RUSSIAN ACADEMY OF SCIENCES

INSTITUTE FOR PROBLEMS IN MECHANICAL ENGINEERING

Proceedings of the XLIII Summer School – Conference

ADVANCED PROBLEMS IN MECHANICS

A P M 2 0 1 5

St. Petersburg
June 22 – July 27, 2015

http://apm-conf.spb.ru

St. Petersburg, 2015

General Information Scientific Committee and Editorial Board

- **D. A. Indeitsev** (IPME RAS, St. Petersburg, Russia) — *Co-Chairman*
- **A. M. Krivtsov** (St. Petersburg State Polytechnical University, IPME RAS, Russia) — *Co-Chairman*
- **I. E. Berinskii** (IPME RAS, St. Petersburg State Polytechnical University, Russia) — *Scientific Secretary*
- **O. S. Loboda** (St. Petersburg State Polytechnical University, IPME RAS, Russia) — *Scientific Secretary*
- **H. Altenbach** (Martin-Luter University Halle Wittenberg, Otto-von-Guericke-University Magdeburg, Germany)
- **A. K. Belyaev** (IPME RAS, St. Petersburg, Russia)
- **I. I. Blekhman** (IPME RAS, Mekhanobr-tekhnika Corp., St. Petersburg, Russia)
- **F. M. Borodich** (Cardiff University, UK)
- **M. Cartmell** (University of Glasgow, UK)
- **A. Castellanos** (University of Seville, Spain)
- **A. V. Cherkaev** (University of Utah, USA)
- **V. A. Eremeyev** (Southern Scientific Center of RAS, Rostov State University, Rostov-on-Don, Russia)
- **A. B. Freidin** (IPME RAS, St. Petersburg, Russia)
- **S. N. Gavrilov** (IPME RAS, St. Petersburg, Russia)
- **S. F. Golovashchenko** (Ford Motor Company, USA)
- **I. G. Goryacheva** (Institute for Problems in Mechanics RAS, Moscow, Russia)
- **E. F. Grekova** (IPME RAS, St. Petersburg, Russia)
- **N. Gupta** (Indian Institute of Technology Delhi, India)
- **D. Harris** (University of Manchester, UK)
- **H. Irschik** (Johannes Kepler University of Linz, Austria)
- **B. L. Karihaloo** (Institute of Theoretical, Applied and Computational Mechanics, UK)
- **A. M. Linkov** (Rzeszow University of Technology, Poland)
- **E. V. Lomakin** (Moscow State University, Russia)
- **A. V. Manzhirov** (Institute for Problems in Mechanics RAS, Moscow, Russia)
- **G. Maugin** (Universite Pierre et Marie Curie, France)
- **A. Metrikine** (TU Delft, The Netherlands)
- **G. Mishuris** (Aberystwyth University, UK)
- **N. F. Morozov** (St. Petersburg State University, IPME RAS, Russia)
- **V. A. Palmov** (St. Petersburg State Polytechnical University, Russia)
- **E. Pavlovskaia** (University of Aberdeen, UK)
- **Y. V. Petrov** (St. Petersburg State University, IPME RAS, Saint-Petersburg, Russia)
- **D. Y. Raychuk** (St. Petersburg State Polytechnical University)
- **M. B. Rubin** (Technion, Faculty of Mechanical Engineering, Haifa, Israel)
- **A. I. Rudskoy** (St. Petersburg State Polytechnical University)
- **S. H. Sargsyan** (National Academy of Sciences, Armenia)
- **E. N. Vilchevskaya** (St. Petersburg State Polytechnical University, IPME RAS, Russia)
- **J. Wang** (Peking University, China)
- **M. Wiercigroch** (University of Aberdeen, UK)
- **M. V. Zakrzhevsky** (Institute of Mechanics Riga Technical University, Latvia)

Preface

Dear Reader,

in this book you will find the Proceedings of the Summer School ĮI Conference "Advanced Problems in Mechanics (APM) 2015". The conference had been started in 1971. The first Summer School was organized by Prof. Ya.G. Panovko and his colleagues. In the early years the main focus of the School was on nonlinear oscillations of mechanical systems with a finite number of degrees of freedom. Since 1994 the Institute for Problems in Mechanical Engineering of the Russian Academy of Sciences organizes the Summer School. The traditional name of "Summer School" has been kept, but the topics covered by the School have been much widened, and the School has been transformed into an international conference. Now it is held under the patronage of the Russian Academy of Sciences. The topics of the conference cover now almost all fields of mechanics, being concentrated around the following main scientific directions:

— aerospace mechanics;
— computational mechanics;
— dynamics of rigid bodies and multibody dynamics;
— fluid and gas;
— mechanical and civil engineering applications;
— mechanics of media with microstructure;
— mechanics of granular media;
— nanomechanics;
— nonlinear dynamics, chaos and vibration;
— molecular and particle dynamics;
— phase transitions;
— solids and structures;
— wave motion.

The Summer School – Conference has two main purposes: to gather specialists from different branches of mechanics to provide a platform for cross-fertilization of ideas, and to give the young scientists a possibility to learn from their colleagues and to present their work. Thus the Scientific Committee encouraged the participation of young researchers, and did its best to gather at the conference leading scientists belonging to various scientific schools of the world.

We believe that the significance of Mechanics as of fundamental and applied science should much increase in the eyes of the world scientific community, and we hope that APM conference makes its contribution into this process.

We are happy to express our sincere gratitude for a partial financial support to Russian Foundation for Basic Research, Russian Academy of Sciences, and St. Petersburg Scientific Center. This support has helped substantially to organize the conference and to increase the participation of young researchers.

We hope that you will find the materials of the conference interesting, and we cordially invite you to participate in the coming APM conferences. You may find the information on the future "Advanced Problems in Mechanics" Schools-Conferences at our website:

`http://apm-conf.spb.ru`

With kind regards,

Co-Chairmen of APM 2015

Dmitri A. Indeitsev, Anton M. Krivtsov

Contents

Numerical investigation of thin films with strain gradient elasticity

B. Emek Abali, Wolfgang H. Müller, Victor A. Eremeyev
abali@tu-berlin.de

Abstract

Thin films are applied in Micro-Electro-Mechanical Systems (MEMS). The mechanical response of thin films on the micrometer length scale is different from their response on the macroscale. In order to model this phenomenon we propose to apply the so-called *strain gradient elasticity*. There are various versions of strain gradient theory available in the literature. After a brief review of our version, we use finite element and finite difference methods for computing the deformation state of thin films by using strain gradient elasticity. Moreover, we perform a numerical study of Cu films of different thicknesses and observe qualitatively the same phenomena as in experiments.

1 Introduction

The miniaturization of electro-mechanical systems requires producing and the use of geometries on the microscale. Nowadays, thin films applied in Micro-Electro-Mechanical Systems (MEMS) are even smaller than 1 µm. As a material for such thin films copper (Cu) is often used due to its high conductance and specific strength. The behavior of Cu on the macroscale can be modeled accurately by using the theory of elasticity. Interestingly, the mechanical response of Cu changes on the micrometer length scale. Especially for Cu thin films this phenomenon has been observed experimentally, see for example Gruber et al. [4] and Wang et al. [11]. Such a change of the mechanical behavior is referred to as (elastic) *size effect*. The ordinary theory of elasticity fails during its characterization, consequently, it needs to be extended. In order to calculate the mechanical behavior of thin films we propose to use the so-called strain gradient elasticity instead. There have been various variants of strain gradient elasticity. For an overview see Gurtin et al. [5, §90]. We give a brief outline of our version based on rational continuum mechanics and then perform a numerical study of Cu thin films.

First, we start with the balance equations of linear and angular momenta. Their flux terms are known to be the stress tensor and the couple stress tensor for a non-polar medium, such as Cu. Second, we apply a suitable method to obtain the necessary constitutive equations for the stress and couple stress tensors. By closing the balance equations with suitable constitutive equations we obtain the field equations. Third, we employ a variational formulation for generating a weak form of the field equations. This weak form can be evaluated computationally by using numerical solution techniques. We use the finite element method

for space discretization and the finite difference method for time discretization, and then solve the weak form by using open-source packages developed under the FEniCS project, see Logg et al. [7]. Thin films made of Cu are simulated with our version of strain gradient elasticity. We perform a numerical study of different thicknesses, and observe qualitatively the same deformation phenomenon as in real experiments.

2 Governing equations

Throughout the paper we use the standard nomenclature of continuum mechanics including the summation convention for repeated indices. We consider a continuum body, $\mathcal{B}_0$, consisting of massive particles at *known* original positions X_i, expressed in Cartesian coordinates. In a material frame the particles are identified by their original positions X_i. As a consequence of (mechanical) loading the body deforms to $\mathcal{B}$ at the present time t and the particles move to $x_i = x_i(X_j, t)$. The objective of continuum mechanics is to calculate this deformation by determining the displacement of each particle:

$$u_i = u_i(X_j, t) = x_i - X_i \ . \tag{1}$$

In the theory of elasticity this is achieved by satisfying the balance of linear momentum. In strain gradient elasticity we need to fulfill also the balance of angular momentum. Both balances of momenta transformed onto the initial frame, $\mathcal{B}_0$, read

$$\begin{aligned} \rho_0 \frac{\partial v_i}{\partial t} - \frac{\partial P_{ji}}{\partial X_j} - \rho_0 f_i = 0 \ , \\ \rho_0 \frac{\partial a_{ik}}{\partial t} - \frac{\partial A_{ijk}}{\partial X_j} - \rho_0 z_{ik} = 0 \ , \end{aligned} \tag{2}$$

where the specific linear momentum (per mass), v_i, and the specific angular momentum, a_{ik}, are the unknowns. The flux terms, P_{ji} and A_{ijk}, will be defined by using constitutive equations. The supply terms, f_i and z_{ik}, are prescribed and known. For a motivation and a derivation of these balance equations from the well-known global balance equations in the current frame we refer to Abali et al. [1]. The specific linear momentum, v_i, is a tensor of rank one. Physically speaking, it is the velocity of the material particles, and given as follows in the initial frame:

$$v_i = \frac{\mathrm{d}x_i(X_j, t)}{\mathrm{d}t} = \frac{\partial x_i(X_j, t)}{\partial t} = \frac{\partial (u_i + X_i)}{\partial t} = \frac{\partial u_i}{\partial t} \ , \tag{3}$$

since the initial positions of particles are constant. The specific angular momentum, a_{ik}, is a tensor of rank two and consists of a spin and a moment of linear momentum. For non-polar materials, such as copper, the spin vanishes and a_{ij} becomes:

$$a_{ik} = X_{[i} v_{k]} = \frac{1}{2}\left(X_i v_k - X_k v_i\right) \ . \tag{4}$$

Hence, in both balances of momenta the displacement field, u_i, occurs, which is the unknown field. After vector multiplication of the balance of linear momentum by the position vector and subsequent substraction from the balance of angular momentum we obtain the balance of spin. It contains a production term. Since the spin vanishes for a non-polar material, its production term has to vanish, too. This restriction requires the Cauchy stress tensor, $\sigma_{ij} = \sigma_{ji}$, *i.e.*, the flux of linear momentum in the current frame, to be

symmetric. The flux of linear momentum in the initial frame is referred to as the first PIOLA-KIRCHHOFF stress tensor:

$$P_{ji} = J(\boldsymbol{F}^{-1})_{jk}\sigma_{ki} \ , \quad J = \det(\boldsymbol{F}) \ , \quad F_{ij} = \frac{\partial x_i}{\partial X_j} \ . \tag{5}$$

Obviously, the first PIOLA-KIRCHHOFF stress fails to be symmetric even in case of a symmetric CAUCHY stress, σ_{ji}. Hence the second PIOLA-KIRCHHOFF is introduced:

$$S_{kj} = P_{ki}(\boldsymbol{F}^{-1})_{ji} \ , \quad S_{kj} = S_{jk} \ . \tag{6}$$

The flux of angular momentum consists of a flux of spin and a moment of flux of linear momentum:

$$A_{ijk} = \mu_{ijk} + X_{[i}P_{jk]} = \mu_{ijk} + \frac{1}{2}\big(X_iP_{jk} - X_kP_{ji}\big) \ . \tag{7}$$

The flux of spin, μ_{ijk}, is also called *couple stress* in the initial frame. We need to find constitutive equations for the stress, S_{ij}, and the couple stress, μ_{ijk}, with respect to the unknowns, *i.e.*, the displacement components, u_i. Then the following two equations lead to the displacement field:

$$\begin{aligned} \rho_0\frac{\partial^2 u_i}{\partial t^2} - \frac{\partial P_{ji}}{\partial X_j} - \rho_0 f_i = 0 \ , \\ \rho_0 X_{[i}\frac{\partial^2 u_{k]}}{\partial t^2} - \frac{\partial \mu_{ijk}}{\partial X_j} - P_{[ik]} - X_{[i}\frac{\partial P_{jk]}}{\partial X_j} - \rho_0 z_{ik} = 0 \ . \end{aligned} \tag{8}$$

The specific supply term for the linear momentum, f_i, is given by the gravitational specific force only, since we neglect electromagnetic interaction in the system. The specific supply term for the angular momentum, z_{ik}, consists of two terms, a specific body force affecting the spin volumetrically, and a moment of the gravitational specific force. Since the material is non-polar the first term is neglected, we have:

$$z_{ik} = X_{[i}f_{k]} = \frac{1}{2}\big(X_if_k - X_kf_i\big) \ . \tag{9}$$

By inserting the latter in Eq. $(8)_2$ we realize that the couple stress has the following symmetry property:

$$\mu_{ijk} = -\mu_{kji} \ . \tag{10}$$

Next, we will define the stress and the couple stress tensors depending on the displacement field. Due to objectivity we need to use the gradient of displacement. In this context we use the GREEN-LAGRANGE strain tensor:

$$E_{ij} = \frac{1}{2}\big(C_{ij} - \delta_{ij}\big) \ , \quad C_{ij} = F_{ki}F_{kj} \ . \tag{11}$$

In the theory of elasticity the stress is given by the strain, which is sufficient to determine the displacements accurately. In strain gradient theory the additional flux term, *i.e.*, the couple stress, is described by the strain gradient, $\partial E_{ij}/\partial X_k$. Theoretically stress may depend on the strain gradient as well as couple stress may depend on the strain. For linear and isotropic materials this is not the case, see dell'Isola et al. [3, §3]. Hence we can define the general *linear* relations for the stress and couple stress as follows

$$S_{ij} = C_{ijkl}E_{kl} \ , \quad \mu_{ijk} = D_{ijklmn}E_{lm,n} \ . \tag{12}$$

The so-called stiffness tensor C_{ijkl} is of rank four and the tensor D_{ijklmn} is of rank six. For isotropic materials the tensorial forms of such material tensors are well-known, see for example Suiker and Chang [10]. Since the strain is symmetric, $E_{ij} = E_{ji}$, we obtain the following stiffness tensor:

$$S_{ij} = \lambda E_{kk}\delta_{ij} + 2\mu E_{ij} \ , \tag{13}$$

where the Lamé parameters are given by the engineering constants, viz., Young's modulus, E, and Poisson's ratio, ν, as follows:

$$\lambda = \frac{E\nu}{(1+\nu)(1-2\nu)} \ , \quad \mu = \frac{E}{2(1+\nu)} \ . \tag{14}$$

Analogously, we obtain the material tensor D_{ijklmn} after using the conditions $E_{ij,k} = E_{ji,k}$ and $\mu_{ijk} = -\mu_{kji}$, such that

$$\mu_{ijk} = \alpha\big(\delta_{ij}E_{km,m} - \delta_{jk}E_{im,m}\big) + \beta\big(\delta_{ij}E_{mm,k} - \delta_{jk}E_{mm,i}\big) + \gamma\big(E_{ij,k} - E_{jk,i}\big) \ . \tag{15}$$

The couple stress possesses three additional material parameters. After measuring E, μ, α, β, γ we can calculate the deformation of thin films. An adequate numerical implementation is presented in the following section.

3 Numerical implementation

The field equations (8) are differential equations in space and time. In order to analyze them numerically we need to discretize the fields and operators in space and time. For discretization in time we use the *finite difference method*:

$$\frac{\partial u_i}{\partial t} = \frac{u_i - u_i^0}{\Delta t} \ , \quad \Delta t = t^{(k+1)} - t^{(k)} \ , \tag{16}$$

This implicit method is stable for real valued problems. For the space discretization we employ the Galerkin-type *finite element method*, where the test functions, δu_i, are chosen from the same Sobolev space as the unknowns, u_i. We use continuous second order elements belonging to

$$\begin{aligned} \mathcal{V} &= \{u_i \in [\mathcal{H}^2(\Omega)]^3 : u_i\big|_{\partial\Omega} = \text{given}\} \ , \\ \hat{\mathcal{V}} &= \{\delta u_i \in [\mathcal{H}^2(\Omega)]^3 : \delta u_i\big|_{\partial\Omega} = \text{given}\} \end{aligned} \tag{17}$$

for the three dimensional domain $\Omega \in \mathbb{R}^3$ and its boundaries $\partial\Omega$. The weak form is obtained by multiplying the field equations with appropriate test functions and then applying integration by parts:

$$\begin{aligned} \mathrm{F} = \sum_{\text{elements}} \int_{\Omega^e} \Big(& \rho_0 \frac{u_i - 2u_i^0 + u_i^{00}}{\Delta t \Delta t}\delta u_i + P_{ji}\delta u_{i,j} - \rho_0 f_i \delta u_i + \\ & + \rho_0 X_{[i}\frac{u_{k]} - 2u_{k]}^0 + u_{k]}^{00}}{\mathrm{d}t\,\mathrm{d}t}\delta u_{k,i} + \mu_{ijk}\delta u_{k,ij} - P_{[ik]}\delta u_{k,i} - X_{[i}P_{jk],j}\delta u_{k,i} - \\ & - \rho_0 l_{ik}\delta u_{k,i} - X_{[i}f_{k]}\delta u_{k,i}\Big)\,\mathrm{d}V - \int_{\partial\Omega}\big(P_{jk}\delta u_k + \mu_{ijk}\delta u_{k,i}\big)N_j\,\mathrm{d}A \ . \end{aligned} \tag{18}$$

This weak form is implemented in Python by using open-source packages developed by the FEniCS project, Logg et al. [7]. Since the weak form is nonlinear, it is linearized by a fully automatized symbolic derivative at the level of partial differential equations, see Alnaes and Mardal [2]. All 2D-plots were created by using the MatpPlotLib packages, see Hunter [6], under NumPy, see Oliphant [9].

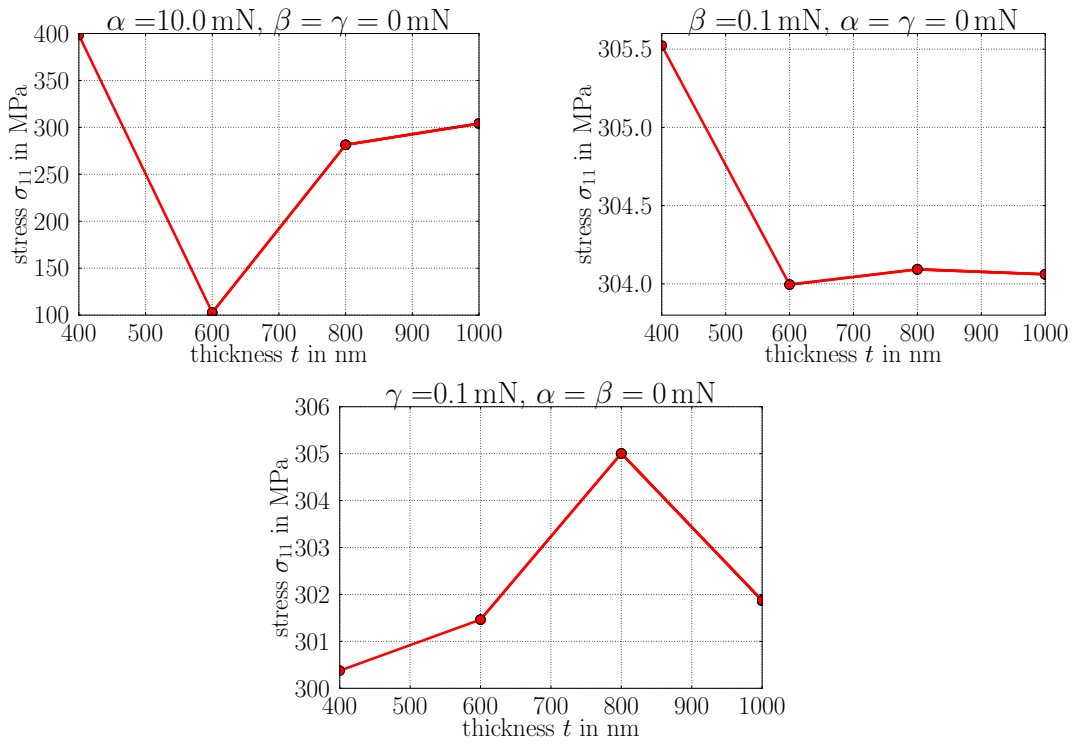

Figure 1: Variation of thickness of thin film out of Cu-HCP. The ordinate refers to the normal stress value at 0.2% of tensile strain.

4 Results and conclusion

The deformation behavior of thin films has been analyzed. We consider a plate with dimensions $10 \times 10 \times 1$ length units on the microscale. By varying the length unit, the length to thickness ratio is kept constant. The geometry remains the same, whereas the geometric scale is changing. In order to perform a somewhat realistic simulation we use the properties of High Conductivity Phosphorus Deoxidized Copper (CU-HCP). The material is modeled as isotropic with Young's modulus taken as $E = 139.9\,\mathrm{GPa}$ at room temperature, see Müller et al. [8]. We assume Poisson's ratio to be $\nu = 0.3$ and take the mass density as $\rho_0 = 8960\,\mathrm{g/\mu m^3}$. The plate is subjected to tensile test conditions: On one end it is clamped by setting the displacements equal to zero. On the other end it is stretched by setting the displacement analogously to a position controlled in tensile testing. For all other boundaries free surface conditions have been implemented, such that the boundary terms vanish. During one "second" the strain is increased linearly up to 0.2% and the stress is computed at that strain. From experiments, see Gruber et al. [4, Fig. 8], we expect approximately 300 MPa of stress at 0.2% of strain. In Fig. 1, at strain $E_{11} = 0.002$ the true stress, namely the Cauchy stress, σ_{11}, is plotted by varying the film thickness. The so-called size effect is obvious. Although the geometric ratios and material parameters remain the same, the behavior alters by varying the thickness. Interestingly this change is not monotonous and seems to be counter-intuitive. We know from the experiments that such a behavior occurs in reality, see Gruber et al. [4, Fig. 9c]. From Gruber et al. [4, Fig. 8] it is known that the material's response up to 0.1% is identical for different thicknesses. In Gruber et al. [4] this discrepancy has been motivated by a possible change in plasticity without any change of the elastic response. However, it is then difficult to

justify the change in the initial yield stress. In this paper we present a simulation with a qualitatively similar response of the material, where the change is explained by our version of strain gradient theory.

We started with a brief outline of the strain gradient theory and its implementation, which are mainly developed in Abali et al. [1]. Additional to the well-known engineering constants three more material parameters were necessary to model a system using strain gradient theory. For simulations of thin films we determined these parameters by free choice and achieved to model the counter-intuitive response of thin films. It is rather challenging to obtain qualitatively accurate results by finding the correct set of parameters.

References

[1] Abali, B. E., Müller, W. H., and Eremeyev, V. A. 2015. Strain gradient elasticity with geometric nonlinearities and its computational evaluation. –submitted–.

[2] Alnaes, M. S. and Mardal, K.-A. 2010. On the efficiency of symbolic computations combined with code generation for finite element methods. ACM Transactions on Mathematical Software, 37(1):6:1–6:26.

[3] dell'Isola, F., Sciarra, G., and Vidoli, S. 2009. Generalized Hooke's law for isotropic second gradient materials. Proceedings of the Royal Society A: Mathematical, Physical and Engineering Science, 465:2177–2196.

[4] Gruber, P. A., Böhm, J., Onuseit, F., Wanner, A., Spolenak, R., and Arzt, E. 2008. Size effects on yield strength and strain hardening for ultra-thin Cu films with and without passivation: A study by synchrotron and bulge test techniques. Acta Materialia, 56(10):2318–2335.

[5] Gurtin, M. E., Fried, E., and Anand, L. 2010. The mechanics and thermodynamics of continua. Cambridge University Press.

[6] Hunter, J. 2007. Matplotlib: A 2d graphics environment. Computing In Science & Engineering, 9(3):90–95.

[7] Logg, A., Mardal, K. A., and Wells, G. N. 2011. Automated solution of differential equations by the finite element method, the FEniCS book, volume 84 of Lecture Notes in Computational Science and Engineering. Springer.

[8] Müller, W. H., Worrack, H., and Zapara, M. 2011. Analysis of nanoindentation experiments by means of atomic force microscopy. PAMM, 11(1):413–414.

[9] Oliphant, T. E. 2007. Python for scientific computing. Computing in Science & Engineering, 9(3):10–20.

[10] Suiker, A. and Chang, C. 2000. Application of higher-order tensor theory for formulating enhanced continuum models. Acta mechanica, 142(1-4):223–234.

[11] Wang, D., Gruber, P. A., Volkert, C. A., and Kraft, O. 2014. Influences of Ta passivation layers on the fatigue behavior of thin Cu films. Materials Science and Engineering: A, 610:33–38.

B. Emek Abali, Technische Universität Berlin, Institute of Mechanics, Einsteinufer 5, D-10587 Berlin, Germany
Wolfgang H. Müller, Technische Universität Berlin, Institute of Mechanics, Einsteinufer 5, D-10587 Berlin, Germany
Victor A. Eremeyev, Otto-von-Guericke-Universität Magdeburg, Institute of Mechanics, Universitätsplatz 2, D-39106 Magdeburg, Germany

Theoretical study of orientation effects during the multi-particle diffuse double layer interaction in monodisperse aqueous zinc oxide nanocolloids

Anton V. Alfimov Elizaveta M. Aryslanova Sergey A. Chivilikhin
alfimov.anton@gmail.com

Abstract

The work presents a theoretical study of the colloid nanoparticle agglomeration with a focus on the morphology of the resulting assemblages. This is achieved by using an original analytical multi-particle interaction model.

It has been shown that the electrosteric repulsion between colloid nanoparticles makes it more energetically favourable to form linear structures; this effect is stronger for particles with higher surface charge. Linear agglomerates, however, turn out to be unstable and subjected to deagglomeration or compaction due to the surface-bound brownian motion of the constituent particles. Therefore the resulting morphology of a nano-agglomerate can be described as the product of a balance between the initial preference for a linear structure formation and further compaction or deagglomeration.

1 Introduction

Nanotechnology is among the fastest growing fields of applied research in the past few decades. An important group of nanomaterials that have found a wide industrial, commercial and scientific application are those based on nanoparticles as their primary structural units. These materials include nanocolloids, aerosols, nanoceramics, etc. and demonstrate a high dependency of bulk material properties on those of the individual nanoparticles [1]. It is important to note that physical and chemical properties of particle-based materials and, therefore, their fate and transport, biological activity and behaviour in the human body are also dependent on the morphology and stability of the particle assemblages [2, 3] in the form of agglomerates and aggregates (terms used in accordance with ISO 14887). Although the agglomeration of nanoparticles has been a subject of extensive studies, only a few works to date have focused their attention on the formation of nano-agglomerate spatial structure [2].

The present work is devoted to the theoretical study of nanoparticle agglomeration in aqueous colloids and is specifically focused on analysing the morphology of forming particle assemblages. Analytical description and analysis of nanoagglomerate structure is achieved by employing a modified version of the original multi-particle colloid interaction model first introduced by the authors in [5]. The model is developed in the framework of the DLVO (Derjaguin, Landau, Verwey, Overbeak) theory that assumes that interparticle interaction

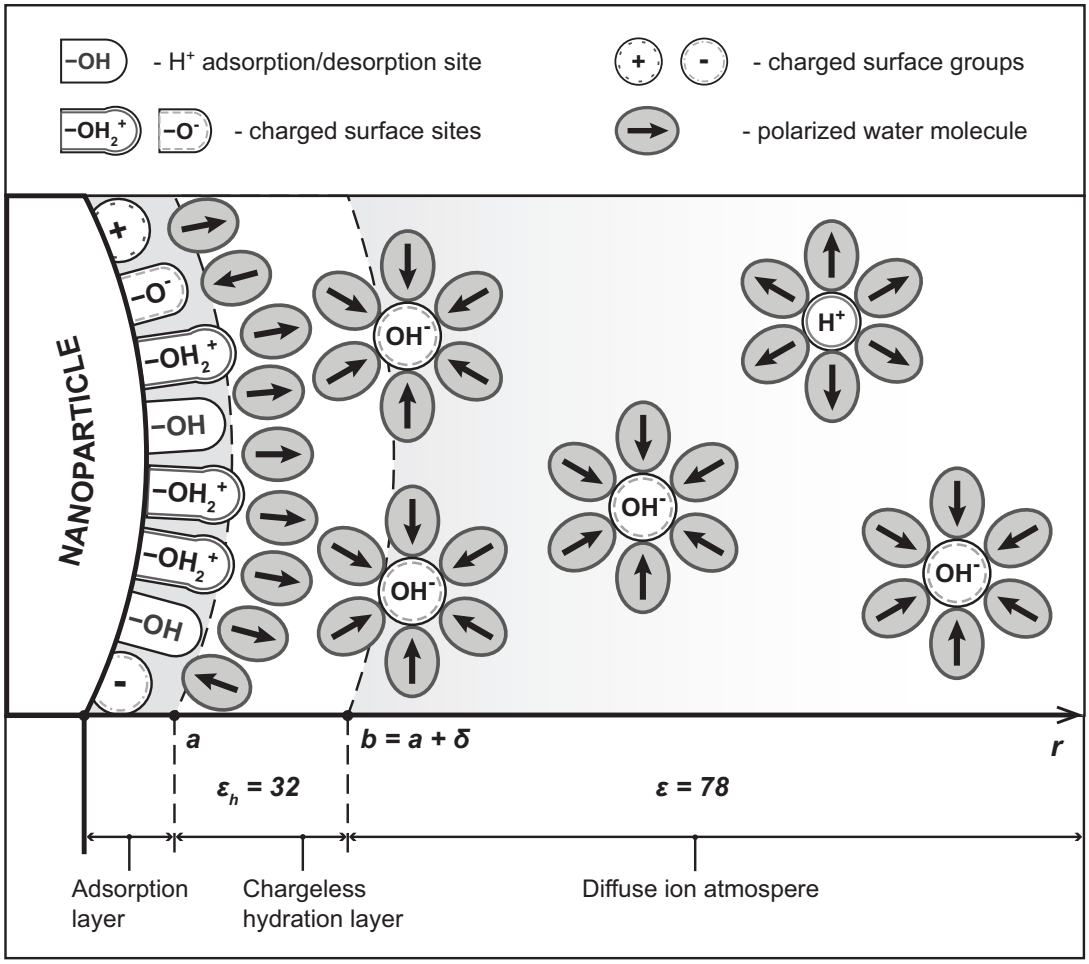

Figure 1: Schematic representation of a colloid ZnO nanoparticle's charged surface and ionic atmosphere.

in colloid solutions is governed by two processes: short-range van der Waals attraction and long-range electroosmotic repulsion due to overlapping electric double-layers (EDL).

2 Methods

2.1 Mathematical model

We consider a spherical nanoparticle suspended in electrolyte solution as a spherically symmetric system with radial coordinate r (see figure 1). The colloid particle obtains surface charge through the processes of adsorption and desorption, which will be discussed in detail later. Thus we assume that the particle and the adsorption layer can be represented as a sphere of the effective radius a and uniform surface charge σ. The charged particle is then subjected to solvation and thus acquires a charge-less hydration shell of roughly two water molecule diameters thickness δ [7]. The layer of polarized H_2O molecules $a < r < b = a + \delta$ (see figure 1) is known to have significantly smaller effective dielectric permittivity in comparison with the bulk water [7]. The hydrated nanoparticle is surrounded by a diffuse ion atmosphere $r > b$ that compensates the particle surface charge. To describe the discussed

EDL structure we therefore have to consider two calculation domains:

$$\begin{array}{ll} \text{I}: & a < r < b, \quad \varepsilon_{\text{I}} = \varepsilon_h \\ \text{II}: & r > b, \qquad \varepsilon_{\text{II}} = \varepsilon \end{array} \tag{1}$$

where the domains I and II correspond to the charge-less gap with the effective dielectric permittivity ε_h and the diffuse layer with the bulk dielectric permittivity ε respectively. The electric potential distribution $\varphi(r)$ in these domains is described by the following Debye-Huckel equation system:

$$\begin{cases} \Delta\varphi_{\text{I}} = 0, & a < r < b \\ \Delta\varphi_{\text{II}} = \kappa^2\varphi_{\text{II}}, & r > b \end{cases} \tag{2}$$

with boundary conditions:

$$\begin{array}{l} \frac{d}{dr}\varphi_{\text{I}}\big|_{r=a} = -\frac{\sigma}{\varepsilon_h\varepsilon_0} \\ \varphi_{\text{I}}(b) = \varphi_{\text{II}}(b) = \varphi_0 \\ \varepsilon_h \frac{d}{dr}\varphi_{\text{I}}\big|_{r=b-} = \varepsilon \frac{d}{dr}\varphi_{\text{II}}\big|_{r=b+} \\ \varphi_{\text{II}}\big|_{r\to\infty} = 0 \end{array} \tag{3}$$

Here κ is the reciprocal of the Debye length:

$$\kappa = \left(\frac{2I}{\varepsilon\varepsilon_0 kT}\right)^{\frac{1}{2}} \tag{4}$$

where $I = \sum_i (z_i)^2 n_i$ - the ionic strength of the solution; i - number of the dissociated solute; z_i - charge number of the ions resulting from the dissociation of the i-th solute; e - elementary charge; ε_0 - dielectric constant; k - Boltzmann constant; T - temperature.
Solving (2) with (3) for the diffuse layer we obtain:

$$\varphi_{II}(r) = \varphi_0 \cdot \frac{b}{r} \cdot \exp\left[-\kappa(r-b)\right] \tag{5}$$

where φ_0 is the zeta-potential:

$$\varphi_0 = \frac{1}{4\pi\varepsilon\varepsilon_0} \cdot \frac{4\pi a^2 \cdot \sigma}{b(1+\kappa b)} \tag{6}$$

The nanoparticle obtains it's surface charge through adsorption and desorption. For amphoteric particles such as ZnO the dominant charging process is competitive protonation and deprotonation of surface $-$OH groups [4, 7], which is demonstrated in figure 1. The corresponding reactions are:

$$\begin{array}{l} -\text{OH} + \text{H}^+ \rightleftarrows -\text{OH}_2^+ \\ -\text{OH} + \text{OH}^- \rightleftarrows -\text{O}^- + \text{H}_2\text{O} \end{array} \tag{7}$$

We assume that all ions in the system except for the H^+ andOH^- are indifferent to the particle surface. Linearisation of the potential-dependent H^+ and OH^- concentrations at

the particle surface in the non-saturated adsorption limit yields a simple expression for the surface charge density σ of a nanoparticle placed in an external electric field:

$$\sigma = \frac{\sigma_0 + e\left[\beta_+ n_{\mathrm{H}}\left(1 - \frac{e\varphi_\Sigma}{kT}\right) - \beta_- n_{\mathrm{OH}}\left(1 + \frac{e\varphi_\Sigma}{kT}\right)\right]}{1 + \frac{e^2[\beta_+ n_{\mathrm{H}} + \beta_- n_{\mathrm{OH}}]}{4\pi\varepsilon\varepsilon_0 \cdot kT}\left[\frac{1}{b(1+\kappa b)} + \frac{b-a}{ab}\right]} \tag{8}$$

where σ_0 - constant portion of the surface charge density due to charged groups that are not involved in any chemical reactions in the considered system; n_{H}, n_{OH} - bulk H^+ and OH^- concentrations in the solution; φ_Σ - local potential of the external electric field; β_+, β_- - model fitting parameters.

Using (6) and the non-saturated charge regulation model (8) we can obtain the expression for the zeta-potential dependency on pH and use for the experimental data fitting and thus obtain the numerical values for the model parameters β_+, β_- (see figure 2). The suggested theoretical approach is suitable for the spherical amphoteric nanoparticles with low surface potential suspended in the aqueous solutions of low ionic strength. Therefore, the zinc oxide nanoparticles were chosen for the modelled system of this work due to their unique semiconductor and chemical properties wide use in customer products.

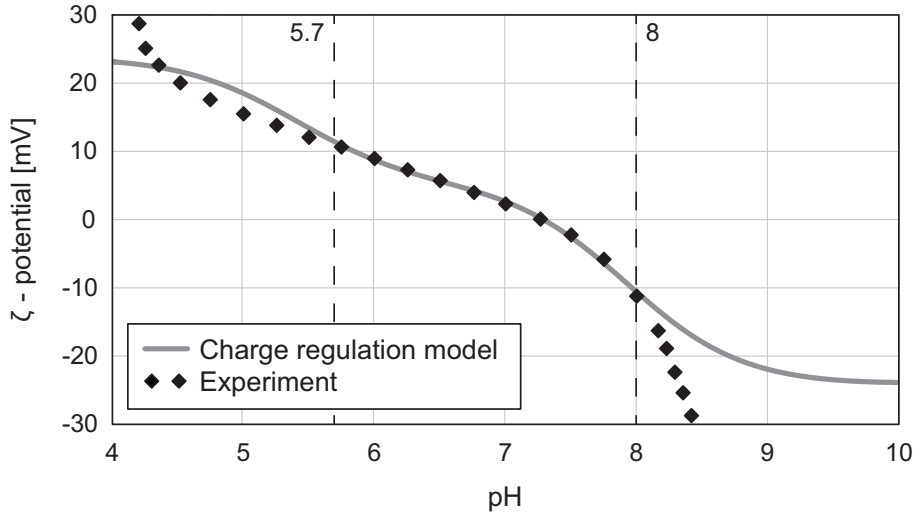

Figure 2: Comparison of the ZnO nanoparticle zeta-potential dependency on pH obtained using the proposed non-saturated charge regulation model (solid line) with the experimental data from [6] (dots). The dashed vertical lines mark the limits of applicability of the model.

Using the monopole approximation, we substitute each particle with its equivalent screened point-charge [8] :

$$Q = 4\pi\varepsilon\varepsilon_0 \cdot \varphi_0 \cdot b\mathrm{e}^{\kappa b} \tag{9}$$

Then the potential energy of a particle number α interacting with multiple other particles can be found as:

$$U_\alpha\left(\{R_{\alpha,\beta}\}\right) = \frac{Q_\alpha}{4\pi\varepsilon\varepsilon_0} \cdot \sum_{\beta\neq\alpha}\left[Q_\beta \cdot \frac{\exp\left(-\kappa R_{\alpha,\beta}\right)}{R_{\alpha,\beta}}\right] + \sum_{\beta\neq\alpha}\left[U_{vdW}\left(R_{\alpha,\beta}\right)\right] \tag{10}$$

where α, β - particle numbers; $R_{\alpha,\beta}$ - centre-to-centre separation between particles α and β; the equivalent charges Q_α can be found from the linear algebraic equation system:

$$Q_\alpha + \sum_{\beta\neq\alpha}\theta_{\alpha,\beta} \cdot Q_\beta = Q_{\mathrm{ISO}} \tag{11}$$

here Q_{ISO} - the equivalent charge of an isolated particle; the matrix coefficients are:

$$\theta_{\alpha,\beta} = \frac{1}{4\pi\varepsilon\varepsilon_0} \cdot \frac{e^2}{kT} \cdot \frac{1}{R_{\alpha,\beta}(1+\kappa b)} \cdot \frac{(\beta_+ n_{\mathrm{H}} + \beta_- n_{\mathrm{OH}}) \cdot \exp\left[-\kappa\left(R_{\alpha,\beta} - b\right)\right]}{1 + \frac{e^2[\beta_+ n_{\mathrm{H}} + \beta_- n_{\mathrm{OH}}]}{4\pi\varepsilon\varepsilon_0 \cdot kT}\left[\frac{1}{b(1+\kappa b)} + \frac{b-a}{ab}\right]} \tag{12}$$

The van der Waals attraction energy in (10) is given by [7]:

$$U_{vdW}(R) = -\frac{A}{6}\left[\frac{2a^2}{R^2-4a^2} + \frac{2a^2}{R^2} + \ln\left(\frac{R^2-4a^2}{R^2}\right)\right] \tag{13}$$

where A - the effective Hamaker constant for the particle interaction through an intervening medium.
Thus we have obtained the expression (10) for the multi-particle colloid interaction potential energy for arbitrary particle positions using the non-saturated charge regulation model (8).

2.2 Model validation

The derived expression for the inter-particle interaction energy allows us to study the potential barrier arising when a nanoparticle is approaching a certain agglomerate configuration. Assuming that the nanoparticle velocity distribution during its Brownian motion approaches the Maxwellian one for times much longer than the duration of a single molecule collision [5], we can calculate the probability of nanoparticle possessing enough kinetic energy overcome the given potential barrier. The corresponding probability function for the particle having the kinetic energy E greater than the potential barrier energy E_b is depicted on figure 3.

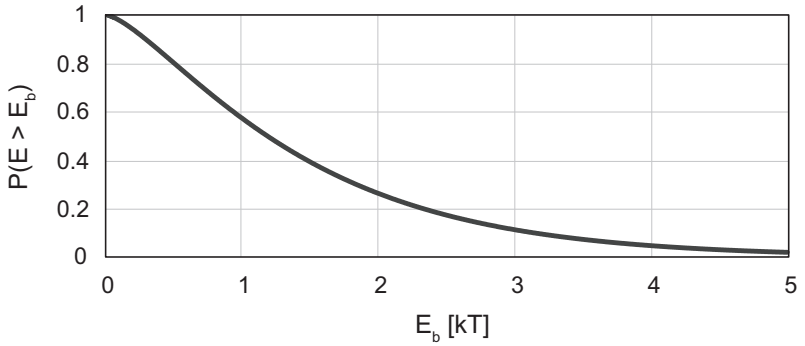

Figure 3: Probability of nanoparticle having the kinetic energy E greater than the potential barrier energy as a function of its value E_b.

For the case of a nanoparticle approaching an agglomerate the proposed model predicts a limited growth of the potential barrier with the increase of the agglomerate's size. After a certain agglomerate size the potential barrier for attachment reaches a plateau and ceases to grow due to the charge redistribution between the particles. The corresponding attachment probability dependency on the agglomerate size is illustrated on figure 4. As shown in the figure, the traditional linear superposition approximation [8] that does not account for the charge regulation predicts the termination of agglomeration for assemblages of more than 13 particles, which significantly contradicts the experiment data (see the inset on figure 4) [6]. On the contrary, the proposed model predicts a limited decrease of the attachment probability reaching a constant high value for the agglomerates of more than 13 constituent particles demonstrating a good qualitative agreement with the experiment.

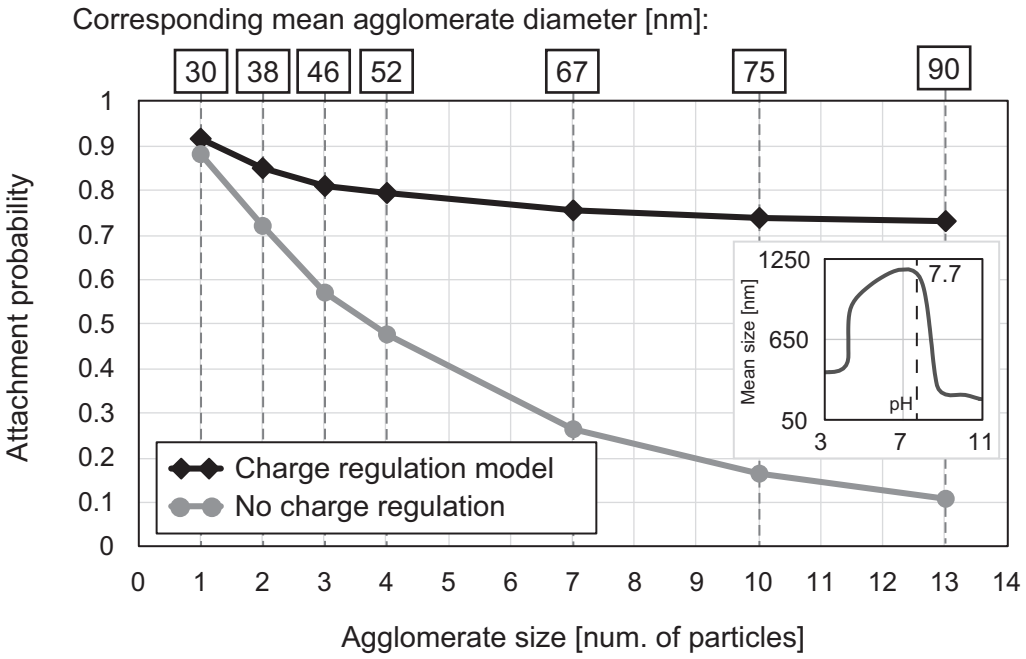

Figure 4: Probability of nanoparticle attachment to an agglomerate as a function of the agglomerate's size (expressed as a number of constituents particles) obtained with and without the charge regulation model for pH = 7.7; the inset illustrates the experimental pH dependency of the mean agglomerate size taken from [6].

3 Results and discussion

The presented multi-particle interaction model was used to study the attachment of a nanoparticle to a certain set of 2-, 3-, 4- and 5-particle agglomerate configurations. To analyse the possible resulting agglomerate morphologies and identify the most energetically favourable of them we have studied the dependency of the interaction potential energy on the location of nanoparticle attachment site on the agglomerate. The resulting potential energy contour plots for the selected agglomerate orientations are depicted in figure 5. The figure shows that the potential barrier due to electroosmotic repulsion is anisotropic with respect to the direction of particle's approach: attachment to a site with more particles in contact results in higher barrier.

The observed electroosmotic orientation effects during agglomeration are further illustrated in figure 6 which demonstrates the dependency of the attachment probability on the direction of the nanoparticle approach for different solution pH values. According to figure 2 pH values that are further away from the neutral pH result in higher particle surface charge and, therefore, the increasing role of electroosmotic repulsion in particle interactions. This explains the corresponding increase of the attachment probability anisotropy for the approach directions found in figure 6.

It is thus shown that with the increase of the nanoparticle surface charge it becomes more and more energetically favourable to initially form linear structures. Figure 6 also shows that for linear agglomerates the attachment of each next particle in a continuation of the linear structure becomes more and more plausible.

The fate of the agglomerate after its initial formation is studied in figure 7. This figure depicts the dependency of the potential well depth on the attachment site location on the agglomerate represented through the angular coordinate. As it should be expected,

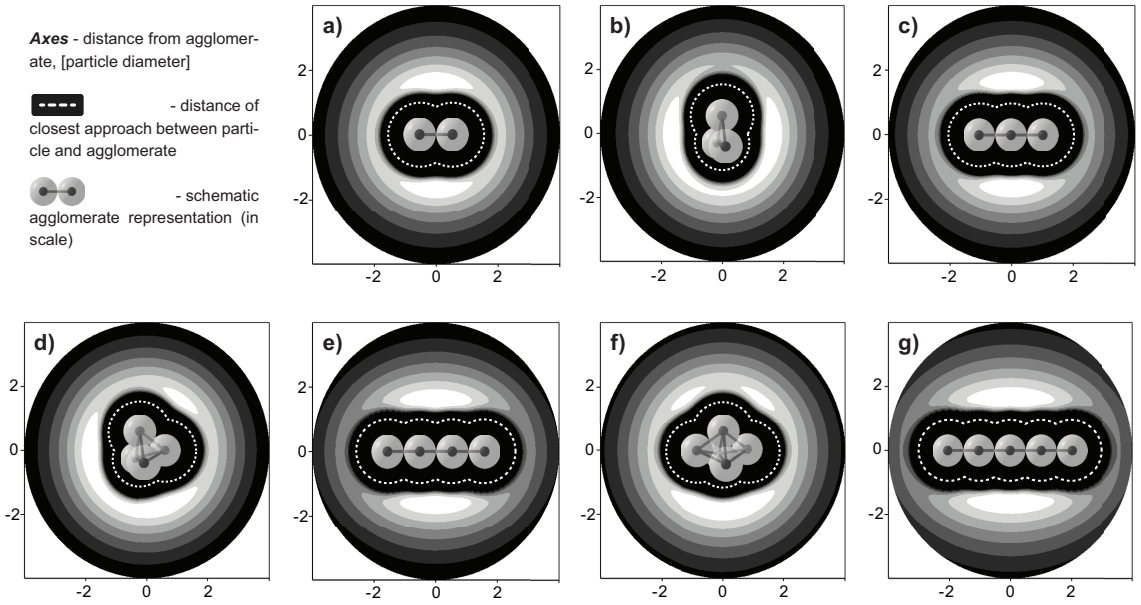

Figure 5: Contour plots of the interaction potential energy between a single mobile nanoparticle and a fixed agglomerate configuration; brighter areas correspond to higher values of the potential energy. The nanoparticle is moving in a plane with a selected orientation relative to the agglomerate. The considered agglomerate configurations are: a) 2-particle agglomerate; b) compact 3-particle agglomerate; c) linear 3-particle agglomerate; d) compact 4-particle agglomerate; e) linear 4-particle agglomerate; f) compact 5-particle agglomerate; g) linear 5-particle agglomerate.

the figure shows that the deepest potential wells correspond to the attachment sites in the closest contact with as many particles as possible. But the most important result is the fact that the van der Waals potential well corresponding to the most favourable sites are highly localised. Away from such positions the potential energy holds constant, which means that the van der Waals attraction will not cause the force on the attached particle unless it is in a very close proximity with the favourable site.

Another notable result in figure 7 is the depths of the potential well corresponding to different attachment sites. Namely, the most energetically favourable from the long-range electroosmotic repulsion point of view sites in contact with only one particle are associated with the potential well of $3kT$. According to figure 3 a particle can escape such a well due to solvent molecules collisions. Potential wells for the sites in contact with two and more particles are deep enough to be considered a permanent attachment.

Therefore, attachment sites with a single particle in contact, which were shown as the most energetically favourable from the electroosmotic repulsion point of view, are unstable due to the surface-bound brownian motion of the attached nanoparticle. The said chaotic motion can either cause the detachment of the particle, or position it near one of the more favourable van der Waals sites and cause the agglomerate compaction.

As a result, according to the proposed model the predominant type of agglomerates in the system with high nanoparticle surface charge will be determined by the balance between the initial linear structure formation and their further gradual deagglomeration or compaction due to the surface-bound brownian motion of the constituent particles and the close-range van der Waals repulsion. The model also predicts the decrease of linear agglomerate fraction in the systems with smaller particle surface charges.

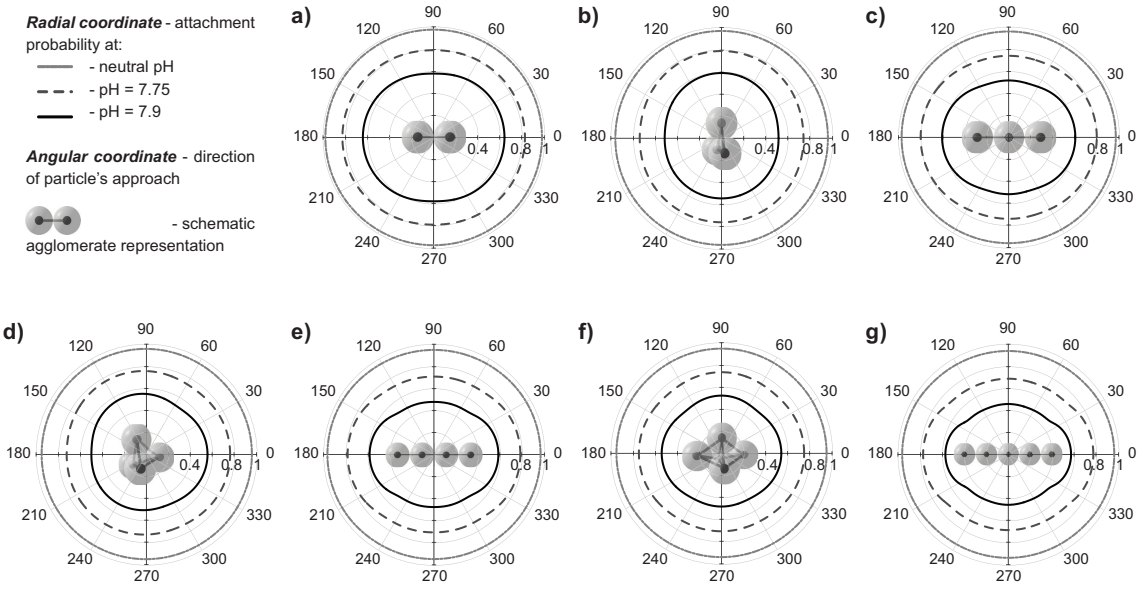

Figure 6: Probability of a nanoparticle attaching to an agglomerate of a specific morphology as a function of the particle's approach direction. The nanoparticle is moving in a plane with a selected orientation relative to the agglomerate. The considered agglomerate configurations are: a) 2-particle agglomerate; b) compact 3-particle agglomerate; c) linear 3-particle agglomerate; d) compact 4-particle agglomerate; e) linear 4-particle agglomerate; f) compact 5-particle agglomerate; g) linear 5-particle agglomerate.

References

[1] E.M. Hotze, T.Phenrat, G.V. Lowry Nanoparticle Aggregation: Challenges to Understanding Transport and Reactivity in the Environment. J. Environ. Qual., 2010 39, p. 1909.

[2] I. Chowdhury, S.L. Walkerb, S.E. Mylon Aggregate morphology of nano-TiO2: role of primary particle size, solution chemistry, and organic matter. Environ. Sci.: Processes Impacts, 2013, 15, p. 275.

[3] M.D. Camejo, D.R. Espeso, L.L. Bonilla Influence of primary particle density in the morphology of agglomerates. Physical Review E, 2014, 90 (01), p. 1.

[4] M. Barisik, S. Atalay, A. Beskok, and S. Qian Size Dependent Surface Charge Properties of Silica Nanoparticles. J. Phys. Chem. C, 2014, 118 (4), p. 1836.

[5] A.V. Alfimov, E.M. Aryslanova, S.A. Chivilikhin An analytical method for determining the interaction energy between multiple identical spherical colloidal zinc oxide nanoparticles. Journal of Physics: Conference Series, 2014, 541 (1), p. 012063.

[6] J.M. Berg, A. Romoser, N. Banerjee, R. Zebda, C.M. Sayes. The relationship between pH and zeta potential of 30 nm metal oxide nanoparticle suspensions relevant to in vitro toxicological evaluations. Nanotoxicology. 3(4). 2009. p. 276.

[7] K.S. Birdi. Handbook of Surface and Colloid Chemistry, Third Edition. CRC Press. 2008. 756 p.

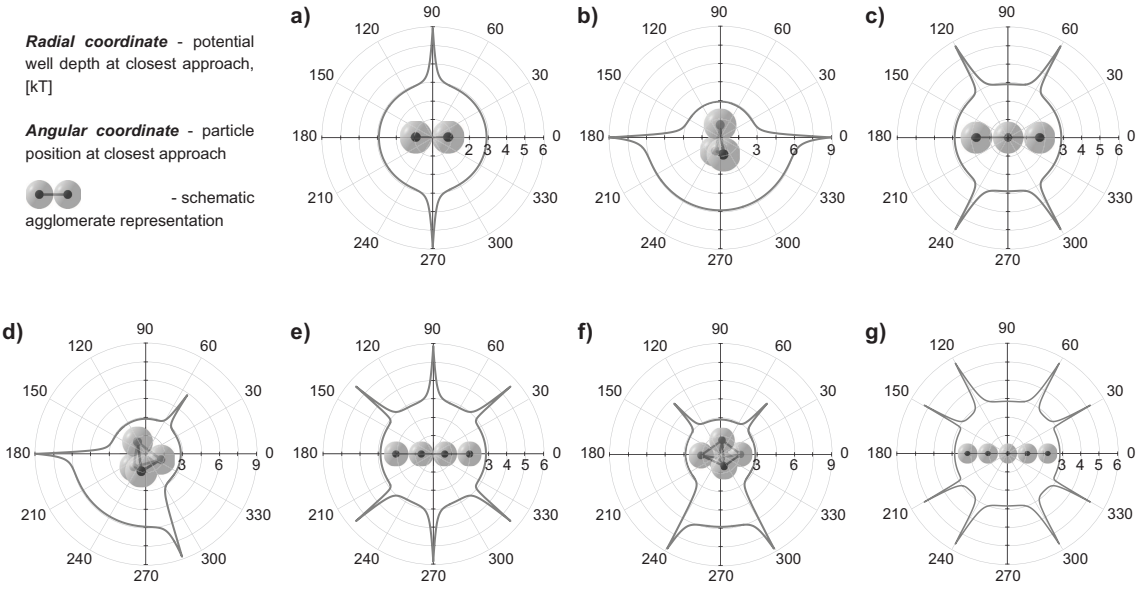

Figure 7: Potential well depth for the nanoparticle attached to the agglomerate of a specific morphology as a function of the attachment site position. The attachment sites lying in a plane with a selected orientation relative to the agglomerate are considered. The agglomerate configurations are: a) 2-particle agglomerate; b) compact 3-particle agglomerate; c) linear 3-particle agglomerate; d) compact 4-particle agglomerate; e) linear 4-particle agglomerate; f) compact 5-particle agglomerate; g) linear 5-particle agglomerate.

[8] H. Ohshima. Effective Surface Potential and Double-Layer Interaction of Colloidal Particles. Journal of Colloid and Interface Science, Volume 174, Issue 1, 1 September 1995, p. 45.

[9] W. Zhang, J. Crittenden, K. Li, Y. Chen. Attachment Efficiency of Nanoparticle Aggregation in Aqueous Dispersions: Modeling and Experimental Validation. Environ. Sci. Technol. 4. 2012. p. 7054.

Anton V. Alfimov, Department of Photonics and Optical Information Technology, ITMO University, St. Petersburg, Russian Federation
Elizaveta M. Aryslanova, Department of Photonics and Optical Information Technology, ITMO University, St. Petersburg, Russian Federation
Sergey A. Chivilikhin, Department of Photonics and Optical Information Technology, ITMO University, St. Petersburg, Russian Federation

Damage and long-term strength criterion of elastic-viscous aging media

Alexander R. Arutyunyan
Robert.Arutyunyan@paloma.spbu.ru

Abstract

The problem of creep, damage and long-term strength of compressible elastic-viscous aging media is considered. The modified Maxwell equation expressed in scale of effective time is used. The parameter of continuity is defined by a value of relative changes of density, which is an integral measure of structure micro defects stored during long-term loading. It is assumed that the rate of brittle fracture depends on stress and the value of stored damage. Taking into account the noted positions the analytical relations for parameter of continuity and long-term strength criteria are derived. The corresponding theoretical curves are plotted.

Financial support of the Russian Foundation for Basic Research (Grant N 14-01-00823) is gratefully acknowledged.

The problem of creep and long-term strength of polymer and composite materials with viscous and brittle mechanical characteristics are discussed. The most polymer (thermosetting plastics, polystyrene, polyacrylates, polyvinyl chloride and other) and composites, based on polymer matrix, fractured when the value of residual deformation is small. During the long-term action of mechanical stresses and temperatures the interrelated processes of deformation and damage occur. Thus the damage parameter has certain physical meaning and is associated with destructive processes, which are consisting of thermal and mechanical stages. In the case of brittle composite materials the damage is defined by degradation processes: loosing of continuity in contact zone fiber-matrix, fracture of fibers in defective volumes, the formation of cracks or voids in the matrix and other. These processes are accompanied by changes of structure and properties as a result of chemical reactions.

In mechanics of scattered damage and brittle fracture the concept of continuity (Kachanov [1]) and damage (Rabotnov [2]) is considered. Following Kachanov, let's introduce the parameter of continuity ψ ($1 \geq \psi \geq 0$), which is defined as a relative volume changes (loosening on the Novozhilov terminology [3]) or density $\psi = \rho/\rho_0$ (where ρ_0 is initial, ρ is current density) [4]. So this parameter is an integral measure of structure micro defects stored during long-term loading. In the world scientific literature there are numerous experimental investigations of the evolution of parameter ψ during creep of metals and composite materials [5-11]. In initial condition $t = 0$, $\rho = \rho_0$, $\psi = 1$ and in fracture moment $t = t_f$, $\rho = 0$, $\psi = 0$.

Since the real materials have random structure, so continuity parameter is a statistical characteristic, which can be defined by some kinetic equation. Form of kinetic equation is determined according the experimental results on long-term strength. In the common

case these equations are based on two hypotheses, which were formulated in [12, 13]. In according to the first hypothesis the rate of brittle fracture depends only on stress $\sigma(t)$

$$\frac{d\psi}{dt} = -f\left[\sigma(t)\right]. \tag{1}$$

In according to the second hypothesis and the conception of statistical physics the rate of brittle fracture depends on stress and the value of stored damage

$$\frac{d\psi}{dt} = -f\left[\sigma(t), \psi\right]. \tag{2}$$

In the equations (1)-(2) $\sigma(t)$ is stress, depending on time. In the creep case on condition $\sigma(t) = \sigma_0 = const$, $1 \geq \psi \geq 0$, $0 \leq t \leq t_f$ from the solution of equations (1), (2) we can obtain the criteria of long-term strength

$$t_f = -1/f(\sigma_0), \tag{3}$$

$$t_f = -\int_t^0 \frac{d\psi}{f(\sigma_0, \psi)}. \tag{4}$$

When formulating the long-term strength criterion in form of relations (1), (2) the condition of a constant stress during creep is accepted. In this regard can be mentioned that the creep experiments are conducted when the applied value of load P is constant. Dropping from time to time the load we can achieve the condition of constant stress. However, the practical realization of this condition is not quite workable. The change of cross section of specimen because of formation of pores and cracks and, accordingly, a correct estimate of the value of true stress is not quite possible.

Let's consider the problem of tensile specimen made of elastic viscous aging material under the action of constant load P. As a rheological equation we will use the modified Maxwell equation, expressed in the scale of effective time [4]

$$\begin{array}{l} \frac{d\varepsilon}{d\omega} = \frac{1}{E}\frac{d\sigma}{d\omega} + \frac{\sigma}{\eta}, \\ d\omega = f_1(\omega, \varepsilon, T, t)dt + f_2(\omega, \varepsilon, T, t)d\varepsilon, \end{array} \tag{5}$$

where ε is strain, T is temperature, t is time, E is the modulus of elasticity, η is coefficient of viscosity.

Parameter ω is considered as a effective time, using which it is possible to describe the deformation aging processes and aging after temper. According to equation (5) during instant active loadings this parameter corresponds to a deformation time ε. In a state of unloading and stabilization the parameter ω describes the kinetics of chemical processes of aging and reduces to a real time t. In the calculation on formula (5) the parameter of effective time is defined by the following relation [14]

$$d\omega = ae^{kt}dt + bd\varepsilon, \tag{6}$$

where a, b, k are constants.

To determine the long-term strength in addition to equations (5)-(6) the relation for a parameter of continuity is considered in the form of a power law [15]

$$\frac{d\psi}{dt} = -\mathrm{A}\sigma^{\mathrm{n}} = -\mathrm{A}\sigma_0^n\psi^n e^{n\varepsilon}, \tag{7}$$

where A, n are constants.

The equation (7) is expressed in a true stress (taking into account the mass conservation law $\rho_0 l_0 F_0 = \rho l F$ we have $\sigma = P/F = \sigma_0 F_0/F = \sigma_0 \psi e^{\varepsilon}$, $\sigma_0 = P/F_0$, $\varepsilon = \ln(l/l_0)$, l_0, F_0 are initial and l, F are current length and cross-section area of specimen, σ is true, σ_0 is engineering stress).
Analytical solutions of interrelated equations (5), (6), (7) are possible in the case of some reasonable consumptions. The equation (1) is solved without account of damage processes. Using the conditions $t = 0$, $\varepsilon = 0$, $\sigma = \sigma_0 = const$, the solution of equation (5), taking into account (6), is written in the form

$$\varepsilon = \frac{\sigma}{E}\left[1 + \frac{a(e^{kt} - 1)}{k\tau\left(1 - \frac{\sigma b}{E\tau}\right)}\right], \tag{8}$$

where $\tau = \eta/E$ is relaxation time.
Introducing the relation (8) into equation (7) and solving it in initial condition $t = 0$, $\psi = 1$, we will obtain

$$\psi = \left\{1 + \frac{A\sigma_0^{n+1} an(1-n)}{E^2\tau\left(1 - \frac{\sigma_0 b}{E\tau}\right)}\left[e^{\frac{n\sigma_0}{E}} - e^{kt}e^{\frac{n\sigma_0}{E}}\left[1 + \frac{a}{E\tau k\left(1 - \frac{\sigma_0 b}{E\tau}\right)}\left(e^{kt} - 1\right)\right]\right]\right\}^{\frac{1}{1-n}}. \tag{9}$$

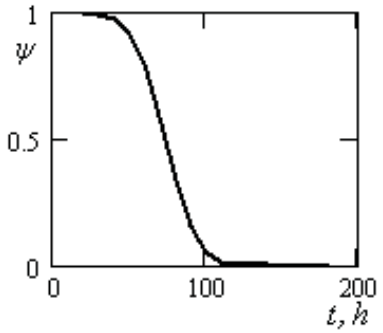

Figure 1: Curve of continuity parameter ψ according formula (9).

Curve of continuity parameter ψ according formula (9) is shown on Fig. 1.
Taking the condition of fracture $t = t_f$, $\psi = \psi_*$ (ψ_* is a value of continuity at fracture time) from (9) we can obtain the relation, which is reduced to the following

$$kt_f + A_1 e^{kt_f} + B = 0, \tag{10}$$

where $A_1 = \frac{n\sigma_0 a}{E^2\tau k\left(1 - \frac{\sigma_0 b}{E\tau}\right)}$, $B = \frac{n\sigma_0}{E} - \frac{n\sigma_0 a}{E^2\tau k\left(1 - \frac{\sigma_0 b}{E\tau}\right)} - \ln\left(e^{\frac{n\sigma_0}{E}} - \frac{(\psi_*^{1-n} - 1)E^2\tau\left(1 - \frac{\sigma_0 b}{E\tau}\right)}{(1-n)A\sigma_0^{n+1} an}\right)$.
The solution of equation (10) is

$$t_f = -\frac{W(A_1 e^{-B}) - B}{k}, \tag{11}$$

where W is Lambert function, which can be defined as

$$W_0(x) = \sum_{n=1}^{\infty} \frac{(-n)^{n-1}}{n!} x^n.$$

Taking into this decomposition only the first two terms of series, we obtain the solution of equation (10) in the form

$$t_f = -\frac{A_1 e^{-B} - (A_1 e^{-B})^2 - B}{k}. \tag{12}$$

In calculations according formulas (9) and (12) the following values of coefficients were used: $E = 2000\,MPa$, $a = 0,8\,[h]^{-1}$, $b = 3$, $\tau = 35\,h$, $n = 2$, $k = 0,1\,[h]^{-1}$, $A = 0,1\,[MPa]^{-2}$, $\sigma_0 = 80\,MPa$, $\psi_* = 0,1$. These coefficients were chosen to obtain a qualitative description of damage parameter and long-term strength curves.
On Fig. 2 the theoretical curve of long-term strength using criterion (12) is shown.

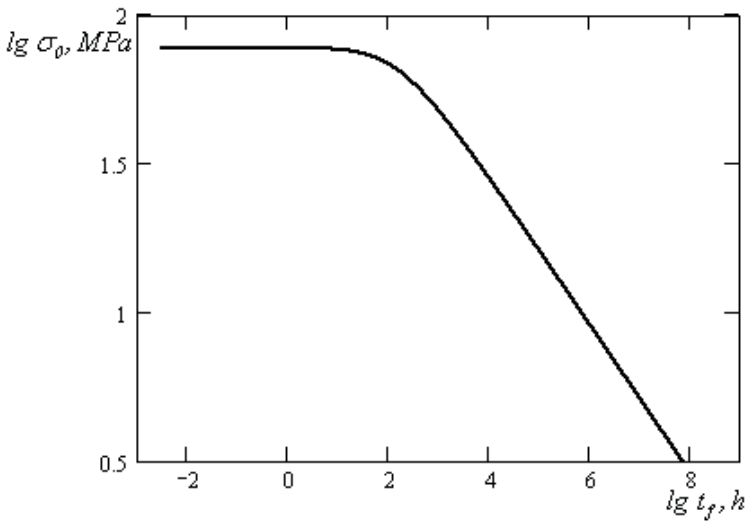

Figure 2: The theoretical curve of long-term strength using criterion (12).

References

[1] Kachanov L.M. Time of fracture under creep // Proceedings USSR Academy of Sciences. OTN. 1958. N 8. P. 26-31. (in Russian).

[2] Rabotnov Y.N. On the mechanism of long-term fracture // Problems of strength of materials and structures. M.: Publishing House of the USSR Academy of Sciences. 1959. P. 5-7. (in Russian).

[3] Novozhilov V.V. On plastic loosening // Applied Mathematics and Mechanics. 1965. N 4. P. 681-689. (in Russian).

[4] Arutyunyan R.A. The problem of strain aging and long-term fracture in mechanics of materials. SPb.: Publishing House of the St. Petersburg State University. 2004. 252p. (in Russian).

[5] Boethner R.C., Robertson W.D. A study of the growth of voids in copper during the creep process by measurement of the accompanying change in density // Trans. of the Metallurg. Society of AIME. 1961. vol. 221. N 3. P. 613-622.

[6] Beghi C., Geel C., Piatti G. Density measurements after tensile and creep tests on pure and slightly oxidised aluminium // J. Mat. Sci. 1970. vol. 5. N 4. P. 331-334.

[7] Brathe L. Macroscopic measurements of creep damage in metals // Scand. J. Metal. 1978. vol. 7. N 5. P. 199-203.

[8] Woodford D.A. Density changes during creep in nickel // Metal science journal. 1969. vol. 3. N 11. P. 234-240.

[9] Kumanin V.I., Kovalev L.A., Alekseev S.V. The durability of the metal in the creep conditions. M.: Metallurgy. 1988. 223p. (in Russian).

[10] Bowring P., Davies P.W., Wilshire B. The strain dependence of density changes during creep // Metal science journal. 1968. vol. 2. N 9. P. 168-171.

[11] Kuznetsov G.B., Covrov V.N. Considering the effects of loosening of highly filled polymer in the equations of hereditary viscoelasticity // Mechanics of Solids. 1994. є N. P. 110-115. (in Russian).

[12] Haward R.N. The extension and rupture of cellulose acetate and celluloid // Trans. Farad. Soc. 1942. v. 38. P. 394-400.

[13] Bokshitskii M.N. Long-term strength of polymers. M.: Chemistry. 1978. 310p. (in Russian).

[14] Arutyunyan R.A. Deformation aging of polymer materials // Proceedings of XXXII Summer School-Conference "Advanced problems in mechanics 2003". June 22-July 2, 2003. Repino, St.-Petersburg. St.-Petersburg: IPME RAS. 2003. P. 17-21.

[15] Arutyunyan R.A. High-temperature embrittlement and creep fracture of metallic materials // Mechanics of Solids. 2015. N 2. P. 96-104. (in Russian).

Alexander R. Arutyunyan, Universitetskii pr., 28, Faculty of Mathematics and Mechanics Sankt-Petersburg State University, Sankt-Petersburg, Petrodvoretz, 198504, Russia.

Thermal brittleness and creep fracture of metallic materials

Robert A. Arutyunyan
Robert.Arutyunyan@paloma.spbu.ru

Abstract

The problem of damage and high-temperature creep fracture of metallic materials is demanded in such areas of modern engineering as the thermal and nuclear power plants, aircraft, spacecraft and others. In this regard, intensive studies on this problem are carried out. It has been found that under the prolonged action of relatively small stresses and high temperatures metallic materials embrittled due to development of damage (cracks, pores etc.). These effects have been studied in details by the methods of physics and materials science. For engineering applications, it became necessary to develop mechanical models of creep damage and fracture. The first such models have been proposed by G. Hoff, L.M. Kachanov, Yu.N. Rabotnov. In these models some controversy assumptions are made, for example the incompressibility condition, which can be overcome, if we formulate the creep fracture criteria using the mass conservation law. Taking into account these propositions and remaining within the concept of damage mechanics, interrelated kinetic equations of creep, damage, and creep fracture criterion are formulated. The proposed approach does not contain the mentioned contradictions and can be considered as the basis for a more accurate description of the damage and fracture of metallic materials and structural elements under the high temperature creep condition.

Financial support of the Russian Foundation for Basic Research (Grant N 15-01-03159) is gratefully acknowledged.

Under the long action of high temperatures and relative small stresses many metallic alloys and pure metals lose plasticity and collapse as brittle (the phenomenon of thermal brittleness). Because these effects are observed in elements of many important engineering objects, in particular, in power and nuclear, the problem of brittle fractures became a subject of numerous theoretical and experimental researches. For the description of brittle fractures the concept of continuity (Kachanov [1]) and damage (Rabotnov [2, 3]) was developed. To materialize the damage parameter various definitions were offered: the relative size of pores or irreversible change of volume (loosening on Novozhilov's terminology [4]) or density (Arutyunyan [5, 6]). In the paper the parameter of continuity is determined by the ratio $\psi = \rho/\rho_0$ (ρ_0 is initial, ρ is current density) and it is an integral measure of the accumulation of structural micro defects during long-term of high-temperature loading [7-16]. In the initial condition $t = 0$, $\rho = \rho_0$, $\psi = 1$, at the time of fracture $t = t_f$, $\rho = 0$, $\psi = 0$.

In the general statement the continuity (damage) parameter ψ and the kinetic equation for this parameter was considered by Haward [17]. According to Haward brittle fracture proceeds with a speed depending on stress $\sigma(t)$

$$\frac{d\psi}{dt} = -f\left[\sigma(t)\right], \tag{1}$$

or, according to representations of statistical physics, from stress and the damage parameter

$$\frac{d\psi}{dt} = -f\left[\sigma(t), \psi\right]. \tag{2}$$

Basic provisions of the concept of Kachanov-Rabotnov brittle fracture are based on the equations (1), (2) which right part is taken in the form of power relation. In the brittle model of Kachanov the continuity parameter ψ $(1 \geq \psi \geq 0)$ is introduced randomly without giving of a certain physical meaning to it. It is supposed that creep deformation doesn't influence fracture processes, and the kinetic equation of the continuity parameter is taken as a power function from effective stress [1]

$$\frac{d\psi}{dt} = -A\left(\frac{\sigma_{\max}}{\psi}\right)^n, \tag{3}$$

where $A > 0$, $n \geq 0$ are empirical constants, not depending on stress, σ_{max}/ψ is effective stress.

The tension problem of specimen stretched under the action of constant load P is solved. It is considered that brittle fracture happens at small deformations therefore it is possible to neglect change of specimen cross section, i.e. the conditions $F = F_0$, $\sigma_{\max} = \sigma = P/F = P/F_0 = \sigma_0 = const$, ($\sigma$ is true stress, σ_0 is nominal stress, F_0, F are the initial and current area of cross section of a specimen) are accepted. At these assumptions the equation (3) can be expressed in the form

$$\frac{d\psi}{dt} = -A\left(\frac{\sigma_0}{\psi}\right)^n. \tag{4}$$

In the Rabotnov's brittle fracture model [3] the damage parameter ω $(0 \leq \omega \leq 1)$ is introduced and it is defined by the following kinetic equation

$$\frac{d\omega}{dt} = A\sigma^n. \tag{5}$$

The damage parameter is introduced as $\omega = F_T/F_0$ (F_T is the total area of pores) and it is characterizes extent of reduction of a specimen area of cross section. Then from condition $F = F_0 - F_T$, we have $F = F_0(1-\omega)$, $\sigma = P/F = \sigma_0 F_0/F = \sigma_0/(1-\omega)$. Taking into account these relations the kinetic equation (5) can be written as

$$\frac{d\omega}{dt} = A\left(\frac{\sigma_0}{1-\omega}\right)^n. \tag{6}$$

The equations (4) and (6) are identical at $\omega = 1 - \psi$, $d\psi = -d\omega$. From the solution of these equations under the initial condition $t = 0$, $\psi = 1$, $\omega = 0$, we have

$$\psi = 1 - \omega = \left[1 - (n+1)A\sigma_0^{nt}\right]^{\frac{1}{n+1}}. \tag{7}$$

Accepting a fracture condition, $t = t_f^b$, $\psi = 0$, $\omega = 1$, from (7) follows the criterion of purely brittle fracture

$$t_f^b = \frac{1}{(n+1)\cdot A\sigma_0^n}. \tag{8}$$

Such an approach provides a physical interpretation of the Kachanov's parameter. However, the condition $F = F_0$, used in the Kachanov's concept, corresponds to zero value of the damage parameter what disagrees with the concept of damage accumulation. Thus, similar interpretation of Kachanov's continuity parameter isn't represented fully correct.
To define the creep deformation Rabotnov [3] introduced a system of two interconnected equations for the rate of creep and damage parameter

$$\frac{d\varepsilon}{dt} = b\sigma^m(1-\omega)^{-q}, \tag{9}$$

$$\frac{d\omega}{dt} = c\sigma^n(1-\omega)^{-r}, \tag{10}$$

where b, c, m, n, q, r are constants, $\varepsilon = \ln(l/l_0)$ is creep deformation, l_0, l are the initial and current length of specimen.
In the case of a purely brittle fracture and small deformations when $F = F_0$, $\sigma = \sigma_0 = const$ solving the system of equations (9)-(10) we will obtained the relation of the creep deformation

$$\varepsilon = \frac{k}{m}\frac{t_f^b}{t_f^v}\left[1 - \left(1 - \frac{t}{t_f^b}\right)^{1/k}\right], \tag{11}$$

where $k = \frac{r+1}{r+1-\mathrm{q}}$, $t_f^b = \frac{1}{c(1+r)\sigma_0^n}$, $t_f^v = \frac{1}{bm\sigma_0^m}$.
Relation (11) is considered as a major result in the Rabotnov's theory, because by using this formula it is possible to describe the third phase of the creep curve, which, in the case of brittle fracture, is completely determined by the damage of material. At the same time, the output of this formula is based on the condition $F = F_0$ and $\omega = 0$, which, as it was noted, is contrary to the very concept of damage. Further, in determining the criteria of ductile-brittle fracture using equations (9)-(10) the condition of incompressibility is introduced, which is also contrary to the damage concept.
To overcome these contradictions in [18] a system of equations for the rate of creep and damage, based on the continuity parameter $\psi = \rho/\rho_0$, have proposed. This paper presents a modified version of these equations, which can describe the main experimental results on creep and creep rupture of metallic materials. Let's consider the following system of equations

$$\frac{d\varepsilon}{dt} = B\sigma^m,$$

$$\psi^\alpha\frac{d\psi}{dt} = -A\sigma^n,$$

where B, α are constants.
The last equation of this system corresponds to the equation (2). Taking into account the mass conservation law $\rho_0 l_0 F_0 = \rho l F$ from which follows the relation $\sigma = \sigma_0\psi e^\varepsilon$ these equations can be written in the form

$$\frac{d\varepsilon}{dt} = B\sigma_0^m\psi^m e^{m\varepsilon}, \tag{12}$$

$$\frac{d\psi}{dt} = -A\sigma_0^n \psi^{n-\alpha} e^{n\varepsilon}. \tag{13}$$

If we consider the case of brittle fracture and small deformations, we can assume $e^{m\varepsilon} \approx 1$, $e^{n\varepsilon} \approx 1$, then the solution of equation (13) with the initial condition $t = 0$, $\psi = 1$ has the form

$$\psi = \left[1 - (\alpha - n + 1)A\sigma_0^{nt}\right]^{\frac{1}{\alpha-n+1}}. \tag{14}$$

Fig. 1 presents the curves, corresponding to equation (14) for various values of the constants: $\alpha = 6$ (curve 1), $\alpha = 4$ (curve 2), $\alpha = 2$ (curve 3) and $\alpha = 1,1$ (curve 4). The curves agree with the experimental curves [7-15]. In the calculations the following values of coefficients were used: $n = 2$, $A = 10^{-9}\,[MPa]^{-2}$, $\sigma_0 = 100\,MPa$.

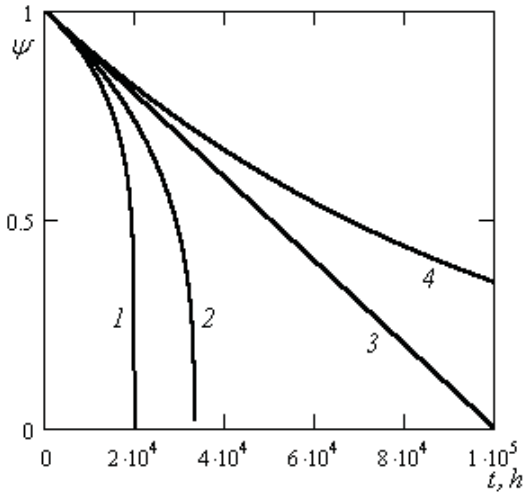

Figure 1: The curves for the parameter of continuity ψ according to the formula (11): $\alpha = 6$ (curve 1), $\alpha = 4$ (curve 2), $\alpha = 2$ (curve 3) and $\alpha = 1,1$ (curve 4).

Taking the fracture condition $t = t_f$, $\psi = 0$, from (14) we obtain the creep fracture criterion

$$t_f^b = \frac{1}{(\alpha - n + 1) \cdot A\sigma_0^n}. \tag{15}$$

When $\alpha = 2n$ the criterion (15) coincides with the Kachanov-Rabotnov criterion (8). On Fig. 2 in the double logarithmic coordinates are shown the creep fracture curves according to the formula (15) for different values of the coefficients: $\alpha = 6$ (curve 1), $\alpha = 4$ (curve 2), $\alpha = 2$ (curve 3) and $\alpha = 1,1$ (curve 4). In the calculations the following values of coefficients were used: $n = 2$, $A = 10^{-9}\,[MPa]^{-2}$.
Taking into account (14) and the initial condition $t = 0$, $\varepsilon = 0$, from equation (12) follows the relation of the creep deformation

$$\varepsilon = \frac{B\sigma_0^{m-n}}{A(\alpha - n + 1)(m - n + 1)} \left\{1 - \left[1 - (\alpha - n + 1)A\sigma_0^{nt}\right]^{\frac{m-n+1}{\alpha-n+1}}\right\}. \tag{16}$$

On Fig. 3 are shown the theoretical creep deformation curves according to the relation (16) for different values of the coefficient α: $\alpha = 8$ (curve 1), $\alpha = 6$ (curve 2) and $\alpha = 1,1$ (curve 3). As can be seen from this figure, the system of equations able to describe the third phase of creep curves, which is determined by the processes of damage accumulation.

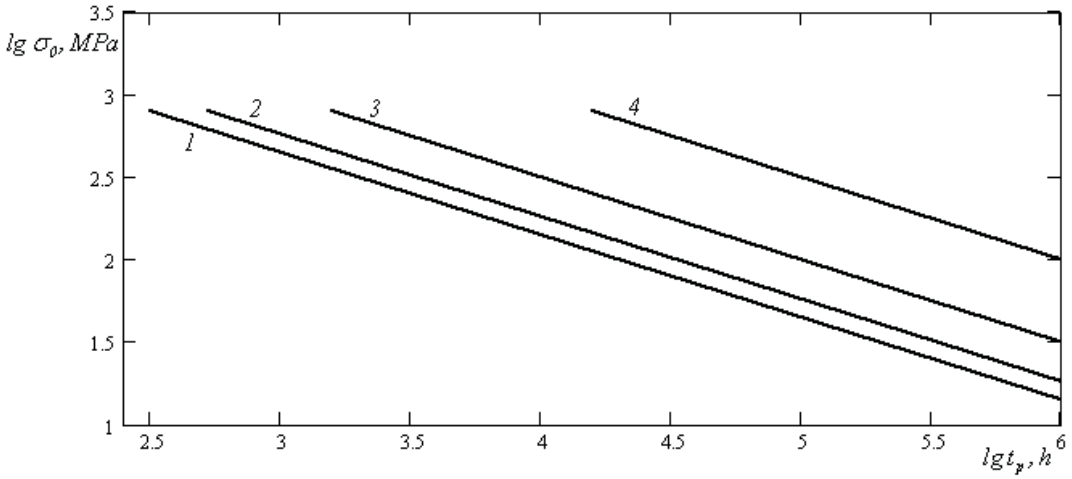

Figure 2: Curves of long-term strength under criterion (15): $\alpha = 6$ (curve 1), $\alpha = 4$ (curve 2), $\alpha = 2$ (curve 3) and $\alpha = 1,1$ (curve 4).

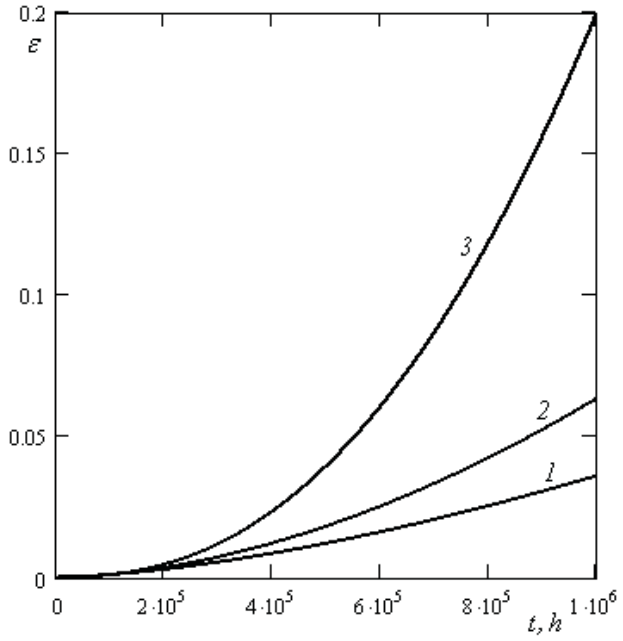

Figure 3: The theoretical creep deformation curves according to the relation (16) for different values of the coefficient α: $\alpha = 8$ (curve 1), $\alpha = 6$ (curve 2) and $\alpha = 1,1$ (curve 3).

In the calculations the following values of coefficients were used: $n = 2$, $m = 4$, $A = 10^{-9}\,[MPa]^{-2}$, $B = 5 \cdot 10^{-17}\,[MPa]^{-4}$, $\sigma_0 = 100\,MPa$.

References

[1] Kachanov L.M. Time of fracture under creep // Proceedings USSR Academy of Sciences. OTN. 1958. N 8. P. 26-31. (in Russian).

[2] Rabotnov Y.N. On the mechanism of long-term fracture // Problems of strength of materials and structures. M.: Publishing House of the USSR Academy of Sciences. 1959. P. 5-7. (in Russian).

[3] Rabotnov Y.N. Creep of elements of designs: M.: Nauka. 1966. 752p. (in Russian).

[4] Novozhilov V.V. On plastic loosening // Applied Mathematics and Mechanics. 1965. N 4. P. 681-689. (in Russian).

[5] Arutyunyan R.A. The problem of strain aging and long-term fracture in mechanics of materials. SPb.: Publishing House of the St.-Petersburg State University. 2004. 252p. (in Russian).

[6] Arutyunyan R.A. Embrittlement problem in mechanics of materials. // Vestn. St. Petersburg. Univ. 2009. ser. 1. vol. 1. P. 54-57. (in Russian).

[7] Rybakina O.G., Sidorin Y.S. Experimental study of the plastic loosening of metals // Proceedings of the Academy of Sciences of the USSR. Mechanics of Solids. 1966. N 1. P. 120-124. (in Russian).

[8] Boethner R.C., Robertson W.D. A study of the growth of voids in copper during the creep process by measurement of the accompanying change in density // Trans. of the Metallurg. Society of AIME. 1961. vol. 221. N 3. P. 613-622.

[9] Beghi C., Geel C., Piatti G. Density measurements after tensile and creep tests on pure and slightly oxidised aluminium // J. Mat. Sci. 1970. vol. 5. N 4. P. 331-334.

[10] Brathe L. Macroscopic measurements of creep damage in metals // Scand. J. Metal. 1978. vol. 7. N 5. P. 199-203.

[11] Ratcliffe R.T., Greenwood G.W. Mechanism of cavitation in magnesium during creep // Phil. Mag. 1965. vol. 12. P. 59-69.

[12] Woodford D.A. Density changes during creep in nickel // Metal science journal. 1969. vol. 3. N 11. P. 234-240.

[13] Kumanin V.I., Kovalev L.A., Alekseev S.V. The durability of the metal in the creep conditions. M.: Metallurgy. 1988. 223p. (in Russian).

[14] Bowring P., Davies P.W., Wilshire B. The strain dependence of density changes during creep // Metal science journal. 1968. vol. 2. N 9. P. 168-171.

[15] Pavlov V.A., Shalaev V.I. Solid solution strengthening due to changes in the stacking fault energy // Alloying and properties of high-temperature alloys. M.: Science. 1971. P. 61-68. (in Russian).

[16] Kuznetsov G.B., Covrov V.N. Considering the effects of loosening of highly filled polymer in the equations of hereditary viscoelasticity // Mechanics of Solids. 1994. N 2. P. 110-115. (in Russian).

[17] Haward R.N. The extension and rupture of cellulose acetate and celluloid // Trans. Farad. Soc. 1942. v. 38. P. 394-400.

[18] Arutyunyan R.A. High-temperature embrittlement and creep fracture of metallic materials // Mechanics of Solids. 2015. N 2. P. 96-104. (in Russian).

Robert A. Arutyunyan, Universitetskii pr., 28, Faculty of Mathematics and Mechanics Sankt-Petersburg State University, Sankt-Petersburg, Petrodvoretz, 198504, Russia.

Directed antenna in block structure

Vladimir A. Babeshko, Olga V. Evdokimova, Olga M. Babeshko,
Igor B. Gladskoi, Elena M. Gorshkova
grigoriev@ispms.tsc.ru

Abstract

It was shown earlier that varying the form of a punch one can achieve a directional radiation of surface waves. A directional radiation is necessary while solving many applications, for example during calculation of acousto-electronic piezoelectric devices on surface waves or during the allocation of hard vibrating equipment, when it's necessary to shade different objects having directed the radiation to a safe side.

In seismic prospecting and defectoscopy the problem of creating a directional radiation of volumetric waves is relevant. Directional seismic antennas are even more widely used during the vibratory examination of the earth's crust and upper Earth mantel, but the optimal characteristics of antenna elements (amplitudes and burden phases) are being determined only empirically, and the use of acoustic antenna theory, formulated to create ideal acoustic circumstances, in case of elastic stratificated circumstances causes great errors. In order to obtain the results, used practically, also the calculation of vertical inhomogeneity and block structure of circumstances realized in this work is important.

Keywords: block element, factorization, topology, integral and differential factorization methods, exterior forms, block structures, boundary problems.

1 Introduction

In this study, the differential factorization method, which has been applied in [1, 2] to an individual convex isotropic elastic body, is extended to the case of block structures, in particular, layered structures. As was noted in [3], this circumstance opens up the possibility to investigate boundary-value problems for differential equations with variable coefficients, as well as nonlinear boundary-value problems.

The formulas derived in [1, 2] for an individual convex elastic body represented an approximate solution describing its stress-strained state. This approximate solution becomes more accurate as the shape of the body approaches a half-space. The approximate equation thus constructed can be refined also by inverting the systems of integral equations presented in the cited works. Similar results can be obtained for block structures [4] but, as is shown below, the large number of blocks and the variety of possible combinations lead to much more complex relationships.

The differential factorization method described in [1, 2] as applied to an individual domain is extended herein to a collection of neightboring domains, which are referred to as block

structures. As applied to boundary value problems for such collections of domains, this method has specificity features that distinguish it from traditional approaches. For example, boundary conditions in the differential factorization method cannot be satisfied in the traditional form by introducing the limiting values of solutions and their derivatives on the boundary. The cause id that the derivatives of the solution constructed by the method on the boundary have mot only classical components but also components in the form of generalizes functions, namely, δ-delta functions and their derivatives [1, 2]. Their origin is explained in detail in [1, 2], and they are not an obstruction to solving boundary value problems. In this paper, we show how to overcome these difficulties when the differential factorization method is applied to block structures.

2 The block element method

By block structures, we mean materials occupying bounded, semibounded, or unbounded domains, which are called contacting blocks. It is assumed that each block in a block structure has its own specific behavioral in response to physical fields of a various nature. It is also assumed that these fields are described by boundary value problems for systems of coupled partial differential equations with constant coefficients. Media of this type are typical of the earth's crust, structural materials under complex physical-mechanical conditions [4], nonmaterials, crystal structures of various arrangements, and electronics materials. A similar structure is also possesse by various materials, including those created by combining only nanoscale components or macro- and nanoscale components.

We consider structures with three-dimensional blocks. The absence of considerable constraints on boundary value problems describing the properties of individual blocks suggests that these block structures can have a wide variety of properties. In the general case, the concept of a block requires that the boundary of the domain a boundary value problem, including multiply connected domains, be unchanged and piecewise smooth. Each block can be bounded or unbounded and can involve coupled processes related to solid and fluid mechanics and electromagnetic, diffusion, thermal, acoustic, and other processes. Block structures are more general objects than piecewise homogeneous structures, in which the physical parameters of the medium are assumed to change in jumps in the transition from one block to another with the preservation of the medium material. The last property means that certain coefficients in the differential equations of a boundary value problem undergo jump variations in the transition from one block to another with the type of the boundary value problem being preserved.

Block structures have a wider range of properties than piecewise homogenous structures. This follows from the variety of blocks' properties, their shapes, and the character of interblock interactions and also results from the interaction of physical fields, some of which are produced or transformed by blocks. A special case of block structures is layered structures. Such structures with plane boundaries for linear boundary value problems can be viewed as fairly thoroughly investigated. Block structures are studied primarily by numerical methods, for which unbounded domains always present difficulties. The differential factorization method, which is a generalization of the integral transform method, gives answers to questions concerning the properties of physical fields in each block even at the stage of solving boundary value problems.

Note that integral transforms in a boundary value problem for partial differential equations in a domain Ω are a convenient research tool when the differential equations, Ω, and the functions describing an integral transform are consistent. By consistency, we mean the possibility of transforming partial differential equations into ordinary ones by applying

an integral transform and the setting of boundary conditions on the boundary described by constant geometric parameter values. This property holds if the integral-transform functions are the eigenfunctions of the differential operator in Ω. In terms of topological algebra, this property holds if the transformation groups generated by an automorphism of the manifold Ω have representations that are invariant under a differentiable mapping of the vector field defined on this manifold. For several simple domains, which are referred to as classical, these are the Fourier transform in domains with plane boundaries, the Bessel transform in domains with circular boundaries, the Bessel-Legendre transform in domains with spherical boundaries, which are applied, for example, to the Helmholtz, Schrodinger, Lame, and Navier–Strokes equations with constant coefficients.

It was shown that these and other integral transforms are consequences of self-mappings of manifolds generating transformation groups of space and their motions. Representations of these groups are obtained by introducing the special functions mentioned above. In the case of classical domains, boundary value problems are relatively easy to solve. Specifically, after applying an integral transform, they are reduced to simple functional or ordinary differential equations and then integral inversion is used.

For boundary value problems in domains of complex geometry, we use the differential factorization method, which reduce them to functional equations with dimension reduction. We formulate the following boundary value problem for a block structure. Assume that the block-structure domain Ω consists of subdomains Ω_b, $b = 1, 2, \ldots, B$ with boundaries $\partial\Omega_b$ It may happen that a portion of the block's boundary is shared with another block, in which case it is a contact boundary. The remaining non-contact portion can be free or subject to external forces. It is assumed that a boundary value problem for systems of partial differential equations with (their own) constant coefficients is set in each domain Ω_b.

For each block, the boundary value problem for the system of P partial differential equations in the three-dimensional block domain Ω can be written as

$$\mathbf{K}_b(\partial x_1, \partial x_2, \partial x_3)\varphi_b = \sum_{m=1}^{M}\sum_{n=1}^{N}\sum_{k=1}^{K}\sum_{p=1}^{P} A^b_{spmnk}\varphi_b p, {}^{(m)(n)(k)}_{x_1\ x_2\ x_3} = 0$$
$$s = 1, 2, \ldots, P_b \tag{1}$$
$$A^b_{sqmnk} = \text{const}, \quad \varphi_b = \{\varphi_{b1}, \varphi_{b2}, \ldots, \varphi_{bP}\}, \quad b = 1, 2, \ldots, B$$
$$\varphi = \{\varphi_s\}, \quad \varphi(\mathbf{x}) = \varphi(x_1, x_2, x_3), \quad \mathbf{x} = \{x_1, x_2, x_3\}, \quad \mathbf{x} \in \Omega_b$$

The following matching conditions are set on the common contact boundary $\partial\Omega_b \cap \partial\Omega_d$

$$\mathbf{R}_b(\partial x_1, \partial x_2, \partial x_3)\varphi_b + \mathbf{R}_d(\partial x_1, \partial x_2, \partial x_3)\varphi_d$$
$$= \sum_{m=1}^{M_1}\sum_{n=1}^{N_1}\sum_{k=1}^{K_1}\sum_{p=1}^{P}\left[B^b_{spmnk}\varphi_{bp,}{}^{(m)(n)(k)}_{x_1\ x_2\ x_3} + B^d_{spmnk}\varphi_{dp,}{}^{(m)(n)(k)}_{x_1\ x_2\ x_3}\right] = f_{bds} \tag{2}$$
$$s = 1, 2, \ldots, s_{b0} < P, \quad \mathbf{x} \in \partial\Omega_b \cap \partial\Omega_d, \quad M_1 < M, \quad N_1 < N, \quad K_1 < K$$
$$b, d = 1, 2, \ldots, B$$

The boundary value problem is studied in the spaces of tempered distributions described in [1].

In the general form, the above boundary conditions describe the contact of blocks with the relevant components of physical fields coinciding on the common boundaries as dedicated by the corresponding physical laws. In particular, conditions (2) can be significantly simpler. For example, they can lack boundary external forces and express only the equality

between the solutions and their derivatives on a common boundary. However, as mentioned above, the derivatives of solutions written in integral form cannot be equated, since their components in the factorization method are generalized functions [2]. On noncontact boundaries, we set the boundary conditions of the boundary value problem considered in [1]. The scheme for applying the differential factorization method to such domains can be described as follows.

Following the differential factorization method [1], the boundary value problem is reduced to a system of functional equations with each domain Ω_b considered separately. As a result, we obtain the system of functional equations.

$$\mathbf{K}_b(\alpha)\varphi_b = \iint\limits_{\partial\Omega_b} \boldsymbol{\omega}_b, \quad \mathbf{K}_b(\alpha) \equiv -\mathbf{K}_b(-i\alpha_1, -i\alpha_2, -i\alpha_3) = \|k_{bnm}(\alpha)\| \qquad b = 1, 2, \ldots, B \tag{3}$$

Here, we used the notation adopted in [1] with additional indices b. For example, ω_b is the vector of exterior forms of the boundary value problem in Ω_b.

Comparing this case with that considered in [1], we note that boundary conditions (2) generally contain the values of the solutions and their derivatives on the boundary at least in two neighboring domains. This is a substantial difference of block structures from objects analyzed in [1].

According to the differential factorization method, the next step consists of factorizing the matrix function $\mathbf{K}_b(\alpha)$ given by (3). For this purpose, we choose a matrix function $\mathbf{K}_b^*(\alpha_3^\nu, m)$ of order $P-1$ obtained by deleting the row and column indexed by m in the adjoint matrix function $\mathbf{K}_b^*(\alpha_3^\nu)$ such that the zeros ξ_n^ν of its determinant $Q_b(\alpha_3^\nu) = \det \mathbf{K}_b(\alpha_3^\nu, m)$ do not coincide with the zeros z_{s+}^v, z_{s-}^v [1].

The elements of the inverse matrix function are denoted by $[\mathbf{K}_b^*(\alpha_3^\nu, m)]^{-1} = \left\|Q_b^{-1}Q_{psb}\right\|$. Then the elements of $\mathbf{K}^{-1}(\alpha_3^\nu, -)$ given by

$$\mathbf{K}_b^{-1}(\alpha_{3,}^v -) = \begin{Vmatrix} 1 & & & & & 0 \\ & 1 & & & & \\ & & \ddots & & & \\ S_{m1} & S_{m2} & \ldots & S_{mm} & \ldots & S_{mN} \\ & & & & \ddots & \\ 0 & & & & & 1 \end{Vmatrix} \tag{4}$$

can be represented in integral the form

$$S_{mp}(\alpha_3^\nu) = \frac{1}{2\pi i} \oint\limits_{\Gamma_\mp} {\sum_{s=1}^{N}}' \frac{Q_{psb}(u_3)M_{sm}(u_3)du_3}{Q_b(u_3)K(u_3)(u_3 - \alpha_3^\nu)} - \left(\frac{1}{2} \mp \frac{1}{2}\right) \frac{R_{mp}(\alpha_3^\nu)}{K(\alpha_3^\nu)}, \quad m \neq p$$

$$\frac{R_{mp}(\alpha_3^\nu)}{K_b(\alpha_3^\nu)} = \frac{Z_{mp}(\alpha_3^\nu)}{Q_b(\alpha_3^\nu)K_b(\alpha_3^\nu)} + \sum_n \frac{Z_{mp}(\xi_n^\nu)}{Q_b'(\xi_n^\nu)K_b(\xi_n^\nu)(\xi_n^\nu - \alpha_3^\nu)}$$

$$S_{mm}(\alpha_3^\nu) = K_b^{-1}(\alpha_3^\nu), \quad \alpha_3^\nu \in \lambda_\mp$$

$$Z_{mp}(\alpha_3^\nu) = {\sum_{s=1}^{N}}' Q_{psb}(\alpha_3^\nu)M_{sm}(\alpha_3^\nu)$$

Here, Γ_+ is a closed contour such that the domain λ_+ contains only the zeros z_{s+}^v, z_{s-}^v and , while the domain λ_- contains only the zeros ξ_n^ν. The closed contour Γ_- encloses

a domain containing all the zeros z_{s+}^{v}, z_{s-}^{v}, and ξ_{n}^{ν}. Representation (4) implies that the elements of $\mathbf{K}_{b}^{-1}(\alpha_{3}^{\nu},-)$ are rational functions with their only singularities being z_{s+}^{v}, z_{s-}^{v}. The term $K_{b}^{-1}(\alpha_{3}^{\nu})$ containing them is given explicitly.

In the case of noncontact boundaries, the boundary conditions in the differential factorization method are set according to the rules described in [1].

The boundary conditions are fulfilled according to the following scheme. First boundary conditions on the noncontact boundary of each block are taken to the corresponding vectors of exterior forms in functional equations (3). For contact blocks, matching conditions (2) hold on the common boundaries of neightboring blocks. Depending on the properties of the described fields, these conditions can include some relations for the solutions and their derivatives. In the simplest case, this is the equality of the solutions and their derivatives on the common boundary in the transition from one block to another. These relations are taken to the corresponding vectors of exterior forms of functional equations (3), which are preliminary solved for the unknown normal derivatives on the boundary. The last procedure ensures the fulfillment of contact boundary conditions (2) in the solution to pseudodifferential equations, which can be proved following the scheme described in [2].

Assume that the blocks are convex. Omitting the intermediate transformations, which can be found in [1], we find that the solution in each block is represented as

$$\varphi_{b}(\mathbf{x}^{\nu})=\frac{1}{8\pi^{3}}\int\limits_{-\infty}^{\infty}\iiint\limits \mathbf{K}_{rb}^{-1}(\alpha_{3}^{\nu})\,\mathbf{K}_{b}^{-1}(\alpha_{3}^{\nu},-)\iint\limits_{\partial\Omega}\boldsymbol{\omega}_{b}e^{-i\langle\alpha_{3}^{\nu}x_{3}^{\nu}\rangle}d\alpha_{1}^{\nu}d\alpha_{2}^{\nu}d\alpha_{3}^{\nu},\quad \mathbf{x}^{\nu}\in\Omega_{b}$$

To illustrate this solution, we evaluate the integral with respect to α_{3}^{ν} by applying Leray's residue form theory to obtain

$$\varphi_{b}(\mathbf{x}^{v})=\frac{1}{4\pi^{2}}\int\limits_{-\infty}^{\infty}\iint\sum_{s}e^{-i\left(\alpha_{1}^{v}x_{1}^{v}+\alpha_{2}^{v}x_{2}^{v}\right)}\left[\mathbf{K}_{rb}^{-1}\left(i\frac{\partial}{\partial x_{3}^{v}}\right)\mathbf{T}_{+b}\left(\alpha_{1}^{v},\alpha_{2}^{v},z_{s+}^{v}\right)e^{-iz_{s+}^{v}x_{3}^{v}}\right.$$
$$\left.-\,\mathbf{K}_{rb}^{-1}\left(i\frac{\partial}{\partial x_{3}^{v}}\right)\mathbf{T}_{-b}\left(\alpha_{1}^{v},\alpha_{2}^{v},z_{s-}^{v}\right)e^{-iz_{s-}^{v}x_{3}^{v}}\right]d\alpha_{1}^{\nu}d\alpha_{2}^{\nu}$$

Here, the boundary $\partial\Omega_{b}$ for the chosen $x_{3}^{\nu}<0$, $\mathbf{x}^{\nu}\in\Omega$ is divided as follows:

$$\iint\limits_{\partial\Omega_{b}}\boldsymbol{\omega}_{b}=\iint\limits_{\partial\Omega_{+b}}\boldsymbol{\omega}_{b}+\iint\limits_{\partial\Omega_{-b}}\boldsymbol{\omega}_{b}$$

$$\iint\limits_{\partial\Omega_{+b}}\boldsymbol{\omega}_{b}\exp(-i\alpha_{3}^{\nu}x_{3}^{\nu})\to 0,\quad \mathrm{Im}\alpha_{3}^{\nu}\to\infty$$

$$\iint\limits_{\partial\Omega_{-b}}\boldsymbol{\omega}_{b}\exp(-i\alpha_{3}^{\nu}x_{3}^{\nu})\to 0,\quad \mathrm{Im}\alpha_{3}^{\nu}\to-\infty$$

If a block degenerates into a half-space or a layered medium, the pseudodifferential equations appearing in the course of solving the boundary value problem degenerate into algebraic equations. The latter are inversed, and the solution is constructed in a finite form [1].

If the block under study is not a convex body, the boundary value problem is analyzed by the generalized factorization method.

3 The block structure

Let us assume that a domain Ω of a block structure consists of contracting convex domains Ω_b, $b = 1, 2, \ldots, B$ with boundaries $\partial\Omega_b$. It may happen that a portion f the boundary $\partial\Omega_{bd}$ of a certain b block coincides with the boundary of another d block $d = 1, 2, \ldots, B$. Such a portion is called contracting. The remaining portions of the boundaries of both domains are noncontracting and will be denoted below by subscripts with one letter: $\partial\Omega_b$, $\partial\Omega_d$. These boundaries can be free of or subjected to external actions. It is assumed that, in each domain Ω_b one of the boundary-value problems considered in [1, 2] is formulated in terms of the systems of differential equations with partial derivatives, the constant coefficients of which are different in each domain.
For each block $b = 1, 2, \ldots, B$ characterized by its own mechanical characteristics, the equations of the isotropic elasticity theory can be written in the following form [1, 2]:

$$\begin{aligned} &(\lambda_b + \mu_b)\,\mathrm{graddiv}\,\mathbf{u}_b + \mu\Delta\mathbf{u}_b - \delta_b\mathbf{u}_b = 0 \\ &\mathbf{u}_b = \{u_{b1}, u_{b2}, u_{b3}\} \end{aligned} \tag{5}$$

where the notation is the same as in the papers cited. On the noncontracting portions of the boundary, traditional boundary conditions of the elasticity theory are set [1, 2]. In the contracting parts, in particular, on $\partial\Omega_{bd}$, the conditions of equality of the stress vectors are formulated as follows:

$$\begin{aligned} &\mathbf{u}_b = \mathbf{u}_d, \quad \mathbf{u}_c = \{u_{c1}, u_{c2}, u_{c3}\} \\ &\mathbf{t}_b{=}\mathbf{t}_d, \quad \mathbf{t}_c = \{t_{c1}, t_{c2}, t_{c3}\}, \quad t_{c1} = \sigma_{c13}, \quad t_{c2} = \sigma_{c23}, \quad t_{c3} = \sigma_{c33} \end{aligned} \tag{6}$$

Using the differential factorization method [1, 2], we reduce the boundary-value problem to the system of functional equations, considering each domain Ω_b individually. As a result, we obtain the following system of functional equations:

$$\begin{aligned} &\mathbf{K}_b(\alpha)\boldsymbol{\varphi}_b = \iint\limits_{\partial\Omega_b} \boldsymbol{\omega}_b, \quad \mathbf{K}_b(\alpha) \equiv -\mathbf{K}_b(-i\alpha_1, -i\alpha_2, -i\alpha_3) = \|k_{bnm}(\alpha)\| \\ &b = 1, 2, \ldots, B \end{aligned} \tag{7}$$

where the notation is the same as in [1, 2] with the addition of subscripts b. In particular, $\boldsymbol{\omega}_b$ is the vector of external forms of the boundary-value problem in domain Ω_b.
Comparing this case with those considered in [1, 2], it should be noted that boundary conditions (2) generally contain stresses and displacements on the boundary from at least two neighboring domains. In this respect, the block structures significantly differ from the individual bodies studied in [1, 2]. According to the algorithm of the differential factorization method, the boundary conditions for noncontracting boundaries are applied according to the rules stipulated in [3].
Without repeating the application of algorithms described in [1, 2], we will present here the final form of pseudodifferential equations for the case of contact between two bodies. Fullfillment of the boundary conditions is ensured as follows. First, the boundary conditions on the noncontracting boundary for each individual block are introduced in the corresponding vectors of exterior forms of functional equations (7). When blocks are in contact, matching conditions (6) on the coinciding boundaries of the neightboring blocks $\partial\Omega_{bd}$ are valid. These relationships should be introduced in the corresponding vector of exterior forms only of one of the functional equations, whereas the vector of exterior forms of the second equation remains unchanged. As was proved in [4], this procedure ensures

fullfillment for the boundary conditions (6) and does not require separation of the generalized functions from classical components appearing in a natural way in solutions obtained using the factorization method.

Having omitted the procedure of applying the differential factorization method to the boundary-value problem under consideration, including its realization in each domain Ω_b and on Ω_d as was performed in [1, 2], we present the pseudodifferential equations for a block structure consisting of two blocks:

$$\begin{aligned}
&\mathbf{M}_c^{\nu}(\alpha_1^{\nu},\alpha_2^{\nu},\alpha_{3r-}^{\nu}(\alpha_1^{\nu},\alpha_2^{\nu}))\mathbf{U}_c^{\nu}(\alpha_1^{\nu},\alpha_2^{\nu},\alpha_{3r-}^{\nu}(\alpha_1^{\nu},\alpha_2^{\nu}))\\
&-\mathbf{D}_c^{\nu}(\alpha_1^{\nu},\alpha_2^{\nu},\alpha_{3r-}^{\nu}(\alpha_1^{\nu},\alpha_2^{\nu}))\mathbf{T}_c^{\nu}(\alpha_1^{\nu},\alpha_2^{\nu},\alpha_{3r-}^{\nu}(\alpha_1^{\nu},\alpha_2^{\nu}))\\
&+{\sum_{\boldsymbol{\tau=1}}^{T}}'\Big[\mathbf{M}_c^{\tau}(\alpha_1^{\nu},\alpha_2^{\nu},\alpha_{3r-}^{\nu}(\alpha_1^{\nu},\alpha_2^{\nu}))\mathbf{U}_c^{\tau}(\alpha_1^{\nu},\alpha_2^{\nu},\alpha_{3r-}^{\nu}(\alpha_1^{\nu},\alpha_2^{\nu}))\\
&-\mathbf{D}_c^{\tau}(\alpha_1^{\nu},\alpha_2^{\nu},\alpha_{3r-}^{\nu}(\alpha_1^{\nu},\alpha_2^{\nu}))\mathbf{T}_c^{\tau}(\alpha_1^{\nu},\alpha_2^{\nu},\alpha_{3r-}^{\nu}(\alpha_1^{\nu},\alpha_2^{\nu}))\Big]=0
\end{aligned}\tag{8}$$

Here, $c=b$ in the case of domain Ω_b and $c=d$ in the case of domain Ω_d.

Applying the methods described in [2] and retaining the notation used in that study, these pseudodifferential equations can be reduced to systems of integral equations. The system of integral equations for domain Ω_b, written with respect to vector t $\mathbf{t}_b^{\nu}$, $\mathbf{t}_d^{\nu}$ for the displacement vectors $\mathbf{u}_b^{\nu}$, $\mathbf{u}_d^{\nu}$ set on noncontracting boundaries, has the following form:

$$\begin{aligned}
&\iint\limits_{\partial\boldsymbol{\Omega}_{b\boldsymbol{\nu}}}\mathbf{k}_b^{\nu}(x_1^{\nu}-\xi_1^{\nu},x_2^{\nu}-\xi_2^{\nu})\mathbf{t}_b^{\nu}(\xi_1^{\nu},\xi_2^{\nu})d\xi_1^{\nu}d\xi_2^{\nu}\\
&+{\sum_{\boldsymbol{\tau=1}}^{T}}'\iint\limits_{\partial\boldsymbol{\Omega}_{b\boldsymbol{\tau}}}\mathbf{k}_b^{\nu\tau}(x_1^{\nu},\xi_1^{\tau},x_2^{\nu},\xi_2^{\tau})\mathbf{t}_b^{\tau}(\xi_1^{\tau},\xi_2^{\tau})d\xi_1^{\tau}d\xi_2^{\tau}=\mathbf{u}_b^{\nu}(x_1^{\nu},x_2^{\nu})\\
&+{\sum_{\tau=1}^{T}}'\iint\limits_{\partial\boldsymbol{\Omega}_{b\boldsymbol{\tau}}}\mathbf{b}_b^{\nu\tau}(x_1^{\nu},\xi_1^{\tau},x_2^{\nu},\xi_2^{\tau})\mathbf{u}_b^{\tau}(\xi_1^{\tau},\xi_2^{\tau})d\xi_1^{\tau}\xi_2^{\tau},\quad x_1^{\nu},x_2^{\nu}\in\partial\boldsymbol{\Omega}_{b\boldsymbol{\nu}},\quad 1\leqslant\nu\leqslant T
\end{aligned}\tag{9}$$

For the domain Ω_d contacting with the domain Ω_b along the boundary $\partial\Omega_{bd}$, the system of integral equations with allowance for boundary conditions (2) takes the following form:

$$\begin{aligned}
&\iint\limits_{\partial\boldsymbol{\Omega}_{p\boldsymbol{\nu}}}\mathbf{k}_d^{\nu}(x_1^{\nu}-\xi_1^{\nu},x_2^{\nu}-\xi_2^{\nu})\mathbf{t}_c^{\nu}(\xi_1^{\nu},\xi_2^{\nu})d\xi_1^{\nu}d\xi_2^{\nu}\\
&+{\sum_{\tau=1}^{T_1}}'\iint\limits_{\partial\boldsymbol{\Omega}_{d\boldsymbol{\tau}}}\mathbf{k}_d^{\nu\tau}(x_1^{\nu},\xi_1^{\tau},x_2^{\nu},\xi_2^{\tau})\mathbf{t}_d^{\tau}(\xi_1^{\tau},\xi_2^{\tau})d\xi_1^{\tau}d\xi_2^{\tau}\\
&+{\sum_{\boldsymbol{\tau=1}}^{T_2}}'\iint\limits_{\partial\boldsymbol{\Omega}_{bd\boldsymbol{\tau}}}\mathbf{k}_d^{\nu\tau}(x_1^{\nu},\xi_1^{\tau},x_2^{\nu},\xi_2^{\tau})\mathbf{t}_b^{\tau}(\xi_1^{\tau},\xi_2^{\tau})d\xi_1^{\tau}d\xi_2^{\tau}=\mathbf{u}_c^{\nu}(x_1^{\nu},x_2^{\nu})\\
&+{\sum_{\boldsymbol{\tau=1}}^{T_1}}'\iint\limits_{\partial\boldsymbol{\Omega}_{d\boldsymbol{\tau}}}\mathbf{b}_d^{\nu\tau}(x_1^{\nu},\xi_1^{\tau},x_2^{\nu},\xi_2^{\tau})\mathbf{u}_d^{\tau}(\xi_1^{\tau},\xi_2^{\tau})d\xi_1^{\tau}\xi_2^{\tau}\\
&+{\sum_{\boldsymbol{\tau=1}}^{T_2}}'\iint\limits_{\partial\boldsymbol{\Omega}_{bd\boldsymbol{\tau}}}\mathbf{b}_d^{\nu\tau}(x_1^{\nu},\xi_1^{\tau},x_2^{\nu},\xi_2^{\tau})\mathbf{u}_b^{\tau}(\xi_1^{\tau},\xi_2^{\tau})d\xi_1^{\tau}\xi_2^{\tau}\\
&x_1^{\nu},x_2^{\nu}\in\partial\boldsymbol{\Omega}_{d\boldsymbol{\nu}};\quad 1\leqslant\nu\leqslant T=T_1+T_2
\end{aligned}\tag{10}$$

Here, $c = d$, $p = d$, if x_1^ν, $x_2^\nu \in \partial\boldsymbol{\Omega}_{b\boldsymbol{\nu}}$; and $c = b$, $p = bd$, if x_1^ν, $x_2^\nu \in \partial\boldsymbol{\Omega}_{bd\boldsymbol{\nu}}$, T_1 and T_2 are the numbers of unity partition of the noncontracting portion of the boundary $\partial\boldsymbol{\Omega}_{b\boldsymbol{\nu}}$ and the contracting portion $\partial\boldsymbol{\Omega}_{bd\boldsymbol{\nu}}$, respectively; and the primed sum symbols imply that the terms with $\nu = \tau$ in these sums are missing if they are present in the same sum symbol. The kernels of the integral equations are as follows (in the notation from [2]):

$$\begin{aligned}
&\mathbf{K}_c^\nu(\alpha_1^\nu, \alpha_2^\nu) = (\mathbf{M}_c^\nu)^{-1}\mathbf{D}_c^\nu, \quad \mathbf{K}^{\nu\tau}(\alpha_1^\nu, \alpha_2^\nu) = (\mathbf{M}_c^\nu)^{-1}\mathbf{D}_c^\tau \\
&\mathbf{B}_c^{\nu\tau}(\alpha_1^\nu, \alpha_2^\nu) = (\mathbf{M}_c^\nu)^{-\mathbf{1}}\mathbf{M}_c^\tau \\
&\\
&\mathbf{k}_c^\nu(x_1^\nu, x_2^\nu) = \mathbf{F}_2^{-1}\mathbf{K}_c^\nu(\alpha_1^\nu, \alpha_2^\nu); \\
&\mathbf{k}_c^{\nu\tau}(x_1^\nu, \xi_1^\tau, x_2^\nu, \xi_2^\tau) = \mathbf{F}_2^{-1}\mathbf{K}_c^{\nu\tau}(\alpha_1^\nu, \alpha_2^\nu)\exp i\langle \mathbf{c}_\tau^\nu\boldsymbol{\alpha}^\nu, \boldsymbol{\xi}^\tau\rangle; \\
&\mathbf{b}_c^{\nu\tau}(x_1^\nu, \xi_1^\tau, x_2^\nu, \xi_2^\tau) = \mathbf{F}_2^{-1}\mathbf{B}_c^{\nu\tau}(\alpha_1^\nu, \alpha_2^\nu)\exp i\langle \mathbf{c}_\tau^\nu\boldsymbol{\alpha}^\nu, \boldsymbol{\xi}^\tau\rangle; \\
&\mathbf{t}_c^\nu(x_1^\nu, x_2^\nu) = \mathbf{F}_2^{-1}\mathbf{T}_c^\nu(\alpha_1^\nu, \alpha_2^\nu); \quad \mathbf{u}_c^\nu(x_1^\nu, x_2^\nu) = \mathbf{F}_2^{-1}\mathbf{U}_c^\nu(\alpha_1^\nu, \alpha_2^\nu).
\end{aligned} \tag{11}$$

The formulas take place for $c = b$ and $c = d$.
If the stress vectors $\mathbf{t}_b^\nu$, $\mathbf{t}_d^\nu$ are given on the boundary, the corresponding system of equations with respect to the displacement vectors $\mathbf{u}_b^\nu$, $\mathbf{u}_d^\nu$ takes the following form:

$$\begin{aligned}
&\iint\limits_{\partial\boldsymbol{\Omega}_{b\boldsymbol{\nu}}} \mathbf{n}_b^\nu(x_1^\nu - \xi_1^\nu, x_2^\nu - \xi_2^\nu)\mathbf{u}_b^\nu(\xi_1^\nu, \xi_2^\nu)d\xi_1^\nu d\xi_2^\nu + \\
&+\sum_{\boldsymbol{\tau}=1}^{T}{}' \iint\limits_{\partial\boldsymbol{\Omega}_{b\boldsymbol{\tau}}} \mathbf{n}_b^{\nu\tau}(x_1^\nu, \xi_1^\tau, x_2^\nu, \xi_2^\tau)\mathbf{u}_b^\tau(\xi_1^\tau, \xi_2^\tau)d\xi_1^\tau d\xi_2^\tau = \mathbf{t}_b^\nu(x_1^\nu, x_2^\nu) \\
&+\sum_{\boldsymbol{\tau}=1}^{T}{}' \iint\limits_{\partial\boldsymbol{\Omega}_{b\boldsymbol{\tau}}} \mathbf{r}_b^{\nu\tau}(x_1^\nu, \xi_1^\tau, x_2^\nu, \xi_2^\tau)\mathbf{t}_b^\tau(\xi_1^\tau, \xi_2^\tau)d\xi_1^\tau\xi_2^\tau \\
&x_1^\nu, x_2^\nu \in \partial\boldsymbol{\Omega}_{b\boldsymbol{\nu}}; \quad 1 \leqslant \nu \leqslant T
\end{aligned} \tag{12}$$

$$\begin{aligned}
&\iint\limits_{\partial\boldsymbol{\Omega}_{p\boldsymbol{\nu}}} \mathbf{n}_d^\nu(x_1^\nu - \xi_1^\nu, x_2^\nu - \xi_2^\nu)\mathbf{u}_c^\nu(\xi_1^\nu, \xi_2^\nu)d\xi_1^\nu d\xi_2^\nu + \\
&+\sum_{\boldsymbol{\tau}=1}^{/T_1} \iint\limits_{\partial\boldsymbol{\Omega}_{d\boldsymbol{\tau}}} \mathbf{n}_d^{\nu\tau}(x_1^\nu, \xi_1^\tau, x_2^\nu, \xi_2^\tau)\mathbf{u}_d^\tau(\xi_1^\tau, \xi_2^\tau)d\xi_1^\tau d\xi_2^\tau + \\
&+\sum_{\boldsymbol{\tau}=1}^{T_2}{}' \iint\limits_{\partial\boldsymbol{\Omega}_{bd\boldsymbol{\tau}}} \mathbf{n}_d^{\nu\tau}(x_1^\nu, \xi_1^\tau, x_2^\nu, \xi_2^\tau)\mathbf{u}_b^\tau(\xi_1^\tau, \xi_2^\tau)d\xi_1^\tau d\xi_2^\tau = \mathbf{t}_c^\nu(x_1^\nu, x_2^\nu) \\
&+\sum_{\boldsymbol{\tau}=1}^{T_1}{}' \iint\limits_{\partial\boldsymbol{\Omega}_{d\boldsymbol{\tau}}} \mathbf{r}_d^{\nu\tau}(x_1^\nu, \xi_1^\tau, x_2^\nu, \xi_2^\tau)\mathbf{t}_d^\tau(\xi_1^\tau, \xi_2^\tau)d\xi_1^\tau\xi_2^\tau \\
&+\sum_{\boldsymbol{\tau}=1}^{T_2}{}' \iint\limits_{\partial\boldsymbol{\Omega}_{bd\boldsymbol{\tau}}} \mathbf{r}_d^{\nu\tau}(x_1^\nu, \xi_1^\tau, x_2^\nu, \xi_2^\tau)\mathbf{t}_b^\tau(\xi_1^\tau, \xi_2^\tau)d\xi_1^\tau\xi_2^\tau, \\
&x_1^\nu, x_2^\nu \in \partial\boldsymbol{\Omega}_{d\boldsymbol{\nu}}; \quad 1 \leqslant \nu \leqslant T = T_1 + T_2;
\end{aligned} \tag{13}$$

where $c = d$, $p = d$, for x_1^ν, $x_2^\nu \in \partial\boldsymbol{\Omega}_{b\boldsymbol{\nu}}$; $c = b$, $p = bd$, for x_1^ν, $x_2^\nu \in \partial\boldsymbol{\Omega}_{bd\boldsymbol{\nu}}$

$$\begin{aligned}
&\mathbf{N}^{\boldsymbol{\nu}}(\alpha_1^\nu, \alpha_2^\nu) = (\mathbf{D}^{\boldsymbol{\nu}})^{-1}\mathbf{M}^{\boldsymbol{\nu}}, \\
&\mathbf{N}^{\nu\tau}(\alpha_1^\nu, \alpha_2^\nu) = (\mathbf{D}^{\boldsymbol{\nu}})^{-1}\mathbf{M}^\tau, \quad \mathbf{R}^{\nu\tau}(\alpha_1^\nu, \alpha_2^\nu) = (\mathbf{D}^\nu)^{-1}\mathbf{D}^\tau, \\
&\mathbf{N}^\nu(\alpha_1^\nu, \alpha_2^\nu) = (\mathbf{D}^{\boldsymbol{\nu}})^{-1}\mathbf{M}^{\boldsymbol{\nu}}, \mathbf{N}^{\boldsymbol{\nu\tau}}(\alpha_1^\nu, \alpha_2^\nu) = (\mathbf{D}^{\boldsymbol{\nu}})^{-1}\mathbf{M}^\tau, \mathbf{R}^{\boldsymbol{\nu\tau}}(\alpha_1^\nu, \alpha_2^\nu) = (\mathbf{D}^{\boldsymbol{\nu}})^{-1}\mathbf{D}^\tau
\end{aligned}$$

$$\mathbf{n}_c^\nu(x_1^\nu, x_2^\nu) = \mathbf{F}_2^{-1}\mathbf{N}_c^\nu(\alpha_1^\nu, \alpha_2^\nu);$$
$$\mathbf{n}_c^{\nu\tau}(x_1^\nu, \xi_1^\tau, x_2^\nu, \xi_2^\tau) = \mathbf{F}_2^{-1}\mathbf{N}_c^{\nu\tau}(\alpha_1^\nu, \alpha_2^\nu)\exp i\langle \mathbf{c}_\tau^\nu \boldsymbol{\alpha}^\nu, \boldsymbol{\xi}^\tau\rangle$$
$$\mathbf{r}_c^{\nu\tau}(x_1^\nu, \xi_1^\tau, x_2^\nu, \xi_2^\tau) = \mathbf{F}_2^{-1}\mathbf{R}_c^{\nu\tau}(\alpha_1^\nu, \alpha_2^\nu)\exp i\langle \mathbf{c}_\tau^\nu \boldsymbol{\alpha}^\nu, \boldsymbol{\xi}^\tau\rangle$$
$$1 \leqslant \nu \leqslant T, \quad c = b,\ d$$

An analysis of these formulas shows that the first integral operators on the left are inverted by the integral factorization method presented in [3, 5, 6] and are principal (as in [1, 2]). Note that, using the above-described derivation of integral equations (9), (10), and (11), (12) for a structure consisting of two blocks, it is not difficult to obtain integral equations for a structure containing an arbitrary number of blocks. Moreover, the system of integral equations for a block structure where domains occupied by blocks are not necessarily convex has a similar form. However, in this case, the principal operators do not need to have kernels dependent on the difference of arguments. In the case of a block structure, as well as in the case of a single body, it is possible to construct an approximate solution discarding small terms. Then, the integral equations can be written as follows:

$$\begin{gathered}
\iint\limits_{\partial\boldsymbol{\Omega}_{b\boldsymbol{\nu}}} \mathbf{k}_b^\nu(x_1^\nu - \xi_1^\nu, x_2^\nu - \xi_2^\nu)\mathbf{t}_b^\nu(\xi_1^\nu, \xi_2^\nu)d\xi_1^\nu d\xi_2^\nu = \mathbf{u}_b^\nu(x_1^\nu, x_2^\nu) \\
x_1^\nu, x_2^\nu \in \partial\boldsymbol{\Omega}_{b\boldsymbol{\nu}}; \quad 1 \leqslant \nu \leqslant T \\
\iint\limits_{\partial\boldsymbol{\Omega}_{p\boldsymbol{\nu}}} \mathbf{k}_d^\nu(x_1^\nu - \xi_1^\nu, x_2^\nu - \xi_2^\nu)\mathbf{t}_c^\nu(\xi_1^\nu, \xi_2^\nu)d\xi_1^\nu d\xi_2^\nu = \mathbf{u}_c^\nu(x_1^\nu, x_2^\nu) \\
x_1^\nu, x_2^\nu \in \partial\boldsymbol{\Omega}_{d\boldsymbol{\nu}}; \quad 1 \leqslant \nu \leqslant T
\end{gathered} \tag{14}$$

$$\begin{gathered}
\iint\limits_{\partial\boldsymbol{\Omega}_{b\boldsymbol{\nu}}} \mathbf{n}_b^\nu(x_1^\nu - \xi_1^\nu, x_2^\nu - \xi_2^\nu)\mathbf{u}_b^\nu(\xi_1^\nu, \xi_2^\nu)d\xi_1^\nu d\xi_2^\nu = \mathbf{t}_b^\nu(x_1^\nu, x_2^\nu), \\
x_1^\nu, x_2^\nu \in \partial\boldsymbol{\Omega}_{b\boldsymbol{\nu}}; \quad 1 \leqslant \nu \leqslant T \\
\iint\limits_{\partial\boldsymbol{\Omega}_{p\boldsymbol{\nu}}} \mathbf{n}_d^\nu(x_1^\nu - \xi_1^\nu, x_2^\nu - \xi_2^\nu)\mathbf{u}_c^\nu(\xi_1^\nu, \xi_2^\nu)d\xi_1^\nu d\xi_2^\nu = \mathbf{t}_c^\nu(x_1^\nu, x_2^\nu), \\
x_1^\nu, x_2^\nu \in \partial\boldsymbol{\Omega}_{d\boldsymbol{\nu}}; \quad 1 \leqslant \nu \leqslant T;
\end{gathered} \tag{15}$$

where $c = d$, $p = d$ for $x_1^\nu, x_2^\nu \in \partial\boldsymbol{\Omega}_{b\boldsymbol{\nu}}$; and $x_1^\nu, x_2^\nu \in \partial\boldsymbol{\Omega}_{b\boldsymbol{\nu}}$; $c = b$, $p = bd$ for $x_1^\nu, x_2^\nu \in \partial\boldsymbol{\Omega}_{bd\boldsymbol{\nu}}$. The modern topological method of solving this problem is presented in [7].

4 Conclusion

Inverting the integral equations and substituting their accurate or approximate solutions in the integral representations of the solutions to the boundary problems, we have

$$\mathbf{u}_c^\nu = \mathbf{F}_3^{-1}(\mathbf{K}_c(\alpha_1^\nu, \alpha_2^{\boldsymbol{\nu}}, \alpha_3^{\boldsymbol{\nu}}))^{-1} \iint\limits_{\partial\boldsymbol{\Omega}_c} \boldsymbol{\omega}_c^\nu, \quad c = b,\ d.$$

Further, one can use the methods described in [1, 2], which make it possible to analyze or calculate two-dimensional integrals.

Acknowledgements

This work was supported in part by the Russian Foundation for Basic Research grants projects No: (14-08-00404), (13-01-12003)-Гœ, (13-01-96502), (13-01-96505), (13-01-96508), (13-01-96509), (15-01-01379), (15-08-01377, project NSh-1245.2014.1, programs of the Presidium of the Russian Academy of Sciences No. 3 and No. 43.

References

[1] V.A. Babeshko, O.V. Evdokimova, and O.M. Babeshko, On the differential Factorization Method in Problems for Continuous Media, Dokl. Phys. **53**, 371 (2008) [Dokl. Akad. Nauk **421**, 37 (2008)].

[2] V.A. Babeshko, O.M. Babeshko, and O.V. Evdokimova, On the differential Factorization Method in Static Problems, Dokl. Phys. **53**, 639 (2008) [Dokl. Akad. Nauk **423** (6), 748 (2008)].

[3] O.V. Evdokimova, O.M. Babeshko, and V.A. Babeshko, On the differential Factorization Method in Inhomogenious Problems Dokl. Math. **77**, 140 (2008) [Dokl. Akad. Nauk **418**, 321 (2008)].

[4] V.A. Babeshko, O.V. Evdokimova, and, O.M. Babeshko, Differential Factorization Method in Block Structures and Nanostructures Dokl. Math. **76**, 614 (2007) [Dokl. Akad. Nauk **415**, 596 (2007)].

[5] V.A. Babeshko, B.V. Glushkov, and N.F. Zinchenko, *Dynamics of Inhomogenious Linearly Elastic Media* (Nauka, Moscow, 1979) [in Russian].

[6] I.I. Vorovich, and V.A. Basbeshko, *Mixed Dynamic Problems of Elasticity Theory in Unbounded Domains* (Nauka, Moscow, 1979) [in Russian].

[7] Babeshko V.A., Evdokimova O.V., and Babeshko O.M. Topological Method of Solving Boundary-Value Problem and Block Elements, Dokl. Phys. **58**, 4 (2013).

Vladimir A. Babeshko, Olga M. Babeshko, Igor B. Gladskoi, Elena M. Gorshkova, Kuban State University, Krasnodar, 350040, Stavropolskiya st. 149, Russia
Vladimir A. Babeshko, Olga V. Evdokimova, Southern Scientific Center RAS, Rostov-on-Don, 344006, Chekhov st., 41, Russia

Nonlinear Vibration Effects in Machinery, Fluid and Combined Media: Development of a Common Research Approach, New Results

I.I.Blekhman, L.I. Blekhman, L.A. Vaisberg, V.B. Vasilkov, K.S. Ivanov, K.S.Yakimova
iliya.i.blekhman@gmail.com

Abstract

New vibration machines and technologies are based on the peculiar effects occurring at high speed impacts on non-linear mechanical systems. Vibrational mechanics and one of its branches, vibrational rheology, represent the general approach to the study of these effects. The report provides an overview of studies covering this type of effects and details the recently discovered new effects and results, which include the phenomenon of vibrational diffusion separation of granular materials, specific behavior of oscillating objects near the interface of two media and increased buoyancy, suspension of particles in near-wall turbulent flows. The new theoretical developments include the expansion of the range of applicability of the vibrational mechanics approach and the method of direct separation of motions; the application of this method to studies of vibrational effects on any dynamic systems, in particular in the field of physics, chemistry and biophysics; and the development of new screening models.

1 Introduction

Vibration acting on nonlinear systems induces certain motion that represents a superposition of rapid oscillations on a slow motion. This slow motion is usually of the main interest and may be described by equations that differ significantly from the original equations of mechanics by the presence of additional forces, which, according to P.L. Kapitsa, are called vibrational forces [1-3]. These forces are the ones inducing the effects that often seem paradoxical, such as the emergence and disappearance of equilibrium positions of systems, changes in stability characteristics of equilibrium positions and motions, changes in rheological properties of materials in relation to slow or static effects, and the apparent changes in the magnitude and direction of the force of gravity. Non-conservative systems "on the average" tend to become potential and "non-smooth" systems acquire a certain "smoothness".

2 Main Areas of Research

The vibrational mechanics approach has been applied to the following classes of problems [1-6]: 1. The effects of vibration on machinery and machine parts (pendulum and pendulum systems), vibration-induced rotation and termination of rotation under vibration, synchronization of rotors; 2. The effects of vibration on industrial processes; 3. Vibrorheology, the effects of vibration on granular materials, fluids, gas-fluid systems, suspensions, dry friction systems; 4. Problems related to the creation of dynamic vibration materials. These studies laid the basis for the development of a number of new vibration processes and vibrational machines.

Figure 1: Photograph of the experimental setup designed to study the classification of granular materials.

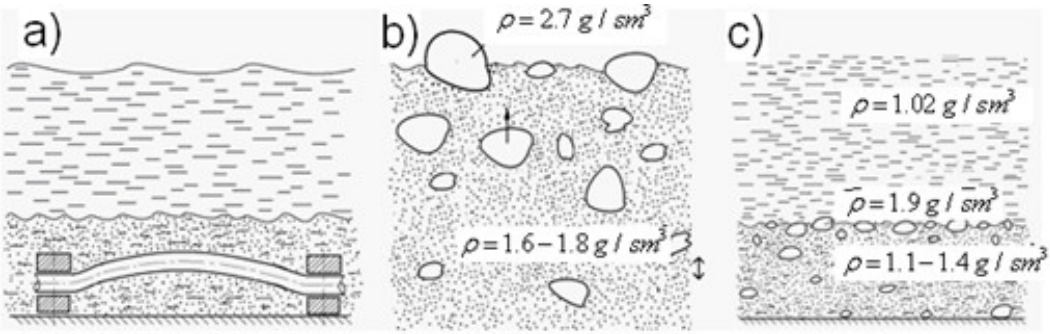

Figure 2: Paradoxical effects under vibration: a) buckling of a pipeline span near the sea bottom, b) buoyancy of boulders in the ground, c) peculiar occurrence of nodules.

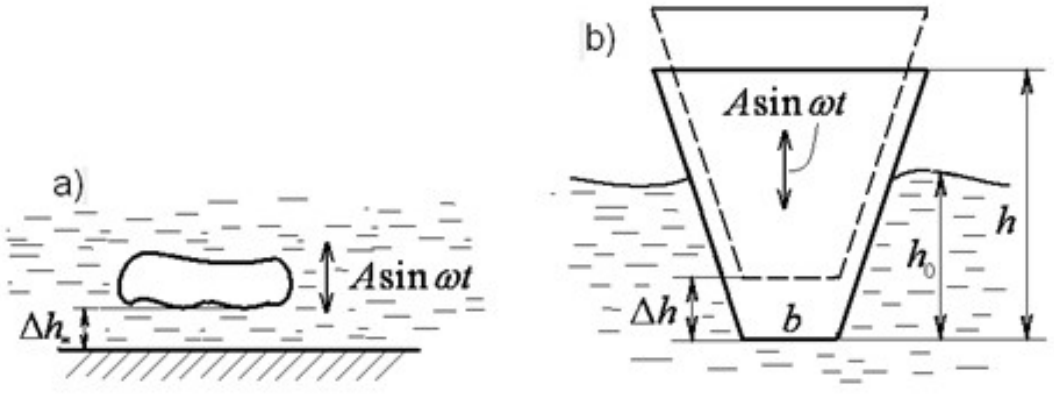

Figure 3: Suspension of vibrating bodies in a fluid: a) suspension of a particle in the bottom fluid flow; b) increased buoyancy of a body with a trapezoidal cross-section.

3 New Results

1) The expanded application of the direct separation of motions in vibrational mechanics [7, 3]. The main results in this field include application of the method for solving systems of equations that do not satisfy the conditions of theorems N.N. Bogolyubov, V.M. Volosov and B.I. Morgunov, and the use of the perturbation method to systems without small parameters.
2) The generalized application of the vibrational mechanics approach to the problems of vibrational effects on any nonlinear dynamic systems (oscillatory strobodynamics). Finding of solutions for a number of problems of such effects on physical, chemical and biological systems [3].
3) The discovery and research of the effect of vibrational diffusion segregation of granular materials [8]. The effect implies that in a granular medium consisting of particles of different sizes, at a sufficiently intense vibration , where A is the amplitude, is the vibration frequency, g is the acceleration of gravity), particles of separate fractions move in the direction opposite to the gradient of concentration of these fractions. In other words, the concentrations of particle fractions tend to equalize, subject to the system of equations similar to nonlinear diffusion equations. This may be illustrated by the following experiment (Fig. 1).
A cylindrical container with circular holes along its side surface of 8 mm in diameter is filled with a mixture of grains of peas ($d2 \approx 6$ mm) and hazelnuts ($d2 \approx 15$ mm) in proportion of 1: 2 by weight. The vessel was subjected to vertical vibration with amplitude A = 2.2 mm and frequency $\omega = 220s^{-1}$ (35 Hz), which corresponds to $A\omega^2/g = 10.8$. During the first few seconds, over 90% of the peas were leaving the vessel, ejected from the holes; after 60 seconds all peas were almost completely gone. This result is explained by the above-mentioned effect of diffusion of peas intensely moving towards the vessel walls where its concentration is less due to its screening through the holes.
The results obtained have already been used to create highly efficient vibrating separators [9].
4) Mathematical models were suggested for abnormal segregation when under the influence of vibration the process of separation of the components of a granular mixture occurs in the direction of increasing the potential energy of the system (the wedge effect, the Brazil nut effect [3, 8]). These allowed to explain and describe such phenomena as floating boulders

in sandy soil under the influence of seismic vibrations, abnormal occurrence of nodules, and buckling of pipeline sections near the sea bottom [10], Fig. 2.
5) The behavior of the oscillating bodies near the boundary of two media [10] was studied. As a result, an explanation and mathematical description were obtained for the effect of suspension of solids in near-wall turbulent flows (hydraulic transportation, Fig. 3a), as well as for the effect of increased buoyancy of oscillating bodies. For example, a body with a trapezoidal cross-section (Fig. 3b) rises above the equilibrium level in the absence of oscillations by the value of

$$\Delta h = \frac{1}{2}\eta^2 \frac{A^2}{b+2h_0\eta}, \qquad \eta = \frac{a-b}{2h}$$

where A is the oscillation amplitude.
The formula takes into account only the conservative (quasi-elastic) component of the additional buoyancy force. A more complex dependence is observed when considering the dissipative forces that also contribute to Δh.
6) New models were developed for the vibratory screening process [11].
7) The effect of vibrational crossing of potential barriers. Detailed studies were conducted for systems in which the barriers are caused by the presence of the gravity force ("vibration against gravity"). These systems have a variety of important technical applications. Two simple basic models of corresponding devices were built.

Acknowledgements

The studies under subparagraphs 1), 2) and 7) in paragraph 3 were supported by the Russian Science Foundation (grant no. 14-19-01190), the work under subparagraphs 3) and 6) was supported by the Ministry of Education (grant no. 14.576.21.0015), and the research under subparagraphs 4) and 5) was supported by the Russian Foundation for Basic Research (grants вhЦ 14-08-00681 and вhЦ 13-08-01201 respectively).

References

[1] Blekhman I.I. Vibrational Mechanics. (Nonlinear Dynamic Effects, General Approach, Applications). вЃY Singapore et al: вЃY World Scientific Publishing Co., 2000. вЃY 510 p.

[2] Selected Topics in Vibrational Mechanics. (Edited by I. Blekhman). - Singapore at al.: World Scientific, 2004, 409 p.

[3] I.I. Blekhman. Theory of Vibration Processes and Devices. Vibrational Mechanics and Vibration Technology. вЃY St. Petersburg: Ore and Metals Publishing House Nauka, 2013, 640 p.

[4] J.J. Thomsen. Vibration and Stability.- Berlin, Heidelberg: Springer, 2003.

[5] A. Fidlin. Nonlinear Oscillation in Mechanical Engineering.- Berlin, Heidelberg: Springer, 2006.

[6] V.B. Vasilkov. Influence of Vibration on Nonlinear Effects in Mechanical Systems. Synopsis of Doctor of Engineering. -St. Petersburg, 2009. http://www.ipme.ru/ipme/edu/diss/vasilkov.pdf (in Russian).

[7] V.S. Sorokin. On the Unlimited Gain of a Nonlinear Parametric Amplifer.- Mechanics Research Communications, 2014, v. 62, pp. 111-116.

[8] I.I. Blekhman, L.I. Blekhman, L.A. Vaisberg, V.B. Vasilkov, K.S. Yakimova, Vibrational Segregation- Simulation, Experiment and Application to Create new Classifying Machines // Proc. of the XLII Summer School-Conference (APM - 2014). St. Petersburg, June 30-July 5, 2014. St. Petersburg, IPME RAS, 2014, pp. 247-257.

[9] L.I. Blekhman, L.A. Vaisberg, V.B. Vasilkov, K.S. Ivanov, RF Patent 139262 (LM). Vibrating Screen. - Published April 10, 2014, Bulletin no. 10.

[10] L.I. Blekhman, Oscillation-induced suspension of solids in fluid and loose media // Bulletin of PNRPU, Mekhanika, Perm: Publishing House of the Perm State Technical University, 2013, no. 2. pp. 52-83 (in Russian).

[11] I.I. Blekhman, L.I. Blekhman, L.A. Vaisberg, K.S. Ivanov, Revisiting the Models of Vibration Screening Process // JVE Intern. LTD. Vibroengineering PROCEDIA. 2014, v.3, pp. 169-174.)

I.I. Blekhman, V.O., Bolshoy pr. 61, St.Petersburg, 199178, Russia

Finite-element modelling of 3d oblique ultrasonically assisted turning of TI-6AL-4V

Laurence A. Coles, Anish Roy and Vadim V. Silberschmidt
L.Coles@lboro.ac.uk & A.Roy3@lboro.ac.uk &
V.Silberschmidt@lboro.ac.uk

Abstract

This study outlines the development of a new three-dimensional FE modelling approach used to study the conventional and ultrasonically assisted oblique turning processes of titanium (Ti-6Al-4V) alloy. Numerical simulations with the models demonstrated that for the chosen machining parameters, the ultrasonically assisted turning (UAT) process resulted in a 20% reduction in the tangential cutting force compared to that in the conventional turning (CT) process. The new approach enables the more accurate prediction of the CT and UAT processes, while allowing the complete control of the machining parameters within the 'real-time' turning simulation. This allows for the prediction of the cutting force, resultant and residual stresses and chip formation.

1 Introduction

Hybrid machining processes have gained sufficient prominence in the manufacturing industry. Ultrasonically assisted machining (UAM) is a hybrid machining technique, in which high-frequency, low-amplitude vibration is superimposed on the cutting tool movement, resulting in several well-documented advantages. Recent studies have seen the development of the ultrasonically assisted turning (UAT) process in which the resultant cutting forces show substantial reduction (in some cases $>70\%$), as well as improved surface finish amongst other advantages [1, 2, 3, 4]. The UAM process has shown advantages when applied to the drilling of composite materials [5].

Direct experimental studies of machining processes are expensive and time-consuming, especially when there is a wide range of machining parameters that affect the complex hybrid thermo-mechanical machining process. In recent years, the use of mathematical simulations and, in particular, finite-element (FE) techniques has gained prominence in the research community; from the application of Smooth-Particle Hydrodynamics (SPH) in the turning of metals [6, 7], to the 2D and 3D FE modelling of both the conventional and ultrasonically assisted turning of many advanced alloys [8, 9, 10]. These modelling approaches are typically restricted to simulations of orthogonal machining, which is not a true representation of the actual cutting process, typically referred to as *oblique machining*.

This study is a part of on-going research at the Wolfson School of Mechanical and Manufacturing Engineering, Loughborough University, UK, on multi-scale FE modelling of

advanced machining processes. This paper outlines the current progress made on the development of a 'real-time' FE models of both the CT and UAT processes.

2 Finite-element model of turning

A schematic of an oblique turning is shown in Figure 1, with the cutting tool geometry taken from [2]. A FE model of the cutting in CT and UAT is shown in Figure 2 with the cutting parameters listed in Table **??**. The modelled domain formed a 5° section of the work piece together with the previous tool path (including the 0.1 mm/rev feed rate off-set). The work piece was fixed with respect to the X-axis (axial direction) and rotated towards the cutting tool. For CT the cutting tool was fixed in the Y (radial) and Z (tangential) directions, with the tool feed rate applied in the X (axial) direction. In UAT, ultrasonic vibration was applied in the Z (tangential) direction as shown in Figure 2. The cutting tool was modelled as a rigid body. This modelling approach allows for the full 3D oblique modelling of the CT and UAT process. This model was develop using the commercial FE software SIMULIA Abaqus/Explicit 6.14.

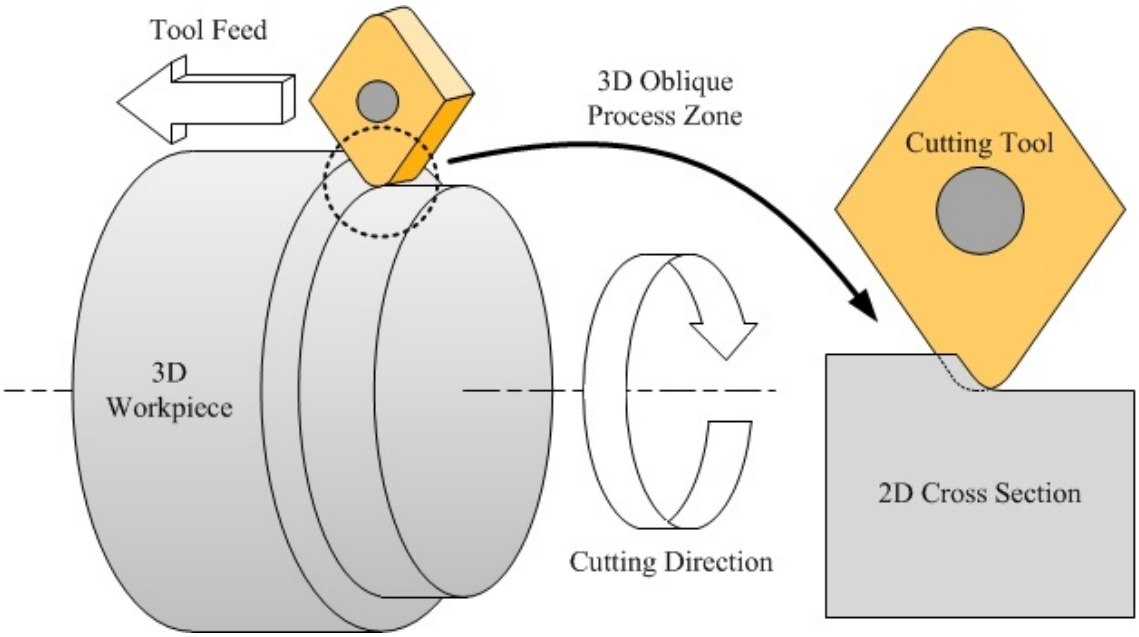

Figure 1: True 3D oblique curved cutting path turning process

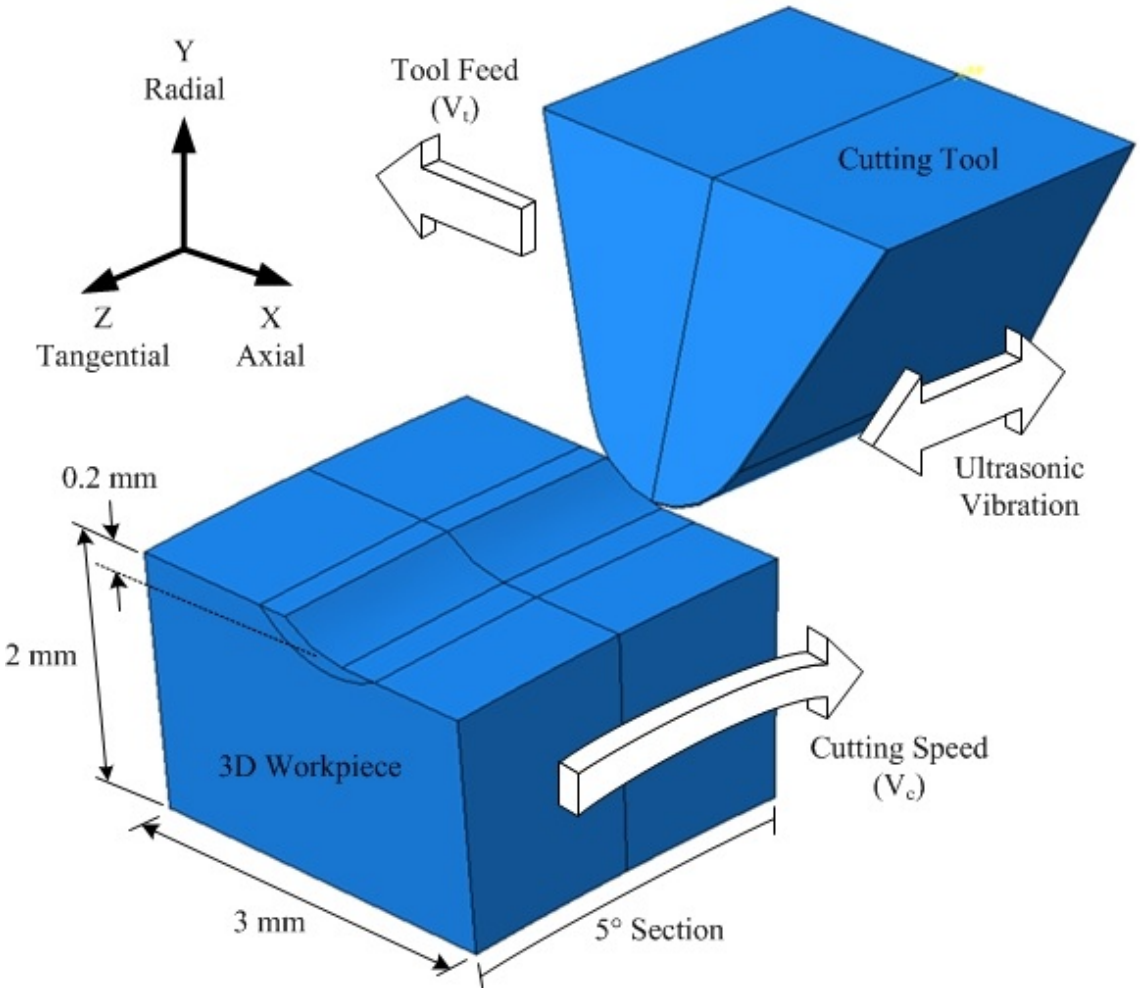

Figure 2: 3D geometry of oblique curved cutting path modelling

Table 1: 3D cutting parameters used in FE Model

Parameter	**Unit**	**Value**
Cutting speed (Surface), V_f	m/min	20
Tool feed, V_t	mm/rev	0.1
Depth of cut	mm	0.2
Ultrasonic frequency, f	Hz	20,000
Ultrasonic amplitude (peak to peak), a	μm	8

The workpiece material was Ti-6Al-4V, with it's behaviour described using a nonlinear temperature- and strain-rate-sensitive Johnson-Cook (JC) material model using parameters A, B, n, C, m, T_m along with other parameters as mentioned in [11] and can be found in Table **??**.
The primary equation of the JC model is

$$\sigma_y = [A + B(\epsilon_p)^n][1 + C\ln(\dot{\epsilon}_p^*)][1 - (T^*)^m)], \tag{1}$$

where

$$\dot{\epsilon}_p^* = \frac{\dot{\epsilon}_p}{\dot{\epsilon}_{p0}}, \qquad T^* = \frac{(T - T_0)}{(T_m - T_0)}. \tag{2}$$

Here, ϵ_p is the effective plastic strain, $\dot{\epsilon}_p$ and $\dot{\epsilon}_{p0}$ are the plastic strain rate and effective plastic strain rate used for the calibration of the model respectively, T and T_0 are the current and reference temperatures respectively.
The workpiece was discretised with a refined mesh around the cutting process zone. For both CT and UAT models, 686565 linear hexahedral coupled temperature-displacement elements (C3D8RT) were used. The cutting tool was meshed using quadratic tetrahedral elements (C3D10M). Contact between the cutting tool and the workpiece was defined as a hard contact for its normal behaviour, with a coefficient of friction of 0.3384 [12] along with a shear stress limit.

Table 2: Material parameters for Ti-6Al-4V

Material parameter	**Symbol (Unit)**	**Value**
Density	$\rho \quad (kg/m^3)$	4428
Elastic modulus	$E \quad (GPa)$	113.8
Poisson's ratio	ν	0.31
JC yield strength	$A \quad (MPa)$	1098
JC hardening coefficient	$B \quad (MPa)$	1092
JC strain hardening exponent	n	0.93
JC strain rate constant	C	0.014
JC softening exponent	m	1.1
Melting temperature	$T_m \quad (K)$	1878
Transition temperature	$T_g \quad (K)$	1163
JC damage constant	d_1	-0.09
JC damage constant	d_2	0.27
JC damage constant	d_3	0.48
JC damage constant	d_4	0.014
JC damage constant	d_5	3.87
Specific heat	$c \quad (J/K)$	560
Heat fraction	α_0	0.9

Given the large deformations observed within the cutting process zone, arbitrary lagrangian eulerian (ALE) re-meshing was employed to allow for increased plastic flow of the material and formation of the chip. ALE re-meshing parameters were calibrated based on the cutting speed and minimum element size. Mass scaling was used to improve computational efficiency for both models. The total modelled machining time was 0.8 ms, which was sufficient for achieving consistent cutting forces.

3 Results and Discussion

The developed fully 3D approach allows the observation of the tangential and axial cutting forces with increased accuracy, the radial forces are still challenging to observe given the

discretised nature of the FE method. At this initial stage, the tangential cutting forces (Z direction) were monitored, with the average force observed from the CT model reaching 50.9 N and for UAT 40.3 N. As a result, it can be shown that the additional ultrasonic vibration leads to an approximate 20% reduction of the tangential cutting forces, which is within the range seen in the previous study. It was found with these models that for the defined turning parameters, the UAT peak cutting force was similar to that of CT but the ultrasonic vibration allowed the tool to dis-engage form the workpiece (decreasing the force) before subsequent re-engaging, resulting in the lower average cutting force.

With reference to Figure 3 it can be seen that stress distributions within the local process zone for both the CT and UAT processes are very similar, showing the shear failure region as expected; still, but shows no significant qualitative differences can be observed. Examining the peak stresses in the process zone for each process, it can be seen that the CT process produces a stress of approximately 1730 MPa and the UAT process produces 1577 MPa and 1728 MPa for maximum retraction and penetration of the ultrasonic cycle, respectively. This modelling approach can then also be used to model the residual stresses induced by CT or UAT.

When examining the initial chip formation in both processes, it can been seen that both chips begin to form full 3D helical shape as commonly observed as a result of real oblique turning. Closer examination suggests that the radii of both chips are similar, but without a longer simulated time the true chip formation and length before breakage cannot be assessed properly. Both the CT and UAT models took approximately 48 hours of computational time to run across 12 cores, demonstrating that the approach remains suitably efficient at this initial stage.

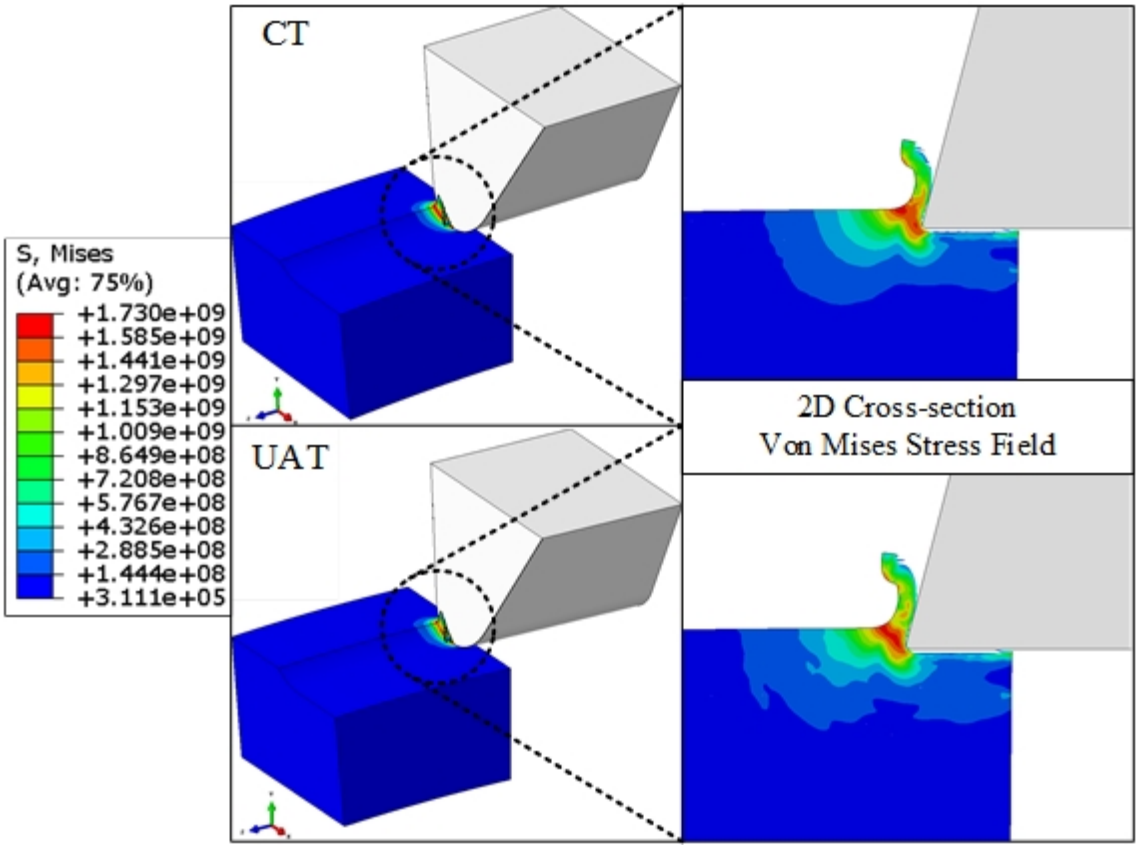

Figure 3: Comparison between von Mises stress fields within process zone for both CT and UAT

4 Conclusions

This paper presents a new modelling approach for simulating both conventional and ultrasonically assisted turning of a titanium alloy. It allows for the complete control of the machining parameters within the simulation, while modelling the 'real-time' turning and workpiece deformation. As a result, this allows for the prediction of the cutting force as well as an assessment of the resultant and residual stresses and chip formation. The following conclusion are made:

1. It can been seen that for the chosen machining parameters the UAT process ofters a 20% reduction in the average tangential cutting force compared to that in the CT process, as expected and found in the literature.

2. This new modelling approach produces a more accurate prediction of the CT and UAT processes taking into account their important 3D cutting geometry which, in turn, enables a greater understanding of the effect of the machining parameters on both processes.

3. The modelling approach shall be developed and taken forward to further investigate and characterisate both processes in more detail, while also make vital comparisons to experimental studies.

5 Acknowledgement

AR and VVS gratefully acknowledges the funding from the Engineering and Physical Sciences Research Council (UK) through grant EP/K028316/1 and Department of Science and Technology (India), project MAST.

References

[1] N. Ahmed, A.V. Mitrofanov, V.I. Babitsky, V.V. Silberschmidt, Analysis of forces in ultrasonically assisted turning. Journal of Sound and Vibration, 2007. 308: p. 845-854.

[2] A. Maurotto, R. Muhammad, A. Roy, V.V. Silberschmidt, Enhanced ultrasonically assisted turning of a β-titanium alloy, Ultrasonics, 2013. 53(7): p. 1242-1250.

[3] R. Muhammad, M.S. Hussain, A. Maurotto, C. Siemers, A. Roy, V.V. Silberschmidt, Analysis of a free machining $\alpha+\beta$ titanium alloy using conventional and ultrasonically assisted turning, Journal of Materials Processing Technology, 2014. 214(4): p. 906-915.

[4] R. Muhammad, A. Maurotto, M. Demiral, A. Roy, V.V. Silberschmidt, Thermally enhanced ultrasonically assisted machining of Ti alloy, CIRP Journal of Manufacturing Science and Technology, 2014. 7(2): p. 159-167.

[5] F. Makhdum, V. A. Phadnis, A. Roy, V. V. Silberschmidt, Effect of ultrasonically-assisted drilling on carbon-fibre-reinforced plastics, Journal of Sound and Vibration, 2014. 333(23): p. 5939-5952.

[6] A. Zahedi, S. Li, A. Roy, V. Babitsky, V. V. Silberschmidt, Application of Smooth-Particle Hydrodynamics in metal machining, Journal of Physics: Conference Series, 2012. 382(1): 012017

[7] A. Zahedi, M. Demiral, A. Roy, V. V. Silberschmidt, FE/SPH modelling of orthogonal micro-machining of f.c.c. single crystal, Computational Materials Science, 2013. 78: p. 104-109.

[8] A.V. Mitrofanov, V.I., Babitsky, V.V. Silberschmidt, Thermomechanical finite element simulations of ultrasonically assisted turning. Computational Materials Science, 2005. 32: p. 463-471.

[9] N. Ahmed, A.V., Mitrofanov, V.I. Babitsky, V.V. Silberschmidt, 3D finite element analysis of ultrasonically assisted turning. Computational Materials Science, 2007. 39: p. 149-154.

[10] R. Muhammad, N. Ahmed, A. Roy, V.V. Silberschmidt, Numerical modelling of vibration-assisted turning of Ti-15333. Procedia CIRP, 2012. 1(0): p. 347-352.

[11] X. Wang, J. Shi, Validation of Johnson-Cook plasticity and damage model using impact experiment, International Journal of Impact Engineering, 2013. 60: p. 67-75.

[12] D. Smolenicki, J. Boos, F. Kuster, H. Roelofs, C.F. Wyen, In-process measurement of friction coefficient in orthogonal cutting, CIRP Annals - Manufacturing Technology, 2014. 63: p. 97-100

Laurence A. Coles, Anish Roy and Vadim V. Silberschmidt, Loughborough University, Wolfson School of Mechanical and Manufacturing Engineering, Loughborough University, Leicestershire, LE11 3TU, UK

The impact of nanoparticles on matrix properties in PMCS

Andrey I. Dmitriev, Werner Österle, Bernd Wetzel, Ga Zhang
dmitr@ispms.tsc.ru

Abstract

The method of movable cellular automata (MCA) was applied to simulate the stress-strain behaviour of a nanocomposite consisting of an epoxy matrix and 5 vol.% silica nanoparticles and for samples of pure components. The size of the elements used for modelling was fixed at 10 nm, corresponding approximately to the diameter of the filler particles. Modelling results were compared with tensile test results of both, pure epoxy as well as the epoxy-5 vol.% SiO_2 composite. Since assuming bulk properties of the two constituents did not yield satisfactory results, slight modifications of the nanoparticle response functions and nanostructures were tested numerically. Finally, slightly increased strength properties of both constituents had to be taken into account for obtaining good correlation between experimental and modelling results. The tendency of model parameter adjustments corroborate expected changes of composite constituents compared to their respective bulk structures.

1 Introduction

The effect of considerably improving of mechanical as well as tribological properties of conventional polymer matrix composites (PMCs) by adding of silica nanoparticles was shown in [1, 2]. The explanation of this influence seems to be quite clear. It is expectable that YoungвЂ™s modulus and strength increases if the epoxy matrix is filled with particles which are much harder than the polymer. On the other hand, it is not easy to estimate this effect quantitatively, especially if the concentration of SNP volume fractions is less than 10% (sometimes no more than 1%) and the particles are very small. The latter circumstance rules out an efficiency of finite element modelling (FEM). In the paper a method of discrete approach - movable cellular automata (MCA) method [3] was used to simulate the mechanical behavior of multi-component nanostructured samples. Within this approach a modelled composite is considered as linked nanoparticles bearing the properties of the different constituents. By introducing criteria for link-breaking and relinking, fracture mechanisms and granular flow can be simulated on the nanoscopic scale. The MCA method have no restriction of particles size, therefore it is especially suitable for modelling the mechanical behaviour of nanocomposites. In the paper the most significant results of our recent research works is presented. More detailed information is summarized in [4].
Within the MCA model the mechanical properties of the nanoconstituents are defined by the corresponding response functions in the form of stress-strain curves. Usually such data

are available only for bulk materials. It is not really clear yet, to what extend bulk properties can be used to characterize nanoparticles. Although there are innumerable papers describing the size, shape and surface functionalities of silica nanoparticles, only very few information on the mechanical properties of such nano-sized objects is available in the literature. Yan et al. have shown that it is in principle possible to determine the elastic modulus of soft and hard nanoparticles embedded in a polymeric matrix by nanoindentation in combination with finite element modelling [5]. Basu et al. have shown that not only elastic properties, but also stress-strain curves can be derived from nanoindentation tests [6]. A great advantage of modelling is that we can vary material parameters hypothetically in a wide range. Thus it is possible to assess the impact of material properties and volume fractions of constituents of a composite material by a series of parameter studies in a theoretical way. The objective of this paper was to find the right range of material parameters in order to reproduce experimental stress stain curves with our model.

2 Experimental data

The raw materials used for preparation of the EP + 5% SiO_2 composite were: a standard diglycidil ether of bisphenol A (DBEBA) offered by DOW as DER331, a cycloaliphatic amine hardener HY 2954 from Huntsman and a colloidal silica masterbatch with a concentration of 40 mass % and a nominal particle diameter of 20 nm in DGBEBA offered as Nanopox F400 from Evonik. A thin slice was prepared from the EP + 5% SiO_2 composite by microtomy and investigated in a Scanning Transmission Electron Microscope (STEM) of type JEOL 2200FS.
Dumbbell-shaped specimens, 4 mm thick, were machined from casted plates and tested according to DIN EN ISO 527 using universal testing machine (Zwick 1474) at room temperature and at a crosshead speed of 0.5 mm/min. The displacement of each specimen during tension was accurately measured by an extensometer with an initial gage length of 20 mm.

3 Numerical model

3.1 A general formalism

The MCA method is based on conventional concept of cellular automata [3, 7]. It is an extension of cellular automaton approach achieved by incorporating some basic postulates and relations of particle-related methods. The movable cellular automaton is an object of finite size, possessing translational and rotational degrees of freedom. Interaction between automata is defined by normal (acting along the line connecting the mass centers) and tangential forces, each of which is the sum of the corresponding potential and the dissipative component. The principles of writing the equation of motion for a system of movable cellular automata and prescribing interactions between them are described in [7].

3.2 Model description

The modelling setup was designed as shown schematically in figure 1a. Two types of the sample were considered: homogeneous sample like pure epoxy and nanocomposite on the basis of epoxy as a polymer matrix filled with silica nanoparticles. Their assumed mechanical properties at room temperature, which are needed to define their stress-strain

behavior, are depicted in figure 1b. Actually, the stress-strain curve for bulk silica was derived from nanoindentation measurements [6], whereas the corresponding dependence of the epoxy matrix was derived experimentally. The significant input parameters to define the mechanical properties of each material are: YoungвЂ™s modulus, Poisson ratio, elastic limit, yield strength, fracture strength, strain at yield strength and strain at fracture.

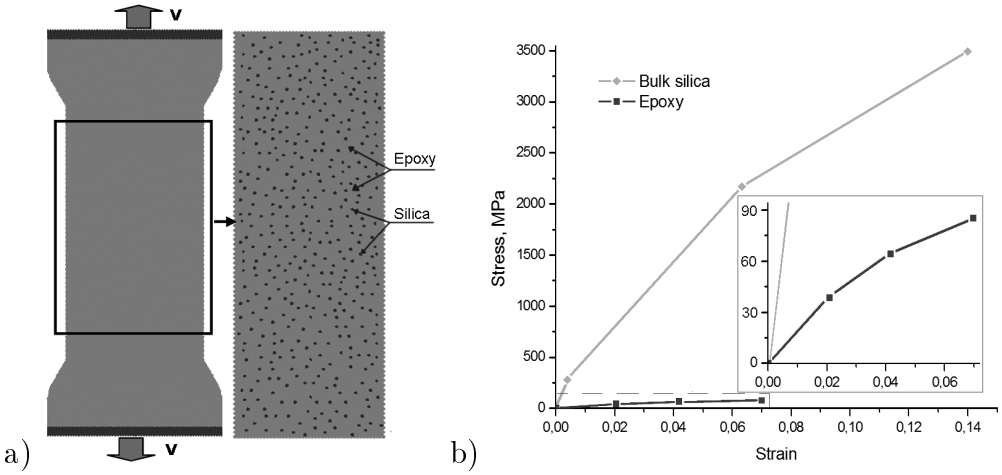

Figure 1: The initial structure of modeled composite and a loading scheme (a); the model response functions of the constitutive elements (b).

The automata size was adjusted to 10 nm according to the smallest size of silica nanoparticles, which are currently used experimentally for polymer matrix composites. A constant velocity (V) equal to 0.2 m/s was applied on all automata of the top and bottom layers of the sample in opposite directions. The geometry of the sample was: 15 μm along loading direction and 3 μm in transvers direction. Thus, the loading conditions similar to uniaxial tension test was reproduced for a small fragment of the real sample. For the composite sample the concentration of silica inclusions embedded in epoxy was kept constant at 5 vol.%. The distribution of silica inclusions in modeled setup was adjusted in a way to achieve best similarity with the real nanostructure. The total number of particles was more than 8000.

4 Results of modelling

4.1 Modelling the stress-strain behavior of pure material

First the uniaxial tensile test of the sample in which the model parameters of all particles were corresponding to the mechanical properties of the pure epoxy was investigated. Verification of the parameters was carried out by comparing the resulting loading diagram with the available experimental data for the similar sample. Figure 2a shows the results of calculations for the homogeneous sample of pure epoxy. The curve marked by filled circles is the experimental stress-strain dependency which was also used as a target response function for defining the behaviour of each element in the setup. Curve no. 1 depicts the stress-strain behaviour resulting from a modelling effort based exactly on this assumption. The resulting curve has the same fracture strain but lower ultimate tensile strength. Curves no. 2 and 3 correspond to the modeled samples in which slightly increased strength properties had to be attributed to the nano-scale elements of the pure epoxy in

order to obtain the desired fit with the experimental data. This can be interpreted in terms of a size effect of mechanical properties, i.e. we should assume higher elastic, yield and strength properties for nanoparticles, compared to bulk properties of the same material. In fact, increased YoungвЂ™s modulus and fracture strength was observed experimentally for silicon as well as silica nanowires [8].
From figure 2b it is clear that the character of the main crack formed when the deformation is about 7% is different from the fracture pattern of the real sample (figure 2c). This distinction can be caused due to the two-dimensional formulation of the numerical model or by the presence of imperfections such as voids or microcracks which are not considered in the model.

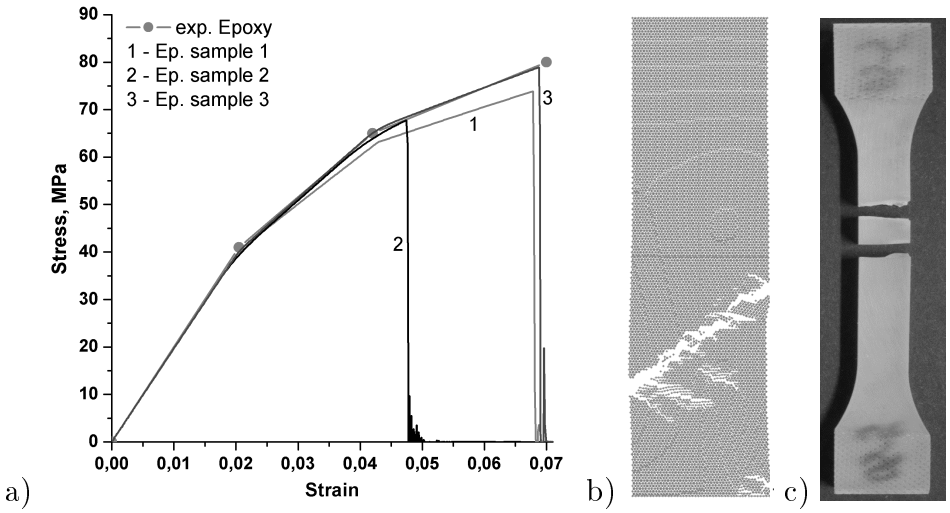

Figure 2: Results of calculation for the pure epoxy sample: resulting loading diagram (a), modeled (b) (sample 3 on fig. 2a) and a real (c) sample after generation of crack.

Similar calculations of the uniaxial tensile tests were carried out for the homogeneous samples in which the model parameters of the response functions for each element were corresponding to the properties of silica nanoparticles. The resulting values for both components were used to generate the composite sample based on the polymer matrix, as described in the next section.

4.2 Modelling the stress-strain behavior of the composite

On the next stage of the investigation the uniaxial tensile test for a composite sample consisting of epoxy matrix filled with 5 vol.% silica nanoparticles was simulated. An attempt to generate a sample, using the previously fitted model parameters of the response functions for both constituents, did not give the expected result. Due to the introduction of the silica nanoparticles the resulting curve shows an increase of stiffness of the composite sample within $7-8\%$ in comparison with the pure epoxy sample (curve no.1 in figure 3a), while the experimental curve corresponds to an increase in stiffness of the composite samples over 20% (filled diamond symbols in figure 3a). At the same time the modeled composite sample (curve no. 1) demonstrates very low fracture strain which can be interpreted as weak adhesion properties between matrix and hard inclusions.
Attempting to achieve a better fit to experimental results, the procedure of the adhesive properties modification at the interface between soft matrix and rigid inclusion was used. For this purpose the parameter which corresponds to the von Mises fracture criterion and

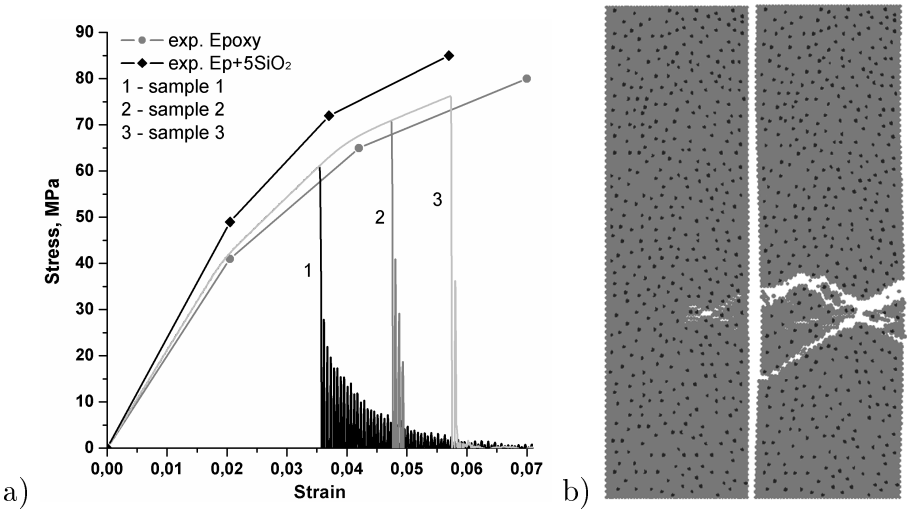

Figure 3: Results of calculation for the composite sample: resulting loading diagrams (a), two consecutive snapshots of the structure evolution of the modeled sample 3 during a generation of the main crack (b).

controls the conditions of the linked to unlinked state transition in the pair of elements of two materials was increased. Other curves depicted in the figure 3a show that the increasing of fracture criterion up to 98 MPa (curve of the sample 2) and 108 MPa (curve of the sample 3) change only the deformation properties of the resulting composite sample, while the slope of the curve is not changed. The resulting structures of the modeled sample 3 at the time of main crack nucleation and propagation are shown in the figure 3b.

4.3 Introduction of additional interface particles

Within the framework of the most recent MCA modelling scheme, the existence of a transition layer can change the response of the system, as shown in [9]. In order to take into account the presence of the interface layer around each hard inclusion additional elements with intermediate mechanical properties defined by the rule described in cited paper were introduced. Briefly the main algorithm to define the certain parameter of intermediate particles can be formulated as

$$P_{new} = P_A C_A + P_B C_B \tag{1}$$

where P_{new} вҐУ calculated value of the selected parameter for the intermediate particle, P_A and P_B вҐУ corresponding value of the same parameter for materials A and B (for, example matrix and inclusion as in our case), C_A and C_B вҐУ corresponding concentration of materials A and B in the intermediate particle. The fracture criteria can be found in the same manner using the rule 1. Simultaneously with the introduction of interphase particles, the absolute number of nanoinclusions was also reduced in order to keep the total volume concentration of silica about the same amount in comparison with the previous calculations. The detail information about the results of calculations with introducing of additional interface particles is given in [4]. In short, the resulting loading diagrams demonstrate that the used technique allowed one to change the angle of slope of the curves in the right direction, while the deformation capacity of the composite sample declined sharply. None of the modifications was capable of describing the experimental curve EP + $5SiO_2$ in respect of predicting the right strain at fracture.

4.4 Modification of the mechanical properties of the matrix

The next step towards defining modelling parameters which should finally enable us to simulate the stress-strain behaviour of the real nanocomposite was a modification of the mechanical properties of the particles of the matrix material, i.e. the epoxy. To go into this direction is justified by the finding that cross-linking of the epoxy molecules is considerably increased in the presence of silica nanoparticles [1, 10].

The result of modifications of epoxy mechanical properties for the satisfying variant of modeled composite sample is shown in Table 3. Numbers in parentheses denote the deviation of given parameter in comparison to the similar bulk epoxy properties. The resulting response function for the considered example is depicted in figure 4.

Table 3: Adjustment of epoxy properties in comparison to bulk one

вГЋђ	bulk(Epoxy)	Epoxy in modeled composite
YoungвГЄs modulus, GPa	2	2
Elastic limit (Y_1), MPa	41	45(10%)
Yield strength (Y_2), MPa	68	73(7%)
Strain at Y_2	0.042	0.042
Ultimate tensile strength (UTS), MPa	88	96(9%)
Ultimate strain	0.075	0.075

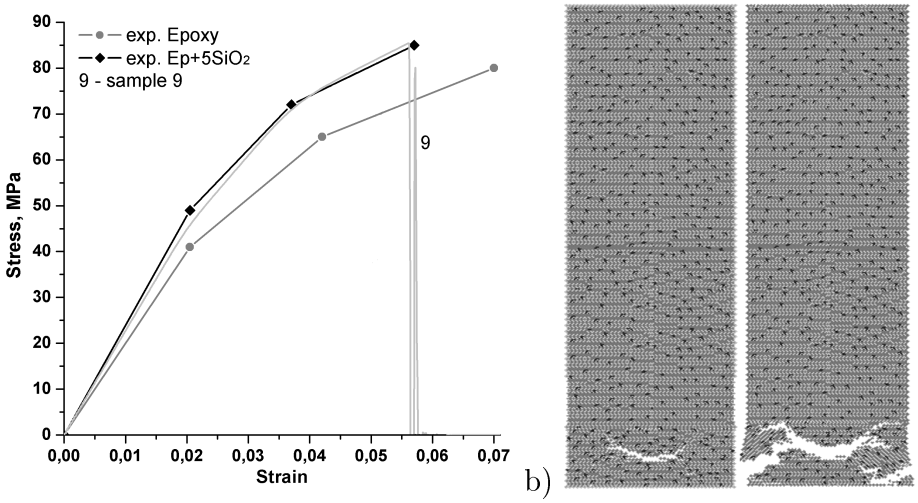

Figure 4: Resulting loading diagrams for the modeled samples (a), two consecutive snapshots of the structure evolution of the modeled sample 9 during a generation of the main crack (b).

5 Conclusion

It has been demonstrated that the MCA-model, has the ability of simulating the tensile properties of a polymer matrix composite filled with silica nanoparticles. Although only a two-dimensional structure was considered, representing a micron-sized flat sample with a thickness corresponding to the element size (10 nm), it was possible to simulate the same stress-strain behaviour and fracture pattern as observed for a macroscopic tensile specimen.
In order to obtain the desired fit between experimental data and modelling results, several modifications of input parameters, which were not a priori obvious, had to be tested numerically. The parameter studies did not only finally provide the best modelling values, but they also shed light on the issue how certain parameters affect the mechanical behaviour of both monolithic as well as composite nanostructures.
The refined response functions obtained by comparison with experimental tensile tests are not only useful for simulating the stress-strain behaviour of a wide range of EP-SiO_2 nanocomposites, but they will also be used in the future for simulating the sliding behaviour of hybrid nanocomposites with exceptional tribological properties [2], as already mentioned in the introduction.

Acknowledgements

This work was supported by RFBR grant no. 14-08-91330a. It is also part of a cooperative research activity funded by the German Research Foundation (DFG) under contract numbers: OS 77/20-1 and ZG 352/3-1.

References

[1] Zhang M.Q., Rong M.Z., Yu S.L., Wetzel B., Friedrich K. Effect of particle surface treatment on the tribological performance of epoxy based nanocomposites, Wear, 253, 1086-1093, 2002.

[2] Zhang G. Structure-tribological property relationship of nanoparticles and short carbon fibers reinforced PEEK hybrid composites, Journal of Polymer Science Part B: Polymer Physics, 48, 801-811, 2010.

[3] Dmitriev A.I., Österle W. Modelling the sliding behavior of tribofilms forming during automotive braking: Impact of loading parameters and property range of constituents, Tribology Letters, 53, 337-351, 2014.

[4] Dmitriev A.I., Häusler I., Österle W., Wetzel B., Zhang G. Modelling of the stress-strain behaviour of an epoxy-based nanocomposite filled with silica nanoparticles, Submitted to Nanoparticle Research, 2015.

[5] Yan W.Y., Pun C.L., Pu Z.H., Simon G.P. Some issues on nanoindentation methods to measure the elastic modulus of particles in composites, Composites Part B, 42, 2093вГY2097, 2011.

[6] Basu S., Moseson A., Barsoum M.W. On the determination of spherical nanoindentation stress-strain curves, Journal of Materials Research, 21, 2628-2637, 2006.

[7] Psakhie S.G., Horie Y., Ostermeyer G.-P. et al. Movable cellular automata method for simulating materials with mesostructure, Theoretical and Applied Fracture Mechanics, 37, 311-334, 2001.

[8] Sundararajan S., Bushan B. Development of AFM-based techniques to measure mechanical properties of nanoscale structures, Sensors and Actuators, A101, 338-351, 2002.

[9] Astafurov S.V., Shilko E.V., Ocharenko V.E. Influence of phase interface properties on mechanical characteristics of metal ceramic composites, Physical Mesomechanics, 17 (4), 282вЃ“291, 2014.

[10] Choi J., Shin H., Yang S., Cho M. The influence of nanoparticle size on the mechanical properties of polymer nanocomposites and the associated interface region: A multiscale approach, Composite Structures, 119, 365вЃ“376, 2015.

Andrey I. Dmitriev, ISPMS SB RAS / TSU, Tomsk Russia
Werner Österle, BAM, Berlin, Germany
Bernd Wetzel, IVW, Kaiserslautern, Germany
Ga Zang, IVW, Kaiserslautern, Germany

Molecular dynamics study of the local frictional contact

Andrey I. Dmitriev, Anton Yu. Nikonov
dmitr@ispms.tsc.ru

Abstract

In the paper simulation of the behavior of copper crystallite under local frictional contact was carried out using the method of molecular dynamics. Loading was realized by the movement of hard indenter along the surface of the sample. Following configurations were considered: initially defect-free crystallite, structure with a symmetrical tilt grain boundary $\Sigma 5$. Influence of the initial structure on the behavior of the crystallite under loading was analyzed. Nucleation of nanofragmentation of the surface layer was displayed. Atomic mechanisms of a process of nanofragmentation were investigated. A detailed analysis of the character of the atomic displacements in emerging blocks shown that they have a rotational nature. Further calculations showed that the amount of disorientation of formed nanoblocks along different directions is not more than 2 degrees. Despite what two limiting cases of arrangement grain boundaries in the material has been studied only, it can be assumed that the behavior of crystallites with defect disposed at an arbitrary angle relative to the free surface is a combination of processes that occur in these cases.

1 Introduction

In many modern applications the state of the surface layer, its hardness, wear resistance, mechanical behavior, processing quality and other characteristics are largely determine the performance properties of the various parts of machines. Therefore, the problem of studying the physical and mechanical properties of the surface and improve its performance by applying various treatment methods to pay close attention [1]. Despite the constant improvement of methods of experimental study, especially the evolution of structure in which these changes occur, are still poorly understood. These difficulties are caused by the simultaneous superposition of a large number of adverse factors occurring at different scales in contact area of the indenter with material surface. Effective solution to this problem, traceable in the modern literature is the use, in combination with experiment, different methods of numerical simulation. Molecular dynamics method still remains the main tool for the theoretical description of the behavior of the modeled system at the atomic scale. With the increasing performance of modern computing its contribution to the treasury of new knowledge acquiring is reinforced. New features allow us to study the evolution of the atomic lattice under dynamic loading with the explicit consideration of the internal structure of the polycrystalline material. Thus, the purpose of the present study was to

investigate with help of the method of molecular dynamics the characteristics of nucleation and development of structural defects in the crystalline material containing grain boundary under a localized loading conditions.

2 The model sample description

A fragment of polycrystalline copper, initially consisting of two grains separated by tilt grain boundary (GB) $\Sigma = 5(210)[001]$ was selected as an object of investigation. Two boundary position, along $X0Z$ and $Y0Z$ as shown in Fig. 1 were simulated. Note that early similar crystallite was used to investigate its behavior under shear loading as initially defect-free sample as well as containing the internal interface of various types [2, 3]. To describe the interatomic interaction the potential built in the framework of the embedded atom method was used [4, 5]. It was previously verified in a number of tests for the calculation of the elastic and energy characteristics.

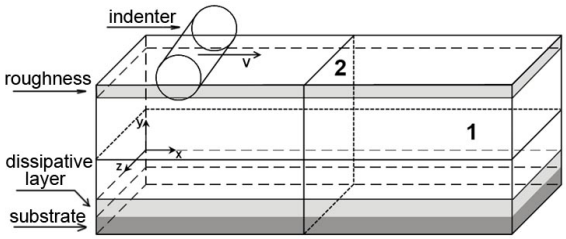

Figure 1: The scheme of the modeled sample.

Along the direction Z in a sample, periodic boundary conditions were set. Along the X-axis free surfaces were simulated. Thus, the considered sample can be represented as a single projection surface of an extended form (so-called pleated surface). The initial roughness of smaller scale was set additionally on the pleated surface. As a result surface stresses due to shear loading distributed unevenly and varied in different parts of the contact patch and further contributed to the redistribution of the local stresses and the formation of structural defects. The bottom layer of atoms (Figure 1) simulated unmovable substrate. Over the substrate a specific "damping" layer of atoms, which used the procedure reducing the kinetic energy was defined. By introducing of such a layer allow us to imitate the distribution of the kinetic energy deep into material along Y direction. The dimensions in the direction of the coordinate axes X, Y and Z were equal to $40.13 \times 24.95 \times 16.63$ nm, respectively. Total number of atoms exceeded 1500000. The equations of motion were integrated with a time step $\Delta t = 0,001$ ps.

Localized shear loading was applied by modeling the interaction of sample surface with microscopic counterbody, which acts as an absolutely rigid indenter. The indenter action has been realized through the force field described by the following formula $F(r) = K(r - R)^2$, where K – constant, r – distance from the center of the cylinder to the atom and the R – radius of the cylinder. At this at $r > R$ $F(r) = 0$. The sample was loaded with the indenter having a radius of 8 nm. The indenter moved in X direction with a constant velocity $V = 10$ m/s, which is close to the maximal available rate of the surface finishing treatment.

3 Results of simulation

Within the first stage the position of $\Sigma 5$ grain boundary, was oriented parallel to a plane $X0Z$ and located in the center of the crystallite (position 1 in Figure 1). To analyze the changing of the crystal lattice structure the algorithm which allows identifying the local topology of inter atomic bonds [6], and reveals the formation of structural defects was applied. The simulation results show that, due to the motion of indenter a lot of stacking faults produced in the bulk of grain. The presence of GB leads to contain the spread of a defect in the neighboring grains. It was also found that as a result of external shear loading the grain boundary starts moving in the direction perpendicular to the plane of the defect. This effect has been studied and described in [2]. Analysis of the structure at different times showed that the motion does not observed for all parts of the defect simultaneously. Parts of the boundary which is located in front and under the indenter move only. This leads to a curvature of the plane of the defect and its output to the free surface. Fig. 2 shows the change in the structure of the simulated sample when the GB under the influence of external localized load rises up to the free surface. The figure marked only the atoms, which local topology of structural relations is differ from the initial fcc lattice. It can be seen that the defects are concentrated in the upper grain. Only after grain boundary beyond the free surface (Figure 2d), structural defects are formed in the lower grain.

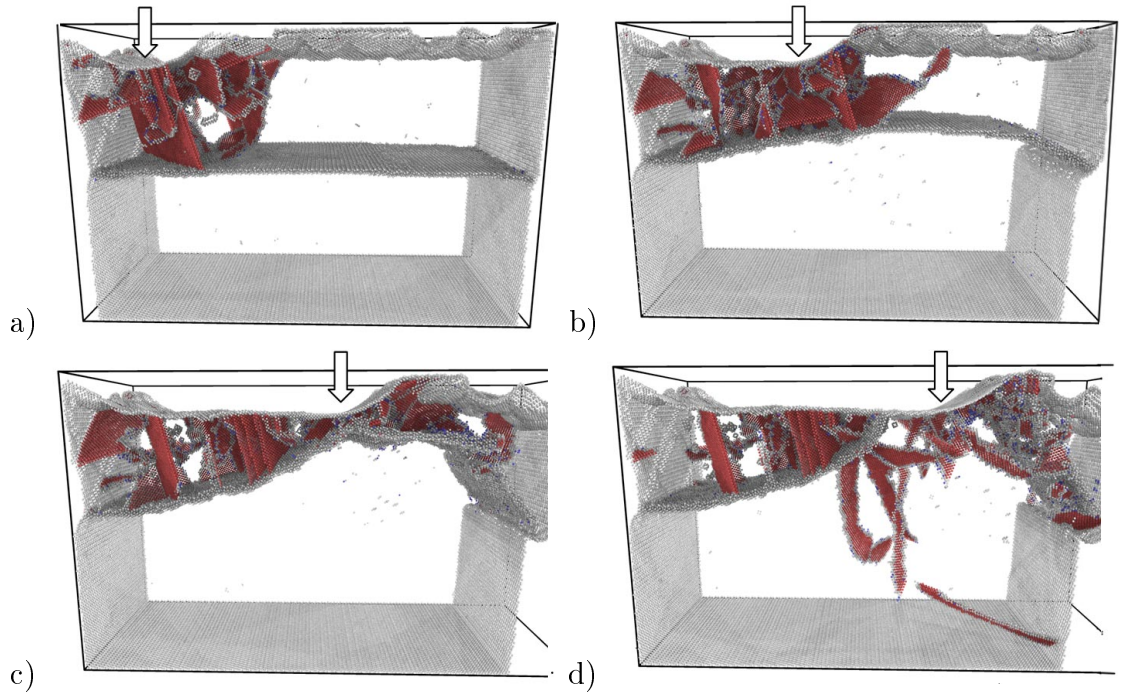

Figure 2: The structure of the modeled fragment at different time steps: a) 0.15 *ns*, b) 1.0 *ns*, c) 2.0 *ns*, d) 2.5 *ns*. Red spheres indicate position of atoms with hcp local topology of atoms relation; gray spheres depict atoms located at the border and close to GB. Hereafter arrows indicate the position of indenter.

Figure 3a demonstrates the position of the grain boundary at different time steps. It is clearly seen that the profile of the border is distorted due to indenter motion. Moving in the direction of the free surface takes place only in the part of the boundary which is situated in front of and under the indenter. Thus, the farther is the part of the border

from the initial position of the indenter along the X axis, the longer time it is subject to shear deformation and the greater distance in the direction perpendicular to the applied stresses, it is shifted. According to the results at time $t = 2.5 \times 10^6 \Delta t$ a part of the grain boundary beyond the free surface. After passing the indenter the position of this section of the border over time remains unchanged.

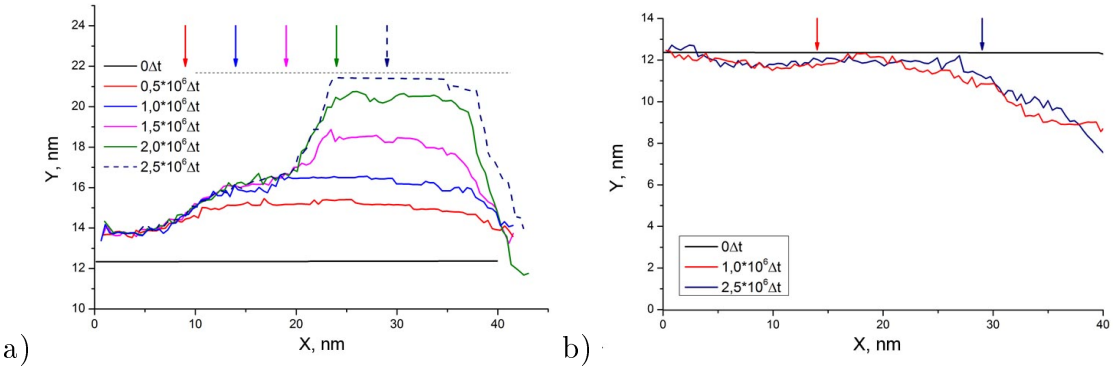

Figure 3: The projection of the grain boundary location on plane $X0Y$ at different time step.

To verify the correlation between the loading direction and the GB structure the similar sample containing a tilt grain boundary $\Sigma 5$, which structure was mirrored relative to the plane of the defect as compared with the above example was simulated. Figure 4 shows the structure of the sample at the same time steps as in Figure 2. It can be seen that the plane of the defect in this case is less distorted. This is because the distance between the grain boundary and indenter increases due to motion of defect far from the free surface in a direction perpendicular to the applied loading. According to the initial distribution of structural defects depicted on the Fig. 4a some defects form in the grain, located below the GB. Closeness to free side surface leads to further annihilation of its (Fig. 4b). So, plural structural defects form only in the grain, which are directly exposed to the action of the indenter (Fig. 4c and 4d).

Figure 3b shows the position of the GB for the described case for two time steps: at the beginning and close to final of the loading. It is seen that in contrast to the previous configuration the resulting position of the grain boundary at the end of loading stage changes only slightly in a direction from the free surface to the substrate. The offset position of the boundary grows up as the distance of this part of the defect increases from the initial position of the indenter. This is due to the peculiarities of redistribution of stresses and strains during the formation of defects in the system containing the grain boundary. Subsequent movement to the grain boundary from free surface to the lower grain is constrained by the presence of a fixed substrate.

The results showed that for both sample configurations the local shear loading leads to formation of numerous structural defects in the volume of the loaded grain. This advantageously stacking faults. Formation numerous defects in the surface layer can also mean a possibility of surface nanofragmentation. In order to identify possible mechanisms leading to the formation of the fragmented structure of the material in the volume of loaded grain atomic displacements at different time intervals for the central layer of the sample were analyzed. The thickness of the selected layer was equal to three atomic planes and its orientation was parallel to the $X0Y$ plane. Figure 5 shows the displacement of the atoms in the central layer of the bicrystal at the time moment near 0.5 ns and during the time

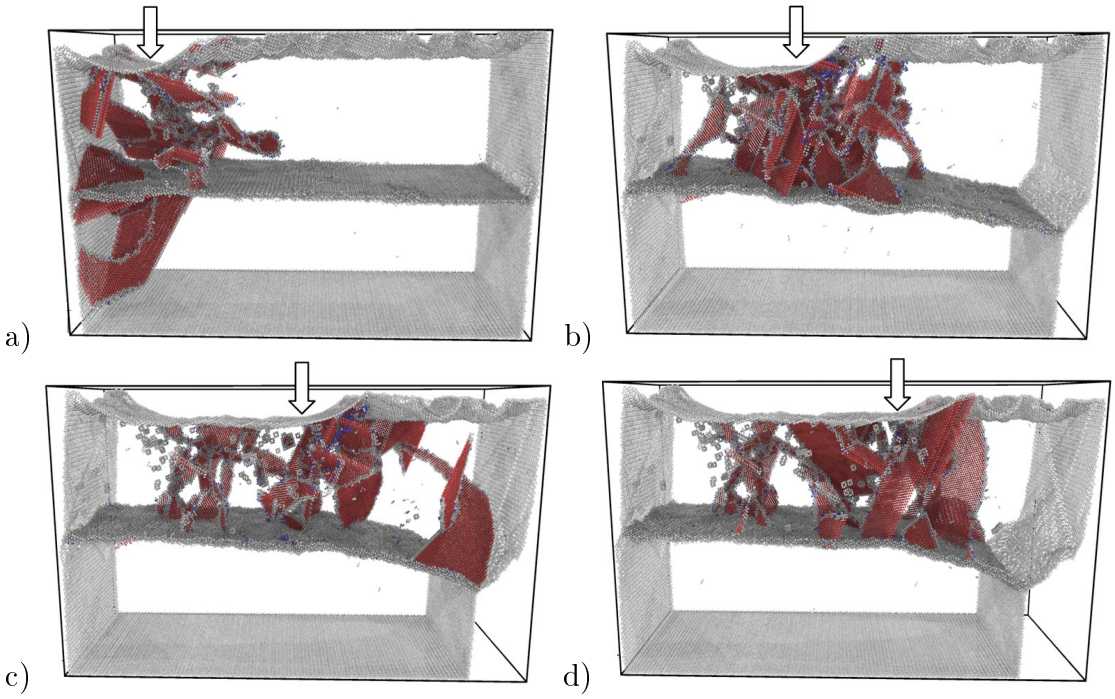

Figure 4: The structure of the modeled sample in which GB was mirrored relative to the plane of the defect as compared with the example shown in Fig. 2 at different time steps: a) 0.15 ns, b) 1.0 ns, c) 2.0 ns, d) 2.5 ns. Red spheres indicate position of atoms with hcp local topology of atoms relation; gray spheres depict atoms located at the border and close to grain boundary.

interval of 50 ps. The structure of building blocks in the upper grain, located in the area close to the indenter is clearly visible.

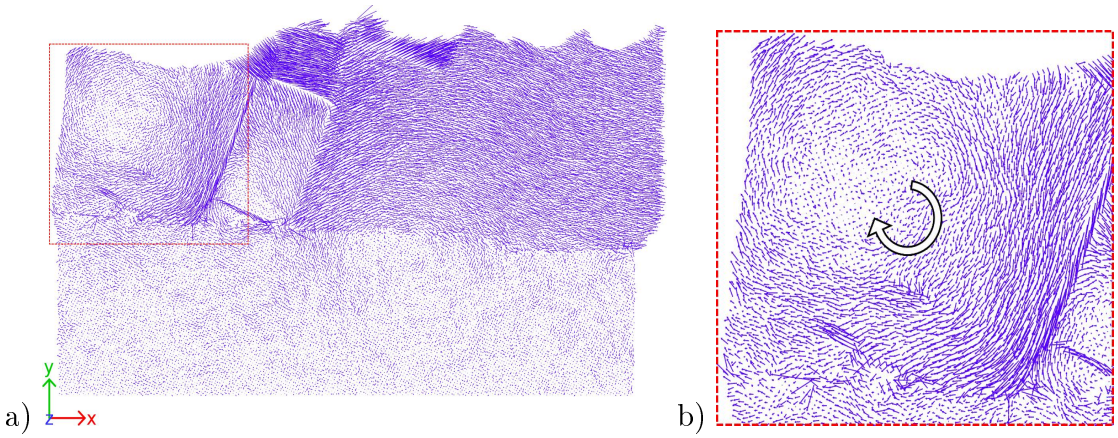

Figure 5: The map of displacements at the time interval $(0.50 - 0.55)$ ns for the atoms of the central cutting of the modeled bicrystal with the thickness of 3 atomic layers. The size of segments is increased up to 5 times for the better visualization. The arrow in zoomed fragment indicates the direction of rotation.

A detailed analysis of the character of the atomic displacements in forming blocks showed that they can carry rotational type. Figure 5 shows enlarged view for one of the blocks

forming in the structure. It is clearly seen that the block as a whole is rotated about an axis parallel to the direction Z. Further calculations showed that the value of such rotations along different directions for forming nanoblocks is no more than 2 degrees.

Similar conclusions can be done by analyzing the displacements of atoms for selected central layer in the subsequent time intervals, depicted in Figure 6.

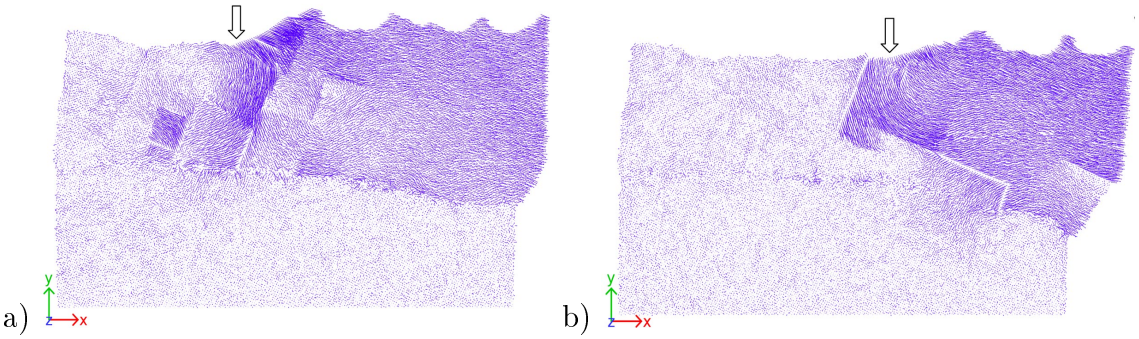

Figure 6: The map of displacements at different time intervals for the atoms of the central cutting layer of the modeled bicrystal with the thickness of 3 atomic layers: a) $(1.0-1.05)$ ns, b) $(2.0-2.05)$ ns. The size of segments is increased up to 5 times for the better visualization.

In the next stage of the research the sample in which the GB was located parallel to the plane $Y0Z$ (position 2 in Figure 1) was generated. Simulation results have shown that the similar action of the indenter on the grain boundary movement along the X axis is not observed. The presence of GB, prevents to the spread of structural defects as in the previous case, but only until the time where the indenter locates at a quite far distance from the position of GB. When the indenter approaches the GB stacking faults occur in the next grain as well. The structures of the modeled fragment for the respective time steps are shown in Figure 7.

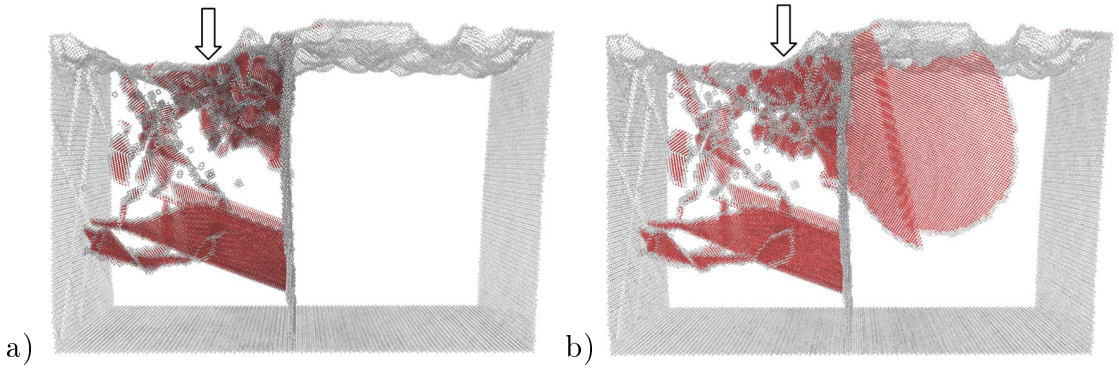

Figure 7: The structure of the modeled fragment with vertical orientation of the GB at different time steps: a) 0.8 ns, b) 0.9 ns. Red spheres indicate position of atoms with hcp local topology of atoms relation; gray spheres depict atoms located at the border and close to grain boundary.

4 Conclusion

In conclusion, we note that the results of computer simulation on the scale of individual atoms revealed the mechanism of plastic deformation of a material with an internal structure in terms of the local shear loading. According to the results, this process can occur through the formation of multiple intersecting planar defects – stacking faults. This leads to the formation of separate fragments of nanoscale size separated by an interface between them. It was found that the displacements of atoms in forming of fragments can have rotational character. Thus, the resulting structure of the modified surface layer is the system of disoriented nanoblocks.
With the help of computer simulations it was shown that the presence of GB in the crystal can limits the propagation of defects into the volume of the sample under shear load and can lead to recrystallization of individual grains only. Despite what it has been studied only the two limiting cases of grain boundaries arrangement in the material, it can be assumed that the behavior of defective crystallites disposed at an arbitrary angle to the free surface is a combination of processes that occur in these cases.
The obtained results can be use as well to understand the process of nanostructuring of the surface during for example finishing treatment.

Acknowledgements

This work was supported by RNF grant no. 14-19-00718.

References

[1] Korzynski M., Pacana A. Centreless burnishing and influence of its parameters on machining effects // J. Mater. Process Techn., 2010, V210(9), P. 1217-1223.

[2] Dmitriev A.I., Nikonov A.Yu., Psakhie S.G. Atomistic mechanism of grain boundary sliding with the example of a large-angle boundary S=5. Molecular dynamics calculation // Phys. Mesomech. 2011, V14(1-2), P. 24-31.

[3] Dmitriev A.I., Nikonov A.Yu. Simulating interaction of two symmetric grain boundaries under shear strain conditions // Tech. Phys. Lett. 2011, V37(9) P.884-887.

[4] Dmitriev A.I., Kuznetsov V.P., Nikonov A.Yu., Smolin I.Yu. Modelling of Nanostructuring Burnishing on Different Scales // Phys. Mesomech. 2014, V17(4) P. 6-13.

[5] Suzuki A., Mishin Y. Atomistic modeling of point defects and diffusion in copper grain boundaries // Interface Sci. 2003, V11(1) P. 131-148.

[6] Dana Honeycutt J., Hans C. Andemen Molecular Dynamics Study of Melting and Freezing of Small Lennard- Jones Clusters // J. Phys. Chem. 1987, V91 P. 4950-4963.

Andrey I. Dmitriev, ISPMS SB RAS / TSU, Tomsk, Russia
Anton Yu. Nikonov, ISPMS SB RAS / TSU, Tomsk, Russia

From localization to zoo of patterns in complex dynamics of ensembles

Antonina N. Fedorova, Michael G. Zeitlin
zeitlin@math.ipme.ru, anton@math.ipme.ru

Abstract

A fast and efficient numerical-analytical approach is proposed for modeling the complex collective behaviour in complex plasma physics models based on the BBGKY hierarchy of kinetic equations. Our calculations are based on variational and multiresolution approaches in the bases of polynomial tensor algebras of high-localized generalized coherent modes generated by action of the internal hidden symmetry of the underlying functional space. We construct the representation for hierarchy of reduced distribution functions via multiscale decomposition in high-localized eigenmodes. Numerical modeling shows the formation of zoo of various internal symmetry-generated structures (patterns) which describe the (meta)stable/unstable type of behaviour in non-equilibrium ensembles.

1 Introduction

The kinetic theory describes a lot of phenomena in beam/plasma physics which cannot be understood on the thermodynamic or/and fluid models level. We mean first of all local/metastable/non-gaussian fluctuations beyond the equilibrium state and collective/relaxation phenomena.
It is well-known that only kinetic approach can describe Landau damping, intra-beam scattering, while, e.g., Schottky noise and associated cooling technique depend on the understanding of spectrum of local fluctuations of the beam charge density [1], [2].
In this paper we review the applications of our numericalanalytical technique based on multiresolution (a.k.a.) wavelet analysis approach for calculations related to description of complex collective behaviour in the framework of general BBGKY hierarchy [3]–[21].
The rational type of nonlinearities allows us to use our results, which are based on the application of wavelet analysis technique and variational formulation of initial nonlinear problems. Wavelet analysis is a set of mathematical methods which give us a possibility to work with well-localized bases in functional spaces and provide maximum sparse forms for the general type of operators (differential, integral, pseudodifferential) in such bases.
It provides the best possible rates of convergence and minimal complexity of algorithms inside and as a result saves CPU time and HDD space.
In part 2 set-up for kinetic BBGKY hierarchy is described. In part 3 we present explicit analytical construction for solutions of hierarchy of equations from part 2 based on tensor algebra extension of multiresolution representation and variational formulation.

We give explicit representation for hierarchy of n-particle reduced/truncated distribution functions in the base of high-localized generalized coherent (regarding underlying affine group) states given by polynomial tensor algebra of base wavelets, which takes into account contributions from all underlying hidden multiscales from the coarsest scale of resolution to the finest one to provide full information about dynamics of complex process.
So, our approach resembles Bogolubov and related approaches but we do not use any perturbation technique (like virial expansion) or linearization procedures.
Numerical modeling shows the creation of different internal (coherent) structures from hidden localized modes, which are related to stable (equilibrium) or unstable/metastable type of behaviour and corresponding pattern (waveleton) formation.

2 Nonequilibrium dynamics: BBGKY hierarchy

Let M be the phase space of ensemble of N particles ($\dim M = 6N$) with coordinates $x_i = (q_i, p_i), \quad i = 1, ..., N, \quad q_i = (q_i^1, q_i^2, q_i^3) \in R^3, \quad p_i = (p_i^1, p_i^2, p_i^3) \in R^3, \quad q = (q_1, \ldots, q_N) \in R^{3N}$. Individual and collective measures are:

$$\mu_i = \mathrm{d}x_i = \mathrm{d}q_i p_i, \quad \mu = \prod_{i=1}^{N} \mu_i \tag{1}$$

Distribution function $D_N(x_1, \ldots, x_N; t)$ satisfies Liouville equation of motion for ensemble with Hamiltonian H_N :

$$\frac{\partial D_N}{\partial t} = \{H_N, D_N\} \tag{2}$$

and normalization constraint

$$\int D_N(x_1, \ldots, x_N; t) \mathrm{d}\mu = 1 \tag{3}$$

where Poisson brackets are:

$$\{H_N, D_N\} = \sum_{i=1}^{N} \Big(\frac{\partial H_N}{\partial q_i} \frac{\partial D_N}{\partial p_i} - \frac{\partial H_N}{\partial p_i} \frac{\partial D_N}{\partial q_i} \Big) \tag{4}$$

Our constructions can be applied to the following general Hamiltonians:

$$H_N = \sum_{i=1}^{N} \Big(\frac{p_i^2}{2m} + U_i(q) \Big) + \sum_{1 \le i \le j \le N} U_{ij}(q_i, q_j) \tag{5}$$

where potentials $U_i(q) = U_i(q_1, \ldots, q_N)$ and $U_{ij}(q_i, q_j)$ are not more than rational functions on coordinates. Let L_s and L_{ij} be the Liouvillean operators (vector fields)

$$L_s = \sum_{j=1}^{s} \Big(\frac{p_j}{m} \frac{\partial}{\partial q_j} - \frac{\partial u_j}{\partial q} \frac{\partial}{\partial p_j} \Big) - \sum_{1 \le i \le j \le s} L_{ij} \tag{6}$$

$$L_{ij} = \frac{\partial U_{ij}}{\partial q_i} \frac{\partial}{\partial p_i} + \frac{\partial U_{ij}}{\partial q_j} \frac{\partial}{\partial p_j} \tag{7}$$

For s=N we have the following representation for Liouvillean vector field

$$L_N = \{H_N, \cdot\} \tag{8}$$

and the corresponding ensemble equation of motion:

$$\frac{\partial D_N}{\partial t} + L_N D_N = 0 \tag{9}$$

L_N is self-adjoint operator regarding standard pairing on the set of phase space functions. Let

$$F_N(x_1, \dots, x_N; t) = \sum_{S_N} D_N(x_1, \dots, x_N; t) \tag{10}$$

be the N-particle distribution function (S_N is permutation group of N elements). Then we have the hierarchy of reduced distribution functions (V^s is the corresponding normalized volume factor)

$$F_s(x_1, \dots, x_s; t) = V^s \int D_N(x_1, \dots, x_N; t) \prod_{s+1 \le i \le N} \mu_i \tag{11}$$

After standard manipulations we arrived to BBGKY hierarchy [2]:

$$\frac{\partial F_s}{\partial t} + L_s F_s = \frac{1}{\upsilon} \int \mathrm{d}\mu_{s+1} \sum_{i=1}^{s} L_{i,s+1} F_{s+1} \tag{12}$$

It should be noted that we may apply our approach even to more general formulation than (12). Some particular case is considered in [22]. For s=1,2 we have from (12):

$$\frac{\partial F_1(x_1; t)}{\partial t} + \frac{p_1}{m} \frac{\partial}{\partial q_1} F_1(x_1; t) = \frac{1}{\upsilon} \int \mathrm{d}x_2 L_{12} F_2(x_1, x_2; t) \tag{13}$$

$$\begin{aligned} &\frac{\partial F_2(x_1, x_2; t)}{\partial t} + \left(\frac{p_1}{m} \frac{\partial}{\partial q_1} + \frac{p_2}{m} \frac{\partial}{\partial q_2} - L_{12} \right) \cdot F_2(x_1, x_2; t) \\ &= \frac{1}{\upsilon} \int \mathrm{d}x_3 (L_{13} + L_{23}) F_3(x_1, x_2; t) \end{aligned} \tag{14}$$

3 Multiscale analysis

The infinite hierarchy of distribution functions satisfying system (12) in the thermodynamical limit is:

$$F = \{F_0, F_1(x_1; t), F_2(x_1, x_2; t), \dots, F_N(x_1, \dots, x_N; t), \dots\}$$

where $F_p(x_1, \dots, x_p; t) \in H^p$, $H^0 = R$, $\quad H^p = L^2(R^{6p})$ (or any different proper functional space), $F \in H^\infty = H^0 \oplus H^1 \oplus \dots \oplus H^p \oplus \dots$ with the natural Fock-space like norm (of course, we keep in mind the positivity of the full measure) introduced by us [3]–[21]:

$$(F, F) = F_0^2 + \sum_i \int F_i^2(x_1, \dots, x_i; t) \prod_{\ell=1}^{i} \mu_\ell \tag{15}$$

$$F_k(x_1, \dots, x_k; t) = \prod_{i=1}^{k} F_1(x_i; t) \tag{16}$$

First of all we consider $F = F(t)$ as function on time variable only, $F \in L^2(R)$, via multiresolution decomposition which naturally and efficiently introduces the infinite sequence of underlying hidden scales into the game [23]. Because affine group of translations and dilations is inside the approach, this method resembles the action of a microscope. We have contribution to final result from each scale of resolution from the whole infinite scale of spaces. Let the closed subspace $V_j (j \in \mathbf{Z})$ correspond to level j of resolution, or to scale j.
We consider a multiresolution analysis of $L^2(R)$ (of course, we may consider any different functional space) which is a sequence of increasing closed subspaces V_j: $...V_{-2} \subset V_{-1} \subset V_0 \subset V_1 \subset V_2 \subset ...$ satisfying the following properties: let W_j be the orthonormal complement of V_j with respect to V_{j+1}: $V_{j+1} = V_j \bigoplus W_j$ then we have the following decomposition:

$$\{F(t)\} = \bigoplus_{-\infty<j<\infty} W_j \tag{17}$$

or in case when V_0 is the coarsest scale of resolution:

$$\{F(t)\} = \overline{V_0 \bigoplus_{j=0}^{\infty} W_j}, \tag{18}$$

Subgroup of translations generates basis for fixed scale number: $\mathrm{span}_{k\in Z}\{2^{j/2}\Psi(2^j t-k)\} = W_j$. The whole basis is generated by action of the full affine group:

$$\mathrm{span}_{k\in Z, j\in Z}\{2^{j/2}\Psi(2^j t - k)\} = \mathrm{span}_{k,j\in Z}\{\Psi_{j,k}\} = \{F(t)\} \tag{19}$$

Let the sequence $\{V_j^t\}, V_j^t \subset L^2(R)$ correspond to multiresolution analysis on time axis, $\{V_j^{x_i}\}$ correspond to multiresolution analysis for coordinate x_i, then

$$V_j^{n+1} = V_j^{x_1} \otimes \cdots \otimes V_j^{x_n} \otimes V_j^t \tag{20}$$

corresponds to multiresolution analysis for n-particle distribution function
$F_n(x_1, \ldots, x_n; t)$.
E.g., for $n = 2$:

$$V_0^2 = \{f : f(x_1, x_2) = \sum_{k_1,k_2} a_{k_1,k_2}\phi^2(x_1 - k_1, x_2 - k_2),\ a_{k_1,k_2} \in \ell^2(Z^2)\}, \tag{21}$$

where $\phi^2(x_1, x_2) = \phi^1(x_1)\phi^2(x_2) = \phi^1 \otimes \phi^2(x_1, x_2)$, and $\phi^i(x_i) \equiv \phi(x_i)$ form a multiresolution basis corresponding to $\{V_j^{x_i}\}$.
If $\{\phi^1(x_1-\ell)\}$, $\ell \in Z$ form an orthonormal set, then $\phi^2(x_1-k_1, x_2-k_2)$ form an orthonormal basis for V_0^2. Action of affine group provides us by multiresolution representation of $L^2(R^2)$. After introducing detail spaces W_j^2, we have, e.g. $V_1^2 = V_0^2 \oplus W_0^2$. Then 3-component basis for W_0^2 is generated by translations of three functions [23]:

$$\begin{aligned}
\Psi_1^2 &= \phi^1(x_1) \otimes \Psi^2(x_2), \\
\Psi_2^2 &= \Psi^1(x_1) \otimes \phi^2(x_2), \\
\Psi_3^2 &= \Psi^1(x_1) \otimes \Psi^2(x_2)
\end{aligned} \tag{22}$$

In general case we can use the rectangle lattice of scales and one-dimentional wavelet decomposition :

$$f(x_1, x_2) = \sum_{i,\ell;j,k} < f, \Psi_{i,\ell} \otimes \Psi_{j,k} > \Psi_{j,\ell} \otimes \Psi_{j,k}(x_1, x_2)$$

where the base functions $\Psi_{i,\ell} \otimes \Psi_{j,k}$ depend on two scales 2^{-i} and 2^{-j}.
Then, after constructing such multidimension bases we can apply some of our variational procedures introduced in [3]-[21]. As a result the solution of equations (12) has the following multiscale/multiresolution decomposition via nonlinear high-localized eigenmodes

$$
\begin{aligned}
F(t, x_1, x_2, \dots) &= \sum_{(i,j)\in Z^2} a_{ij} U^i \otimes V^j(t, x_1, x_2, \dots) \\
V^j(t) &= V_N^{j,slow}(t) + \sum_{l \geq N} V_l^j(\omega_l t), \quad \omega_l \sim 2^l \\
U^i(x_s) &= U_M^{i,slow}(x_s) + \sum_{m \geq M} U_m^i(k_m^s x_s), \quad k_m^s \sim 2^m,
\end{aligned}
\tag{23}
$$

which corresponds to the full multiresolution expansion in all underlying time/space scales.

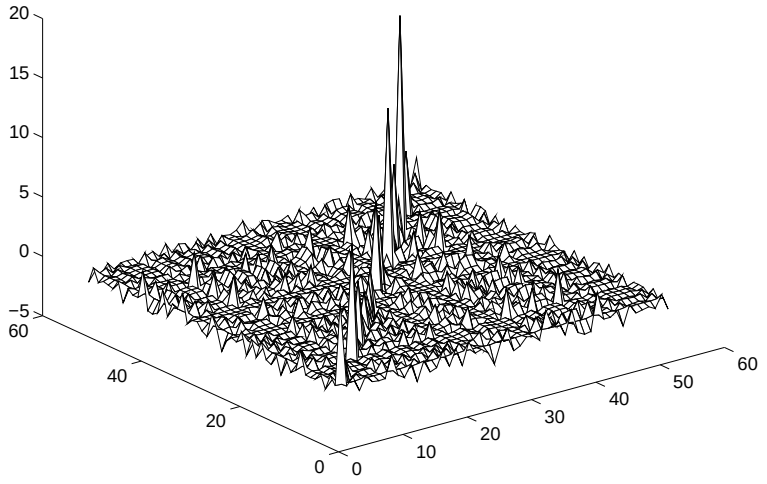

Figure 1: 6-eigenmodes representation for waveletons.

Formal representation (23) provide us with expansion into the slow part $\Psi_{N,M}^{slow}$ (coarse graining) and fast oscillating parts (fine scales) for arbitrary N, M.
So, we can move from coarse scales of resolution to the finest one for obtaining more detailed information about our complex dynamical process.
The first terms in the RHS of formulas (23) correspond on the global level of function space decomposition to resolution space and the second ones to detail space. In this way we collect contributions to the exact solution from each scale of resolution or each hidden time/space scale or from each nonlinear hidden eigenmode [3]–[21].
It should be noted that such representations provide the best possible localization properties in the corresponding (phase)space/time coordinates. In contrast with different approaches representation (23) do not use perturbation technique or linearization procedures.
Numerical calculations are based on compactly supported wavelets and related wavelet families [24] and on evaluation of the accuracy regarding norm (15):

$$
\|F^{N+1} - F^N\| \leq \varepsilon \tag{24}
$$

Fig. 1 demonstrates waveleton (high-localized and metastable) pattern generated at level 6 of the scale/eigenmodes decomposition for solutions of hierarchies like (12).
So, finally, using multiresolution decomposition constructed by properly generated action of hidden symmetry of the underlying functional spaces, we provide the best possible (phase) space/time localization properties and as a result the construction of high-localized metastable waveleton structures in spatially-extended stochastic systems with collective behaviour. Fig. 1 represents some possible image for the energy confinement state in the plasma fusion model [20].

References

[1] *A. H. Boozer*, Rev. Mod. Phys., 76, 1071 (2004).

[2] *R. C. Davidson and H. Qin*, Physics of Intense Charged Particle Beams in High Energy Accelerators (World Scientific, Singapore, 2001); R. Balescu, Equilibrium and Nonequilibrium Statistical Mechanics, (Wiley, New York, 1975).

[3] A.N. Fedorova and M.G. Zeitlin, Quasiclassical Calculations for Wigner Functions via Multiresolution, Localized Coherent Structures and Patterns Formation in Collective Models of Beam Motion, in *Quantum Aspects of Beam Physics*, Ed. P. Chen (World Scientific, Singapore, 2002) pp. 527–538, 539–550; arXiv: physics/0101006; physics/0101007.

[4] A.N. Fedorova and M.G. Zeitlin, BBGKY Dynamics: from Localization to Pattern Formation, in *Progress in Nonequilibrium Green's Functions II*, Ed. M. Bonitz, (World Scientific, 2003) pp. 481–492; arXiv: physics/0212066.

[5] A.N. Fedorova and M.G. Zeitlin, Pattern Formation in Wigner-like Equations via Multiresolution, in *Quantum Aspects of Beam Physics*, Eds. Pisin Chen, K. Reil (World Scientific, 2004) pp. 22-35; Preprint SLAC-R-630; arXiv: quant-ph/0306197.

[6] A.N. Fedorova and M.G. Zeitlin, Localization and pattern formation in Wigner representation via multiresolution, *Nuclear Inst. and Methods in Physics Research, A*, **502A/2-3**, pp. 657 - 659, 2003; arXiv: quant-ph/0212166.

[7] A.N. Fedorova and M.G. Zeitlin, Fast Calculations in Nonlinear Collective Models of Beam/Plasma Physics, *Nuclear Inst. and Methods in Physics Research, A*, **502/2-3**, pp. 660 - 662, 2003; arXiv: physics/0212115.

[8] A.N. Fedorova and M.G. Zeitlin, Classical and quantum ensembles via multiresolution: I-BBGKY hierarchy; Classical and quantum ensembles via multiresolution. II. Wigner ensembles; *Nucl. Instr. Methods Physics Res.*, **534A** (2004)309-313; 314-318; arXiv: quant-ph/0406009; quant-ph/0406010.

[9] A.N. Fedorova and M.G. Zeitlin, Localization and Pattern Formation in Quantum Physics. I. Phenomena of Localization, in *The Nature of Light: What is a Photon? SPIE*, vol.**5866**, pp. 245-256, 2005; arXiv: quant-ph/0505114;

[10] A.N. Fedorova and M.G. Zeitlin, Localization and Pattern Formation in Quantum Physics. II. Waveletons in Quantum Ensembles, in *The Nature of Light: What is a Photon?SPIE*, vol. **5866**, pp. 257-268, 2005; arXiv: quant-ph/0505115.

[11] A.N. Fedorova and M.G. Zeitlin, Pattern Formation in Quantum Ensembles, *Intl. J. Mod. Physics* **B20**(2006)1570-1592; arXiv: 0711.0724.

[12] A.N. Fedorova and M.G. Zeitlin, Patterns in Wigner-Weyl approach, Fusion modeling in plasma physics: Vlasov-like systems, *Proceedings in Applied Mathematics and Mechanics (PAMM)*, Volume **6**, Issue 1, p. 625, p. 627, Wiley InterScience, 2006; arXiv:1012.4971, arXiv:1012.4965.

[13] A.N. Fedorova and M.G. Zeitlin, Localization and Fusion Modeling in Plasma Physics. Part I: Math Framework for Non-Equilibrium Hierarchies, pp.61-86, in *Current Trends in International Fusion Research*, Ed. E. Panarella, R. Raman, National Research Council (NRC) Research Press, Ottawa, Ontario, Canada, 2009; arXiv: physics/0603167.

[14] A.N. Fedorova and M.G. Zeitlin, Localization and Fusion Modeling in Plasma Physics. Part II: Vlasov-like Systems. Important Reductions, pp.87-100, in *Current Trends in International Fusion Research*, Ed. E. Panarella, R. Raman, National Research Council (NRC) Research Press, Ottawa, Ontario, Canada, 2009; arXiv: physics/0603169.

[15] A.N. Fedorova and M.G. Zeitlin, Fusion State in Plasma as a Waveleton (Localized (Meta)-Stable Pattern), p. 272, in *AIP Conference Proceedings*, Volume **1154**, Issue 1, *Current Trends in International Fusion Research*, Ed. E. Panarella, R. Raman, AIP, 2009, doi:10.1063/1.3204585.

[16] A.N. Fedorova and M.G. Zeitlin, Exact Multiscale Representations for (Non)-Equilibrium Dynamics of Plasma, p.291, in *AIP Conference Proceedings*, Volume **1154**, Issue 1, *Current Trends in International Fusion Research*, Ed. E. Panarella, R. Raman, AIP, 2009, doi:10.1063/1.3204592.

[17] A.N. Fedorova and M.G. Zeitlin, Fusion Modeling in Vlasov-Like Models, *Journal Plasma Fusion Res. Series*, Vol. **8**, pp. 126-131, 2009.

[18] A.N. Fedorova and M.G. Zeitlin, Quantum points/patterns, Part 2: from quantum points to quantum patterns via multiresolution, SPIE, vol. 8121, 81210K (2011), doi:10.1117/12.893537; arXiv:1109.5042.

[19] A.N. Fedorova and M.G. Zeitlin, Quantum points/patterns, Part 1. From geometrical points to quantum points in sheaf framework , SPIE, vol. 8121, 81210J (2011), doi:10.1117/12.893502; arXiv:1109.5035.

[20] A.N. Fedorova and M.G. Zeitlin, En route to fusion: confinement state as a waveleton, Journal of Physics CS, vol. 490, 012202, 2014, doi:10.1088/1742-6596/490/1/012202.

[21] *A. N. Fedorova and M. G. Zeitlin*, a list of papers/preprints (including links to arXiv) can be found on web sites below.

[22] *A. N. Fedorova and M. G. Zeitlin*, Fast Modeling for Collective Models of Beam/-Plasma Physics, This Volume.

[23] Y. Meyer, Wavelets and Operators (Cambridge Univ. Press, 1990); G. Beylkin, R. Coifman, V. Rokhlin, Fast Wavelet transform and Numerical Algorithms, Comm. Pure Applid Math, 44, 141-183, 1991.

[24] F. Auger e.a., *Time-Frequency Toolbox* (CNRS, 1996); D. Donoho, *WaveLab* (Stanford, 2000).

Antonina N. Fedorova, Michael G. Zeitlin
Mathematical Methods in Mechanics Group, IPME RAS, V.O. Bolshoj pr., 61, 199178, St. Petersburg, Russia
http://www.ipme.ru/zeitlin.html, http://mp.ipme.ru/zeitlin.html

Fast modeling for collective models of beam/plasma physics

Antonina N. Fedorova, Michael G. Zeitlin
zeitlin@math.ipme.ru, anton@math.ipme.ru

Abstract

We consider an application of modification of our variational-wavelet approach to some nonlinear collective models of beam/plasma physics: the Vlasov/Boltzmann-like truncation of general BBGKY hierarchy related to the modeling of the propagation of intense charged particle beams in high-intensity accelerators and transport systems. We use fast convergent multiscale variational-wavelet representations for solutions which allow to consider the polynomial and rational type of nonlinearities. The solutions are represented via the multiscale decomposition in nonlinear high-localized eigenmodes (waveletons). In contrast to different approaches we do not use perturbation technique or linearization procedures.

1 Introduction

We consider applications of numerical–analytical technique based on modification of our variational-wavelet approach to nonlinear collective models of beam/plasma physics, e.g. some forms of Vlasov/Boltzmann-like reductions of general BBGKY hierarchy (section 2). These equations are related to the modeling of propagation of intense charged particle beams in high-intensity accelerators and transport systems [1], [2]. In our approach we use fast convergent multiscale variational-wavelet representations, which allows to consider polynomial and rational type of nonlinearities [3]-[22]. The solutions are represented via the multiscale decomposition in nonlinear high-localized eigenmodes (some generalization of the so-called Gluckstern modes, in some sense), which corresponds to the full multiresolution expansion in all underlying hidden time/space or phase space scales.
In contrast with different approaches we do not use perturbation technique or linearization procedures.
In section 3 after formulation of key points we consider another variational approach based on ideas of para-products and nonlinear approximation in multiresolution approach, which provides the possibility for computations in each scale separately [23].
We consider representation (4) below, where each term corresponds to the contribution from the scale i in the full underlying multiresolution decomposition as multiscale generalization of old (nonlinear) δF approach [1], [2].
As a result, fast scalar/parallel modeling demonstrates appearance of high-localized coherent structures (waveletons) and (meta)stable pattern formation in systems with complex collective behaviour or the possibility of existence of relatively/locally stable order in the systems with full disorder.

2 Vlasov/Boltzmann–like reductions

Let M be the phase space of ensemble of N particles ($\dim M = 6N$) with coordinates $x_i = (q_i, p_i), \quad i = 1, ..., N, \quad q_i = (q_i^1, q_i^2, q_i^3) \in R^3, \quad p_i = (p_i^1, p_i^2, p_i^3) \in R^3$ with distribution function $D_N(x_1, \ldots, x_N; t)$ and

$$F_N(x_1, \ldots, x_N; t) = \sum_{S_N} D_N(x_1, \ldots, x_N; t) \tag{1}$$

be the N-particle distribution functions (S_N is permutation group of N elements). For s=1,2 we have from general BBGKY hierarchy [22]:

$$\frac{\partial F_1(x_1;t)}{\partial t} + \frac{p_1}{m}\frac{\partial}{\partial q_1} F_1(x_1;t) = \frac{1}{\upsilon}\int \mathrm{d}x_2 L_{12} F_2(x_1, x_2; t) \tag{2}$$

$$\begin{aligned} &\frac{\partial F_2(x_1, x_2; t)}{\partial t} + \Big(\frac{p_1}{m}\frac{\partial}{\partial q_1} + \frac{p_2}{m}\frac{\partial}{\partial q_2} - L_{12}\Big) F_2(x_1, x_2; t) \\ &= \frac{1}{\upsilon}\int \mathrm{d}x_3 (L_{13} + L_{23}) F_3(x_1, x_2; t) \end{aligned} \tag{3}$$

where partial Liouvillean operators are described in [22]. We are interested in the cases when and where

$$F_k(x_1, \ldots, x_k; t) = \prod_{i=1}^{k} F_1(x_i; t) + G_k(x_1, \ldots, x_k; t),$$

where G_k are the correlation patterns, really have additional reductions as in case of the Vlasov-like systems.
Then we have in the equations (2), (3) not more than polynomial type of nonlinearities (more exactly, multilinearities), i.e. we can apply our general approach [3]–[22] based on Local Nonlinear (non-abelian) Harmonic Analysis [23].

3 Multiresolution via para-products

Our goal is the demonstration of advantages of the following formal representation

$$F = \sum_{i \in Z} \delta^i F, \tag{4}$$

for the full exact solution for the systems related to equations (2), (3). It is possible to consider the representation (4) as multiscale generalization of old (nonlinear) δF approach [1], [2]. So, in our modified version of the decomposition (4) each $\delta^i F$ term corresponds to the contribution from the scale i in the full underlying multiresolution decomposition

$$\cdots \subset V_{-1} \subset V_0 \subset V_1 \subset V_2 \ldots \tag{5}$$

of the proper function space (L^2, Hilbert, Sobolev, etc.) to which the tower F really belongs according to the properly chosen physical hypothesis. It should be noted that (4) doesn't based neither on perturbations nor on linearization procedures. Although usually physicists, who prefer computer modeling as a main tool of understanding of the physical reality, don not think about underlying functional spaces, but many concrete features of

complicated complex dynamics are really related not only to concrete form/class of operators/equations but also depend on the proper choice of function spaces where operators actully act. Moreover, we have for arbitrary N in the finite N-mode approximation

$$F^N = \sum_{i=1}^{N} \delta^i F \tag{6}$$

the following more useful decompositions:

$$\{F(t)\} = \bigoplus_{-\infty<j<\infty} W_j \quad \text{or} \quad \{F(t)\} = \overline{V_0 \bigoplus_{j=0}^{\infty} W_j}, \tag{7}$$

in the case when V_0 is the coarsest scale of resolution and where $V_{j+1} = V_j \bigoplus W_j$ and the bases in the scale spaces $W_i(V_j)$ are generated from the base functions $\psi(\varphi)$ by action of the underlying affine group of the translations and dilations (the so called "wavelet microscope"). The following constructions based on the variational approach provide the best possible fast convergence properties in the sense of the combined norm:

$$\|F^{N+1} - F^N\| \leq \varepsilon \tag{8}$$

introduced and considered before in [3]–[22]. Our five basic points after the choice of the model for the functional space are as follows:

1. The ansatz-oriented choice of the (multidimensional) bases related to some polynomial tensor algebra. Some example related to the general BBGKY hierarchy is considered in [22].

2. The choice of the proper variational principle. A few projection/ Galerkin-like principles for the (weak) solution construction are considered in [3] - [21]. It should be noted the advantage of formulation related to biorthogonal (wavelet) decomposition.

3. The choice of base functions in scale spaces W_j from the whole wavelet zoo. They correspond to high-localized (nonlinear) oscillations/excitations, coherent (nonlinear) resonances, etc. Besides the fast convergence properties of the corresponding variational-wavelet expansions it should be noted the minimal complexity of all underlying calculations, especially in case of choice of wavelet packets which minimize Shannon entropy.

4. The operator representations provide the best possible sparse representations for the arbitrary (pseudo) differential/integral operators

   $\mathrm{d}f/\mathrm{d}x, \mathrm{d}^n f/\mathrm{d}x^n, \int T(x,y)f(y)\mathrm{d}y)$, etc [23].

5. (Multi)linearization. Besides variation approach we consider now a different method to deal with (polynomial) nonlinearities.

We modify the scheme of our variational approach in such a way in which we consider the different scales of the multiresolution decomposition (5) separately. For this reason we need to compute errors of approximations. The main problems come, of course, from nonlinear (polynomial) terms. We follow according to the multilinearization (in case below – bilinearization) approach of Beylkin, Meyer etc. from [23]. Let P_j be the projection operators on the subspaces V_j (5):

$$(P_j f)(x) = \sum_k < f, \varphi_{j,k} > \varphi_{j,k}(x) \tag{9}$$

and Q_j are projection operators on the subspaces W_j: $Q_j = P_{j-1} - P_j$. So, for $u \in L^2(R)$ we have $u_j = P_j u \quad$ and $u_j \in V_j$. It is obviously that we can represent u_0^2 in the following form:

$$u_0^2 = 2\sum_{j=1}^{n}(P_j u)(Q_j u) + \sum_{j=1}^{n}(Q_j u)(Q_j u) + u_n^2 \tag{10}$$

In this formula there is no interaction between different scales. We may consider each term of (10) as a bilinear mappings:

$$M_{VW}^j : V_j \times W_j \to L^2(\mathbf{R}) = V_j \oplus_{j' \geq j} W_{j'} \tag{11}$$

$$M_{WW}^j : W_j \times W_j \to L^2(\mathbf{R}) = V_j \oplus_{j' \geq j} W_{j'} \tag{12}$$

For numerical purposes we need formula (10) with a finite number of scales, but when we consider limit $j \to \infty$ we have

$$u^2 = \sum_{j \in \mathbf{Z}}(2P_j u + Q_j u)(Q_j u), \tag{13}$$

which is the very useful para-product of Bony, Coifman and Meyer [23]. Now we need to expand (10) into the wavelet bases. To expand each term in (10) we need to consider the integrals of the products of the basis functions corresponding to decomposition (7), e.g.

$$M_{WWW}^{j,j'}(k,k',\ell) = \int_{-\infty}^{\infty} \psi_k^j(x)\psi_{k'}^j(x)\psi_\ell^{j'}(x)\mathrm{d}x, \tag{14}$$

where $j' > j$ and

$$\psi_k^j(x) = 2^{-j/2}\psi(2^{-j}x - k) \tag{15}$$

are the basis functions proper for (7). For compactly supported wavelets

$$M_{WWW}^{j,j'}(k,k',\ell) \equiv 0 \quad \text{for} \quad |k - k'| > k_0, \tag{16}$$

where k_0 depends on the overlap of the supports of the basis functions and

$$|M_{WWW}^r(k - k', 2^r k - \ell)| \leq C \cdot 2^{-r\lambda M} \tag{17}$$

Let us define j_0 as the distance between scales such that for a given ε all the coefficients in (17) with labels $r = j - j'$, $r > j_0$ have absolute values less than ε. For the purposes of computing with accuracy ε we replace the mappings in (11), (12) by

$$M_{VW}^j : V_j \times W_j \to V_j \oplus_{j \leq j' \leq j_0} W_{j'} \tag{18}$$

$$M_{WW}^j : W_j \times W_j \to V_j \oplus_{j \leq j' \leq j_0} W_{j'} \tag{19}$$

Since

$$V_j \oplus_{j \leq j' \leq j_0} W_{j'} = V_{j_0 - 1},\ V_j \subset V_{j_0 - 1},\ W_j \subset V_{j_0 - 1}$$

we may consider bilinear mappings (18), (19) on $V_{j_0-1} \times V_{j_0-1}$. For the evaluation of (18), (19) as mappings $V_{j_0-1} \times V_{j_0-1} \to V_{j_0-1}$ we need significantly fewer coefficients than for mappings (18), (19). It is enough to consider only coefficients

$$M(k,k',\ell) = 2^{-j/2}\int_{\infty}^{\infty} \varphi(x-k)\varphi(x-k')\varphi(x-\ell)\mathrm{d}x, \tag{20}$$

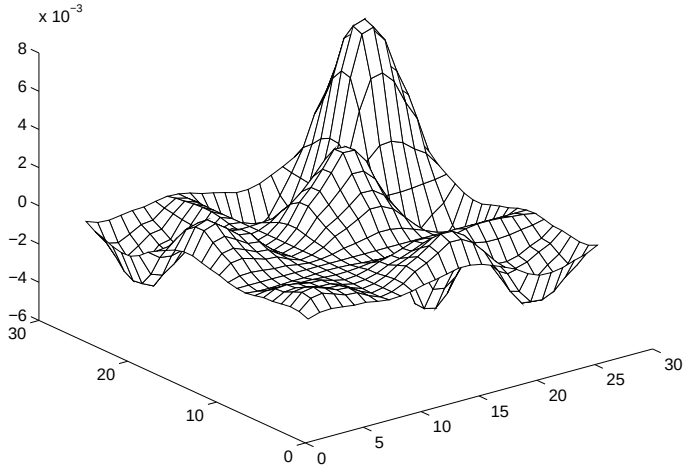

Figure 1: $N = 1$ coarse grain contribution to (6).

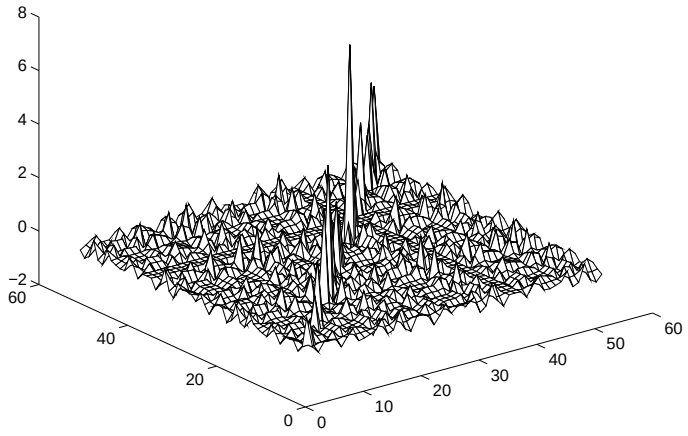

Figure 2: Localized metastable pattern.

where $\varphi(x)$ is scale function. Also we have

$$M(k,k',\ell) = 2^{-j/2} M_0(k-\ell, k'-\ell), \tag{21}$$

where

$$M_0(p,q) = \int \varphi(x-p)\varphi(x-q)\varphi(x)\mathrm{d}x \tag{22}$$

$M_0(p,q)$ satisfy the standard system of linear equations and after its solution we can recover all bilinear quantities (14). Then we may apply some variational approach from [3]-[21] but, in contrast with previous attempts, at each scale separately. Finally, after the application of points 1-5 above, we arrive to the explicit numerical-analytical realization of representations (4) or (6). Fig. 1 demonstrates the coarse grain level contribution to the full solution (6) while Fig. 2 presents our final goal: the localized non-gaussian (meta)stable pattern as the solution of the system like (2),(3). We evaluate the accuracy of calculations according to norm considered for the whole kinetic hierarchy in companion paper [22].

Various images for different types of possible patterns are parametrized by details of the underlying (multi)linear algebra related to aspects of multiresolution decomposition as well as by features related to the internal structure of the underlying functional spaces. Both structures have direct relation to the underlying physics of ensembles.

References

[1] *A. H. Boozer*, Rev. Mod. Phys., 76, 1071 (2004); A. Chao, Handbook of Accelerator Physics, World Scientific, 1999.

[2] *R. C. Davidson and H. Qin*, Physics of Intense Charged Particle Beams in High Energy Accelerators (World Scientific, Singapore, 2001); R. Balescu, Equilibrium and Nonequilibrium Statistical Mechanics, (Wiley, New York, 1975).

[3] A.N. Fedorova and M.G. Zeitlin, Quasiclassical Calculations for Wigner Functions via Multiresolution, Localized Coherent Structures and Patterns Formation in Collective Models of Beam Motion, in *Quantum Aspects of Beam Physics*, Ed. P. Chen (World Scientific, Singapore, 2002) pp. 527–538, 539–550; arXiv: physics/0101006; physics/0101007.

[4] A.N. Fedorova and M.G. Zeitlin, BBGKY Dynamics: from Localization to Pattern Formation, in *Progress in Nonequilibrium Green's Functions II*, Ed. M. Bonitz, (World Scientific, 2003) pp. 481–492; arXiv: physics/0212066.

[5] A.N. Fedorova and M.G. Zeitlin, Pattern Formation in Wigner-like Equations via Multiresolution, in *Quantum Aspects of Beam Physics*, Eds. Pisin Chen, K. Reil (World Scientific, 2004) pp. 22-35; Preprint SLAC-R-630; arXiv: quant-ph/0306197.

[6] A.N. Fedorova and M.G. Zeitlin, Localization and pattern formation in Wigner representation via multiresolution, *Nuclear Inst. and Methods in Physics Research, A*, **502A/2-3**, pp. 657 - 659, 2003; arXiv: quant-ph/0212166.

[7] A.N. Fedorova and M.G. Zeitlin, Fast Calculations in Nonlinear Collective Models of Beam/Plasma Physics, *Nuclear Inst. and Methods in Physics Research, A*, **502/2-3**, pp. 660 - 662, 2003; arXiv: physics/0212115.

[8] A.N. Fedorova and M.G. Zeitlin, Classical and quantum ensembles via multiresolution: I-BBGKY hierarchy; Classical and quantum ensembles via multiresolution. II. Wigner ensembles; *Nucl. Instr. Methods Physics Res.*, **534A** (2004)309-313; 314-318; arXiv: quant-ph/0406009; quant-ph/0406010.

[9] A.N. Fedorova and M.G. Zeitlin, Localization and Pattern Formation in Quantum Physics. I. Phenomena of Localization, in *The Nature of Light: What is a Photon? SPIE*, vol.**5866**, pp. 245-256, 2005; arXiv: quant-ph/0505114;

[10] A.N. Fedorova and M.G. Zeitlin, Localization and Pattern Formation in Quantum Physics. II. Waveletons in Quantum Ensembles, in *The Nature of Light: What is a Photon?SPIE*, vol. **5866**, pp. 257-268, 2005; arXiv: quant-ph/0505115.

[11] A.N. Fedorova and M.G. Zeitlin, Pattern Formation in Quantum Ensembles, *Intl. J. Mod. Physics* **B20**(2006)1570-1592; arXiv: 0711.0724.

[12] A.N. Fedorova and M.G. Zeitlin, Patterns in Wigner-Weyl approach, Fusion modeling in plasma physics: Vlasov-like systems, *Proceedings in Applied Mathematics and Mechanics (PAMM)*, Volume **6**, Issue 1, p. 625, p. 627, Wiley InterScience, 2006; arXiv:1012.4971, arXiv:1012.4965.

[13] A.N. Fedorova and M.G. Zeitlin, Localization and Fusion Modeling in Plasma Physics. Part I: Math Framework for Non-Equilibrium Hierarchies, pp.61-86, in *Current Trends in International Fusion Research*, Ed. E. Panarella, R. Raman, National Research Council (NRC) Research Press, Ottawa, Ontario, Canada, 2009; arXiv: physics/0603167.

[14] A.N. Fedorova and M.G. Zeitlin, Localization and Fusion Modeling in Plasma Physics. Part II: Vlasov-like Systems. Important Reductions, pp.87-100, in *Current Trends in International Fusion Research*, Ed. E. Panarella, R. Raman, National Research Council (NRC) Research Press, Ottawa, Ontario, Canada, 2009; arXiv: physics/0603169.

[15] A.N. Fedorova and M.G. Zeitlin, Fusion State in Plasma as a Waveleton (Localized (Meta)-Stable Pattern), p. 272, in *AIP Conference Proceedings*, Volume **1154**, Issue 1, *Current Trends in International Fusion Research*, Ed. E. Panarella, R. Raman, AIP, 2009, doi:10.1063/1.3204585.

[16] A.N. Fedorova and M.G. Zeitlin, Exact Multiscale Representations for (Non)-Equilibrium Dynamics of Plasma, p.291, in *AIP Conference Proceedings*, Volume **1154**, Issue 1, *Current Trends in International Fusion Research*, Ed. E. Panarella, R. Raman, AIP, 2009, doi:10.1063/1.3204592.

[17] A.N. Fedorova and M.G. Zeitlin, Fusion Modeling in Vlasov-Like Models, *Journal Plasma Fusion Res. Series*, Vol. **8**, pp. 126-131, 2009.

[18] A.N. Fedorova and M.G. Zeitlin, Quantum points/patterns, Part 2: from quantum points to quantum patterns via multiresolution, SPIE, vol. 8121, 81210K (2011), doi:10.1117/12.893537; arXiv:1109.5042.

[19] A.N. Fedorova and M.G. Zeitlin, Quantum points/patterns, Part 1. From geometrical points to quantum points in sheaf framework , SPIE, vol. 8121, 81210J (2011), doi:10.1117/12.893502; arXiv:1109.5035.

[20] A.N. Fedorova and M.G. Zeitlin, En route to fusion: confinement state as a waveleton, Journal of Physics CS, vol. 490, 012202, 2014, doi:10.1088/1742-6596/490/1/012202.

[21] *A. N. Fedorova and M. G. Zeitlin*, a list of papers/preprints (including links to arXiv) can be found on web sites below.

[22] *A. N. Fedorova and M. G. Zeitlin*, From localization to zoo of patterns in complex dynamics of ensembles, This Volume.

[23] Y. Meyer, Wavelets and Operators (Cambridge Univ. Press, 1990); G. Beylkin, R. Coifman, V. Rokhlin, Fast Wavelet transform and Numerical Algorithms, Comm. Pure Applid Math, 44, 141-183, 1991.

[24] F. Auger e.a., *Time-Frequency Toolbox* (CNRS, 1996); D. Donoho, *WaveLab* (Stanford, 2000).

Antonina N. Fedorova, Michael G. Zeitlin
Mathematical Methods in Mechanics Group, IPME RAS, V.O. Bolshoj pr., 61, 199178, St. Petersburg, Russia
http://www.ipme.ru/zeitlin.html, http://mp.ipme.ru/zeitlin.html

The study of structure and mechanical properties of polyethylene - silicate needle nanofiller at the macro and micro level

Oleg K. Garishin, Ilya. A. Morozov, Vladimir V. Shadrin, Victor A. Gerasin, Maria A. Guseva

ilya.morozov@gmail.com

Abstract

The paper presents experimental data obtained by testing composites based on polyethylene and silicate needle filler (palygorskite) of different concentration. At the macro level, stress-strain curves are plotted for materials with different filler concentration, and the mechanical properties of these materials are explored. Research at the micro level examines the microstructure and local mechanical properties of composite materials.

1 Introduction

Nanocomposites based on various types of polyolefins (polyethylene, polypropylene, etc.) and nanodispersed silica ultrafine particles (nanoclay) are currently the subject of intense research. This family of composite materials attracts attention because of their unique physical and chemical properties compared to the conventionally filled polymers. They are known for their high performance, environmental friendliness, relatively low cost and ease of production. Polyolefins are the most popular and accessible group of thermoplastic polymers.

It has been recognized [1, 2] that incorporation of even small quantities of silicate nanoparticles into polymers significantly enhances the diffusion barrier properties of the material, its thermal stability and resistance to thermal buckling. Most likely this is due to the fact that nanostructured materials have some specific features. Firstly, unlike conventional composites, whose individual components are of micron and submicron sizes, nanomaterials have an extremely high interface area enabling the volume concentration of surface layers formed on dispersed particles to very significant. Modifying their physical properties, one can effectively change the macro properties of the material. Secondly, the size and shape anisotropy of filler inclusions contribute much to filler texturing in a polymer. Thirdly, the very small particle sizes inhibit the processes of matrix delamination due to enormous surface tension, which certainly favors the increase in the strength of the composite. Taken together, all these factors provide a considerable improvement of various physical characteristics of nanomaterials at low filler concentration [3].

This paper presents the results of experimental studies of composites based on polyethylene and silicate needle-like nanofiller at the macro and micro levels. At the macroscopic scale, the experimental stress-strain curves obtained for materials with different filler fraction were analyzed. The microstructural and local mechanical properties were studied by the AFM techniques.

2 Fabrication of materials and preparation of samples

Low density polyethylene grade PE 107-02K (ρ = 0.91 g/cm^3) was taken as a polymer matrix. The initial modulus was 85 MPa, and the degree of crystallinity determined by differential scanning calorimetry was equal to approximately 35-40 %.
As a filler (the filling degree varies from 0 to 15 wt. parts), the modified nanoclay based on palygorskite (produced by "Keramzit" Serpukhov) was used. This mineral is water magnesium aluminum silicate. The crystalline structure of palygorskite is intermediate between the so-called belt and layered silicates. Palygorskite crystals are composed of double chains of Si-H tetrahedra interconnected by octahedrally coordinated magnesium and aluminum cations. During the grinding, the mineral breaks into particles having the form of elongated bars вГУ fibers. Under mechanical treatment, needle particles form tangled fibrous aggregates. Palygorskite clay generally has a light gray color, sometimes with a yellowish tinge. Its density is 2000-2300 kg/m^3, and its hardness is 2-2.5 in mineralogical scale and increases significantly after calcination. This mineral in its pure form is widely used in construction as an eco-friendly thermal insulator.
The surface of palygorskite crystals, as well as other clay minerals, is hydrophilic, making it difficult to wetting with hydrophobic organic substances. Before combining with polymers, it must be treated with special surface active substances (surfactants) to create organophilic layers with the necessary level of interaction with a polymer matrix.
For the production of polymer-silicate nanocomposites, a one-step mixing procedure developed at the Institute of Petrochemical Synthesis, Russian Academy of Sciences was applied [4, 5]. This method assumes that a polymer, a silicate and a surfactant are loaded into the extruder simultaneously. Surfactant molecules diffuse to silicate particles directly in a polymer melt.

3 The experiments

Mechanical testing. The mechanical properties of the materials under study were investigated at the macro level on a testing machine Testometric FS-100CT at room temperature. The strain rate was 100%/min. The loading of the samples was carried out until their rupture. For each filler concentration, five experiments were performed.
Atomic force microscopy. The properties of composites at the nano scale were studied by an atomic force microscope (AFM) Dimension Icon in the nanomechanical mapping regime (PeakForce QNM). In this mode an AFM tip performs nanoindentation in each point of the surface with a frequency of 2 kHz. Hence, the following structural-mechanical properties of the surface can be mapped: (a) relief; (b) adhesion force between the tip and the sample; (c) indentation u - the depth of penetration of the tip into the material; (d) Young modulus, i.e. the material stiffness E calculated by the DMT-model. In our experiments, the NSG10 probes (NT-MDT) with a nominal radius of 10 nm and a calibrated stiffness 9 N/m were

used. For each material, ten AFM images of 10x10 μm with a resolution of 1024x1024 points in the xy-plane were captured and analyzed (Fig. 1). Hereinafter, in the lower left-hand corner of the image (Fig. 1) the horizontal line shows the length of the examined segment. To the right of the vertical scale, the range of the measured value and units are given. Apart from needle-shaped palygorskite, the flat and round-shaped inclusions of

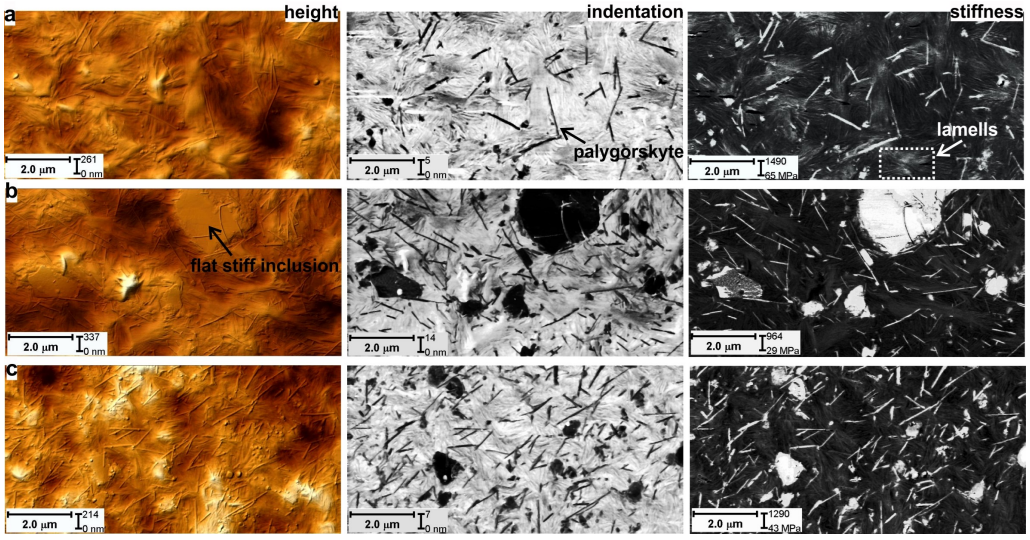

Figure 1: AFM images of the surface (left column) of the appropriate indentation depth (middle column) and stiffness (right column) of materials with filler wt. fractions: (a) вГУ 5, (b) вГУ 10, (c) вГУ 15.

different sizes are clearly visible in the images (see. Fig. 1b); this is probably the clay. Note that the fraction of large inclusions is comparable with the palygorskite fraction.
The microstructure of materials was studied in both the undeformed and stretched states. In the latter case, the samples were fixed and stretched in a special device. The experiments were performed without removing the load from the samples.

4 Results and discussion

Mechanical properties. The averaged engineering stress-strain (σ-ϵ) curves obtained for samples subjected to uniaxial load at constant rates are presented in Fig. 2. At the stage of the plastic flow corresponding to different concentrations, the curves $\sigma^0(\epsilon)$ are very close. Therefore, the evolution of the plastic flow causes actual stresses to become aligned for the systems with different filler concentration. There is a two-fold difference in YoungвГЄs modulus (85 MPa for unfilled polyethylene versus 170 MPa for 15% filler polyethylene). It has been found that incorporation of needle-like filler into the polymer reinforces the material much more strongly than in the case of conventional micro-sized filler. For instance, considering the appropriate concentration obtained by Farris [6] and supposing that the filler density is approximately twice as much as that of the matrix (15% by weight corresponds to the 7.6% by volume), an 1.5 fold increase in the modulus of the polymer filled with conventional micro-particles could be expected.
Microstructural analysis. Despite the fact that the filler is well seen in the maps of mechanical properties (Fig. 1), the polymer-filler interface has never been contrast, yet it has a certain slope up to several tens of nanometers wide. This can be attributed to the fact

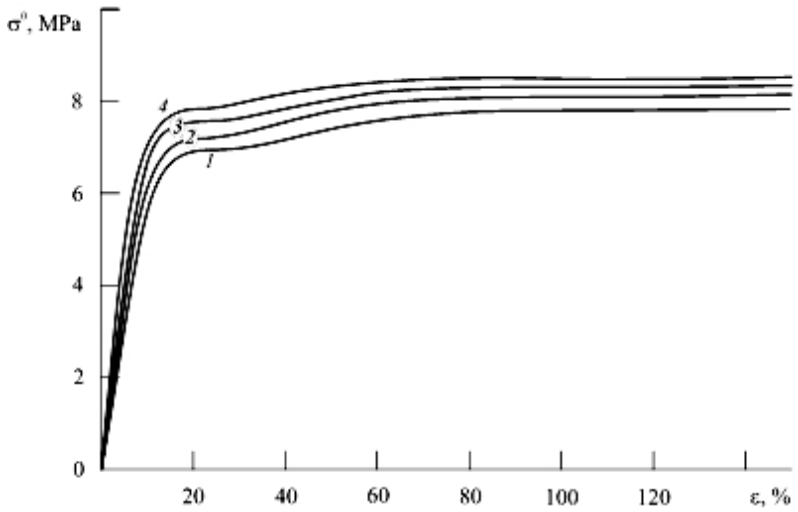

Figure 2: Stress-strain curves obtained for samples tested under uniaxial stretching for filler weight fractions: 1 – 0, 2 – 5, 3 – 10, and 4 – 15.

that some portion of the filler lies hidden under the polymer surface, as well as to the fact that the probe slips over the edge of the filler inclusion. For a quantitative analysis of the filler structure, especially the thickness of palygorskite needles, the criteria for belonging of a certain point in the AFM image to polymer or filler need to be defined. Figure 3 presents the histograms of indentation depth corresponding to the maps given in Fig. 1. For 2.3 nm depth indentation, the distribution histograms for materials with 10 and 15%

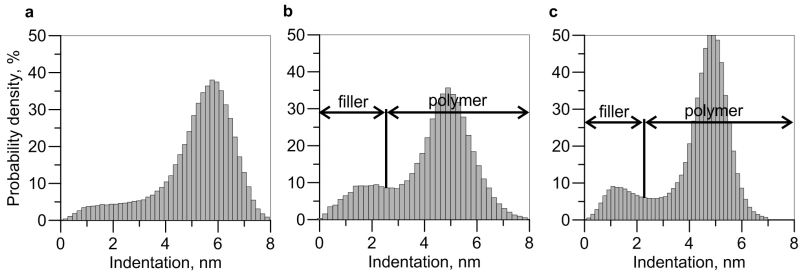

Figure 3: Distribution histograms of indentation depth for the surfaces depicted in Fig. 1. Filler fraction: (a): – 5%, (b) -вГУ 10%, (c) – 15 % wt.

filler content exhibit a local maximum (Fig. 3b, c). A similar pattern was observed for the rest of the images obtained for these materials. Such a pronounced local maximum was not observed for the material with 5% of filler content because of the low filler fraction. Let us assume that in all the images the indentation depth ≤ 2.3 nm corresponds to the filler. Figure 4 shows filler silhouettes isolated in Fig. 1. Further the structural analysis

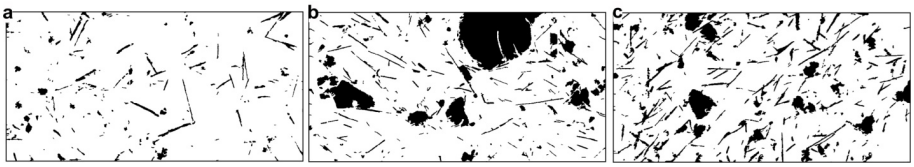

Figure 4: Fig. 4. Filler silhouettes (Fig. 1).

of black-and-white images was carried out. For each material, several hundreds of needles were explored. The average thickness of filler inclusions 27 nm was the same for all materials, and the average length was equal to 0.63, 0.50 and 0.56 microns for different filler concentration. Long needles up to 1.8 microns long were also observed. Palygorskite is able to form in the material secondary structures in the form of multiple stacks of needles arranged in parallel and in close proximity to one another (Fig. 5). It is not always possible

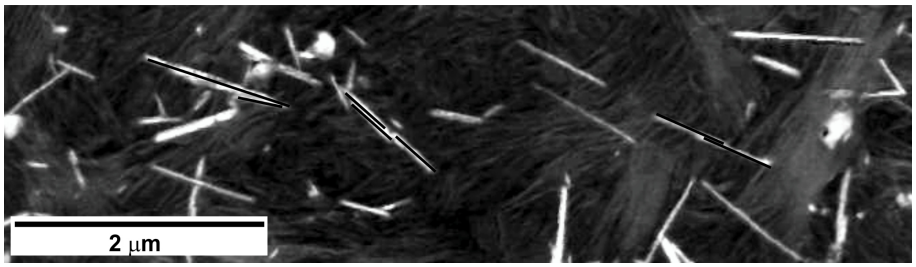

Figure 5: Stiffness map for the material with 10 % of filler. The formation of secondary structures having the form of parallel needles (black lines) is shown. The lamellar structure of polyethylene (gray filaments) is visible.

to unambiguously identify the boundaries of individual needles in agglomerates. This may cause an overestimation of the length and thickness of the objects to be measured. The study of the microstructure of the stretched materials reveals that some needles become wavy shaped (see. Fig. 6a, the axis of elongation is vertical). Apparently, this is due to the non-uniform local deformation of polyethylene and/or the compression of the material in the direction orthogonal to its elongation. Figure 6a shows dense inclusions with round surfaces (shown in boxes) that have good adhesion with a polymer. Inclusions that look like flat tablets are also encountered in the material; the delamination of the polymer, i.e. microcrack nucleation, can be observed near such inclusions (Fig. 6b). An increase in

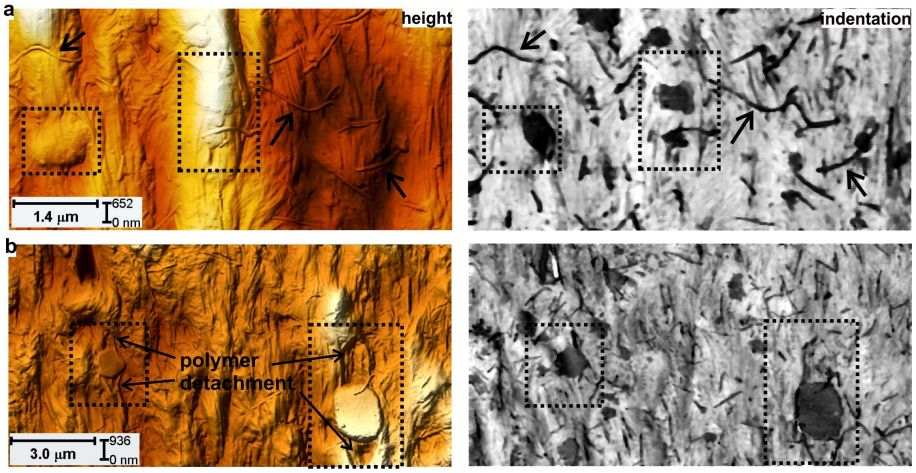

Figure 6: AFM-height images and the corresponding indentation maps of the 10% filled material at 100% tension; the arrows (a) point to the wavy structure of palygorskite; the frames (b) indicate the detachment of the polymer near the large and flat inclusions.

elongation causes the surfaces of the material to become sufficiently inhomogeneous - the

oriented structure of polymer heterogeneities appears on the surface of polyethylene, and the effects observed (palygorskite waving, delaminations) are strengthened.

5 Conclusions

The structure and mechanical properties of polyethylene filled with silicate needle filler (palygorskite) have been studied. Compared to the unfilled polymer, such composites have improved resistance to combustion, i.e. they are less inflammable and toxic.It has been found that the addition of the filler results in a roughly two-fold increase in the initial elastic modulus. At the stage of the plastic flow the mechanical properties of the material differed only slightly. Therefore, it has to be emphasized that the mechanical properties of the material did not worsen. The analysis of the polymer microstructure indicates that some filler needles form in the material secondary structures in the form of stacks. The average thickness of a palygorskite needle is 27 nm, and its length is 0.6 microns. As the stretch of the composite increases, the shape of inclusions becomes wavy.

Acknowledgements

This work is supported by RFBR grants: 13-08-00065(macro experiment), 14-02-96002 r_urals_ a (AFM experiment) and 15-03-08483 (fabrication of nanocomposite specimens).

References

[1] Sheng N., Boyce M.C., Parks D.M., Rutledge G.C., Abes J.I., Cohen R.E. Multiscale micromechanical modeling of polymer/clay nano-composites and the effective clay particle // Polymer. 2004. V. 45. P. 487-506.

[2] Manitiu M., Bellair R.J., Horsch S., Gulari E., Kannan R.M. Supercritical Carbon Dioxide-Processed Dispersed Polystyrene-Clay Nanocomposites // Macromolecules. 2008. V. 41 (21). P. 8038-8046.

[3] Chvalun S.N. Polymer composites // Priroda. 2000, No. 7, P. 22-30.

[4] Ivanyuk A.V., Gerasin V.A., Rebrov A.V., Pavelko R.G., Antipov E.M. Exfoliated clay-polyethylene nanocomposites obtained by in situ polymerization, synthesis. Synthesis, structure, properties. // Journal of Engineering Physics and Thermophysics, 2005, V.78, No. 5, P. 87-92.

[5] Gerasin V.A., Zubova T.A., Bakhov F.N., Barannnikov A.A., Merekalova N.D., Korolev Yu.M., Antipov E.M. Structure of polymer/Na+morillonite nanocomposites prepared by mixing in the melt // Nanotechnologies in Russia (Rossiiskie Nanotekhnologii). 2007. V.2. No. 1-2. P. 90-105.

[6] Farris R.J. Prediction of the viscosity of multimodal suspensions from unimodal viscosity data // Trans. Soc. Rheology. 1968. V. 12. P. 281ВГУ301.

O.K. Garishin, I.A. Morozov, V.V. Shadrin – Institute of Continuous Media Mechanics UB RAS, Perm, Russia
I.A. Morozov, V.V. Shadrin – Perm State University, Perm, Russia

V.A. Gerasin, M.A. Guseva – Institute of Institute of Petrochemical Synthesis RAS, Moscow, Russia

Vibration and wave processes in view of non-linear deformation of components in aircraft engine hydraulic systems

Dinara F. Gaynutdinova Vladimir Ya. Modorsky Vasiliy Yu. Petrov
grigoriev@ispms.tsc.ru

Abstract

We performed numerical studies of hydroelastic vibration and wave processes which included two approaches: one solving coupled problems in ANSYS CFX software package, and another using national algorithm for solving problems of hydroelasticity stated as a couple. In ANSYS CFX package we obtained results of computational modelling of cavitation effect caused by vibrations of the wall in a closed type (return-flow) pipe filled with fluid. We revealed the dependence between the cavitation parameters and the vibration parameters. We also constructed the domain (range) of influence of amplitudes and frequencies of vibration upon concentration of cavitation bubbles. At the second stage of the studies we developed standardized algorithm for solving problems of dynamic hydroelasticity, worked out the model problem of piston motion of piston in the closed type pipe, and conducted a comparative analysis of numerical and analytical solutions of the model problem.

Introduction

Unpredictable failures in the course of operation of hydraulic automatic equipment of aircraft engines occur increasingly often. To predict them is a difficult and time-consuming task. It is true that failures may be related to the drastic increase of operation noise generated by hydraulic systems of aircraft engines, and therefore it might be suggested that they are brought about by cavitation effects in the pipelines caused by vibrations of the component walls. This paper is concerned with the possibility of modelling the cavitation effect during the operation of hydraulic automatic equipment.

1 Solution of the Problem in ANSYS CFX Software Package

Physical Model

To carry out computing experiments we developed a physical model which proposed a three-dimensional statement. In doing so, we took a pipe as the computation domain, compressible fluid (water) as the actuating medium, and sinusoidally movable wall as the loading; assumed that the flow was multiphase (consisting of water as carrier phase, and air as carried phase), the process was adiabatic, and the pipe walls were impenetrable and smooth, and accepted standard ke model of turbulence.

Mathematical Model

In accordance with the accepted physical model, we used a mathematical model based on the mass, momentum and energy conservation laws, and implemented within ANSYS CFX reverse engineering system. It reflected the convection-diffusion transfer of components to be mixed and turbulent flow. The set of equations was enclosed by the initial and boundary conditions. [1]
The finite volume method implemented in ANSYS CFX software package was chosen to solve the original set of equations.

Solid Model and Setting of Initial and Boundary Conditions

The computational domain was divided into finite volumes (400,000 cells). Figure 1 shows the solid model and boundary conditions. The following initial conditions were set: V = 0 m / s; P = 0.1 MPa; T = 293 K; $\rho_w = 1000 kg/m^3$.
The boundary condition adopted for the walls of chamber was "stiff or rigid wall" when the normal velocity component at the boundary was equal to 0. The boundary condition adopted for the mobile body was Ymovable wallY when the normal velocity component at the boundary was set by equation $V = V_0 sin(\omega t)$, where V – flow or fluid velocity, V_0 – wall velocity amplitude, ω – oscillation frequency, and t – time. [2] - [5]

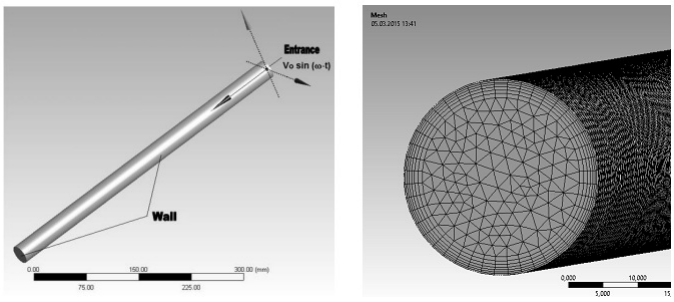

Figure 1: Boundary Conditions and Computational Grid

The time step was set at $5 \cdot 10^{-4}$ sec, and the number of iterations for each calculation did

not exceed 2000. Therefore, each of the options was studied on the real-time interval from 0 to 1 sec. The calculation time was 4 . . . 5 hours.

Analysis of the Results of Computing Experiments

The plan of computing experiments envisaged that V_0 varied in the range $0.001 \ldots 10 m/sec$ and ω - in the range 500 . . . 4000 Hz. All calculations were made on the basis that the initial pressure within an enclosure was 1 MPa at an initial temperature (T) of $20^0 C$.

In accordance with the plan, different values of carried phase concentration were derived from the results of computing experiments.

According to the calculations based on all options of set boundary conditions, we obtained a certain area of cavitation arising due to vibration at various combinations of frequencies and wall velocity amplitudes. In Fig. 2: x-axis is used to specify the change in the speed of oscillation, y-axis to specify the change in the frequency of oscillation, and z-axis Ц the change in the mass content of carried phase. [6]

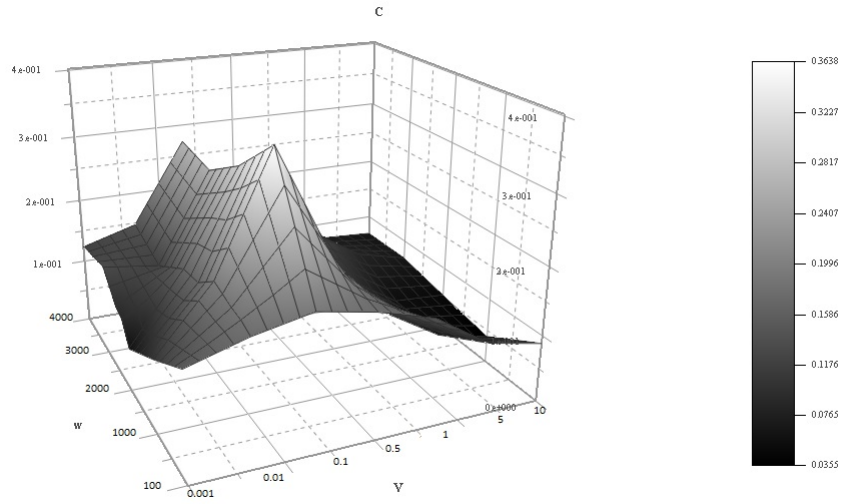

Figure 2: Area of Cavitation Due to Vibration

The analysis of the results revealed a maximum corresponding to the frequency of $2000 Hz$. As the frequency of vibration increased or decreased the concentration decreased. The wall velocity amplitude corresponding to the maximum concentration of the carried phase was $0.1 m/sec$, and as it increased or decreased the concentration decreased as well.

2 Development and Implementation of Standardized Algorithm Based on the Particle-in-Cell Method

At present, with current sanctions against Russia, this is particularly important to develop national algorithms for solving complex interdisciplinary problems, including hydroelasticity.

Physical Model

We developed the physical model that enabled the processes occurring in structure and in fluid to be stated dynamically in two-dimensions; for that purpose, we assumed that the structure was multilayered and made of elastic material; the fluid was compressible and remained in contact with the movable wall; and the pipe walls were impenetrable, impermeable, not heat conducting and smooth; and took no account of gravity.

Mathematical Model

In accordance with the accepted physical model, we constructed a mathematical model of hydrodynamic process based on the mass, momentum and energy conservation laws, control of compressible fluid state, and initial and boundary conditions recorded with due regard for stiffness of loading system.
Mathematical model of deformable structure also included the mass and momentum conservation laws, and was enclosed by Cauchy equations, generalized HookeŸs law, and initial and boundary conditions recorded with due regard for stiffness of loading system.
To develop the original system of differential equations we chose one of the methods of finite differences - the particle-in-cell method.

Standardized Algorithm for Solving Problems of Dynamic Hydroelasticity

Based on the chosen method we developed the algorithm which included several stages (Figure 3). The initial stages were designed to solve the hydrodynamic problem, whereas the subsequent stages were meant to estimate parameters of the dynamic stress-strain state (SSS) or tensely deformed condition (TDC) of structure. [7]

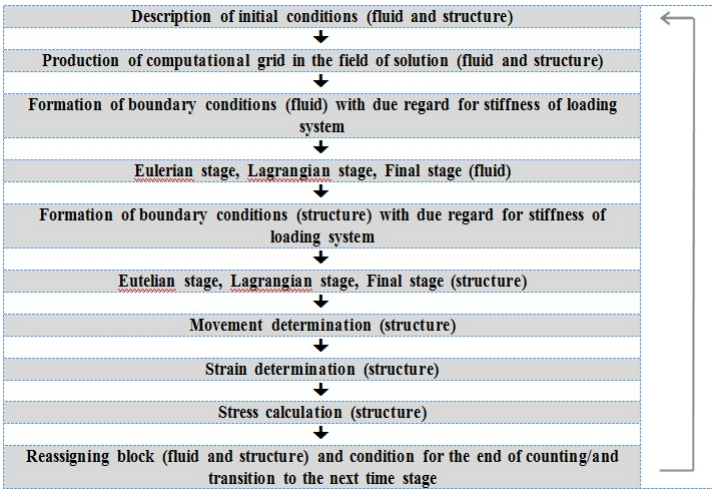

Figure 3: Standardized Algorithm for Solving Problems of Dynamic Hydroelasticity

First, we described the initial conditions and produced a computational grid in the field of solution for both fluid and structure. Then, we formed the boundary conditions for the fluid with due regard for the loading system, and then focused on three successive stages. At the Eulerian stage we neglected all effects associated with the movement of unit cell

(when there was no mass flow through the cell borders), and took into account the effects of material acceleration only through pressures; here we determined intermediate values of the desired flow conditions (characteristics) for a large particle. At the Lagrangian stage we calculated the mass flows crossing the borders of the Eulerian cells. At the final stage, at a new moment we determined the final values of the flow conditions (characteristics) for each cell, and for the entire system on the fixed computational grid. The obtained parameters of hydrodynamic flow were used as the initial data for the subsequent time step and were included in the calculations of the boundary conditions to estimate the dynamic stress-strain state (SSS) or tensely deformed condition (TDC) of structure.
Further, the same three stages were sequentially performed for the structure. The following stages were new from the viewpoint of traditional approaches to the particle-in-cell method and included algorithms to determine the movements, strains and stresses at each time step. That completed the computing cycle of one time step, and the results of calculation at that time step provided a baseline for the next one.
The use of this standardized algorithm for simultaneous solution of hydrodynamic problem and calculation of parameters of the stress-strain state of the structure is an innovation and makes it possible to study and reveal the physical entity of the occurrence and course of abnormal unpredictable hazardous processes and phenomena in case of the nonlinear interaction in the dynamic system using the united methodological tools. This will allow finding ways to ensure operability of expensive high-tech structures yet at the design stage.

Analysis of the Results of Model Problem Solution

Testing of the proposed algorithm for solving problems of dynamic hydroelasticity was conducted in MARS domestic package for the model problem Yabout the motion of piston in the fluid filled pipeY. Design scheme is presented in Figure 4.

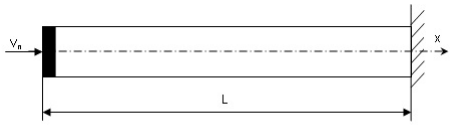

Figure 4: Design Scheme

The following initial conditions were set: $L = 0.5m$ – the pipe length; $P_{in} = 450 \cdot 10^6 Pa$ – internal fluid pressure; $V = 10m/sec$ – the speed of piston; $\rho_w = 1000kg/m^3$ – the liquid density; $K = 5.0$ – fluid adiabatic exponent. In this case, at this stage the structure is not deformable (strained), but this may be considered in future.
Upon starting, the wave of compression will move ahead of the piston at a speed of N1 in a medium at rest (fluid at rest). Once it reaches the wall, the direct wave will reflect from the wall, and the reflected wave will propagate at a speed of N3 in the direction opposite to that of the moving fluid (Figure 5.). [8]

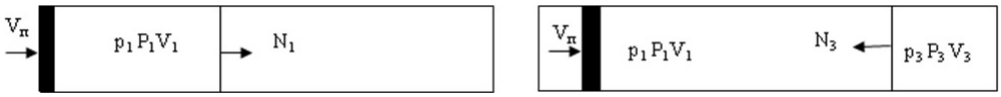

Figure 5: Direct and Reflected Waves

Results of the solution of model problem for the direct wave are given in Figure 6. The figure shows that the front of direct wave has run halfway along the pipe length. Downstream the wave front there are oscillations caused by numerical effects.

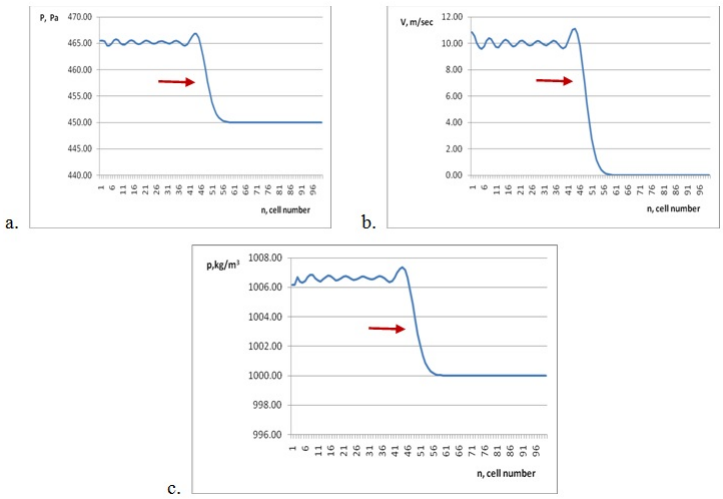

Figure 6: Change in Hydrodynamic Parameters along the pipe length, at $t = 0.16 \cdot 10^{-3} sec$, a. – pressure b. – speed c. – density

Subsequently, after the reflection these effects disappear. Results of the solution of model problem of the reflected wave are shown in Figure 7.

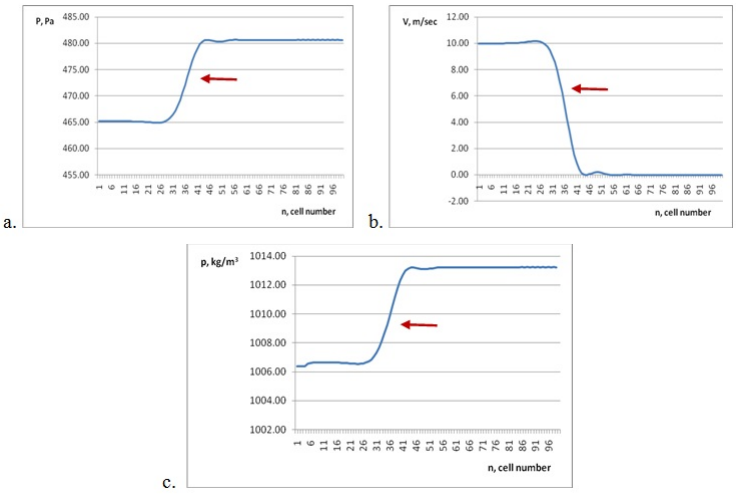

Figure 7: Change in Hydrodynamic Parameters along the pipe length, at $t = 0.57 \cdot 10^{-3} sec$, a. – pressure b. – speed c. – density

To verify the obtained numerical solutions analytical calculations for this model problem were made with the use of known analytical dependences.
Table 1 gives the results of comparison between numerical and analytical solutions in the following parameters: P_1, ρ_1 – pressure and density of the direct wave, respectively; X_1 –displacement of the front of direct shock wave from the original position; N_1 – speed of the front of direct wave; P_3, ρ_3 – pressure and density of the reflected wave, respectively; X_3 – displacement of the front of reflected wave from the original position; N_3 – speed of the front of reflected wave.

Table 4: Comparison between Numerical and Analytical Solutions

Controlled Parameters	Results of Numerical Solution	Results of Analytical Solution
P_1,Pa	$465 \cdot 10^6$	$465 \cdot 10^6$
ρ_1, kg/m^3	1006,6	1006,6
X_1, m	0,24	0,24
N_1, m/sec	1515	1515
P_3, Pa	$480,6 \cdot 10^6$	$480,6 \cdot 10^6$
ρ_3, kg/m^3	1013,3	1013,3
X_3, m	0,36	0,36
N_3, m/sec	1525	1525

The comparative analysis of numerical and analytical solutions has shown that the results of solutions agree very closely. There is a "smearing" of the shock wave front associated with the schematic viscosity.

Conclusions

1. We have carried out the studies using two approaches: on the basis of the solution of the coupled problem in ANSYS CFX commercial package and MARS domestic package, and solved hydroelasticity problems stated as a couple.
2. We have constructed physical and mathematical models for computing experiment and performed numerical computations. We have discovered and constructed the area of cavitation brought about by vibration, and have revealed that the cavitation effect was maximized at certain combinations of amplitudes and frequencies of oscillations.
3. To develop national algorithm for solving coupled problems of dynamic hydroelasticity we have constructed physical and mathematical models, and have developed standardized algorithm. We have solved the model problem of dynamic hydroelasticity stated in one dimension. We have made analytical calculations and comparative analysis with the numerical solution. It has shown that their results agree very closely.

Acknowledgements

The work is carried out with the support of the Russian Foundation for Basic Research, Grant RFFI No. $14-07-96003-r\_ural\_a$.

References

[1] Reverse Engineering System ANSYS CFX-Solver Theory Guide. ANSYS CFX.

[2] The solution of engineering problems on high performance computing complex of the Perm National Research Polytechnic University: monograph edited by V.Ya. Modorsky - Perm: Publishing of the Perm National Research Polytechnic University, 2014. – 314 pp.

[3] A.V. Kozlova, V.Ya. Modorsky. Numerical modeling of the cavitation effects in a closed type pipe with a movable wall. Scientific and Technical Bulletin of Povolzhye. No. 2 2013 – Kazan: Scientific and Technical Bulletin of Povolzhye, 2013. – pp. 132-135.

[4] D.F. Gaynutdinova, A.V. Kozlova, V.Ya. Modorsky, E.V. Mekhanoshina. Numerical modeling of the cavitation effects caused by vibration. Scientific and Technical Bulletin of Povolzhye. No. 6 2013 – Kazan: Scientific and Technical Bulletin of Povolzhye, 2013. – pp. 219-223.

[5] E.V. Mekhanoshina, V.Ya. Modorsky, A.V. Kozlova, D.F. Gaynutdinova, Study of the influence of vibration and pressure on cavitation. Scientific and Technical Bulletin of Povolzhye. No. 6 2013 – Kazan: Scientific and Technical Bulletin of Povolzhye, 2013. – pp. 364-368.

[6] Gaynutdinova D.F., Modorsky V.Ya., Kozlova A.V. Computing modeling of the area of cavitation caused by vibration. Scientific and Technical Bulletin of Povolzhye. No. 6 2014 – Kazan: Scientific and Technical Bulletin of Povolzhye, 2014. – pp. 127-129.

[7] Modorsky V.Ya., Sokolkin Yu.V. Gas Elastic Processes in Power Plants. – M.: Nauka, 2007 – 176 pp.

[8] I.P. Ginzburg Aerogasdynamics. – M.: Vysshaya Schkola, 1966 – 404 pp.

Dinara F. Gaynutdinova, pr. Komsomolsky, 29, Perm, Russian Federation
Vladimir Ya. Modorsky, pr. Komsomolsky, 29, Perm, Russian Federation
Vasiliy Yu. Petrov, pr. Komsomolsky, 29, Perm, Russian Federation

Kinematic fluid dynamos examined by toroidal-poloidal decompositions—An example of combining continuum mechanics and electrodynamic field theory

Sebastian Glane, Felix A. Reich, Wolfgang H. Müller
sebastianglane@mailbox.tu-berlin.de

Abstract

This paper presents a rational approach to the problem of kinematic dynamos in spherical cavities and the related induction equation. An operator notation using poloidal-toroidal decompositions is developed in order to analyze the governing differential equation. A solution of the induction equation is sought by using series expansions. Applying projection methods leads to a fully analytic system of differential equations in one coordinate, *i.e.*, the radius, for the series coefficients.

1 Introduction

Larmor proposed in 1919 that the magnetic field of large astronomical objects, such as the Earth or the Sun, is generated by fluid flow in the interior. This is due to self-excitation processes caused by coupling of fluid- and electromagnetic fields, *cf.*, [11]. The coupling is described by additional terms in Maxwell's equations and the equation of linear momentum. The transfer of kinetic energy to electromagnetic energy can lead to an amplification of the magnetic field. This process is a.k.a. dynamo action.

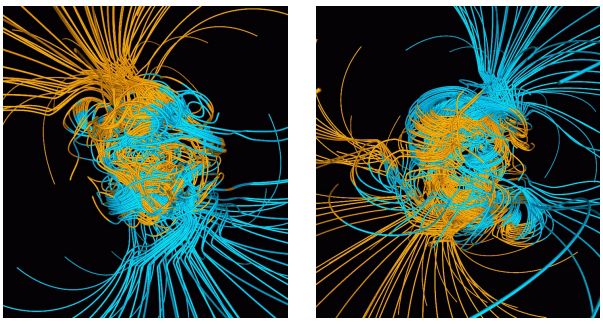

(a) Before dipole reversal. (b) After dipole reversal.

Figure 1: Simulation of a geodynamo in reversal by Glatzmaier, from [6]. Magnetic field lines are shown. Blue/yellow colors indicate the field is directed inward/outward.

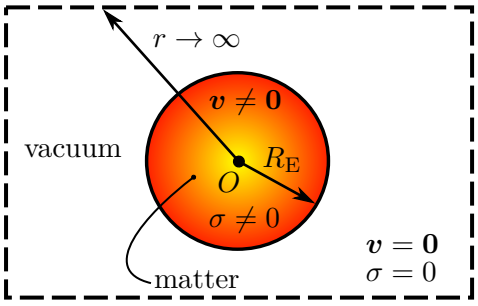

Figure 2: Sketch of the considered problem.

By paleomagnetic investigations, it is known that the Earth's magnetic field is reversing, *i.e.*, changing its polarity, *cf.*, [11]. In order to understand and predict the magnetic field's reversal, the so-called geodynamo is used as a modell. A geodynamo simulation by Glatzmaier illustrating the field reversal is shown in Fig. 1. The origin of the Earth's magnetic field and its reversal is a topic of past and current research. Some aspects of it will be presented in this paper.

2 Induction equation—derivation and discussion

The considered model problem is sketched in Fig. 2. It consists of a spherical cavity filled with a conducting fluid surrounded by vacuum. The governing field equations of electrodynamics of the problem are given by Maxwell's equations. Suppose the fluid is neither polarizable, *i.e.*, $\boldsymbol{P} = \boldsymbol{0}$, nor magnetizable, *i.e.*, $\boldsymbol{M} = \boldsymbol{0}$. In an inertial frame of reference the field equations and related jump conditions read:

$$\nabla \cdot \boldsymbol{B} = 0\,, \qquad [\![\boldsymbol{B}]\!] \cdot \boldsymbol{e} = 0\,, \tag{1a}$$

$$\frac{\partial \boldsymbol{B}}{\partial t} + \nabla \times \boldsymbol{E} = \boldsymbol{0}\,, \qquad [\![\boldsymbol{E}]\!] \times \boldsymbol{e} + [\![\boldsymbol{B}]\!]\, w_\perp = \boldsymbol{0} \tag{1b}$$

$$\varepsilon_0 \nabla \cdot \boldsymbol{E} = 0\,, \qquad \varepsilon_0\, [\![\boldsymbol{E}]\!] \cdot \boldsymbol{e} = \underset{A}{q^\mathrm{f}}\,, \tag{1c}$$

$$\varepsilon_0 \frac{\partial \boldsymbol{E}}{\partial t} - \frac{1}{\mu_0} \nabla \times \boldsymbol{B} = -\boldsymbol{J}^\mathrm{f}\,, \qquad -\frac{1}{\mu_0}\, [\![\boldsymbol{B}]\!] \times \boldsymbol{e} + \varepsilon_0\, [\![\boldsymbol{E}]\!]\, w_\perp = \underset{L}{\boldsymbol{J}^\mathrm{f}}\,. \tag{1d}$$

Note that the Maxwell-Lorentz aether relations have already been inserted in the system above. Moreover, Ohm's law for a *moving* conductor has been used as a constitutive law. Hence, for the diffusive current $\boldsymbol{j}^\mathrm{f}$ we have, *cf.*, [8]:

$$\boldsymbol{j}^\mathrm{f} = \sigma\,(\boldsymbol{E} + \boldsymbol{v} \times \boldsymbol{B})\,. \tag{2}$$

After performing a scaling analysis and by assuming $\|\boldsymbol{v}\| \ll c$ it may be shown that, *cf.*, [9],

$$\mathcal{O}\left(\varepsilon_0 \frac{\partial \boldsymbol{E}}{\partial t}\right) \ll \mathcal{O}\left(\frac{1}{\mu_0} \nabla \times \boldsymbol{B}\right)\,, \quad \mathcal{O}\left(q^\mathrm{f} \boldsymbol{v}\right) \ll \mathcal{O}\left(\frac{1}{\mu_0} \nabla \times \boldsymbol{B}\right)\,, \tag{3}$$

where the Landau symbol $\mathcal{O}$ indicates the order of magnitude. This shows that the convective current is negligibly small w.r.t. the left-hand right of (1d). Hence, the total current $\boldsymbol{J}^\mathrm{f}$ is given by the diffusive Ohmic current $\boldsymbol{j}^\mathrm{f}$ only. Application of Eqns. (2) and (3) to Eqn. (1d) leads to:

$$\frac{1}{\mu_0} \nabla \times \boldsymbol{B} = \sigma\,(\boldsymbol{E} + \boldsymbol{v} \times \boldsymbol{B}) \Leftrightarrow \boldsymbol{E} = \frac{1}{\sigma \mu_0} \nabla \times \boldsymbol{B} - \boldsymbol{v} \times \boldsymbol{B}\,. \tag{4}$$

This analysis is part of the so-called magnetohydrodynamic approximation. If, in addition, we assume that the conductivity σ is constant, which corresponds to a homogeneous conductor, the induction equation is obtained by expressing the curl of the electric field $\boldsymbol{E}$ in Eqn. (1b) through Eqn. (4). Hence, the induction reads, *cf.*, [9]:

$$\frac{\partial \boldsymbol{B}}{\partial t} + \frac{1}{\sigma \mu_0} \nabla \times \nabla \times \boldsymbol{B} = \nabla \times (\boldsymbol{v} \times \boldsymbol{B}) \,. \tag{5}$$

This equation can be interpreted as an evolution equation for the magnetic field $\boldsymbol{B}$. The velocity $\boldsymbol{v}$ is present in the equation above. Consequently, the velocity influences the evolution of the magnetic flux density. From mechanics it is known that the evolution of the velocity is described by the balance of linear momentum. This shows that the equation above can, in general, only be solved in combination with the balance of linear momentum. In this paper we consider so-called kinematic dynamos, which indicates that the velocity field is *prescribed*. Therefore, the balance equations of mechanics are not considered any further.

In what follows we consider the non-dimensional form of the induction equation. It reads:[1]

$$\frac{\partial \boldsymbol{B}}{\partial t} + \nabla \times \nabla \times \boldsymbol{B} = Re_{\text{mag.}} \nabla \times (\boldsymbol{v} \times \boldsymbol{B}) \,, \tag{6}$$

in which $Re_{\text{mag.}}$ is the so-called magnetic Reynolds number. The magnetic Reynolds number relates electromagnetic diffusion to fluid-dynamic transport. For a static velocity field the induction equation can be formulated as a generalized eigenvalue problem. A solution ansatz in exponential form in time leads to:

$$\lambda \boldsymbol{B} + \nabla \times \nabla \times \boldsymbol{B} = Re_{\text{mag.}} \nabla \times (\boldsymbol{v} \times \boldsymbol{B}) \,, \tag{7}$$

in which $\boldsymbol{B}$ is a function of space variables only and λ is the eigenvalue. Eigenvalues with positive/negative real part indicate exponential growth/decay of the related eigenmode $\boldsymbol{B}$. Static solutions both for the magnetic and for the velocity field correspond to $\lambda = 0$. An exponential growth indicates an amplification of a so-called seed field by a given fluid flow. This would demonstrate that dynamo action may be possible.

In order to solve the eigenvalue problem, boundary conditions for the magnetic field at the boundary between the material interior and vacuous exterior, *i.e.*, at $r = 1$, are necessary. It can be shown that for the case of a fixed boundary, $w_\perp = 0$, a continuous transition of the magnetic field results. Hence,

$$[\![\boldsymbol{B}]\!] = \boldsymbol{0} \,. \tag{8}$$

In the presented model the cavity is the only source. Therefore, in the exterior, which is under vacuum, electromagnetic waves travel from the boundary on to infinity. Because of the fact that for the source, *i.e.*, the material interior, the magnetohydrodynamic approximation applies, it also holds for the exterior. In doing so the wave character of the fields is broken. Applying the magnetohydrodynamic approximation to Maxwell's system in vacuum gives:

$$\nabla \cdot \boldsymbol{B} = 0 \,, \quad \nabla \times \boldsymbol{B} = \boldsymbol{0} \,. \tag{9}$$

[1] The choice of reference quantities, *i.e.*, reference length, velocity, and magnetic flux density, inherently determines the form of the non-dimensional induction equation. Other reference quantities may lead to $Re_{\text{mag.}}^{-1}$ in front of the double-curl term.

The solution of these equations is given by a scalar potential ψ describing the spatial behavior of the magnetic field. The time dependence is given by the source, *i.e.*, the material interior. The potential is obtained through LAPLACE's equation and in spherical coordinates its gradient, which is nothing else but the magnetic field, is given by the series:

$$\boldsymbol{B}\left(t,r,\theta,\varphi\right)=\sum_{n=0}^{\infty}r^{-(n+2)}\sum_{m=-n}^{n}c_n^m\left(t\right)\left(-\left(n+1\right)Y_n^m\left(\theta,\varphi\right)\boldsymbol{e}_r+\nabla_{\theta,\varphi}Y_n^m\right)\,. \tag{10}$$

In conclusion, the exterior solution is determined up to time-dependent series coefficients c_n^m, which can be determined by the boundary condition discussed above.

3 Spherical harmonics and poloidal-toroidal decompositions

3.1 Properties of spherical harmonics

We introduce the scalar or inner product of two arbitrary functions f and g on a spherical surface of radius r as:

$$\langle f,g\rangle_{\partial B_r}:=\oiint_{\partial B_r}f\left(\boldsymbol{x}\right)\overline{g}\left(\boldsymbol{x}\right)\frac{1}{\left\|\boldsymbol{x}\right\|^2}\,\mathrm{d}A=\int_0^{2\pi}\int_0^{\pi}f\left(r,\theta,\varphi\right)\overline{g}\left(r,\theta,\varphi\right)\sin\left(\theta\right)\mathrm{d}\theta\,\mathrm{d}\varphi\,. \tag{11}$$

In the context of the HELMHOLTZ equation spherical harmonics Y_n^m occur as the angular part of the solution. In this paper complex spherical harmonics are used and defined by:

$$Y_n^m\left(\theta,\varphi\right):=N_n^m\exp\left(\mathrm{i}m\varphi\right)P_n^{|m|}(\cos\left(\theta\right))\,. \tag{12}$$

The symbol $P_n^{|m|}$ represents the associated LEGENDRE polynomials. As an example two spherical harmonics are plotted in Fig. 3. If the normalization factor N_n^m is chosen

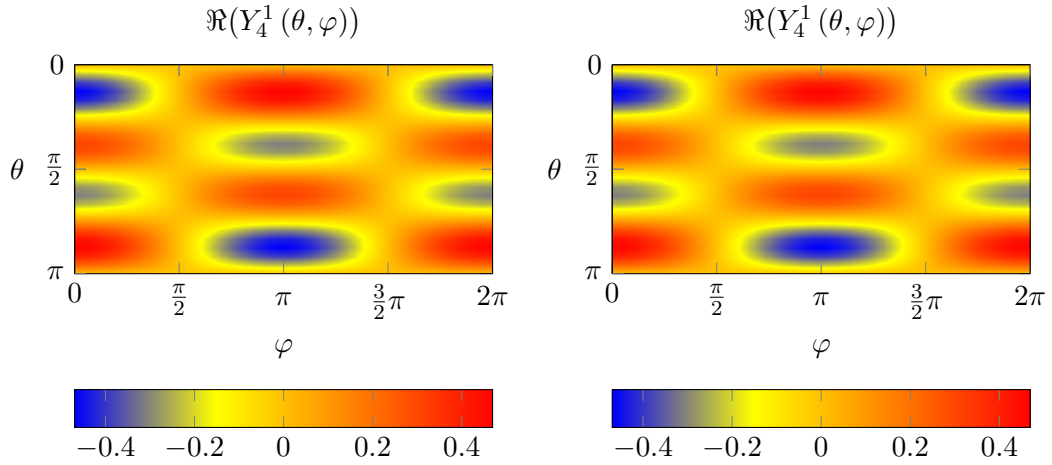

(a) Real part for $m=2$, $n=2$.

(b) Real part for $m=1$, $n=4$.

Figure 3: Plot of spherical harmonics Y_n^m.

appropriately, the spherical harmonics constitute an orthonormal system with respect to the scalar product defined above. Accordingly, the following relation holds:

$$\left\langle Y_n^m,Y_p^o\right\rangle_{\partial B_r}=\delta^{mo}\delta_{np}\,. \tag{13}$$

This orthogonality relation allows for a series expansion of scalar functions in spherical harmonics. In general, the series coefficients may be radially dependent. By further inspection of the HELMHOLTZ equation it can be shown that the spherical harmonics represent the eigenfunctions of the LAPLACE operator on a spherical surface, *viz.*:

$$\Delta_{\theta,\varphi} Y_n^m = -n\,(n+1)\,Y_n^m\,(\theta,\varphi)\ . \tag{14}$$

3.2 Poloidal-toroidal decomposition

It can be shown that every solenoidal, *i.e.*, divergence-free, vector field $\boldsymbol{F}$ can be further decomposed in a toroidal vector field $\boldsymbol{M}$[2] and a poloidal vector field $\boldsymbol{N}$, *cf.*, [12]. Thus, we may write for arbitrary $\boldsymbol{F}$ obeying $\nabla \cdot \boldsymbol{F} = 0$:

$$\boldsymbol{F} = \boldsymbol{M} + \boldsymbol{N}\,. \tag{15}$$

In spherical coordinates, the summands are given by a series of spherical harmonics, *i.e.*:

$$\boldsymbol{M} = \sum_{n=0}^{\infty}\sum_{m=-n}^{n} \boldsymbol{m}_n^m\,, \quad \boldsymbol{N} = \sum_{n=0}^{\infty}\sum_{m=-n}^{n} \boldsymbol{n}_n^m\,. \tag{16}$$

The so-called toroidal and poloidal modes are given by:

$$\boldsymbol{m}_n^m := \nabla \times [r m_n^m\,(r)\,Y_n^m\,(\theta,\varphi)\,\boldsymbol{e}_r] = m_n^m\,(r)\,\boldsymbol{\mathcal{D}}_{\theta,\varphi}[Y_n^m]\ , \tag{17a}$$

$$\begin{aligned}\boldsymbol{n}_n^m :=\ & \nabla \times \nabla \times [r n_n^m\,(r)\,Y_n^m\,(\theta,\varphi)\,\boldsymbol{e}_r] \\ =\ & \frac{n\,(n+1)}{r} n_n^m\,(r)\,Y_n^m\,(\theta,\varphi)\,\boldsymbol{e}_r + D_r^{(1)}[n_n^m]\,\nabla_{\theta,\varphi} Y_n^m\,.\end{aligned} \tag{17b}$$

The symbol $\nabla_{\theta,\varphi}$ represents the gradient on a spherical surface.[3] Moreover, the operators introduced in the equations above are defined as follows:

$$\boldsymbol{\mathcal{D}}_{\theta,\varphi}[f] := \frac{1}{\sin(\theta)}\frac{\partial f}{\partial \varphi}\boldsymbol{e}_\theta - \frac{\partial f}{\partial \theta}\boldsymbol{e}_\varphi\,, \quad D_r^{(1)}[f] := \frac{1}{r}\frac{\mathrm{d}}{\mathrm{d}r}\,[r f\,(r)]\ . \tag{18}$$

The special choices for the toroidal and poloidal fields are motivated by the problem of the vectorial HELMHOLTZ equation, *cf.*, [5]. As an example, a toroidal vector field is shown in Fig. 4b.

3.3 Orthogonality of toroidal and poloidal vector fields

The orthogonality of toroidal and poloidal vector fields is analyzed below with respect to the inner product of two arbitrary vector fields $\boldsymbol{f}$ and $\boldsymbol{g}$:

$$\langle \boldsymbol{f}, \boldsymbol{g} \rangle_{\partial B_r} := \oiint_{\partial B_r} \boldsymbol{f}\,(\boldsymbol{x}) \cdot \overline{\boldsymbol{g}}\,(\boldsymbol{x})\,\frac{1}{\|\boldsymbol{x}\|^2}\,\mathrm{d}A = \frac{1}{r^2}\oiint_{\partial B_r} \boldsymbol{f}\,(\boldsymbol{x}) \cdot \overline{\boldsymbol{g}}\,(\boldsymbol{x})\,\mathrm{d}A\,. \tag{19}$$

We consider the operators $\nabla_{\theta,\varphi}$ and $\boldsymbol{\mathcal{D}}_{\theta,\varphi}$. By using the product rule for the divergence, we may write:

$$\nabla_{\theta,\varphi} f \cdot \boldsymbol{\mathcal{D}}_{\theta,\varphi}[g] = \nabla_{\theta,\varphi} \cdot (f \boldsymbol{\mathcal{D}}_{\theta,\varphi}[g]) - f \nabla_{\theta,\varphi} \cdot \boldsymbol{\mathcal{D}}_{\theta,\varphi}[g]\ . \tag{20}$$

[2] For reasons of notation we use $\boldsymbol{M}$ for toroidal field. This symbol does not represent the magnetization.

[3] The gradient of a function f on a spherical surface is given by:

$$\nabla_{\theta,\varphi} f = \frac{\partial f}{\partial \theta}\boldsymbol{e}_\theta + \frac{1}{\sin(\theta)}\frac{\partial f}{\partial \varphi}\boldsymbol{e}_\varphi\,.$$

After a simple calculation we conclude that:

$$\nabla_{\theta,\varphi} \cdot \boldsymbol{\mathcal{D}}_{\theta,\varphi}[g] = \frac{1}{\sin(\theta)} \left(\frac{\partial}{\partial\theta} \left(\sin(\theta) \frac{1}{\sin(\theta)} \frac{\partial g}{\partial\varphi} \right) - \frac{\partial^2 g}{\partial\varphi\partial\theta} \right) = 0 \,. \tag{21}$$

Hence, the scalar product of the considered operators is:

$$\langle \nabla_{\theta,\varphi} f, \boldsymbol{\mathcal{D}}_{\theta,\varphi}[g] \rangle_{\partial B_r} = \frac{1}{r^2} \oiint_{\partial B_r} \nabla_{\theta,\varphi} \cdot (f \boldsymbol{\mathcal{D}}_{\theta,\varphi}[\overline{g}]) \, \mathrm{d}A = 0 \,. \tag{22}$$

In the last step Gauss' integral theorem was applied to a closed surface, see [4]. Then the boundary integral vanishes because the field of integration is an empty set. By using the product rule and Gauss' integral theorem, we may write:

$$\begin{aligned} \left\langle \nabla_{\theta,\varphi} Y_n^m, \nabla_{\theta,\varphi} Y_p^o \right\rangle_{\partial B_r} = \frac{1}{r^2} \oiint_{\partial B_r} \left(\nabla_{\theta,\varphi} \cdot \left(Y_n^m \nabla_{\theta,\varphi} \overline{Y_p^o} \right) - Y_n^m \Delta_{\theta,\varphi} \overline{Y_p^o} \right) \mathrm{d}A \\ = p\,(p+1) \left\langle Y_n^m, Y_p^o \right\rangle_{\partial B_r} . \end{aligned} \tag{23}$$

This shows that the pairwise orthogonality of the operator $\nabla_{\theta,\varphi}$ is reduced to the orthogonality of the spherical harmonics. The same holds for the operator $\boldsymbol{\mathcal{D}}_{\theta,\varphi}$. Because of the orthogonality of the constitutive operators and spherical harmonics the toroidal and poloidal modes constitute a fully orthogonal set. Hence, in spherical coordinates every solenoidal vector field may be expanded in these orthogonal components, *cf.*, [12].

4 Projection method

In this section we apply the so-called projection method to the induction equation, *i.e.*, the eigenvalue problem (7). This procedure is also presented in [2]. We suppose that the material is compressible. Hence, $\nabla \cdot \boldsymbol{v} = 0$ and the velocity may be expanded in toroidal and poloidal vector fields as well, *cf.*, [2, 4]. We write the magnetic and the velocity field such that:

$$\boldsymbol{B} = \sum_{j=0}^{\infty} \sum_{i=-j}^{j} \left(\boldsymbol{m}_j^i + \boldsymbol{n}_j^i \right) , \quad \boldsymbol{v} = \sum_{l=0}^{\infty} \sum_{k=-l}^{l} \left(\boldsymbol{o}_l^k + \boldsymbol{p}_l^k \right) , \tag{24}$$

where $\boldsymbol{o}_l^k / \boldsymbol{p}_l^k$ represent the toroidal/poloidal modes similar to Eqn. (17). As an example, Fig. 4 shows a prescribed toroidal velocity field. We define the so-called toroidal/poloidal filters $\tilde{\boldsymbol{m}}_n^m$, $\tilde{\boldsymbol{n}}_n^m$ as:

$$\tilde{\boldsymbol{m}}_n^m := \boldsymbol{\mathcal{D}}_{\theta,\varphi}[Y_n^m] \,, \quad \tilde{\boldsymbol{n}}_n^m := \frac{n\,(n+1)}{r} Y_n^m(\theta,\varphi)\, \boldsymbol{e}_r \,. \tag{25}$$

Due to the orthogonality of toroidal and poloidal fields or rather their constitutive operators, the scalar product of the magnetic field and the toroidal/poloidal filters gives:

$$\langle \boldsymbol{B}, \tilde{\boldsymbol{m}}_n^m \rangle_{\partial B_r} = j\,(j+1)\, m_j^i(r)\, \delta^{im} \delta_{jn} \,, \tag{26a}$$

$$\langle \boldsymbol{B}, \tilde{\boldsymbol{n}}_n^m \rangle_{\partial B_r} = \frac{j^2\,(j+1)^2}{r^2} n_j^i(r)\, \delta^{im} \delta_{jn} \,. \tag{26b}$$

This operation is called the projection onto a toroidal or rather poloidal mode. The Kronecker-δ-property may be interpreted as a fully decoupled term. Note that by virtue

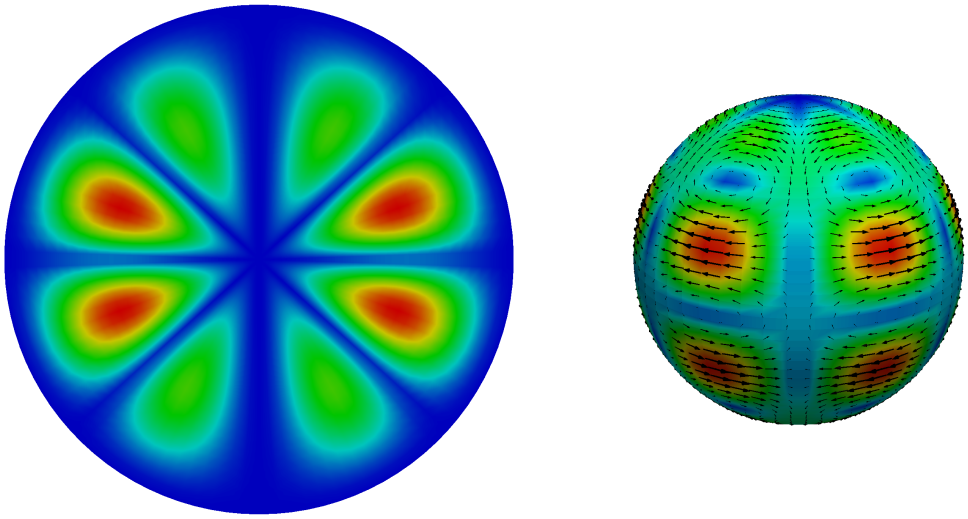

(a) Magnitude in the x-z-plane.

(b) Toroidal vector field on a spherical surface of radius $1/\sqrt{2}$. Colors indicate magnitudes.

Figure 4: Toroidal velocity field with radial function $r^2\left(1-r^2\right)^2$. Vortices indicate a complex 3D fluid flow inside the spherical cavity.

of construction the curl of a toroidal field is a poloidal field and vice versa. It follows that the double curl of either a toroidal or poloidal field is again a toroidal or poloidal field. The projection of the double curl term in equation (7) gives:[4]

$$\langle \nabla \times \nabla \times \boldsymbol{B}, \tilde{\boldsymbol{m}}_n^m \rangle_{\partial B_r} = j\left(j+1\right)\left(j\left(j+1\right)\frac{m_j^i\left(r\right)}{r^2} - D_r^{(2)}\left[m_j^i\right]\right)\delta^{im}\delta_{jn}\,, \tag{27a}$$

$$\langle \nabla \times \nabla \times \boldsymbol{B}, \tilde{\boldsymbol{n}}_n^m \rangle_{\partial B_r} = \frac{j^2\left(j+1\right)^2}{r^2}\left(D_r^{(2)}\left[n_j^i\right] - j\left(j+1\right)\frac{n_j^i\left(r\right)}{r^2}\right)\delta^{im}\delta_{jn}\,. \tag{27b}$$

Since the KRONECKER-δ-property applies again, the double terms do not cause a coupling of the modes.

4.1 Velocity dependent terms

The remaining term in Eqn. (7) is the velocity dependent term. The more complicated nature of this term necessitates a stepwise procedure using operator notation:

1. Exploit linearity of the cross product, the curl, as well as the scalar product;
2. Calculate the cross products (4 terms);
3. Calculate the curl of the cross products (4 terms);
4. Apply the projection to these 4 terms (8 terms).

The resulting terms contain non-linear expressions in terms of spherical harmonics and the operators introduced above. As an example we have:

$$\nabla \times \left(\boldsymbol{o}_l^k \times \boldsymbol{m}_j^i\right) = \frac{o_l^k\left(r\right)m_j^i\left(r\right)}{r}\boldsymbol{\mathcal{D}}_{\theta,\varphi}\left[\mathcal{D}_{\theta,\varphi}\left[Y_l^k, Y_j^i\right]\right]\,, \tag{28a}$$

[4]The operator $D_r^{(2)}$ is defined through the recurrence relation:

$$D_r^{(n)}[f] = D_r^{(1)}\left[D_r^{(n-1)}[f]\right]\,, \quad n \in \mathbb{N}\,.$$

where the anti-symmetric operator $\mathcal{D}_{\theta,\varphi}$ is defined as:

$$\mathcal{D}_{\theta,\varphi}[f,g] := \frac{\partial f}{\partial \theta}\frac{\partial g}{\partial \varphi} - \frac{\partial f}{\partial \varphi}\frac{\partial g}{\partial \theta}\,. \tag{28b}$$

These non-linearities disturb the KRONECKER-δ-property and lead to a coupling of modes. After extensive calculations and application of additional theorems concerning the operators and so-called triple product integrals it can be shown that the coupling structure is governed by the so-called ADAMS-GAUNT- and ELSASSER-integrals K^{ikm}_{jln} and L^{ikm}_{jln}. These integrals are defined as:

$$K^{ikm}_{jln} := \oiint\limits_{\partial B_r} Y^i_j Y^k_l \overline{Y^m_n}\frac{1}{r^2}\,\mathrm{d}A\,, \tag{29a}$$

$$L^{ikm}_{jln} := \oiint\limits_{\partial B_r} \mathcal{D}_{\theta,\varphi}\left[Y^i_j, Y^k_l\right]\overline{Y^m_n}\frac{1}{r^2}\,\mathrm{d}A\,. \tag{29b}$$

In the following, we demonstrate exemplary how the ELSASSER-integral occurs. It may be shown that for arbitrary functions f and g:

$$\boldsymbol{\mathcal{D}}_{\theta,\varphi}[f]\cdot\boldsymbol{\mathcal{D}}_{\theta,\varphi}[g] = \nabla_{\theta,\varphi} f\cdot\nabla_{\theta,\varphi} g\,. \tag{30a}$$

By applying GAUSS' integral theorem analogously to Eqn. (23) and using Eqn. (14), we obtain:

$$\begin{aligned}\oiint\limits_{\partial B_r}\nabla_{\theta,\varphi}\left(\mathcal{D}_{\theta,\varphi}\left[Y^k_l, Y^i_j\right]\right)\cdot\nabla_{\theta,\varphi}\overline{Y^m_n}\frac{1}{r^2}\,\mathrm{d}A &= \oiint\limits_{\partial B_r}\mathcal{D}_{\theta,\varphi}\left[Y^k_l, Y^i_j\right]\Delta_{\theta,\varphi}\overline{Y^m_n}\frac{1}{r^2}\,\mathrm{d}A\\ &= -n\,(n+1)\oiint\limits_{\partial B_r}\mathcal{D}_{\theta,\varphi}\left[Y^k_l, Y^i_j\right]\overline{Y^m_n}\frac{1}{r^2}\,\mathrm{d}A\,.\end{aligned} \tag{30b}$$

Hence:

$$\begin{aligned}&\left\langle\boldsymbol{\mathcal{D}}_{\theta,\varphi}\left[\mathcal{D}_{\theta,\varphi}\left[Y^k_l, Y^i_j\right]\right], \boldsymbol{\mathcal{D}}_{\theta,\varphi}[Y^m_n]\right\rangle_{\partial B_r}\\ &\qquad = -n\,(n+1)\oiint\limits_{\partial B_r}\mathcal{D}_{\theta,\varphi}\left[Y^k_l, Y^i_j\right]\overline{Y^m_n}\frac{1}{r^2}\,\mathrm{d}A = n\,(n+1)\,L^{ikm}_{jln}\,.\end{aligned} \tag{30c}$$

This provides a brief insight into what manipulations are necessary to tackle the velocity dependent terms. The operator notation presented in this paper turned out to be extremely beneficial in context with the projection method. As an example for the components of the velocity dependent terms, we present two expressions:

$$\left\langle\nabla\times\left(\boldsymbol{o}^k_l\times\boldsymbol{m}^i_j\right), \tilde{\boldsymbol{m}}^m_n\right\rangle_{\partial B_r} = -L^{ikm}_{jln}\,n\,(n+1)\,\frac{o^k_l(r)\,m^i_j(r)}{r}\,, \tag{31a}$$

$$\left\langle\nabla\times\left(\boldsymbol{p}^k_l\times\boldsymbol{m}^i_j\right), \tilde{\boldsymbol{n}}^m_n\right\rangle_{\partial B_r} = -L^{ikm}_{jln}\,l\,(l+1)\,n\,(n+1)\,\frac{m^i_j(r)\,p^k_l(r)}{r^3}\,. \tag{31b}$$

Note that the first expression leads to a coupling of the toroidal mode m^i_j and other toroidal modes. The second expression leads to a coupling of the toroidal mode m^i_j with other poloidal modes. The existence of the coupling is governed by the prescribed velocity field. The coupling structure is controlled by the ADAMS-GAUNT- and ELSASSER-integrals, which may be zero or non-zero depending on the index pairs. The values of the ADAMS-GAUNT- and ELSASSER-integrals may be attributed to the so-called WIGNER-3j- symbols, *cf.*, [1, 13]. The WIGNER-3j-symbols obey so-called selection rules and may be numerically calculated using recurrence relations, *cf.*, [10].

4.2 Boundary condition and projection method

In general, from this point on the kinematic dynamo problem is treated numerically by using finite difference methods, *cf.*, [2, 3, 7]. This requires consideration of the boundary condition, *i.e.*, Eqn. (8), in terms of the toroidal-poloidal decomposition. The boundary conditions for the modes, *i.e.*, the radial functions m_j^i and n_j^i respectively are obtained by applying the projection method again. This is convenient since the exterior solution in Eqn. (10) is determined up to a constant c_n^m. If the exponential solution *ansatz* is applied to Eqn. (10) the factor c_n^m is no longer time dependent.

5 Conclusion

A rational approach to dynamo theory based on MAXWELL's equation was presented. A scale analysis lead to the so-called induction equation, *i.e.*, Eqn. (5). In this context kinematic dynamos with a prescribed velocity were addressed in this paper. In case of an exterior vacuum it was shown that the solution for the external magnetic is determined up to a constant.

By using the toroidal-poloidal decomposition for the magnetic and velocity field and by applying the projection method the induction equation was analytically converted to a coupled system of ordinary differential equations. Since in the case of the kinematic dynamo the velocity is prescribed, the unknowns of this system are given by the radial functions m_j^i and n_j^i. The induction equation was therefore treated in a spectral sense with respect. This paper presented a short insight on how the velocity dependent terms need to be addressed mathematically.

References

[1] George B. Arfken and Hans J. Weber. *Mathematical methods for physicists*. 6th ed. Amsterdam, Boston, Heidelberg: Elsevier Academic press, 2005.

[2] Edward Bullard and H. Gellman. "Homogeneous Dynamos and Terrestrial Magnetism". In: *Philosophical Transactions of the Royal Society of London A: Mathematical, Physical and Engineering Sciences* 247.928 (1954), pp. 213–278. ISSN: 0080-4614. DOI: 10.1098/rsta.1954.0018.

[3] M. L. Dudley and R. W. James. "Time-Dependent Kinematic Dynamos with Stationary Flows". In: *Proceedings of the Royal Society of London A: Mathematical, Physical and Engineering Sciences* 425.1869 (1989), pp. 407–429. ISSN: 0080-4630. DOI: 10.1098/rspa.1989.0112.

[4] Walter M. Elsasser. "Induction Effects in Terrestrial Magnetism Part I. Theory". In: *Phys. Rev.* 69 (3-4 Feb. 1946), pp. 106–116. DOI: 10.1103/PhysRev.69.106. URL: http://link.aps.org/doi/10.1103/PhysRev.69.106.

[5] Sebastian Glane. "Untersuchung kinematischer Fluiddynamos über toroidal-poloidale Zerlegungen im Rahmen der rationalen Kontinuumsphysik". master thesis. Berlin Institue of Technology, 2015. URL: http://www.ifm.tu-berlin.de/fileadmin/fg49/AbschlussarbeiteundProjekte/simulation/ThesisGlaneDigital.pdf.

[6] Gary A. Glatzmaier. *The Geodynamo*. 2015. URL: http://es.ucsc.edu/~glatz/geodynamo.html.

[7] David Gubbins et al. “Kinematic dynamo action in a sphere. I. Effects of differential rotation and meridional circulation on solutions with axial dipole symmetry”. In: *Proceedings of the Royal Society of London A: Mathematical, Physical and Engineering Sciences* 456.1998 (2000), pp. 1333–1353. ISSN: 1364-5021. DOI: 10.1098/rspa.2000.0565.

[8] John D. Jackson. *Classical Electrodynamics*. 3rd edition. New York: John Wiley & Sons, 1998.

[9] Attay Kovetz. *Electromagnetic theory*. Oxford University Press Oxford, 2000.

[10] James H. Luscombe and Marshall Luban. “Simplified recursive algorithm for Wigner $3j$ and $6j$ symbols”. In: *Phys. Rev. E* 57 (6 June 1998), pp. 7274–7277. DOI: 10.1103/PhysRevE.57.7274. URL: http://link.aps.org/doi/10.1103/PhysRevE.57.7274.

[11] Michael W. Merrill, Michael W. McElhinny, and Phillip L. McFadden. *The Magnetic Field of the Earth, Volume 63: Paleomagnetism, the Core, and the Deep Mantle*. 1st ed. Academic Press, Aug. 1998.

[12] Julius Adams Stratton. *Electromagnetic theory*. Ed. by Donald G. Dudley. The IEEE Press Series on Electromagnetic Wave Theory. Hoboken, New Jersey: John Wiley & Sons, 2007.

[13] D. E. Winch and R. W. James. “Computations with Spherical Harmonics and Fourier Series in Geomagnetism”. In: ed. by Bruce A. Bolt. Vol. 13. Methods in Computational Physics: Advances in Research and Applications. Academic Press, 1973. Chap. 3, pp. 93–132.

Sebastian Glane, Technische Universität Berlin, Sek. MS 2, Einsteinufer 5, 10587 Berlin; present address: Institute of Continuum Mechanics and Material Mechanics, Hamburg University of Technology, Eißendorfer Str. 42, 21073 Hamburg, Germany

Felix A. Reich, Technische Universität Berlin, Sek. MS 2, Einsteinufer 5, 10587 Berlin

Wolfgang H. Müller, Technische Universität Berlin, Sek. MS 2, Einsteinufer 5, 10587 Berlin

Photoacoustic thermoelastic imaging of indented areas in metals

Alexei L. Glazov Kyrill L. Muratikov
klm.holo@mail.ioffe.ru

Abstract

Non-destructive evaluation of metals with residual stresses was performed by the photoacoustic method. Main attention was paid to experimental investigations of areas inside Vickers and Rockwell indentations in metal samples under external loading. It is shown that external normal and shear stresses influence on the behavior of the photoacoustic signal inside indented areas in metals. The obtained results can be used for estimating sensitivity of the photoacoustic method to mechanical stress determination in metals. The theoretical model of the photoacoustic thermoelastic effect in solids is proposed for the explanation of the obtained results. It is based on the modified nonlinear model of elastic body that takes into account a possible dependence of YoungвЃ Єs modulus of a metal on temperature. The proposed model is applied for the explanation of the photoacoustic signal behavior in indented areas of metals and its modifications under residual and external stresses. Theoretical and experimental study of the photoacoustic signal behaviour resulted in a new method of residual stress evaluation based on thermoelastic photoacoustic effect and Vickers indentation.

1 Introduction

Recent investigation of the thermoelastic photoacoustic (TEPA) effect in solids reveals the dependence of thermal, thermoelastic and elastic properties on the internal stress [1, 2, 5, 4, 5, 6, 7, 8, 9]. These works open new possibilities for the non-destructive evaluation of objects with residual stresses at a microscopic level. It has an utmost practical as well as fundamental significance. A long history of the technique and industries shows the vitality of the residual stresses for the life expectance and reliability, whereas the mechanisms of stress effect are far from the deep consideration. Because of the universal character of The photothermoacoustic methods they can be apply for investigating the great diversity of materials.

Previously, the residual stress effect on thermal and thermoelastic properties was investigated experimentally for several ceramic composites [4, 5, 8, 9]. It was clearly demonstrated under external subjection like temperature and pressure, that the internal stress very strongly influences on the photoacoustic piezoelectric signal. Our experimental approach consisting in applying simultaneously different photothermoacoustic methods reveals main mechanisms of the TEPA signal formation in the investigated ceramics.

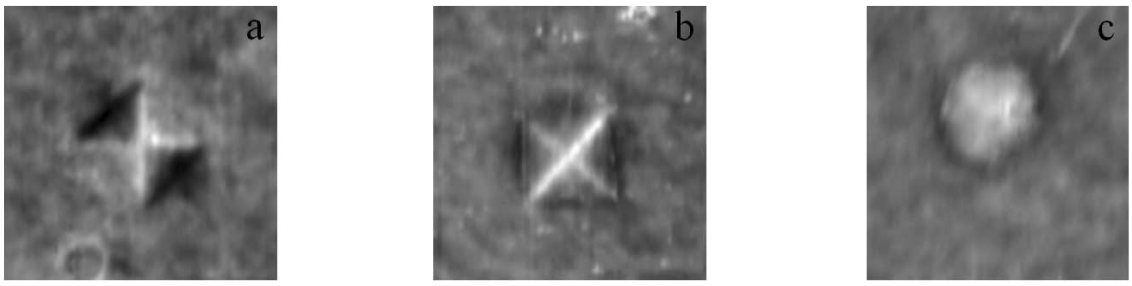

Figure 1: The photoacoustic piezoelectric images of two Vickers indented areas (a, b) and a Rockwell indented area (c) in steel smple. The size of the each image is 0.6x0.6 mm^2. The modulation frequency is 142 kHz.

To interpret the obtained results a non-linear model of the TEPA effect in solids with residual stress was developed. The model quantitatively explains the behaviour of the TEPA signal, for example, near vertical crack tips [8, 10, 11].
The photoacoustic methods provide unique opportunity for the microscopic study of the residual stress. In this case a three dimensional model for inhomogeneous objects is needed for a quantitative analysis. Here we present analytical expressions for the TEPA signal obtained in the framework of the perturbation theory.
Experimental part of the work is devoted to the photoacoustic investigation of metals with residual stresses. The objects of study were steel samples with Vickers and Rockwell indentation.

2 Experimental results and discussion

For microscopic study of the thermoelastic properties of solids we use photothermoacoustic microscope with built-in compressive mechanism that allows us to investigate samples under external load up to 2000 N parallel to the sample surface. The microscope provides scan images with minimal step 2.5 μm in two directions. Thermal waves and acoustic vibrations were excited in the sample by radiation of an argon-ion laser modulated by an acoustooptic modulator. The radiation was absorbed at the front surface of a sample. To detect the photoacoustic signal a piezoelectric detector was attached to the rear side of the sample and had an operation frequency about 140 kHz. The modulation frequency in photoacoustic microscopy is one of the pacing factors of spatial resolution. For instrumental steel U8 the corresponding thermal wave length is about 3 μm.
In this work we focused on studying steel samples. Residual stresses were produced in the sample by Vickers or Rockwell indentation. The indentation load was 98 N. In these materials there was no cracks unlike the case of ceramics [8, 10], so, the main attention was paid to the TEPA signal behaviour inside the prints and in the nearest vicinities.
Fig. 1 presents images of indented areas of a steel sample. There are two Vickers indentations made at angle 45° and Rockwell indentation. The load of indentations is 98 N. One of the features of such images is high amplitude of the TEPA signal along the Vickers indentation diagonals which are the strong stress concentrators. The highest signal is in the indentation center. Its magnitude is about two to three times larger than the average signal outside the indentation zone. In this case a signal higher than average corresponds to the compressive stress and a lower signal corresponds to the tensile stress, which is similar to the case of ceramics [10].

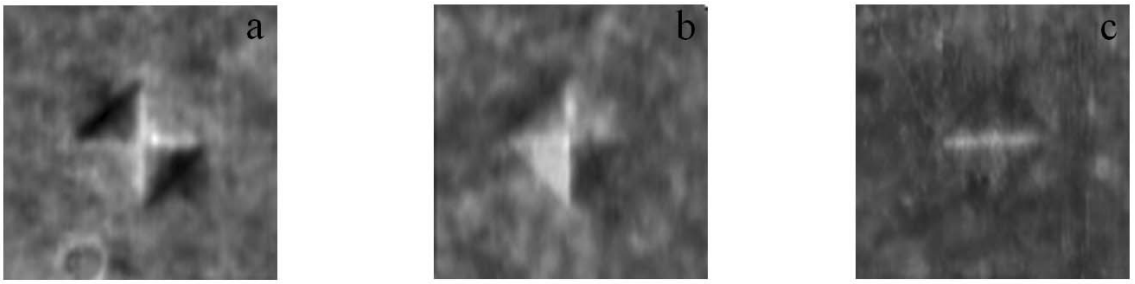

Figure 2: The photoacoustic piezoelectric images of a Vickers indented area while annealing 870°C. (A) is an image of the initial state, (b) is an image after 1h annealing and cooling in air, (c) is an image after the following 1h annealing and cooling in athe furnace. The image size is 0.6x0.6 mm^2. The modulation frequency is 142 kHz.

To reveal the nature of photoacoustic piezoelectric response from metals with residual steress we performed experiments with thermal development of the samples. For this purpose we have made images of the indented areas after two annealing circles. The annealing was made at 870°C. The first stage was one hour heating and cooling in air. The second stage was one hour heating also but cooling in the furnace. Fig. 2 shows three images of one of the indents before and after the two annealing circles. The image after the first circle (Fig. 2b) exibits a certain decrease of the TEPA signal deviation from the average value but together with appearence of some new features corresponding to thermal stresses induced by the quick cooling in the air. The second annealing circle with the slow cooling results in a much more smooth image with a maximum signal of 160% of the average amplitude along one diagonal only (Fig. 2c). We propose that this signal feature may be due to plastic deformation. Elimination of other features implies that the main part of residual stresses disappeared during annieling. So we confirmed once more that the TEPA signal is well attributed to stress field in objects.

Let us consider now an external load influence on indentation images and residual stress distribution. Fig. 3 presents behavior of the TEPA images of two Vickers indentation oriented at different angles to the external load axe. The indentation were made at the same sample not far from each other. The initial free state of the sample is shown in Fig. 3a and 3b. The difference of the images may be both due to initial residual stress before indentation and orientation of the prints relative to the piezoelectric detector. According to images 3c and 3d, there was a strong redistribution of the stresses inside the indentation print under moderate external pressure 24 MPa. After cancelling the load indentation image of the first indentation returned to the initial state because images 3c and 3e are similar. This means that all changes under the load were forced by elastic deformations. Signal behavior across the indent diagonal is shown in Fig. 4. The normed signal changed from 1.5 to 3.0 under the load and relaxed down to 1.7 after the load cancel. So the difference in signal between 1.7 and 1.5 corresponds to the plastic deformation and that between 3.0 and 1.7 corresponds to the elastic deformation under external pressure 24 MPa. The most interesting peculiarity of image 2c is opposite change of th signal on the two diagonals. According to our above suggestions one diagonal is subjected to compressive and the other one to tensile stress, although the both diagonals are at the angles close to 45° to the load axe. That means that the stress field is redistributed inside the indent print.

The other indent exibits a different behavior under the same external load. One can see from Fig. 3f that the load cancel does not change practically the TEPA image. This means that the all changes have the plastic character. Apparengly, the residual compressive

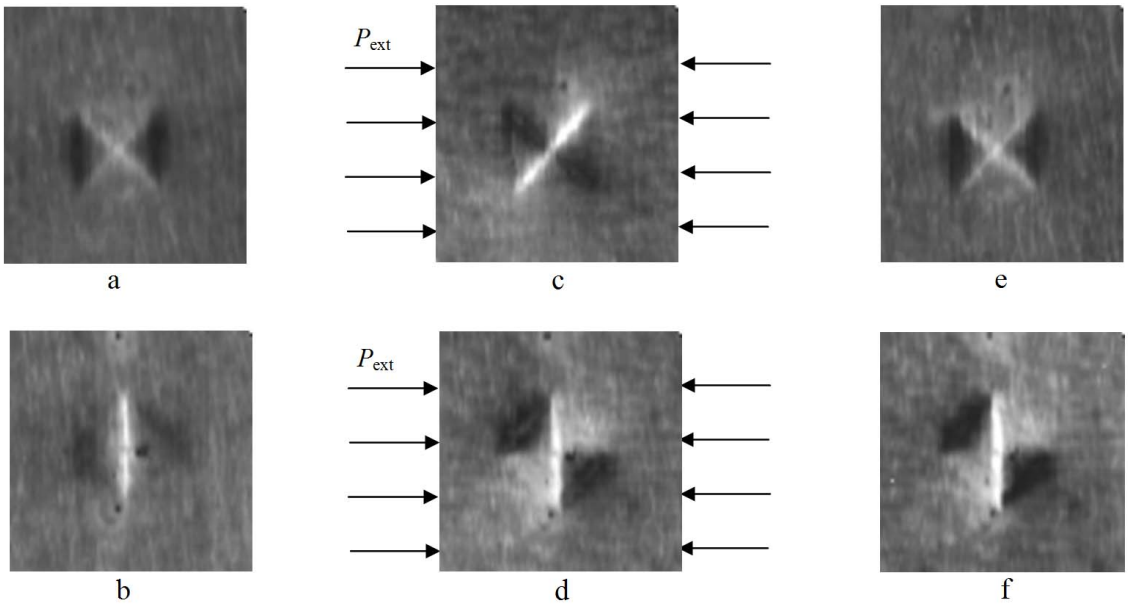

Figure 3: The photoacoustic piezoelectric images of two Vickers indented areas in the steel sample. Arrows denote external pressure direction. The image size is 0.6x0.6 mm^2. The modulation frequency is 142 kHz. (A) and (b) are the different indentations in free state, (c) and (d) are the images of the sample under external load 24 MPa, (e) and (f) are the images after the load cancel.

stress concentrated along one diagonal was so high that the low external pressure was enough to produce plastic deformation. At that, irreversible changes took place not only at this diagonal but in the whole area of the indentation. In this experiments the Vickers indentation behaves itself as one system with connections between its parts.

3 Theoretical model of the thermoelastic photoacoustic effect in inhomogeneous solids

The theoretical model of the TEPA effect in solids with residual stresses was proposed in our previous works [4, 5, 6]. Here we present the further three-dimensional development of the model for a case of inhomogeneous objects with non-uniform mechanical stress fields. We consider the residual stress influence on the properties of a material by introducing the dependence of thermoelastic constant on elastic deformations. Previously, the photoacoustic signal variations resulted from non-uniform residual stresses was obtained for the case of fixed sample boundary [12]. Here we need an expression for TEPA signal for the case of a free sample surface. The non-stationary deformations can be defined by solving the general equation of motion for elastic solids [13]

$$\rho \frac{\partial^2 u_{\mathrm{i}}}{\partial t^2} = \frac{\partial \sigma_{ij}}{\partial x_j}, \tag{1}$$

where ρ is the density of deformed body, u_i are the displacement components, σ_{ij} are the stress tensor components accounting the thermoelastic effect

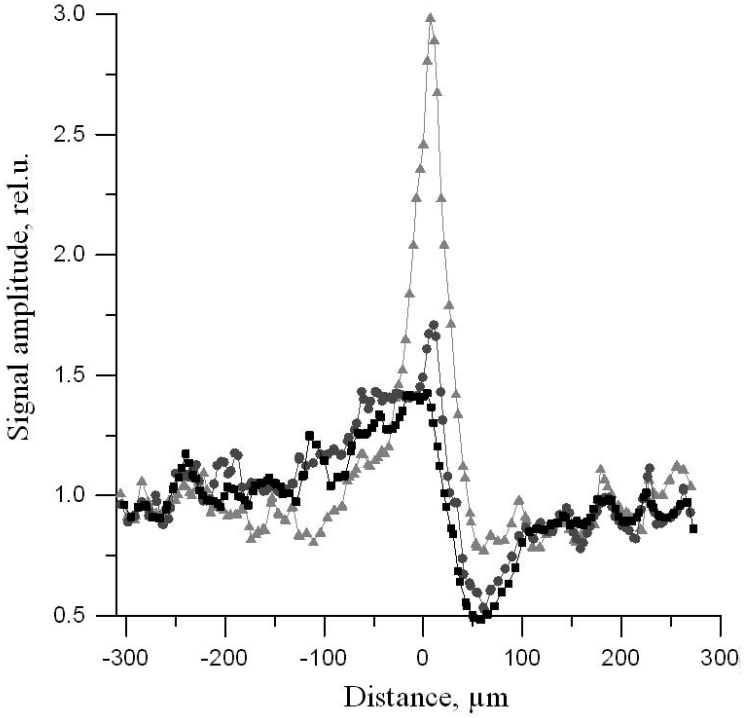

Figure 4: Distribution of the photoacoustic signal amplitude across the upper right part of diagonal of the indent shown in Figs. 3a, 3c and 3e. Black squares correspond to the initial state, grey circles correspond to the sample under the external pressure of 24 MPa, light grey triangles correspond to the sample after cancelling the load.

$$\sigma_{ij} = 2\mu(\vec{r})u_{ij} + [\lambda(\vec{r})u_{kk} - \gamma(\vec{r})(T - T_0)]\delta_{ij}, \tag{2}$$

μ and λ are the Lame coefficients, γ is the thermoelastic coupling coefficient, u_{ij} is the tensor of the total strain of the body, T is the object temperature, and T_0 is the environmental temperature.

In line with the assumption made in [12], we will consider only the thermoelastic coupling coefficient depending on the object nonhomogeneity. Namely, $\gamma = \gamma_0 + \gamma_1(\vec{r})$, where γ_0 is the thermoelastic coupling coefficient of the homogeneous object and γ_1 corresponds to the nonhomogeneity. If the variations of the elastic deformation are small and nonhomogeneity is weak we can use the perturbation theory approximation. We believe that for weak nonhomogeneity $\gamma_0 \gg \gamma_1$. Than in the frame of the perturbation theory the temperature variation in the object resulted from the laser irradiation and the thermoelastic displacement components are $\Delta T = \Delta T^{(0)} + \Delta T^{(1)}$ and $\Delta u_i = \Delta u_i{}^{(0)} + \Delta u_i{}^{(1)}$ with $\Delta T^{(0)} \gg \Delta T^{(1)}$ and $\Delta u_i = \Delta u_i{}^{(0)} + \Delta u_i{}^{(1)}$.

For the case of a free surface the boundary conditions are

$$\sigma_{iz} n_z \big|_{z=0} = 0, \tag{3}$$

where n_i are the components of the normal to the surface, and z=0 corresponds to the illuminated surface.

To solve the problem we can follow the work [13]. The general expressions are very complex. For the case $z^2 \gg (x-x_0)^2+(y-y_0)^2$, where (x_0, y_0) is the center of the laser beam; the TEPA signal may be expressed in a simplified form

$$\Delta V = -C\frac{(1-4\nu^2)(1+\nu)}{\pi E(1-\nu)}\frac{1}{z^2}\int dx' \int dy' \gamma_1(x', y', 0)\Delta T^{(0)}(x', y', 0), \tag{4}$$

where C is a coefficient depending on the piezoelectric detector, ν is Poisson's ratio, E is Young's modulus, z is the sample thickness.
Expression (4) can be used for definition of internal stress influence on the TEPA signal behaviour around indentation zones, where the signal magnitude is small. At this, the following circumstances must be taken into account. Firstly, according to results of works [**? ? ? ?**] changes of the thermoelastic constant of a material due to internal stress near the sample surface may be considered proportional to $\sigma_{xx}+\sigma_{yy}$. Secondly, the residual stress distribution around the indentation may be considered as spherically symmetric [14], and then $\sigma_{xx}+\sigma_{yy}$ is proportional to σ_r, where according to Yoffe [14]

$$\sigma_r = -\frac{\sigma_r^{(0)} r_0^2}{r^2}, \tag{5}$$

where r_0 is the indentation size, $\sigma_r^{(0)}$ is an average stress at the indentation border.
The experimental average TEPA signal distribution along lines passing through the center of the Vickers print in various directions demonstrate r^{-2} dependence in accordance with the obtained expression.
Of cause, the proposed model does not take into account the residual stress existing in a sample before indentation and its application to the 2-order central symmetrical Vickers indentations would be *a priori* incorrect.

4 Conclusion

To investigate residual stress influence on the thermoelastic properties of metals we have studied theoretically and experimentally the TEPA effect in steel under subjection of thermal development and external pressure. The imaging of Vickers indented areas showed strong dependence of residual stress localization on initial stresses in the samples. Using the photoacoustic microscope combined with press machine we have demonstrated the possibility to chose external pressure for reproducing initial stress effect on the TEPA images of Vickers indentations. So, the combination of the TEPA microscopy and Vickers indentation technique may result in a simple method of the local residual stress estimation in metals. To develop the method we plan to apply and study different types of indentations. We have continued also developing non-linear model of TEPA effect in solids with residual stresses. The paper presents an expression for TEPA signal for solids with weakly heterogeneous thermoelastic properties obtained within the framework of the perturbation theory. It was successfully applied for the description of the TEPA signal behaviour around Vickers indentations.

Acknowledgments

This work was supported by Russian Science Foundation, project no. 15-19-00182.

References

[1] J.H. Cantrell, M. Qian, M.V, Ravichandran and K.M Knowles. Appl. Phys. Lett., vol.57, pp.1870-1872, 1990.

[2] R.M.Burbelo, A.L.Gulyaev, L.I.Robur, M.K.Zhabitenko, B.A.Atamanenko, and Ya.A.Kryl, J. de Phys. 4, vol.C7, pp.311-314, 1994.

[3] H. Zhang, S. Gissinger, G. Weides and U. Netzelman. J. de Phys. 4, vol.C7, pp.603-606, 1994.

[4] K.L.Muratikov, Tech. Phys. Lett., vol.24, pp.536-538, 1998.

[5] K.L.Muratikov, Tech. Phys., vol.44, pp.792-796, 1999.

[6] K.L.Muratikov, A.L.Glazov, D.N.Rose, and J.E.Dumar, J. Appl. Phys., vol.88, pp.2948-2955, 2000.

[7] A.L.Glazov, K.L.Muratikov, V.I.Nikolaev, and S.A.Pulnev, Tech. Phys. Lett., vol.36, pp.699-702, 2010.

[8] K.L. Muratikov, A.L. Glazov, D.N. Rose and J.E. Dumar. Tech. Phys. Lett., 2002, vol.28, pp.377-381,2002.

[9] K.L. Muratikov, A.L. Glazov, D.N. Rose and J.E. Dumar. High Temperatures-High Pressures, vol.33, pp.285-292, 2001.

[10] K.L. Muratikov, A.L. Glazov, D.N. Rose and J.E. Dumar. Rev. Sci. Instrum., vol.74, pp.3531-3535, 2003.

[11] K.L.Muratikov, and A.L.Glazov, Central European J. of Phys., vol.3, pp.485-515, 2003.

[12] K.L. Muratikov. Tech. Phys. Lett., vol.30, pp.956-958, 2004.

[13] L.D. Landau and E.M. Lifshitz. Theory of Elasticity, 187 p., Pergamon, New York (1986).

[14] Yoffe E H, Philosophical Magazine A, vol.46, pp.617-628, 1982.

Alexei L. Glazov, Ioffe Physical-Technical Institute, Polytekhnicheskaya 26, 124021 St.Peterburg, Russia
Kyrill L. Muratikov, Ioffe Physical-Technical Institute, Polytekhnicheskaya 26, 124021 St.Peterburg, Russia

The system of inverted pendulums

Mikhail A. Guzev, Alexander S. Losev
guzev@iam.dvo.ru

Abstract

We present a mathematical model of the inverted pendulums. Theoretical analysis is carried out for the system of two objects. The stability problem of N inverted pendulums is analysed numerically.

1 Introduction

From the point of view of studying various physical processes the system of coupled pendulums is an instructive model. The case of small linear oscillations in a vicinity of the stable equilibrium position is described in the literature [1]. In the unstable (inverted) position there are interesting features in the behavior. For example, the upper vertical position of the pendulum might be stable when the driving frequency is fast [2],[3]. Pyotr Kapitza was the first to analyze this highly unusual phenomenon in 1951 [4].
Stability of two inverted connected pendulums was investigated in [5]. The stability problem of a finite number of inverted pendulums in a linear interaction hasn't been considered yet. It is pointed that behavior of the inverted pendulums is linked with the study of the domino effects [6] . In particular it is shown [7]-[9] that the domino-structure plays an essential role in determination of rock brittleness and instability at failure. Therefore, the inverted interacting pendulums are naturally called domino system with weak interaction. This paper presents a mathematical model of the inverted pendulums and examines its properties.

2 Construction of the Lagrangian

We determine the Lagrangian and the equation of motion of the following chain. The вГЁchainвГ№ is a set of massless upright pendulums with $N+1$ mass points . A mass m is fixed to one end of a massless bar; the other end of the bar is fixed to a hinge. The $N+1$ hinges are placed in the vertical direction and divided by the constant distance a. The pendulums of equal length l are connected by a non-linear spring, and the coupling is not weak in the general case (Figure. 1.).
Let the displacement of the mass j be denoted by $\mathbf{r}_j = (x_j,\ y_j)$. Then we have the following presentation

$$(x_j,\ y_j) = (aj + l\cos\varphi_j,\ l\sin\varphi_j), \quad j = 0, 1, \ldots, N \tag{1}$$

where φ_j is an angle between the bar and the horizontal axis. We introduced plane polar coordinates for the problem and adopt the set of the polar angles $\{\varphi_j\}$ as generalized coordinates of the chain.

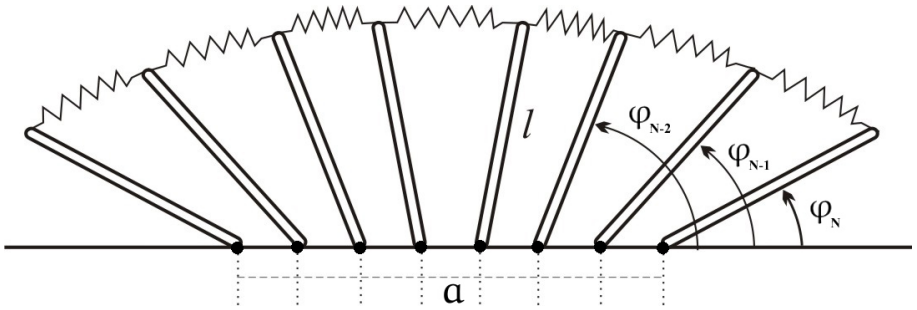

Figure 1: Interacting dominoes.

The Lagrangian of the system is equal to $L = T - P$. The kinetic energy of the chain T is calculated in accordance with the formula

$$T = \sum_{j=0}^{N} m\frac{1}{2}(\dot{x}_j^2 + \dot{y}_j^2) = \sum_{j=0}^{N} m\frac{(l\dot{\varphi}_j)^2}{2}. \tag{2}$$

The total potential energy P of the chain is given by the expression

$$P = P_g + P_{nonlin}. \tag{3}$$

Here P_g is the potential energy corresponding to the external uniform gravity and P_{nonlin} arises from internal forces of the interacting masses. The potential energy of a mass due to uniform gravity is $P(j)_g = mgl\sin\varphi_j$ then the corresponding potential energy of the chain is

$$P_g = \sum_{j=0}^{N} P(j)_g = \sum_{j=0}^{N} mgl\sin\varphi_j\ . \tag{4}$$

The internal potential energy function P_{nonlin} depends on a potential interaction between the masses:

$$P_{nonlin} = \sum_{j=0}^{N-1} U(l_{j,j+1}) \tag{5}$$

here $l_{j,j+1}$ is the distance between neighboring masses. We use (1) for calculation of $l_{j,j+1}$:

$$l_{j,j+1} = \sqrt{[a + l(\cos\varphi_{j+1} - \cos\varphi_j)]^2 + l^2(\sin\varphi_{j+1} - \sin\varphi_j)^2}. \tag{6}$$

From (2)-(5) we have the Lagrangian of the system

$$L = T - P = \sum_{j=0}^{N}[m\frac{(l\dot{\varphi}_j)^2}{2} - mgl\sin\varphi_j] - \sum_{j=0}^{N-1} U(l_{j,j+1})\ . \tag{7}$$

3 Background equations

Lagrange's equations corresponding to the Lagrangian (7) are the following ones:

$$\frac{d}{dt}\frac{\partial L}{\partial\dot{\varphi}_j} - \frac{\partial L}{\partial\varphi_j} = \frac{d}{dt}\frac{\partial T}{\partial\dot{\varphi}_j} + \frac{\partial U}{\partial\varphi_j} \Leftrightarrow$$

$$\Leftrightarrow ml^2\ddot{\varphi}_j = mgl\cos\varphi_j + \frac{\partial U(l_{j-1,j})}{\partial\varphi_j} + \frac{\partial U(l_{j,j+1})}{\partial\varphi_j}. \tag{8}$$

The two last derivatives are equal to

$$\frac{\partial U(l_{j-1,j})}{\partial\varphi_j} + \frac{\partial U(l_{j,j+1})}{\partial\varphi_j} = \frac{\partial U(l_{j-1,j})}{\partial l_{j-1,j}}\frac{\partial l_{j-1,j}}{\partial\varphi_j} + \frac{\partial U(l_{j,j+1})}{\partial l_{j,j+1}}\frac{\partial l_{j,j+1}}{\partial\varphi_j}. \tag{9}$$

It is clear that:

$$\frac{\partial l_{j,j+1}}{\partial\varphi_j} = \frac{1}{2l_{j,j+1}}\frac{\partial l^2_{j,j+1}}{\partial\varphi_j}, \quad \frac{\partial l_{j-1,j}}{\partial\varphi_j} = \frac{1}{2l_{j-1,j}}\frac{\partial l^2_{j-1,j}}{\partial\varphi_j}. \tag{10}$$

The distance $l_{j,j+1}$ is expressed in the terms of the quantities

$$\varphi_{+,j} = \frac{\varphi_{j+1}+\varphi_j}{2},\ \varphi_{-,j} = \frac{\varphi_{j+1}-\varphi_j}{2}.$$

For this purpose we use the formulae

$$\cos\varphi_{j+1} - \cos\varphi_j = -2\sin\frac{\varphi_{j+1}+\varphi_j}{2}\sin\frac{\varphi_{j+1}-\varphi_j}{2},$$

$$\sin\varphi_{j+1} - \sin\varphi_j = 2\cos\frac{\varphi_{j+1}+\varphi_j}{2}\sin\frac{\varphi_{j+1}-\varphi_j}{2}$$

and rewrite (6) in the form

$$l_{j,j+1} = \sqrt{a^2 - 4al\sin\varphi_{+,j}\sin\varphi_{-,j} + 4l^2\sin\varphi_{-,j}}. \tag{11}$$

Since

$$\frac{\partial\varphi_{+,j}}{\partial\varphi_j} = \frac{1}{2},\ \frac{\partial\varphi_{-,j}}{\partial\varphi_j} = -\frac{1}{2}$$

we substitute (11) into (10), and it results in

$$\frac{\partial l^2_{j-1,j}}{\partial\varphi_k} = -2al\cos\varphi_{+,j-1}\sin\varphi_{-,j-1} - 2al\sin\varphi_{+,j-1}\cos\varphi_{-,j-1} + 4l^2\sin\varphi_{-,j-1}\cos\varphi_{-,j-1},$$

$$\frac{\partial l^2_{j,j+1}}{\partial\varphi_k} = -2al\cos\varphi_{+,j}\sin\varphi_{-,j} + 2al\sin\varphi_{+,j}\cos\varphi_{-,j} - 4l^2\sin\varphi_{-,j}\cos\varphi_{-,j}. \tag{12}$$

If we consider the weak coupling between the pendulums then the potential $U(l_{j,j+1})$ can be written in the traditional form

$$U(l_{j,j+1}) \equiv \frac{k}{2}(\varepsilon_j)^2, \quad \varepsilon_j \equiv \frac{l_{j,j+1}-a}{a}, \tag{13}$$

where ε_j is the relative deformation. The particlesвЃ Є displacements are not small in the general case, i.e. $\varphi_k \sim 1$. But the relative deformation ε_j is supposed to be a first order linear with respect to $\varphi_{-,k}$ then from (11), (13) one has

$$|\varepsilon_j| \approx \frac{2l}{a}|\varphi_{-,j}|\sin\varphi_{+,j} \ll 1. \tag{14}$$

Forces that keep the pendulums together are assumed to be a first order linear with respect to the relative deformation ε_j. It allows us to replace $\sin\varphi_{-,j} \to 0$ and $\cos\varphi_{-,j} \to 1$ in (12) and remain the linear term with respect to $\varphi_{-,j}$ in $l_{j,j+1}$:

$$\frac{\partial l^2_{j-1,j}}{\partial\varphi_j} \approx -2al\sin\varphi_{+,j-1},\ \ l_{j,j-1} \approx a - 2\varphi_{-,j-1}l\sin\varphi_{+,j-1},$$

$$\frac{\partial l_{j,j+1}^2}{\partial \varphi_j} \approx 2al\sin\varphi_{+,j}, \quad l_{j,j+1} \approx a - 2\varphi_{-,j} l\sin\varphi_{+,j}.$$

From here and (10) we obtain

$$\frac{\partial l_{j,j+1}}{\partial \varphi_j} = l\sin\varphi_{+,j}, \frac{\partial l_{j-1,j}}{\partial \varphi_j} = -l\sin\varphi_{+,j-1}, \tag{15}$$

including the leading order with respect to $|\varphi_{-,k}| \ll 1$. Substitution of the expression (15) into (9) results in

$$\frac{\partial U(l_{j-1,j})}{\partial \varphi_j} + \frac{\partial U(l_{j,j+1})}{\partial \varphi_j} = l\frac{\partial U(l_{j-1,j})}{\partial l_{j-1,j}}\sin\varphi_{+,j-1} - l\frac{\partial U(l_{j,j+1})}{\partial l_{j,j+1}}\sin\varphi_{+,j}. \tag{16}$$

Combination of (16) and (8) allows us to obtain the corresponding equations of a discrete chain:

$$\begin{aligned}
&ml^2\ddot{\varphi}_0 - k\left(\frac{l}{a}\right)^2(\varphi_1-\varphi_0)\sin^2\varphi_{+,0} + mgl\cos\varphi_0 = 0,\\
&ml^2\ddot{\varphi}_j - k\left(\frac{l}{a}\right)^2[(\varphi_{j+1}-\varphi_j)\sin^2\varphi_{+,j} - (\varphi_j-\varphi_{j-1})\sin^2\varphi_{+,j-1}] + mgl\cos\varphi_j = 0,\\
&ml^2\ddot{\varphi}_N + k\left(\frac{l}{a}\right)^2(\varphi_N-\varphi_{N-1})\sin^2\varphi_{+,N-1} + mgl\cos\varphi_N = 0, \quad j = 1,\dots,N-1.
\end{aligned} \tag{17}$$

Introducing the pendulum time $t_0 = \sqrt{l/g}$ of the chain, we can go to $t \to t\sqrt{l/g}$ and write the motion equation (17) in the following form

$$\begin{aligned}
&\ddot{\varphi}_0 - \frac{1}{p^2}(\varphi_1-\varphi_0)\sin^2\varphi_{+,0} + \cos\varphi_0 = 0, \quad p^2 = \frac{mgl}{k\left(\frac{l}{a}\right)^2},\\
&\ddot{\varphi}_j - \frac{1}{p^2}[(\varphi_{j+1}-\varphi_j)\sin^2\varphi_{+,j} - (\varphi_j-\varphi_{j-1})\sin^2\varphi_{+,j-1}] + \cos\varphi_j = 0,\\
&\ddot{\varphi}_N + \frac{1}{p^2}(\varphi_N-\varphi_{N-1})\sin^2\varphi_{+,N-1} + \cos\varphi_N = 0, \quad j = 1,\dots,N-1.
\end{aligned} \tag{18}$$

4 Analysis of the two pendulum model

The system (18) for the two pendulums can be written as

$$\ddot{\varphi}_0 - \frac{1}{p^2}(\varphi_1-\varphi_0)\sin^2\varphi_{+,0} + \cos\varphi_0 = 0, \quad \ddot{\varphi}_1 + \frac{1}{p^2}(\varphi_1-\varphi_0)\sin^2\varphi_{+,0} + \cos\varphi_1 = 0. \tag{19}$$

We use functions $\varphi_{+,0}$, $\varphi_{-,0}$ (12) in (19):

$$\ddot{\varphi}_{+,0} + \cos\varphi_{+,0}\cos\varphi_{-,0} = 0, \quad \ddot{\varphi}_{-,0} + \frac{2\varphi_{-,0}}{p^2}\sin^2\varphi_{+,0} - \sin\varphi_{+,0}\sin\varphi_{-,0} = 0. \tag{20}$$

Since there is the condition (14) we can replace $\cos\varphi_{-,0} \to 1$ with accuracy of $(\varphi_{-,0})^2\cos\varphi_{+,0}$ and $\sin\varphi_{-,0} \to \varphi_{-,0}$ with accuracy of $(\varphi_{-,0})^3\sin\varphi_{+,0}$ in (20). The system (20) is reduced to

$$\ddot{\varphi}_{+,0} + \cos\varphi_{+,0} = 0, \quad \ddot{\varphi}_{-,0} + \left[\frac{2}{p^2}\sin^2\varphi_{+,0} - \sin\varphi_{+,0}\right]\varphi_{-,0} = 0.$$

The first equation coincides with the equation of the nonlinear pendulum. It has a stationary solution $\varphi_{+,0} = \pi/2$. In this case $\varphi_{-,0}$ satisfies the equation

$$\ddot{\varphi}_{-,0} + \left[\frac{2}{p^2} - 1\right] \varphi_{-,0} = 0.$$

Behavior of $\varphi_{-,0}$ over time depends on the value of the parameter p . It is clearly that the condition

$$p_*^2 = \frac{mgl_*}{k_*(l_*/a_*)^2} = 2 \tag{21}$$

determines the critical value $p_* = \sqrt{2}$ separating different regions of behavior. If there is the condition $p < \sqrt{2}$ then the solution $\varphi_{-,0}$ is oscillatory one. In the case of the enequality $p > \sqrt{2}$ function $\varphi_{-,0}$ contains exponentially growing contributions.
The system (18) was investigated numerically using an implicit Runge-Kutta method with the help of the package "Mathematica 9.0". We supposed that the initial speed was equal to zero. It is shown that decrease of the parameter p^2 results in increase of the oscillation frequency. In particular, the corresponding elliptical trajectories for $p^2 = 2$ and $p^2 = 1.5$ are shown in (Figure. 2). They indicates the existence of the stability regions in a vicinity

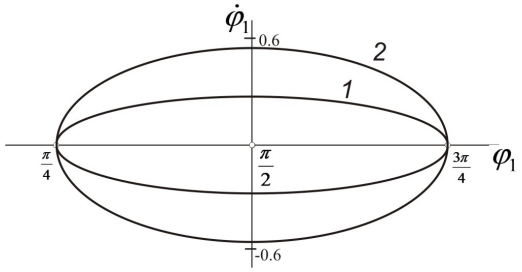

Figure 2: Phase portraits for $N = 2$ at $p^2 = 2$ (curve 1) and $p^2 = 1.5$ (curve 2).

of $(0,\ \pi/2)$. The phase portrait of the second pendulum is identical to the first one on condition that $\dot{\varphi}_1 = -\dot{\varphi}_2$.
Numerical investigation of the system (18) at $p^2 > 2$ shows that the elliptical trajectories disappear and an unstable trajectories appear. This confirms the analytical formula (21) for the critical value of the parameter p_*.

5 Investigation of stability for N pendulums

Model of two pendulums showed that the quantity p^2 is a control parameter of the system. In particular, the value of $p^2 = 2$ is the highest value of the parameter p for which the stable equilibrium is observed for $N = 2$. This allows us to formulate a heuristic idea of separating stable trajectories for $N > 2$.
We begin to calculate the trajectories of the system (18) starting from $p^2 = 2$ for different initial angles at zero initial velocity. Reducing p^2 we control the appearance of elliptic trajectories in the phase plane by means changing the initial angle and analyzing the phase trajectories of each pendulum. If there is an elliptic point on the plane than the position of a pendulam is a stable one. This procedure allows us to calculate the critical value p_* of the system. The software package Mathematica 9.0 was used to construct the solution for $N = 4;\ 6;\ 8;\ 10$ pendulums.

It is shown that the critical value p_* decreases monotonically with respect to N. Analytical investigation of stability of the system (18) was carried out on the information about zeroes of the matrix determinant in a small vicinity of the equilibrium. The asymptotic formula is obtained in case of small p_* and written in the form

$$\frac{1}{p_*^2} = \frac{2\cos\frac{\pi}{N+1}\cos^2\frac{\pi}{2(N+1)}}{\sin\frac{\pi}{2(N+1)}} - 1. \tag{22}$$

But we expand (22) for the finite p_* as well and the calculated values are presented in the Table 1.

Table 5: Numerical and asymptotic values of with respect to N.

N	Asymptotic values p_*^2	Numerical values p_*^2
2	2.0000	2.000
4	0.2676	0.560
6	0.1493	0.220
8	0.1053	0.120
10	0.0819	0.085

6 Discussion

We constructed the 1D model of the inverted interacting pendulums. It was found that in the case of two inverted connected pendulums the upper vertical position of the system has a critical behavior with respect to the interaction parameter p. The relative angle between two pendulums contains wavy terms when $p < \sqrt{2}$. If the parameter $p > \sqrt{2}$ the solution behaves monotonically.
For a finite number N of inverted pendulums critical behavior of the parameter p is defined by the value of N. The asymptotic formula for the critical value of p with respect to N is proposed in the work. It is shown that the critical value leads to its decrease. Hence the kinematic characteristic N influences on physics behaviour effectively.

Acknowledgements

This work was supported by the Russian Scientific Foundation (grant no. 13-01-00275).

References

[1] A. Sommerfeld, Vorlesungen Гёber Theoretische Physik, Band 1: Mechanik. Verlag Harri Deutsch thun Frahkfurt/M, 1994.

[2] A. Stephenson, On an induced stability. Phil. Mag. 1908, 15, pp. 233-236.

[3] A. Stephenson, On a new type of dynamical stability. Mem. Proc. Manch. Lit. Phil. Soc. 1908, 52, pp. 1-10.

[4] P. L. Kapitza, Pendulum with Vibrating Suspension. UFN, 1951, vol.44, pp. 7-20 (in Russian).

[5] A. P.Markeev, A motion of connected pendulums // Nonlinear dynamics, 2013, Vol. 9, вЊ 1, pp. 27-38 (in Russian)

[6] J. M. J. van Leeuwen, The Domino Effect, arXiv:physics/0401018v1 (2008).

[7] B.G. Tarasov, Intersonic shear rupture mechanism. I. J. Rock Mech. Min. Sci. 45, 6, 2008, pp. 914-928.

[8] B.G. Tarasov, M.F. Randolph, I. J. Rock, Superbrittleness of rocks and earthquake activity // Mech. Min. Sci. 48, 2011, pp. 888-898.

[9] B.G. Tarasov, M.A. Guzev, Mathematical Model of Fan-head Shear Rupture Mechanism Materials Structure & Micromechanics of Fracture VII, Key Engineering Materials Vols. 592-593, 2014, pp. 121-124

Mikhail A. Guzev, 7 Radio st., Vladivostok, Russian Federation
Alexander S. Losev, 7 Radio st., Vladivostok, Russian Federation

A mixed time-frequency domain method to describe the dynamic behaviour of a discrete medium bounded by a linear continuum

Jeroen S. Hoving Andrei V. Metrikine
J.S.Hoving@tudelft.nl

Abstract

To minimize the calculation time required by numerical models that describe dynamic interactions involving nonlinear behaviour, it is useful to divide the model into two separate domains. One domain close to the interaction point, which consists of a sophisticated model capable of describing nonlinear phenomena, and another domain at a distance from the interaction point where only linear behaviour remains. The key issue in such numerical models is the coupling of the two domains. The presence of said nonlinear phenomena implies the necessity to work in the time domain rather than in the frequency domain. Nevertheless, frequency domain approaches are preferred as they allow for much faster calculations than time domain approaches. So-called hybrid models exist that attempt to maximize the use of frequency domain approaches for the modelling of nonlinear dynamic behaviour, but these models are often iterative, thereby increasing calculation times.

This contribution presents a non-iterative method to describe the non-smooth dynamic behaviour of a significantly nonlinear system coupled to a linear continuum. Although this method shows the potential to be particularly effective for applications in two- or three-dimensional media, this paper treats the coupling of a one-dimensional linear medium to illustrate this method.

1 General Introduction

To determine the loads on a structure due to the dynamic interaction of a structure with its environment, it is vital to correctly model the response of the environment. In this paper, we focus only on the response of the environment and include the structure as an external load applied to an environment. Near the point of interaction between structure and environment, the behaviour of the environment may be governed by nonlinear phenomena and is therefore modelled by a medium capable of describing these nonlinear phenomena, which typically occur in soil-structure and ice-structure interaction. From a numerical point of view, it is desirable to keep the domain of this nonlinear medium as small as possible to minimize the required calculation time. Therefore, the environment is divided into two separate media; a sophisticated nonlinear medium in the region of interaction with the structure, and a linear-elastic medium at such distance from the interaction point that its

response is always linear. As nonlinear phenomena are difficult to capture by continuum models [2], we use a discrete lattice model in the near-field. Applications of lattice models are for example found in the fields of fracture mechanics [5] and micromechanics [4], but also in the field of ice-structure interaction [1]. The linear-elastic far-field response is modelled by a semi-infinite continuum, thus providing the lattice model with a non-reflective boundary.

In some cases, the system of equations of motion for a coupled one-dimensional model can be analytically derived in the time domain. However, as soon as multiple dimensions are considered, a time domain solution can no longer be obtained analytically. Instead, the system of equations of motion has to be derived in the frequency domain and the integration involved with the inverse transformation from the frequency to the time domain must be performed numerically [3]. For a coupled system that is completely linear, one needs to solve the algebraic system of equations of motion in the frequency domain once and then apply numerical integration at every time step to obtain the time domain solution. This requires severely less numerical effort than to solve the system of differential equations in the time domain at every time step. Unfortunately , nonlinear phenomena cannot be described in the frequency domain and thus, coupled systems that incorporate nonlinear phenomena must generally be solved in the time domain. Nevertheless, the nonlinearities in the dynamic response of lattice models may generally be described to be significantly nonlinear, i.e. the dynamic properties change at any given moment in time, but the change in behaviour is instant. In other words, every single time a nonlinearity occurs the system changes instantly, while the system itself still behaves in a linear manner during the following time steps. Thus, for the period between any two nonlinearities, the system of equations of motion can still be solved algebraically in the frequency domain. Assuming that the featured nonlinearities are significantly nonlinear thus allows us to describe the dynamic response of a nonlinear medium to be piecewise linear. The approach described in this paper can be considered as a mixed time-frequency domain (MTFD) method as the nonlinearities are applied between time steps and thus in the time domain, while the response of the coupled model, during each piecewise linear period, is found by solving the corresponding algebraic system of equations of motion in the frequency domain. This approach is somewhat superfluous for one-dimensional models, as the coupling between one-dimensional media may often be solved analytically, but shows the potential to be particularly effective for the modelling of coupled two- or even three-dimensional media. Nevertheless, the method is here explained on the basis of the one-dimensional coupled linear-elastic system depicted in figure 1, because its system of equations of motion for the coupled linear elastic model can be solved in both the frequency domain and directly in the time domain, and therefore the correct application of the MTFD-method can be easily verified for this system.

In the following, we will first discuss the methodology of the mixed time-frequency domain approach. Consecutively, we will derive the system of equations of motion for the one-dimensional discrete-continuous linear-elastic system in the time domain for zero initial conditions, which serves as a benchmark for the MTFD-method. The derivation of the system of equations of motion for the MTFD-approach including nonzero initial conditions is then discussed in section 4. In section 5, an improved statement for the inverse Laplace transform is presented that allows for its numerical application for a system with nonzero initial conditions. Subsequently, the results of the MTFD-method are compared to the benchmark system in section 6.

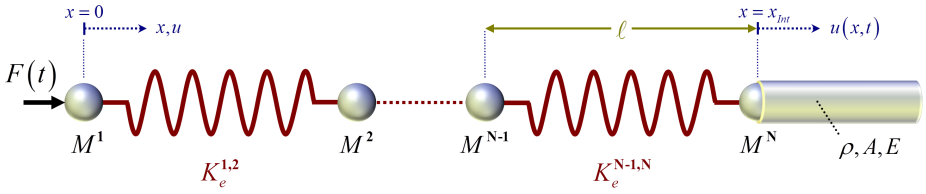

Figure 1: The one-dimensional semi-infinite discrete-continuous linear-elastic system

2 Methodology of the mixed time-frequency domain approach

Let us consider an arbitrary system of particles that may respond significantly nonlinear to an applied load. When the system is at rest and has zero initial conditions, it is safe to assume that this system will initially respond in a linear manner. To describe the response of said system for the time period until the occurrence of the first nonlinear event, we describe the system in the frequency domain using the Laplace transform and solve the resulting algebraic system of equations of motion yielding the frequency domain response of the system. We then obtain the time domain response for the system by straightforwardly applying the inverse Laplace transform at every time step. This method remains valid for as long as the system behaves linearly.

Now, suppose that at a given time $t = t_0$, a significant nonlinear event occurs. Due to the significant nonlinear event, the behaviour of the system changes, but the change is instant and the response of the system after this significant nonlinear event, i.e. for $t > t_0$, is once again linear. That is, for the time period until the next significant nonlinear event. As the response of the system for the time period between any two nonlinear events is always linear, we can again obtain this response by describing the system in the Laplace domain and solving the corresponding algebraic system of equations, but now for its new properties and with nonzero initial conditions. As the nonzero initial conditions represent the response of the system prior to $t = t_0$, we may consider the system for the time period between the first and second nonlinear event, to start anew at $t = t_0$. To properly consider the new situation for the system that starts at $t = t_0$ in both the time and the Laplace domain, we reset the time domain and describe the new situation for the system to start at $t = 0$, but with nonzero initial conditions. The time domain response after the significant nonlinear event is then once again obtained by solving the corresponding algebraic system in the frequency domain and applying the inverse Laplace transform. This new time domain is valid until the next nonlinear event. Each time the time domain is reset, the response of the system prior to the occurrence of the nonlinear event is included in the new time domain through the nonzero initial displacement at $t = 0$. Note here that, since the initial conditions are nonzero and different for each piecewise linear time period, we here apply the Laplace transform rather than the Fourier transform as the Laplace transform takes the initial conditions into account in the frequency domain, while the Fourier transform neglects the initial conditions in the frequency domain. The procedure described here has been visualized in figure 2.

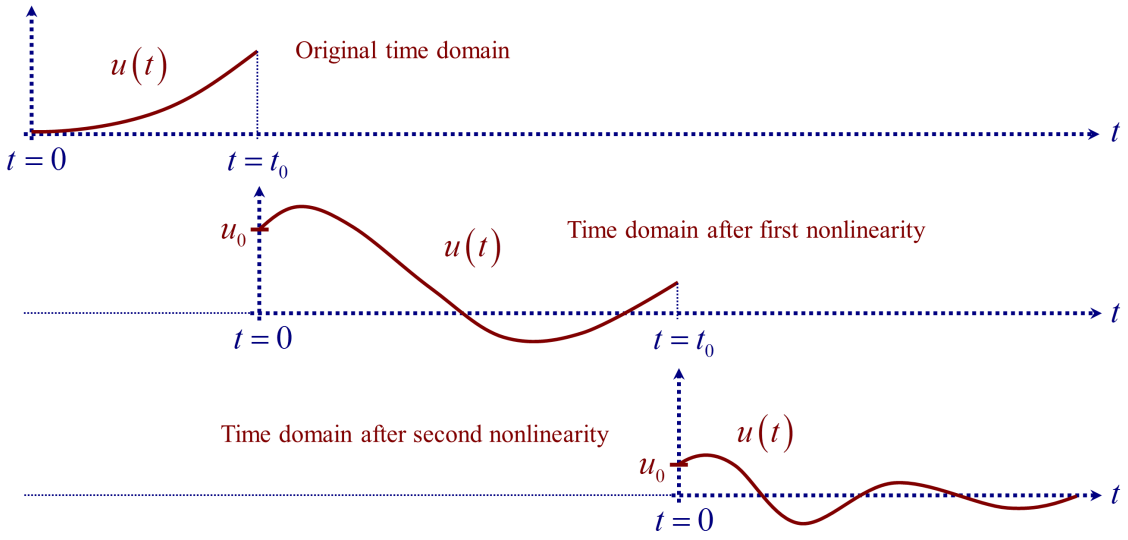

Figure 2: Resetting the time domain every time a nonlinear event occurs

3 Governing equations for the discrete-continuous system in the time domain

The one-dimensional semi-infinite discrete-continuous linear-elastic system, previously depicted in figure 1, is comprised of a one-dimensional linear-elastic discrete lattice composed of **N** particles in series, and a semi-infinite linear-elastic rod. Each particle **n** has a dimensionless mass $M^{\mathbf{n}}$ and the distance between any two adjacent nodes is ℓ. Each two adjacent particles **n** and **n+1** are kinematically related by a spring with a dimensionless stiffness $K_e^{\mathbf{n},\mathbf{n+1}}$. The linear-elastic rod has a density ρ, cross-section area A and Young's modulus E. The discrete lattice and the semi-infinite linear-elastic rod are connected at particle **N** with coordinate $x = x_{Int}$. The coupling between the one-dimensional Hooke system and the linear-elastic rod is described by the equation of motion of particle **N**.
The dimensionless equations of motion for particles **n=1...N-1** respectively read:

$$M^{\mathbf{1}}\ddot{u}^{\mathbf{1}} - K_e^{\mathbf{1,2}}e^{\mathbf{1,2}} = F(t) \tag{1}$$

$$M^{\mathbf{n}}\ddot{u}^{\mathbf{n}} + K_e^{\mathbf{n\text{-}1,n}}e^{\mathbf{n\text{-}1,n}} - K_e^{\mathbf{n,n+1}}e^{\mathbf{n,n+1}} = 0 \tag{2}$$

Here, $e^{\mathbf{n,n+1}}$ denotes the elongation of the kinematic element between particles **n** and **n+1**. Furthermore, dimensionless time and space are respectively introduced as $t \to t\omega_0$ and $x \to x\omega_0/c$, where ω_0 and c are respectively the natural frequency of and the wave speed in the system.
To assure homogeneity between lattice and rod, their material properties are matched. The relation between the material properties of the lattice and the rod is established by matching the equation of motion for the rod with the homogeneous equation of motion for an arbitrary particle inside the lattice in the long-wave limit. Applying the Taylor expansion to the equation of motion for an arbitrary particle inside the lattice by replacing the particle displacement $u^{\mathbf{n}}$ by the continuum displacement $u(x,t)$ and replacing the displacements of the adjacent particles, $u^{\mathbf{n\text{-}1}}$ and $u^{\mathbf{n+1}}$, by the second order Taylor polynomial of the corresponding continuum displacement $u(x \pm \ell, t)$ yields the equation of motion for an

arbitrary particle inside the lattice in the long-wave limit [7]. Comparing the resulting expression with the equation of motion for the rod shows that the mass of a particle inside the homogeneous system is found as $M = \rho A \ell$ and the spring stiffness of the springs inside the homogeneous system is found as $K_e = EA/\ell$. Therefore, the dimensionless mass of a particle $\mathbf{n}$ and the dimensionless stiffness of the spring between particles $\mathbf{n}$ and $\mathbf{n+1}$ in equations (1) and (2) are generally introduced as $M^{\mathbf{n}} \rightarrow M^{\mathbf{n}}/M$ and $K_e^{\mathbf{n,n+1}} \rightarrow K_e^{\mathbf{n,n+1}}/K_e$. For a homogeneous system, we thus find that $M^{\mathbf{n}} = K_e^{\mathbf{n,n+1}} = 1$.
The equation of motion of particle $\mathbf{N}$, also denoted as the interface equation, is obtained by combining the one-dimensional wave equation for the semi-infinite rod and the interface conditions that follow from respectively the equilibrium of forces and the displacement relation at the lattice-continuum interface. In the time domain, the dimensionless coupling statement reads:

$$\ddot{u}(x,t) - u''(x,t) = 0 \tag{3}$$

$$u'(x_{Int},t) = M^{\mathbf{N}}\ddot{u}^{\mathbf{N}} + K_e^{\mathbf{N\text{-}1,N}} e^{\mathbf{N\text{-}1,N}} \tag{4}$$

$$u(x_{Int},t) = u^{\mathbf{N}} \tag{5}$$

Solving the one-dimensional wave equation (3) in the Laplace domain accounting for the appropriate behaviour of the linear-elastic rod for $x \rightarrow \infty$, and inserting the resulting Laplace domain displacement along the semi-infinite rod into the interface conditions (4), as well as taking into account (5), yields the interface equation in the Laplace domain. Subsequently applying the inverse Laplace transform to the resulting Laplace domain expression then yields the interface equation, i.e. the equation of motion for particle $\mathbf{N}$, in the time domain as:

$$M^{\mathbf{N}}\ddot{u}^{\mathbf{N}} + K_e^{\mathbf{N\text{-}1,N}} e^{\mathbf{N\text{-}1,N}} + \dot{u}^{\mathbf{N}} = 0 \tag{6}$$

By choosing the point of coupling between lattice and rod at a particle and keeping the distance between the particles equal to ℓ, it follows from the systems' geometry that particle $\mathbf{N}$ only represents half the length ℓ. To maintain a homogeneous distribution of mass and spring stiffness along the coupled system, it then follows that $M^{\mathbf{N}} = \frac{1}{2}$ and $K_e^{\mathbf{N\text{-}1,N}} = 1$. Note here that different combinations of mass and stiffness may be chosen at the discrete-continuous interface as testified by Metrikine et al. [4], where it is shown that there will be no reflection at the lattice-rod interface in the long-wave limit as long as the interface mass and stiffness are related as:

$$K_e^{\mathbf{N\text{-}1,N}} = \frac{2}{1 + 2M^{\mathbf{N}}} \tag{7}$$

Together, equations (1), (2) and (6) give the full system of dimensionless equations of motion for the one-dimensional coupled system in the time domain.

4 Laplace domain equations for the coupled 1D-system for nonzero initial conditions

In the previous section, we have derived the equations of motion for the one-dimensional coupled linear-elastic system in the time domain assuming zero initial conditions. For the application of the MTFD-method however, we require the corresponding system of equations to account for nonzero initial conditions in the Laplace domain. Applying the unilateral Laplace transform to equations (3) to (5) with respect to time, which accounts for possible nonzero initial conditions, yields the dimensionless coupling statement in the Laplace domain as:

$$s^2\tilde{u}(x,s) - \tilde{u}''(x,s) = su_0(x) + v_0(x) \tag{8}$$

$$\tilde{u}'(x_{Int},s) + M^{\mathbf{N}}(su_0^{\mathbf{N}} + v_0^{\mathbf{N}}) = M^{\mathbf{N}}s^2\tilde{u}^{\mathbf{N}} + K_e^{\mathbf{N\text{-}1,N}}\tilde{e}^{\mathbf{N\text{-}1,N}} \tag{9}$$

$$\tilde{u}(x_{Int},s) = \tilde{u}^{\mathbf{N}} \tag{10}$$

Here, the tilde denotes a variable in the Laplace domain, while s is the complex Laplace parameter. Furthermore, $u_0(x)$ and $v_0(x)$ are respectively the initial displacement and initial velocity along the linear-elastic rod, while $u_0^{\mathbf{N}}$ and $v_0^{\mathbf{N}}$ denote the initial displacement and initial velocity of the interface particle. Accounting for the appropriate behaviour of the rod for $x \to \infty$ and noting that $Re(s) > 0$, the general solution to equations (8) reads:

$$\tilde{u}(x,s) = C_1e^{-sx} + \tilde{u}_p(x,s) \tag{11}$$

The first right-hand-side term is the solution to the homogeneous equation, where C_1 is derived by considering the boundary condition at x_{Int}. Furthermore, $\tilde{u}_p(x,s)$ denotes the yet unknown particular solution. For zero initial conditions, equation (8) reduces to a homogeneous equation, so that the particular solution is exclusively related to the nonzero initial conditions. Applying the differentiation to space to equation (11) and rearranging yields:

$$\tilde{u}'(x,s) = -s\tilde{u}(x,s) + s\tilde{u}_p(x,s) + \tilde{u}_p'(x,s) \tag{12}$$

Substituting equation (12) into equation (9), as well as taking equation (10) into account, yields the interface equation in the Laplace domain as:

$$M^{\mathbf{N}}s^2\tilde{u}^{\mathbf{N}} + K_e^{\mathbf{N\text{-}1,N}}\tilde{e}^{\mathbf{N\text{-}1,N}} + s\tilde{u}^{\mathbf{N}} = M^{\mathbf{N}}(su_0^{\mathbf{N}} + v_0^{\mathbf{N}}) + f_0(s) \tag{13}$$

$$where: f_0(s) = s\tilde{u}_p(x_{Int},s) + \tilde{u}_p'(x_{Int},s) \tag{14}$$

Note here that all terms related to the nonzero initial conditions are collected at the right-hand-side of equation (13).

The particular solution to equation (8) is found using a Green's function approach. To this purpose, we replace the right-hand-side of equation (8) by the Dirac delta function. Applying the Fourier transform with respect to space to the resulting equation of motion then yields the corresponding GreenвГЄs displacement in the frequency-wavenumber domain. Applying the inverse Fourier transform using contour integration by means of the residue theorem yields the Green's displacement of the linear-elastic rod in the Laplace domain as $\tilde{g}_u(x,s) = \frac{1}{2s}e^{-s|x|}$. Consequently, we find the particular solution at $x = x_{Int}$ as:

$$\tilde{u}_p(x_{Int},s) = \frac{1}{2s}\int_0^\infty e^{-s|x_{Int}-\xi|}(su_0(\xi)+v_0(\xi))d\xi \tag{15}$$

Using Leibniz' rule for differentiation under the integral sign to obtain the spatial derivative of the particular solution and subsequently substituting equation (15) and its spatial derivative into equation (14) then yields the expression $f_0(s)$ as:

$$f_0(s) = \int_{x_{Int}}^\infty e^{-s(\xi-x_{Int})}(su_0(\xi)+v_0(\xi))d\xi \tag{16}$$

Equation (16) denotes the contribution of the rod's initial conditions to the interface equation. If we only allow loads to be applied inside the lattice, it is evident that at any time moment the response of the rod is due to the input at its interface with the lattice, and thus, we can express the displacement and velocity along the rod in terms of the response of the interface particle **N**. The relation between the time domain response of the rod and that of the interface particle can be derived by considering the boundary value problem for the rod assuming zero initial conditions. In the Laplace domain, the relation between the displacement along the rod and that of the interface particle is found as $\tilde{u}(x,s) = \tilde{u}^{\mathbf{N}}e^{-s(x-x_{Int})}$. Applying the inverse Laplace transform then yields the corresponding relation in the time domain as $u(x,t) = u^{\mathbf{N}}(t-(x-x_{Int}))H(t-(x-x_{Int}))$. Deriving the velocity relation accordingly and substituting both displacement and velocity relations into equation (16), as well as replacing the variable of integration ξ by the variable of integration $\tau = \xi - x_{Int}$ then yields the expression $f_0(s)$ as:

$$f_0(s) = \int_0^{t_0} e^{-s\tau}(su_0^{\mathbf{N}}(t_0-\tau)+v_0^{\mathbf{N}}(t_0-\tau)d\tau \tag{17}$$

The remaining expression for $f_0(s)$ can now be interpreted as a convolution integral over the time domain prior to the time moment t_0 at which the system was reinitiated and new nonzero initial conditions were specified. Consequently, equations (13) and (17) together describe the Laplace domain interface equation exclusively in terms of the discrete lattice. The Laplace domain system of equations of motion for the one-dimensional coupled linear-elastic system that accounts for nonzero initial conditions is completed by including the Laplace domain equations of motion for the particles **n=1...N-1** that read:

$$M^{\mathbf{1}}s^2\tilde{u}^{\mathbf{1}} - K_e^{\mathbf{1,2}}\tilde{e}^{\mathbf{1,2}} = \tilde{F}(s) + M^{\mathbf{1}}(su_0^{\mathbf{1}}+v_0^{\mathbf{1}}) \tag{18}$$

$$M^{\mathbf{n}}s^2\tilde{u}^{\mathbf{n}} + K_e^{\mathbf{n\text{-}1,n}}\tilde{e}^{\mathbf{n\text{-}1,n}} - K_e^{\mathbf{n,n+1}}\tilde{e}^{\mathbf{n,n+1}} = M^{\mathbf{n}}(su_0^{\mathbf{n}}+v_0^{\mathbf{n}}) \tag{19}$$

Here, $\tilde{F}(s)$ is the Laplace domain expression for the external force applied at particle **1**. Note here that, once the time domain is reinitiated at a time t_0 this must also be accounted for in the Laplace domain expression of the applied load.

5 Transformation to the time domain accounting for nonzero initial conditions

Solving the algebraic system of equations of motion given by equations (13) and (17) to (19) yields the Laplace domain displacements of all particles in the one-dimensional lattice. The time domain displacements of all particles in the lattice are then obtained by applying the inverse Laplace transform to the corresponding Laplace domain displacements. The inverse Laplace transform of these Laplace domain displacements can not be derived analytically and must therefore be obtained numerically. As a consequence, the semi-infinite domain of integration of the inverse Laplace transform has to be truncated. This truncation leads to several problems, in particular for nonzero initial conditions. If we describe the inverse Laplace transform in terms of frequency, rather than in terms of the complex Laplace operator s, we may find the time domain displacement of a particle $\mathbf{n}$ in the lattice as:

$$u^{\mathbf{n}} = \frac{e^{\sigma t}}{\pi} \int_0^{\omega_{tr}} Re\left\{\tilde{u}^{\mathbf{n}} e^{i\omega t}\right\} d\omega \tag{20}$$

Here, ω_{tr} is the truncation frequency. The corresponding velocities and accelerations may then be obtained by taking the first and second time derivatives of equation (20), which is equivalent to respectively applying the inverse Laplace transform to $\tilde{v}^{\mathbf{n}} = su^{\mathbf{n}}$ and $\tilde{a}^{\mathbf{n}} = s^2 u^{\mathbf{n}}$. Now, we may only apply the inverse Laplace transform numerically, if their integrands are sufficiently convergent within the truncated domain of integration. Solving equation (19) for $\tilde{u}^{\mathbf{n}}$ shows that, taking nonzero initial conditions into account, the Laplace domain displacement has a convergence ω^{-1} for $\omega \to \infty$. Consequently, it follows that the Laplace domain velocity and acceleration, i.e. $\tilde{v}^{\mathbf{n}}$ and $\tilde{a}^{\mathbf{n}}$, are both non-convergent. As shown by figure 3, the lack of convergence is due to the nonzero initial conditions; Figure 3a shows the convergent Laplace domain displacement, velocity and acceleration of a particle $\mathbf{n}$ for zero initial conditions, while figure 3b gives the response for nonzero initial conditions.

As an alternative, and in correspondence with the Laplace transform, we may respectively describe the velocity and acceleration in the Laplace domain as $\tilde{v}^{\mathbf{n}} = su^{\mathbf{n}} - u_0^{\mathbf{n}}$ and $\tilde{a}^{\mathbf{n}} = s^2 u^{\mathbf{n}} - su_0^{\mathbf{n}} - v_0^{\mathbf{n}}$. Substituting $\tilde{u}^{\mathbf{n}}$, found from solving equation (19), into these expressions shows that the Laplace domain velocity and acceleration now both have the same convergence for $\omega \to \infty$ as the Laplace domain displacement. Although the given Laplace domain expressions for displacement, velocity and acceleration are now convergent, these expressions still do not lead to a proper numerical application of the inverse Laplace transform. To illustrate this, let us consider the inverse Laplace transform and note that by applying the causality principle, the integrand of the inverse Laplace transform may alternatively be described as either one of $Re\left\{\tilde{u}^{\mathbf{n}} e^{i\omega t}\right\} = 2Re\left\{\tilde{u}^{\mathbf{n}}\right\} cos(\omega t) = -2Im\left\{\tilde{u}^{\mathbf{n}}\right\} sin(\omega t)$. These integrands may however only be interchanged if, and only if, the limit $\omega \to \infty$ is taken into account. For either integrand, numerically applying the integration over its truncated domain yields an incorrect behaviour of the time domain displacement near the nonzero initial conditions as depicted in figure 4. Due to the finite domain of integration,

the integrand with the term $sin(\omega t)$ must always give a zero displacement at time $t = 0$ of the time domain reinitiated at $t = t_0$. Additionally, taking the time derivative of the integrand with the term $cos(\omega t)$ shows that $\dot{u}_0 = \sigma u_0$, where σ is the small positive real value of the complex Laplace parameter. Consequently, the corresponding time domain displacement has a slope that is significantly smaller than the slope of the exact solution. To improve the behaviour of the inverse Laplace transform with a truncated domain of integration for a system that, in the time domain, has nonzero initial conditions, we extract the initial conditions from the corresponding Laplace domain expression and separately include the contribution of the initial conditions in the time domain. As a consequence, the remaining Laplace domain expression, henceforth denoted as the improved Laplace domain expression, can be considered as a Laplace domain expression for a system with zero initial conditions, thereby improving its behaviour in the time domain. To obtain expressions for the displacement, velocity and acceleration that appreciate the rules of differentiation, we do not only extract the initial displacement from the Laplace domain displacement, but we also extract the contributions of the initial velocity and initial acceleration. Consequently, the time domain expressions for the displacement, velocity and acceleration of an arbitrary particle $\mathbf{n}$ in the lattice now become:

$$u^{\mathbf{n}} = \frac{e^{\sigma t}}{\pi} \int_0^{\omega_{tr}} Re\left\{\tilde{u}^{\mathbf{n}}_{imp} e^{i\omega t}\right\} d\omega + u^{\mathbf{n}}_0 + v^{\mathbf{n}}_0 t + a^{\mathbf{n}}_0 \frac{t^2}{2} \tag{21}$$

$$\dot{u}^{\mathbf{n}} = \frac{e^{\sigma t}}{\pi} \int_0^{\omega_{tr}} Re\left\{s\tilde{u}^{\mathbf{n}}_{imp} e^{i\omega t}\right\} d\omega + v^{\mathbf{n}}_0 + a^{\mathbf{n}}_0 t \tag{22}$$

$$\ddot{u}^{\mathbf{n}} = \frac{e^{\sigma t}}{\pi} \int_0^{\omega_{tr}} Re\left\{s^2\tilde{u}^{\mathbf{n}}_{imp} e^{i\omega t}\right\} d\omega + a^{\mathbf{n}}_0 \tag{23}$$

Here, the improved Laplace domain displacement is found as:

$$\tilde{u}^{\mathbf{n}}_{imp} = \tilde{u}^{\mathbf{n}} - \frac{u^{\mathbf{n}}_0}{s} - \frac{v^{\mathbf{n}}_0}{s^2} - \frac{a^{\mathbf{n}}_0}{s^3} \tag{24}$$

Substituting $\tilde{u}^{\mathbf{n}}$, found from solving equation (19), into equation (24), shows that the improved Laplace domain displacement now has a convergence ω^{-3} for $\omega \to \infty$. Figure 5

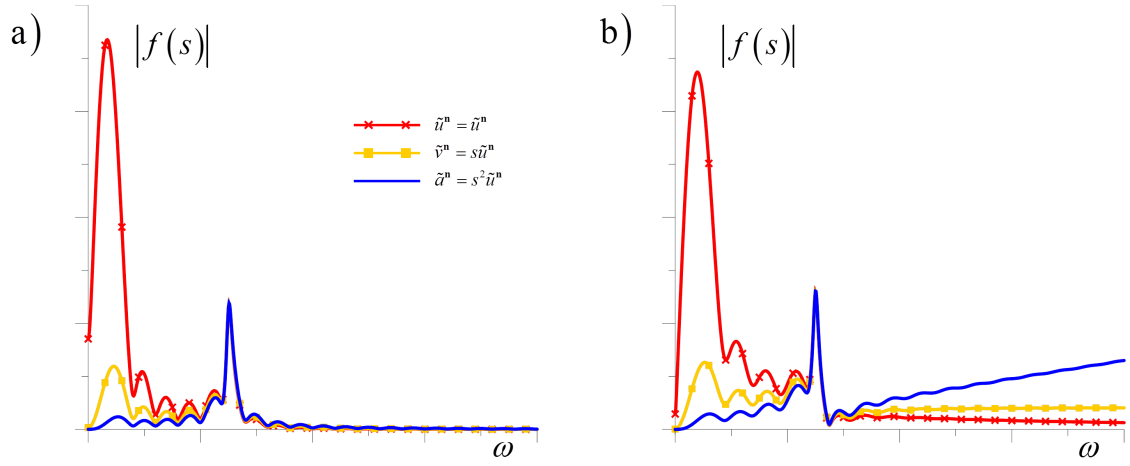

Figure 3: Absolute Laplace domain displacement, velocity and acceleration for: a) zero initial conditions; b) nonzero initial conditions.

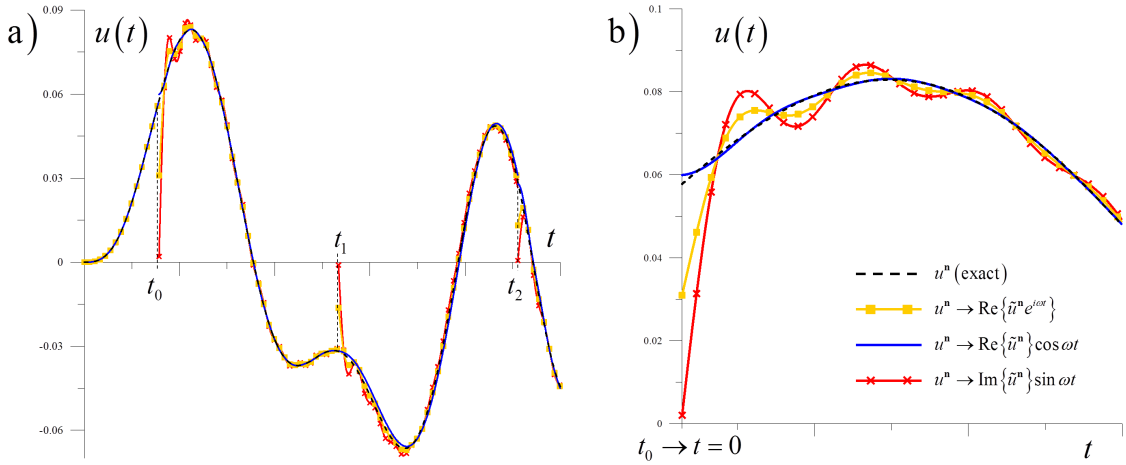

Figure 4: Displacement for a truncated domain of the inverse Laplace transform: a) in the original time domain; b) close-up in the time domain reinitiated at t_0.

shows the displacement of particle **n** obtained using the improved statement for the inverse Laplace transform given by equation (21).

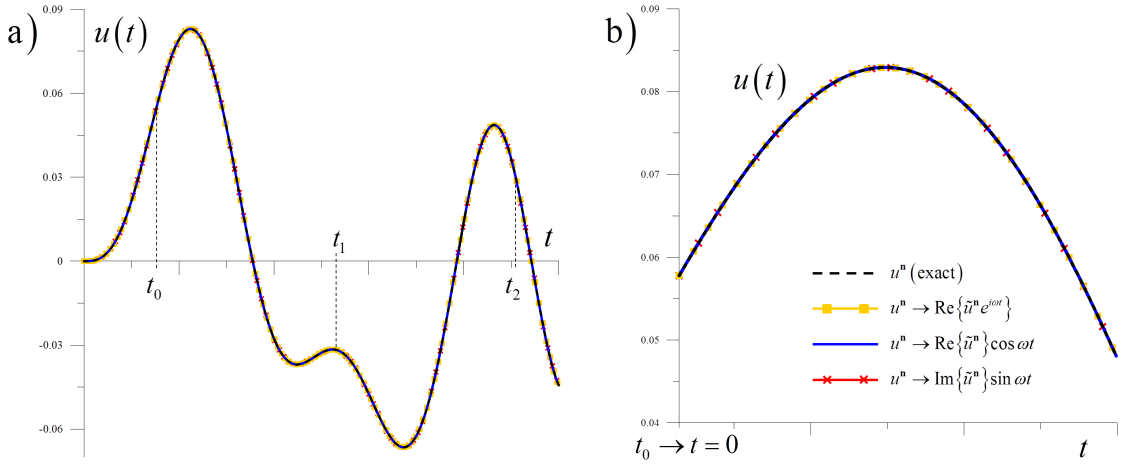

Figure 5: Displacement obtained using the improved statement: a) in the original time domain; b) close-up in the time domain reinitiated at t_0.

6 The mixed time-frequency domain method applied to the coupled 1D-system

Figure 6 shows the longitudinal displacements along the one-dimensional discrete-continuous linear-elastic system due to an applied single-sinus pulse load at 6 consecutive time moments. The discrete lattice consists of 80 particles at an inter-particle distance of $\ell = 0,2m$ and the linear-elastic rod has a density $\rho = 1960kg/m^3$, a cross-section area $A = 1m^2$ and a Young's modulus $E = 19,6MPa$.
The continuous line shows the displacements that result from applying the MTFD-method, while the dashed line shows the resulting displacements from applying a Runge-Kutta scheme to solve the system directly in the time domain, here denoted as the TD-method.

The simulation consists of a 1000 time steps and for the application of the MTFD-method, the system was reinitiated after every 100 time steps. Figure 6 verifies that the MTFD-method yields the proper response of the system. Although the MTFD-method is here applied to a rather simplistic linear-elastic coupled system, and thereby hardly yields any computational profit, its real gain is found in the application of the MTFD-method to a coupled system consisting of a nonlinear lattice bounded by a viscoelastic environment, especially, for multi-dimensional systems.

References

[1] O. Dorival, A.V. Metrikine and A. Simone, A lattice model to simulate ice-structure interaction, Proceedings of the ASME 27th international OMAE conference, p. 989-996, Estoril, Portugal, 2008.

[2] J.S. Hoving, F. Molenkamp, A.V. Metrikine and A.C.W.M. Vrouwenvelder, The dynamic response of a discrete lattice containing dry-friction elements to a surface load, Proceedings of the XXXIII APM Conference, p. 224-232, St. Petersburg, Russia, 2005.

[3] J.S. Hoving and A.V. Metrikine, On the coupling of nonlinear discrete element models with continua in the time domain, Proceedings of the XXXVIII APM Conference, p. 274-281, St. Petersburg, Russia, 2010.

[4] M. Ostoja-Starzewski, Lattice models in micromechanics, Applied Mechanics Reviews 55(1), p.35-60, 2002.

[5] E. Schlangen and J.G.M. van Mier, Simple lattice model for numerical simulation of fracture of concrete materials and structures, Materials and Structures 25, p. 534-542, 1992.

[6] A.S.J. Suiker, A.V. Metrikine and R. de Borst, Dynamic behaviour of a layer of discrete particles, part 1: Analysis of body waves and eigenmodes, Journal of Sound and Vibration 240, p. 1-18, 2001.

[7] A.A. Maradudin, E.M. Montroll, and G.H. Weiss, Theory of Lattice Dynamics in the Harmonic Approximation, Solid State Physics, Vol. Supplement 3. New York: Academic Press, 1963.

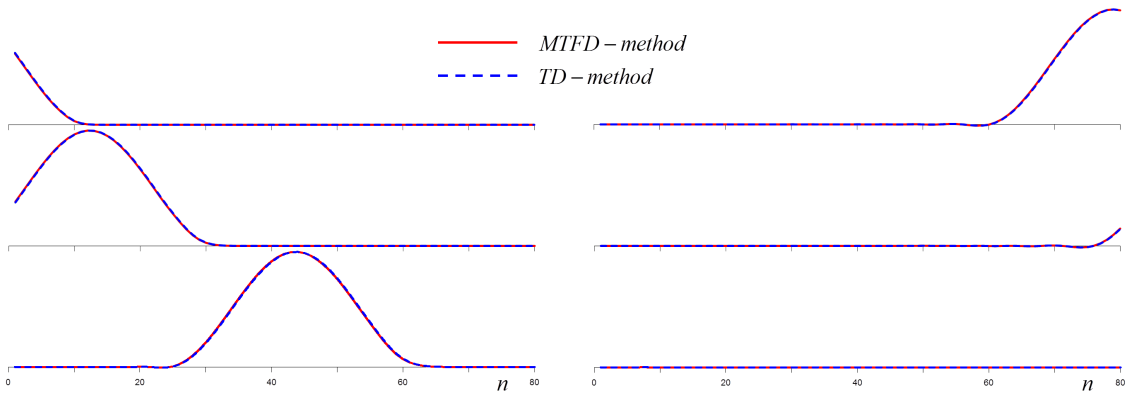

Figure 6: Longitudinal displacement along the one-dimensional discrete-continuous linear-elastic system at successive time moments due to a single-sinus pulse.

[8] A.V. Metrikine, A.M. Kudarova, J.S. Hoving, R. van Vliet, On the minimization of wave reflection at the interface of a discrete system and a dispersively-similar continuum, Journal of Sound and Vibration 346, p. 191-199, 2015

Jeroen S. Hoving, Delft University of Technology, Faculty of Civil Engineering and GeoSciences, P.O. Box 5048, 2600 GA, The Netherlands
Andrei V. Metrikine, Delft University of Technology, Faculty of Civil Engineering and GeoSciences, P.O. Box 5048, 2600 GA, The Netherlands

A semi-analytical impulse response method for transient laminar flow in hydraulic networks

Antonio Jarquin-Laguna, Apostolos Tsouvalas
A.JarquinLaguna@tudelft.nl

Abstract

Transient analysis in hydraulic networks has been well recognized of high importance due to sudden changes in flow or pressure introduced by valve closures or component failures. Therefore, accurate and robust numerical models are necessary to analyse the travelling pressure waves as a result of such abrupt changes, i.e. waterhammer effects. This work presents the formulation of a semi-analytical impulse response method applied to transient laminar flow in hydraulic networks. The method is based on the exact solution of a two-dimensional viscous model in the frequency domain with various interface and boundary conditions. The numerical computations are based on the use of the fast Fourier transform and a discrete numerical convolution with respect to time. A numerical example is presented and the results are compared with the method of modal approximations which is widely used in practice. The results show that the proposed method is able to predict the transient behaviour with better accuracy and without the need of spatial discretization. Thus, it is expected that for large networks, the computational cost of the impulse response method will have a great advantage when compared to existing grid-space methods.

1 Introduction

Transient flow in hydraulic networks is a common phenomenon as a result of either accidental or normal operation of hydraulic systems. The study and analysis of unsteady-flow conditions is very important due to the large disturbances in pressure and flow conditions that might be introduced [1]. Several numerical methods exist to model fluid transients [2, 3]. To date, the method of characteristics (MOC) is the most popular one due to its accuracy, simplicity and ability to include different boundary conditions in the one dimensional case [4]. This method has also been adapted for two dimensional cases to account for the frequency dependence of the friction forces [5, 6] and extended to be applied in more complex hydraulic networks,

[7, 8]. However, the MOC together with other discrete formulations such as finite differences [9], require a spatial discretization of the lines in the network, which turns to be computationally demanding as discussed in [10].

For laminar flow, another approach to model the fluid transients is possible through modal approximations. The idea behind this technique is to represent the transcendental expressions in the frequency domain, as a finite summation of low-order polynomial transfer functions. Thus, it is possible to approximate each mode of the transmission line by a second order linear differential equation [11, 12, 13, 14]. The modal method can also be formulated directly in the time domain using a variational method [15].The modal approximation has certain advantages when used in time domain simulations, not only because it is easily coupled to other mechanical or hydraulic subsystems, but additionally because it can be implemented and solved numerically with a variable time step ODE solver. Furthermore, several studies have shown that modal methods are more convenient and numerically stable when compared, for example, with discrete methods [16, 17]. On the contrary, when modal approximations are used to construct hydraulic networks as a part of a complex fluid power system, i.e. through bond-graph models [18, 19], each line in the network should include enough number of modes to cover the frequency range of interest of both the overall system and input disturbance. Due to the different line geometries and interface conditions, the selection of the required number of modes for each line is not straightforward. Therefore, the modal method has the disadvantage of lacking a direct control on the accuracy of the results due to a propagation error introduced by the number of modes used for each line.

A semi-analytical approach is presented in this paper based on the impulse response method (IRM). This method has been extensively used for dynamic analyses in other areas, like for example vibrations of mechanical systems, however its use in hydraulic systems has not been completely exploited. A variation of this method has already been used for analysis of a single pipeline as referred in [20, 21]. This work presents a direct extension towards a solution of a hydraulic network system consisting of multiple lines including dissipative boundary conditions. The approach is remarkably simple in its application. It consists of a solution of a coupled system of linear algebraic equations and the use of the Fourier transform. The method is accurate and reliable for the solution of large networks, overcoming the disadvantages of several other approaches.

The paper is composed as follows. Section 2 revises the mathematical formulation of the two dimensional viscous compressible model for a single pipeline together with the exact solution of a hydraulic network in the frequency domain. Section 3 describes the application of the impulse response method to solve a hydraulic network using the equations of the previous section. In section 4, a numerical example of a simple hydraulic network is presented in which the time-domain results are compared with the ones obtained by the use of the modal method. Finally the conclusions are presented in the last section.

2 Mathematical formulation and exact solution in the frequency domain

2.1 Transient laminar flow

Consider a laminar, axisymmetric flow of a Newtonian fluid through a constant diameter line with constant material properties, in which the mean fluid velocity is considerably less than the acoustic velocity and the thermodynamic effects are neglected. The velocities in the axial x-coordinate and radial r-coordinate are denoted by $u(x,r,t)$ and $v(x,r,t)$, respectively. Assuming that the motion in the radial direction is negligible compared to the motion in the axial direction $u >> v$, the radial pressure distribution is constant across the cross-sectional area, i.e. $P(x,t)$.

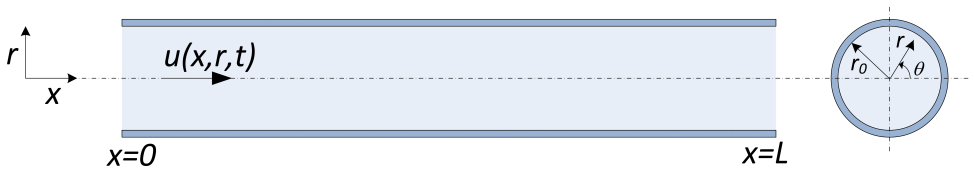

Figure 1: Schematic of a single hydraulic line

The fluid properties are designated through the fluid density ρ, the fluid dynamic viscosity μ and the fluid bulk modulus of elasticity K. Hence, the partial differential equations corresponding to the mass conservation and the momentum equilibrium in the axial direction, are reduced to [1],

$$\frac{\partial P(x,t)}{\partial t} + c^2\rho\left[\frac{\partial u(x,r,t)}{\partial x} + \frac{\partial v(x,r,t)}{\partial r} + \frac{v(x,r,t)}{r}\right] = 0 \tag{1}$$

$$\frac{\partial u(x,r,t)}{\partial t} + \frac{1}{\rho}\frac{\partial P(x,t)}{\partial x} = \mu\left[\frac{\partial^2 u(x,r,t)}{\partial r^2} + \frac{1}{r}\frac{\partial u(x,r,t)}{\partial r}\right] \tag{2}$$

where the effective speed of sound in the fluid is $c = (K_e/\rho)^{1/2}$; the effective bulk modulus of the fluid K_e takes into account the flexibility of the pipeline, compressibility of the hydraulic fluid and the effect of any entrapped air into the system.

The cross-sectional volumetric flow is obtained through the integration of the axial velocity across the cross-sectional area of the line with finite radius r_0. The volumetric flow is also defined as the product of the average velocity $\bar{u}(x,t)$ and the cross-sectional area.

$$Q(x,t) = \pi\, r_0^2\, \bar{u}(x,t) = \int_0^{r_0} u(x,r,t)\, 2\pi r\, dr \tag{3}$$

The previous equations correspond to what is known as a two-dimensional viscous compressible model or dissipative friction model [2, 3].

2.2 General solution of a single line

The general solution of equations 1 and 2 can be obtained in the frequency domain by using the Fourier transform with respect to time according to the following transformation pair,

$$\tilde{f}(\omega) = \int_{-\infty}^{\infty} f(t)\, e^{-j\omega t} dt \tag{4}$$

$$f(t) = \frac{1}{2\pi} \int_{-\infty}^{\infty} \tilde{f}(\omega)\, e^{j\omega t} d\omega \tag{5}$$

here ω represents the frequency and $j = \sqrt{-1}$ is a complex value. The average velocity and the pressure are then given by the following two equations [1],

$$\bar{U}(x,\omega) = \left[A(\omega) \cos\frac{j\omega\beta}{c} x + B(\omega) \sin\frac{j\omega\beta}{c} x \right] \frac{J_0\left[j \left(\frac{j\omega\, r_0^2}{\nu} \right)^{\frac{1}{2}} \right]}{\beta^2} \tag{6}$$

$$\bar{P}(x,\omega) = \left[A(\omega) \sin\frac{j\omega\beta}{c} x - B(\omega) \cos\frac{j\omega\beta}{c} x \right] \frac{\rho c}{\beta} J_0 \left[j \left(\frac{j\omega\, r_0^2}{\nu} \right)^{\frac{1}{2}} \right] \tag{7}$$

in which $A(\omega)$ and $B(\omega)$ are the unknown integration constants to be obtained from the applied boundary conditions; $\nu = \mu/\rho$ is the kinematic viscosity of the fluid and the constant β is expressed through the Bessel functions of the first kind $J_n(z)$ with $n = 0, 1$.

$$\beta = \left(\frac{2}{j \left(\frac{j\omega\, r_0^2}{\nu} \right)^{\frac{1}{2}}} \frac{J_1\left[j \left(\frac{j\omega\, r_0^2}{\nu} \right)^{\frac{1}{2}} \right]}{J_0\left[j \left(\frac{j\omega\, r_0^2}{\nu} \right)^{\frac{1}{2}} \right]} - 1 \right)^{-\frac{1}{2}} \tag{8}$$

Using the boundary conditions at the upstream section where $x = 0$, and at the downstream section with $x = L$, the integration constants $A(\omega)$ and $B(\omega)$ are obtained for a single pipeline. Hence the velocity and pressure at the upstream side $\bar{U}_u(\omega)$, $\bar{P}_u(\omega)$ can be expressed in terms of the downstream velocity and pressure $\bar{U}_d(\omega)$, $\bar{P}_d(\omega)$. If the volumetric flow is used instead of the average velocity using equation 3, the following relations are formulated in matrix form,

$$\begin{bmatrix} P_u(\omega) \\ Q_u(\omega) \end{bmatrix} = \begin{bmatrix} \cos\frac{j\omega\beta L}{c} & -\frac{\beta\rho c}{\pi r_0^2} \sin\frac{j\omega\beta L}{c} \\ \frac{\pi r_0^2}{\beta\rho c} \sin\frac{j\omega\beta L}{c} & \cos\frac{j\omega\beta L}{c} \end{bmatrix} \begin{bmatrix} P_d(\omega) \\ Q_d(\omega) \end{bmatrix} \tag{9}$$

A most common representation of the previous equation is done in terms of hyperbolic functions instead of trigonometric functions. The hyperbolic notation is a popular way to show the solution for a single line and its derivation is found in the Appendix.

Two pipeline parameters are introduced, the line impedance constant Z_0 and the dissipation number of the line D_n are defined respectively as:

$$Z_0 = \frac{\rho\, c}{\pi r_0^2} \tag{10}$$

$$D_n = \frac{\nu L}{r_0^2 c} \tag{11}$$

2.3 Extension towards the solution of a hydraulic network

The solution of a complete hydraulic network consisting of multiple lines is an extension of the solution given by equations 6 and 7. Using equation 3, a general solution for the flow and pressure of each of the lines of the network, denoted by the subscript i, is given by:

$$Q_i(x,\omega) = \left[A_i(\omega)\cos\frac{j\omega\beta_i}{c}x + B_i(\omega)\sin\frac{j\omega\beta_i}{c}x\right]\frac{\rho c}{Z_{0,i}}\frac{J_0\left[j\left(\frac{j\omega\, r_{0,i}^2}{\nu}\right)^{\frac{1}{2}}\right]}{\beta_i^2} \tag{12}$$

$$P_i(x,\omega) = \left[A_i(\omega)\sin\frac{j\omega\beta_i}{c}x - B_i(\omega)\cos\frac{j\omega\beta_i}{c}x\right]\frac{\rho c}{\beta_i}J_0\left[j\left(\frac{j\omega\, r_{0,i}^2}{\nu}\right)^{\frac{1}{2}}\right] \tag{13}$$

The difference from the solution for a single pipeline is that the integrations constants for the pressure and flow descriptions cannot be determined explicitly for each of the lines of the hydraulic network. Instead they are obtained numerically by solving a linear system of coupled equations compiled from the various boundary and interface conditions according to the particular configuration of the system. The system of equations written in matrix form is

$$\mathbf{A}\,\vec{x} = \vec{b} \tag{14}$$

where $\mathbf{A}$ is the global system matrix, whose elements are frequency dependent. The vector $\vec{x}$ corresponds to the unknown integration constants for the network consisting of n lines.

$$\vec{x} = \left[\ A_1(\omega),\ B_1(\omega),\ A_2(\omega),\ B_2(\omega), ...,\ A_n(\omega),\ B_n(\omega)\ \right]^T \tag{15}$$

The right-hand side vector $\vec{b}$ corresponds to the external forcing terms at the boundary conditions or interfaces. Thus, the solution of a complex network is only limited by the computational considerations to solve a system of algebraic linear equations. The order of this system of equations is twice the number of lines in the hydraulic network, $2n$.

2.3.1 Interface and boundary conditions

The interface conditions correspond to the junction points or nodes in systems of branching pipes. At these particular locations, the continuity equation is used to relate the inflows and outflows of the discharges at each node or junction, see equation 16. In addition, another set of equations is obtained through the general assumption of uniqueness of the pressure at each junction or node k according to equation 17.

$$\sum Q_{in}(x_k, \omega) - \sum Q_{out}(x_k, \omega) = 0 \tag{16}$$

$$P^{l}(x_k, \omega) = P^{r}(x_k, \omega) \tag{17}$$

The different boundary conditions at the terminations of the lines could include any linear static or dynamic hydraulic component. An example of a static boundary condition is a resistive component, which relates the volumetric flow with the pressure difference across the element at each moment of time through the hydraulic resistance R; in the frequency domain this condition is given by,

$$P_a(\omega) - P_b(\omega) - R\, Q_b(\omega) = 0 \tag{18}$$

A dynamic termination as a boundary condition is also possible, (i.e. a line termination with a large volume of fluid or an actuator). For this example the relation is given through a first order linear differential equation for the pressure P_b, where the hydraulic capacitance C_1 accounts for the fluid compressibility. The representation in both time and frequency domain is given as,

$$C_1 \frac{dP_b(t)}{dt} - Q_b(t) = 0 \tag{19}$$

$$C_1\, j\omega\, P_b(\omega) - Q_b(\omega) = 0 \tag{20}$$

The treatment of a non-linear boundary condition at one of the terminations is also possible through this method; in this case a simultaneous numerical solution of the non-linear boundary condition equation and the convolution integral at the boundary is required. An example is shown in [20], for the particular case of a non-linear valve description.

3 Impulse response method for hydraulic networks

The impulse response method makes use of the superposition property of linear systems; if an arbitrary but known input is decomposed to a series of impulses of

different amplitudes, the response of the system is obtained by the superposition of the responses of each impulse. Thus, if the system or hydraulic network pressure and/or flow response to an impulse is known in the time domain, its response to a general forcing function can be obtained through the convolution of the impulse response and the forcing function.

A known input at one of the boundaries of the hydraulic network can be given as either a pressure function $\Delta P(t)$ or flow function $\Delta Q(t)$. The pressure response of the system at a given location $P(x,t)$ is therefore provided by the convolution of the pressure response at the same location to a pressure impulse $r_{P\,x}(t)$ and the desired pressure input function $\Delta P(t)$,

$$P(x,t) = \int_0^t r_{P\,x}(t-\tau)\,\Delta P(\tau)\,d\tau \tag{21}$$

in which τ is a time variable used for the convolution. Or in the case of a flow input $\Delta Q(t)$ the convolution uses the pressure response to a flow impulse $r_{Q\,x}(t)$ and the flow input function,

$$P(x,t) = \int_0^t r_{Q\,x}(t-\tau)\,\Delta Q(\tau)\,d\tau \tag{22}$$

Hence, in order to obtain the system response to an impulse, the complete hydraulic network is first solved in the frequency domain $r_x(\omega)$. Afterwards, the inverse Fourier transform of the pressure and/or flow is applied at the desired locations to obtain the time domain description $r_x(t)$.

$$r_x(t) = \frac{1}{2\pi}\int_{-\infty}^{\infty} r_x(\omega)\,e^{j\omega t}d\omega = \frac{1}{\pi}Re\left[\int_0^{\infty} r_x(\omega)\,e^{j\omega t}d\omega\right] \tag{23}$$

An efficient way to obtain such response from a numerical perspective, is to use the discrete fast Fourier transform (FFT). Although the FFT is based on a fixed discrete time step, the impulse response has only to be calculated once for the whole network. Once this response is available for the particular configuration, the numerical convolution is obtained in a separate step for any desired input without the necessity to solve the system once more. Furthermore the convolution can also be implemented for a variable step approach.

3.1 Computational efficiency comparison

For large hydraulic networks, the computational efficiency of the proposed method can be compared with other approaches. A general overview is observed in table 1.

Hence let us consider a network comprising of $n_{lines} = 100$. In the MOC, first of all an internal discretization is required; assuming that ten elements are used per line, a final grid of around $1,000$ points is obtained. Every time step, a solution using finite differences is found for all the points in the grid. With the modal method no discretization is required, however a few modes are needed at least to model each

Table 1: Overview of calculation requirements for hydraulic networks

Approach	Calculation requirements per Δt
MOC	Solution required at all interior points of the grid; results are approximate.
Modal method	Solution to a system of linear ordinary differential equations $n_{lines}(4n_{modesperline}+1)$; results are approximate.
IRM	Solution to a system of linear algebraic equations $2n_{lines} \times 2n_{lines}$; exact results in freq domain, accuracy in time domain depends on FFT required at the end of the method.

line $n_{modesperline} = 4$. Assuming that four modes are used to describe accurately each line, a system of 900 ode's is obtained. It is important to mention that the order of the final system might be considerably higher as the number of modes per line is independent and some lines would require higher modes in order to obtain a minimum accuracy. Finally the IRM requires the solution of an independent linear system of equations of 200×200 per frequency (which is equivalent as per time step in the frequency domain), where the obtained solution is exact. At the end of the method, an inverse FFT is required but the computational cost of this operation is also independent of the number of lines in the network.

4 Numerical results

In order to illustrate the proposed method and to compare the predictions with the modal approach proposed in the literature [18], three cases are solved numerically based on the simple hydraulic network shown in figure 2. The forcing input function $\Delta P(t)$ is a unit step pressure at the upstream side $x = 0$. The examples include different linear terminations and the input parameters for each case are summarized in table 2. It is important to note that the dissipation numbers of each line are relatively high $D_n >> 0.0001$. D_n is an adimensional number which is used to characterize both transient and frequency response of a pipeline and given by equation 11; a high value implies that the energy dissipation due to the shear friction at the wall of the line is important. Therefore the dissipative model with frequency-dependent friction will give a more accurate description of the transient behaviour than the linear friction model.

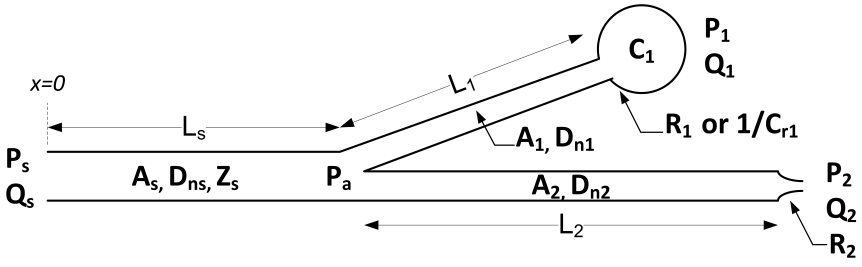

Figure 2: Schematic of the hydraulic network used for the numerical simulations

In general, there exist two unknown integration constants for each line comprising the network. This means that for the particular configuration shown in figure 2, six independent linear equations are required. The first equation corresponds to the boundary condition at the upstream side of the supply line where the required pressure impulse is applied at $x = 0$. Three more equations are obtained from the interface conditions at the branching node a; one for the continuation of flows; the other two from the uniqueness assumption of the pressure. The supply line of the network is noted by the subscript s, while the two other branch lines are noted by the subscripts 1 and 2 respectively.

$$\text{at } x = 0 \qquad P_s(0,\omega) = 1 \tag{24}$$

$$\text{at } x = L_s \qquad Q_s(L_s,\omega) - Q_1(L_s,\omega) - Q_2(L_s,\omega) = 0 \tag{25}$$

$$P_s(L_s,\omega) - P_1(L_s,\omega) = 0 \tag{26}$$

$$P_s(L_s,\omega) - P_2(L_s,\omega) = 0 \tag{27}$$

The fifth and sixth equations are derived from the boundary conditions at the terminations of the hydraulic lines 1 and 2. Once the integration constants are obtained for all the lines in the network, the average velocity and pressure can be evaluated at any desired location by equations 12 and 13. The time domain response of the pressure impulse is obtained numerically through the discrete inverse FFT. For all cases, the number of samples used was $N = 2^{16}$, with a discrete step time of $0.0001s$. The selected time step allows to follow the pressure wave propagation along the spatial coordinate with sufficient detail. Furthermore, it includes frequency components up to $5000Hz$ which are sufficient to describe the step input considered in the examples. The final step is to convolute numerically the impulse response with a step function to obtain the desired step response of the system in the time domain.

Table 2: Numerical parameters for the different cases taken from [18]

	D_{ns}	D_{n1}	D_{n2}	L_1/L_s	L_2/L_s	A_1/A_s	A_2/A_s	R_1/Z_s	R_2/Z_s	C_1/C_c*
Case 1	0.1	0.1	0.1	1	1	1	1	∞	3	-
Case 2	0.01	0.01	0.1	1	5	1	0.5	∞	∞	-
Case 3	0.01	0.1	0.1	5	10	0.5	1	2	6	0.25

* with $C_c = \pi L_s r_s^2/\rho c^2$

4.1 Model comparison and discussion

The results for each case are compared with the results of the same network using the modal method. The modal method is based on four modes for each of the lines in the hydraulic network as presented in [18].

4.1.1 Case 1

All the lines have the same geometric characteristics; one of the terminations of the pipeline is blocked while the other consist of a linear resistance element; the

boundary conditions are shown in equations 28 and 29.

$$\text{at } x = L_1 \qquad Q_1(L_1, \omega) = 0 \tag{28}$$

$$\text{at } x = L_2 \qquad P_2(L_2, \omega) - R_2 Q_2(L_2, \omega) = 0 \tag{29}$$

The pressure response to an impulse at the locations P_a, P_1, P_2 is shown in figure 3(a); this response is numerically convoluted with a unit step input to obtain the results of figure 3(b). Figure 3(c) shows the comparison of results with the modal method. The pressure transient shows a smooth response which is accurately described, with minor differences, by both methods. However, the modal method contains spurious oscillations at the initial moments in time, which are not present in the results of the IRM. The oscillations present in the modal method are impossible to eliminate since this would require the inclusion of infinitely many modes. In the presented method such oscillations are absent since the solution is exact.

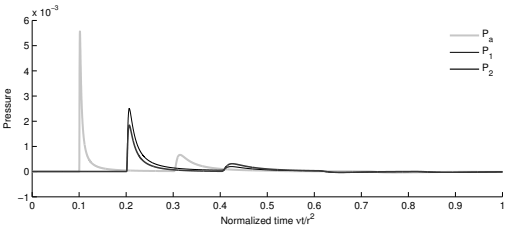

(a) Impulse response

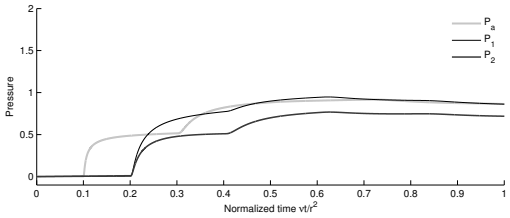

(b) Step response

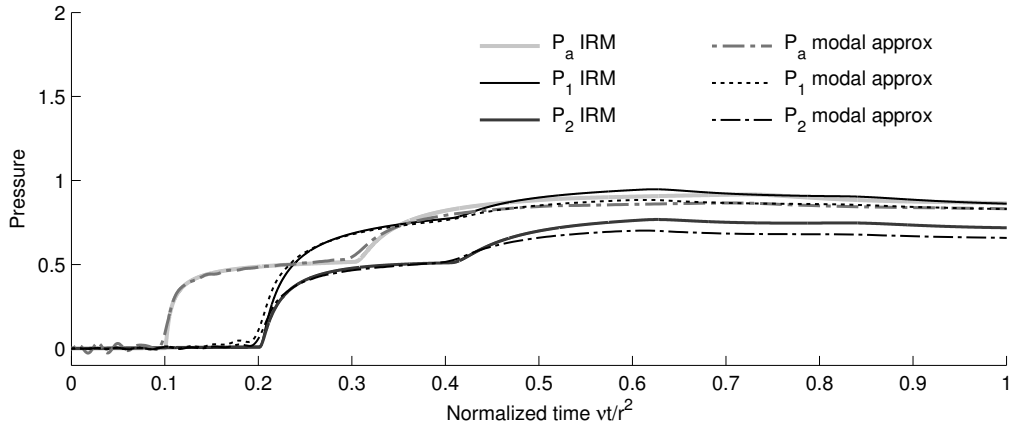

(c) Step response comparison between the IRM and modal approximations

Figure 3: Time domain response comparison of case 1

4.1.2 Case 2

In this case, different geometries of the lines are used and both terminations are blocked; the respective boundary conditions are given in equations 30 and 31.

$$\text{at } x = L_1 \qquad Q_1(L_1, \omega) = 0 \tag{30}$$

$$\text{at } x = L_2 \qquad Q_2(L_2, \omega) = 0 \tag{31}$$

As seen in figure 4, when blocked terminations are used, the modal approximations are inadequate to provide an accurate response of the system. Spurious oscillations are again present at the initial moments of time for the reason explained previously. In addition, a higher dissipation of the transient response is observed in the modal approximations together with a phase difference.

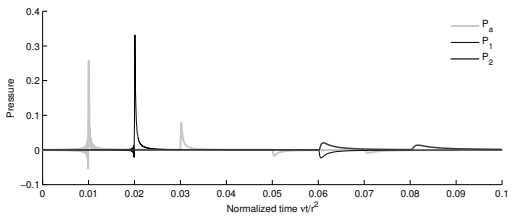

(a) Impulse response

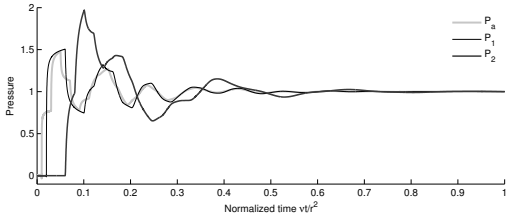

(b) Step response

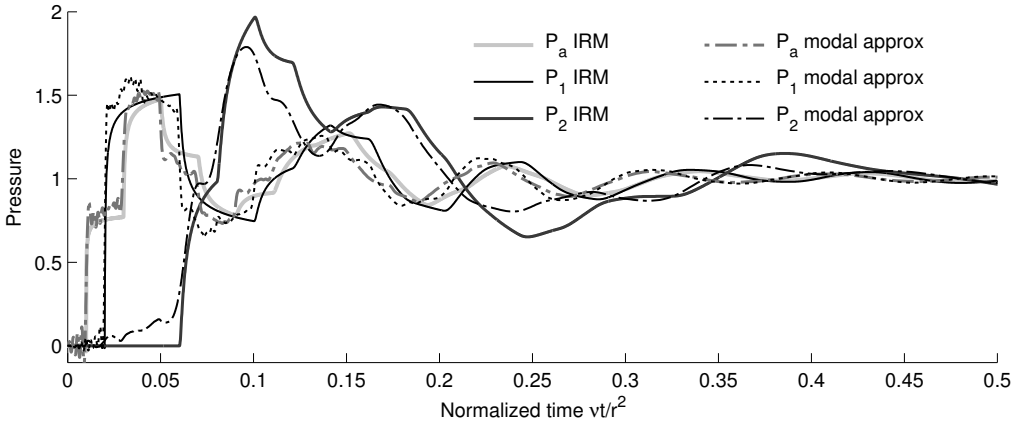

(c) Step response comparison between the IRM and modal approximations

Figure 4: Time domain response comparison of case 2

The results provided by the IRM method also show sharp variations in the pressure response due to reflected wave fronts, however this effect is not captured correctly by the modal method.

4.1.3 Case 3

In the final case 3, different geometries are present with both dynamic and static terminations, such boundaries are given through equations 32 and 33.

$$\text{at } x = L_1 \qquad P_1(L_1, \omega) - \left(\frac{1}{C_1 j\omega} + R_1\right) Q_1(L_1, \omega) = 0 \tag{32}$$

$$\text{at } x = L_2 \qquad P_2(L_2, \omega) - R_2\, Q_2(L_2, \omega) = 0 \tag{33}$$

In figure 5 the results show a relatively smooth response for both methods. As can be seen, the pressure response P_a at the hydraulic branch using modal approximations, presents large oscillations specially after the first wave front surpasses the branch junction. The oscillations might be reduced by increasing the number of modes for this particular line. Hence, it is evident that even for a relatively simple network the modal method has not direct control in the required number of modes for each line.

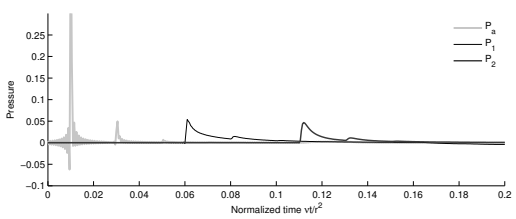

(a) Impulse response

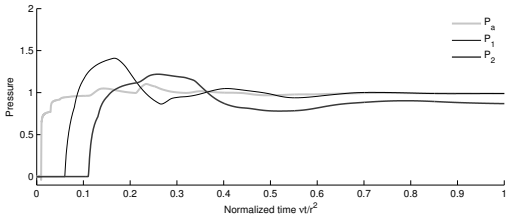

(b) Step response

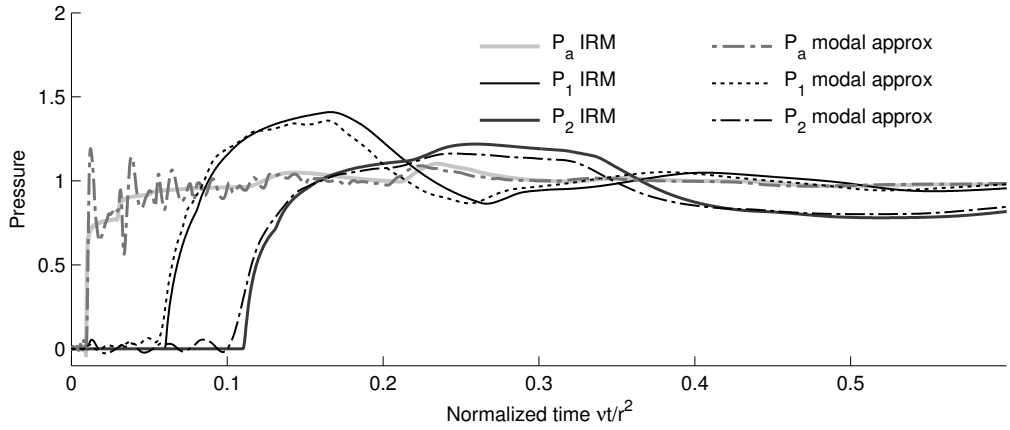

(c) Step response comparison between the IRM and modal approximations

Figure 5: Time domain response comparison of case 3

From the results presented in the previous cases, it is clear that sharp wave fronts and reflections cannot be approximated with a few number of modes. For larger networks with multiple number of lines, the inclusion of a large number of modes per line can be both computationally demanding and inexact. On the contrary, the adopted IRM method is based on an exact solution in the frequency domain, making this approach more accurate and reliable for the solution of larger networks, overcoming the disadvantages of several other approaches.

5 Conclusions

An application of a semi-analytical impulse response method to hydraulic networks was presented for transient laminar flow using a two-dimensional viscous compressible model. By solving analytically the complete network in the frequency domain, a unique impulse response of pressure and/or volumetric flow is obtained in the time-domain through the inverse FFT. A discrete numerical convolution with respect to time is then applied separately to obtain the response of the complete network to a chosen arbitrary input. Although the application of the method was shown for a simple hydraulic network, it can be easily extended to networks with large numbers of lines with various interface and boundary conditions.

Since the IRM does not require any spatial discretization, it is expected that the computational cost has a great advantage, specially for applications in large networks, when compared to existing grid-space methods. The method is only limited by the numerical considerations to solve a system of coupled linear algebraic equations and the fast Fourier transform. This means that for large networks, the increase in computational cost is only determined by the order of the global system matrix, which is linearly dependent to the number of lines forming the system.

In addition, the presented results show that the adopted IRM method provides a more accurate description of the transient behaviour than the modal approximation of individual lines used for network modelling. For a large network, the modal method might provide inaccurate results, as the required number of modes for each line is not *a priori* known.

References

[1] D'Souza, A.F., and Oldenburger, R., 1964, "Dynamic Response of Fluid Lines," J. Basic Eng., **86**, pp. 589–598.

[2] Goodson, R.E., and Leonard, R.G., 1972, "A Survey of Modeling Techniques for Fluid Line Transients," J. Basic Eng., **94**, pp. 47482.

[3] Stecki, J., and Davis, D., 1986, "Fluid Transmission Lines-Distributed Parameter Models, Part 1: A Review of the State of the Art," Proc. Inst. Mech. Eng., Part A, **200**, pp. 215228.

[4] Wylie, E., Streeter, V., and Suo, L., 1993, *Fluid Transients in Systems*, Prentice-Hall.

[5] Zielke, W., 1968, "Frequency-Dependent Friction in Transient Pipe Flow," J. Basic Eng., **90**, pp. 109115.

[6] Trikha, A.K., 1975, "An Efficient Method for Simulating Frequency- Dependent Friction in Transient Liquid Flow," ASME Trans. J. Fluids Eng., **97**, pp. 97105.

[7] Karney, B. W., and McInnis, D., 1992, "Efficient calculation of transient flow in simple pipe networks," J. Hyd. Eng., **118**(7), pp. 1014–1030.

[8] Wichowski, R., 2006, "Hydraulic transients analysis in pipe networks by the method of characteristics (MOC)," Archives of Hydro-Engineering and Environmental Mechanics, **53**(3), pp. 267–291.

[9] Pezzinga, G., 1999, "Quasi-2D model for unsteady flow in pipe networks," J. Hyd. Eng., **125**(7), pp. 676–685.

[10] Wood, D.J., Lingireddy, S., Boulos, P.F., Karney, B.W., McPherson, D.L., 2005, "Numerical methods for modeling transient flow in distribution systems," Journal American Water Works Association,**97**(7), pp. 104–115.

[11] Hsue, C.Y., and Hullender, D.A., 1983, "Modal Approximations for the Fluid Dynamics of Hydraulic and Pneumatic Transmission Lines," *Fluid Transmission Line Dynamics*, M. E. Franke and T. M. Drzewiecki, eds., ASME Special Publication, New York, pp. 51-7.

[12] Yang, W. C., and Tobler, W. E., 1991, "Dissipative Modal Approximation of Fluid Transmission Lines Using Linear Friction Model" J. Dyn. Syst. Meas. Control, **113**, pp. 152162.

[13] Van Schothorst, G., 1997, "Modeling of Long-Stroke Hydraulic Servo-Systems for Flight Simulator Motion Control and System Design," Ph.D. thesis, Delft University of Technology, The Netherlands.

[14] Ayalew, B., and Kulakowski, B. T., 2005, "Modal Approximation of Distributed Dynamics for a Hydraulic Transmission Line With Pressure Input-Flow Rate Output Causality," J. Dyn. Syst. Meas. Control, **127**, pp. 503507.

[15] Mäkinen, J., Piche R., and Ellman, A., 2000, "Fluid Transmission Line Modeling Using a Variable Method," J. Dyn. Syst. Meas. Control, **122**, pp. 153162.

[16] Watton, J., and Tadmori, M., 1988, "A Comparison of Techniques for the Analysis of Transmission Line Dynamics in Electrohydraulic Control Systems," Appl. Math. Modelling, **12**, pp. 457-66.

[17] Soumelidis, M.I., Johnston, D.N., Edge K.A., and Tilley, D.G., 2005, "A Comparative Study of Modelling Techniques for Laminar Flow Transients in Hydraulic Pipelines," JFPS conf.

[18] Margolis, D. L., and Yang, W. C., 1985, "Bond Graph Models for Fluid Networks Using Modal Approximation," J. Dyn. Syst. Meas. Control, **107**, pp. 169175.

[19] Yang, L., Hals, J., and Moan, T., 2012, "Comparative study of bond graph models of hydraulic transmission lines with transient flow dynamics," J. Dyn. Syst. Meas. Control, **134**, 031005.

[20] Suo, Lisheng, and Wylie, E.B., 1989, "Impulse response method for frequency-dependent pipeline transients," ASME Trans. J. Fluids Eng., **111**, pp. 478483.

[21] Kim, S., 2011, "Holistic unsteady-friction model for laminar transient flow in pipeline systems" J. Hyd. Eng., **137**(12), pp. 1649–1658.

Appendix

The matrix solution for a single line can also be expressed in terms of the complex Laplace variable $s = \sigma + j\omega$; where σ is a decay factor and ω represents the frequency. Hence, equation 9 is rewritten as,

$$\begin{bmatrix} P_u(s) \\ Q_u(s) \end{bmatrix} = \begin{bmatrix} \cos \frac{s\beta L}{c} & -\frac{\beta \rho c}{\pi r_0^2} \sin \frac{s\beta L}{c} \\ \frac{\pi r_0^2}{\beta \rho c} \sin \frac{s\beta L}{c} & \cos \frac{s\beta L}{c} \end{bmatrix} \begin{bmatrix} P_d(s) \\ Q_d(s) \end{bmatrix} \tag{34}$$

The previous equation can also be expressed in terms of hyperbolic functions instead of trigonometric function using the relations $\sin jx = j \sinh x$ and $\cos jx = \cosh x$. The hyperbolic notation is the most usual way to show the solution for a single line as it is expressed only in terms of the line characteristic impedance $Z_c(s)$ and the propagation operator $\Gamma(s)$ [2, 3].

$$\begin{bmatrix} P_u(s) \\ Q_u(s) \end{bmatrix} = \begin{bmatrix} \cosh \Gamma(s) & Z_c(s) \sinh \Gamma(s) \\ \frac{1}{Z_c(s)} \sinh \Gamma(s) & \cosh \Gamma(s) \end{bmatrix} \begin{bmatrix} P_d(s) \\ Q_d(s) \end{bmatrix} \tag{35}$$

This general notation allows to use the solution for the different distributed parameters models (i.e. 1D inviscid model, 1D linear friction model) depending on the expression used for the terms $Z_c(s)$ and $\Gamma(s)$. Using the normalized Laplace operator $\overline{s} = s/\omega_c$, where $\omega_c = \nu/r_0^2$ is the viscosity frequency, the line characteristic impedance $Z_c(\overline{s})$ and the propagation operator $\Gamma(\overline{s})$ are given by,

$$Z_c(\overline{s}) = Z_0 \left[1 - \frac{2}{j(\overline{s})^{\frac{1}{2}}} \frac{J_1\left(j(\overline{s})^{\frac{1}{2}}\right)}{J_0\left(j(\overline{s})^{\frac{1}{2}}\right)} \right]^{-\frac{1}{2}} \tag{36}$$

$$\Gamma(\overline{s}) = D_n \overline{s} \left(1 - \frac{2}{j(\overline{s})^{\frac{1}{2}}} \frac{J_1\left[j(\overline{s})^{\frac{1}{2}}\right]}{J_0\left[j(\overline{s})^{\frac{1}{2}}\right]} \right)^{-\frac{1}{2}} \tag{37}$$

Antonio Jarquin-Laguna, Technical University of Delft, Stevinweg 1 2628CN, Delft, the Netherlands

Apostolos Tsouvalas, Technical University of Delft, Stevinweg 1 2628CN, Delft, the Netherlands

Numerical simulation of ceramic plate penetration by cylindrical plunger

Nikita Kazarinov, Vladimir Bratov, Yuri Petrov, Lucjan Witek, Arkadiusz Bednarz

nkazarinov@gmail.com

Abstract

In this paper dynamic fracture process due to high-speed impact of steel plunger into ceramic sample is simulated. The developed numerical model is based on finite element method and a concept of incubation time criterion, which is proven to be applicable in order to predict brittle fracture under high-rate deformation. Simulations were performed for ZrO2(Y2O3) ceramic plates. To characterize fracture process quantitatively fracture surface area parameter is introduced and controlled. This parameter gives the area of new surface created during dynamic fracture of a sample and is essentially connected to energetic peculiarities of fracture process. Multiple simulations with various parameters made it possible to explore dependencies of fracture area on plunger velocity and material properties. Energy required to create unit of fracture area at fracture initiation (dynamic analogue of Griffith surface energy) was evaluated and was found to be an order of magnitude higher as comparing to its static value.

1 Introduction

The investigation of fracture properties of ceramics is of big interest due to application of these materials in protection systems. Multi-layered ceramic composites are used in bulletproof vests and demining devices due to their exceptional properties (good impact energy absorption, low weight). In order to optimize construction and design of protection systems elaborate numerical schemes for simulation of impact into ceramic targets should be developed. Such numerical models should take into account peculiar properties of dynamic fracture [1]. Despite considerable advances in theoretical studies of impact problems, generally applicable fracture criteria for ceramic materials have not been developed yet [2]. In the presented paper the numerical scheme involves incubation time fracture criterion which is proven to be an effective tool for fracture process simulation for a wide range of brittle and quasi-brittle materials subjected to dynamic loading [3, 4]. The developed scheme is based on finite element method and is used to simulate impact of steel cylindrical plunger into round ceramic plate. Due to obvious axial symmetry of the problem two-dimensional formulation is used. Both bodies (target and plunger) are supposed to show

purely elastic behavior up to the moment of fracture. Temperature effects are neglected in the presented research. Such simplifications of the model made it possible to concentrate on fundamental features of dynamic fracture process вЂ“ evolution of fracture surface in the target, fragmentation and surface energy (analogous to GriffithвЂ™s surface energy) calculation.

2 Problem formulation

Plunger and target are supposed to be linear elastic bodies and their stress-strain state is defined by Lame equations and Hook's law:

$$\rho \frac{\partial^2 U_i}{\partial t^2} = (\lambda + \mu) \nabla_i \left(\nabla \bullet \bar{U} \right) + \mu \Delta U_i, \tag{1}$$

$$\sigma_{i,j} = \delta_{i,j} \lambda \nabla \bullet \bar{U} + \mu \left(\frac{\partial U_i}{\partial x_j} + \frac{\partial U_j}{\partial x_i} \right). \tag{2}$$

The ceramic plate is supposed to be fixed on its outer radius. The plunger initial velocity V is in the direction normal to the plate surface.
Material properties for the target are typical for ZrO2(Y2O3) ceramics [5, 6]. The plunger is supposed to have properties of steel. Tables 1 and 2 give the material properties utilized for the simulation.

Density, ρ, $\frac{kg}{m^3}$	6000
Young's modulus, E, MPa	200
Poisson's ratio, ν,	0.25
Critical stress intensity factor, $K_{IC}, MPa\sqrt{m}$	13.3
Ultimate tensile stress, σ_c, MPa	750

Table 6: Target material properties

Density, ρ, $\frac{kg}{m^3}$	7860
Young's modulus, E, MPa	200
Poisson's ratio, ν,	0.25

Table 7: Plunger material properties

3 Fracture criterion and simulation technique

To perform correct simulation of fracture in ceramics due to impact of a plunger one should choose an adequate fracture criterion which will be able to predict fracture in transient loading conditions. While classical fracture criteria (like critical stress criteria or criteria based on dynamic fracture toughness concept) tend to be inapplicable for dynamic loading cases [7], incubation time fracture criterion may be regarded as a universal tool for dynamic fracture prediction [8, 9]. It is supposed that a similar approach can be used to predict

fracture initiation, evolution and arrest in ceramic materials [10] for the studied class of problems. The criterion for fracture event at point x, at time t, is formulated in the following way [11]:

$$\frac{1}{\tau}\int_{t-\tau}^{t}\frac{1}{d}\int_{x-d}^{x}\sigma(x',t')dx'dt' \geq \sigma_c, \tag{3}$$

where τ is the microstructural time of a fracture process (or fracture incubation time) - a parameter characterizing the response of the material to applied dynamical loads (i.e. τ is constant for a given material and does not depend on problem geometry, the way a load is applied, the shape of a load pulse or its amplitude). d is the characteristic size of a fracture process zone and is constant for the given material and chosen scale. d is calculated in the following way $d = \frac{2}{\pi}\frac{K_{IC}^2}{\sigma_c^2}$ [1]. $\sigma(x,t)$ is stress at a point x, changing with time, and σ_c is its critical value (ultimate stress or critical tensile stress found in quasi-static experiments).
Fracture criterion (3) is integrated into numerical scheme which is based on finite element method. ANSYS software package is used as a solver and fracture criterion is implemented via ANSYS user programmable feature (UPF) in FORTRAN. In addition to this external program in C++ is used to control and optimize solution progress and manage output data. Element size in the mesh is chosen to be equal d and thus minimal length of a microcrack in the sample will be also equal d which is in agreement with approach based on (3). Time step of the solution is chosen to be smaller than time needed for the fastest wave to pass through single element of the mesh.
In the constructed mesh each element has its own set of nodes - neighbor elements do not have common nodes, however nodes with equal coordinates have coupled degrees of freedom. This means that while condition (3) is false they behave as a single node, and as soon as (3) is true the nodes are separated and new surface appears.

4 Results

Experiments for incubation time evaluation in ceramics have not been performed yet and value of τ for $ZrO_2(Y_2O_3)$ ceramic is unknown. However this makes it possible to investigate influence of incubation time alternation on fracture process features. Reasonable range for possible incubation time variation was chosen keeping in mind values typical for other brittle materials [9].

4.1 Fracture surface evolution

At each step of the solution fracture surface area is calculated in the external program. While fracture surface area is calculated axial symmetry of the problem is considered: length of each microcrack is multiplied by the distance to symmetry axis and then added to the total fracture surface area. When fracture surface area stops to increase the solution is stopped. Typical graph of fracture surface area - time dependence is presented in figure 1.
It should be noticed here, that parts of the ceramic target separated in course of the fracture process do not interact with each other, which is, of course, a significant simplification of the model. This simplification can have a kind of physical reasoning, connected to removal of energy from the system (as separated parts are no longer interacting with the fracturing media), that in real experiment is consumed by fracture, including heating, surface energy, acoustic emissions, material dumping, etc. Possibly, interaction of separated particles with

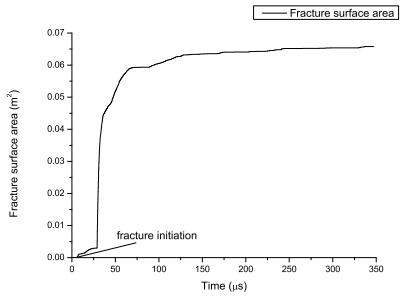

Figure 1: Fracture surface area as a function of time.

other particles, plunger and the resting bulk of ceramic material should not be neglected, but this is the topic for a future study.
As plunger initial velocity is altered the amount of energy spent for fracture changes. Thus the induced damage also changes. Figure 2 depicts dependence of final fracture surface area on plunger initial velocity. These calculations were performed for 1 μs incubation time value. Variation of incubation time value provided dependence of final fracture surface area on τ (see figure 3). As seen from the graph higher incubation time values correspond to bigger final fracture surface area. This may be referred to the fact that greater incubation time values induce fracture closer to the sample edges. The data was obtained for $100 m/s$ velocity of the plunger. Variation of the incubation time used in fracture criterion (3) in fact, means the variation of the material as the incubation time is a material property responsible for material response to dynamic loading.

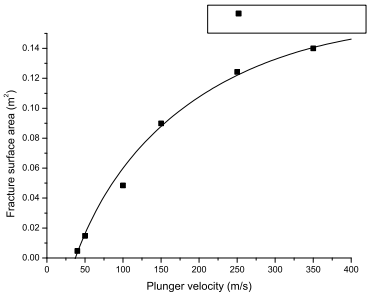

Figure 2: Fracture surface area - plunger initial velocity dependence.

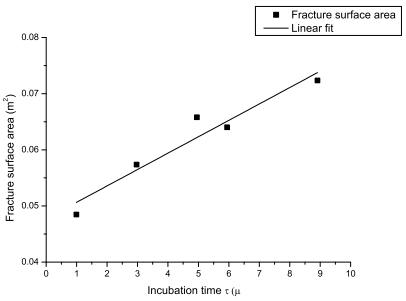

Figure 3: . Final fracture surface area as a function of the fracture incubation time.

4.2 Fragmentation

In this study the mesh of the target is interpreted as a graph with elements being nodes of this graph. If two elements are separated by a microcrack two nodes of the graph have no edge between them. Such approach allows application of well developed algorithms from graph theory to investigate fragments of the target (connected components from the graph theory point of view). Variation of the incubation time value provided an opportunity to investigate dependence of number of separate fragments appearing as a result of fracture on incubation time. This dependence is presented in figure 4. As incubation time increases number of fragments drops. In addition to this distribution of sizes of fragments was studied (figure 5). One should note here that several points were eliminated from the graph to highlight zone of interest (middle-sized fragments).

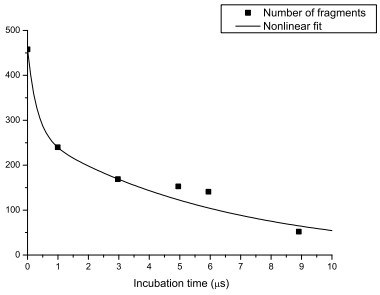

Figure 4: Number of fragments in the end of fracture as function of incubation time.

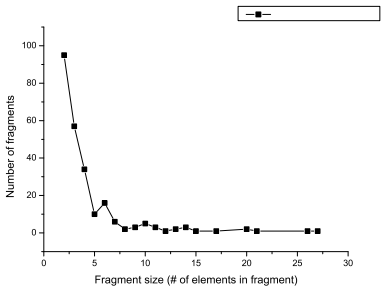

Figure 5: Number of fragments of each size for the plunger velocity 250 m/s and 1 μs incubation time value.

4.3 Surface energy. Dynamic analogue of Griffith's constant

The classical approach to fracture mechanics going back to Griffith [12] is based on the statement that a crack propagates if this process leads to a decrease in the total energy Π of the system. For a plate of unit thickness, the crack-growth conditions can be written as

$$-\frac{\partial \Pi}{\partial L} = 2\gamma. \tag{4}$$

Griffith initially interpreted the quantity 2γ as the surface energy, because it represented the specific work (per unit area) expended to form a new surface. Irwin and Orowan showed that this quantity should be interpreted as the total work (including the plastic one) in the fracture zone. This work can be taken as the resistance to a certain dissipative process proceeding in a small region near the crack tip. The study of this characteristic includes the determination of its physical origin (different for different classes of materials) and its measurement.
For the case of linearly elastic body the Griffith's constant is equal to

$$\gamma = \frac{K_{Ic}^2}{2E}, \tag{5}$$

where E is Young's modulus and K_{Ic} is critical stress intensity factor for mode I loading. Thus, γ can be indirectly determined in this case from the standard tests. However it was shown [13] that in case of dynamic loading surface energy appears to be much higher than values obtained for static cases.
In the present study the energy spent for fracture Π is calculated as difference between initial (E) and residual (E_r) kinetic energies of the plunger. These energies are calculated using formulas $E = mV^2/2$ and $E_r = mV_r^2/2$ where m is the plunger mass and V and V_r are initial and residual velocities of the plunger. To calculate dynamic analogue of Griffith's energy - γ_d - one should apply the following formula:

$$\gamma_d = \left.\frac{d\Pi}{dS}\right|_{S=0}, \tag{6}$$

where S is the area of fracture surface created in a result of interaction. Calculation of γ_d using (6) gives $\gamma_d = 1171\frac{J}{m^2}$ for the studied case. This value is considerably higher (approximately an order of magnitude) than fracture surface energy evaluated in quasi-static loading conditions [14].

5 Conclusions

The presented research is the first attempt to analyze and simulate dynamic fracture of ceramics due to impact of steel plunger applying incubation time approach. Dependencies of final fracture surface area and fragmentation properties on incubation time (and thus material) were investigated. Moreover fracture surface area for dynamic fracture was calculated appearing to be an order of magnitude higher than the value for static loading conditions.

6 Acknowledgments

The authors acknowledge Saint Petersburg State University for a research grant 6.39.319.2014. The research and publication preparation was also supported by RFBR research grants 14-01-00814 and 13-01-00598, the President Grant for Government Support of Young Russian Scientists MK–7596.2015.1 and the academic programs of the Russian Academy of Science and FP7 EU MARIE CURIE Project TAMER No. 610547

7 References

References

[1] Petrov Y V 1991 On "Quantum" Nature of Dynamic Fracture of Brittle Solids. *Dokl. Akad. Nauk USSR* **321**,66-8

[2] Ravi-Chandar K 2004 *Dynamic Fracture* (Elsevier) 264

[3] Bratov V 2011 Incubation time fracture criterion for FEM simulations *Acta Mechanica Sinica* **27(4)** 541-49

[4] Bratov V, Petrov Y 2007 Application of incubation time approach to simulate dynamic crack propagation *AInternaitional Journal of Fracture* **146** 53-60

[5] Masaki T 1986 Mechanical Properties of Toughened ZrO2-Y2O3 Ceramics *Journal of American Mechanical Society* **69(8)** 638-40

[6] Winnbust A J A, Keiser K, Burggraaf A J 1983 Mechanical Properties and Fracture Behaviour of ZrO2-Y2O3 Ceramics *Journal of Materials Science* **18** 1958-66

[7] Bratov V A, Morozov N F, Petrov Yu V 2009 *Dynamic Strength of Continuum* (St. Petersburg University Press, Saint Petersburg) 224

[8] Kazarinov N, Bratov V, Petrov Y 2014 Simulation of Dynamic Crack Propagation under Quasi-Static Loading *Doklady Physics* **59(2)** 99-102

[9] Smirnov V, Petrov Yu V, Bratov V 2014 Energy of a solid sphere under nonstationary oscillations *Science China Physics, Mechanics and Astronomy* **55(1)** 78-85

[10] Petrov Y V, Taraban V V 1999 On Process Zone Size Criteria of Fracture In Brittle Solids *Physico-Chemical Mechanics of Materials* **1** 77-82

[11] Morozov N, Petrov Y 2000 *Dynamics of fracture* (Springer-Verlag, Berlin.)

[12] Griffith A 1921 Phenomena of Rupture and Flow in Solids *Philosophical transactions of the Royal Society of London* **A221** 163-98

[13] Bratov V A, Gruzdkov A A, Krivosheev S I, Petrov Yu V 2004 Energy balance in the crack growth initiation under pulsed-load conditions *Doklady Physics* **49(5)** 338-41

[14] Lawn B 1993 *Fracture of Brittle Solids ϭΓ′Y Second Edition* (Press Syndicate of the University of Cambridge, Melbourne) 378

Nikita Kazarinov, Saint Petersburg State University, Universitetskaya Emb. 7-9, 199034, Russia
Vladimir Bratov, Saint Petersburg State University, Universitetskaya Emb. 7-9, 199034, Russia
Yuri Petrov, Saint Petersburg State University, Universitetskaya Emb. 7-9, 199034, Russia
Lucjan Witek, Rzeszow University of Technology, al. PowstaEЋcΓγw Warszawy 12, 35-959 Rzeszow, Poland
Arkadiusz Bednarz, Rzeszow University of Technology, al. PowstaEЋcΓγw Warszawy 12, 35-959 Rzeszow, Poland

A simple numerical model of a geometrically nonlinear Timoshenko beam

Chris Keijdener, Andrei V. Metrikine
c.keijdener@tudelft.nl

Abstract

In the original problem for which this model was developed, one-dimensional flexible objects interact through a non-linear contact model. Due to the non-linear nature of the contact model, a numerical time-domain approach was adopted.

One of the goals was to see if the coupling between axial and transverse deformations had an influence on the results and so this capacity had to be included. In addition, large deformations should be allowed as well as non-prismatic, non-symmetrical cross-sections and inhomogeneous constitutive properties. To accommodate these requirements the linear model which was being used, was upgrade to meet these requirements.

The model created with the procedure explain in this paper consist of discrete masses connected by a set of nonlinear springs. The expressions for the masses and springs are obtained by discretization of the continuum representation of a Timoshenko beam. The required number of springs is proportional to the desired order of geometrical nonlinearity the model should accurately capture.

This paper explains the procedure to create a model which can accurately capture geometrically nonlinear effects up to a desired order..

1 Introduction

While studying the interaction between level ice and a downward sloping structures, the question arose whether axial deformation and buckling had an effect on the breaking length of the ice. To investigate this, the linear discrete element model of a Timoshenko beam was improved so that it could accurately capture geometrically nonlinear (GN) effects as well as non-prismatic, non-symmetrical cross-sections and inhomogeneous constitutive properties. The linear model used falls in the category of discrete models whose origin is generally credited to [4] whom introduced the framework method to solve the plane stress problem. The earliest derivation found of a discrete system which accurately captures a Timoshenko beam was done by [3]. These models have been applied to study cracked beams [1] and moving loads [9].
In all works listed above, the authors assumed an element layout (the number of springs and their geometry) which involves some level of judgment and trial and error to obtain an element layout which can be matched to the continuum. The matching results in

expressions for the parameters of the discrete model, such as the springsвЂ˜Є stiffness and their geometry, in terms of quantities of the continuum such as the area, YoungвЂ˜Єs modules or density. In this paper we take the more traditional approach by directly discretizing a continuum. A consequence of directly discretizing the continuum, is that the element layout is obtained as a result of the derivation rather than a starting point like it was in previous works. The linear models and their element geometries can be obtained by linearizing the GN models derived in this paper.
In the first part of this paper the procedure is derived for obtaining discrete models which can accurately capture GN effects up to a given order. Next, using this procedure, the simplest possible model is created and is used to validate the procedure.

2 The discrete element

In this paper we start with the kinematic assumptions as defined in [6, 7]:

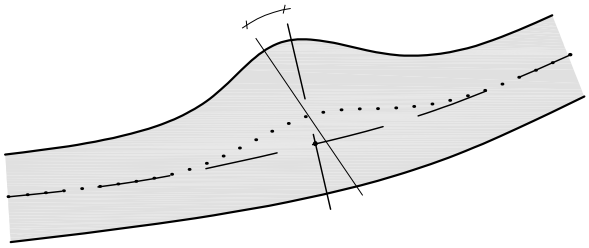

Figure 1: A non-prismatic, non-symmetric beam. The dashed line is the chosen reference axis while the dotted line is the neutral axis of the cross-section. The distance r_1 is the offset between the two. For beams with a cross-section which is symmetric with respect to its neutral axis, r_1 will be zero for all elements. However, for non-symmetric beams r_1 will be none zero and vary along the length. The coordinate s runs along the chosen reference axis and the coordinate h runs tangential to it.

To ensure that the deflections of the beam reside in the x,z-plane, the cross-section and loading are assumed to be symmetric with respect to this plane. From this continuous beam a piece is cut with a length l. The potential energy of this piece is:

$$\begin{aligned} \mathbb{V}_{piece,\varepsilon} &= \frac{1}{2}\int_{s_n-l/2}^{s_n+l/2}\int_{A(s)} \sigma\left(s,h\right)\varepsilon\left(s,h\right)\,dA\,dx \\ \mathbb{V}_{piece,\gamma} &= \frac{1}{2}\int_{s_n-l/2}^{s_n+l/2}\int_{A(s)} \tau\left(s,h\right)\gamma\left(s,h\right)\,dA\,dx \end{aligned} \tag{1}$$

where s_n is the midpoint of the piece, σ is the normal stress, ϵ is the normal strain, τ is the shear stress and γ is the shear strain and all the constitutive properties are allowed to be a function of s. This continues piece is now discretized using finite differences. In this paper a two-point discretization scheme is used for simplicity, resulting in a linear element as can be seen in the figure below.

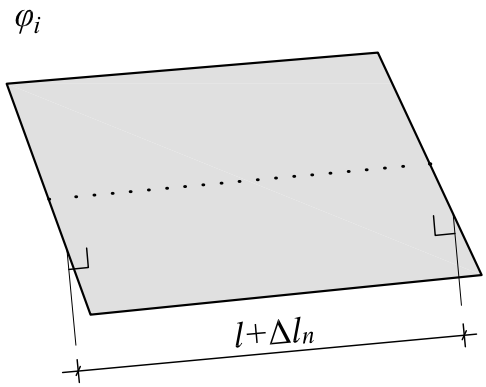

Figure 2: The element n which is part of a Timoshenko beam and connects nodes i and j.

Due to the presence of two nodes per element, the following expressions relate the continuum and the discrete element:

$$x_j - x_i = l\frac{\partial x(s)}{\partial s}\bigg|_{s=s_n} + O\left(l\right), \ \frac{x_j + x_i}{2} = x\left(s\right)|_{s=s_n} + O\left(l^2\right) \tag{2}$$

In these equations the x-displacement was used but the same relations apply to any property which is a function of s, such as $z(s,h)$ or $\gamma(s,h)$. These relations also show that for all s-dependent constitutive properties, the value half-way the element should be used, again resulting in a second order error in their discretization. This will be denoted with a subscript n, so for instance E_n stand for $E(s)|_{s=s_n}$. This discretization also requires the inhomogeneous or non-prismatic nature of the beam to be smooth so that higher order derivatives with respect to s are small.
After discretization the integral over s becomes trivial as all s-dependencies have been removed and so the expression for the potential energy (Eq. (1)) of the discrete element becomes:

$$\begin{aligned} \mathbb{V}_{n,\varepsilon} &= \frac{l}{2}\int_{A_n} \sigma_n\left(h\right)\varepsilon_n\left(h\right)\, dA \\ \mathbb{V}_{n,\gamma} &= \frac{l}{2}\int_{A_n} \tau_n\left(h\right)\gamma_n\left(h\right)\, dA \end{aligned} \tag{3}$$

where σ_n, ϵ_n, τ_n and γ_n are the stresses and strains of the element. These will be defined in the next section which covers to potential energy of the element. The kinetic energy is discussed afterwards.

2.1 Potential energy

The following geometrical relations apply the element shown in Figure 2 (note that all coordinates are global):

$$\begin{aligned} \hat{x}_i\left(h\right) &= x_i + \left(h + r_{1,n}\right)\cos\left(\varphi_i + \pi/2\right) = x_i - \left(h + r_{1,n}\right)\sin\left(\varphi_i\right) \\ \hat{z}_i\left(h\right) &= z_i + \left(h + r_{1,n}\right)\sin\left(\varphi_i + \pi/2\right) = z_i + \left(h + r_{1,n}\right)\cos\left(\varphi_i\right) \\ \hat{x}_j\left(h\right) &= x_j - \left(h + r_{1,n}\right)\sin\left(\varphi_j\right) \\ \hat{z}_j\left(h\right) &= z_j + \left(h + r_{1,n}\right)\cos\left(\varphi_j\right) \end{aligned} \tag{4}$$

Similarly to what is done in infinitesimal strain theory, [8] the normal and shear strains are defined using the relations in Eq. (4):

$$\varepsilon_n(h) = \frac{l_n(h) - l}{l} = \frac{\Delta l_n(h)}{l} = \frac{1}{l}\left(\sqrt{\Delta X_n^2(h) + \Delta Z_n^2(h)} - l\right) \tag{5}$$

$$\begin{aligned} -\gamma_n(h) &= \frac{\gamma_i(h) + \gamma_j(h)}{2} - \frac{\pi}{2} - \gamma_{0,n} \\ &= \frac{1}{2}\left(\left(\varphi_i + \frac{\pi}{2}\right) - \alpha_n(h) + \left(\varphi_j + \frac{\pi}{2}\right) - \alpha_n(h)\right) - \frac{\pi}{2} - \gamma_{0,n} \\ &= \frac{\varphi_i + \varphi_j}{2} - \alpha_n(h) - \gamma_{0,n} = \varphi_n - \alpha_n(h) - \gamma_{0,n} \\ &\rightarrow \gamma_n(h) = \alpha_n(h) - \varphi_n + \gamma_{0,n} \end{aligned} \tag{6}$$

$$\begin{aligned} \alpha_n(h) &= \arctan\left(\frac{\Delta Z_n(h)}{\Delta X_n(h)}\right) \\ \Delta X_n(h) &= \hat{x}_j(h) - \hat{x}_i(h)\,,\ \Delta Z_n(h) = \hat{z}_j(h) - \hat{z}_i(h) \end{aligned} \tag{7}$$

where l_n is the current length of the element, Δl_n is the elongation of the element, γ_n is the shear angle of the element where $-\pi/2$ subtracts the default shear angle which account for the fact that by default the cross-section is perpendicular to the beam axis and $\gamma_{0,n}$ accounts for any non-zero shear angle in the undeformed state, Δx_n and Δz_n are the distance between the two nodes in their respective direction and is the undeformed length (element size) given by $L(N+1)$ where L is the length of the beam and N is the total number of elements.
Next the following linear stress-strain relations are assumed:

$$\begin{aligned} \sigma_n &= E_n \varepsilon_n(h) = \frac{E_n}{l}\Delta l_n(h) \\ \tau_n &= G_n \gamma_n(h) \end{aligned} \tag{8}$$

Usage of nonlinear materials is also possible as long as both stresses remain uncoupled. Using these relations, the potential energy of the element becomes:

$$\begin{aligned} \mathbb{V}_{n,\varepsilon} &= \frac{l}{2}\int_{A_n} \frac{E_n}{l^2}\Delta l_n^2(h)\ dA \\ \mathbb{V}_{n,\gamma} &= \frac{l}{2}\int_{A_n} G_n \gamma_n^2(h)\ dA \end{aligned} \tag{9}$$

The next step is to solve the two cross-sectional integrals.

2.2 Solving the cross-sectional integrals

Due to the complexity of the expressions for the elongations, analytically solving the cross-sectional integrals (CSI) in Eq. (9) results in so many terms that it makes evaluation impractically slow. Because of this, we seek to find an approximate system for which the integral can be solved, whose error compared to the exact solution of the CSI is acceptable. The first step in finding this approximate system is to investigate a Taylor series expansion (TSE) of the squared strains. The TSE is done for an element which is part of a beam whose undeformed shape is a straight line and which is not subjected to any pre-stress.

The approximate system will prove to be independent of these two assumptions. The TSE of the element can be written in the following form:

$$\begin{aligned}\mathbb{V}_{n,\varepsilon} &= \frac{l}{2}\frac{E_n}{l^2}\int_{A_n} B_{n,0}h^0 + B_{n,1}h^1 + B_{n,2}h^2 + .. + B_{n,\infty}h^\infty \\ \mathbb{V}_{n,\gamma} &= \frac{l}{2}G_n\int_{A_n} C_{n,0}h^0 + C_{n,1}h^1 + C_{n,2}h^2 + .. + C_{n,\infty}h^\infty\end{aligned} \tag{10}$$

where the coefficients B_0 and C_0 contain all terms which are proportional to h^0 of their respective strain and so on. The order of h-dependency goes up to infinity because the normal strain contains a square root and the shear strain an arctangent.
Because the strains were assumed to be constant over the width of the beam, the CSI is only dependent on h. Looking at Eq. (8) however, these h-dependencies are all multiplications with a certain order of h. These simple dependencies on h allow the CSIs to be calculated in a trivial manner if two assumption are made: 1) that the elasticity of the material is uniform over the cross-section and 2) that all terms which result from the TSE have the same profile over the height as the strain they originate from. This implies that higher order strain components, for instance say those in $B_{n,5}$, have the same profile as the normal strain they originates from, which is a linear profile. Under these assumptions the integral in Eq. (10) evaluates to:

$$\begin{aligned}\mathbb{V}_{n,\varepsilon} &= \frac{l}{2}\frac{E_n}{l^2}\int_{A_n} B_{n,0}h^0 + B_{n,1}h^1 + B_{n,2}h^2 + .. + B_{n,\infty}h^\infty \\ \mathbb{V}_{n,\gamma} &= \frac{l}{2}G_n\int_{A_n} C_{n,0}h^0 + C_{n,1}h^1 + C_{n,2}h^2 + .. + C_{n,\infty}h^\infty\end{aligned} \tag{11}$$

Both equations contain infinitely many terms. However, if this expansion is truncated at a certain order ϖ, which then defines the *maximum order of geometrical nonlinearity* of the discrete system, the expansion only contains a finite number of orders:

$$\begin{aligned}\mathbb{V}^{(\varpi)}_{n,\varepsilon} &= \frac{l}{2}\frac{E_n}{l^2}\left(A_nB_{n,0} + A_nr_{1,n}B_{n,1} + I_nB_{n,2} + .. + A_nr_{\varpi,n}B_{n,\varpi}\right) \\ \mathbb{V}^{(\varpi)}_{n,\gamma} &= \frac{l}{2}G_n\left(\kappa_{0,n}A_nC_{n,0} + \kappa_{1,n}A_nr_{1,n}C_{n,1} + \kappa_{2,n}I_nC_{n,2} + .. + \kappa_{\varpi,n}A_nC_{n,\varpi}\right)\end{aligned} \tag{12}$$

The order of GN of a term in the expansion is defined as the total number of s-dependent variables in that term. The relation between the total number of unique solutions to the CSIs and ϖ is shown in the table below:

	$\varpi=1$	$\varpi=2$	$\varpi=3$	$\varpi=4$	$\varpi=5$	$\varpi=6$
ϵ_n	3	3	3	4	5	6
γ_n	1	2	3	4	5	6

Table 8: The total number of unique solutions to the CSI for different orders of GN (ϖ) for both strains

To give an example, the 3 unique solutions to the CSIs in the potential energy of ϵ_n truncated at $\varpi = 1$ are A_n, $A_nr_{1,n}$ and I_n. Apart from an anomaly in the lower orders of the normal strain, there is a linear relation between ϖ and the highest order of ϖ-dependency in the CSIs. This relation forms the basis of the approximation of the CSIs. If the discrete system is only required to be accurate up to a certain order ϖ, the number

of solutions to the CSIs is finite. To ensure that the approximate system can accurately capture all GN effects up to order ϖ, a solution is sought in the following form which is based on Eq. (9):

$$\begin{aligned}\hat{\mathbb{V}}_{n,\varepsilon}^{(\varpi)} &= \frac{l}{2}\int_{A_n}\frac{E_n}{l^2}\sum_{q=1}^{Q_\varepsilon} k_{n,q}\Delta l_n^2\left(h=h_{n,q}\right)\,dA \\ \hat{\mathbb{V}}_{n,\gamma}^{(\varpi)} &= \frac{l}{2}\int_{A_n} G_n\sum_{q=1}^{Q_\gamma} g_{n,q}\gamma_n^2\left(h=\eta_{n,q}\right)\,dA\end{aligned} \tag{13}$$

where $k_{n,q}$ and $g_{n,q}$ are unknown dimensionless scaling factors, $h_{n,q}$ and $\eta_{n,q}$ are unknown offsets of the springs with respect to the chosen reference axis and Q_ϵ and Q_γ are the total number of springs. The evaluation of the strains at a specific offset ($h_{n,q}$ and $\eta_{n,q}$) effectively turns the continuously distributed elasticity into a discrete spring with a certain offset, visualized below.

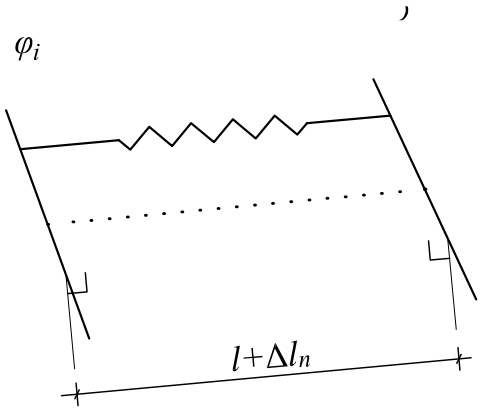

Figure 3: The continuously distributed normal strain has been replaced by a spring with a certain offset $h_{n,q}$. The same applies to the shear strain.

This means that the integral over the cross-section has been replaced by a summation of springs, each with an unknown scale and offset. To understand the implications of this approximation, the truncated TSE of the approximate form (Eq. (11)) and the exact form (Eq. (13)) are compared (the exact same can be for the shear energy):

$$\begin{aligned}\mathbb{V}_{n,\varepsilon}^{(\varpi)} &= \frac{l}{2}\frac{E_nA_n}{l^2}\left(B_{n,0}+r_1B_{n,1}+..+r_\varpi B_{n,\varpi}\right) \\ \hat{\mathbb{V}}_{n,\varepsilon}^{(\varpi)} &= \frac{l}{2}\frac{E_nA_n}{l^2}\sum_{q=1}^{Q_\varepsilon} k_{n,q}\left(\hat{B}_{n,0}h_{n,q}^0+\hat{B}_{n,1}h_{n,q}^1+..+\hat{B}_{n,\varpi}h_{n,q}^\varpi\right)\end{aligned} \tag{14}$$

At this point it is important to understand how the approximation differs from the exact solution, but, more importantly, how they are similar. Because the вГЁstrain equationвГ№ for each spring is based on those of the continuously distributed strain, their TSE will be exactly the same apart from their dependence on h. This means that for any given state of the elements the strain components which are contained in their respective TSE will be exactly the same. This means that $B_0=\hat{B}_0$ and $C_0=\hat{C}_0$ and the same holds for all other orders. The different dependence on h results in a different type of solution to the CSIs: for the continuum the integral actually integrates over different orders of h while

the approximate system has become independent of h due to the substitution and so the integral evaluates to A_n for all terms. However, as the approximate system still has two unknowns per spring, the two equations in Eq. (14) can be matched, so that the CSI of both systems ends up being the same. This results in the following set of equations:

$$\begin{cases} \sum_{q=1}^{Q_\varepsilon} k_{n,q} h_{n,q}^{0} = 1 \\ \sum_{q=1}^{Q_\varepsilon} k_{n,q} h_{n,q}^{1} = r_{1,n} \\ \dots \\ \sum_{q=1}^{Q_\varepsilon} k_{n,q} h_{n,q}^{\varpi} = r_{\varpi,n} \end{cases}, \quad \begin{cases} \sum_{q=1}^{Q_\gamma} g_{n,q} \eta_{n,q}^{0} = \kappa_{0,n} \\ \sum_{q=1}^{Q_\gamma} g_{n,q} \eta_{n,q}^{1} = \kappa_{1,n} \\ \dots \\ \sum_{q=1}^{Q_\gamma} g_{n,q} \eta_{n,q}^{\varpi} = \kappa_{\varpi,n} \end{cases} \tag{15}$$

where $r_{0..\varpi,n} = 1/A_n \int_{A_n} h^{0..\varpi}\, dA$, $\kappa_{0,n}$ is the Timoshenko shear correct factor and $\kappa_{1..\varpi,n}$ are its higher order equivalents. The right hand side of both sets are different as the continuous normal and shear strains have a different distribution along the height. The total number of equations to be satisfied is equal to the number of unique solutions to the CSIs, which was shown in Table 1. Each spring has a total of two unknowns: its offset and scaling factor. Since the same number of unknown is needed as their are equations, the required number of springs (Q_ϵ and Q_γ) becomes:

$$Q_\varepsilon = \max\left(\lceil \varpi/2 \rceil, 2\right), \; Q_\gamma = \lceil \varpi/2 \rceil \tag{16}$$

where the brackets indicate the ceiling function and the minimum of two normal springs is due to linear bending effects being proportional to I_n.

With all the unknowns determined the discrete element can accurately capture the potential energy up to the specified order of geometrical nonlinearity ϖ. This means that the resulting discrete element is not an exact solution to the CSI and thus will have an error compared to that exact solution. This error is independent of the mesh size and manifests itself as an incorrect solution to the CSIs for orders higher than ϖ. The error can be reduced by increasing ϖ but for a given order of ϖ there will be a non-converging error. Note that higher order (in terms of h) CSIs are also multiplied with higher order (in terms of ϖ) strain components. The error in the incorrect solution to the CSI is therefore only as important as the вГЁmagnitudeвГ№ of the strain component it is multiplied with. As the influence on the solution (displacements, stresses, etc.) diminishes as the order of the strain components increases, the influence of the error to the CSI also diminishes.

The final item to consider is the state which was used to perform the TSE and whether this has any influence on the matching process. A different state does result in a different TSE of the potential energies but can always be rewritten in the form show in Eq. (10). The strain components contained in $B_{n,0..\infty}$ and $C_{n,0..\infty}$ will be different they will still be equal to $\hat{B}_{n,0..\infty}$ and $\hat{C}_{,0..\infty}$ since both are based on the same strain equations. This means that the matching process is independently of the state used for the TSE. The absolute value of the non-converging error will be slightly different for each state, as in each state the importance of higher order is slightly different. However, in general the importance of higher orders is small and so the overall magnitude of the non-converging error will be independent of the state of the system.

This ends the discretization of the potential energy. The next step is to consider the kinetic energy.

2.3 Kinetic energy

The kinetic energy requires the velocities. Based on Eq. (2) the expressions for the velocities of the element are:

$$\begin{aligned}\dot{\hat{x}}_n &= \frac{\partial\left(\hat{x}_i+\hat{x}_j\right)/2}{\partial t} = \frac{1}{2}\left(\dot{x}_i-(h+r_1)\cos\left(\varphi_i\right)\dot{\varphi}_i+\dot{x}_j-(h+r_1)\cos\left(\varphi_j\right)\dot{\varphi}_j\right)\\ \dot{\hat{z}}_n &= \frac{\partial\left(\hat{z}_i+\hat{z}_j\right)/2}{\partial t} = \frac{1}{2}\left(\dot{z}_i-(h+r_1)\sin\left(\varphi_i\right)\dot{\varphi}_i+\dot{z}_j-(h+r_1)\sin\left(\varphi_j\right)\dot{\varphi}_j\right)\end{aligned} \tag{17}$$

Using these relations the kinetic energy of an element becomes:

$$\mathbb{T}_n = \frac{l}{2}\int_A \rho\left(\dot{\hat{x}}_n^2+\dot{\hat{z}}_n^2\right)\,dA \tag{18}$$

Luckily, the expressions for the velocities are much simpler than those of the strains and so the CSI can be solved analytically under the assumption that the density is uniform over the cross-section:

$$\begin{aligned}\mathbb{T}_n = {}& \frac{J_n}{8}\left(\left(-\cos\left(\varphi_i\right)\dot{\varphi}_i-\cos\left(\varphi_j\right)\dot{\varphi}_j\right)^2+\left(-\sin\left(\varphi_i\right)\dot{\varphi}_i-\sin\left(\varphi_j\right)\dot{\varphi}_j\right)^2\right)\\ &+\frac{m_n}{4}\left(\dot{x}_i-r_{1,n}\cos\left(\varphi_i\right)\dot{\varphi}_i+\dot{x}_j-r_{1,n}\cos\left(\varphi_j\right)\dot{\varphi}_j\right)^2\\ &+\frac{m_n}{4}\left(\dot{y}_i-r_{1,n}\sin\left(\varphi_i\right)\dot{\varphi}_i+\dot{y}_j-r_{1,n}\sin\left(\varphi_j\right)\dot{\varphi}_j\right)^2\end{aligned} \tag{19}$$

where $J_n = \int_{A_n}\rho_n h^2 l\;dA = \rho_n l\left(I_n + r_{1,n}A_n\right)$ and $m_n = \int_{A_n}\rho_n l\;dA = \rho_n A_n l$. With this, both the kinetic and potential energy of the discrete element have been defined and so the Lagrangian of the system if known.
Finally, to avoid numerical issues the arctan2 function should be used when computing the shear angle γ_n. In addition, the vector containing the shear angle of all elements can contain jumps of 2π because the range of α_n is limited to the range of the arctan2 ($[-\pi,\pi]$) while γ_n does not have this limitation. These jumps should be removed from the vector.

3 Model validation

This chapter will validate the methodology derived in this paper. The first step is to create a model. The model is then validated against solutions found in the literature.

3.1 Creating a simple beam model

The only step to be done in creation of the model is to perform is matching in Eq. (15). To perform the matching, the order of GN of the model has to be set. ϖ is set to 1 as this results in the fastest model possible and its performance is already sufficiently accurate.
To further simplify the model, the anomaly visible in Table 1 is investigated to see which terms are proportional to I_n as those are the once which necessitate the second axial spring. An investigation shows that the anomaly is caused by linear bending effects, e.g $\int_A Ez^2\phi_{xx}\,dA = EI\phi_{xx}$. This strain component could be capture by the second axial spring, as previously suggested, but can also be captured by a rotational spring. As the rotational spring is faster, we opt for that solution. This results in the following set of equations, similar to Eq. (15):

$$\left\{\begin{array}{c}k_n h_n^0 = 1\\ k_n h_n^1 = r_{1,n}\end{array}\right.,\quad \left\{\begin{array}{c}g_n\eta_n^0 = \kappa_{0,n}\\ g_n\eta_n^1 = \kappa_{1,n} = \kappa_{0,n}r_{1,n}\end{array}\right.,\quad \left\{\frac{l}{2}k_{n,rot} = \frac{l}{2}\frac{E_n I_n}{l^2}\right. \tag{20}$$

where $k_{n,rot}$ is the unknown stiffness of the rotational spring. This set of equations is readily solved. The equations of motion (EOMs) can now be obtained using the Euler-Lagrange equation. The EOMs were implemented in matlab at used to compute the results in the following section.

3.2 Validation

The model is now validated against solutions found in existing literature:

- Cantilever with small point load at the end (linear behavior): quadratic convergence
- Cantilever with large point load at the end (GN behavior) (from [2]): initial converges quadratically but then converges to a non-decaying error, see below:

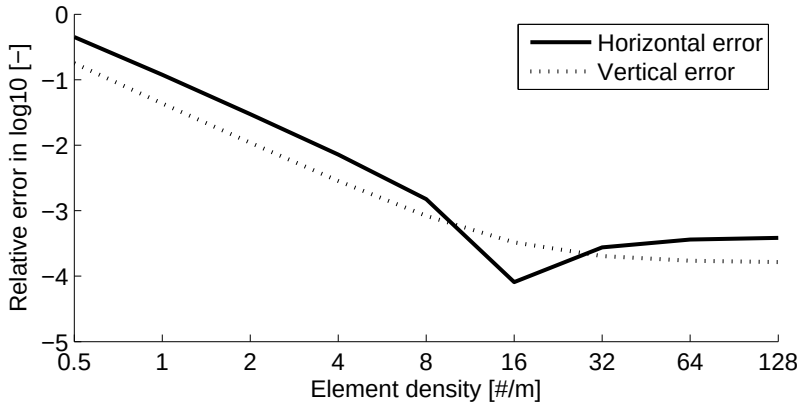

- GN cantilever with large moment causing the beam to roll up to a circle: exact (error is equal to the error of the Newton-Rapson scheme used to solve the nonlinear problem):

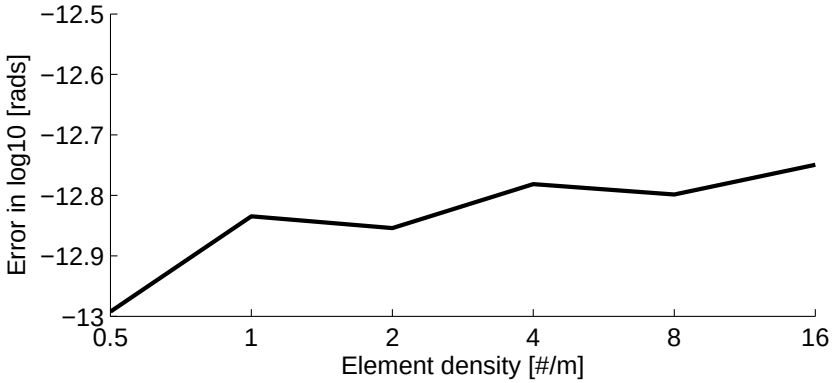

- Axial buckling: the converged predicted buckling load has an error of about 0.44 % when compared with the buckling load given by EulerвЂ˜Cs formula.
- Eigenfrequencies (from [2]): quadratic convergence
- GN cantilever with follower load (from [5]): good agreement, see below:

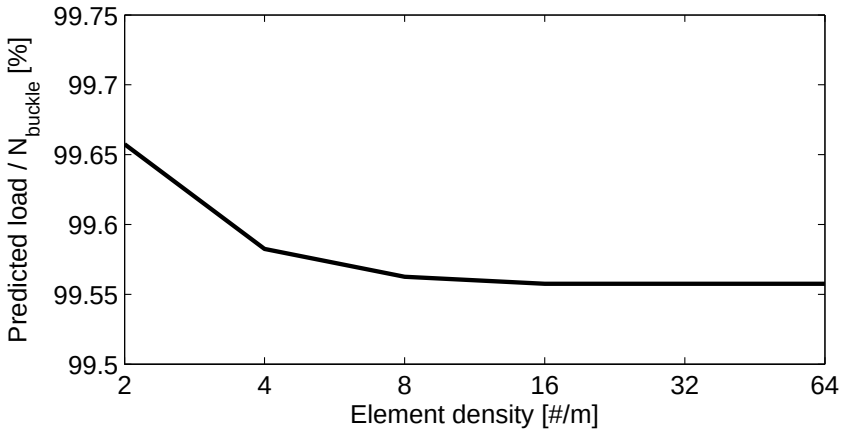

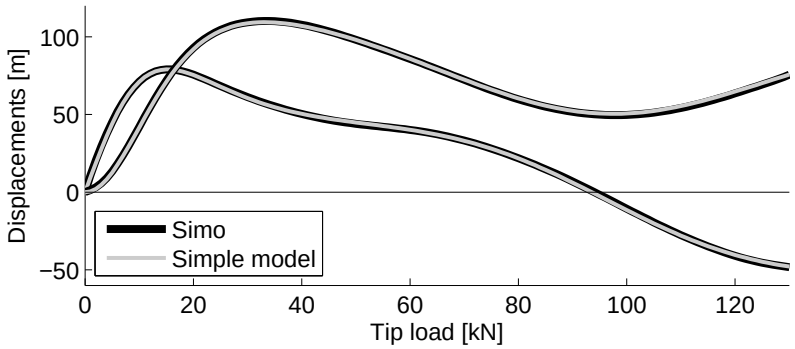

4 Conclusion

A simple way to derive a discrete model of a geometrically nonlinear Timoshenko beam has been presented. The model does not include warping effects and there are no compressive effects in transversal direction. However, for problems where these effects can be ignored, the results of the model are in good agreement with existing formulation. The relative ease at which the model can be implemented makes it ideal for educational purposes.

Acknowledgements

The authors wish to acknowledge the support from the Research Council of Norway through the Centre for Research-based Innovation SAMCoT and the support from all SAMCoT partners.

References

[1] Attar, M., Karrech, A., & Regenauer-Lieb, K. (2014). Free vibration analysis of a cracked shear deformable beam on a two-parameter elastic foundation using a lattice spring model. Journal of Sound and Vibration, 333, 2359вЃ“2377. doi:10.1016/j.jsv.2013.11.013

[2] Gerstmayr, J., Matikainen, M. K., & Mikkola, A. M. (2008). A geometrically exact beam element based on the absolute nodal coordinate formulation. Multibody System Dynamics, 20, 359вЃ“384. doi:10.1007/s11044-008-9125-3

[3] Heinsbroek, A. G. T. J., & Blauwendraad, J. (1989). Reinforced concrete beams under shock loading, linear and nonlinear response. Heron, 34(3).

[4] Hrennikoff, A. (1941). Solution of Problems of Elasticity by the Frame-Work Method. Applied Scientific Research, A8, 169вЂ“175.

[5] Simo, J. C., & Vu-Quoc, L. (1986). A three-dimensional finite-strain rod model. part II: Computational aspects. Computer Methods in Applied Mechanics and Engineering. doi:10.1016/0045-7825(86)90079-4

[6] Timoshenko, S. P. (1921). On the correction factor for shear of the differential equation for transverse vibrations of bars of uniform cross-section. Philosophical Magazine, 744.

[7] Timoshenko, S. P. (1922). On the transverse vibrations of bars of uniform cross-section. Philosophical Magazine, 125.

[8] Wikipedia. (2015). Geometric derivation of the infinitesimal strain tensor. Retrieved February 18, 2015, from http://en.wikipedia.org/wiki/Infinitesimal_strain_theory

[9] Yavari, A., Nouri, M., & Mofid, M. (2002). Discrete element analysis of dynamic response of Timoshenko beams under moving mass. Advances in Engineering Software, 33(3), 143вЂ“153. doi:10.1016/S0965-9978(02)00003-0

Chris Keijdener, Stevinweg 1, 2628 CN Delft, The Netherlands
Andrei V. Metrikine, Stevinweg 1, 2628 CN Delft, The Netherlands

High-Order Numerical Scheme for Attached Vortex Layer Intensity Computation in 2D Vortex Element Method

Kseniya S. Kuzmina, Ilia K. Marchevsky
kuz-ksen-serg@yandex.ru, iliamarchevsky@mail.ru

Abstract

The numerical simulation of two-dimensional viscous incompressible flow around airfoils by using vortex element method is considered. The numerical scheme and the corresponding algorithm for this method are usually presuppose the replacement of the airfoil with the polygon which consists of panels, and the unknown vortex layer intensity is assumed to be piecewise-constant on the panels. The accuracy of this scheme varies from $O(h^2)$ to $O(h^3)$ for different airfoils (h is the panels' length). In the present research new high-order numerical scheme is developed. The solution approximation as well as airfoil boundary approximation is improved — vortex layer intensity assumed to be not piecewise-constant, but piecewise-linear or piecewise-quadratic on the panels, and the curvilinearity of the airfoil's boundary is taken into account. In order to obtain linear algebraic equations system least squares method is used instead of collocation-type conditions in separate control points or on average on the panels. It is shown that the developed scheme has higher accuracy order than the previously known schemes. For some particular model problems (flow around circular, elliptical and Zhukovsky airfoils) this approach allows to obtain solution with accuracy $O(h^5)$.

1 Introduction

Vortex Element Method that belongs to particle-type meshless Lagrangian CFD method is very useful when solving number of engineering problems, especially fluid-structure interaction (FSI) problems, when the fluid domain varies in time and the flow can be considered incompressible.

In 2D case there are some approaches for solving the Navier — Stokes equations by using vortex methods, one of the most useful is Viscous Vortex Domains Method (VVD) which is based on the so-called 'diffusive' velocity computation for vortex wake evolution simulation [1]. The accuracy of the flow simulation and aerodynamic loads computation depends on many factors. The most important factors are:

- the accuracy of the airfoil approximation;
- the accuracy of vortex layer intensity on the airfoil surface computation;

- the accuracy of the vortex wake approximation and its evolution simulation.

Normally in 2D Vortex Element Method the intensity of vortex layer is computed as solution of singular boundary integral equation of the 1-st kind [2], and this approach sometimes leads to significant errors and even to qualitatively wrong results [3]. However, there exists the alternative approach that corresponds to solving Fredholm-type integral equation of the 2-nd kind [4]. The authors have developed this approach and it allows to raise the accuracy considerably [3].
But the further accuracy improvement is restricted to the accuracy of the airfoil approximation. In the present research the algorithm is developed and the corresponding quadrature formulae are derived which allow to take into account the curvature of the airfoil. This approach allows to consider the solution to be piecewise-linear or piecewise-quadratic along every curvilinear part of the airfoil whereas in traditional approaches the solution is assumed to be piecewise-constant along straight airfoil's panels.
The mentioned ideas are very close to well-known 'panel methods' [5], but there are some significant differences. Firstly, we don't assume the solution to be continuous along the airfoil — it is important for correct flow simulation around airfoils with angle points and sharp edges. Secondly, in order to obtain linear algebraic equations system we use least squares method along the curvilinear parts of the airfoil instead of collocation-type conditions in separate control points. And thirdly, we provide integration along the curvilinear parts of the airfoil using Gaussian quadratures instead of series expansions which are usually used in panel methods.
The developed approach and numerical algorithm allow to raise significantly the accuracy of vortex layer intensity computation in Vortex Element Method.

2 Governing Equations

Viscous incompressible media movement is described by Navier — Stokes equations

$$\nabla \cdot \vec{V} = 0, \qquad \frac{\partial \vec{V}}{\partial t} + (\vec{V} \cdot \nabla)\vec{V} = \nu \Delta \vec{V} - \nabla \left(\frac{p}{\rho} \right),$$

where $\vec{V}(\vec{r}, t)$ is flow velocity, $p(\vec{r}, t)$ — pressure, $\rho = \text{const}$ — density of the media, ν — kinematic viscosity coefficient. No-slip boundary condition on the airfoil surface and boundary conditions of perturbation decay on infinity

$$\vec{V}(\vec{r}, t) = 0, \quad \vec{r} \in K; \qquad \vec{V}(\vec{r}, t) \to \vec{V}_\infty, \quad p(\vec{r}, t) \to p_\infty, \quad |\vec{r}| \to \infty$$

should be satisfied.
Navier — Stokes equations can be written down in Helmholtz form using vorticity vector $\vec{\Omega}(\vec{r}, t) = \nabla \times \vec{V}(\vec{r}, t)$:

$$\frac{\partial \vec{\Omega}}{\partial t} + \nabla \times (\vec{\Omega} \times \vec{U}) = 0. \tag{1}$$

Here $\vec{U}(\vec{r}, t) = \vec{V}(\vec{r}, t) + \vec{W}(\vec{r}, t)$, $\vec{W}(\vec{r}, t)$ is the so-called 'diffusive velocity', which is proportional to viscosity coefficient [1]:

$$\vec{W}(\vec{r}, t) = \nu \frac{(\nabla \times \vec{\Omega}) \times \vec{\Omega}}{|\vec{\Omega}|^2}.$$

Equation (1) means that the vorticity which exists in the flow moves with velocity $\vec{U}$. 'New' vorticity is being generated only on airfoil surface, so we can consider that the vorticity distribution in the flow $\vec{\Omega}(\vec{r},\, t)$ is always known.
The streamlined airfoil influence is equivalent to superposition of the attached vortex $\gamma_{att}(\vec{r},\, t)$ and source $q_{att}(\vec{r},\, t)$ layer influences and free vortex layer $\gamma(\vec{r},\, t)$ influence. All these layers are located on the airfoil surface,

$$\gamma_{att}(\vec{r},\, t) = \vec{V}_K(\vec{r},\, t) \cdot \vec{\tau}(\vec{r},\, t), \quad q_{att}(\vec{r},\, t) = \vec{V}_K(\vec{r},\, t) \cdot \vec{n}(\vec{r},\, t), \quad \vec{r} \in K,$$

where $\vec{n}(\vec{r},\, t)$ and $\vec{\tau}(\vec{r},\, t)$ are normal and tangent unit vectors [6, 3].
In the present research the airfoil is assumed to be rigid and immovable, so $\gamma_{att}(\vec{r},\, t) = 0$, $q_{att}(\vec{r},\, t) = 0$. If the vorticity distribution is known, flow velocity can be reconstruted using the Biot — Savart law:

$$\vec{V}(\vec{r},\, t) = \vec{V}_\infty + \frac{1}{2\pi} \int_S \frac{\vec{\Omega}(\vec{s},\, t) \times (\vec{r} - \vec{s})}{|\vec{r} - \vec{s}|^2} dS + \frac{1}{2\pi} \oint_K \frac{\vec{\gamma}(\vec{s},\, t) \times (\vec{r} - \vec{s})}{|\vec{r} - \vec{s}|^2} dl_s. \tag{2}$$

Here $\vec{V}_\infty = \text{const}$ is uniform flow velocity, S is flow region, K is airfoil surface; vortex layer intensity and vorticity vectors are $\vec{\gamma} = \gamma\vec{k}$ and $\vec{\Omega} = \Omega\vec{k}$, where $\vec{k}$ is unit vector orthogonal to the flow plane; for each point at the airfoil surface $\vec{n}(\vec{r}) \times \vec{\tau}(\vec{r}) = \vec{k}$.
Vortex layer intensity $\gamma(\vec{s},\, t)$ can be found from no-slip boundary condition on airfoil surface:

$$\vec{V}(\vec{r},\, t) = \vec{0}, \quad \vec{r} \in K.$$

For simplicity we consider the model problem and assume that there is no vorticity in the flow ($\Omega(\vec{r},\, t) = 0$) and we need to compute the vortex layer intensity on airfoil surface. From mathematical point of view this problem is equivalent to ideal incompressible steady flow simulation around the airfoil. In real unsteady viscous flow similar problem should be solved every time step.

3 The integral equation for vortex layer intensity computation

According to (2) and taking into account that the unknown vortex layer intensity $\gamma(\vec{s},\, t)$ concerns to free vorticity which is part of vortex wake, it could be shown that the limit value of flow velocity on the airfoil surface is equal to (time dependence hereafter is omitted)

$$\vec{V}_-(\vec{r}) = \vec{V}_\infty + \frac{1}{2\pi} \oint_K \frac{\vec{\gamma}(\vec{s}) \times (\vec{r} - \vec{s})}{|\vec{r} - \vec{s}|^2} dl_s - \Big(\frac{\vec{\gamma}(\vec{r})}{2} \times \vec{n}(\vec{r})\Big), \quad \vec{r} \in K. \tag{3}$$

Classical approach which is normally being used in vortex element method, presupposes that the unknown function $\gamma(\vec{r})$ should be found from the equality to zero of *normal* component of the flow velocity limit value at the airfoil's surface:

$$\vec{V}_-(\vec{r}) \cdot \vec{n}(\vec{r}) = 0, \quad \vec{r} \in K. \tag{4}$$

This integral equation is singular and the principal value of the corresponding integral should be understood in Cauchy sense [2]. This approach sometimes leads to significant errors and even qualitatively wrong solution can be obtained.

In order to solve such problems another approach can be implemented. It is shown [4] that 'boundary condition' (4) is equivalent to the following condition

$$\vec{V}_-(\vec{r}) \cdot \vec{\tau}(\vec{r}) = 0, \quad \vec{r} \in K, \tag{5}$$

which corresponds to the equality to zero of *tangent* component of the flow velocity limit value.
It should be noted that in case of smooth airfoils (5) leads to Fredholm-type integral equation of the 2-nd kind with bounded kernel:

$$\frac{1}{2\pi} \oint_K \frac{\vec{n}(\vec{r}) \cdot (\vec{r} - \vec{s})}{|\vec{r} - \vec{s}|^2} \gamma(\vec{s}) dl_s - \frac{\gamma(\vec{r})}{2} = -\vec{V}_\infty \cdot \vec{\tau}(\vec{r}). \tag{6}$$

The equation (6) as well as the singular equation which follows from (4) has infinitely many solutions; in order to select the unique solution an additional equation should be solved together with them:

$$\oint_K \gamma(\vec{s}) dl_s = \Gamma. \tag{7}$$

Total circulation Γ of the vorticity layer on the airfoil can be found from problem statement. For some simplest airfoils it is possible to construct conformal mappings to the circle and to solve the problem analytically. Exact solutions are found for elliptical airfoils and Zhukovsky airfoils [3].

4 Numerical scheme for vortex layer intensity computation

4.1 Numerical scheme with straight panels

Normally in vortex methods curvilinear airfoil surface is being approximated with polygon (whose legs are usually called 'panels' and have lengths L_i), and vortex layer intensity is supposed to be piecewise-constant function on the legs.
For this approach the integral in equation (6) can be replaced with the sum of integrals over panels, which are proportional to vortex layer intensities on these panels. The most accurate results can be obtained if we satisfy equation (6) not in separate points on airfoil surface, but on the average on the panels:

$$\frac{1}{2\pi L_i} \sum_{j=1}^{N} \gamma_j \int_{K_i} \left(\int_{K_j} \frac{\vec{n}_i \cdot (\vec{r} - \vec{s})}{|\vec{r} - \vec{s}|^2} dl_s \right) dl_r - \frac{\gamma_i}{2} = -\vec{V}_\infty \cdot \vec{\tau}_i, \quad i = 1, \ldots, N.$$

Coefficients of this linear algebraic system can be calculated analytically [7].
Numerical experiments show that the accuracy of this approach varies from $O(h^2)$ to $O(h^3)$ for different airfoils (fig. 1).

4.2 Numerical scheme with curvilinear panels

In order to construct more accurate numerical scheme we should take into account that the panels in reality are curvilinear and piecewise-constant approximation of the vortex layer intensity also can cause the error. It is possible to develop new numerical scheme

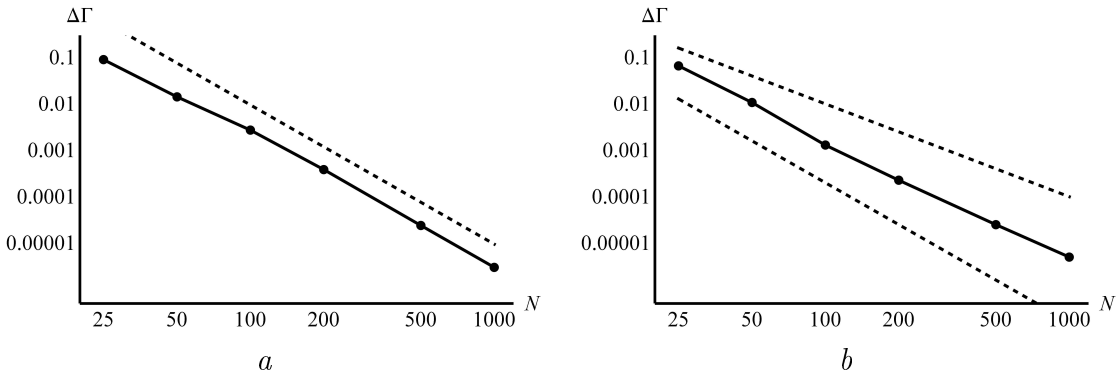

Figure 1: Error of vortex element's circulations (in logarithmical scale) for numerical scheme [3]: a — elliptical airfoil, dashed line corresponds to $O(h^3)$ error; b — Zhukovsky airfoil, dashed lines correspond to $O(h^2)$ and $O(h^3)$ error; h is average panel length

which is based on curvilinear approximation of the airfoil's surface and piecewise-linear or piecewise-quadratic vorticity distribution along panels.

It is well-known [2] that vortex layer intensity is unbounded near angle points of the airfoil, so when constructing high-order accuracy numerical schemes it is important to approximate the airfoil by a smooth curve. We assume the airfoil's geometry to be known exactly by its parametric equations $x = x(t)$, $y = y(t)$, $t \in [0,\, 2\pi)$, so it is possible to calculate not only coordinates of points on the airfoil's surface, but also tangent directions at these points. We demand that the curve which approximates the airfoil on the particular panel, passes over endings of the panel and has the same tangent directions as the original airfoil. Let's denote the beginning of the i-th panel as C_i and its ending as C_{i+1} (these points correspond to t_i and t_{i+1} parameter's value); $\vec{\tau}_i^{\,0}$ is unit vector which is collinear to $\overrightarrow{C_iC_{i+1}}$; $\vec{n}_i^{\,0}$ is unit normal vector which is orthogonal to $\vec{\tau}_i^{\,0}$ (fig. 2).

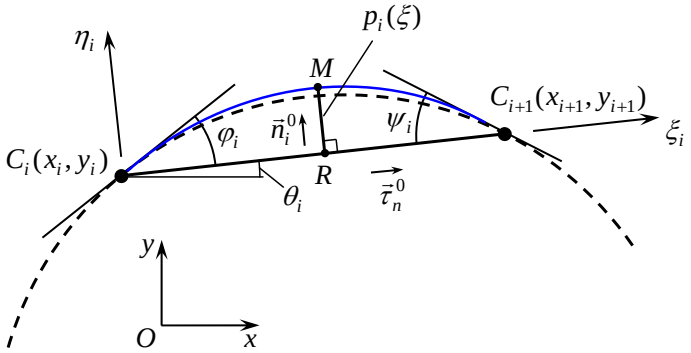

Figure 2: Piecewise-polynomial approximation of airfoil's surface. Dashed line is the original airfoil's surface, solid line is its polynomial approximation

For every panel we introduce 'local' coordinate system $C_i\xi_i\eta_i$, then points C_i and C_{i+1} correspond to $\xi = 0$ and $\xi = L_i$, where $L_i = |\overrightarrow{C_iC_{i+1}}|$. In order to construct the interpolation curve we firstly calculate tangents of angles φ_i and ψ_i by using the following formulae:

$$\tan\varphi_i = \frac{y'_+(t_i) - x'_+(t_i)\tan(\theta_i)}{x'_+(t_i) + y'_+(t_i)\tan(\theta_i)}, \quad \tan\psi_i = -\frac{y'_-(t_{i+1}) - x'_-(t_{i+1})\tan(\theta_i)}{x'_-(t_{i+1}) + y'_-(t_{i+1})\tan(\theta_i)}.$$

Here θ_i is angle between i-th panel and Ox axis; x'_+, x'_-, y'_+, y'_- denote right-hand and left-hand derivatives with respect to t correspondingly.
The equation of the interpolation curve on i-th panel in local coordinates is

$$p_i(\xi) = \frac{\xi(L_i - \xi)}{L_i}\Big(a_i + b_i\frac{\xi}{L_i}\Big),$$

where the conditions $p_i(0) = 0$, $p_i(L_i) = 0$ are satisfied automatically, coefficients a_i and b_i can be calculated from the conditions $p'_i(0) = \tan\varphi_i$, $p'_i(L_i) = -\tan\psi_i$:

$$a_i = \tan\varphi_i, \quad b_i = \tan\psi_i - \tan\varphi_i.$$

So the position vector of arbitrary point M which lies on the interpolation curve and has coordinate ξ in local system is

$$\overrightarrow{OM}(\xi) = \overrightarrow{OC_i} + \xi\vec{\tau}_i^{\,0} + p_i(\xi)\vec{n}_i^{\,0}.$$

Assuming the original airfoil to be C^4-smooth on the panel, the difference between the constructed interpolation curve and the original airfoil is $O(L_i^4)$. It can be proved using Taylor series expansions.
We approximate vorticity layer intensity distribution along the i-th curvilinear panel by quadratic polynomial:

$$\gamma_i(\xi) = \alpha_i + \beta_i\frac{\xi}{L_i} + \delta_i\frac{\xi^2}{L_i^2}.$$

Unknown coefficient values α_i, β_i, δ_i, $i = 1, \ldots, N$ can be found from integral equation (6) with additional condition (7). In order to obtain the approximate solution of this equation we use least-squares method and minimize function

$$\Psi = \oint_K \left(\frac{1}{2\pi}\oint_K \frac{\vec{n}(\vec{r})\cdot(\vec{r}-\vec{s})}{|\vec{r}-\vec{s}|^2}\gamma(\vec{s})dl_s - \frac{\gamma(\vec{r})}{2} + \vec{V}_\infty\cdot\vec{\tau}(\vec{r})\right)^2 dl_r - \\ - \lambda\left(\oint_K \gamma(\vec{r})dl_r - \Gamma\right) \to \min \quad (8)$$

with respect to α_i, β_i, δ_i, λ.
Both outer and inner integrals in (8) can be replaced with the sums of integrals along curvilinear panels:

$$\Psi = \sum_{i=1}^{N}\int_{K_i}\left(\frac{1}{2\pi}\sum_{j=1}^{N}\int_{K_j}\frac{\vec{n}(\vec{r})\cdot(\vec{r}-\vec{s})}{|\vec{r}-\vec{s}|^2}\gamma(\vec{s})dl_s - \frac{\gamma(\vec{r})}{2} + \vec{V}_\infty\cdot\vec{\tau}(\vec{r})\right)^2 dl_r - \\ - \lambda\left(\sum_{i=1}^{N}\int_{K_i}\gamma(\vec{r})dl_r - \Gamma\right) \to \min. \quad (9)$$

All the integrals are calculated in local coordinates, so on i-th panel $\vec{r} = \vec{r}_i(\xi)$, on j-th panel $\vec{s} = \vec{s}_j(\zeta)$:

$$\vec{r}_i(\xi) = \overrightarrow{OC_i} + \xi\vec{\tau}_i^{\,0} + p_i(\xi)\vec{n}_i^{\,0}, \quad \vec{s}_j(\zeta) = \overrightarrow{OC_j} + \zeta\vec{\tau}_j^{\,0} + p_j(\zeta)\vec{n}_j^{\,0}.$$

Introducing Jacobian of coordinates transformation

$$J_i(\xi) = \frac{dl_r}{d\xi}\Big|_{\vec{r}=\vec{r}_i(\xi)} = \sqrt{1 + \big(p'_i(\xi)\big)^2}\Big|_{\vec{r}=\vec{r}_i(\xi)},$$

according that $\gamma(\vec{r}_i(\xi)) = \gamma_i(\xi)$ and denoting $\vec{n}(\vec{r}_i(\xi)) = \vec{n}_i(\xi)$, $\vec{\tau}(\vec{r}_i(\xi)) = \vec{\tau}_i(\xi)$, we can write down function (9) in the following form:

$$\Psi = \sum_{i=1}^{N} \int_0^{L_i} \left(\frac{1}{2\pi} \sum_{j=1}^{N} \int_0^{L_j} \frac{\vec{n}_i(\xi) \cdot \left(\vec{r}_i(\xi) - \vec{s}_j(\zeta)\right)}{|\vec{r}_i(\xi) - \vec{s}_j(\zeta)|^2} \gamma_j(\zeta) J_j(\zeta) d\zeta - \frac{\gamma_i(\xi)}{2} + \right.$$
$$\left. + \vec{V}_\infty \cdot \vec{\tau}_i(\xi) \right)^2 J_i(\xi) d\xi - \lambda \left(\sum_{i=1}^{N} \int_0^{L_i} \gamma_i(\xi) J_i(\xi) d\xi - \Gamma \right) \to \min . \quad (10)$$

Unit tangent vector $\vec{\tau}_i(\xi)$ is calculated not for original curve, but for obtained interpolation:

$$\vec{\tau}_i(\xi) = \frac{\vec{\tau}_i^{\,0} + p_i'(\xi)\vec{n}_i^{\,0}}{\left|\vec{\tau}_i^{\,0} + p_i'(\xi)\vec{n}_i^{\,0}\right|}.$$

Unit normal vector $\vec{n}_i(\xi)$ is orthogonal to $\vec{\tau}_i(\xi)$.
The only unknown functions in (10) are $\gamma_i(\xi)$, but they are quadratic functions with respect to ξ, so

$$\Psi = \sum_{i=1}^{N} \int_0^{L_i} \left(\frac{1}{2\pi} \sum_{j=1}^{N} \left(\alpha_j \int_0^{L_j} \frac{\vec{n}_i(\xi) \cdot \left(\vec{r}_i(\xi) - \vec{s}_j(\zeta)\right)}{|\vec{r}_i(\xi) - \vec{s}_j(\zeta)|^2} J_j(\zeta) d\zeta + \right.\right.$$
$$+ \beta_j \int_0^{L_j} \frac{\vec{n}_i(\xi) \cdot \left(\vec{r}_i(\xi) - \vec{s}_j(\zeta)\right)}{|\vec{r}_i(\xi) - \vec{s}_j(\zeta)|^2} \frac{\zeta}{L_j} J_j(\zeta) d\zeta + \delta_j \int_0^{L_j} \frac{\vec{n}_i(\xi) \cdot \left(\vec{r}_i(\xi) - \vec{s}_j(\zeta)\right)}{|\vec{r}_i(\xi) - \vec{s}_j(\zeta)|^2} \frac{\zeta^2}{L_j^2} J_j(\zeta) d\zeta \Bigg) -$$
$$- \frac{1}{2} \left(\alpha_i + \beta_i \frac{\xi}{L_i} + \delta_i \frac{\xi^2}{L_i^2} \right) + \vec{V}_\infty \cdot \vec{\tau}_i(\xi) \Bigg)^2 J_i(\xi) d\xi -$$
$$- \lambda \left(\sum_{i=1}^{N} \int_0^{L_i} \left(\alpha_i + \beta_i \frac{\xi}{L_i} + \delta_i \frac{\xi^2}{L_i^2} \right) J_i(\xi) d\xi - \Gamma \right) \to \min . \quad (11)$$

Denoting

$$\int_0^{L_j} \frac{\vec{n}_i(\xi) \cdot (\vec{r}_i(\xi) - \vec{s}_j(\zeta))}{|\vec{r}_i(\xi) - \vec{s}_j(\zeta)|^2} \frac{\zeta^r}{L_j^r} J_j(\zeta) d\zeta = I_{ij}^{(r)}(\xi), \quad \int_0^{L_i} J_i(\xi) \frac{\xi^r}{L_i^r} d\xi = J_i^{(r)},$$

we obtain

$$\Psi = \sum_{i=1}^{N} \int_0^{L_i} \left(\frac{1}{2\pi} \sum_{j=1}^{N} \left(\alpha_j I_{ij}^{(0)}(\xi) + \beta_j I_{ij}^{(1)}(\xi) + \delta_j I_{ij}^{(2)}(\xi) \right) - \frac{1}{2} \left(\alpha_i + \beta_i \frac{\xi}{L_i} + \delta_i \frac{\xi^2}{L_i^2} \right) + \right.$$
$$\left. + \vec{V}_\infty \cdot \vec{\tau}_i(\xi) \right)^2 J_i(\xi) d\xi - \lambda \left(\sum_{i=1}^{N} \left(\alpha_i J_i^{(0)} + \beta_i J_i^{(1)} + \delta_i J_i^{(2)} \right) - \Gamma \right) \to \min .$$

The minimum of this function corresponds to the equality to zero of all partial derivatives

with respect to α_i, β_i, δ_i, λ:

$$\frac{\partial\Psi}{\partial\alpha_k} = \sum_{i=1}^{N}\int_0^{L_i} 2\left(\frac{1}{2\pi}\sum_{j=1}^{N}\left(\alpha_j I_{ij}^{(0)}(\xi) + \beta_j I_{ij}^{(1)}(\xi) + \delta_j I_{ij}^{(2)}(\xi)\right) - \right.$$
$$\left. - \frac{1}{2}\left(\alpha_i + \beta_i\frac{\xi}{L_i} + \delta_i\frac{\xi^2}{L_i^2}\right) + \vec{V}_\infty\cdot\vec{\tau}_i(\xi)\right)\left(\frac{I_{ik}^{(0)}(\xi)}{2\pi} - \frac{1}{2}\right)J_i(\xi)\,d\xi - \lambda J_k^{(0)} = 0,$$

$$\frac{\partial\Psi}{\partial\beta_k} = \sum_{i=1}^{N}\int_0^{L_i} 2\left(\frac{1}{2\pi}\sum_{j=1}^{N}\left(\alpha_j I_{ij}^{(0)}(\xi) + \beta_j I_{ij}^{(1)}(\xi) + \delta_j I_{ij}^{(2)}(\xi)\right) - \right.$$
$$\left. - \frac{1}{2}\left(\alpha_i + \beta_i\frac{\xi}{L_i} + \delta_i\frac{\xi^2}{L_i^2}\right) + \vec{V}_\infty\cdot\vec{\tau}_i(\xi)\right)\left(\frac{I_{ik}^{(1)}(\xi)}{2\pi} - \frac{1}{2}\frac{\xi}{L_k}\right)J_i(\xi)\,d\xi - \lambda J_k^{(1)} = 0,$$

$$\frac{\partial\Psi}{\partial\delta_k} = \sum_{i=1}^{N}\int_0^{L_i} 2\left(\frac{1}{2\pi}\sum_{j=1}^{N}\left(\alpha_j I_{ij}^{(0)}(\xi) + \beta_j I_{ij}^{(1)}(\xi) + \delta_j I_{ij}^{(2)}(\xi)\right) - \right.$$
$$\left. - \frac{1}{2}\left(\alpha_i + \beta_i\frac{\xi}{L_i} + \delta_i\frac{\xi^2}{L_i^2}\right) + \vec{V}_\infty\cdot\vec{\tau}_i(\xi)\right)\left(\frac{I_{ik}^{(2)}(\xi)}{2\pi} - \frac{1}{2}\frac{\xi^2}{L_k^2}\right)J_i(\xi)\,d\xi - \lambda J_k^{(2)} = 0,$$

$$\frac{\partial\Psi}{\partial\lambda} = \sum_{i=1}^{N}\left(\alpha_i J_i^{(0)} + \beta_i J_i^{(1)} + \delta_i J_i^{(2)}\right) - \Gamma = 0.$$

These expressions can be simplified. If we denote integrals of known functions as

$$J_{mnk}^{(p,q)} = \int_0^{L_m} I_{mn}^{(p)}(\xi) I_{mk}^{(q)}(\xi) J_m(\xi)\,d\xi, \qquad J_{mn}^{(p,r)} = \int_0^{L_m} I_{mn}^{(p)}(\xi)\frac{\xi^r}{L_m^r}J_m(\xi)\,d\xi,$$

and introduce variable $\gamma_j^{(u)}$, where

$$\gamma_j^{(0)} = \alpha_j, \quad \gamma_j^{(1)} = \beta_j, \quad \gamma_j^{(2)} = \delta_j, \quad j = 1,\,2,\,\ldots,\,N,$$

the system of linear algebraic equations can be written down in compact form:

$$\sum_{j=1}^{N}\sum_{u=0}^{2}\gamma_j^{(u)}\left(\frac{1}{2\pi^2}\sum_{i=1}^{N}J_{ijk}^{(u,r)} - \frac{1}{2\pi}\sum_{i=1}^{N}\left(J_{ij}^{(u,r)}\frac{L_i^r}{L_k^r}\right) - \frac{1}{2\pi}J_{jk}^{(r,u)} + \frac{1}{2}J_j^{(u+r)}\frac{L_i^r}{L_k^r}\right) - \lambda J_k^{(r)} =$$
$$= -\sum_{i=1}^{N}\int_0^{L_i}\left(\vec{V}_\infty\cdot\vec{\tau}_i(\xi)\right)\left(\frac{1}{\pi}I_{ik}^r(\xi) - \frac{\xi^r}{L_k^r}\right)d\xi, \quad k = 1,\,2,\,\ldots,\,N, \quad r = 0,\,1,\,2,$$

$$\sum_{j=1}^{N}\sum_{u=0}^{2}\gamma_j^{(u)}J_j^{(u)} = \Gamma. \tag{12}$$

If we assume the solution to be piecewise-linear on the panels, variables r and u in system (12) take the values 0 and 1.

In order to calculate all the integrals in (12) numerically we use Gaussian quadrature formula, according to which

$$\int_a^b f(x)\,dx \approx \sum_{k=1}^{n_{gp}} \omega_k f(x_k),$$

where weights ω_k values and gaussian points positions x_k are known [8]. In the present research $n_{gp} = 7$; in that cases when approximate integration accuracy is not enough, special numerical integration procedure, implemented in Wolfram Mathematica, is used.

5 Numerical experiment

We consider circular airfoil with radius $R = 1$, elliptical airfoil with semiaxes $a = 1.0$, $b = 0.5$ and Zhukovsky airfoil with parameters ($a = 3.5$, $d = 0.4$, $h = 0.3$) under angle of incidence $\beta = \pi/6$.
Using the developed numerical scheme with curvilinear panels we firstly compute vortex layer intensity distribution along the panels (α_i, β_i and δ_i values) and then integrate it in order to obtain total circulation on each panels:

$$\Gamma_i = \int_0^{L_i} \left(\alpha_i + \beta_i \frac{\xi}{L_i} + \delta_i \frac{\xi^2}{L_i^2}\right) J_i(\xi) d\xi, \quad i = 1, 2, \ldots, N.$$

Then using the analytical solution [3] exact values of Γ_i^* are computed and then error can be found:

$$\Delta\Gamma = \max_i |\Gamma_i - \Gamma_i^*|.$$

The results of numerical experiments are nearly the same both for piecewise-linear and piecewise-quadratic vorticity distribution, but in case of piecewise-quadratic solution matrix of the system (12) sometimes becomes ill-conditioned.
In all cases (for circular, elliptical and Zhukovsky airfoils) the accuracy of the developed approach is close to $O(h^5)$ (fig. 3).

Conclusion

For flow simulation by using vortex methods new numerical scheme is suggested for vortex layer intensity computation on an airfoil's surface. The developed approach allows to take into account airfoil's curvature, which is important for solution of the integral equation with high accuracy. Vorticity distribution assumed to be piecewise-linear or piecewise-constant on the panels. It allows to reproduce discontinuous solutions, which take place on airfoils with sharp edge (Zhukovsky airfoil). The numerical experiment showed that the developed scheme has 5-th accuracy order.

Acknowledgements

The work was supported by Russian Federation President's Grant for young PhD-scientists [proj. MK-3705.2014.8].

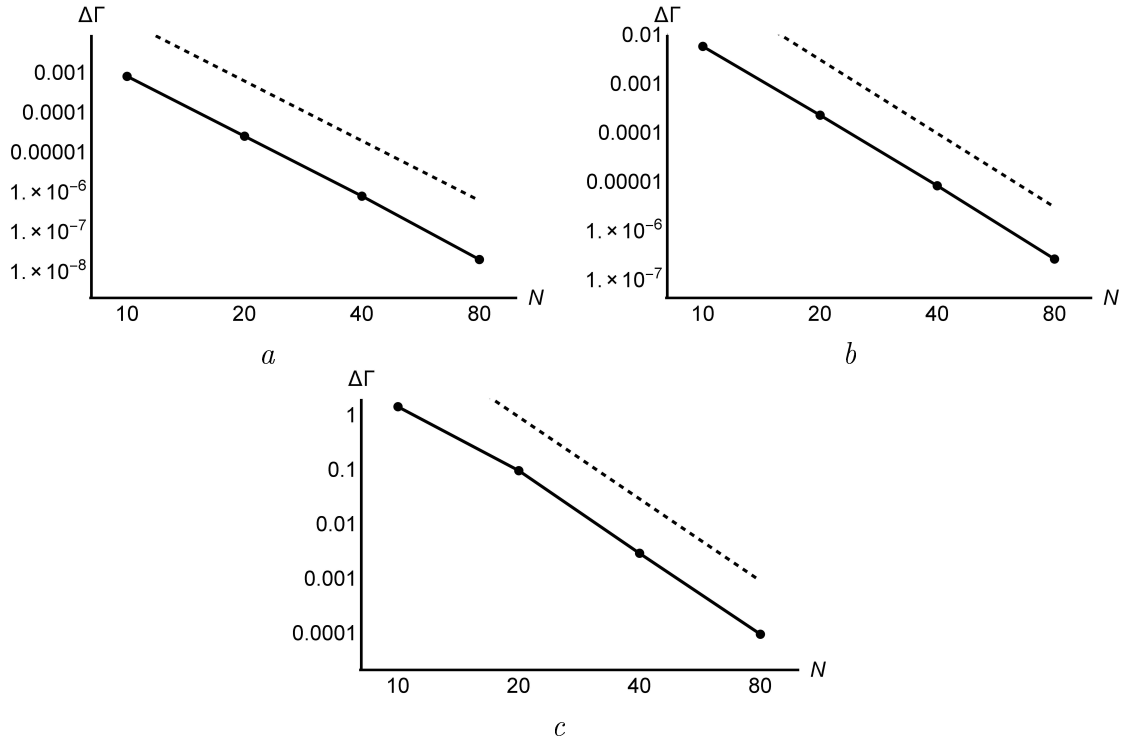

Figure 3: Error of total circulation on the panels circulations (in logarithmical scale) for the developed numerical scheme (12): a — circular airfoil; b — elliptical airfoil; c — Zhukovsky airfoil; dashed lines in all cases correspond to $O(h^5)$ error; h is average panel length

References

[1] Dynnikova G.Ya. Vortex Motion in Two-Dimensional Viscous Fluid Flows // Fluid Dynamics. 2003. V. 38, No. 5. P. 670–678.

[2] Lifanov I.K., Belotserkovsky S.M. Methods of Discrete Vortices. CRC, 1992.

[3] Kuzmina K.S., Marchevsky I.K. On Numerical Schemes in 2D Vortex Element Method for Flow Simulation Around Moving and Deformable Airfoils // Proceedings of Summer School-Conference "Advanced Problems in Mechanics 2014". St.-Peterburg, 2014. P. 335–344. URL: http://www.ipme.ru/ipme/conf/APM2014/2014-PDF/2014-335.pdf

[4] Kempka S.N., Glass M.W., Peery J.S., Strickland J.H. Accuracy Considerations for Implementing Velocity Boundary Conditions in Vorticity Formulations. SANDIA REPORT SAND96-0583 UC-700, 1996.

[5] Vaz G., Falcao de Campos J.A.C., Eca L. A numerical study on low and higher-order potential based BEM for 2D inviscid flows // Computational Mechanics. 2003, V. 32, Is. 4–6. P. 327–335.

[6] Andronov P.R., Guvernyuk S.V., Dynnikova G.Ya. Vortex Methods for Unsteady Hydrodynamic Loads. Moscow, MSU, 2006. [in Russian]

[7] Marchevsky I.K., Moreva V.S. Vortex Element Method for 2D Flow Simulation with

Tangent Velocity Components on Airfoil Surface // ECCOMAS 2012 — Europ. Congr. on Comp. Meth. in Ap. Sc. and Eng., e-Book. 2012. P. 5952–5965.

[8] Abramowitz M., Stegun I.A. Handbook of Mathematical Functions with Formulas, Graphs, and Mathematical Tables. New York, Dover, 1965.

Kseniya S. Kuzmina, Russia, 105005 Moscow, 2nd Baumanskaya st., 5
Ilia K. Marchevsky, Russia, 105005 Moscow, 2nd Baumanskaya st., 5

Fracture Processes in Cortical Bone: Effect of Microstructure

Simin Li, Mayao Wang, Xing Gao, Elizabeth A. Zimmermann, Christoph Riedel, Bjrn Busse and Vadim V. Silberschmidt*
V.Silberschmidt@lboro.ac.uk

Abstract

Understanding of bone fracture can improve medical and surgical procedures. Therefore, investigation of the effect of boneвЂ™s microstructure and properties as well as loading conditions on crack initiation and propagation is of great importance. In this paper, several modelling approaches are used to study fracture of cortical bone tissue at various length scales and different types of loading. Two major problems are tackled: crack propagation under impact loading and bone cutting in surgical procedures.

In the former case, a micro-scale finite-element (FE) fracture model was suggested, accounting for boneвЂ™s microstructure and using X-FEM for crack-propagation analysis [1, 2]. The cortical bone tissue was modelled as four-component heterogeneous materials. The morphology of a transverse-radial cross section captured with optical microscopy was used to generate FE models; extensive experimental studies provided necessary mechanical input data [3]. The problem of bone cutting was treated within the framework of tool-bone interaction analysis [4, 5]. A two-domain approach was used, with a process zone simulated using a smooth-particle hydrodynamics method. This zone was embedded in a continuum domain with macroscopic anisotropic properties obtained in experiments. This study is supported by analysis of damage induced by interaction between the cutting tool and the bone tissue using wedge-indentation tests and considering also the anisotropic behaviour of the bone.

1 Introduction

Research into mechanical behaviour of a natural composite material - cortical bone tissue - has attracted great attention over the past few decades, not only because of its important role in structural integrity of a musculoskeletal system, but also due to the boneвЂ™s intrinsic hierarchical heterogeneous structure and anisotropic mechanical properties. Macroscopically, deformation mechanisms of bones differ from those of metals, polymers and composites since bones consist of a living tissue with a continuously evolving microstructure. Mechanical properties of cortical bone vary not only from bone to bone; they demonstrate a spatial viability even within the same bone related to changes of the underlying microstructure [3, 6]. Dissimilar mechanical properties measured with

indentation at different anatomical positions provide further information on its heterogeneity and anisotropic mechanical behaviour [7]. Considering the wide spectrum of material properties of cortical bone and its intricate deformation processes associated with various loading modes and orientations, a further investigation is needed to comprehend variations of material properties in relation to the local regions and underpinning microstructural constituents.
Microscopically, complex micro-architecture of the cortical bone tissue has a significant effect on its mechanical and fracture properties. Anisotropic deformation and fracture behaviours observed at macroscopic level [8] are largely attributed to preferential alignment of micro-constituents at respective length scales, such as osteons and Haversian canals at micro-scale, or collagen fibrils and mineral crystals at nano-scale. From a fracture-toughness perspective, those intricate structural hierarchy and material heterogeneity observed in cortical bone tissues can often lead to an improved fracture resistance thanks to various toughening mechanisms [8, 9].

2 Mechanical behaviour of cortical bone tissue

2.1 Variability of anisotropic mechanical behaviour in tension and compression

Uniaxial tensile and compressive tests were conducted on specimens of cortical bone to characterise its deformation behaviours at different loading conditions and orientations.
The specimens used for this study were obtained from mid-diaphysis of fresh bovine femoral bones from a local butchery shop soon after slaughter since the mechanical behaviours of bovie and human bones are close. Specimen preparation and storage procedures followed exactly the generally adopted methods [3, 6]; details can be found in [4, 6]. Dumb-bell-shape specimens (15 mm in gauge length $\times 5mm \times$ 2 mm) oriented along both the longitudinal and transverse directions of the bone were prepared and divided into four groups according to their anatomical position (cortices, or quadrants): anterior, medial, posterior and lateral for uniaxial tension tests (Fig. 1). The same categorisation was applies to cylindrical specimens (Ø5 mm $\times$ 5 mm) for uniaxial compression test.
Experiments with specimens from four different quadrants of the bone were performed on an Instron 3366 (Instron, USA) system with a 10 kN load cell under quasi-static loading conditions. Displacements were measured using an extensometer (2630 Series, Instron) and a linear variable differential transducer (LVDT) sensor (2601 Series, Instron) in the uniaxial tensile and compressive tests, respectively. The detailed experimental procedure can be found in [6].

2.1.1 Results and analysis

The obtained results (detailed in [6]) correlate well with those reported in literature [10] and indicate that mechanical responses of cortical bone diverge dramatically under different loading conditions and orientations. Transverse specimens loaded in tension appeared to be rather brittle and failed at much lower strains compared with those for the longitudinal direction, but the difference for compression is less prominent (Fig. 2). Regardless of the loading mode, specimens loaded in the longitudinal direction always demonstrate a higher stiffness (a higher Youngвs modulus) and strength (higher ultimate stress) than those in the transverse direction. Among the material properties measured for four anatomic

quadrants, two orientations and two loading modes, the anterior quadrant had the highest Youngвґєs modulus in the longitudinal direction, while the medial quadrant has the highest one in the transverse direction. The lowest values are for the lateral and posterior quadrants for the longitudinal and transverse directions, respectively. A difference between the highest and lowest values of the Youngвґєs modulus in each orientation was more than 20%. The relations across different quadrants (Factor A) and loading modes (Factor B) were compared in terms of significance of variances using a two-way ANOVA analysis ($\alpha = 0.05$) with a Tukey HSD test. Overall, the results showed a statistical significance in factor A (between cortices), but there is no uniform significance in factor B (between loading modes). The interaction between the two factors appears to be negative, which means that loading modes do not have effective contribution to variability across the cortices and vice versa. Results of the detailed Tukey HSD tests together with pairwise comparisons between the studied factors are summarised in [6].

2.2 Fracture toughness of cortical bone tissue

Fracture toughness of cortical bone in different orientations is studied in this section to deepen our understanding of anisotropy and variability of fracture resistance of the cortical bone tissue.

Fifteen specimens cut from each cortex of fresh bovine femurs were notched to allow crack growth along three different orientations relative to the bone axis вґЎY longitudinal, transverse and radial as shown in Fig. 1. After cutting, specimens were polished and then checked under microscope to insure that their surfaces were free from scratches and damage. Specimens were kept hydrated in a 0.9% physiological saline solution prior to tests. All specimens were prepared with the same dimensions, according to British Standard: BS 7448-1: 25 mm $\times 2.72 mm \times$ 5.43 mm (total length $\times width \times$ thickness). Also, a very fine slit of 2.7 mm was produced using a low-speed diamond blade for all specimens according to the same standard.

The fracture toughness tests were performed on an Instron 3345 single-column bench-top machine. All specimens were loaded quasi-statically up to failure with a displacement-controlled loading rate of 1 mm/min. The load was measured using a 5 kN load cell and the corresponding load-line displacement was acquired synchronously using a LVDT sensor (2601 Series, Instron, USA), see Fig. 3. The obtained load-displacement curves were then analysed according to the classification described in BS 7448-1. After tests, fracture surfaces of all the specimens were gold-coated and analysed using scanning electron microscopy (SEM).

2.2.1 Results and analysis

Critical values of fracture toughness J_C of the cortical bone tissue were calculated for three crack-growth directions: longitudinal, radial and transverse; in addition, anisotropy ratios of the fracture-toughness values were analysed. The obtained experimental data demonstrated that all specimens exhibited signes of a non-linear fracture process; hence, the J-integral (Table 1) was used to quantify fracture toughness based on British Standard: BS 7448-1.

It can be noticed from these results that the fracture-toughness values for specimens cut from different cortices vary significantly. In general, cortical bone shows higher resistance to fracture when a crack grows perpendicular to the osteon direction and lower resistance for those grow parallel to osteons (i.e. radial and longitudinal directions, respectively). For a crack growing in the transverse direction, specimens from the medial quadrant had

the highest critical value of J-integral while those from the posterior quadrant had the lowest. The Tukey HSD test ($\alpha = 0.05$) demonstrated statistically significant differences between medial to posterior ($p = 0.035$) and posterior to lateral ($p = 0.028$) cortices. On the other hand, specimens with radially extended cracks had the highest fracture toughness for the lateral quadrant and the lowest for the posterior one. The calculated critical values of J-integral for the radial cracks, ranging from 983 N/m to 2664 N/m, are significantly lower compared with specimens with transverse cracks. Considerable differences were found between anterior to lateral ($p = 0.027$) and posterior to lateral ($p = 0.015$) quadrants. Finally, for specimens with cracks extending along the direction parallel to osteons (longitudinal cracks), the critical J-integral values were comparable with those for radial cracks, and their highest value was found for the lateral quadrant whereas anterior specimens demonstrated the lowest. Statistically significant differences in this case were found between anterior to medial ($p = 0.043$) and anterior to lateral ($p = 0.02$) quadrants. Generally, comparing the data between cortices, higher levels of fracture toughness was usually found in specimens cut from the medial and lateral quadrants. The disparity between these two groups ranged from as low as 18.3% up to 171%.

Such non-uniform fracture resistance across different cortices of the bovine femur implies that the variation of microstructure has a great impact on the local fracture processes. Previous research [3, 6] showed that a change in the volume fraction of constituents at a microstructural level largely affected local material properties, such as elastic modulus, yield stress, ultimate strength, which, in turn, influenced fracture properties. Preferential alignment of microstructural constituents also has an important effect on anisotropy of fracture toughness. Higher resistance to fracture was found for cracks propagating perpendicular to osteons, while lower resistance for cracks extending parallel to osteons. The fracture anisotropy ratios (calculated as ratios of respective values of J_C) between transversely-orientated cracks and longitudinally- or radially-orientated cracks varied for different cortices, ranging from 2.13 to 4.36, with the lowest ratio found in the lateral quadrant and the highest ratio in the anterior quadrant.

Fracture surfaces were analysed for all the tests using SEM. The results obtained for different crack-extension directions and cortex positions are grouped in Fig. 4. Dissimilar characters of fracture-surface roughness were evident among the four cortex positions вΓ an indication of a variety of fracture-toughening mechanisms acting in different cortex positions. A transition of the underlying microstructure from one type to another could be the reason for these differences. As shown in Fig. 4, the fracture surfaces from the anterior and posterior quadrants were relatively smooth compared with those for the medial and lateral quadrants. Empirical evidence suggested that the surface roughness was associated with the amount of energy required to generate the fracture surface: a lower level of fracture energy indicates a smoother fracture surface.

Additionally, a combination of microstructural changes and different crack-extension directions triggered complicated toughening mechanisms, which, in turn, were reflected in diverse fracture-toughness values and levels of surface roughness. Generally, for the longitudinal fracture specimens, with crack fronts propagating along the direction parallel to the osteons, the fracture toughening mechanism was dominated by uncracked-ligament bridging during the process of osteons splitting, rupture, interface failure and fibre delamination (see Fig. 5 L_a, L_b). Similarly, for cracks propagating in the radial direction, the toughening mechanism was still governed by uncracked-ligament bridging as a result of osteon splitting or fibre delamination. However, a slight difference in this case was the existence of interface areas or empty spaces such as cement line or Haversian canals that had a larger contribution towards crack arrest in these regions. As a result, twists and

kinks of osteons were observed in the current analysis (see Fig. 5 R_a, R_b). In contrast to the previous two cases, cracks growing along the transverse direction required a larger traction force for the crack front to penetrate and cross the osteons as longitudinal strength of osteons was much higher than transverse one. Cracks were therefore more likely to be deflected due to imperfections and heterogeneity of the microstructure or cause complete pull outs of osteons (see Fig. 5 T_a). Consequently, higher values of fracture toughness were obtained and rougher crack surfaces were observed. In the elastic-plastic fracture regime, the tensional field at the back of the crack tip also promoted a multi-scale bridging effect through shear sliding between interface regions at different levels (see Fig. 5c).

3 Numerical modelling of fracture process of cortical bone under impact loading

3.1 Model configuration for Izod test

An extended finite-element method (X-FEM) was adopted to study crack propagation in human cortical bone under dynamic loading condition. This model was developed according to the Izod test configuration shown in Fig. 6 [1]. A cortical-bone specimen was modelled as a rectangular beam with a pre-notch. Its model had two sections: a microstructured area 1.278 mm in length and 0.958 mm in width was located in front of the pre-notch as an area of interest, and a surrounding area of a homogenized bone material (50 mm in length and 8 mm in width) was implemented to reduce the overall computational cost. According to the Izod test, a loading condition was set as that of a rotational impact with 5.33 rad/s immediately before the contact with the specimen. A hammer was modelled as made of carbon steel, with isotropic material properties. Its elastic modulus, PoissonвГЄs ratio and density were 210 GPa, 0.3 and 7850 kg/m^3, respectively. A master-and-slave contact interaction between the hammer and the specimen was defined during the impact process. The bottom half of the specimen was fixed completely using an encastre-type constraint. A 4-node bilinear plain-strain quadrilateral (CPE4R) element was used in this simulation. Mechanical properties of different microstructural constituents, such as osteons, interstitial area and cement line were based on the research from Li et al. [2]. The elastic modulus of cement line was 25% lower than that of the osteons following a suggestion in Budyn et al. [11].

The model employed X-FEM to simulate crack propagation in the bone specimen. This simulation technique allows a crack to initiate and propagate along an arbitrary, solution-dependent path, subject to a local material response. The local crack initiation and evolution criteria were established using a surface-based cohesive traction-separation criterion. The initial horizontal 300 Bxm-long crack (pre-notch) was embedded into the homogenized area next to the microstructured domain (Fig. 6). Crack initiation in a cortical bone is commonly described as strain-driven; hence, a fracture strain of 0.6% was chosen based on our previous study [6]. When the fracture strain was reached, damage evolution took place. The evolution criterion was defined in terms of the fracture energy based on the fracture-toughness alues obtained in the experimental part of this study (Table 2).

3.2 Results and analysis

Four models with different statistical realizations of morphologies, obtained for four types of patients, were developed using random distributions of microstructural constituents (details in [2, 12]). The results of simulations indicated that the calculated crack-propagation paths were different for the studied groups, due to variations in spatial distributions of the microstructural constituents. Crack paths for four groups demonstrated different crack-deflection characteristics (Fig. 7) [3], with the young group having a lowest extent of deflections. For the diseased and treated groups, the crack paths exhibited more kinks compared to the other two groups. Generally, crack propagation was more influenced by surrounding cement lines and tended to go through Haversian canals. It was previously indicated that the presence of cement lines might prevent a crack from destroying other Haversian systems during the fracture process [6].
Comparing the evolution of crack lengths with time for all the studied groups, the difference was not significant, with a 6.75% standard deviation, for an average crack length of 1.419 mm. Of all the groups, the young group had the lowest crack length (1.37 mm), while it took the longest time for the crack to propagate through the microstructured area. This means that the micromorphological characteristics of bone in the young group hindered crack propagation. According to the trend curves of four groups (Fig. 7), the senior group had the lowest toughness, while the young group had the highest. For the initial 0.1 ms, the four groups had similar crack growth rates, with the senior group demonstrating a higher crack-growth rate after this. Apart from the senior group, the similar trends of crack propagation were observed in other three groups prior reaching a length of 0.4 mm; then, the crack in the diseased group began to accelerate quicker than those in the young and treated groups, confirming a considerable improvement for the treated group compared to the non-treated group. The results obtained with the developed FE models demonstrated that micromorphology of bone played a key role in influencing the crack propagation.

4 Experimental and numerical investigation of anisotropic fracture process of cortical bone due to wedge test

To further elusidate the effect of microstructure on damage initiation and evolution in cortical bone, a study employing wedge indentation was implemented.

4.1 Experimental analysis

A total number of 40 specimens (30 mm $\times 3mm \times$ 3 mm) were prepared from the mid-diaphysis of bovine femur for both longitudinal and transverse directions (Fig. 9b) using a low-speed band saw and then a diamond-coated precision blade (Isomet Low-Speed Saw, Buehler) under water irrigation. The specimens were further categorised into four groups according to their anatomic quadrants (anterior, posterior, medial and lateral) in order to reduce inconsistency caused by material variability across different regions [6]. Penetration tests were performed using Instron MicroTester 5848 with a 2 kN load cell. The specimens were kept hydrated in saline solution prior to the experiments and then glued to the testing base. Four penetrations were made for each cutting direction: perpendicular to osteons (L-C and L-R planes, Fig. 9a) and along them (C-L and C-R planes) using a standard sharp cutting tool under quasi-static loading conditions (displacement rate of 1.8 mm/min). A high-speed camera (Fastcam SA-3, Photron) equipped with a micro-lens (AF Micro-Nikkor

105mm f/2.8D, Nikon, 5000-7500 fps) was employed to capture the deformation process at micro-scale.

4.2 Modelling approach

A 3D finite-element modelling approach вГЎ encompassing both conventional and smoothed-particle-hydrodynamics (SPH) elements вГЎ was implemented using Abaqus/-Explicit. The developed FE model was configured in accordance with our experimental setup. A plane-strain condition was assumed throughout the thickness of the tested specimen, and, therefore, to improve the computational efficiency; the cortical-bone specimen was modelled with the following dimensions: (6 mm $\times 3mm \times$ 0.02 mm) (length $\times width \times$ thickness), with symmetric boundary conditions applied to both front and back sides in the x-y plane as shown in Fig. 9d. The bottom surface of the specimen was fully constrained, while two lateral edges were constrained in the y-z plane. Particle elements (PC3D) were implemented in the middle part of the specimen with a width of 0.4 mm in the x-y plane (Fig. 9d). The remaining two sections were modelled using continuum elements (C3D8R). Tie constrains were applied at the boundaries between continuum and particle elements. The cutting tool was modelled as an analytical rigid body with its geometry measured using optical microscopy.
The bovine cortical-bone specimen was modelled as transversely isotropic elasto-plastic material incorporating the HillвГЄs anisotropic yield criteria and progressive degradation. The material properties used in the model were obtained mostly in the experiments performed in this study (see Table 1 & 3).

4.3 Results and analysis

Penetration of the cutting tool was implemented in different directions: perpendicular to osteons (L-C and L-R planes) and parallel to osteons (C-L and C-R planes). The obtained results indicated strong correlation between the penetration force and orientation of the microstructure, and varied considerably across different cortices. Generally, cortical bone exhibited a higher peak force when the tool penetrated perpendicular to osteons (L-C and L-R) with more energy required to cause damage; and a significantly lower peak force when the penetration direction was parallel to osteons (C-L and C-R), due to relatively low levels of stiffness and toughness. The anisotropic ratios defined as the ratios between penetrations perpendicular to osteons and parallel to them are demonstrated in Table 4. Apparently, the anisotropy ratio varied from one cortex to another in the range from 1.43 to 2.15, with the lowest ratio found in the lateral quadrant and the highest ratio in the posterior one.
Images taken from the high-speed camera also revealed distinct deformation and damage phenomena which were largely affected by the underlying microstructures and their orientation [5]. Various microstructure-related toughening mechanisms were observed for different penetration directions. Generally, for penetration along the longitudinal axis (C-L direction) and radial direction (C-R), damage was well ahead of the cutting tip and mainly caused by material separation and subsequent crack propagation along the penetration direction (Figs.10). Deformation and damage around the cutting tip happened in a rather brittle fashion which was driven predominantly by the low stiffness in the transverse direction and the less effective longitudinal fracture resistance. As a result, low penetration forces were measured. In contrast to the previous two cases, penetrating perpendicular to osteons (L-C and L-R) required much higher force and energy due to the fact that the

stiffness and fracture toughness along bone's longitudinal direction are much higher than the radial and circumferential directions. Damage was therefore more likely to be formed laterally to the penetration direction. Additionally, there were two types of damage patterns observed during our experiments on penetration perpendicular to osteons: a more brittle damage pattern involving fragmentation and materialвГЄs peeling off was predominantly observed at the plexiform bone region; a more diffused ductile damage pattern was associated with large deformation of the osteonal structure.
Images taken with the high-speed camera also revealed distinct deformation and damage phenomena, which were largely affected by the underlying microstructures and their orientation [5]. Various microstructure-related toughening mechanisms were observed for different penetration directions. Generally, for penetration along the longitudinal axis (C-L direction) and the radial direction (C-R), damage was well ahead of the cutting tip and mainly caused by material separation and subsequent crack propagation along the penetration direction (Figs. 10). Deformation and damage around the cutting tip happened in a rather brittle fashion, driven predominantly by low stiffness in the transverse direction and the less effective longitudinal fracture resistance. As a result, low penetration forces were measured. In contrast to the previous two cases, indentations perpendicular to osteons (L-C and L-R) required much higher forces and energy due to the fact that the levels of stiffness and fracture toughness along the bone's longitudinal direction are much higher than those for the radial and circumferential directions. Damage was therefore more likely to be formed laterally to the penetration direction. Additionally, there were two types of damage patterns observed during our experiments on penetration perpendicular to osteons: (i) a more brittle damage pattern involving fragmentation and materialвГЄs peeling off was predominantly observed at the plexiform bone region; (ii) a more diffused ductile damage pattern was associated with large deformation of the osteonal structure.
To gain further detailed understanding on anisotropic deformation and fracture responses to penetration of cortical bone in the vicinity of the cutting tip, numerical simulations were conducted using a SPH-based FE approach. Eight models were developed for two penetration directions (perpendicular and parallel to osteons) for each of four cortices. The performed simulations clearly demonstrated that progressive damage mechanisms strongly affected the deformation process. A comparison between the simulations and the experimental data for relationships between the levels of specific force (per unit width) and displacement demonstrated that the obtained numerical results were well within the range of the experimental measurements (see details in [5]) for different cutting directions and cortices. Apparently, the relationships between the cutting force and the penetration depth were linearly correlated up to a point somewhat below the maximum cutting force, and their initial slopes for both cutting directions were similar (Fig. 11). However, the levels of maximum force and corresponding displacement for specimens cut parallel to osteons' directions (C-L or C-R) were much lower than those for other directions. This orientation-dependent load-bearing capacity was directly affected by the distinct orientation-dependent deformation and damage mechanisms observed in our experiments (Fig. 10). By incorporating these orientation-dependent material formulation and damage mechanisms, the developed models were capable to reproduce the anisotropic character of failure, with both forces and displacements predicted adequately for various cutting directions and cortices.

5 Conclusion

In this paper, the study was focused on the fracture processes in cortical bone at various length scales. To implement it, mechanical behaviour of the cortical bone tissue was charac-

terise for elastic, post-yield and damage regimes. The results from our studies demonstrate specific features of varying anisotropic deformation and fracture behaviours of the cortical bone tissue, which also depend on the applied loading conditions. Due to a natural loading regime exerted by species' weight and muscle forces, long bones are normally exposed to combined loading conditions that are spatially non-uniform [6]. As it is well known from the literature [8], bone is a dynamic tissue that reacts to mechanical loading by adapting its shape, internal microstructure and material properties to meet requirements of external loading environment. The differences in the values of the YoungвЃ™s modulus and fracture toughness (critical J-integral) could be the outcome of bone adaptation to its natural non-uniform loading conditions.
Combining the characterised local material properties and crack initiation and evolution techniques based on fracture mechanics, the developed microstructured model of the bone tissue adequately characterizes the non-linear fracture processes in it caused by impact loading. The further implementation of the hybrid SPH/continuum FE model enables the numerical realisation of the anisotropic deformation and damage evolution in the vicinity of the tool-bone interaction zone and povides valuble insights for further development of advanced surgical devices.

Acknowledgements

The authors acknowledge the financial support from EPSRC UK (Grant no. EP/G048886/1) and from the 7^{th} European Community Framework Programme through a Marie Curie International Research Staff Exchange Scheme (IRSES) Project TAMER (Grant PIRSES-GA-2013-610547).

References

[1] A. Abdel-Wahab, A. Maligno; V.V. Silberschmidt,Dynamic properties of cortical bone tissue: Izod tests and numerical study. CMC: Computers, Mater. Continua, 2010, Vol. 19, pp. 217-238.

[2] S. Li, A. Abdel-Wahab, E. Demirci, V.V. Silberschmidt, Fracture process in cortical bone: X-FEM analysis of microstructured models, Int. J. Fracture, 2013, Vol. 184(1), pp. 43-55.

[3] A. Abdel-Wahab, K. Alam, V.V. Silberschmidt, Analysis of anisotropic viscoelasto-plastic properties of cortical bone tissues. J. Mech. Behav. Biomed. Mater., 2011, Vol. 4, pp. 807-820.

[4] S. Li, A. Abdel-Wahab, V.V. Silberschmidt, Analysis of fracture processes in cortical bone tissue, Engng. Fracture Mech., 2013, Vol. 110, pp. 448-458.

[5] S. Li, A. Abdel-Wahab, E. Demirci, V.V. Silberschmidt, Penetration of cutting tool into cortical bone: Experimental and numerical investigation of anisotropic mechanical behaviour. J. Biomech., 2014, Vol. 47, pp. 1117-1126.

[6] S. Li, E. Demirci, V.V. Silberschmidt, Variability and anisotropy of mechanical behavior of cortical bone in tension and compression. J. Mech. Behav. Biomed. Mater., 2013

[7] S. Li, E. Demirci, V.V. Silberschmidt, Analysis of Deformation Characteristics of Cortical Bone Tissue, Solid State Phenom. 188, 118-123

[8] Ritchie, R.O., Kinney, J.H., Kruzic, J.J., Nalla, R.K., A fracture mechanics and mechanistic approach to the failure of cortical bone, Fatigue Fract Engng Mater Struct 28 345-371(2005)

[9] M.E. Launey, M.J. Buehler, R.O. Ritchie, On the mechanistic origins of toughness in bone, Annu. Rev. Mater. Sci. 40 25-53(2010).

[10] D.T. Reilly, A.H. Burstein, The elastic and ultimate properties of compact bone tissue, J. Biomech. 8 393-405(1975).

[11] ГҚ. Budyn, & T. Hoc, European Journal of Computational Mechanics/Revue EuropГқenne de MГқcanique NumГқrique, 16(2), 213-236. (2007).

[12] M. Wang, X. Gao, S.Li, A. A. Abdel-Wahab, E. A. Zimmermann, C. Riedel, B. Busse, & V. V. Silberschmidt, Effect of Micromorphology of Cortical Bone Tissue on Crack Propagation under Dynamic Loading, DYMAT. (in press)

Figures:

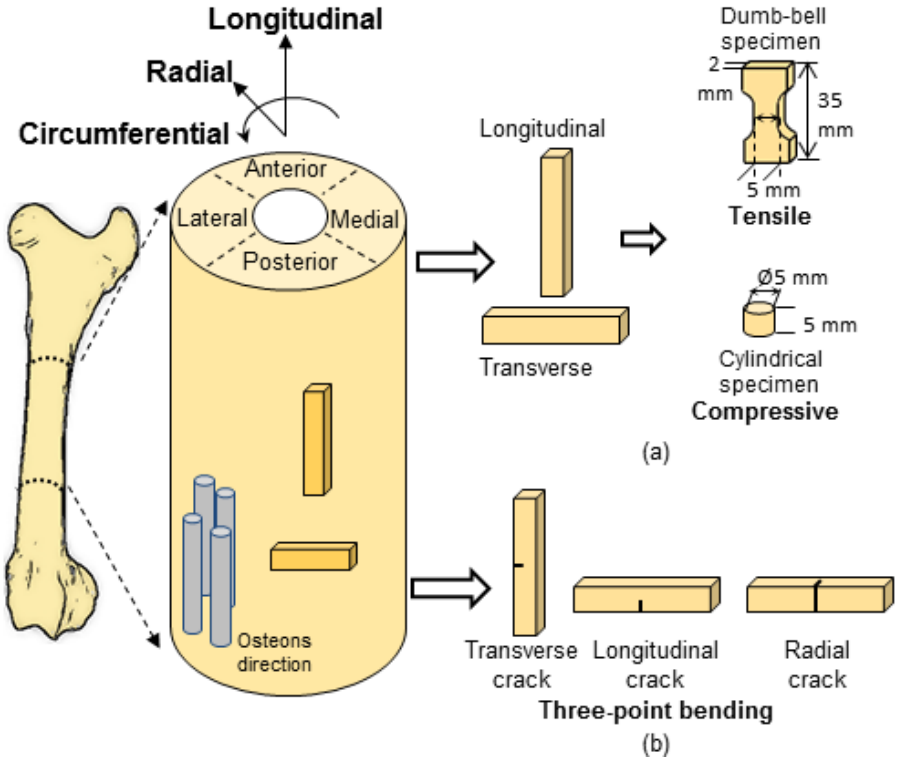

Figure 1: Fig. 1 Schematic illustration of specimen preparation process for: (a) uniaxial tension and compression tests; (b) three-point bending tests

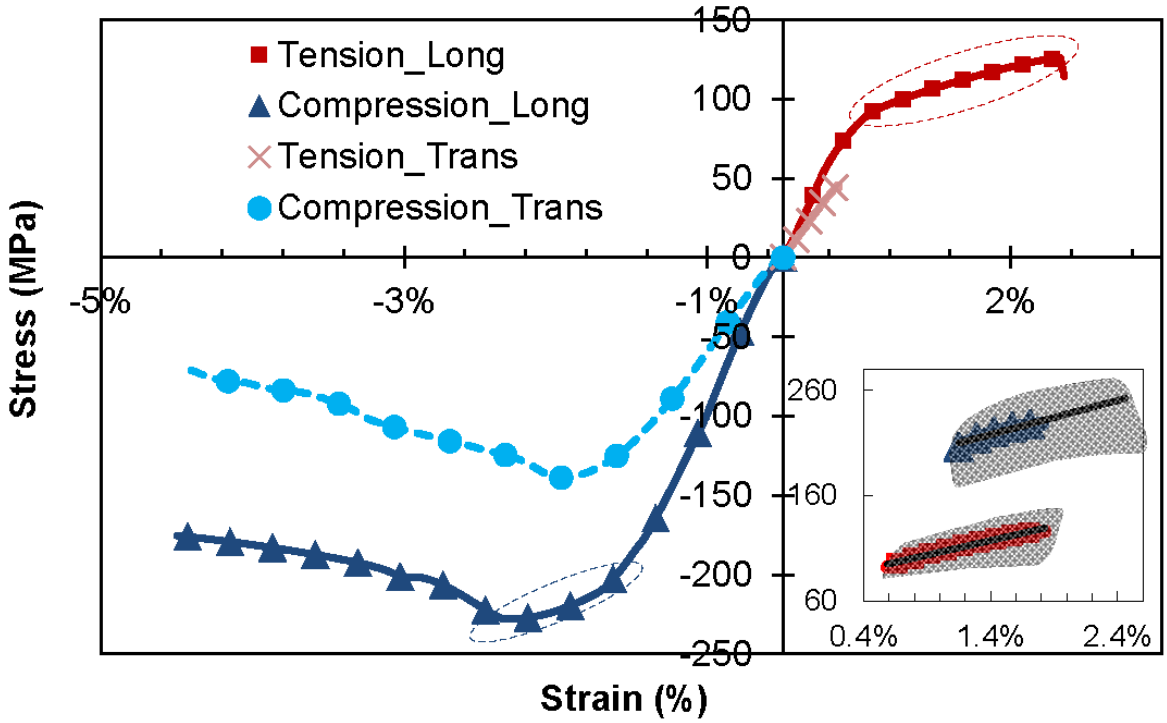

Figure 2: Fig. 2 Typical stress-strain curves for longitudinal & transverse specimens in tension and compression (anterior quadrant); Inserts show strengthening portions for longitudinal specimens

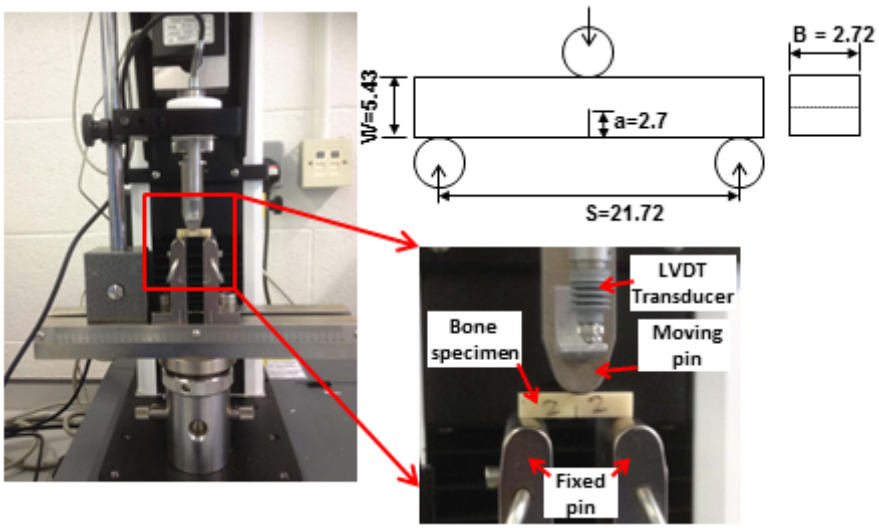

Figure 3: Fig. 3 Three-point bending test with single-edge-notch cortical bone specimen and LVDT mounted on Instron 3345

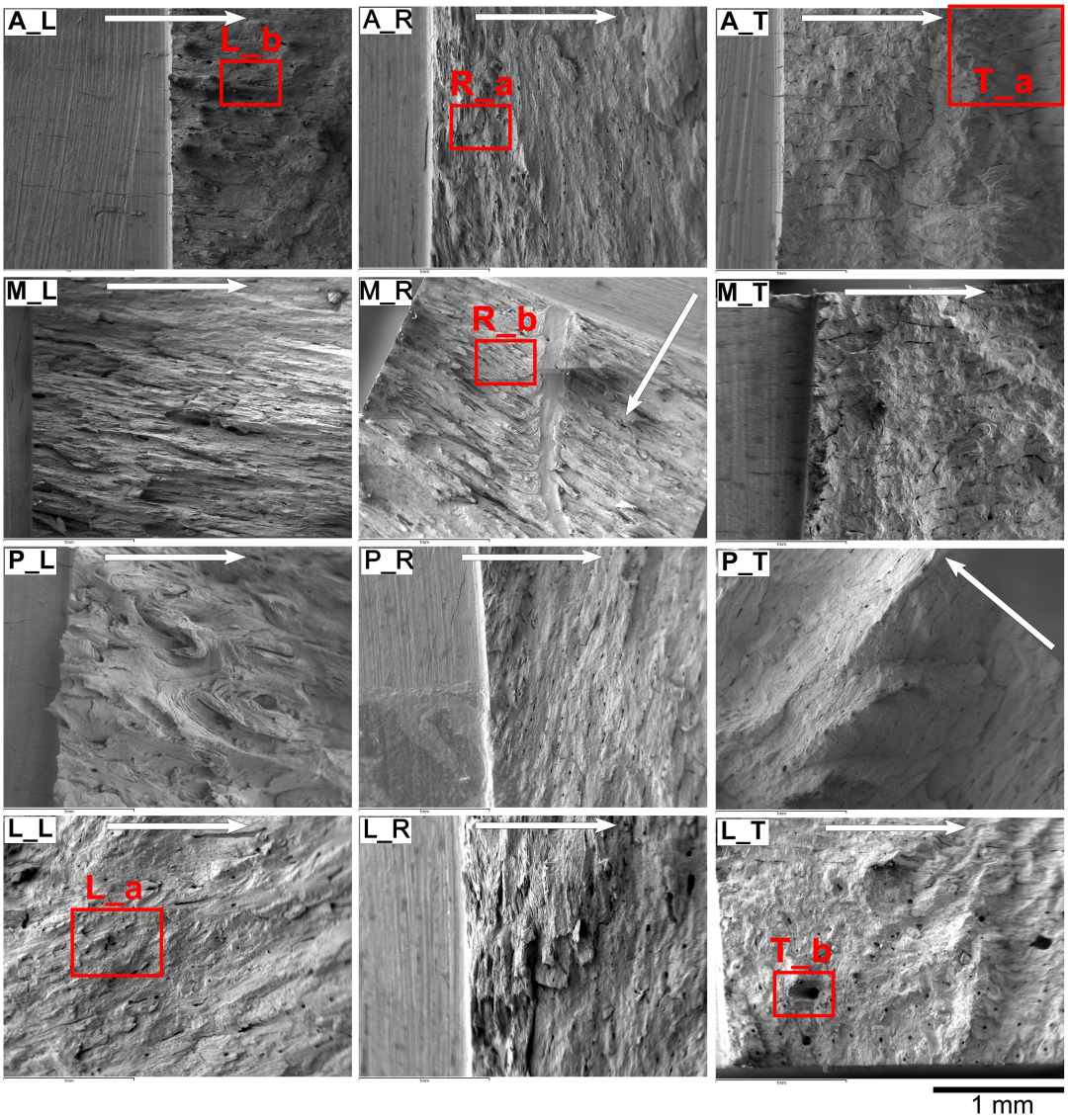

Figure 4: Fig. 4 SEM images of fracture surfaces for various cortex positions and crack propagation directions: A, M, P, L denote anterior, medial, posterior and lateral; _L, _R, _T denote crack propagation directions for longitudinal, radial and transverse ones, respectively, white arrows indicate crack growing direction

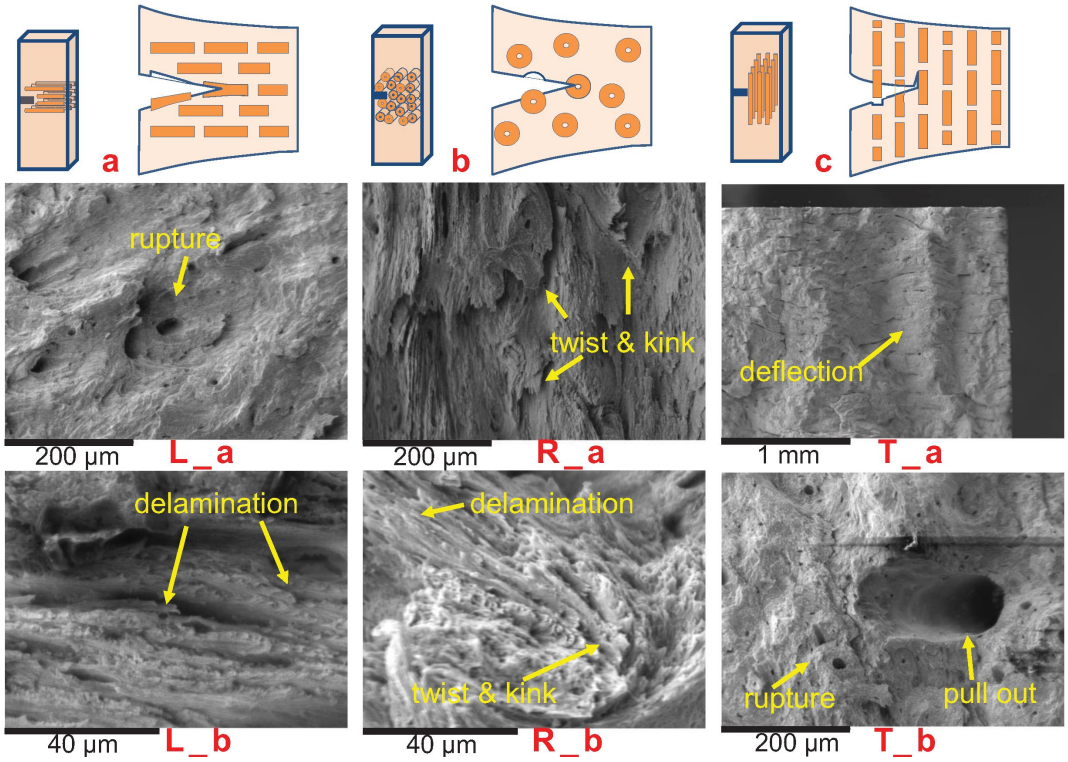

Figure 5: Fig. 5 Schematic illustrations and SEM images of various toughening mechanisms for longitudinal (a), radial (b) and transverse (c) cracks-growth directions, Labels at the bottom of each image indicate the corresponding magnified areas in Fig. 4

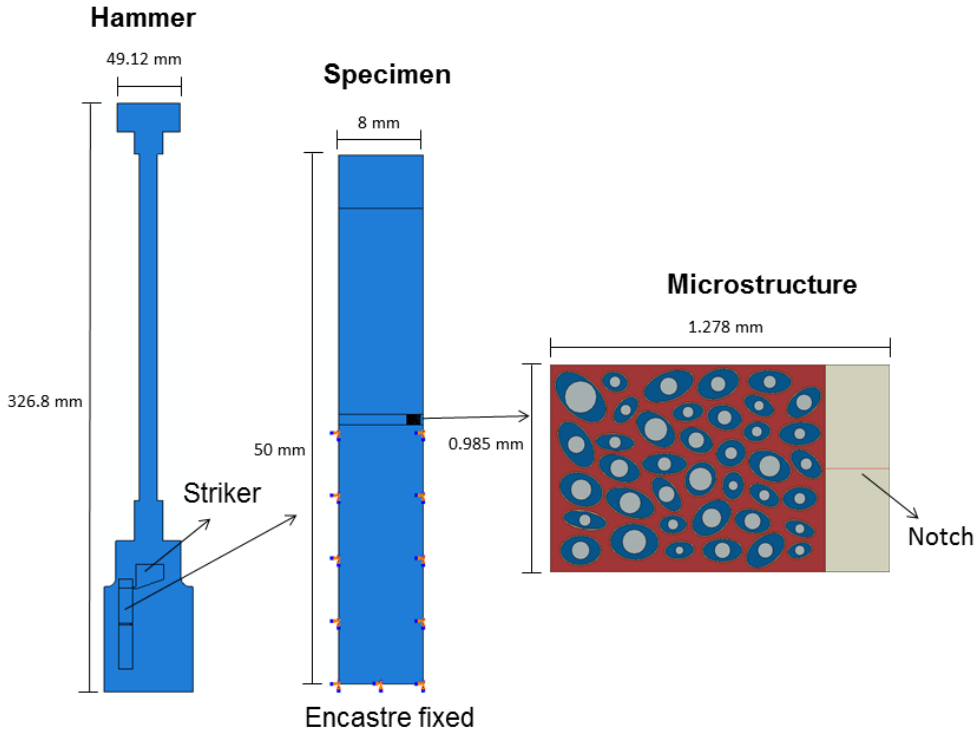

Figure 6: Fig. 6 Schematic illustrations of model configurations for Izod impact testing using microstructural bone model

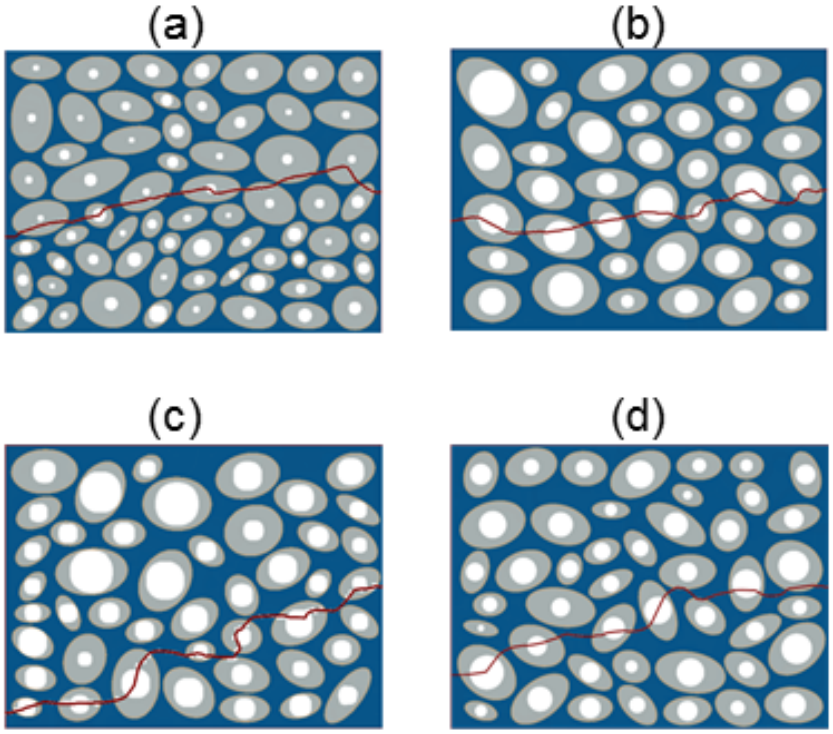

Figure 7: Fig. 7 Typical crack propagation of four different microstructure realizations (a) Young (b) Senior (c) Diseased (d) Treated

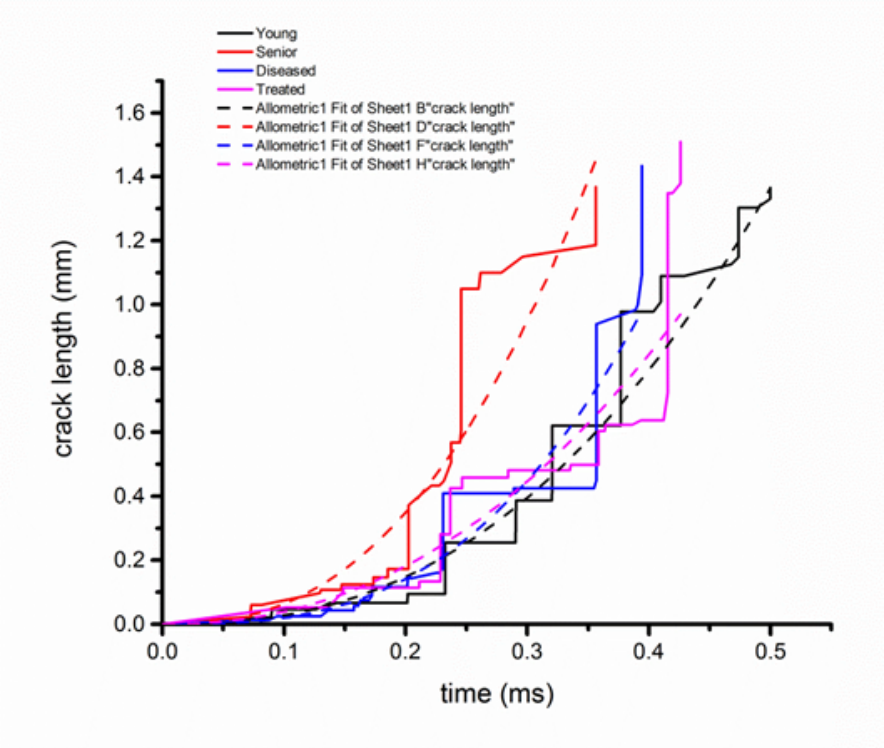

Figure 8: Fig. 8 Typical crack length versus time curves for different microstructural realizations

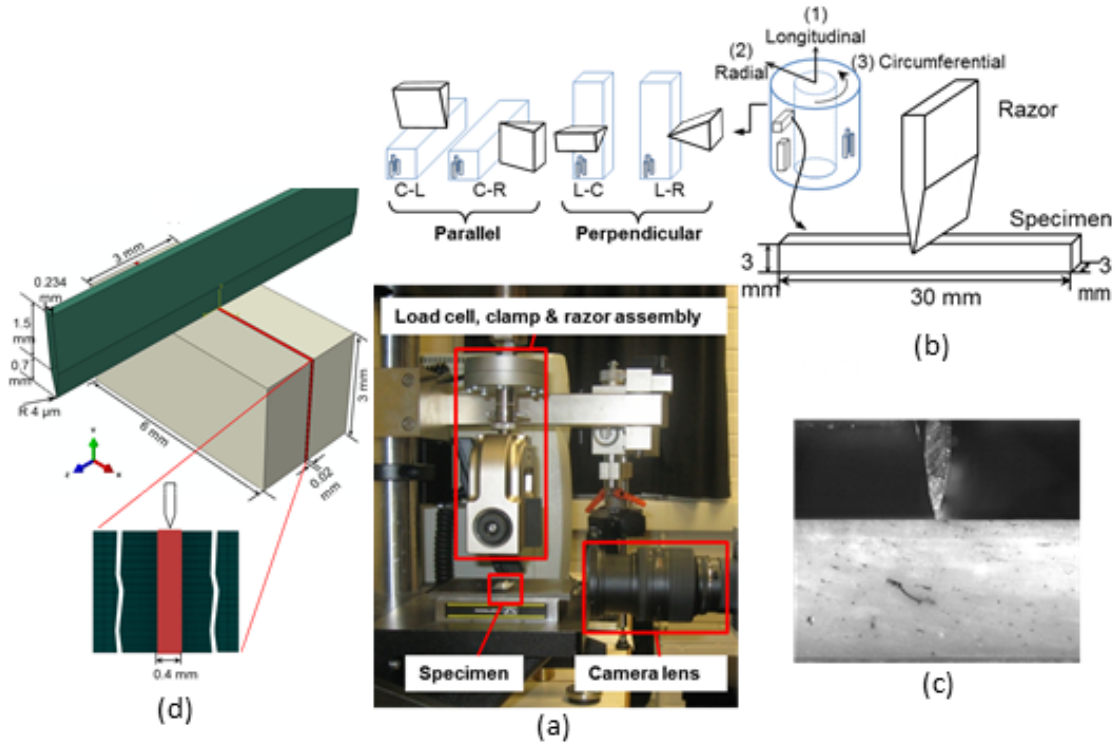

Figure 9: Fig. 9 (a) Notation of penetration directions according to ASTM E399 standard; (b) schematic of specimen preparation and cutting configuration; (c) setup for cutting experiments mounted on Instron MicroTester 5848; (c) superimposed image of razor and cortical-bone specimen taken with high-speed camera (Fastcam SA-3, Photron); (d) specification of model geometry

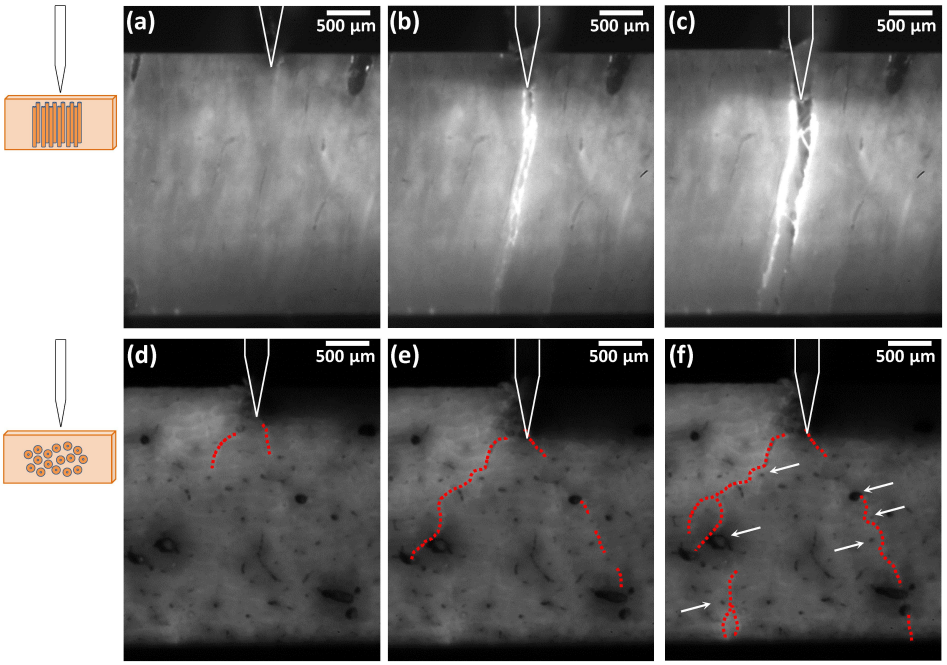

Figure 10: Fig. 10 High-speed-camera images of distinct damage processes in cutting parallel to osteons' direction,: (a-c) C-L direction; (d-f) C-R direction; white lines designate profile of razor blade, red dotted lines indicate crack path and white arrows point at positions of osteons

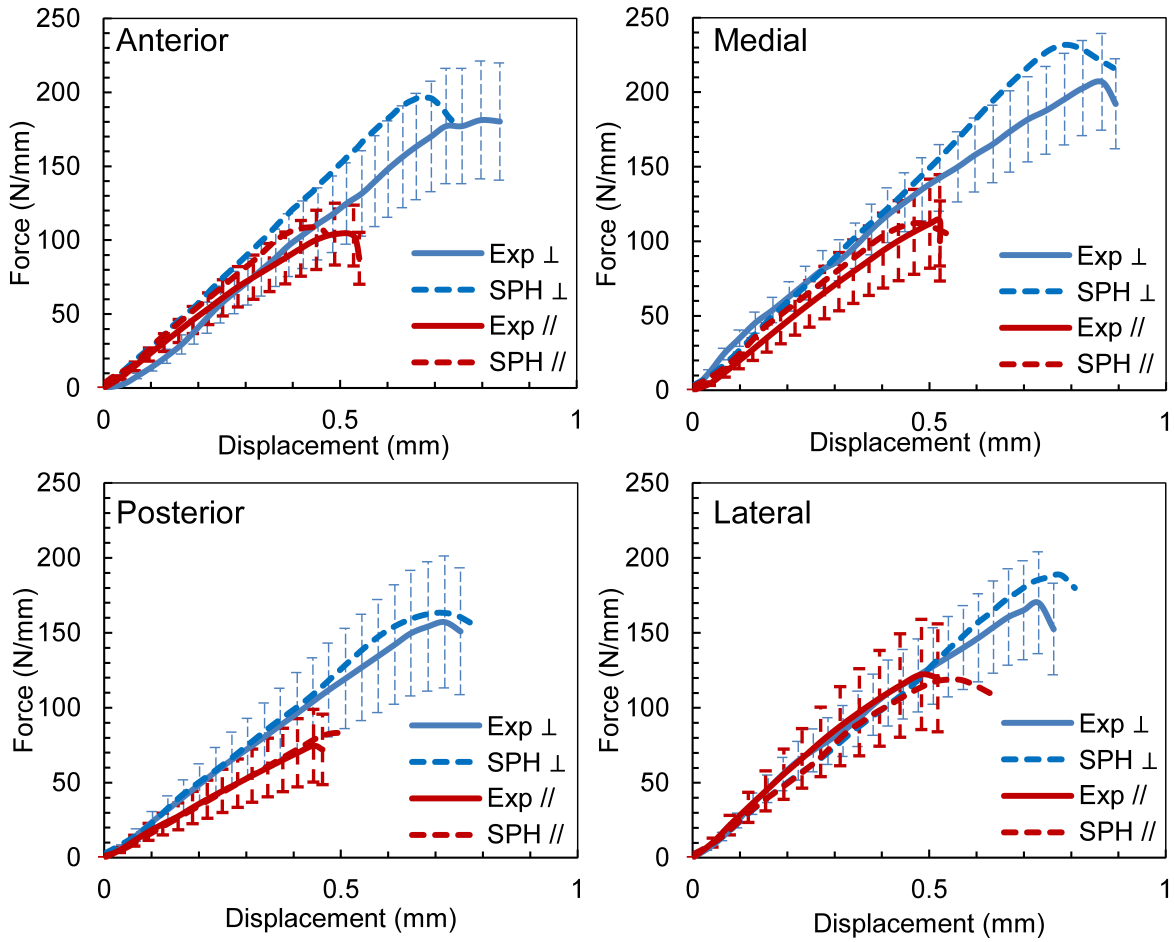

Figure 11: Fig. 11 Force (per unit width) - displacement diagrams for cutting of cortical bone in different orientations across four cortices; ⊥ and // denote penetration perpendicular and parallel to osteons' direction, respectively

Units: N/m	Anterior	Medial	Posterior	Lateral
	Mean SD	Mean SD	Mean SD	Mean SD
Longitudinal	1033.9 ±254.5	1768.5 ±98.8	1165.7 ±340.1	2034.3 ±509.9
Radial	1199.1 ±153.1	1418.2 ±97.2	983.0 ±369.5	2664.2 ±554.4
Transverse	4509.1 ±422.1	5925.5 ±802.9	3876.7 ±847.3	5661.6 ±452.7

Figure 12: Table 1 Average and standard deviation of critical J-integral values for all cortex positions and crack growth directions

	Elastic Modulus (GPa)	Poisson's Ratio	Strain Energy-Release Rate (N/mm)
Homogeneous material	10.46	0.167	0.422
Osteon	9.13	0.17	0.86
Interstitial matrix	14.122	0.153	0.238
Cement line	6.85	0.49	0.146

Figure 13: Table 2 Material properties of microstructural constituents of cortical-bone tissue and homogenous material

	Anterior	Posterior	Medial	Lateral
Density (kg/m^3)	2	2	2	2
E_1 (GPa)	23.2	19.3	21.1	15.1
E_2, E_3 (GPa)	13.2	9.9	14.7	11.2
v_{12}, v_{13}	0.27	0.27	0.27	0.27
v_{23}	0.39	0.39	0.39	0.39
G_{12}, G_{13} (GPa)	6.1	6.1	6.1	6.1
ε_{y1} (%)	1	1	1	1
ε_{f1}, ε_{f2} (%)	2	2	2	2
J_{IC1} (N/m)	1653	1534	1868	2664
J_{IC2} (N/m)	4087	3029	4765	4296

Figure 14: Table 3 Material properties used in simulations

Anisotropic ratio	Anterior	Posterior	Medial	Lateral
perpendicular /parallel	1.80	2.15	1.95	1.43

Figure 15: Table 4 Anisotropic ratios for different penetration directions for four anatomic cortices

Vadim V. Silberschmidt Wolfson School of Mechanical and Manufacturing Engineering Loughborough University Loughborough Leicestershire LE11 3TU, U.K.

Generalized Continua and Size Effects in Elastostatic Bending Experiments

Christian Liebold, Wolgfang H. Müller
Christian.Liebold@TU-Berlin.de

Abstract

In this work we deal with a finite element approach to the modified strain gradient theory, which will be used to describe size dependent material behavior within the framework of an elastic theory. The couple stress-, strain gradient-, and material surface theories are analyzed in context with beam bending. The derivation of a variational formulation of the modified strain gradient theory is presented and implemented in an open-source FE-environment for solution. By using an atomic force microscope to record force and deflection data of micro-cantilevers made of the material epoxy, a size effect is revealed and higher-order material coefficients could be measured and obtained.

Introduction

Driven by miniaturization and by the quest for reducing the costs of materials the simulation and the valuation of reliability of engineering materials grows in importance. Size effects in elasticity need to be accounted for, either in a physically detailed manner, or as an alternative technique of homogenization. Materials with intrinsic micro- or nano-structure may show size-dependent material behavior, which is reflected by a stiffer or softer elastic response to external forces when the size of the material body is reduced. This has been observed in several experiments on metals and polymers, for example, in copper [8], silver [15], zinc oxide [21], lead [4], carbon nanotubes [20], epoxy [3] and polypropylene [16]. Conventional (Cauchy-) continuum theory is unable to predict size effects. Several continua of higher order were proposed in the literature, such as *non-local theories* [7], *strain gradient theories* [18], *micropolar theories* [5, 19], *theories of material surfaces* [10] or *fractional continuum mechanics* [2].

1 Some continuum mechanical theories of higher order

With respect to size effects we distinguish between micromorphic and strain gradient theories [7] as an extension to the conventional CAUCHY continuum. Additionally, the theory of elastic material surfaces [10] is taken into account. The origin of generalized continua is detailed in [1]. By quoting ERINGEN (*cf.* [6], pp. 33) we may state that "a *micromorphic continuum* may be thought of as a classical continuum to each point of which is associated another continuum." The additional continuum, thought as a continuous distribution of deformable point particles, is restricted to homogeneous deformations[1]. The intrinsic deformation of the point particles is described by directors, which are first-order tensors "attached" to each material point. A second-order tensor Q_{ij} maps the particle's orientation and deformation between different configurations. In the special case of a *micropolar continuum*, Q_{ij} is an arbitrary proper orthogonal tensor. The point particles are restricted to rotations only. In the Couple Stress-, or pseudo-COSSERAT continuum (CS), the rotational degree of freedom φ_i of the associated continuum is related to the macroscopic rotation vector $\frac{1}{2}\epsilon_{ijk}u_{k,j}$, where use is made of the summation convention on repeated indices. In what follows comma separated indices denote partial spatial derivatives with respect to a Cartesian coordinate system defined in the current frame.
The theory of material surfaces, a.k.a. *Surface Elasticity* (SE), captures surface characteristics that may differ from those of the volume. For example, these differences are caused by surface oxidation, aging, coating, atomic and molecular rearrangement or even surface roughness. Discrete formulae for the problem of simple beam bending are given, using the EULER-BERNOULLI assumptions for the displacement field u_i. From these relations, generalized elastic moduli for isotropic materials of the CS- and SE theory read [22, 17]:

$$E_{\mathrm{CS}} = E\left(1 + 6\frac{\ell^2}{T^2}\right), \quad E_{\mathrm{SE}} = E + E^{\mathrm{surf}}\left(\frac{6}{T} + \frac{2}{W}\right), \tag{1}$$

where E denotes the conventional YOUNG's modulus, and T the thickness of beams with rectangular cross-sections, W being their width, and ℓ, as well as E^{surf} the corresponding additional material parameters of the underlying higher order theory.

In contrast to micromorphic continua and to the theory of material surfaces, the idea behind *Strain Gradient theories* (SG) is the extension of the kinematic variables by defining second order derivatives of the displacement vector, without introducing additional degrees of freedom. Hence, the gradient of the small strain tensor $\tilde{\eta}_{ijk} = \varepsilon_{kj,i}$ is used explicitly in the strain energy density u and it is connected to stress measures as follows [18]:

$$u^{\mathrm{SG}} = u(\varepsilon_{ij}, \tilde{\eta}_{ijk}) \ , \quad \sigma_{ij} = \frac{\partial u^{\mathrm{SG}}}{\partial \varepsilon_{ij}} \ , \quad \mu_{ijk} = \frac{\partial u^{\mathrm{SG}}}{\partial \tilde{\eta}_{ijk}} \ , \tag{2}$$

where σ_{ij} denotes the CAUCHY stress tensor and μ_{ijk} the higher-order stress tensors.

[1] The displacement gradient is constant for the (sub-)body.

2 The Modified Strain Gradient theory (MSG)

The decomposition of $\tilde{\eta}_{ijk}$ in combination with utilizing the macroscopic rotation vector φ_i results in a reduction of independent additional material parameters from five down to three. Fleck & Hutchinson (1997) [9] first introduced independent metrics of $\eta_{ijk} = u_{k,ij}$ and decomposed the second order displacement gradient into its symmetric and anti-symmetric part, $\bar{\bar{\eta}}_{ijk}$ and η^{A}_{ijk}:

$$\bar{\bar{\eta}}_{ijk} = \tfrac{1}{3}\left(u_{k,ij} + u_{i,jk} + u_{j,ki}\right) \ , \quad \eta^{\mathrm{A}}_{ijk} = \tfrac{2}{3}\left(\epsilon_{ikl}\bar{\eta}_{lj} + \epsilon_{jkl}\bar{\eta}_{li}\right) \ , \tag{3}$$

where $\bar{\eta}_{ij} = \varphi_{i,j}$ is the gradient of rotation (decomposed into its symmetric and anti-symmetric part, χ^{S}_{ij} and χ^{A}_{ij} as well):

$$\bar{\eta}_{ij} = \tfrac{1}{2}\epsilon_{ilk}u_{k,lj}\,, \quad \varphi_i = \tfrac{1}{2}\epsilon_{ilk}u_{k,l}\,, \quad \chi^{\mathrm{A}}_{ij} = \tfrac{1}{2}\left(\varphi_{i,j} - \varphi_{j,i}\right), \quad \chi^{\mathrm{S}}_{ij} = \tfrac{1}{2}\left(\varphi_{i,j} + \varphi_{j,i}\right), \tag{4}$$

ϵ_{ilk} being the alternating tensor (Levi-Civita symbol). $\bar{\bar{\eta}}_{ijk}$ is further decomposed into its spherical and deviatoric parts, $\eta^{(0)}_{ijk}$ and $\eta^{(1)}_{ijk}$. $\eta^{(0)}_{ijk}$ is related to χ^{A}_{ij} and the dilatation gradient $\varepsilon_{mm,i}$ in the following manner [9]:

$$\eta^{(0)}_{ijk} = \tfrac{1}{5}(\delta_{ij}\bar{\bar{\eta}}_{mmk} + \delta_{jk}\bar{\bar{\eta}}_{mmi} + \delta_{ki}\bar{\bar{\eta}}_{mmj}) \ , \quad \bar{\bar{\eta}}_{mmi} = \varepsilon_{mm,i} + \tfrac{2}{3}\epsilon_{iln}\chi^{\mathrm{A}}_{ln} \ . \tag{5}$$

By assuming symmetry of the couple stress tensor μ_{ij}, the anti-symmetric part of the gradient of rotation does not influence the strain energy, as shown in [13, 22]. A linear strain energy density for nonsimple isotropic materials of the modified gradient type reads:

$$u^{\mathrm{MSG}} = \hat{u}(\varepsilon_{ij}, \varepsilon_{mm,i}, \eta^{(1)}_{ijk}, \chi^{\mathrm{S}}_{ij}) = \tfrac{1}{2}\sigma_{ij}\varepsilon_{ij} + \tfrac{1}{2}p_i\varepsilon_{mm,i} + \tfrac{1}{2}\mu^{(1)}_{ijk}\eta^{(1)}_{ijk} + \tfrac{1}{2}\mu_{ij}\chi^{\mathrm{S}}_{ij} \ , \tag{6}$$

and the corresponding work-conjugated stress measures are:

$$\begin{aligned} \sigma_{ij} &= \frac{\partial u^{\mathrm{MSG}}}{\partial \varepsilon_{ij}} = \lambda\varepsilon_{kk}\delta_{ij} + 2\mu\varepsilon_{ij} \quad , \quad p_i = \frac{\partial u^{\mathrm{MSG}}}{\partial \varepsilon_{nn,i}} = 2\mu\ell_0^2\varepsilon_{mm,i} \\ \mu^{(1)}_{ijk} &= \frac{\partial u^{\mathrm{MSG}}}{\partial \eta^{(1)}_{ijk}} = 2\mu\ell_1^2\eta^{(1)}_{ijk} \quad , \qquad \mu_{ij} = \frac{\partial u^{\mathrm{MSG}}}{\partial \chi^{\mathrm{S}}_{ij}} = 2\mu\ell_2^2\chi^{\mathrm{S}}_{ij} \ . \end{aligned} \tag{7}$$

λ and μ are Lamé's constants, whereas $\ell_0 = \ell_1 = \ell_2 = \ell$ denote the additional material length scale parameters, which are chosen to be equal to ℓ without providing further arguments.

3 Finite element approach

A solution strategy for the modified strain gradient theory is presented using finite elements in context with the open-source FE-project FEniCS©, [14]. It allows to directly implement variational formulations of partial differential equations.

3.1 Variational formulation of MSG theory

The starting point is the local form of the equilibrium equation of the linear momentum of MSG theory, given by [12]:

$$\sigma_{ik,i} - p_{i,ik} - \mu^{(1)}_{ijk,ij} - \tfrac{1}{2}\epsilon_{jlk}\mu_{ij,il} + f_k = \rho\ddot{u}_k \ . \tag{8}$$

The variational formulation of the strain energy in a global formulation results after multiplication of an arbitrary first-order tensor function for displacements (so-called test function) δu_k:

$$\int\limits_V \Big(\sigma_{ik,i}\delta u_k - p_{i,ik}\delta u_k - \mu^{(1)}_{ijk,ij}\delta u_k - \tfrac{1}{2}\epsilon_{jlk}\mu_{ij,il}\delta u_k\Big)\,\mathrm{d}V = 0 \ , \tag{9}$$

where the body-force vector f_k is set to be equal to zero and static conditions are assumed. In view of the so-called test function u_k, Eqn. (9) represents a partial differential equation of fourth order. Reduction from fourth-order to a third-order differential equation is achieved by applying, first, the product rule for differentiation to each summand:

$$\begin{aligned}
\int\limits_V \sigma_{ik,i}\delta u_k \mathrm{d}V &= \int\limits_V \left(\sigma_{ik}\delta u_k\right)_{,i}\mathrm{d}V - \int\limits_V \sigma_{ik}\delta u_{k,i}\mathrm{d}V \ , \\
\int\limits_V p_{i,ik}\delta u_k \mathrm{d}V &= \int\limits_V \left(p_{i,i}\delta u_k\right)_{,k}\mathrm{d}V - \int\limits_V p_{i,i}\delta u_{k,k}\mathrm{d}V \ , \\
\int\limits_V \mu^{(1)}_{ijk,ij}\delta u_k \mathrm{d}V &= \int\limits_V \left(\mu^{(1)}_{ijk,i}\delta u_k\right)_{,j}\mathrm{d}V - \int\limits_V \mu^{(1)}_{ijk,i}\delta u_{k,j}\mathrm{d}V \ , \\
\int\limits_V \tfrac{1}{2}\epsilon_{jlk}\mu_{ij,il}\delta u_k \mathrm{d}V &= \int\limits_V \left(\tfrac{1}{2}\epsilon_{jlk}\mu_{ij,i}\delta u_k\right)_{,l}\mathrm{d}V - \int\limits_V \tfrac{1}{2}\epsilon_{jlk}\mu_{ij,i}\delta u_{k,l}\mathrm{d}V \ ,
\end{aligned} \tag{10}$$

and, second, Gauss' theorem to transform volume into surface integrals:

$$\begin{aligned}
\int\limits_V \sigma_{ik,i}\delta u_k \mathrm{d}V &= \oint\limits_{\partial V} \sigma_{ik}\delta u_k n_i \mathrm{d}A - \int\limits_V \sigma_{ik}\delta u_{k,i}\mathrm{d}V \ , \\
\int\limits_V p_{i,ik}\delta u_k \mathrm{d}V &= \oint\limits_{\partial V} p_{i,i}\delta u_k n_k \mathrm{d}A - \int\limits_V p_{i,i}\delta u_{k,k}\mathrm{d}V \ , \\
\int\limits_V \mu^{(1)}_{ijk,ij}\delta u_k \mathrm{d}V &= \oint\limits_{\partial V} \mu^{(1)}_{ijk,i}\delta u_k n_j \mathrm{d}A - \int\limits_V \mu^{(1)}_{ijk,i}\delta u_{k,j}\mathrm{d}V \ , \\
\int\limits_V \tfrac{1}{2}\epsilon_{jlk}\mu_{ij,il}\delta u_k \mathrm{d}V &= \oint\limits_{\partial V} \tfrac{1}{2}\epsilon_{jlk}\mu_{ij,i}\delta u_k n_l \mathrm{d}A - \int\limits_V \tfrac{1}{2}\epsilon_{jlk}\mu_{ij,i}\delta u_{k,l}\mathrm{d}V \ .
\end{aligned} \tag{11}$$

The reduction from a third-order to a second-order differential equation is achieved by a second manipulation of this kind to Eqns. $(11)_2$, $(11)_3$ and $(11)_4$:

$$\begin{aligned}
\int_V p_{i,i}\delta u_{k,k}\mathrm{d}V &= \oint_{\partial V} p_i\delta u_{k,k}n_i\mathrm{d}A - \int_V p_i\delta u_{k,ki}\mathrm{d}V\ ,\\
\int_V \mu^{(1)}_{ijk,i}\delta u_{k,j}\mathrm{d}V &= \oint_{\partial V} \mu^{(1)}_{ijk}\delta u_{k,j}n_i\mathrm{d}A - \int_V \mu^{(1)}_{ijk}\delta u_{k,ji}\mathrm{d}V\ ,\\
\int_V \tfrac{1}{2}\epsilon_{jlk}\mu_{ij,i}\delta u_{k,l}\mathrm{d}V &= \oint_{\partial V} \tfrac{1}{2}\epsilon_{jlk}\mu_{ij}\delta u_{k,l}n_i\mathrm{d}A - \int_V \tfrac{1}{2}\epsilon_{jlk}\mu_{ij}\delta u_{k,li}\mathrm{d}V\ .
\end{aligned} \tag{12}$$

We now insert Eqns. (11) and (12) into (9) and separate volume from surface integrals:

$$\begin{aligned}
&-\int_V \left(\sigma_{ik}\delta u_{k,i} + p_i\delta u_{k,ki} + \mu^{(1)}_{ijk}\delta u_{k,ji} + \tfrac{1}{2}\epsilon_{jlk}\mu_{ij}\delta u_{k,li}\right)\mathrm{d}V =\\
&\oint_{\partial V}\left(-\sigma_{ik}n_i\delta u_k + p_{i,i}n_k\delta u_k + \mu^{(1)}_{ijk,i}n_j\delta u_k + \tfrac{1}{2}\epsilon_{jlk}\mu_{ij,i}n_l\delta u_k\right)\mathrm{d}A -\\
&\qquad\oint_{\partial V}\left(p_in_i\delta u_{k,k} + \mu^{(1)}_{ijk}n_i\delta u_{k,j} + \tfrac{1}{2}\epsilon_{jlk}\mu_{ij}n_i\delta u_{k,l}\right)\mathrm{d}A\ .
\end{aligned} \tag{13}$$

We identify the resulting boundary conditions for the surface-traction vector $\bar{t}_k$:

$$\begin{aligned}
&\oint_{\partial V}\left(\sigma_{ik}n_i - p_{i,i}n_k - \mu^{(1)}_{ijk,i}n_j - \tfrac{1}{2}\epsilon_{jlk}\mu_{ij,i}n_l\right)\delta u_k\mathrm{d}A =\\
&\qquad\oint_{\partial V}\underbrace{\left(\sigma_{ik} - p_{j,j}\delta_{ik} - \mu^{(1)}_{lik,l} - \tfrac{1}{2}\epsilon_{jik}\mu_{lj,l}\right)n_i}_{\bar{t}_k}\delta u_k\mathrm{d}A\ ,
\end{aligned} \tag{14}$$

the surface double-traction tensor $\bar{m}_{jk}$, as well as the surface dilatation vector $\bar{p}_i$:

$$\begin{aligned}
&\oint_{\partial V}\left(p_in_i\delta u_{k,k} + \mu^{(1)}_{ijk}n_i\delta u_{k,j} + \tfrac{1}{2}\epsilon_{jlk}\mu_{ij}n_i\delta u_{k,l}\right)\mathrm{d}A\ =\\
&\oint_{\partial V}\underbrace{p_i}_{\bar{p}_i}n_i\delta u_{k,k}\mathrm{d}A + \oint_{\partial V}\underbrace{\left(\mu^{(1)}_{ijk} + \tfrac{1}{2}\epsilon_{ljk}\mu_{il}\right)n_i}_{\bar{m}_{jk}}\delta u_{k,j}\mathrm{d}A\ .
\end{aligned} \tag{15}$$

$\bar{m}_{jk}$ and $\bar{p}_i$ are set equal to zero, since in practice they are difficult to realize and apply anyway. The final variational formulation of the MSG theory reads:

$$\boxed{\int_V \left(\sigma_{ik}\delta u_{k,i} + p_i\delta u_{k,ki} + \mu^{(1)}_{ijk}\delta u_{k,ji} + \tfrac{1}{2}\epsilon_{jlk}\mu_{ij}\delta u_{k,li}\right)\mathrm{d}V = \oint_{\partial V}\bar{t}_k\delta u_k\mathrm{d}A}\ . \tag{16}$$

3.2 Model implementation and boundary conditions

We follow a three-dimensional elasto-static finite element analysis of a cantilever beam (clamped on one side). DIRICHLET boundary conditions are applied to the surface at $x = 0$, and a surface-traction vector $\bar{t}_k = (0, 0, \text{-}F/A)$ acts on the surface at $x = L$, where F and A are a single point force and the cross-sectional area of the beam, respectively, *cf.* Fig. (1). The GALERKIN method is used for spatial discretization. The mesh consists of equidistantly distributed tetrahedral continuous LAGRANGE elements with a polynomial degree of two, corresponding to the order of the resulting partial differential equation (16). The system matrix is solved by using the method of GAUSSian elimination (LU, for a lower/upper decomposition) with low effort in time. The conventional elastic coefficients were chosen to be $E = 3.8$ GPa and $\nu = 0.38$, which are suitable for the material epoxy [11].

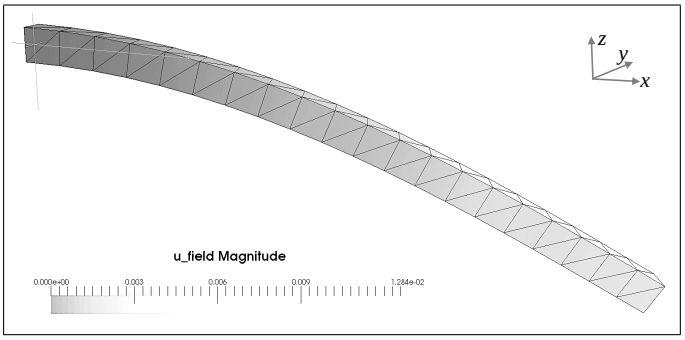

Figure 1: Mesh and deformation of a cantilever beam calculated in FeniCS©.

3.3 Analysis of the FE model

In a post-processing algorithm of the numerical solution, the present FE-model is analyzed regarding to the behavior of the higher-order stress measures presented in Eqn. (7). In addition to the deflection u_z we calculate the following quantities:

- the y-component of the rotation vector: $\varphi_y = \frac{1}{2}\epsilon_{yij}\, u_{j,i}$,
- an equivalent dilatation stress: $p_{\text{eqv}} = \sqrt{p_i p_i}$,
- an equivalent couple stress: $\mu_{\text{eqv}} = \sqrt{\mu_{ij}\mu_{ij}}$,
- an equivalent strain: $\varepsilon_{\text{eqv}} = \sqrt{\varepsilon_{ij}\varepsilon_{ij}}$,
- and an equivalent double-stress: $\mu^{(1)}_{\text{eqv}} = \sqrt{\mu^{(1)}_{ijk}\mu^{(1)}_{ijk}}$,

each along a line at $y = W/2$ and $z = T$ (cf. Fig. (2), (3) and (4)), where T is the thickness of the beam.

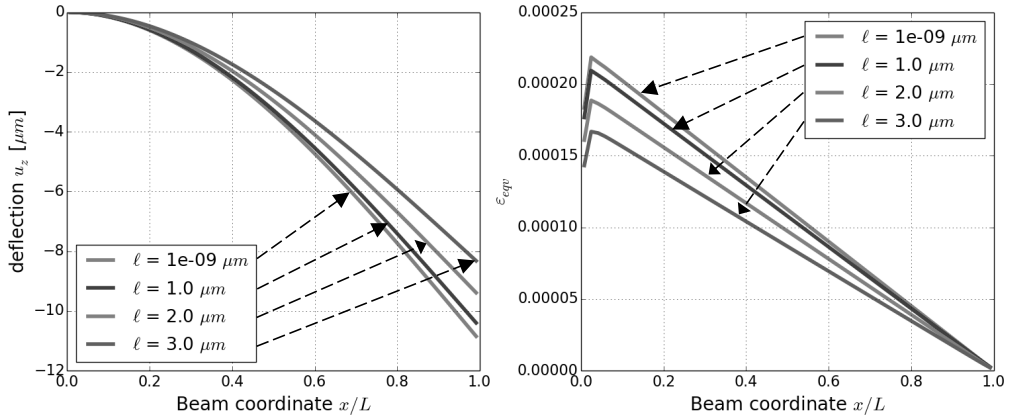

Figure 2: Deflections and equivalent strains along the line at $z = T$.

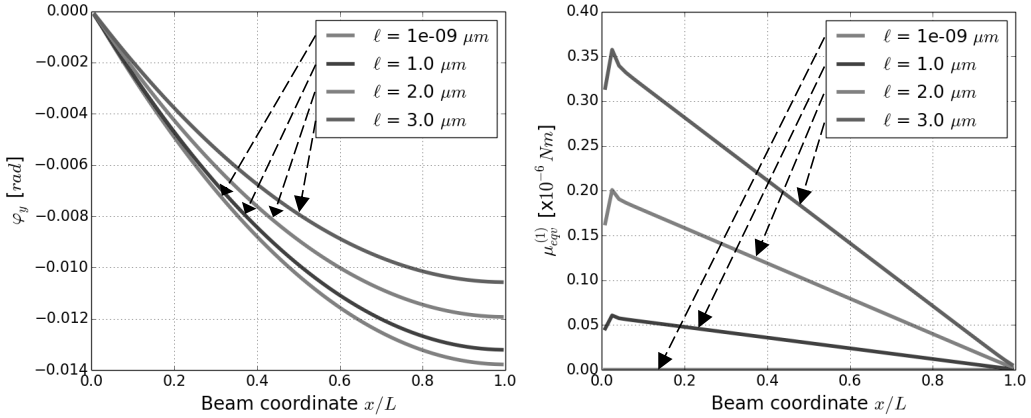

Figure 3: y-component of the rotation vectors and equivalent double-stresses.

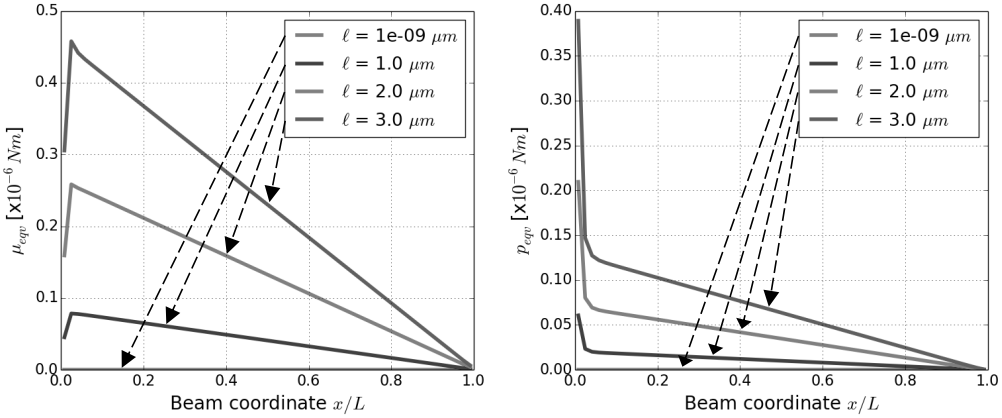

Figure 4: Equivalent couple stresses and equivalent dilatation stresses.

If ℓ is set equal to zero (ℓ=1x10^{-15} m), the solutions converge to the classical continuum solution, where there is no p_{eqv}, μ_{eqv}, and $\mu^{(1)}_{\mathrm{eqv}}$. If ℓ is increased, u_z, φ_y and $\varepsilon_{\mathrm{eqv}}$ decrease, while the corresponding higher-order stress measures p_{eqv}, μ_{eqv}, and $\mu^{(1)}_{\mathrm{eqv}}$ increase. The deviations close to the beam coordinate at $x=0$ in Fig's. (2), (3) and (4) are caused by a more complex stress state due to the boundary condition that is used for the clamped surface.

4 Experimental analysis

Static bending tests were performed on freestanding micro-beam structures made of epoxy. A load of $0.5 < F < 250$ μN was applied by using an off-axis laser-reflective Atomic Force Microscope (AFM) and deflections of 40 nm $< w <$ 10.0 μm were recorded. By assuming rectangular cross-sections of the specimens, the classical relation,

$$E^* = \frac{4L^3}{WT^3}\frac{F}{w} \,, \tag{17}$$

between the AFM measures (F/w) and the elastic modulus from the measurement E^* was used, where L is the length of the beam. The specimens had ratios of width to thickness of $W/T \approx 2$–5 and length to thickness of $L/T \approx 15$–40.

5 Results and conclusions

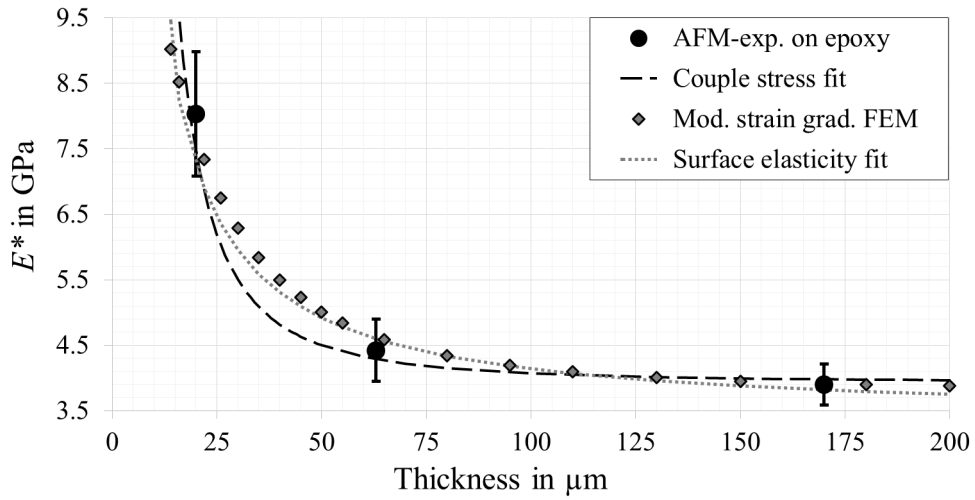

Figure 5: Results of the experiments, the couple stress model (Eqn. $(1)_1$), the surface elastic model (Eqn. $(1)_2$) and the finite element approach of the MSG theory

The results for the increasing elastic moduli are in very good agreement to the results of the couple stress and the surface elasticity analysis (both based on the Euler-Bernoulli assumptions) and to the AFM-experiments as well. The method of least squares gives the following values for the bulk elastic modulus and the corresponding additional material parameter: $E = 3.93$ GPa and $\ell = 7.75$ μm for the CS theory and $E = 3.37$ GPa and $E^{\text{surf}} = 1.3$ kN/m for the surface theory of elasticity. The FE-model for the MSG theory gives proper results in case of $E = 3.7$ GPa and $\ell = 7.9$ μm, see Fig. (5).

References

[1] Altenbach J., Altenbach H., Eremeyev V.A.: *On generalized Cosserat-type theories of plates and shells: A short review and bibliography.* Arch. Appl. Mech., **80**, pp. 73–92 (2010)

[2] Carpinteri A.: *Fractal nature of material microstructure and size effects on apparent mechanical properties.* Mechanics of Materials, **18**, pp. 89–101 (1994)

[3] Chong C.M.: *Experimental investigation and modeling of size effect in elasticity.* Dissertation, Hong Kong University of Science and Technology, 2002.

[4] Cuenot S., Fretigny C., Demoustier-Champagne S., Nysten B.: *Surface tension effect on the mechanical properties of nanomaterials measured by atomic force microscopy.* Physical Review B, **69**, pp. 01–05 (2004)

[5] Eringen A.C.: *A unified theory of thermomechanical materials.* Int. J. Engng. Sci., **4**, pp. 179–202 (1966)

[6] Eringen A.C.: *Continuum Physics. Vol. IV – Polar and nonlocal field theories.* Academic Press, INC. New York (1976)

[7] Eringen A.C.: *Nonlocal Continuum field theories.* Springer-Verlag, NY (2010)

[8] Fleck N.A., Muller G.M., Ashby M.F., Hutchinson J.W.: *Strain gradient plasticity: Theory and experiment.* Acta metall. mater., **42**(2), pp. 475–487 (1994)

[9] Fleck N.A., Hutchinson J.W.: *Strain gradient plasticity.* In: Hutchinson J.W., Wu T.Y. (Eds.), Adv. in Appl. Mech., **33**, Academic Press, NY, pp. 295–361 (1997)

[10] Gurtin M.E., Murdoch A.I.: *A continuum theory of elastic material surfaces.* ARMA, **57**(4), pp. 291–323 (1975)

[11] Lam D.C.C., Yang F., Chong C.M., Wang J., Tong P.: *Experiments and theory in strain gradient elasticity.* J. Mech. Phys. Sol., **51**(8), pp. 1477–1508 (2003)

[12] Li X.-F., Wang B.-L., Lee K.Y.: *Size Effect in the Mechanical Response of Nanobeams.* J. of Adv. Research in Mech. Eng., **1**(1), pp. 4–16 (2010)

[13] Liebold C., Müller W.H.: *Measuring material coefficients of higher gradient elasticity by using AFM techniques and Raman-spectroscopy.* In: Generalized continua as models for materials (Eds. Altenbach H., Forest S., Krivtsov A.), Advanced Structured Materials **22**, 2013, pp. 255–271.

[14] Logg A., Mardal K.-A., Wells G.N. et al.: *Automated solution of differential equations by the finite element method.* Springer, 2012, [doi:10.1007/978-3-642-23099-8].

[15] Ma Q., Clarke D.R.: *Size dependent hardness of silver single crystals.* Journal of Materials Research, **10**(4), pp. 853–863 (1995)

[16] McFarland A.W., Colton J.S.: *Role of material microstructure in plate stiffness with relevance to microcantilever sensors.* Journal of Micromechanics and Microengineering, **15**(5), pp. 1060–1067 (2005)

[17] Miller R.E., Shenoy V.B.: *Size-dependent elastic properties of nanosized structural elements.* Nanotechnology, **11**, pp. 139–147 (2000)

[18] Mindlin R.D., Eshel N.N.: *On first strain-gradient theories in linear elasticity.* International Journal of Solids and Structures, **4**, pp. 109-124 (1968)

[19] Nowacki W.: *Theory of micropolar elasticity.* CISM, Udine (1972)

[20] Salvetat J.-P., Kulik A.J., Bonard J.M., Briggs G.A.D., Stöckli T., Metenier K., Bonnamy S., Beguin F., Burnham N.A., Forró L.: *Elastic modulus of ordered and disordered multiwalled carbon nanotubes.* Adv. Mater. Weinheim, Ger., **11**, pp. 161165 (1999-b)

[21] Stan G., Ciobanu C.V., Parthangal P. M., Cook R.F.: *Diameter-dependent radial and tangential elastic moduli of ZnO nanowires.* Nano Letters, **7**(12), pp. 3691–3697 (2007)

[22] Yang F., Chong C.M., Lam D.C.C., Tong P.: *Couple stress based strain gradient theory for elasticity.* Int. J. of Sol. and Struct., **39**(10), pp. 2731–2743 (2002)

Christian Liebold, Wolfgang H. Müller
Berlin University of Technology, Faculty of Mechanics,
Chair of Continuum Mechanics and Materials Theory
Einsteinufer 5, 10587 Berlin, Germany

Indentation in single crystals

Qiang Liu, Murat Demiral, Anish Roy, Vadim V. Silberschmidt
A.Roy3@lboro.ac.uk

Abstract

The process of indentation in three types of single crystals (FCC copper, BCC Ti-64 and Ti-15-3-3) was investigated using crystal-plasticity modelling. In order to investigate the effects of strain gradient on nanoindentation, both conventional single-crystal-plasticity and mechanism-based strain-gradient crystal-plasticity models were employed. For each type of single crystal, idealized conical and spherical indenters were incorporated into indentation simulations. The simulation results indicate that realization of indentation size effect was significantly affected by the indenter geometry and imposed strain gradient. Indentation hardness decreased with depth for a conical indenter but increased for a spherical one in the range of small indentation depths.

1 Introduction

Modelling of micro-/nano-indentation of single crystals has been developed extensively to elucidate experimentally observed features such as the size effect, pile-up phenomenon and lattice rotations. For instance, Liu et al. [1] performed crystal-plasticity (CP) finite-element (FE) numerical simulations and micro-indentation experiments to determine mechanical properties of single-crystal copper. Lee and Chen [2] adopted a mechanism-based strain-gradient crystal-plasticity (MSGCP) theory to model the size effect in micro-indentation in the same material. Wang et al. [3] studied an effect of crystallographic orientation on pile-up patterns and micro-textures using a CP FE model for single-crystal copper. Correct numerical predictions of the surface pile-up patterns were achieved; however, a difference of an order of a magnitude in the load-displacement curve between experiments and simulations was reported. Liu et al. [1] performed a similar study using a spherical indenter instead of a conical one, where satisfactory agreements between the numerical and experimental load-displacement curves were demonstrated. However, different magnitudes of a coefficient of friction were used to represent a contact condition between the indenterвЂ™s tip and the workpiece material for different orientations to match numerically obtained surface profiles with the experimental data. An error of up to 50% was reported for a magnitude of the maximal pile-up. In the study of Demiral et al. [4], where both the incipient and evolving strain gradients were considered in the calibration procedure (unlike prior studies), a better agreement for the load-displacement curves and maximum pile-up heights was obtained. Zahedi et al. [5][6] studied the effects of crystal orientation on a cutting force and chip morphology in metal machining, where the continuum CP FE method was combined with smoothed particle hydrodynamics to overcome the problem of element distortion in CP FE simulations.

Some numerical studies have attempted to analyse physical deformation mechanisms leading to lattice rotations. For instance, Wang et al. [3] demonstrated lattice rotations for a single crystal of Cu with different orientations using a 3D elastic viscoplastic CP FE technique. Zaafarani et al. [7] proposed a physically based CP model based on dislocation-rate formulations to explain potential reasons for deformation-induced patterns consisting of multiple narrow zones with alternating crystalline rotations. However, the model consistently overestimated the extent of lattice rotations in the experiment. Demiral et al. [8] developed a 3D FE model of nano-indentation incorporating an enhanced model of the strain-gradient crystal plasticity [9] to simulate accurately deformation of a body-centred cubic metallic material. It was noted that deformation-induced lattice rotations can be predicted correctly using the strain-gradient CP theory since the effect of GNDs was accounted for (via strain gradients). This study demonstrated that the introduction of strain gradients altered the activity of slip systems and the relative contribution to the overall plastic slip.

2 Model

In this part, the indentation size effect(ISE) of three types of single crystals, namely, FCC copper, BCC β phase of Ti-6Al-4V (β-Ti-64) and BCC β phase of Ti-15V-3Cr-3Al-3Sn (β-Ti-15-3-3-3), was investigated using crystal-plasticity models. In indentation modelling, idealised conical and spherical indenters were chosen to study the effects of indenter's geometry on the mechanical response of the tested material. The chosen half-angle of the conical indenter was 72° and the radius of spherical indenter 2.5μm; dimensions of the modelled work-piece were $(16 \times 16 \times 8)\mu m^3$. The top surface of the modelled workpiece was free of constraints and normal displacements of all the other faces were fixed. Friction between the indenter and the indented surface was ignored for simplicity. The maximum indentation depths for all simulations was $h_{max} = 0.5\mu m$.
A crystal plasticity model was used to describe the material's behaviour of these single crystals during nanoindentation. It is well known that conventional CP models do not account for the deformation mechanism at the smallest length-scale accurately as they do not consider dislocation evolution and propagation explicitly. In our study, a conventional single-crystal plasticity (SCP) model [10] and the MSGCP model [11] were employed to compare and contrast the (de)merits of the two models. Both models had a similar constitutive framework, with the latter accounting for the effect of strain-gradients. The relationship between the shear rate $\dot{\gamma}^{(\alpha)}$ and resolved shear stress $\tau^{(\alpha)}$ on the slip system α is expressed by the power law proposed by Hutchinson [12], as

$$\dot{\gamma}^{(\alpha)} = \dot{\gamma}_0 |\frac{\tau^{\alpha}}{g^{\alpha}}|^n sgn(\tau^{\alpha}) \tag{1}$$

where $\dot{\gamma}_0$ is the reference shear rate, $g^{(\alpha)}$ is the slip resistance and n is the rate-sensitivity parameter. The evolution of $g^{(\alpha)}$ is given by

$$\dot{g}^{(\alpha)} = \sum_{i=1}^{n} h_{\alpha\beta} |\dot{\gamma}^{(\beta)}| \tag{2}$$

where $h_{\alpha\beta}$ is the hardening modulus that is calculated from the relation propose by Hutchinson [12]:

$$h_{\alpha\alpha} = h_0 sech^2(\frac{h_0\gamma}{\tau_s - \tau_0}), h_{\alpha\beta} = q h_{\alpha\alpha} (\alpha \neq \beta), \gamma = \sum_{\alpha} \int_0^t |\dot{\gamma}^{(\alpha)}| dt. \tag{3}$$

Here, h_0 is the initial hardening modulus, q is the latent hardening ratio, τ_0 and τ_s are the shear stresses at the onset of yield and the saturation of hardening, respectively. The accumulative shear strain over all the slip systems is represented by γ. Generally, τ_0 is equal to the value of initial slip resistance $\tau_0 = g^{(\alpha)}|_{(t=0)} = g_0$.
The sole difference between SCP and MSGCP is the calculation of the slip resistance $g^{(\alpha)}$. In the SCP model, $g^{(\alpha)}$ was only determined by SSDs. In contrast, the contribution of GNDs was also taken into account in the MSGCP model, and $g^{(\alpha)}$ was redefined as

$$g_T^{(\alpha)} = \sqrt{(g_{SSD}^{(\alpha})^2 + (g_{GND}^{(\alpha})^2}, \tag{4}$$

where, $g_{SSD}^{(\alpha)}$ and $g_{GND}^{(\alpha)}$ are contributions to the slip resistance caused by SSDs and GNDs, respectively. The evolution of slip resistance $g_{SSD}^{(\alpha)}$ was given by a strain-hardening equation:

$$\dot{g}_{SSD}^{(\alpha)} = \sum_{i=1}^{n} h_{\alpha\beta} |\dot{\gamma}^{(\beta)}| \tag{5}$$

The slip resistance $g_{GND}^{(\alpha)}$ was determined by the effective density of GNDs :

$$g_{GND}^{(\alpha)} = \alpha\mu\sqrt{b\eta_G^{(\alpha)}} \tag{6}$$

$$\eta_G^{(\alpha)} = |\mathbf{m}^{(\alpha)} \times \sum_{\beta} (s^{\alpha\beta} \bigtriangledown \gamma^{(\alpha)}) \times \mathbf{m}^{(\beta)}|. \tag{7}$$

In equation (6), b and μ are the Burgers vector and shear modulus, respectively. In equation (7), $\mathbf{m}^{(\alpha)}$ is the normal unit vector of slip plane, $s^{(\alpha)}$ and $s^{(\beta)}$ define the slip direction. Consequently, the MSGCP model could be reduced to the SCP model if $g^{(\alpha)} = g_T^{(\alpha)} = g_{SSD}^{(\alpha)}$.
The two types of crystal-plasticity models were implemented in the commercial FE code ABAQUS/Standard by using the user interface subroutine, UMAT. Calculation of a strain gradient in the MSGCP model was realized with the use of C3D8 element available in the FE package. The simulation results were reported in the form of hardness-indentation depth curves. Hardness H was defined as

$$H = \frac{F_{max}}{A}, \tag{8}$$

where F_{max} was the maximum load applied in indentation and A was the projected area of contact between the indenter and the work-piece. The contact area was determined by accounting for the contact nodes on the surface of the work-piece as outlined in the work of Lee and Chen [2]. To capture an accurate description of the contact area, a finer local mesh was used in regions underneath the indenter tip.

3 Results and Discussions

3.1 Indentation of FCC copper single crystal

The material parameters used in the work of Lee and Chen [2] was adopted for copper single crystal. The magnitude of Burgers vector for copper is $b = 0.255nm$, shear modulus $\mu = 42.0GPa$ and the empirical coefficient in the Taylor model is $\alpha = 0.5$. For the investigated FCC copper single crystal, the slip was assumed to occur on the usual twelve $\{111\}\langle 110\rangle$

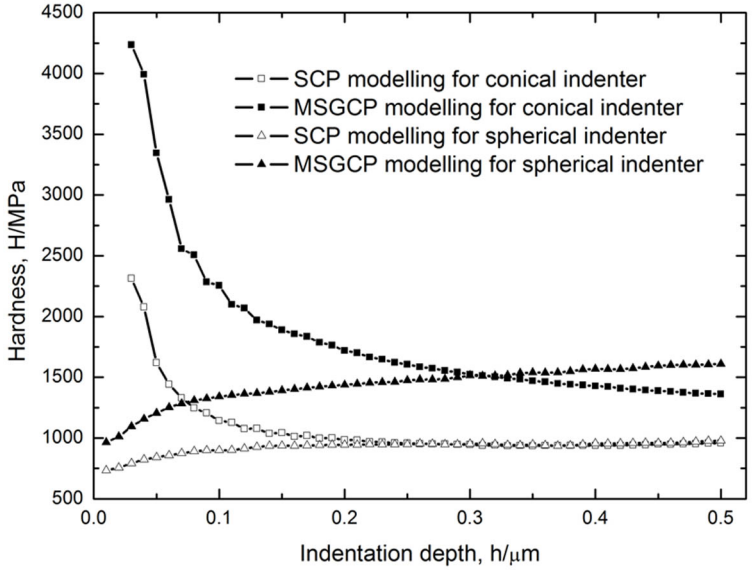

Figure 1: Indentation size effect for copper single crystal for conical and spherical indenters

slip systems. For both conical and spherical indenters, the indentation simulations were performed on the crystallographic plane of the work-piece.

Variations of hardness with indentation depth in nanoindentation with conical and spherical indenters are presented in Figure 1. ISE was clearly observed for the two types of indenter, although the hardness-indentation depth curves for the spherical indenter exhibited lower depth sensitivity. Interestingly, the trend of the change in hardness with indentation depth was different for conical and spherical indenters. We observed that the reported hardness reduce with increasing depth for the conical indenter, however, the trend was opposite for the spherical one. Therefore, the indenter geometry not only affected the magnitude of calculated hardness but also the nature of ISE. Our study demonstrated that the difference in hardness related to indenter geometry was more significant at lower indentation depths.

For the two types of indenters, it was clear that predictions based on the MSGCP model were significantly different from those with the SCP model, as shown in Figure 1. This implies that strain gradients played a pivotal role in defining hardness (and overall deformation). It also infers that strain gradient lead to an increase in hardness at smaller indentation depths for the conical indenter; however, the tendency was reversed for the spherical indenter. For the simulation results based on SCP modelling, it was noted that the hardness became insensitive to the depth when the indentation depth exceeded 0.2 μm. This phenomenon was different for MSGCP modelling. A gradual decrease or increase of hardness with higher indentation depth was observed for conical and spherical indentations, respectively. Therefore, the effect of indenter geometry on hardness was observed even at a large indentation depth due to the effect of strain gradients.

3.2 Indentation of BCC Ti-64 single crystal

Material parameters used for modelling the BCC β-Ti-64 single crystal were cited in literature [13][14]. The magnitude of Burgers vector $b = 0.286nm$, the shear modulus

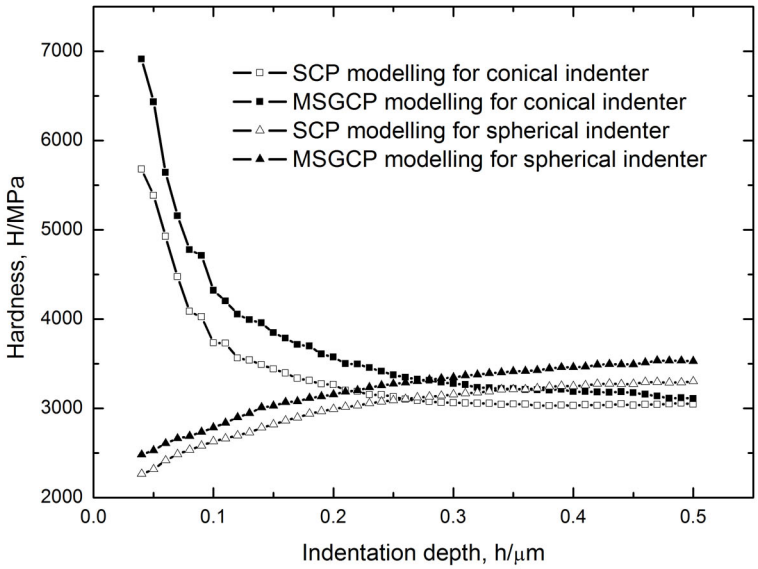

Figure 2: Indentation size effect for copper single crystal for conical and spherical indenters

$\mu = 42.085GPa$ [15] and $\alpha = 0.5$ were chosen based on prior studies. Twelve $\{110\}\langle 111\rangle$ slip systems were considered for β-Ti-64. For both conical and spherical indenters, the simulations were performed on the [110] crystallographic plane.
In Figure 2, the variations of hardness with indentation depth are shown demonstrating a significant ISE. For both SCP and MSGCP simulation results, there was an evident discrepancy in hardness caused by the indenter geometry. At a small indentation depth, the hardness obtained for the conical indenter was larger than that for the spherical one; however, a higher hardness was observed for the spherical indenter at large indentation depths. It is important to point out that the discrepancy in hardness between the two types of indenters existed even if the effect of strain gradients was neglected. Note that Ti-64 has a much higher slip resistance than Cu. For the range of indentation depths studied, the proportion of plasticity to elasticity in the contact area of Cu is larger than that in Ti-64. Thus, an increase in hardness was observed when using the spherical indenter due to its propensity to induce elastic deformation. At each indentation depth, the strain-gradient effect was small.

3.3 Indentation of BCC Ti-15-3-3 single crystal

Material parameters of a BCC β-Ti-15-3-3 single crystal were obtained by calibrating experimental results in our previous work [4]. Here, twelve $\{112\}\langle 111\rangle$ were taken as the dominant the slip systems. For both conical and spherical indenters, the indentation simulations were performed on the [110] crystallographic plane of the material.
The ISE in Ti-15-3-3 is shown in Figure 3. The hardness magnitudes obtained for the conical indenter exhibit a significant depth-dependence in comparison to those for the spherical indenter. For the SCP model, the effect of indenter geometry on hardness was considerable when the indentation depth was smaller than 0.25 μm but could be neglected at larger depths, similar to the results for the FCC Cu single crystal (Figure 1). In contrast, the results from the MSGCP model indicate that a difference in hardness for the two types

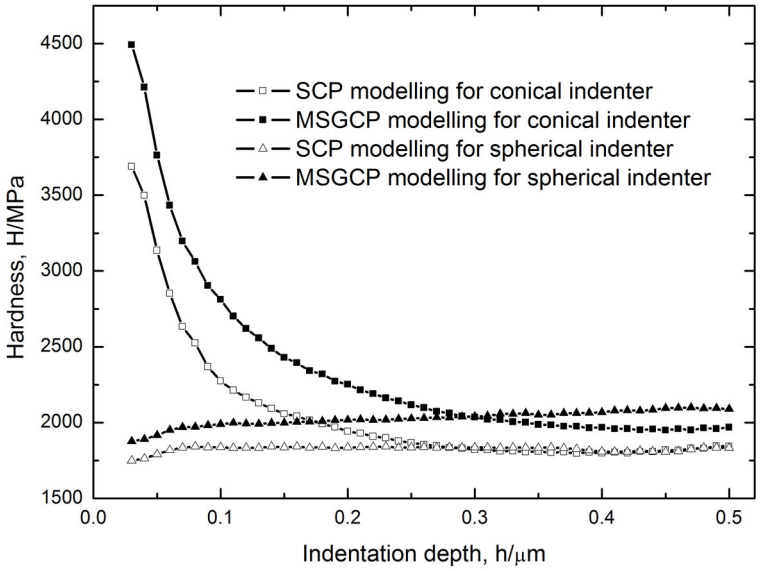

Figure 3: Indentation size effect for copper single crystal for conical and spherical indenters

of indenters exists, but is less significant than that for BCC Ti-64 (Figure 2).

4 Conclusions

The ISE was observed for nanoindentation of the three investigated single crystals for both conical and spherical indenters at small indentation depth. The indenter geometry had a significant effect on the features of ISE: the calculated hardness magnitude decreased with the indentation depth for the conical indenter but increased for the spherical one. Therefore, a great discrepancy in hardness for different types of indenters was observed, especially when the indentation depth was relatively small. However, hardness became less sensitive to the depth at larger indentation depths. For all the three types of single crystals studied, the variation of hardness with indentation depth was higher for the conical indenter. In these monocrystals, strain gradients played different roles in nanoindentation. It is emphasized that both the effects of indenter geometry and strain gradients were related to each other. The difference in hardness caused by the indenter geometry could be neglected when the effects of strain gradients were not considered for metal single crystals with low slip resistance (FCC copper and BCC Ti-15-3-3 single crystals). The indenter geometry also influenced strain gradients that, in turn, affected hardness. The discrepancy in hardness between the results of MSGCP and SCP models decreased with indentation depth for the conical indenter but the trend was opposite for the spherical indenter. The presented simulation results indicate that there are several geometrical and mechanical factors, which affect the data obtained with nanoindentation of single crystals. The modelling approach such as described here helps to elucidate the mechanisms that lead to deformation in the small scale.

5 Acknowledgement

Funding from the Engineering and Physical Sciences Research Council (UK) through grant EP/K028316/1 and Department of Science and Technology (India), project MAST, is gratefully acknowledged.

References

[1] Y Liu, S Varghese, J Ma, M Yoshino, H Lu, and R Komanduri. Orientation effects in nanoindentation of single crystal copper. International Journal of Plasticity, 24(11):1990вГ“Y2015, 2008.

[2] WB Lee and YP Chen. Simulation of micro-indentation hardness of FCC single crystals by mechanism-based strain gradient crystal plasticity. International Journal of Plasticity, 26(10):1527вГ“Y1540, 2010.

[3] Y Wang, D Raabe, C Kluüber, and F Roters. Orientation dependence of nanoindentation pile-up patterns and of nanoindentation microtextures in copper single crystals. Acta Materialia, 52(8):2229вГ“Y2238, 2004.

[4] M Demiral, A Roy, and VV Silberschmidt. Indentation studies in bcc crystals with enhanced model of strain-gradient crystal plasticity. Computational Materials Science, 79:896вГ“Y902, 2013.

[5] A Zahedi, S Li, A Roy, V Babitsky, and VV Silberschmidt. Application of smooth-particle hydrodynamics in metal machining. In Journal of Physics: Conference Series, 382, 012017. 2012.

[6] SA Zahedi, M Demiral, A Roy, and VV Silberschmidt. FE/SPH modelling of orthogonal micro-machining of FCC single crystal. Computational Materials Science, 78:104-109, 2013.

[7] N Zaafarani, D Raabe, F Roters, and S Zaefferer. On the origin of deformation induced rotation patterns below nanoindents. Acta Materialia, 56(1):31вГ“Y42, 2008.

[8] M Demiral, A Roy, T El Sayed, and VV Silberschmidt. Influence of strain gradients on lattice rotation in nano-indentation experiments: A numerical study. Materials Science and Engineering: A, 608:73вГ“Y81, 2014.

[9] M Demiral. Enhanced gradient crystal-plasticity study of size effects in bcc metal. PhD thesis, Loughborough University, 2012.

[10] Y Huang. A User-material Subroutine Incroporating Single Crystal Plasticity in the ABAQUS Finite Element Program. Harvard Univ., 1991.

[11] C-S Han, H Gao, Y Huang, and W D Nix. Mechanism-based strain gradient crystal plasticity-I. theory. Journal of the Mechanics and Physics of Solids, 53(5):1188-1203, 2005.

[12] JW Hutchinson. Bounds and self-consistent estimates for creep of polycrystalline materials. Proceedings of the Royal Society of London. Series A, Mathematical and Physical Sciences, 101-127, 1976.

[13] AC Lewis, SM Qidwai, and AB Geltmacher. Slip systems and initiation of plasticity in a body-centered-cubic titanium alloy. Metallurgical and Materials Transactions A, 41(10):2522–2531, 2010.

[14] J Thomas, M Groeber, and S Ghosh. Image-based crystal plasticity FE framework for microstructure dependent properties of Ti–6Al–4V alloys. Materials Science and Engineering: A, 553:164–175, 2012.

[15] XG Fan and He Yang. Internal-state-variable based self-consistent constitutive modeling for hot working of two-phase titanium alloys coupling microstructure evolution. International Journal of Plasticity, 27(11):1833–1852, 2011.

Qiang Liu, Wolfson School of Mechanical and Manufacturing Engineering, Loughborough University, LE11 3TU, UK
Murat Demiral, Department of Mechanical Engineering, University of Turkish Aeronautical Association, Ankara, Turkey, 06790
Anish Roy, Wolfson School of Mechanical and Manufacturing Engineering, Loughborough University, LE11 3TU, UK
Vadim V. Silberschmidt, Wolfson School of Mechanical and Manufacturing Engineering, Loughborough University, LE11 3TU, UK

Finite element investigation of the gravitational and rotational deformation of the Earth

P. Lofink Wolfgang H. Müller
paul.lofink@tu-berlin.de

Abstract

In this paper we investigate the deformation of Earth due to self-gravitation and constant rotation, *i.e.* centrifugal accelerations. A first rough estimate of a rotating, self-gravitating sphere made of iron using linear elasticity and infinitesimal strains shows that the deformations due to gravity alone are about 14 percent. These are comparatively large deformations. Consequently, we apply the concept of finite deformations instead and solve the local balance equations for mass and linear momentum in the current configuration, using the Almansi strain tensor. The stress and strain measures are related by a constitutive law similar to St.Venant-Kirchhoff. In order to solve this highly nonlinear problem, finite element calculations are conducted by using the research tool FEniCS [**?**]. Results show that the purely gravitational displacements are about two magnitudes larger compared to the ones from centrifugal forces, which has an impact on the accuracy of the so-called flattening parameter. We treat this problem by a thorough investigation of the magnitude of all participating terms, which leads to a decoupling of the system of highly non-linear differential equations. We compare the results with previously conducted analytical work presented in [**?**].

1 State of work and guide to the paper

The problem we investigate in this article is not completely new and was initially discussed by the masters of the old days, namely Newton [**?** **?**], Sommerfeld and Klein [**?**]. However, nowadays computational power is steadily increasing and numerical calculations enable us to tackle the subject by using advanced numerical techniques. Our initial investigations will concern the prediction of the so-called flattening parameter, which describes Earth's ellipsoidal shape. Newton himself found an approximate analytical expression for the flattening of Earth [**?**]:

$$f_{\text{Newton}} = \frac{a-c}{c} = \frac{5}{4}\frac{\omega_0^2\, a^3}{G\, m} = 4.35 \cdot 10^{-3} \ , \tag{1}$$

a and c being the equatorial and polar radius, ω_0 the angular velocity, m the mass of Earth and $G = 6.673 \cdot 10^{-11}\,\mathrm{m^3/kg\,s^2}$ the gravitational constant. We will try to recover Newton's result by performing a 3D finite element analysis of an rotating sphere with the elastic properties of iron. This is the natural choice, since it is nowadays commonly accepted that Earth's inner core is essentially made of that. Moreover, initially we will assume the deformation to be small. Consequently, we will apply geometrically linear elastic theory in combination with an isotropic Hooke's law. First results will reveal deformations of a size that definitely challenges the validity of a geometrically linear theory. Hence, we will eventually switch to finite deformations, while concentrating exclusively on self-gravity, which is the dominant force to begin with. By doing so we end up with a radially symmetric, highly non-linear problem. Again, we will apply an isotropic constitutive relation for the Cauchy stresses, *i.e.*, $\boldsymbol{\sigma}$. However, this time we will base the deformation on the Green-Almansi strain tensor, $\boldsymbol{e}$, and assume a homogeneous initial mass distribution with an average *current* mass density, $\rho_0 = 5515\,\mathrm{kg/m^3}$. This seems to be a reasonable estimate since mass is a conserved quantity. The governing differential equation will then be recast into dimensionless form containing Poisson's ratio, ν, and an additional parameter, $\alpha_k = \frac{4\pi G \rho_0^2 r_0^2}{3k}$, which accounts for the influence of self-gravitation and effective stiffness of the Earth (r_0 refers to Earth's average current outer radius). Since we have no direct knowledge regarding the effective bulk modulus, k, of Earth, we will use the modulus of iron leading to $\alpha_k = 1.976$. Unfortunately the direct finite element solution of the nonlinear problem, based on the Newton-Raphson algorithm, will not be successful. However, by incrementally increasing α_k we will be able to handle α_k-values of up to $\alpha_k = 1.1$ leading to displacements of about 20 % of the current outer radius, r_0. Results are shown for both linear and non-linear modeling in Section 4 after a continuum theory based description of the mechanical problem in Sections 2 and 3.

2 Theoretical background

In this section we derive the equations governing the problem of a self-gravitating rotating Earth. We start with the global balance equations for mass and linear momentum:

$$\frac{\mathrm{d}}{\mathrm{d}t}\int_{V_t} \rho \,\mathrm{d}V = 0\,, \quad \frac{\mathrm{d}}{\mathrm{d}t}\int_{V_t} \rho \boldsymbol{v} \,\mathrm{d}V = \oint_{\partial V_t} \boldsymbol{n}\cdot\boldsymbol{\sigma}\,\mathrm{d}A + \int_{V_t} \rho \boldsymbol{f}\,\mathrm{d}V \tag{2}$$

ρ denoting the current mass density, $\boldsymbol{v}$ the velocity, $\boldsymbol{\sigma}$ the Cauchy stress tensor, $\boldsymbol{n}$ the outward normal vector, and $\boldsymbol{f}$ the specific body force. It is convenient to transform the equations onto a frame co-moving at the center of Earth, *i.e.*, rotating at a constant angular velocity $\boldsymbol{\omega} = \omega_0 \boldsymbol{e}_z$. To this end, we perform a Euclidian transformation [**?** , Chap. 8], where dashed quantities always describe entities in the co-moving frame:

$$\boldsymbol{x} = \boldsymbol{x}' - \boldsymbol{b}' \quad \text{or} \quad x_i(t)\,\boldsymbol{e}_i = x_i'(t)\,\boldsymbol{e}_i'(t) - b_i'(t)\,\boldsymbol{e}_i'(t)\,. \tag{3}$$

In this and all the following relations we use Einstein's summation convention. Now we investigate this equation component-wise and calculate the time derivatives. The

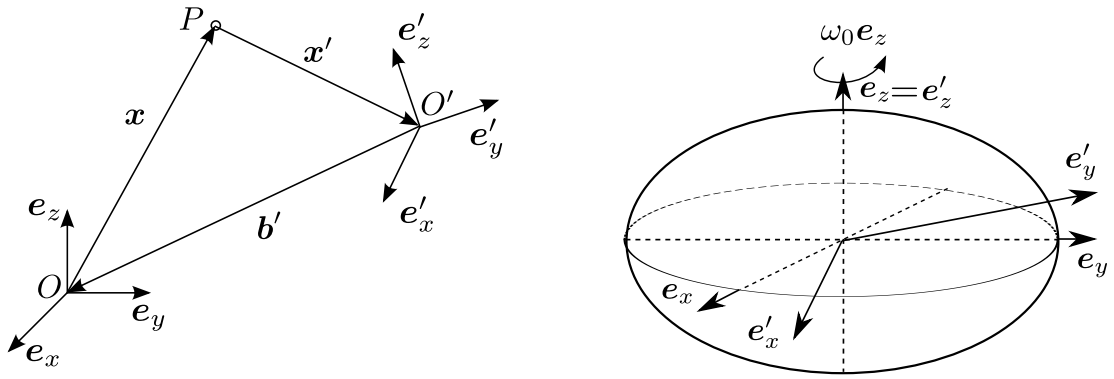

Figure 1: The co-moving basis vectors and quantities for the Euclidian transformation.

change of basis vectors is a pure rotation with the angular velocity $\boldsymbol{\omega}$ where the origins O and O' of the systems coincide (*cf.*, Fig. 1):

$$\boldsymbol{v} = \dot{x}_i \boldsymbol{e}_i = \dot{x}'_i \boldsymbol{e}'_i + x'_i \boldsymbol{\omega}' \times \boldsymbol{e}'_i \ , \quad \boldsymbol{a} = \ddot{x}'_i \boldsymbol{e}'_i + 2\dot{x}'_i \boldsymbol{\omega}' \times \boldsymbol{e}'_i + x'_i \boldsymbol{\omega}' \times (\boldsymbol{\omega}' \times \boldsymbol{e}'_i) \, . \quad (4)$$

Since we use the co-moving system we may assume a stationary configuration, where Earth particles have no relative motion $\dot{x}'_i, \ddot{x}'_i = 0$ and therefore:

$$\boldsymbol{v} = \boldsymbol{\omega}' \times \boldsymbol{x}' \ , \quad \boldsymbol{a} = -\boldsymbol{\omega}' \times (\boldsymbol{\omega}' \times \boldsymbol{x}') \, . \quad (5)$$

These results are necessary for obtaining the *local* balance equations. To this end we apply Reynold's transport theorem and assume the global balances to be valid for every sub-domain. Therefore the integrand itself has to be equal to zero:

$$\frac{\mathrm{d}\rho}{\mathrm{d}t} + \rho \nabla \cdot \boldsymbol{v} = 0 \ , \quad \rho \boldsymbol{a} = \nabla \cdot \boldsymbol{\sigma} + \rho \boldsymbol{f} . \quad (6)$$

In context with Euclidian tensor properties of the occurring fields the following useful relations apply:

$$\rho = \rho' \ , \quad \nabla = \frac{\partial}{\partial x_i} \boldsymbol{e}_i = \frac{\partial}{\partial x'_i} \boldsymbol{e}'_i \ , \quad \boldsymbol{\sigma} = \sigma_{ij} \boldsymbol{e}_i \otimes \boldsymbol{e}_j = \sigma'_{ij} \boldsymbol{e}'_i \otimes \boldsymbol{e}'_j \ , \quad \boldsymbol{f} = f_i \boldsymbol{e}_i = f'_i \boldsymbol{e}'_i . \quad (7)$$

By assuming a constant angular velocity in $\boldsymbol{e}'_3$ - direction, a further simplification results:

$$-\rho' \boldsymbol{\omega}' \times (\boldsymbol{\omega}' \times \boldsymbol{x}') = -\rho' \omega_0^2 \, (x'_1 \boldsymbol{e}'_1 + x'_2 \boldsymbol{e}'_2) = \nabla' \cdot \boldsymbol{\sigma}' + \rho' \boldsymbol{f}' . \quad (8)$$

The body forces $\boldsymbol{f}'$ result from self-gravity only. Since the gravitational force is conservative we may derive it from a scalar potential, U', obeying Poisson's equation:

$$\boldsymbol{f}' = -\nabla' U' \ , \quad \nabla' \cdot (\nabla' U') = 4\pi G \rho' . \quad (9)$$

For the sake of brevity we will omit dashes in what follows. We will see later that a formulation in the reference configuration is useful for deriving certain required relations for the unknown fields. The corresponding basic transformations read:

$$\mathrm{d}\boldsymbol{x} = \boldsymbol{F} \cdot \mathrm{d}\boldsymbol{x}_0 \ , \quad \boldsymbol{n} \, \mathrm{d}A = J \boldsymbol{F}^{-T} \cdot \boldsymbol{n}_0 \, \mathrm{d}A_0 \ , \quad \mathrm{d}V = J \, \mathrm{d}V_0 \ , \quad (10)$$

with the deformation gradient:

$$\boldsymbol{F} = \frac{\partial z^i}{\partial Z^j} \boldsymbol{g}_i \otimes \boldsymbol{g}_0^j \ , \quad J = \det \boldsymbol{F} \ , \tag{11}$$

z^i and Z^j being the coordinates and $\boldsymbol{g}_i$ and $\boldsymbol{g}_0^j$ the (potentially) curvilinear base vectors in the current and referential configurations, respectively. With these identities we may write for the balance of mass:

$$\frac{\mathrm{d}}{\mathrm{d}t} \int_{V_0} \rho J \, \mathrm{d}V_0 = 0 \ , \quad \frac{\mathrm{d}}{\mathrm{d}t} \left(\rho J \right) = 0 \ , \quad \rho J = \rho_0 = \text{const.} \ , \tag{12}$$

and for the balance of linear momentum:

$$\frac{\mathrm{d}}{\mathrm{d}t} \int_{V_0} \rho J \boldsymbol{v} \, \mathrm{d}V_0 = \oint_{\partial V_0} J \left(\boldsymbol{F}^{-T} \cdot \boldsymbol{n}_0 \right) \cdot \boldsymbol{\sigma} \, \mathrm{d}A_0 \quad \text{or} \quad \rho_0 \boldsymbol{a} = \nabla_{\boldsymbol{x}_0} \cdot \boldsymbol{P} + \rho_0 \boldsymbol{f}. \tag{13}$$

Herein we have used the first Piola-Kirchhoff stress tensor $\boldsymbol{P} = J \boldsymbol{F}^{-1} \cdot \boldsymbol{\sigma}$.

3 Constitutive equations

In order to close the system of equations we have to specify constitutive relations, which connect the stress tensors $\boldsymbol{\sigma}$ or $\boldsymbol{P}$ with quantities of deformation. In the geometrically linear case we use well known Hooke's law:

$$\boldsymbol{\sigma} = \lambda \, \mathrm{tr} \left(\boldsymbol{\varepsilon} \right) \, \mathbf{1} + 2\mu \boldsymbol{\varepsilon} \quad \text{with} \quad \boldsymbol{\varepsilon} = \frac{1}{2} \left(\nabla_{\boldsymbol{x}} \otimes \boldsymbol{u} + \left(\nabla_{\boldsymbol{x}} \otimes \boldsymbol{u} \right)^T \right). \tag{14}$$

If we adopt the concept of finite deformations in the reference configuration we may use the St. Venant-Kirchhoff law, which relates the second Piola-Kirchhoff stress tensor, $\boldsymbol{S}$, and the Green-Lagrange strain tensor, $\boldsymbol{E}$:

$$\boldsymbol{S} = \lambda \, \mathrm{tr} \left(\boldsymbol{E} \right) \, \mathbf{1} + 2\mu \, \boldsymbol{E} \ , \quad \boldsymbol{S} = J \ \boldsymbol{F}^{-1} \cdot \boldsymbol{\sigma} \cdot \boldsymbol{F}^{-T} \ , \quad \boldsymbol{E} = \frac{1}{2} \left(\boldsymbol{F}^T \cdot \boldsymbol{F} - \mathbf{1} \right). \tag{15}$$

If we prefer to stay in the current configuration we may use a constitutive equation based on the Almansi strain tensor, $\boldsymbol{e}$:

$$\boldsymbol{\sigma} = \lambda \, \mathrm{tr} \left(\boldsymbol{e} \right) \, \mathbf{1} + 2\mu \, \boldsymbol{e} \ , \quad \boldsymbol{e} = \frac{1}{2} \left(\mathbf{1} - \boldsymbol{B}^{-1} \right) \ , \quad \boldsymbol{B} = \boldsymbol{F} \cdot \boldsymbol{F}^T. \tag{16}$$

If infinitely small deformations are assumed, all three constitutive equations coincide, *cf.*, [**?**].

4 Results

In order to prepare the balance equations for a finite element analysis, we have to generate weak forms. Therefore we apply the procedure described in [**?**], *i.e.*,

we multiply by a test function, $\delta\boldsymbol{u}$, integrate over the entire domain, and perform integration by parts:

$$\int_{V_t} \boldsymbol{\sigma}\cdot(\nabla_{\boldsymbol{x}} \otimes \delta\boldsymbol{u})\,\mathrm{d}V - \oint_{\partial V_t} \boldsymbol{n}\cdot\boldsymbol{\sigma}\cdot\delta\boldsymbol{u}\,\mathrm{d}A = \int_{V_t} \rho\boldsymbol{f}\cdot\delta\boldsymbol{u}\,\mathrm{d}V + \int_{V_t} \rho\omega_0^2\,(x_1\boldsymbol{e}_1 + x_2\boldsymbol{e}_2)\cdot\delta\boldsymbol{u}\,\mathrm{d}V. \tag{17}$$

Analogously we derive for the potential, U, with a test function, δU:

$$-\int_{V_t} \nabla_{\boldsymbol{x}} U \cdot \nabla_{\boldsymbol{x}}\delta U\,\mathrm{d}V + \oint_{\partial V_t} \boldsymbol{n}\cdot\nabla_{\boldsymbol{x}} U\,\delta U\,\mathrm{d}A = \int_{V_t} 4\pi G\rho\,\delta U\,\mathrm{d}V. \tag{18}$$

For completion of the boundary value problem we require the following conditions to hold:

$$U|_{\boldsymbol{x}=\boldsymbol{0}} = 0\ , \quad \boldsymbol{u}|_{\boldsymbol{x}=\boldsymbol{0}} = \boldsymbol{0} \quad \text{and} \quad \boldsymbol{n}\cdot\boldsymbol{\sigma}|_{\boldsymbol{x}\in\partial V_t} = \boldsymbol{0}. \tag{19}$$

In the last equation we neglect surface stresses since they are very small compared to the stresses in the interior. We simulated the geometrically linear case with linear continuous Galerkin elements (tetrahedra). Both Eqns. (17) and (18) were written in weak form and solved simultaneously. Additionally, we incorporated a spatially

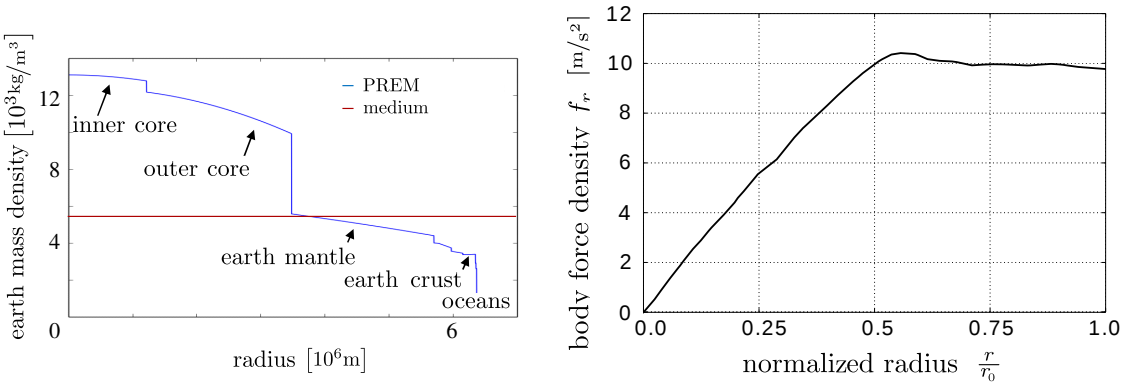

Figure 2: Mass density distribution according to PREM (left) and the corresponding gravitational acceleration (right) [**?**].

varying mass density, ρ, (see Fig. 2) of the PReliminary Earth Model (PREM, [**?**]) derived from a study of propagation velocities for seismic waves. The results in Fig. 3 show that for an earth-like celestial body deformations due to self-gravitation are beyond the validity of linear deformation theory. By comparing the curve for the total displacements, u_r^{tot}, *i.e.*, gravity plus centrifugal acceleration, and purely gravitational displacements, u_r^{grav}, there is almost no difference. By plotting the rotational displacements exclusively, we realize a difference of about two or three magnitudes. The flattening parameter of Eqn. (1) can now be calculated by taking the difference between displacements along the equatorial plane and poles:

$$f = \frac{u_r^{\mathrm{rot}}\,(\vartheta = \pi/2) - u_r^{\mathrm{rot}}\,(\vartheta = 0)}{r_0} = 1.1\cdot 10^{-3}. \tag{20}$$

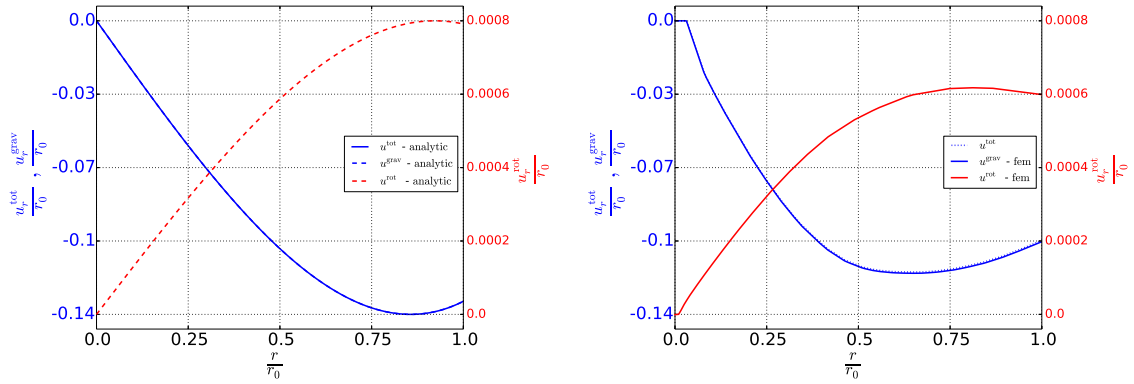

Figure 3: Analytic results from [**?**] based on a constant average mass density (left) and FE-results for normalized displacements along the equatorial plane from a 3D Cartesian simulation with the PREM mass density (right).

Consequently, from now on we concentrate on deformation by gravity alone and use non-linear theory. Now we have two possibilities: Either we transform all equations onto the reference configuration or onto the current configuration. The reference configuration has one major drawback, namely the unknown initial radius, R_0. A possible solution is to determine the radius iteratively by adjusting the radius in a stepwise manner, and always comparing the result to the real current outer radius. However, it is more convenient to transform all equations onto the current configuration and to use the real outer radius for the mesh. If we omit rotation we have a purely radially symmetric problem. Therefore, we switch to spherical coordinates and assume the deformation to be purely radial as well:

$$Z^1 = R\left(r\ ,\vartheta\ ,\varphi\right) = r - u_r\left(r\right)\ , \quad Z^2 = \Theta\left(r\ ,\vartheta\ ,\varphi\right) = \vartheta\ , \quad Z^3 = \Phi\left(r\ ,\vartheta\ ,\varphi\right) = \varphi, \tag{21}$$

with corresponding base vectors:

$$\boldsymbol{g}^i = \left\{\boldsymbol{e}_r\ , \frac{1}{r}\,\boldsymbol{e}_\vartheta\ , \frac{1}{r\sin\vartheta}\,\boldsymbol{e}_\varphi\right\} \quad \text{and} \quad \boldsymbol{g}_{0_k} = \left\{\boldsymbol{e}_R\ , R\boldsymbol{e}_\Theta\ , R\sin\Theta\boldsymbol{e}_\Phi\right\}. \tag{22}$$

This motion results in the following deformation measures:

$$\boldsymbol{F}^{-1} = \begin{bmatrix} \frac{\mathrm{d}R}{\mathrm{d}r} & 0 & 0 \\ 0 & 1 & 0 \\ 0 & 0 & 1 \end{bmatrix}_{\boldsymbol{g}_{0_i}\otimes\boldsymbol{g}^k} = \begin{bmatrix} \left(1-\frac{\mathrm{d}u_r}{\mathrm{d}r}\right) & 0 & 0 \\ 0 & \frac{R}{r} & 0 \\ 0 & 0 & \frac{R}{r} \end{bmatrix}_{\boldsymbol{e}_{0_i}\otimes\boldsymbol{e}^k}, \quad J = \left(1-\frac{\mathrm{d}u_r}{\mathrm{d}r}\right)^{-1}\left(\frac{r}{R}\right)^2. \tag{23}$$

With the help of the deformation gradient we may derive the only non-zero Green-Almansi strain components:

$$e_{rr} = \frac{\mathrm{d}u_r}{\mathrm{d}r}\left(1-\frac{1}{2}\frac{\mathrm{d}u_r}{\mathrm{d}r}\right), \quad e_{\vartheta\vartheta} = e_{\varphi\varphi} = \frac{u_r}{r}\left(1-\frac{1}{2}\frac{u_r}{r}\right). \tag{24}$$

With Eqn. (16) we can now detail the Cauchy stress components. It is reasonable to normalize them by the bulk modulus, k:

$$t_{rr} = \frac{\sigma_{rr}}{k} = \frac{3\left(1-\nu\right)}{1+\nu}\frac{\mathrm{d}u_r}{\mathrm{d}r}\left(1-\frac{1}{2}\frac{\mathrm{d}u_r}{\mathrm{d}r}\right) + \frac{2\nu}{1+\nu}\frac{u_r}{r}\left(1-\frac{1}{2}\frac{u_r}{r}\right), \tag{25}$$

$$t_{\vartheta\vartheta} = t_{\varphi\varphi} = \frac{\sigma_{\vartheta\vartheta}}{k} = \frac{\sigma_{\varphi\varphi}}{k} = \frac{\nu}{1+\nu}\frac{\mathrm{d}u_r}{\mathrm{d}r}\left(1 - \frac{1}{2}\frac{\mathrm{d}u_r}{\mathrm{d}r}\right) + \frac{3}{1+\nu}\frac{u_r}{r}\left(1 - \frac{1}{2}\frac{u_r}{r}\right). \tag{26}$$

If the balance equation (13) is observed it turns out that only the radial component is different from zero. In addition to introducing normalized stresses, we define a dimensionless current radius, $x = {}^{r}/_{r_0}$, and a dimensionless displacement, $u = {}^{u_r}/_{r_0}$, by dividing both by the outer radius of the Earth, $r_0 = 6378\,\mathrm{km}$:

$$\frac{\mathrm{d}t_{rr}}{\mathrm{d}x} + \frac{1}{x}\left(2\,t_{rr} - t_{\vartheta\vartheta} - t_{\varphi\varphi}\right) = -\frac{\rho\, r_0}{k} f_r \ . \tag{27}$$

For a radial mass distribution Eqn. (9) reduces to:

$$\frac{1}{r^2}\frac{\mathrm{d}}{\mathrm{d}r}\left(r^2\frac{\mathrm{d}U}{\mathrm{d}r}\right) = 4\pi G\rho\,(r) \quad \Rightarrow \quad \frac{\mathrm{d}U}{\mathrm{d}r} = \frac{1}{r^2}\int_{\tilde{r}=0}^{\tilde{r}=r} 4\pi\rho\,(\tilde{r})\,\tilde{r}^2\,\mathrm{d}\tilde{r}\ , \tag{28}$$

and therefore the gravitational accelerations are given by:

$$f_r = -\frac{Gm\,(r)}{r^2} = -\frac{Gm\,(R)}{r^2} = -\frac{G\,\frac{4}{3}\pi\rho_0 R^3}{r^2} = -\frac{4}{3}\pi G\rho_0\left(1 - \frac{u_r}{r}\right)^3 r\ . \tag{29}$$

Herein we have used a homogeneous medium mass density, $\rho_0 = 5515\ {}^{\mathrm{kg}}/_{\mathrm{m}^3}$ (see Fig. 2). By inserting this result in Eqn. (27) and by using Eqn. $(23)_2$ we get:

$$\frac{\mathrm{d}t_{rr}}{\mathrm{d}x} + \frac{1}{x}\left(2\,t_{rr} - t_{\vartheta\vartheta} - t_{\varphi\varphi}\right) = \alpha_k\left(1 - \frac{u}{x}\right)^5\left(1 - \frac{\mathrm{d}u}{\mathrm{d}x}\right)x\ , \quad \alpha_k = \frac{4\,\pi\,G\,\rho_0^2\,r_0^2}{3\,k}. \tag{30}$$

Simulations were carried out for different parameters α_k, always keeping Poisson's ratio at $\nu = 0.3$ (Fig. 4, left) and $\nu = 0.38$ (Fig. 4, right), respectively. The results

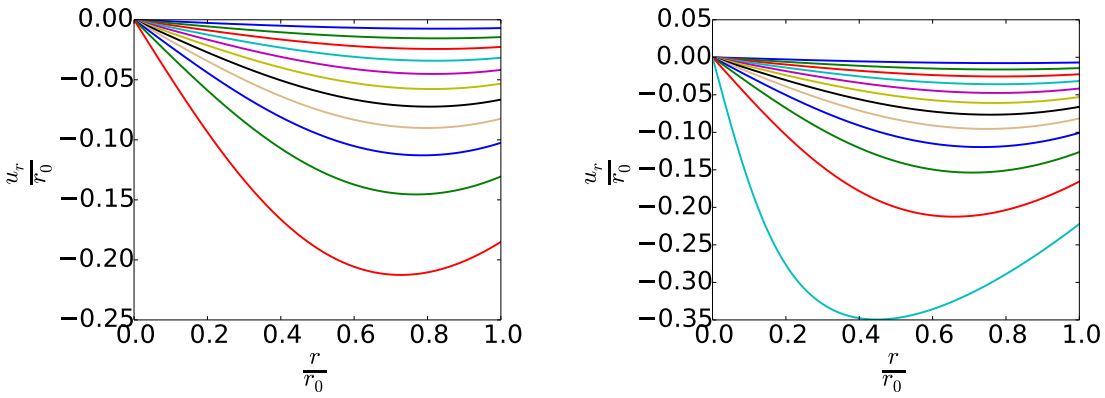

Figure 4: Nonlinear solution for $\nu = 0.3$, starting from $\alpha_k = 0.1$, upper blue line, to $\alpha_k = 1.1$, lower red line in steps of 0.1 (left), and for $\nu = 0.38$ and $\alpha_k = 0.1 \cdots 1.2$ (right).

(see Fig. 4) show once more very clearly that purely gravitational deformations of a massive, earth-like celestial body are beyond the validity of linear geometric theory. Therefore finite deformation theory was applied to the radially symmetric self-gravitational problem of a sphere and results are shown for different constellations of parameters. Unfortunately no convergence was achieved for the case when

α_k turned to 1.976, which corresponds to $\alpha = 2.45$ when referring to the alternative mass-stiffness parameter $\alpha = \alpha_k \frac{2(1+\nu)}{3(1-\nu)}$ of the paper by Müller and Weiss [**?**] in the same proceedings. Their largest converging value of α is 1.76, obtained with the finite difference technique for $\nu = 0.38$. This corresponds to $\alpha_k = 1.18$, which is almost exactly the same value we were able to achieve (see Fig. 4 (right)) with the finite element algorithm. We tried to solve the differential equation by adaptively refining the mesh at regions were the displacement gradient is large, but to no avail: Convergence could not be achieved for larger values of α_k.

Paul Lofink, Technische Universität Berlin, Sekr. MS 2, Einsteinufer 5, 10587 Berlin
Wolfgang H. Müller, Technische Universität Berlin, Sekr. MS 2, Einsteinufer 5, 10587 Berlin

On the existence of a critical speed of a rotating ring under a stationary point load

Tao Lu Andrei V. Metrikine
T.Lu-2@tudelft.nl

Abstract

It is known that critical speeds exist for a constant load uniformly moving around an elastic ring, which is elastically connected to an immovable axis. However, in the inverted case, namely in the case of a rotating ring subject to a stationary constant load, the existence of such critical speeds is still being debated by the research community. Various rotating thin ring/shell models are available in literature. Especially active is the tire research community within which the rotating ring/shell models are often employed to mimic vibrations of the tire tread of pneumatic tires. The theoretical predictions of the critical speeds made on the basis of the existing models are not convincing and sometimes confusing. Properly formulated governing equations including the pretension due to rotation and a due linearization are needed to predict the critical speeds correctly. In this paper, a rotating thin ring elastically mounted on an immovable axis and subjected to a stationary point load is investigated. The governing equations are obtained by modifying one of the most widely used rotating ring models in order to describe the pretension in a more accurate way. The parameters are adopted from a pneumatic tire. Free and forced vibrations are investigated. Instability and stationary modes are found which were not reported in literature before. The results of the forced vibration clearly reveal that a critical speed of a rotating ring does exist. The deformation patters of the ring rotating at the sub-critical and super-critical speeds are shown and discussed.

1 Introduction

The in-plane vibration of rotating thin rings and shells has wide engineering applications. A special position among those is occupied by the pneumatic tires, whose dynamics has been investigated by many researchers with the help of rotating ring models. Such simplistic models are useful because the predicted natural frequencies are in good agreement with the ones measured in experiments. Various rotating thin ring models have been developed and, among those, the models based on the LoveвЂ™s thin shell theory in Ref. [1, 2, 3] are most commonly used. Critical speed clearly exists for a constant load moving around an elastic ring [4] but the existence of the critical speed for a rotating ring subjected to a stationary constant load is still being debated. Significant wave-like deformation was observed when a pneumatic tire rolls on the ground with a speed higher than a certain critical value

which suggests a rotating ring may have a critical rotation speed. However, the theoretical predictions for the critical speed are not convincing and, sometimes, confusing when use is made of the existing rotating ring models. Some references gave a prediction for the critical speed but the pretension due to rotation was not properly included or even not included at all, e.g. Ref. [5, 6]. Many other references did not mention the critical speed problem, e.g. in [2, 3]. In Ref. [7], Huang and Hsu concluded that no critical rotational speeds exist for the forced response to a stationary constant point load subjected to a rotating thin shell. The aim of this paper is to show that there exist critical speeds for rotating thin rings but a modification of the model is needed to predict those. The rotating thin ring model used in this paper is a modified version of that presented in ref. [2].The modification concerns the pretension caused by rotation. Parameters from a pneumatic tire are applied. The physical parameters of the ring are obtained by matching the natural frequencies predicted by the adopted analytical model with the measured ones from ref. [8]. Free vibrations are studied first in order to show the effect of the gyroscopic forces. Thereafter, the ring response to a constant stationary point load is analyzed.

2 Governing Equations

In this paper, pneumatic tires are chosen as the engineering application of rotating ring model. The tire is modeled as a thin ring with a uniform rectangular cross section. Radial and circumferential distributed springs are used to model the sidewall of the tire. It is assumed that the center of the ring is fixed and the ring rotates about it.
The rotating ring model and the reference systems are shown in Figure 1. It is assumed that the mean radius of the ring is R, whereas w and u are the small displacements in the radial and circumferential directions, respectively. p is the internal air pressure of the tire. The stiffnesses of the radial and circumferential springs per unit length are designated as k_r and k_c, respectively. It is also assumed that all springs possess viscosity per unit length equal to σ. Furthermore, ρ is the mass density of the rim, E is the YoungвГЄs modulus, A is the cross-sectional area and I is the cross sectional moment of inertia. P is the magnitude of the constant radial point load which represents the contact force between the tire and the ground. Ω is the angular frequency of the tire rotation.
The linearized equations governing the model vibrations in the nonrotating reference system are the same as in ref. [2] and can be written as

$$\begin{aligned}
&\rho A\ddot{u} + 2\rho A\Omega(\dot{u}' + \dot{w}) - \rho A\Omega^2(u - 2w' - u'') + \frac{EI}{R^4}(w''' - u'') \\
&\quad - \frac{EA}{R^2}(w' + u'') + N(u - w') + k_c u + \sigma(\dot{u} + \Omega u') = 0, \\
&\rho A\ddot{w} + 2\rho A\Omega(\dot{w}' - \dot{u}) - \rho A\Omega^2(w + 2u' - w'') + \frac{EI}{R^4}(w'''' - u''') \\
&\quad + \frac{EA}{R^2}(w + u') + N(u' - w'') + k_r w + \sigma(\dot{w} + \Omega w') = P\delta(\theta),
\end{aligned} \tag{1}$$

where the overdot and the prime designate the partial derivatives with respect to time and the angle θ, respectively.
Note that because of rotation, the ring has a static radial deformation w_e and the pretension $N = EAw_e/R$ (see Ref. [2]). Equation (1) governs small vibrations about the static equilibrium.
In Ref. [1, 2, 3] and in most of the other references, the pretension is approximated by

$$N = pbR + \rho AR^2\Omega^2. \tag{2}$$

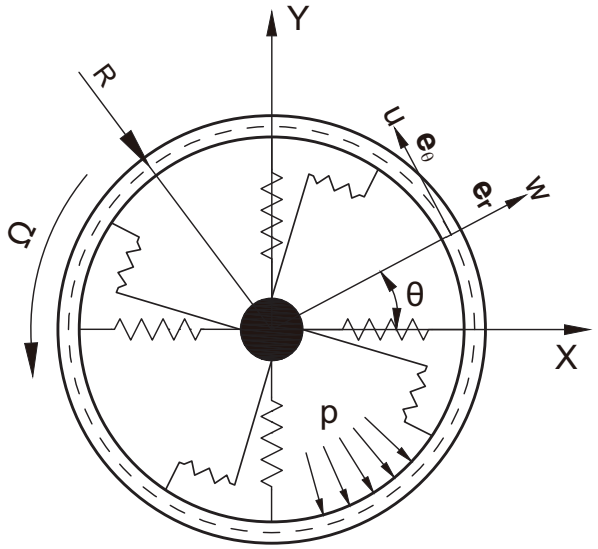

Figure 1: Rotating ring

A proper approximation for the pretension due to rotation is needed to predict the critical speed. If we take an element of the rotating ring and analyze the force equilibrium, the pretension can be shown to be described by

$$N = \frac{EA}{R}\frac{pbR + \rho AR^2\Omega^2}{EA/R + k_r R}. \tag{3}$$

If $EA/R >> k_r R$, i.e. if the extensional stiffness EA of the tire treadband is very high, then the approximation $N = pbR + \rho AR^2\Omega^2$ can be applied. However, in the present paper, the more general equation (3) is retained. Consequently, the static radial deformation is taken as

$$w_e = \frac{pbR + \rho AR^2\Omega^2}{EA/R + k_r R}. \tag{4}$$

3 Identification of the parameters

One of the main factors the validity of the rotating thin ring model depends upon is the estimation of the values for the parameters in the governing equations. A reasonable way to determine those is to match the natural frequencies predicted by the analytical model with those measured using nonrotating tires [2, 8].
Let us derive expressions for the natural frequencies. To this end, we assume the following form of the solution:

$$w(\theta, t) = We^{\mathrm{i}(n\theta + \omega_n t)}, \quad u(\theta, t) = Ue^{\mathrm{i}(n\theta + \omega_n t)}. \tag{5}$$

Substituting the above expressions into the governing equation (1), one can obtain the frequency equation in the form of a fourth order polynomial:

$$\omega_n{}^4 + a_3\omega_n{}^3 + a_2\omega_n{}^2 + a_1\omega_n + a_0 = 0. \tag{6}$$

For brevity, the expressions for the coefficients of the above polynomial are omitted. These coefficients are functions of all the model parameters, as well as of the mode number n and speed of rotation Ω.
Generally, the geometrical and material parameters ρ,A,R,b,h(b is the width and h the thickness of the ring), are obtained based on the tire geometry and its material properties. In contrast, the equivalent parameters EA,EI,k_r,k_c are identified from experimental modal analysis. By comparing the measured natural frequencies and natural frequencies predicted by equation (5), the values of EA,EI,k_r,k_c can be identified. The experimental natural frequencies, along with geometrical and material parameters used in this paper are taken from Ref. [8] for a 195/70R14 radial tire. The geometrical and material parameters are

$$b = 0.16m,\ h = 0.01m,\ A = 0.0016m^2,\ R = 0.285m,$$
$$\rho = 2.28 \times 10^3 kg/m^3,\ p = 2.5 \times 10^5 N/m^2$$

Table 9: The measured and theoretically predicted natural frequencies

	Mode number	n=1	n=2	n=3	n=4	n=5	n=6	n=7	n=8
1	f_n(Hz):measured	-	108.53	132.38	158.30	186.92	213.60	248.14	287.54
2	f_n(Hz):predicted	91.14	108.53	132.38	159.32	186.92	215.17	245.92	287.54

The first row in Table 9 lists the measured natural frequencies of the tire adopted from Ref. [8]. The second row contains the natural frequencies predicted by the model whose parameters were chosen such as to give a close correspondence between the measured and calculated frequencies. In order to determine four equivalent parameters, namely EA,EI,k_r,k_c four measured natural frequencies were substituted in the characteristic equation (6).
The natural frequencies of n=2, 3, 5, 8 were used. Upon solving the four obtained nonlinear algebraic equations the following figures for the equivalent parameters were obtained:

$$EA = 13374.99N,\ EI = 17.37Nm^2,\ k_r = 4.49 \times 10^6 N/m^2,\ k_c = 1.16 \times 10^6 N/m^2$$

Substituting the above figures to equation (6) and solving it for the frequency, the natural frequencies shown in the last row of Table 9 were obtained. Table 9 demonstrates good agreement between the theoretical and measured natural frequencies. Note that in Table 9, the measured natural frequencies are associated with the dominant bending modes. Since no inextensibility assumption is employed here, the natural frequencies of the extensional modes can be obtained as well by solving equation (6).

4 Free vibration

Making use of the identified equivalent parameters, the natural frequencies of the rotating ring can be obtained. The dependence of the natural frequencies on the rotation speed for the modes from 0 to 5 are shown in Figure 2. The absolute values of the real part of the natural frequencies are shown.
The following conclusions can be drawn from Figure 2:
1. Frequency bifurcation. The nonrotating ring has two distinct natural frequencies (for each mode number) associated predominantly with the radial and circumferential vibrations. Usually, the lower one corresponds to the predominantly radial motion while the higher one is associated with the predominantly circumferential motion(for $n \geq 2$). When the ring rotates, for any mode number greater than zero, both the lower and the higher

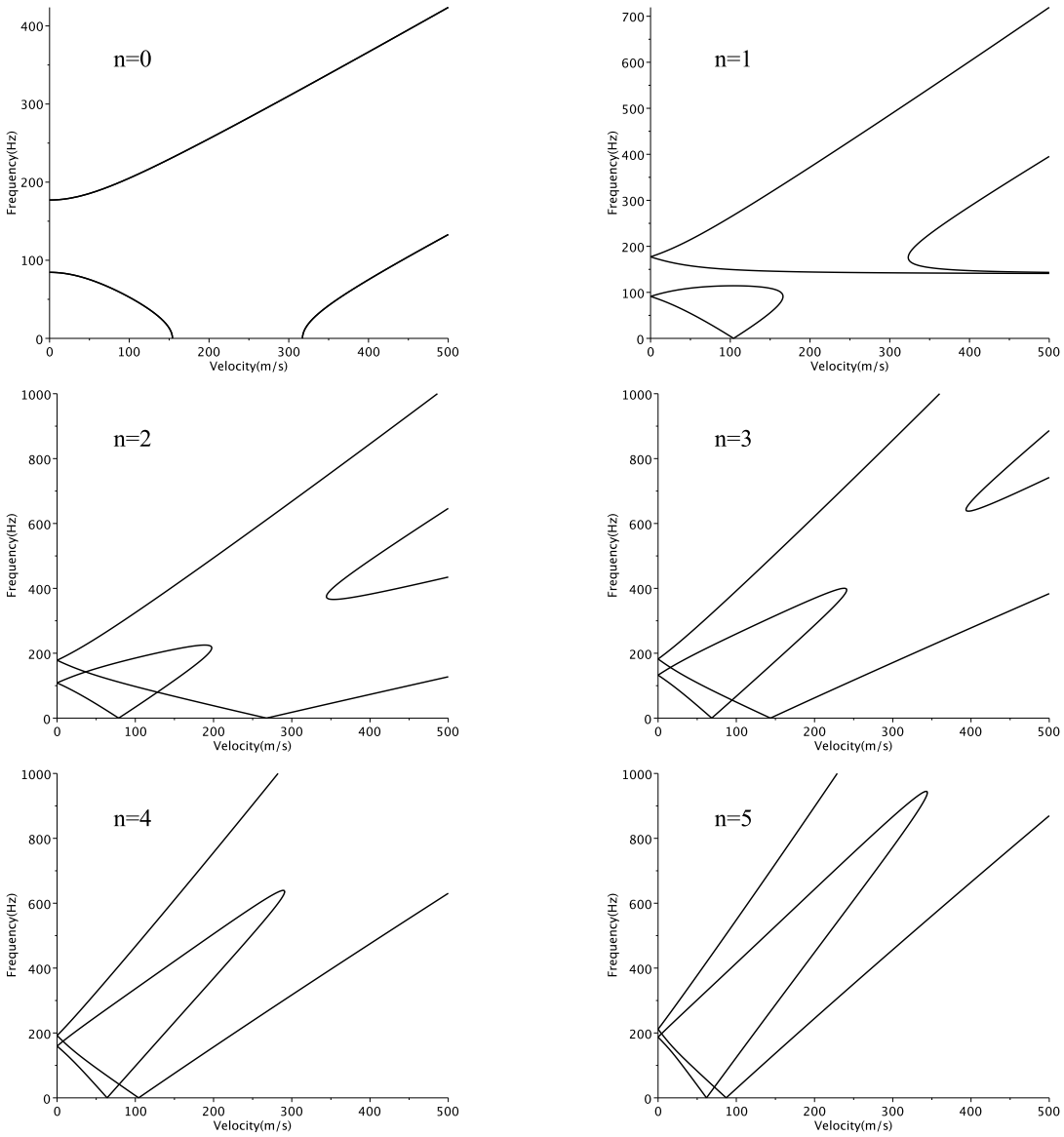

Figure 2: Natural frequencies versus rotation speeds

natural frequencies split into two different frequencies which results in four distinct natural frequencies. This phenomenon is referred to as the frequency bifurcation. One needs to note that the natural frequencies corresponding to n=0 do not bifurcate.

2. Instability. For mode 0, the higher natural frequency increases monotonically as the rotation speed grows, whereas the lower one first decreases to zero and then its real part turns to zero at certain velocity. This means that as from this velocity (and up to the velocity at which the real part becomes nonzero again) the natural frequency is purely imaginary which indicates that the system is unstable and the type of the instability is divergence. For the modes $n \geq 1$, the two distinct natural frequencies of the lower set coalesce into one at a particular velocity and become complex-valued after this velocity. When the speed of rotation increases further, the natural frequencies may become real again. Since the coefficients of the characteristic polynomial (6) are all real, the complex roots appear in conjugate pairs. Therefore, there must be at least one root with negative imaginary part. This means the motion in unstable and flutter instability may occur.

3. Stationary modes. For the modes $n \geq 1$, zero natural frequencies are observed at certain speeds of rotation for both predominantly radial and predominantly circumferential vibrations. In the case of zero frequency, equation (5) reduces to

$$w(\theta, t) = We^{in\theta}, \quad u(\theta, t) = Ue^{in\theta} \tag{7}$$

and the deformation of the ring becomes time independent. This means that the modes corresponding to zero natural frequencies are stationary with respect to an earth-bound observer. This phenomenon was not reported in literature.
4. The natural frequencies of both the radial and circumferential modes are nearly the same in the case of a nonrotating tire ($\Omega = 0$). This fact has been confirmed by many modal tests in literature, for example in Ref. [9].
The maximum velocity in Figure 2 is 500m/s. The operational speed of a tire cannot reach such high a velocity in reality. Furthermore, even if it would, the validity of the model would be jeopardized by a very large static deformation. Therefore, the predictions of the natural frequencies for the high rotation speeds are provided herein for the sake of the completeness of the mathematical analysis only.

5 Steady-state response of a rotating ring

In this section, the forced vibration of a rotating ring is computed. The so-called вГЁmethod of imagesвГ№ is employed to solve the governing equations. This method was first used to solve the response of an elastic ring subject to a moving load in Ref. [4] and recently applied for computing the response of a rotating train wheel in [10]. The parameters have been given in Section 3.

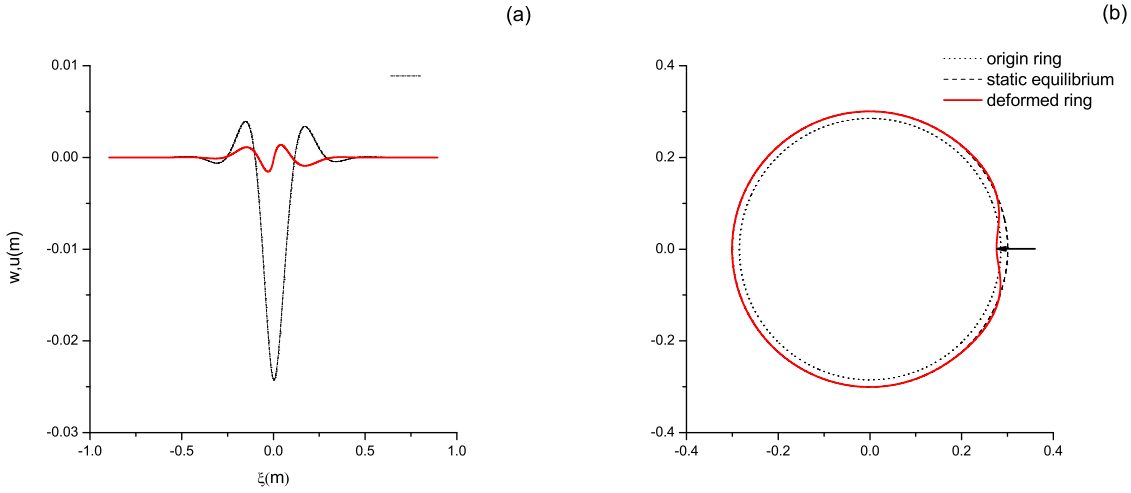

Figure 3: v=50m/s

Figures 3-5 show the radial displacement w, the circumferential displacement u and the corresponding ring shapes for three different rotating speeds. The magnitude of the applied force is $1.0 \times 10^4 N$ and the damping σ used is $500 Ns/m^2$. In figures 3-5(a), the radial and circumferential displacements are plotted versus the distance from the load ξ ($\xi = 0$ is the loading point,$\xi > 0$ corresponds to the position when $0 < \theta \leq \pi$, $\xi < 0$ corresponds to the position when $\pi < \theta \leq 2\pi$). In figures 3-5(b), the dotted line represents the original

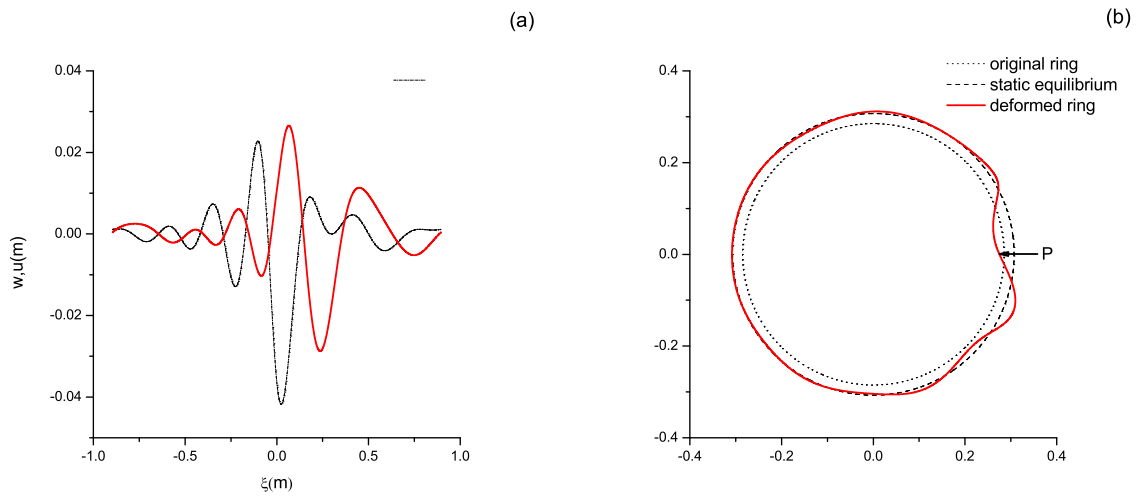

Figure 4: v=70m/s

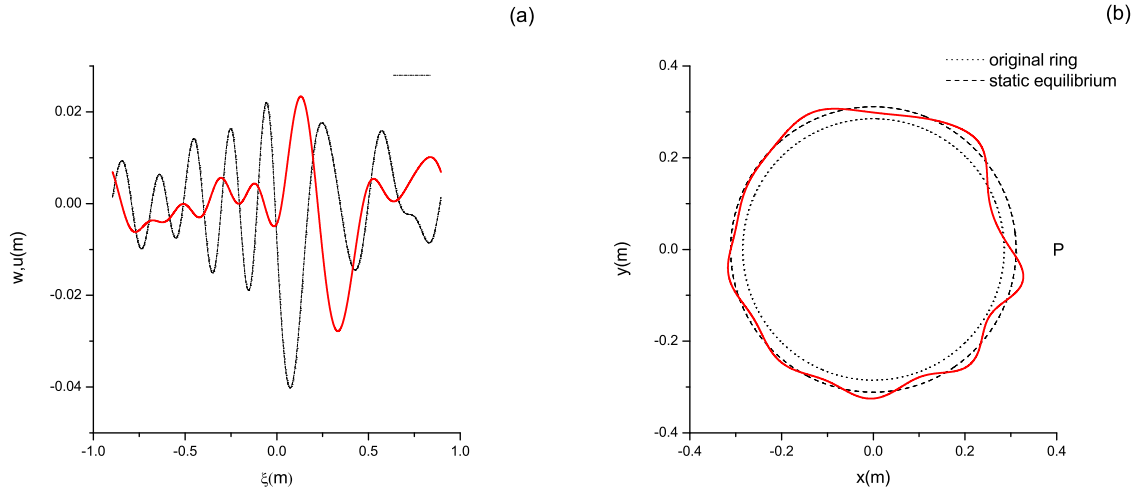

Figure 5: v=80m/s

undeformed ring, the dash line represents the static equilibrium of the ring obtained by equation (4). The ring shape after deformation is depicted by solid line. Note that in all the figures, the ring rotates anticlockwise.

Three different velocities are considered. In Figure 3, the ring rotates with velocity $v = 50m/s$, it is clearly seen that the ring deflections are symmetrical with respect to the loading point (the ring deflections are not perfectly symmetrical because of the damping, but if there is no damping or the rotating speed is small enough, the deflections will be perfectly symmetrical). In this case, it is obvious that the ring rotates at sub-critical speed. In Figure 4, the response for $v = 70m/s$ is shown. Both the radial and the circumferential displacements become wave-like which indicates that the ring now is rotating at a velocity that is higher than the critical speed. The displacements become more wavy and spread from the loading point to the whole ring in Figure 5 when the rotating speed increases to $v = 80m/s$. Further calculation shows the critical speed to be about the same as the

minimum phase speed $v = 62m/s$ of a stationary ring with the same parameters.

6 Comments on other rotating ring models

In most publications, researchers claim that no critical speeds exist for rotating thin ring models, see for example Ref. [1]. As shown in this paper, when the model in Ref. [2] is chosen as a basis in our study, together with a modified pretension, steady state wave-like deformations are predicted. If one follows the procedure proposed in this paper and modifies the pretension to the form of equation (3), one may wonder if other rotating ring models are also capable of predicting the standing waves. Following the procedure presented in this paper, the other two popular rotating thin ring models proposed in Ref. [2, 3] are examined. The examinations show that they can predict critical speed as well, and the resulting critical speeds are similar to those obtained in Section 4 of this paper.

7 Conclusions

In this paper, the following conclusions are made:
Stationary modes for both bending dominant modes and extension dominant modes are reported for a rotating ring using the parameters of a pneumatic tire.
Critical speed is successfully predicted for a rotating ring.
The above formulated conclusions are based on one of the most popular rotating ring models with the modification of the pretension caused by rotation. Other rotating ring models may also be capable of predicting the existence of the critical speed provided that the same modification is implemented.

References

[1] S.C. Huang, W. Soedel, Response of rotating rings to harmonic and periodic loading and comparison with the inverted problem. Journal of Sound and Vibration, 118(2), 253-270, 1987.

[2] S. Gong, A study of in-plane dynamics of tires. PhD Thesis, Delft University of Technology, 1993.

[3] Y.J. Kim, J.S. Bolton, Effects of rotation on the dynamics of a circular cylindrical shell with application to tire vibration. Journal of Sound and Vibration, 275(3), 605-621, 2004.

[4] A.V. Metrikine, M.V. Tochilin, Steady-state vibrations of an elastic ring under a moving load. Journal of Sound and Vibration, 232(3), 511-524, 2009..

[5] J. Padovan, On viscoelasticity and standing waves in tires. Tire Science and Technology, 4(4), 233-246, 1976.

[6] G.R. Potts, C.A. Bell, L.T. Charek, T.K. Roy, Tire vibrations. Tire Science and Technology, 5(4), 202-225, 1977.

[7] S.C. Huang, B.S. Hsu, Resonant phenomena of a rotating cylindrical shell subjected to a harmonic moving load. Journal of Sound and Vibration, 136(2), 215-228, 1990.

[8] Y.T. Wei, L. Nasdala, H. Rothert, Analysis of forced transient response for rotating tires using REF methods. Journal of Sound and Vibration, 320(1), 145-162, 2009.

[9] L.H. Yam, D.H. Guan, A.Q. Zhang, Three-dimensional mode shapes of a tire using ex-perimental modal analysis. Experimental mechanics, 40(4), 369-375, 2000.

[10] T. Lu, A. Metrikine, A rotating ring in contact with a stationary load as a model for a flexible train wheel. EURODYN 2014: Proceedings of the 9th International Conference on Structural Dynamics, Porto, Portugal, 30 June-2 July 2014. Faculty of Engineering of University of Porto, 2014.

Tao Lu, Faculty of Civil Engineering and Geosciences, Delft University of Technology Stevinweg 1, 2628 CN Delft, The Netherlands
Andrei V. Metrikine, Faculty of Civil Engineering and Geosciences, Delft University of Technology Stevinweg 1, 2628 CN Delft, The Netherlands

Steady streaming in a vibrating container at high Reynolds numbers

A. Morgulis, K. Ilin
morgulisandrey@gmail.com

Abstract

We consider the fluid flows in a variable vibrating container while assuming that the width of the Stokes layer is of the same order as the magnitude of the vibration. With no additional assumptions we build the asymptotic expansions of the general vibrational flow. In particular, we get an explicit form of the general equations and boundary conditions for the mean flow ('steady streaming'). We apply these results to exploring the steady 3D streaming in a round pipe due to the transverse deformation of the pipe wall spreading in the form of spiral wave.

1 The steady streaming and the Stokes drift

Let us consider a viscous incompressible and homogeneous flow confined within a container which moves itself and/or changes the shape of itself periodically but with no displacement or deformation on average. The characteristic scales of such motion are: the averaged size of the container, the magnitude of the displacement or deformation, and the correspondent frequency. We denote them as L, A and Ω, respectively. We take L as the unit of length , Ω^{-1} as the unit of time, $U = A\Omega$ as the unit of velocity, and $\rho AL\Omega^2$ as the unit of pressure (where ρ stands for the fluid density). The Navier-Stokes eqs. take the form

$$\mathbf{v}_\tau + \delta(\mathbf{v}, \nabla)\mathbf{v} = -\nabla p + \epsilon^2 \Delta \mathbf{v},\ \nabla \cdot \mathbf{v} = 0 \text{ in } D(\tau); \quad \mathbf{v}(\bar{x} + \delta\tilde{Y}, \tau) = \tilde{Y}_\tau, \bar{x} \in \bar{S}. \quad (1)$$

Here $\tau = \Omega t$, $\delta = A/L$, $\epsilon^2 = \nu/(\Omega L^2)$, where ν is the viscosity of the fluid. Further, $D(\tau)$ stands for the current liquid domain, $\tilde{Y} = \tilde{Y}(\bar{x}, \tau, \delta)$ describes the current displacement of the wall, $\bar{S}$ is the reference ('averaged') position of the wall and $\bar{D}$ denote the reference domain which is confined within $\bar{S}$. The Reynolds number is $Re = (LU)/\nu = LA\Omega/\nu = \delta/\epsilon^2$.

While letting $\epsilon \to +0$ and $\delta \to +0$ in (1) we formally arrive at the vibrational limit which is linear Euler system $\mathbf{v}_{0\tau} = -\nabla p_0$, $\operatorname{div} \mathbf{v}_0 = 0$ endowed with an extra boundary condition, namely $\mathbf{v}_0 = \tilde{Y}_{0\tau}$ on $\bar{S}$. Thus, the leading approximation gives an irrotational ($\operatorname{curl} \mathbf{v}_0 = 0$) flow in the bulk of the fluid while the effect of the viscosity as well as the vorticity concentrate themselves within the Stokes layer alongside $\bar{S}$ the thickness of which is of order ϵ. However the senior approximations discover a *global* steady vortex flow which is widely known as *'steady streaming'*.

In spite of its relative weakness the steady streaming is capable of making effect on the long-term mixing processes. For clarity, let us consider the dimensionless equation of the

fluid particles which is written in the form $dx/dT = \delta^{-1}\mathbf{v}(x,\tau,\delta)$, where $T = \delta^2\tau$ is the 'slow' time. Assume $\mathbf{v} = \tilde{\mathbf{v}}(x,\tau) + \delta(\bar{\mathbf{v}}(x) + \tilde{\mathbf{v}}_1(x,\tau)) + O(\delta^2)$, $\delta \to 0$ where 'tilde'-terms vanish on average. Then $x = \bar{x}(T) + \delta(\bar{x}_1(T) + \tilde{x}(\tau,T)) + O(\delta^2)$, $\delta \to 0$ where $d\bar{x}/dT = \bar{\mathbf{v}}(x) + \overline{[\tilde{\mathbf{v}},\tilde{\mathbf{w}}]}/2$ and the square brackets denote the common commutator of vector fields, and $\tilde{\mathbf{v}} = \tilde{\mathbf{w}}_\tau$. Generically, both summands in $d\bar{x}/dT$ possess vorticity[1] and the latter is known as the Stokes correction.

There is a number of different treatments of the steady streaming depending on the assumptions about dimensionless quantity $\mathrm{Re}_s = (\Omega A^2)/\nu = \delta^2/\epsilon^2$ which is widely known as the streaming Reynolds number. In fact, $\sqrt{\mathrm{Re}_s}$ is nothing more than the ratio of amplitude of the displacements of the boundary to the thickness of the Stokes layer. Assume that they are of the same order *i.e.*

$$\delta \to 0,\ \epsilon \to 0, \quad \sqrt{Re_s} = \delta/\epsilon \stackrel{\text{def}}{=} \beta \equiv \text{const} \sim 1, \quad Re = \beta\epsilon^{-1} \to \infty. \tag{2}$$

Considering of such scales goes back to Craik and Leibovich (1976), Duck and Smith (1979), Haddon and Riley, (1979), Gopinath (1993) [2]. Our approach is more formal and general. We develop asymptotic expansion of general problem (1) with the use of the Vishik-Lyusternik method. V. Levenshtam (2000) employed similar approach in the case of a constant domain and vibrating mass force. Our analysis results in the universal description of the steady streaming and Stokes drift with no use of special assumptions about the flow except for those of (2). On such base we easily treat a number of important particular cases.

2 Governing equation

We start with a number of auxiliary matters. Given a vector field $\mathbf{a}$ on $\bar{D}$ consider the orthogonal (in the natural metric of the energy) decomposition $\mathbf{a} = \mathbf{b} + \nabla\chi$ and associated projectors $\Pi : \mathbf{a} \mapsto \nabla\chi \quad \Pi' : \mathbf{a} \mapsto \mathbf{b}$, where $\mathbf{b}$ is divergent-free field being tangential to $\bar{S}$. Let $\bar{g} = \bar{g}(\cdot)$ be the averaged value of $g = g(\cdot,\tau)$ with respect to τ. We set $\tilde{g} = g - \bar{g}$. Apparently, $\tilde{\bar{g}} = \bar{\tilde{g}} = 0$. In what follows we overline the non-oscillating terms and put tilde over the terms vanishing on average. The integration operator $\partial_\tau^{-1} : g \mapsto f$, $\partial_\tau f = g$ is well-defined in the space of time-periodic $g : \bar{g} = 0$.

Let a be a power expansion. Denote as ${}_m a$ the $m-$th order polynomial obtained by the truncating of a. Further, let $b, c, \ldots$ be polynomials perhaps with variable and vector-valued coefficients. Denote as $\mathrm{op}(b,c,\ldots)$ an algebraic expression over $b, c...$, may be, involving the derivatives of the coefficients.

We seek asymptotic solution $\mathbf{v}, p$ to the system (1) subject to assumptions (2) in the form $(\mathbf{v},p) = (\mathbf{v}^\imath,p^\imath) + (\mathbf{v}^\flat,p^\flat)$ where $\imath$ -terms are to describe the inner flow inside the bulk of the fluid while $\flat$ -terms are to describe the flow near the boundary within the Stokes layer the width of which is of order ϵ. Both $\mathbf{v}^\imath, p^\imath$ and $\mathbf{v}^\flat, p^\flat$ are expanded in ϵ^k, $k = 0,1,2,\ldots$. The coefficients $(\mathbf{v}_k^\imath, p_k^\imath)$ and $(\mathbf{v}_k^\flat, p_k^\flat)$ of both expansions have to be smooth in $x \in \bar{D}$ and 2π -periodic in τ. In addition, $\flat$ - coefficients depend on $\eta = \rho/\epsilon$, where ρ is a non-tangential coordinate nearby $\bar{S}$. These dependencies have to be such that $(\mathbf{v}_k^\flat, p_k^\flat)(\cdot,\eta) = o(\eta^{-n})$ for every n.

[1] The commutator of two irrotational generically has nonzero curl

[2] We omit the detailed references for the sake of compactness. The details can be found in the articles listed at the end of this one. They all are readily accessible via arxiv.org or www.researchgate.net

With this in mind we substitute the unknowns in (1) with the above expansions and arrive at the chain of equation for $\imath$ - coefficients: $\partial_\tau \mathbf{v}^\imath_k = -\nabla p^\imath_k + \mathbf{f}_k$, $\nabla \cdot \mathbf{v}^\imath_k = 0$ inside $\bar{D}$, $\mathbf{v}\cdot\mathbf{n} = \gamma_k$ on $\bar{S}$, where $\mathbf{f}_k = \mathbf{op}(\,_{k-1}\mathbf{v}^\imath)$, $\gamma_k = \mathrm{op}(\,_{k-1}\mathbf{v}^\flat, \,_{k-1}\mathbf{v}^\imath, \,_k\tilde{Y})$ and $\mathbf{n}$ stands for the *inward* normal filed on $\bar{D}$. There exists a solution provided that $\Pi'\mathbf{f}_k = 0$ and no solutions exist otherwise; the solution (if any) is defined up to the mean field $\bar{\mathbf{v}}^\imath_k$. We have to find the mean field while reducing the solvability condition for the next approximation.
Let us come through more details. Let $\mathbf{N}\tilde{\gamma}$ denote the velocity of the irrotational flow the normal component of which on $\bar{S}$ is equal to $\tilde{\gamma}$. To get the iterating started, we set $\mathbf{f}_0 = 0$, $\tilde{\gamma}_0 = \bar{\mathbf{n}}\cdot\tilde{Y}_{0\tau}$, where $\bar{\gamma}_0 = 0$ as the boundary does not vary on average, and $\tilde{Y}_0 = \tilde{Y}(x,\tau,0)$. Then $\mathbf{v}^\imath_0 = \bar{\mathbf{v}}^\imath_0 + \mathbf{N}\tilde{\gamma}_0$; $\nabla\tilde{p}^\imath_0 = -\partial_\tau\mathbf{N}\tilde{\gamma}_0$. While calculating the first-order terms, we face the solvability condition which coincides with the steady incompressible Euler equation in $\bar{D}$. In sec. 3 we'll see that we have to seek the solution obeying both no-flux and no-slip boundary conditions. Such problem seems to be overdetermined but there always exists the trivial solution $\bar{\mathbf{v}}_0 \equiv 0$. Although another choice can be of sense too we do not explore such possibility here.
Thus the first-order term $\bar{\mathbf{v}}_1$ is the leading one for the steady streaming. Next we pass to the second order terms but the evaluating of them produce no equation for $\bar{\mathbf{v}}_1$ as the correspondent solvability condition turns out to be always satisfied. The solvability condition for the third-order terms takes the following form

$$\Delta\bar{\mathbf{v}}^\imath_1 - \nabla H_1 = \beta\bar{\boldsymbol{\omega}}^\imath_1\times\mathbf{V};\ \nabla\cdot\bar{\mathbf{v}}^\imath_1 = 0;\ \mathbf{V} = \bar{\mathbf{v}}^\imath_1 + \beta\overline{[\boldsymbol{\xi}_\tau,\boldsymbol{\xi}]}/2,\ \boldsymbol{\xi} = \mathbf{N}(\partial_\tau^{-1}\tilde{\gamma}_0) \tag{3}$$

where $\bar{\boldsymbol{\omega}}^\imath_1 = \nabla\times\bar{\mathbf{v}}^\imath_1$.[3] Thus, $\mathbf{V}$ is the total drift velocity which is responsible for the transporting of the mean vorticity into the bulk of the fluid. The averaged commutator $\beta\overline{[\boldsymbol{\xi}_\tau,\boldsymbol{\xi}]}/2$ is nothing more then the Stokes correction.

3 Boundary condition.

Currently, our target is the deriving of the boundary conditions for the mean flow. To this end, we have to consider asymptotic expansion inside the Stokes layer. To do so we employ coordinates $x\mapsto(\rho,\theta)$ where $\rho(x) = \mathrm{dist}(x,\bar{S})$, θ is the point in $\bar{S}$ which is nearest to x. Such mapping induces the decomposition $\mathbf{h} = \mathbf{h}^{\shortparallel} + \mathbf{h}_{\mathfrak{n}}$, where the former summand is the tangential component and the latter one is the normal component of $\mathbf{h}$.[4] We rewrite system (1) relative to the coordinates (ρ,θ) and then separate the normal and tangential projections of it. Next we inflate the Stokes layer with the stretched normal coordinate $\eta = \rho/\epsilon$. We use slightly different expansions for the normal and tangential velocities as well as for the pressure; namely $(\mathbf{v}^\flat_0)_{\mathfrak{n}} = p^\flat_0 = p^\flat_1 = 0$, $(\mathbf{v}^\flat_{k+1})_{\mathfrak{n}} = u^\flat_k$, $p^\flat_{k+2} = P^\flat_k$, $\mathbf{w}^\flat_k = (\mathbf{v}^\flat_k)^{\shortparallel}$ $k = 0,1,\ldots$. Then the equations for the boundary layer corrections and boundary conditions take the form

$$\left(\partial_\tau + \beta\tilde{\gamma}_0\partial_\eta + \partial^2_\eta\right)\mathbf{w}^\flat_k = \mathbf{F}_k;\quad \partial_\eta u^\flat_k = S_k;\quad \partial_\eta P^\flat_k = R_k;\quad \eta > \beta\tilde{\eta}_0(\theta,\tau); \tag{4}$$

$$\mathbf{w}^\flat_k = \beta^k(\tilde{Y}_{k\tau} - \mathbf{b}_k)^{\shortparallel} - \mathbf{w}^\imath_k;\quad u^\imath_k = \beta^k(\tilde{Y}_{k\tau} - \mathbf{b}_k)_{\mathfrak{n}} - u^\flat_{k-1};\quad \text{if } \eta = \beta\eta_0, \tag{5}$$

$$\tilde{\eta}_0(\theta,\tau) = \partial_\tau^{-1}\tilde{\gamma}_0(\theta,\tau) = (\tilde{Y}_0)_{\mathfrak{n}}|_{\rho=0};\quad (\mathbf{w}^\flat_k, u^\flat_k, P^\flat_k) = o(\eta^{-s}),\ \eta\to\infty\ \forall s>0; \tag{6}$$

$$\mathbf{b}_k = \mathbf{op}(\,_{k-1}\mathbf{v}^\imath, \,_{k-1}\mathbf{w}^\flat, \,_{k-1}u^\flat, \,_k\tilde{Y});\quad S_k = \mathrm{op}(\,_k\mathbf{v}^\imath, \,_kp^\imath, \,_{k-1}u^\flat, \,_{k-1}P^\flat, \,_k\mathbf{w}^\flat); \tag{7}$$

$$\mathbf{F}_k = \mathbf{op}(\,_{k-1}u^\flat, \,_{k-1}\mathbf{w}^\flat, \,_{k-1}P^\flat, \,_{k-1}\mathbf{v}^\imath, \,_{k-1}p^\imath);\quad R_k = \mathrm{op}(\,_k\mathbf{v}^\imath, \,_kp^\imath, \,_ku^\flat, \,_{k-1}P^\flat, \,_k\mathbf{w}^\flat). \tag{8}$$

[3] For the deriving of Eq.(3) we employ the equality $\mathbf{a}\times[\mathbf{b},\mathbf{c}]+\mathbf{c}\times[\mathbf{a},\mathbf{b}]+\mathbf{b}\times[\mathbf{c},\mathbf{a}] = \nabla(\mathbf{a}\cdot(\mathbf{b}\times\mathbf{c}))$ which is valid for every three of the divergence free fields.

[4] Now we direct the normal towards the bulk of the fluid.

Here all the $\imath-$terms or their derivatives are restricted onto $\bar{S}$ i.e. to $\rho = \eta = 0$. Note also that $\mathbf{F}_k$, R_k and S_k possesses the decay rate (6) provided that the $\flat-$terms they involve possesses the same decay rate.

Substituting η with $s = \eta - \beta\eta_0 > 0$ transforms the first equation of (4) into the canonical heat equation in a semi-plane $\{(s,\tau) : s > 0\}$ and the first boundary condition (5) then moves to the line $s = 0$. Note that the appearing of the advection in the first equation of (4) is the direct consequence of assumption (2).

The oscillating projection of the first equation in (5) gives boundary condition to the first equation in (4) while the oscillating projection of the second gives the boundary condition to the normal velocity of the inner flow. The averaging of the both gives the boundary values for $\bar{\mathbf{v}}_k^\imath$ i.e. for the mean flow. The calculating of them involves $\bar{\mathbf{w}}_k^\flat$ and $\bar{u}_k^\flat$ which one can get via the averaging of the first and second equations of (4) with account of the decay condition. We emphasize that the averaging is always performed relative to the moving frame *i.e.* we *first* write all the things using s-variable first and *next* perform the averaging.

System (4-8) possesses triangular structure which allows us to find $\mathbf{w}_k^\flat$ first, $u_k^\flat$ next and $P_k^\flat$ finally. To get the process started we set $\mathbf{b_0} = 0$, $\mathbf{F}_0 = 0$. Then $\bar{\mathbf{w}}_0^\imath = 0$ and $\bar{\gamma}_0 = 0$ as stated in Sec. 2.

Now we formulate the boundary conditions for $\bar{\mathbf{v}}_1^\imath$. We denote as $\hat{h}_m$, $m \in \mathbb{Z}$ the Fourier coefficients for periodic function h. Also, $\hat{Y}_m$ stands for the Fourier coefficient of $\tilde{Y}_0 = \tilde{Y}(x,\tau,0)$. On $\bar{S}$, we define a vector field $\mathbf{q} = \tilde{Y}_0 - \boldsymbol{\xi}$, $\mathbf{q} \parallel \bar{S}$. Thus,

$$\begin{aligned}
&\beta^{-1}\bar{\mathbf{w}}_1^\imath\big|_{\bar{S}} = \overline{(\nabla^{\shortparallel}\cdot\mathbf{q})\mathbf{q}_\tau}/2 - \sum |m|\left(\nabla^{\shortparallel}|\hat{\mathbf{q}}_m|^2 + 4(\nabla^{\shortparallel}\cdot\hat{\mathbf{q}}_m)\hat{\mathbf{q}}_{-m}\right)/4 - \overline{[\tilde{Y}_{0\tau}^{\shortparallel},\tilde{Y}_0^{\shortparallel}]}/2 - \\
&-\frac{1}{2}\sum |m|\left(\nabla^{\shortparallel}\cdot(\hat{Y}_m\times\nabla\rho)\right)(\nabla\rho\times\hat{\mathbf{q}}_{-m}) - 2\overline{(\operatorname{curl}(\boldsymbol{\xi}\times\nabla\rho)\cdot\nabla\rho - \tilde{\eta}_0\Delta\rho)\mathbf{q}_\tau} - \\
&-\overline{\tilde{\eta}_0\nabla^{\shortparallel}\tilde{\eta}_{0\tau}} - 2\overline{\tilde{\eta}_{0\tau}(\tilde{Y}_0^{\shortparallel},\nabla)\nabla\rho} - \overline{(\nabla^{\shortparallel}\cdot(\tilde{Y}_0\times\nabla\rho))(\nabla\rho\times\boldsymbol{\xi}_\tau)} - \nabla^{\shortparallel}\overline{(\boldsymbol{\xi}_\tau^{\shortparallel}\cdot\tilde{Y}_0^{\shortparallel})} - \qquad (9)\\
&-\beta\overline{(\tilde{Y}_0^{\shortparallel}\cdot\nabla\tilde{\eta}_0)\,\mathbf{W}_s|_{s=0}};\quad \mathbf{W}_\tau = \mathbf{W}_{ss},\ s>0,\ \mathbf{W}(0,\tau) = \mathbf{q}_\tau,\ \mathbf{W}(\infty,\tau) = 0.\\
&\beta^{-1}\bar{u}_1^\imath\big|_{\bar{S}} = \beta^{-1}\bar{\gamma}_1^\imath = \overline{[\boldsymbol{\xi},\boldsymbol{\xi}_\tau]_{\mathfrak{n}}}/2. \qquad (10)
\end{aligned}$$

Equations (3) and boundary conditions (9-10) gives us the total drift velocity $\mathbf{V}$. Note that $\mathbf{V}$ is always tangential to $\bar{S}$.

4 Examples

1. The tangential and torsional vibrations are natural provided that a subgroup of the motions acts on $\bar{S}$. For such vibrations, the Stokes term is always equal to zero.

For instance, consider the tangential vibrations of a circular pipe. Then $\bar{D} = \{r < 1\}$, and $\rho = 1 - r$ (relative to proper cylindrical coordinates). Every tangential motion of the boundary can be written as $Y_0 = \tilde{\kappa}_0(\tau)\mathbf{e}_\theta + \tilde{\kappa}_1(\tau)\mathbf{e}_z = \mathbf{q}$. where $\tilde{\kappa}_0(\tau)$ and $\tilde{\kappa}_1(\tau)$ are given scalar periodic functions. Apparently, $\nabla^{\shortparallel}\cdot\mathbf{q} = 0$, $\nabla^{\shortparallel}|\hat{\mathbf{q}}_k|^2 = 0$ and $\nabla^{\shortparallel}\cdot(\hat{\mathbf{q}}_k\times\nabla\rho) = 0$ once again. Thus, *translational-rotational tangential vibrations of the circular pipe produce no steady streaming in the leading approximation.*

Consider now *the torsional oscillations of a ball submerged in unbounded fluid.* Then the averaged flow domain is $\bar{D} = \{r > 1\}$, $r = |x|$, $\bar{S} = \{r = 1\}$, $\rho = r - 1$, $\nabla\rho = \theta = x/r$. Let $\tilde{Y}_0 = \mu(\tau)\mathbf{k}\times\boldsymbol{\theta}$, where $\mathbf{k} \equiv \text{const}$, $|\mathbf{k}| = 1$, μ is scalar 2π-periodic function vanishing on average. Then $\hat{\mathbf{q}}_m = \hat{\mu}_m\mathbf{k}\times\boldsymbol{\theta}$ and no one term on the righthand side of (9) contributes in $\bar{\mathbf{w}}_1^\imath$ except for $-\frac{1}{4}\sum|m|\nabla^{\shortparallel}|\hat{\mathbf{q}}_m|^2$ and for $-\frac{1}{2}\sum|m|\left(\nabla^{\shortparallel}\cdot(\hat{Y}_m\times\nabla\rho)\right)(\nabla\rho\times\hat{\mathbf{q}}_{-m})$. In the end, we get $\bar{\mathbf{w}}_1^\imath|_{\bar{S}} = -(\kappa\beta/4)\sin 2\psi\mathbf{e}$, $\kappa = \sum|m||\hat{\mu}_m|^2$, $\cos\psi = \mathbf{k}\cdot\boldsymbol{\theta}$ here ψ is the

latitude on S, $\psi = \pi/2$ on the equator and $\mathbf{e}$ is the unit vector associated with ψ; on the equator, $\mathbf{e}$ is directed as $\mathbf{k}$. Thus, *the steady streaming driven by the torsional oscillations of a submerged ball moves the fluid from the poles towards the equator* that is in agreement with the experiments of Hollerbach *et al* (2009), see Morgulis (2010) for more detailed analysis.

Consider *the translational vibrations of a submerged ball.* Then $\tilde{Y}_0 = \mu(\tau)\mathbf{k}$ (with the same $\bar{D}$, $\bar{S}$, μ and $\mathbf{k}$ as in the case of the torsional vibration). Such vibrations are not tangential but produce no Stokes correction again, *i.e.* $\overline{[\boldsymbol{\xi}_\tau, \boldsymbol{\xi}]} = 0$ everywhere in the flow domain. As a result, $\bar{u}_1^i = 0$ on $\bar{S}$, see (10). Furthermore, $\mathbf{q} = 3\mu(\boldsymbol{\theta} \times (\mathbf{k} \times \boldsymbol{\theta}))/2$. No one term on the righthand side of (9) contributes in $\bar{\mathbf{w}}_1^i$ except for $-\frac{1}{4}\sum |m| \left(\nabla^{\shortparallel}|\hat{\mathbf{q}}_m|^2 + 4(\nabla^{\shortparallel} \cdot \hat{\mathbf{q}}_m)\hat{\mathbf{q}}_{-m}\right)$, and $\bar{\mathbf{w}}_1^i = (45\kappa\beta/16)\sin 2\psi \mathbf{e}$. This time, *the steady streaming driven by the translational oscillations of a submerged ball moves the fluid from the equator towards the poles.*

2. The normal vibrations are such that $\tilde{Y}_0^{\shortparallel} = 0$. Then $\tilde{Y}_0 = \tilde{\eta}_0 \nabla\rho$, $\mathbf{q} = -\boldsymbol{\xi}^{\shortparallel}$. For instance, consider *the normal vibrating of the lid of a liquid half-space.* Let $\mathbf{e}_x, \mathbf{e}_y, \mathbf{e}_z$ be the unit vectors of Cartesian coordinates system $Oxyz$ relative to which $\bar{D} = \{z > 0\}$, $\bar{S} = \{z = 0\}$ and $\rho = z$. Let $\tilde{\eta}_0 = \tilde{\eta}_0(x, \tau)$. Then $\boldsymbol{\xi} = \xi\mathbf{e}_x + \eta\mathbf{e}_z$, $\tilde{\eta}_0 = \eta|_{z=0}$ and $\mathbf{q} = -\xi\mathbf{e}_x$. Further, $\operatorname{curl}(\boldsymbol{\xi} \times \nabla\rho) \cdot \nabla\rho = -\xi_x$, and $\Delta\rho = 0$. Then

$$\bar{\mathbf{w}}_1^i|_{\bar{S}} = w\mathbf{e}_x,\ w = \beta\overline{\tilde{\eta}_{0x}\tilde{\eta}_{0\tau}} - (3\beta/2)(\overline{\xi_x\xi_\tau} + (\partial_x/2)\sum |k||\hat{\xi}_k|^2)|_{z=0};$$
$$\tfrac{\beta}{2}\overline{[\boldsymbol{\xi}_\tau, \boldsymbol{\xi}]} = \beta(\bar{\psi}_z\mathbf{e}_x - \bar{\psi}_x\mathbf{e}_z);\quad \bar{u}_1^i = \beta\bar{\psi}_x|_{z=0},\quad \bar{\psi} = \overline{\eta\xi_\tau};.$$

Consider now normal vibration being produced with *a planar traveling wave, i.e.* set $\tilde{\eta}_0(x, \tau) = f(\alpha x - \tau)$, where $f(\sigma) = \sum \hat{f}_k \mathrm{e}^{ik\sigma}$ is prescribed. Then

$$\eta = \sum \hat{f}_k \mathrm{e}^{-\alpha|k|z + ik\sigma};\ \xi = -i\sum \hat{f}_k \operatorname{sgn} k \mathrm{e}^{-\alpha|k|z+ik\sigma};\ \sigma = \alpha x - \tau;$$
$$\overline{\tilde{\eta}_{0x}\tilde{\eta}_{0\tau}} = \overline{\xi_x\xi_\tau}|_{z=0} = -\alpha\overline{f'^2};\ \bar{\psi} = -\sum |\hat{f}_k|^2|k|\mathrm{e}^{-2|k|\alpha z};$$
$$\bar{u}_1^i = 0,\ \bar{\mathbf{v}}_1^i = w\mathbf{e}_x,\ w = \alpha\beta\overline{f'^2}/2 \equiv \text{const},$$
$$\tfrac{\beta}{2}\overline{[\boldsymbol{\xi}_\tau, \boldsymbol{\xi}]} = \beta\bar{\psi}'(z)\mathbf{e}_x = 2\beta\alpha\sum |\hat{f}_k|^2 k^2 \mathrm{e}^{-2|k|\alpha z}.$$

Here the mean field $\bar{\mathbf{v}}_1^i$ is constant. The total drift velocity is

$$\mathbf{V} = W(z)\mathbf{e}_x,\ \text{where } W(z) = \alpha\beta\overline{f'^2}/2 + 2\beta\alpha(\sum |\hat{f}_k|^2 k^2 \mathrm{e}^{-2|k|\alpha z}).$$

Thus *the steady streaming being induced by the spreading of the normal displacements in the form of a planar wave traveling along the lid of a liquid semi-space moves the drifting particles in the direction of the wave propagation (as $W(z) > 0$ for every $z > 0$). The streamlines are everywhere parallel to the direction of the wave propagation. The velocity magnitude depends on the depth only and attains a nonzero limit far down from the lid as the Stokes correction becomes negligible.*

Finally, consider *the normal vibrations of the wall of a circular pipe being produced with a spiral traveling wave.* Again, $\bar{D} = \{r < 1\}$, $\bar{S} = \{r = 1\}$ and $\rho = 1 - r$ relative to the cylindrical coordinates r, θ, z, and

$$\tilde{\eta}_0(\theta, z, \tau) = f(\alpha z + n\theta - \tau),\ n \in \mathbb{N},\quad f = f(\sigma) = \sum \hat{f}_k \mathrm{e}^{ik\sigma}.$$

We treat this case by analogy with the previous one. As usual, $I_p(s)$, $p \in \mathbb{N}$, stands for modified Bessel function of first kind (bounded for $s \to +0$) of order p. For the sake of convenience, define

$$\chi_{k,n,\alpha}(s) = \tfrac{d}{2ds}\left(\frac{I_{n|k|}(s)}{I'_{n|k|}(\alpha n|k|)}\right)^2;\ \mu_{k,n,\alpha} = \frac{I_{|k|n}(\alpha|k|)}{I'_{|k|n}(\alpha|k|)},\quad k \in \mathbb{Z};$$

The tangential and normal components of the mean velocity on $\bar{S}$, the mean velocity itself, the Stokes correction, and the drift velocity field have the forms

$$\bar{\mathbf{w}}_1^i = \beta C_{n,\alpha}\,(n\mathbf{e}_\theta + \alpha\mathbf{e}_z)\,;\, \bar{u}_1^i = 0;\ \bar{\mathbf{v}}_1^i = \beta C_{n,\alpha}(nr\mathbf{e}_\theta + \alpha\mathbf{e}_z); \tag{11}$$

$$C_{n,\alpha} = \sum k^2|\hat{f}_k|^2\left(\tfrac{3}{2}(1+\tfrac{n^2}{\alpha^2})\mu_{k,n,\alpha}^2 - \tfrac{2\mu_{k,n,\alpha}}{|k|\alpha} - 1\right); \tag{12}$$

$$(\beta/2)\overline{[\boldsymbol{\xi}_\tau, \boldsymbol{\xi}]} = \beta(v_{n,\alpha}(r)n\mathbf{e}_\theta + w_{n,\alpha}(r)\alpha\mathbf{e}_z); \tag{13}$$

$$v_{n,\alpha} = \tfrac{1}{r}\sum k^2|\hat{f}_k|^2\left(\chi'_{k,n,\alpha}(\alpha|k|r) - \tfrac{\chi_{k,n,\alpha}(\alpha|k|r)}{\alpha|k|r}\right); \tag{14}$$

$$w_{n,\alpha} = \sum k^2|\hat{f}_k|^2\left(\chi'_{k,n,\alpha}(\alpha|k|r) + \tfrac{\chi_{k,n,\alpha}(\alpha|k|r)}{\alpha|k|r}\right); \tag{15}$$

$$\mathbf{V} = (\beta/2)[\boldsymbol{\xi}_\tau, \boldsymbol{\xi}] + \bar{\mathbf{v}}_1^i = \beta\left(v_{n,\alpha}^d n\mathbf{e}_\theta + w_{n,\alpha}^d\alpha\mathbf{e}_z\right); \tag{16}$$

$$v_{n,\alpha}^d = rC_{n,\alpha} + v_{n,\alpha};\ w_{n,\alpha}^d = C_{n,\alpha} + w_{n,\alpha} \tag{17}$$

Thus the steady streaming being induced with the spreading of the normal displacements in the form of a spiral wave traveling along the wall of a circular pipe gives rise to a translational-rotational motion of the drifting particles. The axial and rotational velocities depend only on the distance from the pipe axis and the streamlines are helixes.

The Stokes corrections to the axial and rotational velocities are always positive *i.e.* the directions of the correspondent rotating and translating of the drifting particles are the same as those of the deforming wave. Indeed, the modified Bessel equation implies that

$$\left(I'_pI_p\right)' + s^{-1}I'_pI = I'^2_p + (1+s^{-2}p^2)I_p^2;$$
$$\left(I'_pI_p\right)' - s^{-1}I'_pI = \left(I'_p - s^{-1}I_p\right)^2 + (1+(p^2-1)s^{-2})I_p^2.$$

Then every summand in (14-15) is positive. Despite of this observation, the components of total drift velocity (17) can change their signs, *i.e.* the directions of the translating or revolving of different layers of the fluid can be opposite one to another. Indeed, consider the long-wave limit *i.e.* let $\alpha \to 0$. For simplicity, let f be a trigonometric polynomial of degree N. Then

$$C_{n,\alpha} = \sum k^2|\hat{f}_k|^2\left(1/2 - 2/(|k|n) + O(\alpha)\right),\ \alpha\to 0;$$
$$v_{n,\alpha}^d\Big|_{r=1} = \sum k^2|\hat{f}_k|^2\left(5/2 - 4/(|k|n) + O(\alpha)\right),\ \alpha\to 0;$$
$$w_{n,\alpha}^d\Big|_{r=1} = \sum k^2|\hat{f}_k|^2\left(5/2 - 2/(|k|n) + O(\alpha)\right),\ \alpha\to 0;$$

Thus $C_{n,\alpha}$ can be negative, that is, the rotational and axial components of mean velocity can be directed oppositely to those of the deforming wave provided that $n = 1, 2, 3$ while α is small enough. If $n = 1$ in addition then $v_{n,\alpha}^d$ can be negative for $r = 1$, that is, the rotating of the drifting material particle can be opposite to that of the deforming wave near the wall[5] of the pipe. Finally, $w_{1,\alpha}^d$ is positive in the long-wave limit, that is, the axial drift always follows the wave near the pipe wall.

Consider now the vicinity of the pipe axis. It is convenient to watch the behaviour of angular velocity. Then

$$\lim_{r\to+0}\tfrac{v_{n,\alpha}(r)}{r} = \alpha^2\sum_{0<n|k|\le 2}\tfrac{k^2|\hat{f}_k|^2}{4^{|kn|}I'^2_{n|k|}(\alpha|k|)};\qquad n = 1,2;$$

$$\lim_{r\to+0}\tfrac{v_{n,\alpha}}{r} = 0,\ n>2;\quad w_{1,\alpha}|_{r=0} = \tfrac{5|\hat{f}_1|^2}{2I'^2_1(\alpha)},\ w_{1,\alpha}|_{r=0} = 0,\ n>1.$$

[5] "Near the wall" means that the distance from the wall is small enough but still much greater when the width of the boundary layer (which is of order ϵ)

We conclude that in the long-wave limit, $w^d_{n,\alpha}$, $n = 1, 2, 3$ can be negative on the axis but always positive near the wall. Consequently, the axial drift of the material particles can change its direction in the bulk of the fluid; namely, the axial drift always follows the wave near the pipe wall but the counter drifting can occur near the axis. However if $n = N = 1$ then the axial drift follows the wave on the axis too. (We remind that N is the degree of polynomial f).
Consider now the long-wave limit for the angular velocity $\Gamma_{n,\alpha}(r) = C_{n,\alpha} + r^{-1}v_{n,\alpha}$. If $n > 3$ then the drifting particles and the deforming wave revolve themselves in the same direction. Otherwise the rotating keeps the same direction near the pipe wall while the counter revolving can occur near the axis. If $n = 1$ there is an extra possibility: the counter revolving occurs both near the wall and near the axis and so happens inevitably provided that $n = N = 1$, see Fig. 1.
On Fig. 1, the profiles of the angular velocity of the total drift vs the distance from the pipe axis are presented for the case of the vibrations being produced by single harmonic, that is, for $f(\sigma) = \cos\sigma$. The right hand panel displays the plots for different azimuthal wave numbers while the wave length is fixed. The left hand panel displays plots for different wave lengths while azimuthal wave number is fixed. It is worth to note that there are such the values of the wave length that the angular velocity turns out to be much smaller near the pipe wall than near the axis. While looking at the right hand panel, it can be seen that the doubling of the azimuthal wave number is able to re-direct the rotating of all of the drifting particles. Further increase of the wave number from doubled to tripled changes the direction of the rotation again; however, the changing happens not everywhere but near the axis only.

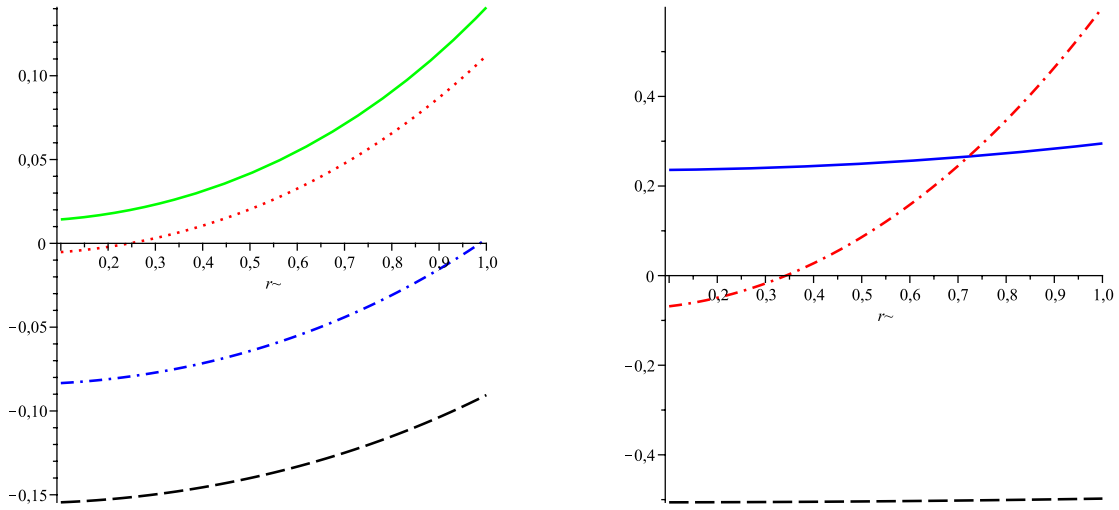

Figure 1: The left hand panel displays $\Gamma_{n,\alpha}$ vs r where $n = 1$ while $\alpha = 1.13$ (solid line), $\alpha = 1.1$ (dotted line), $\alpha = 0.99$ (dash-dotted line) and $\alpha = 0.9$ (dashed line). The right hand panel displays $\Gamma_{n,\alpha}$ vs r where $\alpha = 0.5$ while $n = 1$ (dashed line), $n = 3$ (dash-dotted line) and $n = 2$ (solid line).

Acknowledgements

The research constituting the contribution of A. Morgulis into this article had been fulfilled within the project being a part of Russian governmental task in the sphere of scientific

activity No. 1.1398.2014/K.

References

[1] Ilin K., Morgulis A. Steady streaming between two vibrating planes at high Reynolds numbers. arXiv:1108.2710v1 [physics.flu-dyn] 2011.

[2] On The Steady Streaming Induced By Vibrating Walls. SIAM J. Appl. Math. 2012. Vol. 72, No. 5. Pp. 1406 - 1427.

[3] Morgulis A.B. High frequency asymptotic for the viscous fluid flow due to the torsional oscillations of a submerged ball. Modern Problems in Cont. Mech. Proc. of XIV Int. Conf. Vol.1. C. 235–240. Rostov-on-Don, 2010 (Russian). http://mcc-conf.ru/results.html

Morgulis A.B., Inst. for Math. Mech. and Comp. Sci, Southern Federal University, Milchakova 8a, Rostov-na-Donu, Russia
Ilin K.I., Dept. of Math., The University of York, Heslington,York,UK

Hyperelastic structural-mechanical model of filled rubber. Influence of filler dispersion and interfacial properties

Ilya A. Morozov, Lyudmila A. Komar
ilya.morozov@gmail.com

Abstract

The microstructure of filled rubber (heterogeneous filler network in rubber matrix) is modelled by a volume filled with thousands of rigid spherical inclusions. Inclusions could be grouped into secondary structures вГУ fractal clusters. Inclusions are connected by damageable links representing the mechanical behaviour of the elastomer in the gaps between filler particles. The formation of the interfacial polymer layer is taken into account. The volume is subjected to stepwise deformation. Hysteresis losses under cyclic loading conditions are modelled by way of breaking links. The influence of the microstructure (filler fraction, cluster/random filler distribution) and properties of interfacial layers, on the macroscopic characteristics of filled elastomers are discussed.

1 Introduction

Reinforcement of elastomers by active fillers, in particular carbon black (CB) improves the mechanical and strength characteristics of rubbers. Elastic properties inherent in unfilled vulcanizates remain unchanged. CB is represented by the primary indivisible aggregates of the order of 0.1...0.2 μm. However, the filler is added to the polymer in a pelletized form (grains of size 1 вГУ- 3 mm). During the process of mixing of composite ingredients these grains are somehow separated and distributed throughout the matrix. Depending on the mixing parameters and elastomer viscosity, part of the filler is left in the composite in the form of bulk inclusions вГУ micropellets. At the same time CB aggregates in the polymer matrix form secondary structures вГУ fractal clusters. At some volume fraction, the filler in the matrix forms a continuous network of clusters. Experimental studies have revealed that the surface of active filler in a rubber is surrounded by a reduced-mobility polymer layer [1]. The thickness of this layer is 2 nm, and it exhibits properties similar to the polymer in a glassy-like state. According to some hypotheses [2], the mobility of molecules increases gradually outward from the surface and at a distance of 10 nm passes into the matrix. One of the effective ways of explaining the mechanical properties of the composites is structural-mechanical modeling. The finite element method is used in the works [5, 6] to determine the macroscopic properties of filled rubber. On the basis of the periodicity cell, the authors examine the stress-strain state, depending on the location

[5, 6] and shape [6] of inclusions. Both works describe the effect of stress softening. In the first case [5] stress softening effect is modeled by reducing (result of local ruptures) the number of elastic macromolecular segments in the second [6] - due to the viscoelastic properties of the binder. FEM models are limited by large computational costs and the complexity of calculations arising from the large deformations and on the borders of the hard and soft phases. In the work of Xi and Hentschke [7] filled elastomer is presented by the volume of elements, each of which is either part of the filler or fragment of matrix. The force interactions between the elements exist. Introducing the force response under low shear stress, the authors simulate the Payne effect. We should also mention the work of Garishin and Moshev [8], which is describe the discrete model of behavior of random filler structure in an elastomer matrix under uniaxial loading. In the present work, a structural-mechanical model for filled elastomers is proposed which takes into account the peculiar microstructural features of the material. Inclusions are connected by hyperelastic links. The mechanical properties of these links are dependent on the size of the gap between inclusions and the characteristics of hypothetical interfacial layers.

2 Concept of the model

The structure of the composite is represented as a system of rigid spherical inclusions. For modelling of interfacial interactions the links are used (Fig.1), which are, in fact, the rods pivotally connected to the centres of inclusions and working in tension and compression only. Two types of links are considered: 1. Links between inclusions with the initial gap

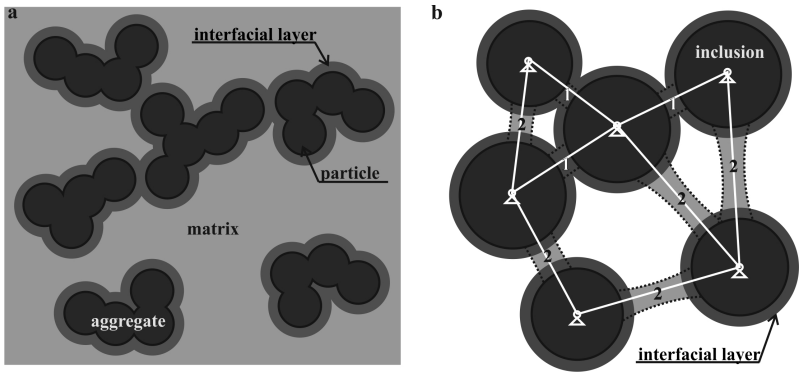

Figure 1: Continuum structure (a) and discrete model (b) of the filled elastomer. Different types of links are indicated by the numerals (description is given in the text).

δ_0 <20 nm, which has a common special layer with a thickness 10 nm. 2. Links between inclusions that do not have common intersecting layers ($\delta_0 \geq 20$ nm) and interact in the material via the elastomer matrix. The external load changes the location of inclusions and the configuration of links. Shortly speaking, the links are irreversibly broken under a particular load. In addition, the case where the special layers are absent, i.e. the properties of links coincide with the properties of the matrix, is analyzed.

3 Mechanical interaction of the pair of inclusions in the elastomer

The force due to the stretching or compression of the link between two inclusions was determined by the finite element method by analyzing the stress-strain state in the gap between two rigid inclusions embedded in a hyperelastic low compressible polymer (Poisson ratio – 0.495). In the calculation, an elastomeric matrix was assigned the properties of unfilled styrene butadiene vulcanizate, and the corresponding experimental uniaxial tension curve was approximated by the third-order Ogden potential.
For simplicity, we suggest that the forces occur in the gaps between the nearest carbon black particles of the neighboring aggregates (Fig.2a). The particle radius is assumed to be equal to 15 nm. The special layer is divided into 5 equal parts with the corresponding elastic modulus: E_i = 60, 30, 7, 5, 3 MPa (Fig. 2b). The modulus of the matrix is 1 MPa. In the case of inclusion interaction in the absence of a special layer, E_i = 1 MPa. It is assumed that the inclusion is an absolutely rigid one, and the interface between the inclusion and the matrix is in perfect adhesion. As a cohesive failure criterion for the

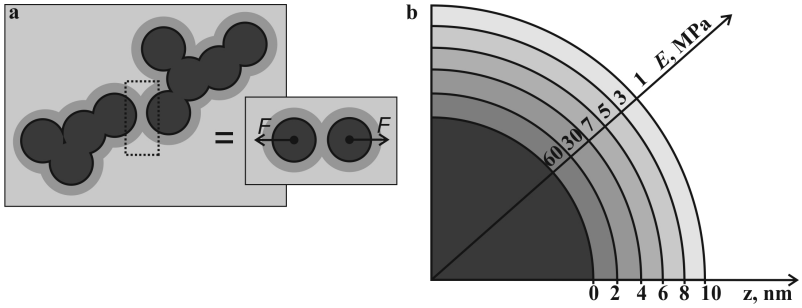

Figure 2: Carbon black aggregates in the matrix surrounded by a special layer and the structural element for calculating force interactions (a); elastic modulus of the layer versus the distance from the surface (b).

structural element, we have taken the Gent approach [3]: $< \sigma > = 5/6E$, where $< \sigma >$ is the hydrostatic stress in the center of the gap between inclusions; E is the elastic modulus in the center of the gap. The plots of force F versus elongation in the gap λ_g up to the point at which the fracture begins are presented in Fig.3. The results indicate that the structural elements with specific layers begin to fracture at lower deformation, and the resulting force is twice as much as the force for elements without specific layers.

4 Structural – mechanical modelling

The microstructure is modelled as a cube non-uniformly filled with spheres of equal size. The minimum acceptable space between the spheres is 2 nm. The spheres are assembled into fractal clusters. Comprehensive analysis of fractal structure and the synthesis algorithms are given in work [4]. Apart from the clustered structure, the case of random filler distribution is also considered. The filler volume fraction in the investigated structures is 0.13 (30 weight parts of filler).
By virtue of the constancy of the volume, the structure is deformed by the step-wise displacement of inclusions. After each deformation step, the coordinates of inclusions are refined in the context of forces that occur in links. This is done by minimizing the local

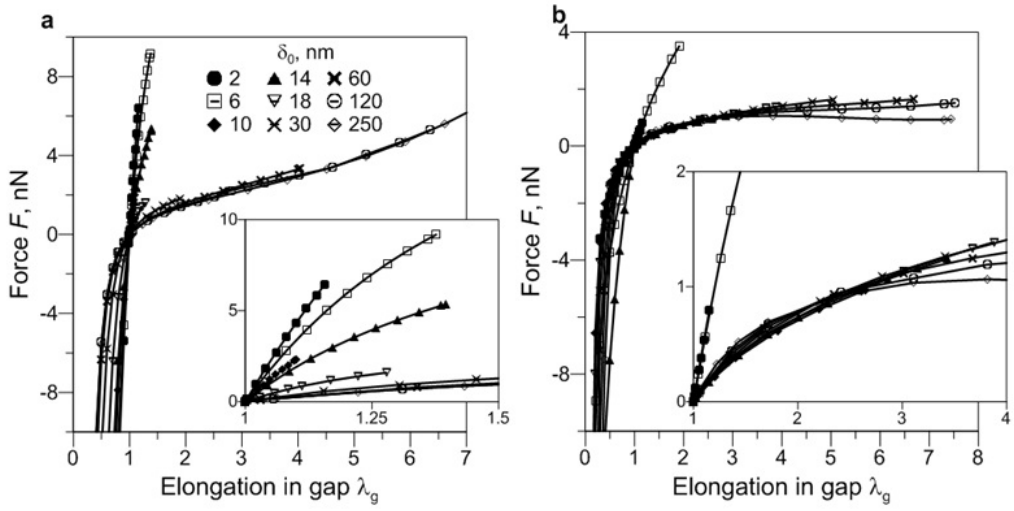

Figure 3: Plots of force F versus elongation in the gap for different initial gaps δ_0: (a) вГУ inclusions are surrounded by a specific layer; (b) вГУ characteristics of the layer coincide with the matrix.

elastic energy of links. The minimization is performed by the Nelder вГУ- Mead method. On achieving the optimal state of all the inclusions, the configuration of links is specified: at maximum elongation, the link is broken. The part of the material in the gap with the broken link begins to respond to compressive forces only and makes no resistance in other cases. If the breakage of links takes place, then the equilibrium seeking for the system is repeated. When a new optimal state of the structure is found, the structural-mechanical characteristics of the system are determined, and the next step of loading is performed.

5 Results and discussion

Two uniaxial stretching вГУ compression cycles with an increasing amplitude (elongation ratio λ was equal to 2 and 4) were applied to each structure. Example of the initial and stretched 4-times structure is shown in Fig. 4. At a certain local elongation of the

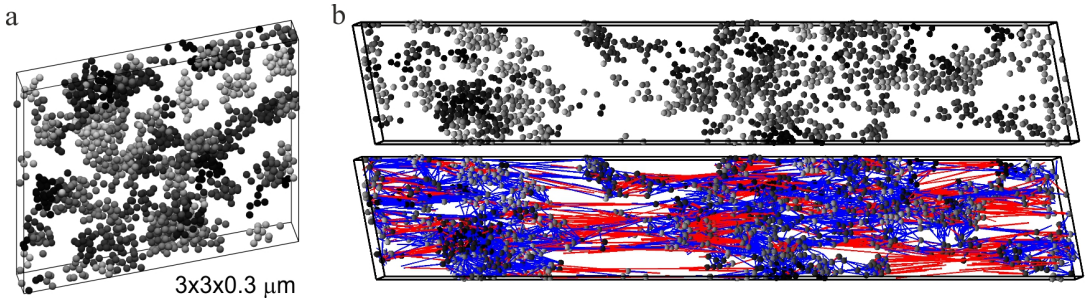

Figure 4: Fragment of the model clustered structure before loading (a), after stretching 4 times (b). Unbroken links are shown in green and blue, and broken links in red. Clusters are shown in different shades of gray.

gap between inclusions the corresponding link was broken. The typical behaviour of the rupture of the links is shown in Fig. 5a. At λ less than the maximum value (unloading or

repeating loading), the number of broken links remains unchanged. Thus, the rupture of links leads to the hysteresis of the stress-strain curve (Fig. 5b), which is typical of filled rubbers. The stress of links of the clustered model without layers, starting at $\lambda = 2.5$

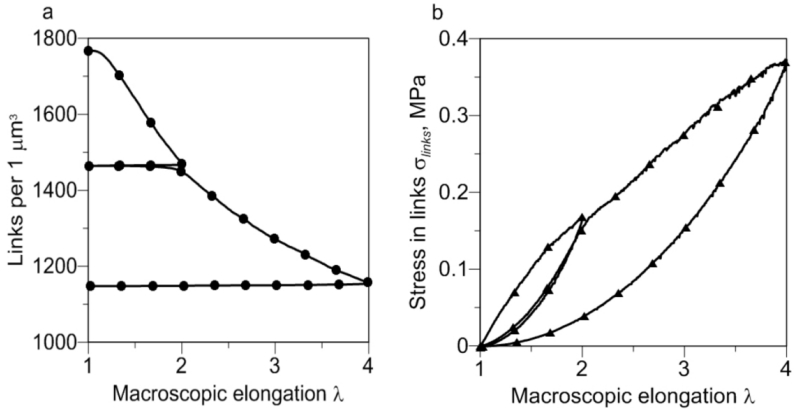

Figure 5: Typical response of the structure to elongation вГ Y number of links (a) and their stress (b).

in Fig. 6a, reaches its maximum and then begins to diminish; no material reinforcement takes place. The reason is that the forces caused by the deformation of the material in the gap between two inclusions without layers (Fig.3b) do not increase for $\delta_0 > 20$ nm. At the same time, despite the fact that the links in the material with layers are broken at lower elongation, their elastic properties of layers have the reinforcement effect on the composite. Based on the obtained results, it can be concluded that the model with the layers with variable stiffness is more appropriate to describe the mechanical behavior of filled elastomers than others. The stresses in randomly filled structure are higher than in

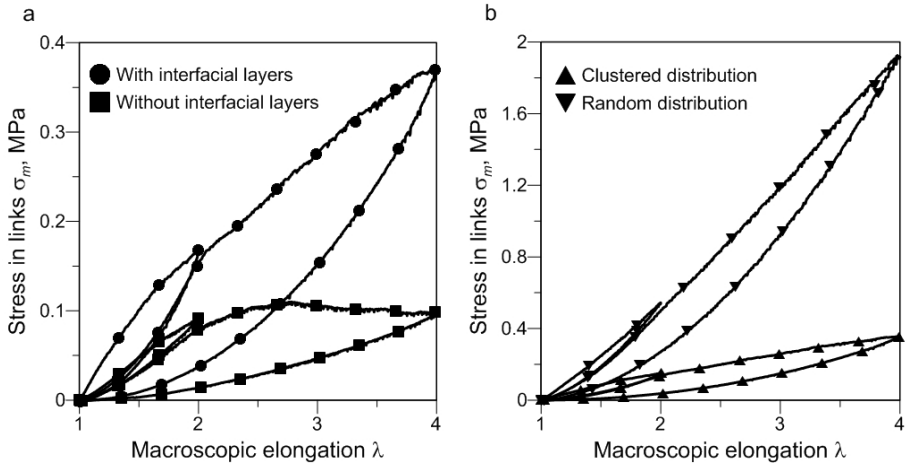

Figure 6: Stress in links vs. elongation of the structure: (a) вГ Y comparison of the structures with and without layers; (b) вГ Y comparison of clustered and random distribution.

the clustered (Fig. 6b). This is due to the fact that the random distribution of inclusions is more homogeneous compared to that of clusters. Hence, in the structural-mechanical model of random structure many through-matrix links occur, that is, the matrix fraction working under deformation increases. So, this is accompanied by an increase in stresses.

6 Conclusions

A structural-mechanical model for describing the eleastic behavior of filled elastomers has been proposed. The model explicitly takes into account the peculiar properties of the microstructure of the material and interphase interactions in it. The behavior of part of the polymer placed in the gaps between inclusions has been modeled by links with nonlinear elastic force response. At some stretch factor the elastomeric link is broken, which allows us to model the Mullins effect at the macrosopic level.
The results of simulation of cyclic stretching-compression of materials with clustered and random distribution of inclusions are presented. The cases where polymer layers with variable stiffness are present or absent around inclusions (the layer of macromolecules adsorbed on the active surface of inclusions) have been examined. Based on the structural-mechanical model, it can be concluded that the absence of interfacial layers of variable stiffness does not lead to the reinforcement effect characteristic of filled vulcanizates.

Acknowledgements

The work is supported by the RFBR-grants 15-08-03881a and 13-01-96016a.

References

[1] Litvinov V.M., Steeman P.A.M., EPDM-carbon black interactions and the reinforcement mechanisms, as studied by low-resolution 1H NMR // Macromolecules. 2009. V. 32. P. 8476 - 8490.

[2] Fukahori, Y., New progress in the theory and model of carbon black reinforcement of elastomers // J. Appl. Polym. Sci. 2005. V. 95. P. 60 - 67.

[3] Cho K., Gent A.N., Cavitation in model elastomeric composites // J. Mat. Sci. 1988. V. 23. P. 141 - 144.

[4] Morozov I.A., Lauke B., Tada T., Structural modelling and stiffness of filled elastomers // Compos. B: Eng. 2014. V. 60. P. 555 - 560.

[5] Y. Tomita, W. Lu, M. Naito, Y. Furutani. Numerical evaluation of micro- to macroscopic mechanical behavior of carbon-black-filled rubber // International Journal of Mechanical Science. 2006. V. 48. P. 108Ц116.

[6] M. Naito, K. Muraoka, K. Azuma, Y. Tomita 3D modeling and simulation of micro to macroscopic deformation behavior of filled rubber // Proceedings of 5th European conference on Constitutive Models for Rubber, ECCMR 2007, Paris, France, 4Ц7 September 2007. P.141Ц146.

[7] H. Xi, R. Hentschke. The Influence of Structure on Mechanical Properties of Filler Networks Via Coarse-Grained Modeling // Macromolecular Theory and Simulations. 2014. V. 23. є 6. P. 373Ц382.

[8] O.K. Garishin, V.V. Moshev. Damage model of elastic rubber particulate composites // Theoretical and applied fracture mechanics. 2002. V. 38. є 1. P. 63Ц69.

Ilya A. Morozov, Institute of Continuous Media Mechanics UB RAS, Perm, Russia
Lyudmila A. Komar, Institute of Continuous Media Mechanics UB RAS, Perm, Russia

Large strain theory applied to self-gravitating bodies: A numerical approach

Wolfgang H. Müller, Wolf Weiss
wolfgang.h.mueller@tu-berlin.de

Abstract

This paper presents an analysis of the deformation in terrestrial objects, such as the inner planets, rocky moons, or asteroids, which is due to self-gravitation. The problem of modeling such structures is quite old and goes back to the work of Kelvin, Rayleigh, Love, and Jeans in the late 1800. In those days a linear-elastic, closed-form solution was presented and studied. However, it turns out that in the case of huge objects, such as Earth or Venus, the resulting strains can become quite large. Thus, in the sixties, non-linear elasticity was used and large strains were taken into account. The conclusion was that some crucial parameters, *e.g.*, the location of the Love radius, do not change much when switching from the linear to the non-linear regime. However, this is true only for certain choices of effective stiffness parameters for the celestial body. At that time this was difficult to see, because the non-linear analysis is based on numerical solution procedures, which were less developed back then.

In this paper we will first present some of the history of the problem, then show the breakdown of the linear-elastic solution and, finally, use modern continuum mechanics tools to derive the underlying non-linear equations. We will solve them by applying two numerical techniques, namely Runge-Kutta methods for the solution of differential equation as well as finite differences.

At the end we will discuss the limits of the numerical approaches and present an outlook to further alternatives.

1 Introduction and problem statement

The problem of modeling the deformation, *i.e.*, the displacements, stresses and strains in self-gravitating terrestrial bodies by suitable constitutive equations for solids is quite old. In what follows we will restrict ourselves to homogeneous solid spheres, so that the problem reduces to a fully radially symmetric case. First attempts at finding such solutions were based on the linear theory of elasticity, *i.e.*, on

the combination of the static balance of momentum with Hooke's law, formulated at small strains. A rather extensive exposition of this problem for a constant, homogeneous mass density, including also the effects of centrifugal forces, can be found in [**Hoskins1910**]. A corresponding analytical result for the radial displacement is presented in [**Love1927**], Sect. 98. Most recently, results for this problem have been summarized resulting in concise formulae in [**MuellerEtAl2015**]. The differential equation for the radial displacement in the linear small strain case reads (dashes denote differentiations w.r.t. the radius, r, $G = 6.67410^{-11}\mathrm{m}^3\mathrm{kg}^{-1}\mathrm{s}^{-2}$ is the gravitational constant, ρ_0 is the (constant) mass density, $\lambda = \frac{E\nu}{(1-2\nu)(1+\nu)}$, $\mu = \frac{E}{2(1+\nu)}$ are Lamé's constants, E and ν are Young's modulus and Poisson's ratio, respectively):

$$u_r^{''} + 2\frac{u_r^{'}}{r} - 2\frac{u_r}{r^2} = \frac{4\pi G\rho_0^2}{3(\lambda+2\mu)}r, \tag{1}$$

and its solution is given by:

$$u_r = -\frac{\alpha_k}{30}\frac{1+\nu}{1-\nu}\left(\frac{3-\nu}{1+\nu} - \frac{r^2}{r_0^2}\right)r, \quad \alpha_k = \frac{4\pi G\rho_0^2 r_0^2}{3k}. \tag{2}$$

where $k = \frac{E}{3(1-2\nu)}$ is the (homogenized, *i.e.*, effective) bulk modulus of the terrestrial body (a.k.a. elastic modulus of compressibility), and r_0 denotes the outer radius. This relation can be used to determine the position where the radial strain changes sign. This was first done in [**Love1927**] where it was found that:

$$r_{\mathrm{Love}} = r_0\sqrt{\frac{3-\nu}{3(1+\nu)}}. \tag{3}$$

The radial strain is of tensile nature above this position and compressive below. Note that the circumferential strain is always compressive. Love did not say if he intended this quantity to be more than just a curiosity. We may speculate that the tensile nature of a principal strain could be used in context with a damage criterion, but we will not discuss this any further in this paper. Eqn. (2) was used to calculate the strain on the surface for various terrestrial bodies based on data compiled in [**MuellerEtAl2015**], as a function of varying effective compressibility. The latter is hard to specify in each particular case, especially since the planets are not completely solid. Therefore, a range of reasonable values for k should be examined. The results are shown in Fig. 1. On the left we see plots for the inner planets (Mercury and Mars in red and dashed-black, respectively, nearly coinciding, Venus in green, and Earth in blue). On the right we see results for Earth's Moon (red), Io (green), Europa (blue), Ganymede (black), Callisto (magenta), and Titan (cyan). For the moons, Mercury, and Mars the strains are small enough in order to accept linear small strain elasticity as a viable tool for computing the deformation. In the case of Venus and of Earth the strains are *not* small. Rather they turn out to be of the order of 10 percent and more, which is alarmingly high, to say the least.

Thus, in the sixties there was a revival of the problem. First, because based on seismic measurements more complex models of the density distribution of the Earth became available, *e.g.*, [**Pan1963**], [**Samanta1966**], and, second, because

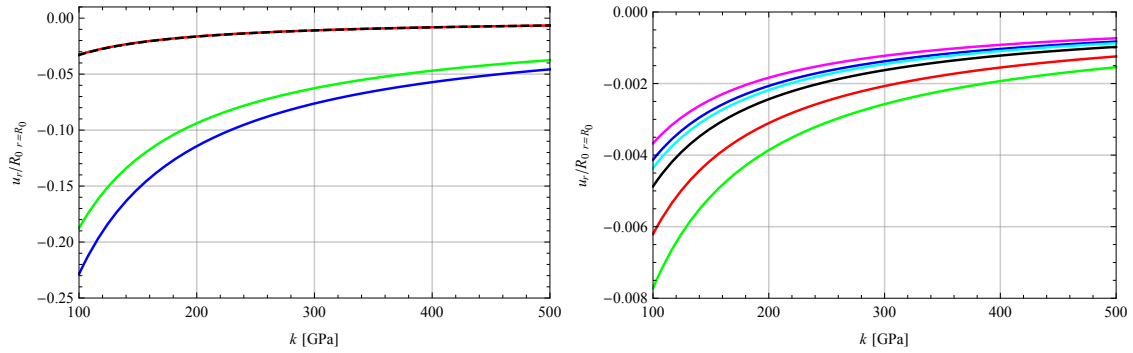

Figure 1: Strains on the periphery of various terrestrial bodies as a function of effective compressibility (for color code see text).

of the conclusion that linear strain theory might be insufficient to describe the situation in rather massive terrestrial bodies. This concern was expressed explicitly in [**BoseChattarji1963**] and [**Pan1963**]. This analysis was based on the paper by Seth [**Seth1935**] on finite elasticity, which operates in current space, uses the Eulerian-Almansi tensor as a strain measure, and related it to the current Cauchy stress in terms of a quasi Hookean equation. The numerical approach used infinite series for a displacement related quantity in context with a corresponding highly linear differential equation stemming from the static equation of momentum in the current configuration together with empirically motivated equations for the mass density and the corresponding self-gravitating force field. We will elaborate on this in the next section.

2 The governing equations in the nonlinear case

We consider the purely radially symmetric case of self-gravitation for a sphere with a homogeneous mass density ρ_0 in the unstressed reference configuration, $\mathcal{B}_0$. In fact, just like the effective compressibility, k, this is a parameter, which is relatively hard to assess. Indeed, frequently we do know the total mass, m, of a terrestrial object. However, we do not know its outer radius R_0 before gravity has been "switched on," so-to-speak. Therefore, the equation $\rho_0 = \frac{m}{\frac{4\pi}{3}R_0^3}$ cannot directly be used to determine the reference mass density. However, we shall see later that ρ_0 and the effective elastic parameters of the terrestrial object in question form a dimensionless factor, α. It is this factor we will vary within reasonable bounds, since the effective elastic parameters are just as elusive as the mass density of the reference configuration.

It is for such reasons that it is useful to formulate the continuum mechanics equations w.r.t. the current configuration, $\mathcal{B}(t)$, and *not* w.r.t. $\mathcal{B}_0$. This contradicts to a certain degree standard procedures of modern continuum mechanics, which has a certain preference for the use of the reference configuration in terms of a full description in material space. It is interesting to note that the need for the concept of a reference configuration for self-gravitating bodies was anticipated quite early in the papers of Jeans [**Jeans1903**] and Lord Rayleigh [**Rayleigh1906**], respectively. It has also received further attention more recently, *e.g.* in [**Geller1988**]. However,

as indicated above, this is a treacherous way to go, at least from a practical point-of-view, since the outer radius of an undeformed planet is not a directly measurable quantity. With this in mind we will start from the static balance of momentum in *current* spherical coordinates. In the totally radially symmetric case only the radial component is different from zero and reads (*cf.*, [**mueller2014**], pg. 116, σ_{ij} denote the Cauchy stresses in spherical coordinates):

$$\frac{\mathrm{d}\sigma_{rr}}{\mathrm{d}r}+\frac{2\sigma_{rr}-\sigma_{\vartheta\vartheta}-\sigma_{\varphi\varphi}}{r}=-\rho f_r\,,\ \rho=\frac{\rho_0}{\det\boldsymbol{F}}\,,\ f_r=-\frac{Gm(r_0)}{r^2}. \tag{4}$$

In the present case it is reasonable to make the ansatz $r=r(R)\Leftrightarrow R=R(r)$ for the deformation (r refers to the current radial and R to the radial position in the reference configuration, respectively). Hence the deformation gradient, $\boldsymbol{F}$, and the Euler-Almansi strain tensor, $\boldsymbol{e}$, read in spherical coordinates:

$$\boldsymbol{F}=\begin{pmatrix}\frac{\mathrm{d}r}{\mathrm{d}R}&0&0\\0&\frac{r}{R}&0\\0&0&\frac{r}{R}\end{pmatrix}\ \Rightarrow\ 2\boldsymbol{e}=\begin{pmatrix}1-\left(\frac{\mathrm{d}R}{\mathrm{d}r}\right)^2&0&0\\0&1-\left(\frac{R}{r}\right)^2&0\\0&0&1-\left(\frac{R}{r}\right)^2\end{pmatrix}. \tag{5}$$

From Eqn. $(5)_1$ we find immediately that $\det\boldsymbol{F}^{-1}=\frac{\mathrm{d}R}{\mathrm{d}r}\left(\frac{R}{r}\right)^2$. Moreover, the form of the body force in Eqn. (4) deserves a comment: At the current position r of a sphere with an exclusively radial mass density distribution, $\rho(r)$, the attraction is directed toward the center and dictated by the total mass, $m(r)$, situated beneath this position. However, due to mass conservation we have $m(r)\equiv m(R)=\frac{4\pi}{3}\rho_0R^3$. In this context it should be noted that Eqn. $(4)_3$ is a direct and exact consequence of Poisson's equation for the potential, U, in case of a radially symmetric mass distribution, $\rho(r)$:

$$\frac{1}{r^2}\frac{\mathrm{d}}{\mathrm{d}r}\left(r^2\frac{\mathrm{d}U}{\mathrm{d}r}\right)=4\pi G\rho(r)\ \Rightarrow \tag{6}$$

$$f_r\equiv-\frac{\mathrm{d}U}{\mathrm{d}r}=-\frac{4\pi G}{r^2}\int_{r=0}^{r=r_0}r^2\rho(r)\mathrm{d}r\equiv-\frac{Gm(r_0)}{r^2}.$$

We now turn to the constitutive equation for the stress-strain relations. Following [**Seth1935**], pg. 234 these are given by Hooke's law where the linear strains, ε_{ij}, have been replaced by the nonlinear ones, e_{ij}, $j\in r,\vartheta,\varphi$. Therefore the non-vanishing Cauchy stress components, σ_{ij}, read:

$$\sigma_{rr}=(\lambda+2\mu)\,e_{rr}+\lambda(\,e_{\vartheta\vartheta}+e_{\varphi\varphi})\,,\ \sigma_{\vartheta\vartheta}\equiv\sigma_{\varphi\varphi}=2(\lambda+\mu)\,e_{\vartheta\vartheta}+\lambda\,e_{rr}. \tag{7}$$

If Eqns. (4)-(6) are inserted into each other a nonlinear differential equation of second order for $r(R)$ results, which can be rewritten in terms of the radial displacement $u_r(r)\equiv r-R(r)$. It is instructive to convince oneself that this equation reduces to Eqn. (1) of the linear case if all nonlinear terms are neglected. Clearly, the nonlinear differential equation must be analyzed numerically. For this purpose it is useful to, first, change to dimensionless coordinates by normalizing the current radius with the current outer radius, r_0, so that $x=r/r_0$ and $u(x)=u_r/r_0$. Second, following [**BoseChattarji1963**], we introduce an auxiliary quantity, $\beta(x)$, by

$R(r) = r\beta(r) \;\Rightarrow\; u_r(r) = r[1-\beta(r)]$. This will prove to be beneficial during the numerical analysis. Hence, we arrive at:

$$\frac{\mathrm{d}}{\mathrm{d}x}\left[3\beta^2 + \left(\beta'^2 + \frac{2\beta\beta'}{x}\right)x^2\right] + \frac{2(1-2\nu)}{1-\nu}x\beta'^2 = -\alpha(\beta + x\beta')\beta^5 x, \tag{8}$$

where the factor $\alpha = \frac{8\pi G\rho_0^2 r_0^2}{3(\lambda+2\mu)}$ has been introduced, which bears a certain similarity to the one in Eqn. $(1)_2$. Both differential equations are of second order and need two boundary conditions for their analytical or numerical treatment, respectively. In the case of Eqn. (8) these result from the requirement that the (normalized) radial displacement, $u(x)$, must be an odd function in x, *i.e.*, $\beta'(0) = 0$. Moreover, the surface of the sphere is traction-free, *i.e.*, $\sigma_{rr}|_{r=r_0} = 0$, which is equivalent to $\frac{1+\nu}{1-\nu}[1-\beta^2(1)] - [\beta'^2(1) + 2\beta(1)\beta'(1)] = 0$.

3 Numerical analysis and discussion

At the beginning of this section it should be mentioned that in the work by Bose and Chattarji [**BoseChattarji1963**] and Pan [**Pan1963**] a solution for $\beta(x)$ was sought in form of a Taylor power series. In fact, this is a very tedious and sometimes inaccurate approach, in particular, if more complex density distributions are studied. The latter affect directly the right hand side of Eqn. $(4)_1$. In fact, these authors insert highly nonlinear expressions for ρf_r, because they want to model the impact of Earth's heterogeneous mass distribution.

Interestingly $\rho(r)$ and $f_r(r)$ are given in separate, but related[†] equations based on some earlier work by Bolt [**Bolt1957**]. The right hand side of Eqn. (8) is highly linear, too, despite the fact that the reference density is homogeneous. Clearly, our current density is not homogeneous because of Eqn. $(4)_2$. However, in contrast to the previous authors, it is not neither phenomenological nor assumed. Rather it is a straightforward continuum mechanics result from the assumption of a *single* reference mass density. In other words, the current distribution of the mass density can be calculated once we have solved the boundary value problem for $\beta(x)$. Moreover, f_r is nonlinear because of the nonlinearity inherent to Eqn. $(4)_3$. It is an *exact* expression for purely radial mass density distributions, $\rho(r)$, and that is all there is to it.

We now turn to a numerical solution of Eqn. (8). The first technique to be used is based on the NDSolve command from Mathematica ([**Wolfram2014**]). NDSolve is based on Runge-Kutta integration techniques for ODEs. In addition we used the option "stiffness switching," since Eqn. (8) reacts in a stiff manner, due to its inherent singularity at $r = 0$ or $x = 0$. The latter is already present in the linear case described by Eqn. (1). However, there it can simply be excluded by putting the corresponding constant of integration in the analytical solution equal to zero. Moreover, it should be pointed out that despite this optional choice, we were not able to obtain a solution for the proper boundary condition $\beta'(0) = 0$. Rather we had to choose $\beta'(\epsilon) = 0$ with $\epsilon = 10^{-3}$.

[†]by Newton's gravitational principle

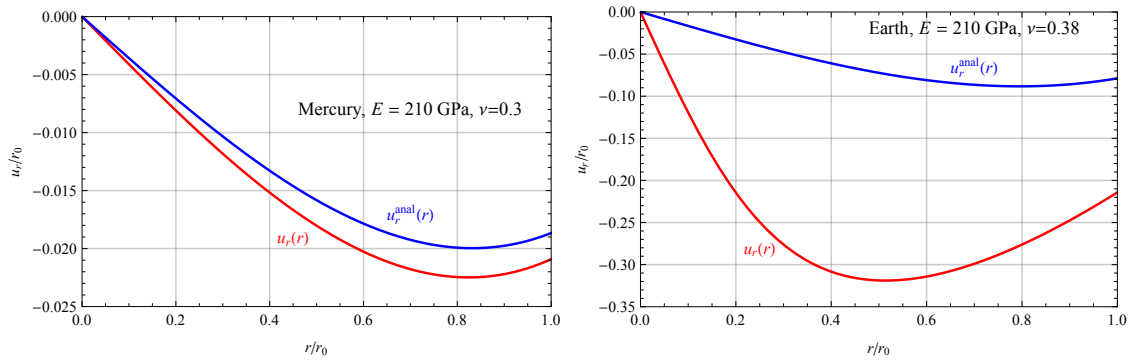

Figure 2: Radial displacement as a function of radial position.

Two results are shown in Fig. 2. For the plots geometry and mass data for Mercury and Earth were chosen from [**MuellerEtAl2015**]. It should be pointed out that ρ_0 was estimated by using the relation $\frac{m}{\frac{4\pi}{3}r_0^3}$, *i.e.*, the current outer radius of the planets. In the case of Mercury the values of iron were chosen for Young's modulus and Poisson's ratio, leading to $\alpha \approx 0.35$. If the same elastic data was used for Earth α increased up to 1.96. For this value convergence could no longer be obtained. Hence, Poisson's ratio was raised to 0.38, which is equivalent to $\alpha \approx 1.75$. The reason for the lack of convergence becomes apparent by looking at the plots: In the case of Mercury, there is already a slight discrepancy to the analytical solution, $u_r^{\mathbf{anal}}(r)$, shown in Eqn. $(2)_1$. The analytical solution *underestimates* the displacement. This is not surprising since a radial strain, which is roughly given by u_r/r_0, of more than two percent is already testing the limits of a linear theory.

In the case of Earth the situation is much more dramatic. First, the difference between the analytical and the numerical solution is huge and, second, even the analytical solution already predicts strains of almost 10%, whereas the numerical solution amounts to 30% and more. Note that the curvature of $u_r(r)$ "on the left" becomes more and more pronounced when the α-values increase. For large values of α, *i.e.*, for large values of reference density and small values of Young's modulus and/or Poisson's ratio, the $u_r(r)$-curve will first decline very steeply and then show an essentially linear behavior with a moderate slope. Such extreme gradients with kinks are very difficult to master numerically.

It is for this reason that we now turn to a potentially alternative numerical method, namely a finite-difference scheme. Eqn. (8) is transformed into a set of non-linear coupled equations, resulting in a sparsely populated matrix, by approximating the solution in discrete points, $i = 1..., i_{\max}$ on the interval $x \in [0, 1]$ separated by the distance Δx. "In the flesh" we use finite difference approximations of $\mathcal{O}(\Delta x^2)$ for the first and second order differential quotients as follows:

$$\beta'(x) \approx \frac{\beta(i+1) - \beta(i-1)}{2\Delta x}\,, \quad \beta''(x) \approx \frac{\beta(i-1) - 2\beta(i) + \beta(i+1)}{\Delta x^2}. \tag{9}$$

At the left and right hand side of the $[0, 1]$-interval we use for the first derivatives with the same degree of accuracy:

$$\beta'(0) = \frac{-3\beta(1) + 4\beta(2) - \beta(3)}{2\Delta x} + \mathcal{O}(\Delta x^2), \tag{10}$$

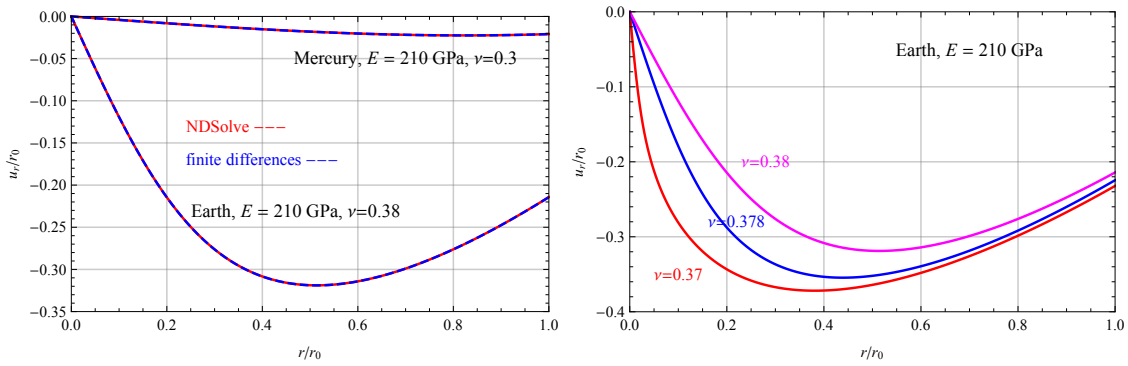

Figure 3: Finite difference vs. Runge-Kutta method.

$$\beta'(1) = \frac{\beta(i_{\max} - 2) - 4\beta(i_{\max} - 1) + 3\beta(i_{\max})}{2\Delta x} + \mathcal{O}(\Delta x^2).$$

Some results are shown in Fig. 3. The plots on the left show that the finite difference method leads to exactly the same results of the NDSolve command, at least as long as the parameter α does not reach a certain threshold. This is explored in the plots on the right. Recall that $\nu = 0.38$, $E = 210$ MPa with Earth parameters, *i.e.*, $\alpha \approx 1.75$ was the convergence limit in case of NDSolve. The finite difference technique allows to go a little beyond this value up $\nu = 0.37$, *i.e.*, $\alpha \approx 1.86$. The plots show that an increasing value of α leads to an increase of strain, as anticipated. Moreover, the initial slope of the displacement curves increases rapidly. Then, at larger values of r/r_0, the displacement shows a more or less linear behavior. If we keep increasing α the transition zone is governed by huge gradients and turns essentially into a kink. However, this is very hard to capture numerically. In fact, the finite difference method fails to converge above the afore-mentioned α value. It might be an alternative to use a non-equidistant discretization. However, this is left to future research. Moreover, another numerical alternative might be to use finite elements. This will be explored in these proceedings in the paper by Müller and Lofink.

The curves in Fig. 3 also indicate that the position of the Love radius, *i.e.*, the position of the minimum of the u_r-curves, as predicted by the analytical solution shown in Eqn. (3) will change in the case of massive terrestrial objects. This is explored in detail in the plots of Fig. 4. The left inset presents three curves. First, the dependence of the Love radius according to Eqn. (3), which is labeled as the "analytical solution." Second, the plot called "Mercury," for which mass and geometry data of Mercury were used. Moreover, Young's modulus was that of iron, Poisson's ratio varied within the possible bounds, and the NDSolve command was applied to find a numerical solution of the nonlinear boundary-value problem. Thus, α-values changed between 0.47 and 0, when ν increased from 0 to 0.5. The result confirms the statements in [**BoseChattarji1963**] or [**Pan1963**] according to which the location of the Love radius is hardly affected by the nonlinear treatment of the deformation problem. However, this is only true, if α stays small, which is not guaranteed for a large object, such as Earth. This is shown in the third plot of Fig. 4 (left). In this case α varied between 0 and 1.75 when ν decreased from 0.5 to 0.38. Obviously, the difference to the analytical solution can become very large.

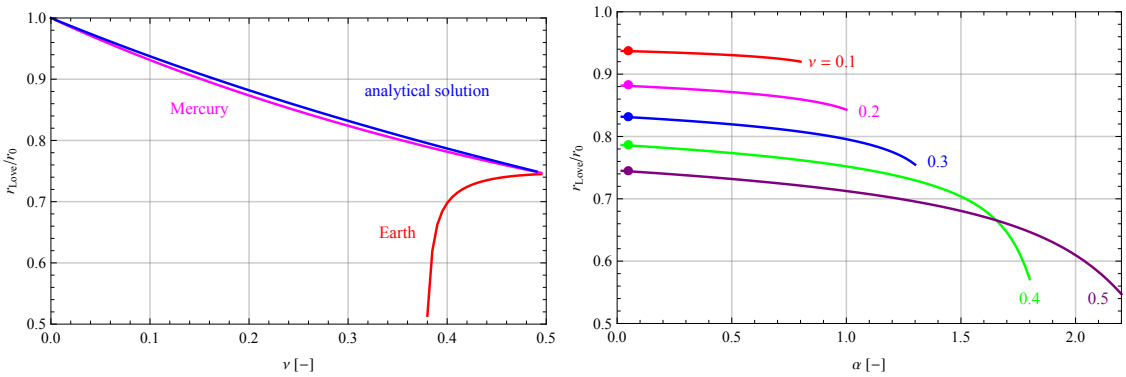

Figure 4: Position of the Love radius (see text).

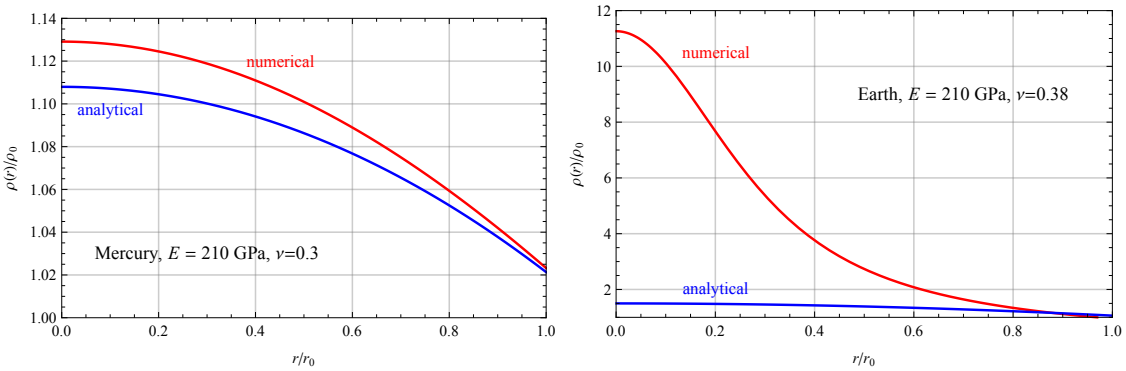

Figure 5: Normalized distribution of mass density predicted.

In summary, the location of the Love radius depends on *two* parameters, Poisson's ratio (which is the *only* parametric dependence in the analytical solution) *and* the mass-stiffness parameter, α. The plot on the right hand side of Fig. 4 explores this in more detail: The Love radius is plotted *vs.* α for various values of ν. The corresponding values for the Love radius according to the analytical solution are indicated by circles. They are valid for small values of α.

We now turn to the assessment of the redistribution of density due to the deformation. The non-linear numerical analysis is based on Eqn. $(4)_2$, which leads us to conclude that:

$$\frac{\rho}{\rho_0} = [\beta(x) + x\beta'(x)]\beta^2(x). \tag{11}$$

In the case of the analytical solution from Eqn. (2) we may write:

$$\frac{\rho}{\rho_0} = 1 - u_r'(x) - 2\frac{u_r(x)}{x}. \tag{12}$$

Fig. 5 shows results obtained by evaluating both equations. Clearly, the mass density increases toward the center of a planet even if the reference mass density is homogeneous and constant. In the case of a small planet (like Mercury) the density distributions from both equations are relatively close together. In the case of a large

planet (like Earth) the numerical, *i.e.*, the solution from the non-linear equation of deformation leads to densities at the center much larger than those obtained from the linear solution. In other words: The nonlinearity allows us to understand and potentially model the dramatic increase of mass density in the center of massive terrestrial planets without assuming a denser core to begin with.

As a matter of fact, the increase in mass density shown on the right hand side of Fig. 5 is much too large. This is due to the assumption that the effective elasticity of Earth is essentially that of iron, which it is *not*, *and* that the Earth was homogeneous in the beginning when it formed, which it was certainly *not*. Indeed, the plot is intended to demonstrate the potential of a nonlinear description of deformation, a fact which, to the best knowledge of the authors, has not been emphasized in the literature so far. Indeed, the density distribution of the PREM model [**DziewonskiAnderson1981**] are phenomenologically based on seismic measurements which were analyzed by using (anisotropic) linear elasticity. All we wish to say at this point is that modeling the density distribution of Earth should be attempted in combination with a nonlinear deformation theory.

4 Summary and conclusion

In this paper we have analyzed the deformation in self-gravitating, initially homogeneous, solid spheres. An analytical solution valid for linear, small strain theory was juxtaposed to a numerical one of the corresponding boundary-value problem based on nonlinear, elastic, large strain theory. Problems in context with the numerical treatment of the nonlinear equation were discussed. It turns out that two dimensionless parameters govern the deformation problem, first, Poisson's ratio, ν, and, second, a mass-stiffness parameter, $\alpha = \frac{8\pi G\rho_0^2 r_0^2}{3(\lambda+2\mu)}$, characteristic of a particular sphere, *i.e.*, terrestrial planet. Presently, convergence of the numerical solution can only be guaranteed within a certain range of α. Further investigations, based on adaptive meshing techniques, are currently underway to expand this range. However, it can already be said that in contrast to previous statements in the literature, the location of the Love radius, *i.e.*, the transition between compressive to tensile radial strains within the sphere, is affected if nonlinear is used *and* the body in question is sufficiently massive and not too stiff.

Acknowledgements

The authors are grateful to Dr. Joydev Chattopadhyay, Editorial Secretary of the Calcutta Mathematical Society for providing us with a copy of the paper by [**BoseChattarji1963**].

Wolfgang H. Müller and Wolf Weiss, Technische Universität Berlin, Institute of Mechanics, Einsteinufer 5, D-10587 Berlin, Germany

Indentation study of mechanical behaviour of Zr-Cu-based metallic glass

V. Nekouie, A. Roy, V.V. Silberschmidt
V.Nekouie2@lboro.ac.uk

Abstract

It has been well known that plastic deformation of bulk metallic glasses (BMGs) is localised in thin shear bands. So, initiation of shear bands and related deformation should be studied for comprehensive understanding of deformation mechanisms of BMGs. In this paper, indentation techniques are extensively used to characterise elastic deformation of Zr-Cu-based metallic glass, followed by a systematic analysis of initiation and evolution of shear bands in the indented materials. Our results, obtained with a suggested wedge-indentation technique, demonstrated initiation of shear bands in materialвґЄs volume.

Key words: Metallic glass; shear bands; indentation.

1 Introduction

Modern high-tech industries rely on the manufacture and synthesis of advanced materials that are stronger than conventional ones. Bulk metallic glasses (BMGs) have received much scientific and technological attention due to their advanced mechanical properties such as a high ratio of elastic limit to the Youngвґ Єs modulus and higher fracture toughness, when compared to their crystalline counterparts of the same composition. This is typically attributed to the absence of a long-range order in their atomic structure and a lack of defects such as dislocations, which control ductility in traditional metallic materials. BMGs are brittle and exhibit negligible plasticity in the macro-scale. Some recent experiments on sub-micron and nano-sized BMG specimens showed that the process of shear localisation become more stable and less catastrophic, when compared to a response exhibited by large-size samples [1]. These desirable and unique properties of metallic make them an ideal candidate for many applications such as MEMS (micro-electromechanical systems), miniaturised biomedical devices and implants as well as in micro-robotics. A number of mechanistic theories have been proposed to describe the plastic flow and deformation behaviour of BMGs. Some popular theories are concepts of free volume and shear transformation zones (STZs) proposed in Argon and Spaepenвґ Єs model, based on motion of atoms [2, 3]. The deformation mechanism of metallic glasses based on these concepts is realised homogenously or inhomogenously, depending on the levels of strain rate, temperature and applied stress [4]. A significant amount of experiments was carried out to understand deformation mechanisms. Prior studies showed that shear bands

with a characteristic thickness of the order of 10-20 nm were responsible for deformation of BMGs at low temperatures and/or high stresses. More recently, deformation-induced crystallisation was observed in a number of BMGs that led to substantial plastic deformation [5]. These changes in shear bands were not only induced by bending or compression of BMGs [6], but were the results of their nanoindentation or microhardness testing [7], ball milling or cold rolling process [8]. However, various research groups suggested contradicting conclusions on shear band crystalisation, based on similar experiments performed with various BMG systems [4, 9]. Thus, a question on propensity for crystallisation is still open. Traditional indentation techniques have been used extensively over years to determine mechanical properties and deformation mechanisms of metallic glasses [10]. These techniques helped researchers to perform mechanical characterisation at micro-scale and analyse the mechanism of plastic flow in BMGs. Although shear bands typically initiate beneath the indenter, in nano- and micro-indentation experiments, by their very nature, shear bands could be observed only after they evolved to the surface. So, a wedge indentation experiment was designed to overcome the limitation of nano- and micro-indentation to observe the initiation and propagation of shear bands under the indenter surface [1]. As the length of the wedge indenter was considerably larger than its width, the wedge indentation experiments also allow numerical modelling to be simplified to a 2D formulation. There are different, sometimes contradicting hypotheses about the deformation mechanisms of BMGs at microscale. Hence, further studies are required to understand initiation and propagation of shear bands in the volume and at the surface of metallic glasses. In this study, a Zr-Cu-based metallic glass is characterised using nano- and micro-indentation techniques. A thorough structural characterisation of shear bands around the indented region was carried out to understand the nature of shear banding in BMGs.

2 Experimental procedure

For our studies, a beam-shaped alloy with nominal composition of $Zr_{48}Cu_{36}Al_8Ag_8$ was prepared at IFW Dresden, Institute for Complex Materials, , Germany by arc-melting the pure elements (99.9% Zr, 99.99% Cu). BMG specimens were cut and polished to mirror-like finish with the roughness of some 5 nm. Indentation tests were conducted to characterise the shear bands with a nano indentation test system (Micro Materials Ltd.) using a spherical and Vickers indenters. A series of nano- and micro-indentations were conducted on the polished surface of the samples with a loading rate of 2 mN/s. A wedge indenter made of high-speed steel, with a nominal angle of 60Bə and an edge radius of 19.5 Oëm was designed and manufactured in-house (Figure 1). The indentation tests reported here were conducted at ambient temperature. XRD analysis of as-cast samples was carried out to study formation of crystalline phases. In order to reconfirm the crystallography, the samples were thinned to electron transparency and observed using transmission electron microscopy (TEM). Scanning electron microscopy (SEM) was used to observe evolution of shear bands on the deformed surfaces.

3 Results and Discussion

The amorphous nature of the supplied samples of BMG was initially investigated using X-ray diffraction (Figure 2); their microstructure was further characterised with TEM.

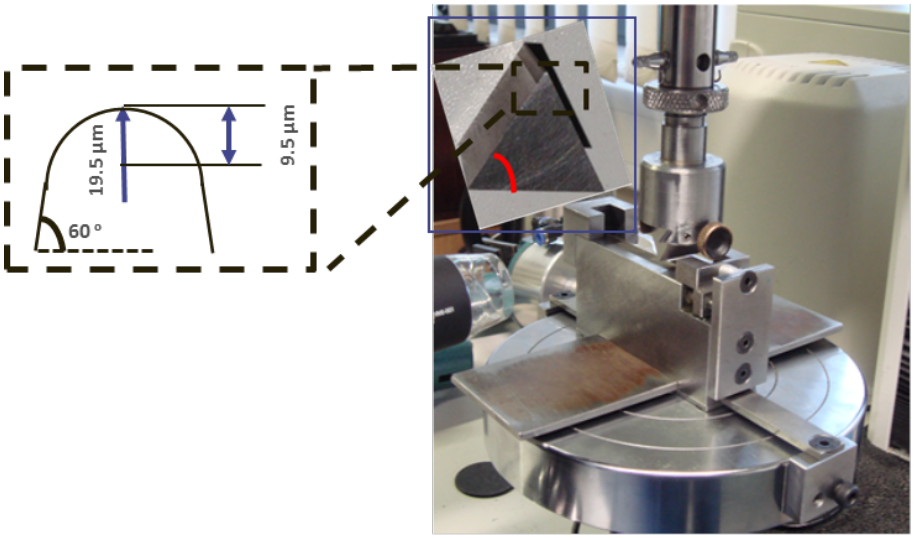

Figure 1: Experimental set-up for wedge indentation and its dimension

The TEM results confirmed the amorphous nature of the alloy, as the first halo ring of a Selected Area Electron Diffraction (SAED) pattern did not show any presence of nanocrystals.

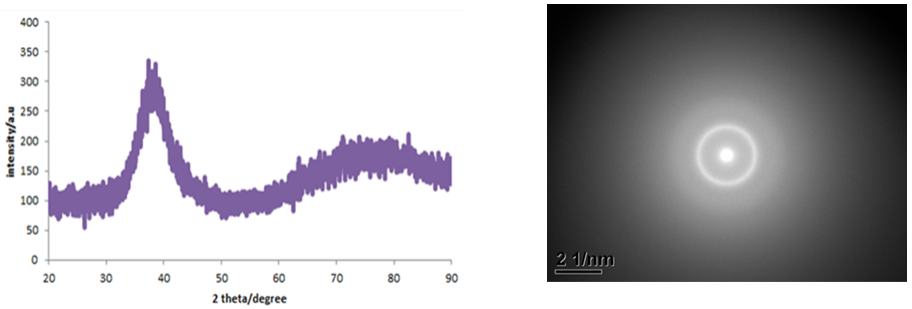

Figure 2: (a) XRD pattern of as cast $Zr_{48}Cu_{36}Al_8Ag_8$, (b) corresponding SAED patterns.

3.1. Microindentation

Multiple unloading-reloading experiments were conducted using a spherical indenter with diameter of 50 Bχm at loading rate of 2 mN/s to investigate the variation of elastic modulus with depth in BMG specimens. The maximum indentation depth ranged from 6 Bχm to 18 Bχm, and three partial unloads down to 20% of the peak load at each step were applied in these steps. Shear bands formed at loads in excess of 10 N. As shown in Fig. 3, shear bands moving from various initiation points crossed each other; however, shear bands nucleated later were arrested by already nucleated ones. Instability of shear bands was observed in the form of nucleation of several secondary shear bands from the primary ones in the course of deformation. A large plastic zone was formed under the indenter tip during indentation [12, 13]. It contained a high density of shear bands; this is ideal for investigation of deformation-induced hardening and softening effects [14]. The obtained results showed a dependence of elastic modulus on penetration depth, indicating a work-

softening phenomenon in the studied metallic glass, especially at microscale. The values of reduced (Er) and elastic (E) moduli obtained from the curve using the Oliver-Pharr method are given in Table 1. The reduced and elastic moduli decreased from 48 GPa to 38 GPa and 41 GPa to 33 GPa, respectively. This phenomenon is often referred as indentation size effect (ISE) [12, 15], manifested by a decrease in the elastic modulus with an increase in the indentation depth. A large number of shear bands were activated by indentation; this reduced the reaction force on the indenter, leading to a reduction in material stiffness.

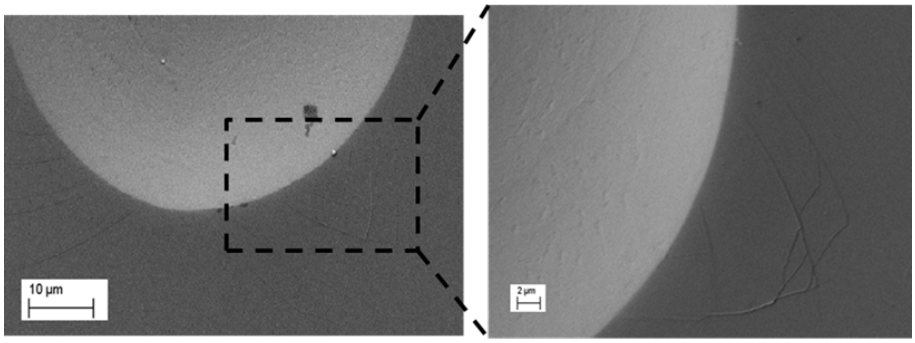

Figure 3: SEM images of micro-indentation in $Zr_{48}Cu_{36}Al_8Ag_8$.

Table 10: Reduced modulus (Er) and elastic modulus (E) of $Zr_{48}Cu_{36}Al_8Ag_8$ at various depth.

Cycle	Indentation depth (μm)	Reduced modulus (GPa)	YoungвЃ Єs modulus (GPa)
1	6.2	48	41.7
2	12.1	40	34.8
3	18.2	38	33.06

3.2 Shear-band initiation

The aim of this experiment was to characterise initiation of the first plastic event in order to calculate the required stress for shear bands initiation of the metallic glass investigated in this study. Based on the nano-indentation experiments [1], the first pop-in event occurred at applied force of 4 mN resulted in indentation depth of 0.060 Bҳm. The corresponding total area of contact and stress required for the first pop-in were 1.88 Bҳm2 and 2.12ГЧ109 N/m2, respectively. It is necessary to determine the contact area A_c in wedge-indentation experiments in order to predict the approximate force necessary for initiation of shear bands. This force can be obtained using the following equation:

$$F = \sigma A_c \qquad Eq.1$$

It was found that the required load would be around 500 N; hence, testing was carried out using the beam-shaped samples in a compression mode with a constant displacement rate of 0.05 mm/min using the wedge indentation technique and the load levels between 200 N and 500 N. To avoid contact problem at low loads, surfaces of the wedge indenter were prepared with the use of a surface grinder in an attempt to make the surface uniform while maintaining the 60Bə angle.

The wedge indenter has an edge radius of 8 Oëm and height of 5 Oëm. Evolution of deformation pattern on the front surface of the specimen is presented in Fig. 4. The plastic depth increased from 5 Bҳm to 13 Bҳm by increasing the load from 200 N to 500

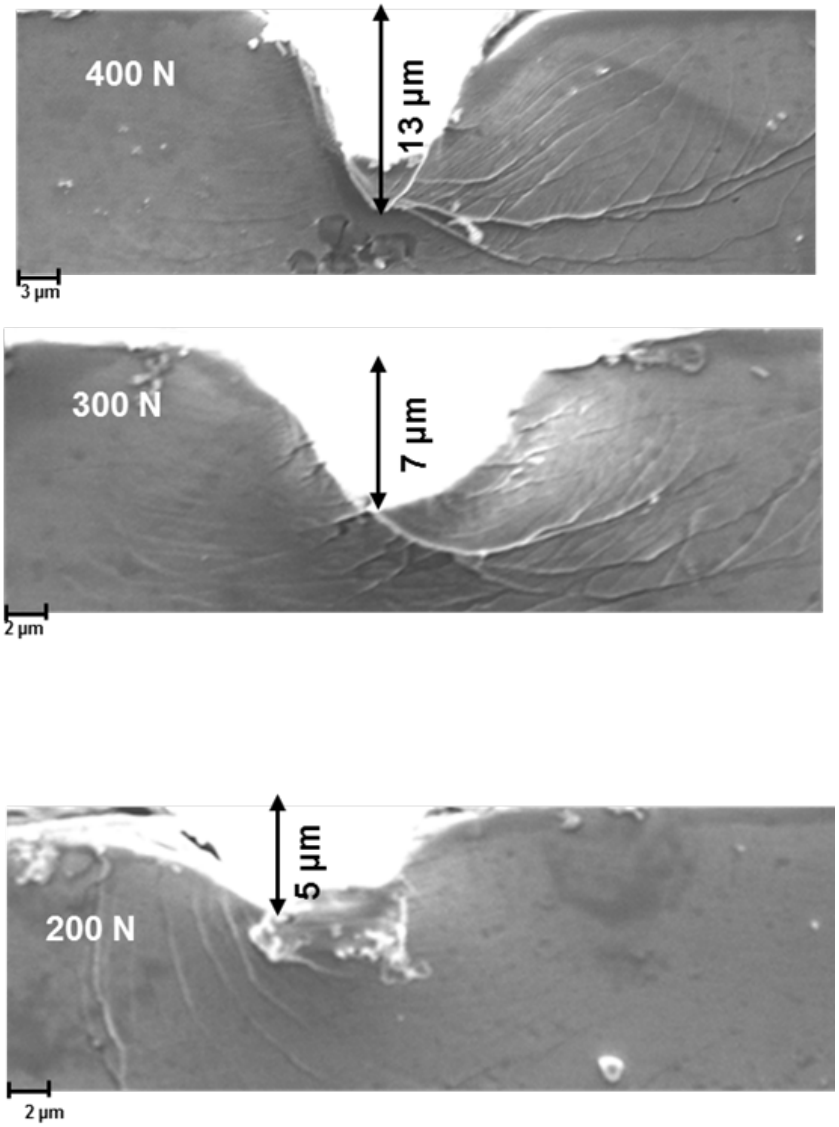

Figure 4: Evolution of shear bands pattern with load under wedge indentation: (a) 400 N, (b) 300 N, (c) 200 N.

N, and serrated semi-circular slip-steps formed by shear bands were observed. The results show that the nucleation and initial propagation of shear bands occurred at loads below 200 N; there were no shear bands at 100 N load. For 200 N, the indentation depth was 22.17 Bxm before unloading obtained from F-D curve. The calculated stress was :

$$\sigma = \frac{F}{A_c} = 0.886GPa$$

At 100 N, the shear band initiation stress was approximately 0.7 GPa, therefore, it can be estimated that, in wedge indentation the stress level required to initiate shear-band formation is between 0.7-0.9 GPa. Due to different shear bands morphology in wedge indentation, this value is not similar to the calculated stress required for shear bands initiation in nanoindentation with spherical indenter.

3.3 Comparison between glass and metallic glass

The purpose of this study was to compare fracture surfaces of soda-lime-silica glass and the studied Zr-Cu-based metallic glass using the wedge indentation technique at room temperature. The relationship established between mechanical behaviour and fracture feature can assist in elucidating the fracture mechanism. Wedge indentation was applied to both glass and metallic-glass specimens with dimensions of 40 mm x 4 mm x 2mm using loads of 500 N, 1 kN and 1.3 kN. Fractography studies showed that fracture surfaces of materials that fail in a brittle manner from surface cracks are characterized by a sequence of three distinct fracture features including mirror, mist and hackle regions, depending on the loading mode. For instance, there was no mist region observed on fracture surfaces formed in the mixed-mode failure [17]. A side view of wedge indentation for a glass specimen is presented in Fig. 5; here, classical concentric cone cracks were observed. The contact radius at maximum pressure was just within the outermost surface ring in Fig. 5, confirming that the cone fractures formed in the region of weak tension outside the subsurface compression zone. In addition, there was no detectable deformation observed beneath the contact circle; essentially, the material behaved as an ideally homogeneous solid. As shown in micrographs of subsurface damage at higher magnification in Fig. 5(c), hackle marking on the fracture surfaces of soda glass appeared as lances. Observation of fracture surfaces indicated that the propagating crack did not experience any energy-dissipation process such as plasticity or crack bridging, which could result in retarding the crack growth in a substantial manner.

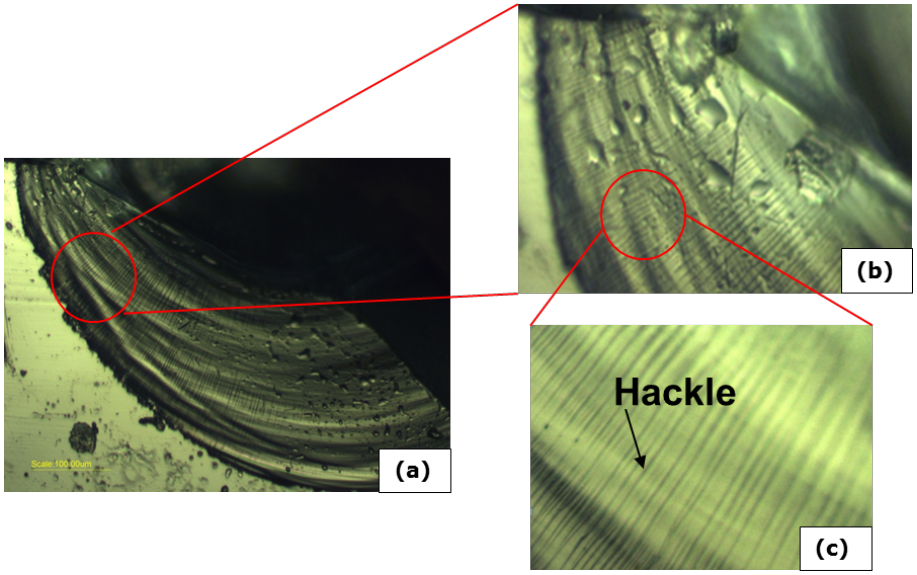

Figure 5: Optical micrographs of indented soda-lime-silica glass after applying 1.3 kN showing cone fracture form (a)and hackle fracture (b and c).

As shown in Fig. 6, significant differences were found in the appearance of the fracture surfaces of specimens of the traditional and metallic glasses at microscale. In contrast to the former, shear bands in BMGs were not brittle and provided the ability to deform plastically, with many semi-circular shear bands created beneath the indenter. Shear bands bifurcate with increasing distance from the indenter tip, indicating branching and healing mechanisms contributing to energy-dissipation processes, which led to plastic deformation at microscale.

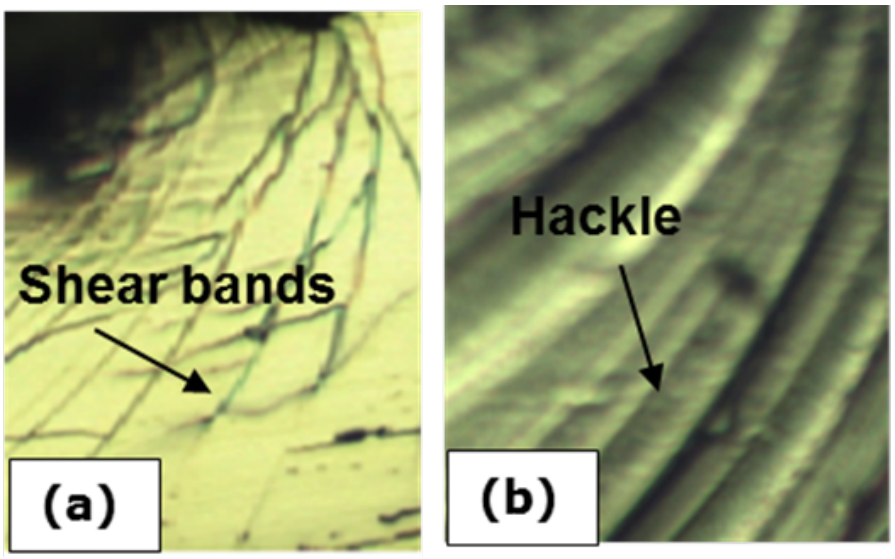

Figure 6: Optical micrograph of 1 kN wedge indentation on as-cast $Zr_{48}Cu_{36}Al_8Ag_8$ metallic glass (a) and soda-lime-silica glass (b).

4 Conclusions

The microhardness study perfomed on $Zr_{48}Cu_{36}Al_8Ag_8$ clearly indicated the dependence of its elastic modulus on penetration depth at microscale due to activation of a large number of shear bands. A relatively new technique вГЎ wedge indentation вГЎ was employed to calculate the required stress for shear bands initiation of the metallic glass. It was estimated that the level of stress required to initiate shear bands was between 0.7-0.9 GPa in wedge indentation. The wedge indentation technique was also applied to compare fracture surfaces of the soda-lime-silica glass and the studied Zr-Cu-based metallic glass at microscale. Observation of fracture surfaces indicated that the propagating cracks did not experience any energy dissipation in the traditional glass; on the contrary, the shear-band evolution in the metallic glass showed branching and healing mechanisms contributing to the plastic deformation at microscale.

References

[1] Nekouie, V., Abeygunawardane-Arachchige, G., Roy, A., Silberschmidt V.V.: Indentation-induced deformation localisation in Zr-Cu-based metallic glasses. J. Alloys Compd. 615, 93-97 (2014)

[2] Argon, A.: Plastic deformation in metallic glasses. Acta Metall. 27(1), 47вГЎ58 (1979)

[3] Spaepen, F.: A microscopic mechanism for steady state inhomogeneous flow in metallic glasses. Acta Metall. 25(4), 407вГЎ415 (1977)

[4] Schuh, C.A., Hufnagel, T.C., Ramamurty, U.: Mechanical behavior of amorphous alloys. Acta Mater. 55(12), 4067вГЎ4109 (2007)

[5] Chen, M., Inoue, A., Zhang, W., Sakurai, T.: Extraordinary of ductile bulk metallic glass. Phys. Rev. Lett. 96(24), 1382-1396 (2006)

[6] Jiang, M.Q., Ling, Z., Meng, J.X., Dai, L.H.: Energy dissipation in fracture of bulk metallic glasses via inherent competition between local softening and quasi-cleavage. Philosophical Magazine. 88(3), 407-426 (2008)

[7] Kim, J., Choi, Y., Suresh, S., Argon, A.S.: Nanocrystallization during nanoindentation of a bulk amorphous metal alloy at room temperature. Sci. 295, 654-656 (2002)

[8] El-Eskandarany, M., Sherif, S., Inoue, A. Room-temperature mechanically induced solid-state devitrifications of glassy Zr65Al7.5Ni10Cu12.5Pd5 alloy powders. Acta Mater. 51(15), 4519-4532 (2003)

[9] Greer, A.L., Cheng, Y.Q., Ma, E.: Shear bands in metallic glass. Mater. Sci. Eng. 74(4), 71-132 (2013)

[10] Gouldstone, A., Chollacoop, N., Dao, M., Li, J., Minor, A.: Indentation across size scales and discipline: Recent development in experimentation and modelling. Acta Mater. 55(12), 4015-4039 (2007)

[11] Bhowmick, R., Raghavan, R., Chattopadhyay, K., Ramamurty, U.: Plastic flow softening in a bulk metallic glass. Acta Mater. 54(16), 4221вГ4228 (2006)

[12] Jana, S., Bhowmick, R., Kawamura, Y., Chattopadhyay, K., Ramamurty, U.: Deformation morphology underneath the Vickers indent in a Zr-based bulk metallic glass. Intermetallics 12(10), 1097вГ1102 (2004)

[13] Zhang, H., Jing, X., Subhash, G., Kecskes, L.J., Dowding, R.J.: Investigation of shear band evolution in amorphous alloys beneath a Vickers indentation. Acta Mater. 53(14), 3849вГ3859 (2005)

[14] Bei, H., Xie, S., George, E.P: Softening caused by profuse shear banding in a bulk metallic glass, Phys. Rev. Lett., 96 (10), 105503 (2006)

[15] Cai, H., Kalceff, M.A.S, Lawn B.R.: Deformation and fracture of mica containing glass ceramics in Hertzian contacts. J. Mater. Res. 9(3), 762-770 (1994)

[16] Lam, D.C., Chong, A.C.: Model and experiments on strain gradient hardening in metallic glass, Mater. Sci. Eng.: A, 318 (1) 313-319 (2001)

[17] Gopalakrishnan, K., Mecholsky, J.: Quantitative fractography of mixed mode fracture in glass and ceramics. J. Eur. Ceram. Soc. 34(14), 3247-3254 (2014)

V. Nekouie, A. Roy & V. V. Silberschmidt, Wolfson School of Mechanical and Manufacturing Engineering, Loughborough University, UK

Stationary energy partition between modes in the one-dimensional carbyne chain

Svetlana P. Nikitenkova, Dmitry A. Kovriguine
spnikitenkova@yandex.ru

Abstract

The stationary patterns of energy partition between waves in a one-dimensional carbyne chain at ambient temperatures are investigated, taking into account central and noncentral interactions between carbon atoms. The study is carried out by standard asymptotic methods of nonlinear dynamics in the framework of classical mechanics, based on a simple mathematical model. Within the first-order nonlinear approximation analysis the triple-phonon resonant ensembles of quasi-harmonic waves are revealed. Each resonant triad consists of a single primary high-frequency longitudinal mode and a pair of secondary low-frequency transverse modes of oscillations. In general, the carbyne chain is described as a superposition of resonant triads of various spectral scales. It is found that the stationary energy distribution in a carbyne is obeyed to the classical Rayleigh-Jeans law, with the allowances for the proportional amplitude dispersion, which influences upon the results of theoretical estimations in several percents, comparing to the linear theory prediction.

1 Introduction

Carbyne, a one-dimensional carbon allotrope, has been first found and studied in the early sixties of the last century [1]. This is a natural material, since its presence had been detected in meteorites [2]. Carbyne is of particular interest for nanotechnology, being the most hard of all known materials [3] up today, strongly than a diamond. At the same time, the specific heat capacity of carbyne is larger than the heat capacity of graphite, and the latter is higher than a diamond. This ordering is due to the spatial framework of these carbon allotropes [1]. The flexibility of carbyne has approximately the same order as most polymers, though this can be efficiently controlled by attaching to the ends of a chain some chemicals [3]. In this case, the carbyne chain can be turned from a random coil, with the persistent length of order 14 $[nm]$, into a strong string of extremely small diameter and extremely large value of the Young's modulus. The bending of carbyne chains is resulted in an additional voltage between the carbon atoms to exhibit the semiconducting properties. This feature can be utilized in NEMS as a precision sensor. In addition to the strength properties, carbyne displays a number of other unique properties, opening prospects for the using in hydrogen storage technologies to produce ecologically friendly batteries. These unique properties stimulate an intensive discussion over the synthesizing a carbyne from a liquid carbon [4, 5, 6].

Based on a most simple mathematical model of a carbyne chain, the three-wave resonances are investigated, which arise due to the nonlinear coupling between central and noncentral bonds of nearest neighborhood carbon atoms. It is shown that the low-frequency longitudinal waves are almost always unstable. These break up into pairs of secondary low-frequency transverse waves, unless the frequency of the primary longitudinal mode does not exceed a certain critical value. Otherwise, the three-wave resonant processes are forbidden, and the standard Rayleigh–Jeans law holds true, prescribing an equal energy partition among degrees of freedom. Thus, for the short-wave processes, the stationary pattern of energy distribution between waves is highly simplified. It is found that the law of stationary energy partition in a carbyne chain at room temperature is close, within the high-frequency spectral band, to the Rayleigh–Jeans law. Some differences arise due to the presence of triple-wave resonant processes at low-frequency vibrations. This can affect the specific heat, thermal conductivity and other phenomenological parameters of the system, especially at low temperatures.

2 Mathematical model

We consider mechanical vibrations of a simple one-dimensional chain consisting of particles of equal masses m, at equal distances a. Each particle has two degrees of freedom on the plane of oscillation. The forces between the particles are both central and noncentral. Accounting for noncentral forces leads to appearance of the so-called *bending* oscillatory modes. An absolute elongation of a segment in the chain λ_n, and the curvature of the median line κ_n, in the vicinity of the atom number n can be expressed as it follows:

$$\lambda_n = \sqrt{\left(a + (u_n - u_{n-1})\right)^2 + (w_n - w_{n-1})^2} - a;$$

$$\kappa_n = \arctan\left(\frac{w_n - w_{n-1}}{a + u_n - u_{n-1}}\right) - \arctan\left(\frac{w_{n+1} - w_n}{a + u_{n+1} - u_n}\right),$$

where u_n and w_n are the longitudinal and transverse components of the displacement, respectively. The Lagrangian of the system, within a harmonic approximation, has the following form

$$L = \frac{m}{2}\sum_{n=-Z}^{Z}\left(\dot{u}_n^2 + \dot{w}_n^2\right) - \frac{1}{2}\sum_{n=-Z}^{Z}\left(\alpha\lambda_n^2 + \beta\kappa_n^2\right), \tag{1}$$

where α and β are the force constants; the dot denotes derivative with respect to the time t. The number of elemental cells Z in the chain is supposed to be large enough, i.e. $Z \to \infty$. Equations governing the dynamics of the chain of particles are derived with the help of the Euler-Lagrange principle of variations. For the convenience of asymptotic procedures we introduce a small parameter $\mu \ll 1$, using the following similarity transform: $u_n \to \mu u_n$, $w_n \to \mu w_n$. In the linear limit, as $\mu \to 0$, equations become linear. Spectral parameters of the linearized set are completely characterized by the following dispersion relations

$$\omega_l(k) = \sqrt{\frac{2}{m}\alpha\left(1 - \cos ka\right)}; \quad \omega_b(k) = 2\sqrt{\frac{\beta}{m}}\frac{(1 - \cos ka)}{a}, \tag{2}$$

where $\omega_l(k)$ and $\omega_b(k)$ stand for the natural frequencies of the normal harmonic waves, depending upon the wave number k.

3 Average Hamiltonian. Resonance

Let the small parameter of the problem μ be non-zero. The solution to the linearized set can be adopted to have some useful information on the nonlinear system characterized by the Lagrangian (1), by varying the complex amplitudes of quasi-harmonic waves at the time:

$$\begin{aligned} U_n(t) &= \int\limits_{-\infty}^{\infty} \left(A_l(k,\tau_1,\tau_2,...)\, e^{i\phi_l(k,t)} + c.c.\right) dk + \sum_{m=1}^{\infty} \mu^m u_n^{(m)}(t); \\ W_n(t) &= \int\limits_{-\infty}^{\infty} \left(A_b(k,\tau_1,\tau_2,...)\, e^{i\phi_l(k,t)} + c.c.\right) dk + \sum_{m=1}^{\infty} \mu^m w_n^{(m)}(t). \end{aligned} \tag{3}$$

Here A_l and A_b are the complex amplitudes (*c.c.* are the corresponding complex conjugates of the preceding terms); $\phi_l(k,t) = \omega_l(k)\,t + kan$ and $\phi_b(k,t) = \omega_b(k)\,t + kan$ denote fast-rotating phases of the transverse and longitudinal waves, respectively; $\tau_n \to \mu^n t$ are the slow temporal time scales; $u_n^{(m)}(t)$ and $w_n^{(m)}(t)$ are small nonresonant corrections to the basic solution. The Lagrange function, with the help of anzats (3), being averaged over the fast rotating phases, appears in the form of so-called average Lagrangian $\langle L\rangle$. In turn, the arguments are of this function are proportional to the canonically conjugate variables. If one enters by a standard way the generalized momenta, p_{A_l} and p_{A_b}, then the average Lagrangian $\langle L\rangle$ can be rewritten as the average Hamiltonian $\langle H\rangle = \dot{A}_l p_{A_l} + \dot{A}_l^* p_{A_l^*} + \dot{A}_b p_{A_b} + \dot{A}_b^* p_{A_b^*} - \langle L\rangle$. The advantage of the Hamiltonian description is obvious: at least the one integral of energy is already known *a priori*, $\langle H\rangle = H_0$, where H_0 is a of integration. The average Hamiltonian, as a power series in μ, has a simple structure:

$$\langle H\rangle = \mu^2 \langle H_2\rangle + \mu^3 \langle H_3\rangle + ...$$

The first term $\langle H_2\rangle$ is identically zero by virtue of the dispersion relations (3). The term $\langle H_3\rangle$ is a cubic polynomial dependent upon the new generalized coordinates, namely, the complex conjugate amplitudes of longitudinal and transverse waves. This term carries all the information about the dynamic properties of the system within the first-order nonlinear approximation. Let $\langle H_3\rangle$ be not identically zero. Then the system experiences the first-order *resonance*, due to the nonlinear coupling between triads of modes being in phase, known as the *resonant triplets*.

4 Triple-mode resonant ensembles

For the benefit of nonlinear triple-mode resonant interaction between waves, any dynamical system requires an appropriate type of quadratic nonlinearity in the equations of motion, together with fulfilling the following *phase-matching* conditions

$$\omega_1 = \omega_2 + \omega_3; \quad k_1 = k_2 + k_3. \tag{4}$$

Here ω_n are the natural frequencies and k_n are the corresponding wave numbers of waves, satisfying the dispersion relations (2). The frequencies are numbered following the natural order: $\omega_1 \geq \omega_2 \geq \omega_3$. Based on the analysis of the dispersion and the structure of nonlinearity, one can establish that the triple-mode resonance in a carbyne chain can be of the one single type: each triple can consist of the primary high-frequency longitudinal mode with a pair of transverse low-frequency satellites, being in phase.

Real solutions to the dispersion equation (2), satisfying the phase-matching conditions (4), can be determined graphically. These solutions do exist in the wide permissible range of wave numbers, though the wave number of the longitudinal mode k_1 should not belong to the following "forbidden" interval:

$$k_1 \notin [k^*, 2\pi - k^*], \text{ where } k^* = \arctan\left(\frac{8\sqrt{\alpha\beta}\left(\alpha a^2 - 4\beta\right)a}{\alpha^2 a^4 - 24\beta\alpha a^2 + 16\beta^2}\right)/a.$$

5 Evolution equations of a single triad

Let the high-frequency mode of the resonant triad be a longitudinal wave. Then, after substituting the following representation of the solution:

$$\begin{aligned} u_n(t) &= A_1(\tau)\exp i\left(\omega_1 t + k_1 an\right) + c.c.; \\ w_n(t) &= A_2(\tau)\exp i\left(\omega_2 t + k_2 an\right) + A_3(\tau)\exp i\left(\omega_3 t + k_3 an\right) + c.c., \end{aligned} \tag{5}$$

into the Lagrangian (1), where ω_m and k_m are the spectral parameters of waves entering the resonant triple; $A_m(\tau)$ are the complex amplitudes of quasi-harmonic waves that slowly varying in the time $\tau = \mu t$; *c.c.* denotes the complex conjugate of the preceding terms, the evolution equations describing the evolution of the first-type triad take the following form:

$$2im\omega_j \frac{dA_j}{d\tau} = \frac{\partial \mathrm{H}}{\partial A_j^*}; \quad -2im\omega_j \frac{dA_j^*}{d\tau} = \frac{\partial \mathrm{H}}{\partial A_j}. \tag{6}$$

Here $\mathrm{H} = ic\left(A_1^* A_2 A_3 - A_1 A_2^* A_3^*\right)$ is the average potential of the triplet; c is the coefficient of the nonlinear coupling.

6 Conservation laws for isolated triads

The evolution equations (6) possess the first integrals. Obviously, one of them, is the average Hamiltonian: $\mathrm{H} = constant$, while the others are known as the Manley-Rowe relations [7]:

$$\begin{aligned} \omega_1 \left|A_1(\tau)\right|^2 + \omega_2 \left|A_2(\tau)\right|^2 &= c_{1,2}; \\ \omega_2 \left|A_2(\tau)\right|^2 - \omega_3 \left|A_3(\tau)\right|^2 &= c_{2,3}, \end{aligned} \tag{7}$$

where $c_{1,2}$, $c_{2,3}$ are arbitrary integration constants determined from the initial conditions to the Cauchy problem.

7 The superposition of triads

The average Hamiltonian, related to N resonant triads in a carbyne chain, can be written as it follows

$$\mathrm{H} = i\sum_{n=1}^{N} c_n \left(A_{3n-2}^* A_{3n-1} A_{3n} - A_{3n-2} A_{3n-1}^* A_{3n}^*\right),$$

where c_n are the nonlinearity coefficients related to the n-th resonant triplet; $A_m \quad \left(m = \overline{1,\, 3N}\right)$ are the complex amplitudes of waves, slowly varying in the time τ. The evolution equations of the triad chain are derived from the Hamiltonian formalism of mechanics:

$$2im\omega_n \frac{dA_n}{d\tau} = \frac{\partial \mathrm{H}}{\partial A_n^*}; \quad -2im\omega_n \frac{dA_n^*}{d\tau} = \frac{\partial \mathrm{H}}{\partial A_n}. \quad \left(n = \overline{1, 3N}\right) \tag{8}$$

These equations can be rewritten in polar coordinates:
$A_n(\tau) = a_n(\tau) \exp i\varphi_n(\tau) \quad \left(n = \overline{1, 2N+1}\right)$.

8 Stationary energy partition in a carbyne chain

The first-principle estimates of the carbyne chain parameters are the following [3]: $E = 32.71\ [TPa]$; $a = 32.71 \times 10^{-10}\ [m]$; $r = 0.366 \times 10^{-10}\ [m]$; $m = 1.994 \times 10^{-26}\ [kg]$. These parameters are sufficient for calculating the specific values of the coefficients: $F = \pi r^2 = 0.149 \times 10^{-20}\ \left[m^2\right]$; $J = \pi r^4/4 = 0.017 \times 10^{-40}\ \left[m^4\right]$; $\alpha = EF/a = 5.969 \times 10^{-10}\ [TPa \times m]$; $\beta = JF/a = 0.222 \times 10^{-30}\ \left[TPa \times m^3\right]$. Here F and J denote the effective cross-section square and moment of inertia, respectively. The flexural rigidity of carbyne at ambient temperatures corresponds to the persistence length about 110 carbon atoms along the chain [3]. The ratio of the de Broglie wavelength to the distance between the nearest neighborhood carbon atoms is about 10^{-1}. This indicates the possibility of studying the wave dynamics of carbyne in the framework of the classical mechanics. Carbyne chain has a small flexural rigidity that satisfies the inequality $\beta/\alpha a^2 \ll 1$. This indicates that the complex cascades of energy exchange between the modes of oscillations are absent in the system. Within the first-order nonlinear approximation analysis, only the three-wave resonant interactions between high-frequency longitudinal and pairs of low-frequency transverse waves are involved in the formation of steady states. The stationary solution for a single resonant triplet is following

$$\varpi_1\omega_1 a_1^2 = \varpi_2\omega_2 a_2^2 = \varpi_3\omega_3 a_3^2 = \varpi_1\varpi_2\varpi_3\omega_1\omega_2\omega_3/c^2,$$

where ϖ_i are the nonlinear Stokes corrections to the natural frequencies ω_i. In the first-order approximation, the nonlinear triple wave resonant ensembles represent closed and isolated dynamical objects. Therefore, the principle of linear superposition for any set of triplets should be valid. Therefore, there are infinitely many different patterns of the stationary energy distribution between the individual modes of oscillations of the system, from a formal point of view. Among all these possible stationary distributions, one should choose the single steady state that is implemented in practice. A selection rule provides the Boltzmann theorem on the energy equipartition between degrees of freedom from the statistical mechanics, declaring the proportionality of the average kinetic energy of a particle to the temperature of the system. At the thermal equilibrium, the energy is divided equally between all the modes. In the context of the problem of the stationary energy partition in a carbyne, the following sequence of constructions is evident. At the first step, it is reasonable to assume that nonlinear interactions between the modes are negligible, i.e., the system represents an ideal gas of quasi-particles without collisions. Then the stationary distribution of energy in the chain will be exactly described by the classical Rayleigh–Jeans law, since the total kinetic energy of the system is equal to

$$\mathrm{K} = \sum_{n=1}^{3N} \mathrm{K}_n = \sum_{n=1}^{3N} \omega_n^2 a_n^2 = 3Nk_BT\left(a^2\alpha\right)^{-1},$$

where k_B and T are the Boltzmann constant and the temperature, respectively; $3N$ is the total number of modes entering N different resonant triads. Every oscillatory mode, by virtue of the equipartition theorem, has the energy portion $\mathrm{K}_n = \omega_n^2 a_n^2 = k_B T \left(a^2 \alpha\right)^{-1}$.
Let us assumed now an essential nonlinearity of the system under consideration. The total kinetic energy is also conserved:

$$\mathrm{K} = \sum_{n=1}^{3N} \mathrm{K}_n = constant.$$

The portions of the binding energy are represented by the Hamiltonians of N individual resonant triplets: $\mathrm{H}_n = -2c_n a_{3n-2} a_{3n-1} a_{3n}$. Using the Lagrange method, we introduce the following function

$$\Lambda_{\mathrm{K}} = \sum_{n=1}^{N} \mathrm{H}_n + \sum_{n=1}^{3N} \lambda_n \left(\omega_n^2 a_n^2 - \mathrm{K}_n\right),$$

where λ_n are the Lagrange multipliers, which should be determined together with the amplitudes of oscillations a_n. A minimization of this function leads to the standard Rayleigh–Jeans law:

$$a_{3n-i} = \sqrt{k_B T \left(\alpha a^2 \omega_{3n-i}^2\right)^{-1}} \quad \left(i = \overline{0,2}; \quad n = \overline{1,N}\right).$$

This expression manifests on the proportional amplitude dispersion: the frequency corrections of nonlinear stationary waves, Ω_n, are directly proportional to the natural frequencies of the linear oscillators, ω_n. The coefficients of proportionality is $\sigma_n = c_n \sqrt{k_B T} / \left(2a\sqrt{\alpha}\omega_{3n-2}\omega_{3n-1}\omega_{3n}\right)$. As one can see, the generalization of the Rayleigh–Jeans law for nonlinear stationary processes is reduced to a frequency shift of linear harmonics, characterized by the ratio: $1 + \mu\sigma_n$, where the small parameter is defined by the maximal amplitude of the given triad: $\mu = \max\left(a_n\right)$.
For example, let us consider a resonant triad with the following spectral parameters, almost at the boundary of the "forbidden" zone: $\omega_1 = 0.297$; $\omega_2 = 0.560$; $\omega_3 = 0.261$; $c_1 = 0.298$. Let the temperature be $T = 300$ $[K]$. The minimum of the functional $\Lambda_{\mathrm{K}} = -0.987 \times 10^{-4}$ is achieved at the point $\varpi_2 = 0.061$. The proportionality coefficient is $\sigma_1 = 0.234$. The maximal amplitude of the stationary process equals to $\mu = a_3 = 0.039$. One can see that the frequency ratio, caused by the proportional amplitude dispersion at room temperature, can be clearly distinguished experimentally: $\mu\sigma_1 = 0.009$, i.e., being about a percents higher, compared to that of the linear theory. At the temperature $T = 600$ $[K]$, this frequency ratio arises almost up to two percents: $\mu\sigma_1 = 0.018$, and so on.
The problem formulation for any arbitrary set of resonant triads in a carbyne chain is reduced to the linear superposition of all waves entering these ensembles, being the closed and isolated dynamical systems, at least within the first-order nonlinear approximation.

9 Conclusion

Central and noncentral interactions between carbon atoms in a carbyne chain are taken into account to investigate the stationary energy partition between waves at ambient temperatures. The study used standard asymptotic methods of nonlinear dynamics, in the framework of classical mechanics, based on most simple mathematical model. The first-order nonlinear approximation analysis revealed the triple-wave resonant ensembles

of quasi-harmonic waves. These ensembles are formed due to a quadratic nonlinearity of the system, provided that the triple-mode phase-matching conditions are satisfied. Each resonant triad consists of a single primary high-frequency longitudinal mode and a pair of secondary low-frequency transverse modes of oscillations. It was shown that low-frequency quasi-harmonic longitudinal waves, caused by the central forces, are almost always unstable. These break up into pairs of secondary low-frequency transverse waves, unless the frequency of the primary longitudinal mode does not exceed some critical limit, defined by some "forbidden" zone. In general, the carbyne chain is described as a superposition of resonant triads of different spectral scales. We found that the stationary energy distribution in carbyne chains is described by the standard Rayleigh–Jeans law. This describes an equal energy distribution over the degrees of freedom. Some differences arise due to the effect of the proportional amplitude dispersion, leading to a temperature-dependent shift of wave frequencies in several percents, that can be clearly distinguished in experiments. These dispersion effect gets higher the theoretical value of the specific heat, and, in turn, can influence upon the thermal conductivity and other phenomenological parameters of the carbyne chain, especially at low temperatures, at which the tools of classical mechanics cannot be applied jet. The present study may be of interest for some applications of nanotechnology, dealing with NEMS or delicate water purification sets.

References

[1] Sladkov A.M. *Carbyne – the third allotropic form of carbon*, Moscow: Nauka, 2003.

[2] Smith, P.P.K.; Buseck, P.R. *Carbon in the Allende meteorite – Evidence for poorly graphitized carbon rather than carbyne*. In: Lunar Planetary Science Conference and, 12th, Houston, TX, March 16–20, 1981, Proceedings. Section 2. (A 82-31677 15-91) New York and Oxford: Pergamon Press, 1982, pp. 1167–1175.

[3] Liu M, Artyukhov VI, Lee H, Xu F, Yakobson BI: Carbyne from first Principles: Chain of C Atoms, A nanorod or A nanorope, *Acs Nano*, 2013, doi: 10.1021 / nn404177r

[4] Asinovskii E.I., Kirillin A.V., Kostanovskii A.V. Experimental investigation of the thermal properties of carbon at high temperatures and moderate pressures, *Physics-Uspekhi*, 2002,45(8), pp. 869-882.

[5] Savvatimskii A.I.. Melting point of graphite and liquid carbon,*Physics-Uspekhi*, 2003, 46(12), pp. 1295-1303.

[6] Belenkov E, Mavrinsky V. Crystal structure of a perfect carbyne, *Crystallgraph Rep.*, 2008, 53(1), pp. 83-90.

[7] Kaup, P.J., A. Reiman & A. Bers. Space-time evolution of nonlinear three-wave interactions. Interactions in a homogeneous medium, *Rev.of Modern Phys.*, 1979, vol. 51, no. 2, pp. 275-309.

Svetlana P. Nikitenkova,Lobachevsky State University of Nizhni Novgorod, Russia
Dmitry A. Kovriguine, Nizhny Novgorod State Technical University na RE Alekseev, Russia

Molecular dynamics simulations of the collapse of a hollow thick-walled cylinder

Anton Yu. Nikonov, Andrey I. Dmitriev
nikonov@usgroups.com

Abstract

In the paper simulation of the deformation of copper single crystal under high-speed axisymmetric loading was carried out using the method of molecular dynamics. Sample in the form of a hollow thick-walled cylinder was simulated. It is found that the compressive deformation when reaching a certain value leads to the formation of stacking fault in the inner surface of the cylinder. It is shown that depending on the orientation of a single crystal lattice stacking fault formation comes in various planes. It was found that the order of the plane of motion of dislocations depends on the angle between the plane and the direction of loading. Agreement of the results with the experimental data allows the use of modeling techniques to the study of the basic laws of plastic deformation in single crystals. The observed regularities of formation of localized deformation bands can be used to understand the processes of deformation of pure single crystals.

1 Introduction

Despite some progress, associated with using, both modern experimental research methods and new theoretical approaches, It is attending to the issue of studying the characteristics of localization of plastic deformation in crystalline materials [1, 2]. Increased interest caused by the fact that an understanding of the basic mechanisms of plastic deformation of crystalline materials is directly related to the ability to control their strength and deformation characteristics.

It should be noted that the most common strain localization phenomenon is seen in the cases of high degrees, high speeds and temperatures of deformation. This is manifested as the forming of stationary bands, also known as the term Вкshear bandsВь and represents an area of the material in which the strain rate is much higher deformation rates in the other volumes [3, 4]. The formation of Вкshear bandsВь plays a crucial role in the further deformation, because in most cases they are the harbinger of destruction of the material. At the same time it is known that with increasing of the deformation the scale of manifestations of its localization varies from block to grain from grain to grain complex and further to the sample as a whole. Thus, this process is multi-layered. Therefore, the initial stage of the origin and development of the process of localization of deformation is inextricably linked with the features of material response to the load on the microscale [5, 6]. In the transition to microscale research conducted on single crystals become important.

In [7], devoted to high-speed axisymmetric loading of copper single crystals noted that the spatial position of the centers of localization of deformation is determined by crystallography of active slip systems. Thus, the order of connection of a close-packed direction of sliding is determined by the corresponding factor Schmid. Note that in the cited paper the method of explosive loading of a hollow thick-walled cylinder was used. The advantage of this approach is the possibility of combining in one experiment all possible orientations of the single crystal relative to the applied load in the plane defined by the base plane of the sample. Since for the experimental solution of the problem requires laborious preparation of the corresponding single-crystal samples, taking into account their small spatial scales the issue can be effectively studied using modern methods of computer simulation [8].
Thus, the aim of this work is a theoretical study of the origin and development of the process of deformation localization on the scale of individual atoms depending on the crystallographic orientation of the plane of the base of the hollow cylindrical sample under high speed axisymmetric loading.

2 The results of computer simulation

2.1 The results of sample loading with the base plane (001) and (111)

For research of high-speed loading of single-crystal sample of copper on the scale of individual atoms the method of molecular dynamics using the software package LAMMPS was chosen. The interaction between the particles is described by means of the embedded atom method [**?** 9]. Simulated sample was a defect-free hollow copper cylinder whose axis of symmetry was directed along the Z-axis of the laboratory system of coordinates. The inner and outer radii of the cylinders is $36,15$ Å and $144,6$ Å. The height of the cylinder was set equal to $108,45$ Å. Initially two samples were considered. Orientation of their crystal lattice has been chosen so that the axis of the laboratory coordinate system X, Y and Z correspond to the crystallographic directions [100], [010] and [001] and [11$\bar{2}$], [$\bar{1}$10] and [111]. Axisymmetric loading was simulated by specifying an atom located on the outer surface of a cylinder of constant velocities. Velocities were directed toward the center of the cylinder in a plane parallel to the base sample, and velocity magnitudes are equal to 10 m/s. The thickness of the loaded layer was 5 Å. Periodic boundary conditions was modelling along the cylinder axis Z. The initial kinetic temperature of the simulated sample was 140 K. High-speed algorithm Werle was used for integrating the equations of motion. Total number of atoms exceeded 500000.
In this paper the evolution of the structure of the sample as a result of the applied axisymmetric compression was analyzed using a search algorithm of changes of the local topology of the atomic bonds [10]. It is found that the compressive deformation when reaching a certain value leads to the formation of defects in the inner surface of the cylinder structure. Fig. 1 shows the evolution of the structure of two simulated crystallites, which shows only the atoms with the local topology of atomic bonds differs from the original fcc lattice. On Figure 1 gray color mark atoms that locate on the inner and outer free surfaces. Red color indicates atoms with hcp a local topology of atomic bonds. It is clearly seen that the bands of localized atomic displacements that are formed on the inner surface of a hollow cylinder, formed mainly by atoms with a local topology of the atomic bonds are close to the hcp lattice. Thus, the obtained structural defects correspond to the stacking fault. With further loading of the simulated sample the number of stacking faults increases, and

they extend from the inner free surface where the strain reaches a maximum value in the volume of the material.

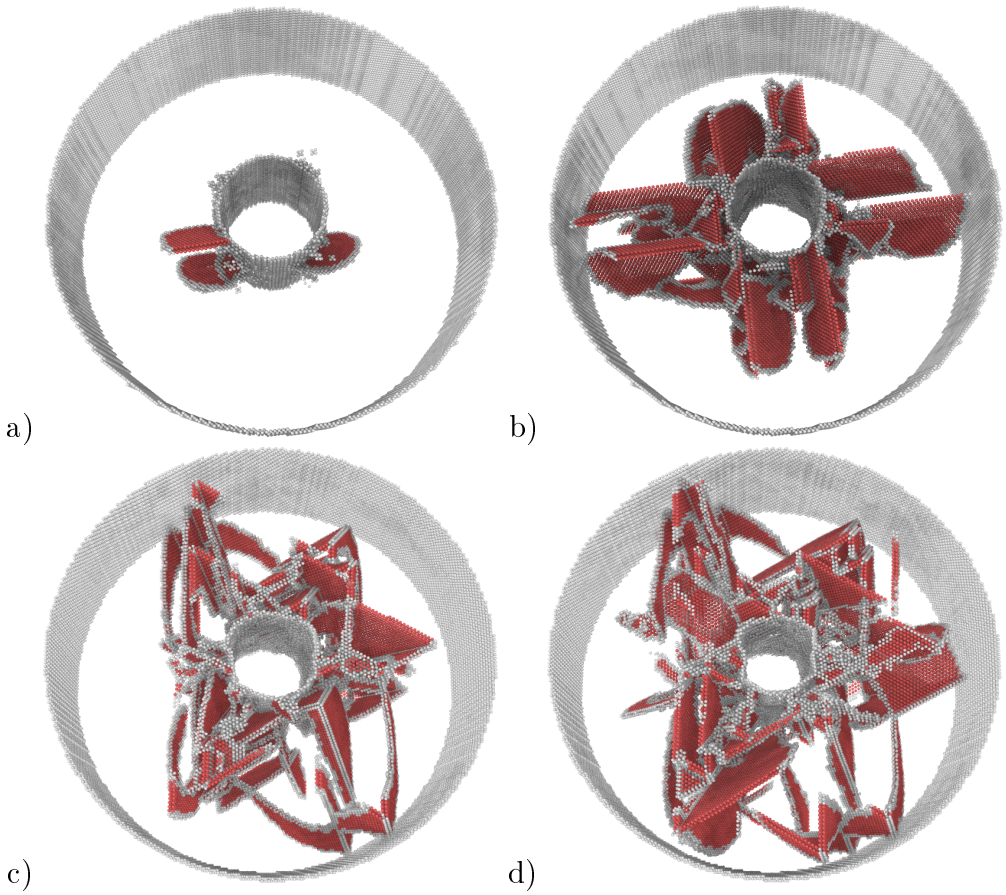

Figure 1: A three-dimensional image of the structure of the simulated crystallites at the stage of strain localization at different times. For a cylinder with the orientation of the base (001): a) $t = 39\ ps$, b) $t = 45\ ps$. For a cylinder with the orientation of the base (111): c) $t = 39\ ps$, d) $t = 45\ ps$.

Note that the generation of defects in the structure of the sample with orientation of the base (001) begins at time $t = 38\ ps$, whereas for the sample with orientation (111), this process occurs at $t = 27\ ps$. The difference between the behaviour of both of loaded crystallites is also the angle between the slip planes and the axis of the cylinder. Thus, for the sample with the crystallographic orientation of the base plane (001), the angle $\phi \approx 54,74°$, a sample with a base (111) $\phi \approx 70,53°$. This leads to difference in the start time of defect formation. Thus, the order of priority activity of slip systems in the considered samples are not observed, and the bands of localized atomic displacements are formed simultaneously on all possible slip planes.

2.2 The loading of the sample with the base plane (134)

To study the effect of crystallographic orientation of the base plane of cylindrical sample at its deformation properties, we modelled the axisymmetric high-speed loading of copper single crystal, the shape and dimensions of which were similar to the cases described above.

The crystallographic orientation of the lattice in the sample was as follows: along the cylinder axis (axis Z) direction [134] along the X and Y axes – $[11\bar{1}]$ and $[\bar{7}5\bar{2}]$, respectively. As before, the formation of stacking faults was observed near its inner free surface at certain degree of deformation of sample. Fig. 2 shows the structure at consecutive sample instant of time. It is possible to select a sequence in the formation of bands of localized atomic displacements in the sample under loading. Initially bands arise in a plane , which extends at an angle 90° to the axis of the cylinder (Fig. 2a). Then, stacking fault begin to form in the plane ($\phi = 76,9°$ to the cylinder axis) (Fig. 2b). The plane with a misorientation angle $\phi = 47,2°$ becomes the third slip plane (Figure 2c). The latter stacking faults appear in the (111) plane (misorientation angle $\phi = 25,1°$) (Figure 2d). Thus, in sequence of formed atomic displacements localized bands order was observed and associated with a decrease of the misorientation angle between the cylinder axis and corresponding slip plane. This result is fully consistent with the physics of the phenomenon under study and is in good agreement with data of experimental studies [7].

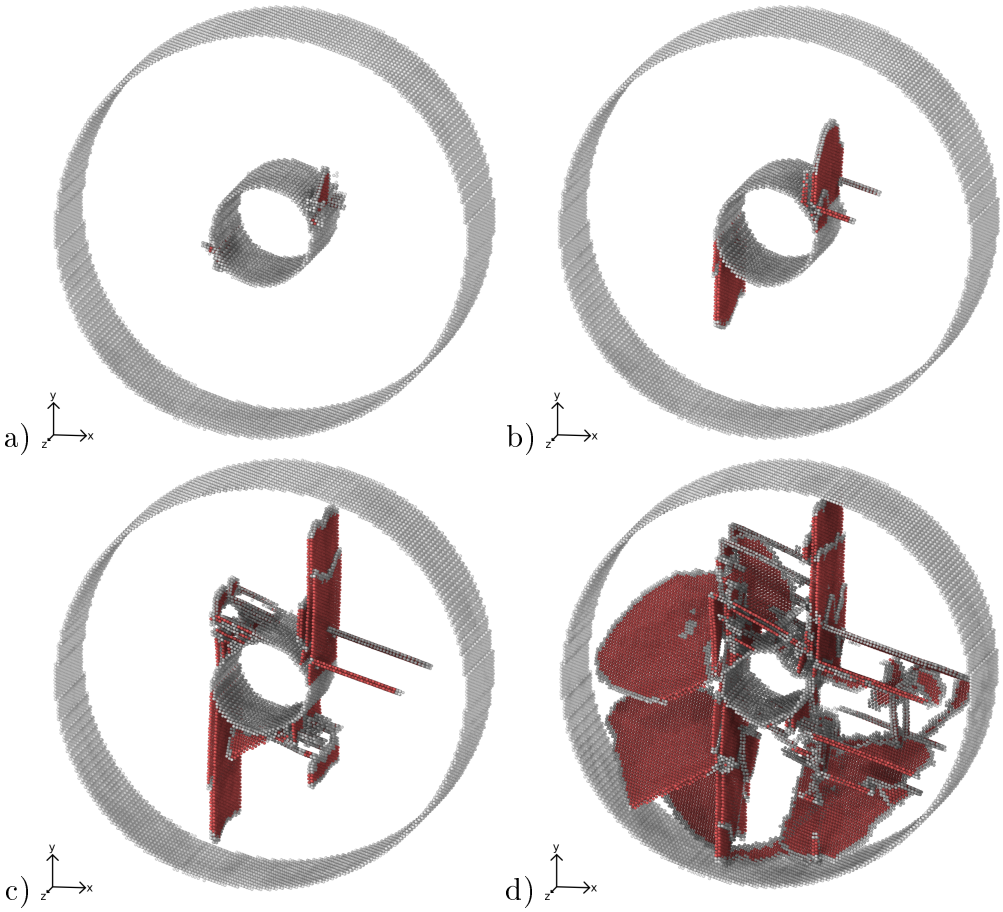

Figure 2: A three-dimensional image of the structure of the simulated crystallite at the stage of strain localization at different times: a) 26 *ps*, b) 28 *ps*, c) 33 *ps*, d) 47 *ps*.

2.3 Influence of crystallographic orientation on the magnitude of deformation.

In this study we evaluated the strain under which the localized atomic displacements appear in the crystallites. The deformation amount was calculated by the following formula:

$$\varepsilon = ln(r_0/r) \tag{1}$$

where r and r_0 вГ Y the current and the initial distance from the center of the cylinder to the selected atoms. The calculation results of deformation depending on the time of loading in case of the cylinder with the orientation of the base (001) was shown in Fig. 3. The position of selected atoms in the sample for which the value of the deformation calculated, observed in Fig. 3 in the upper left corner. Along the Z-axis atoms were selected in the atomic plane situated in the middle of the sample.

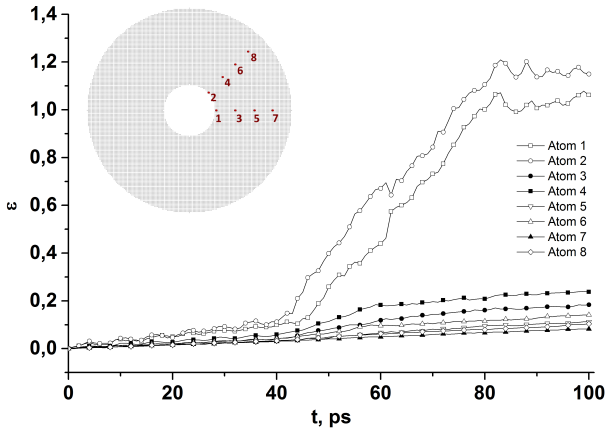

Figure 3: The time dependence of the calculated amount of deformation for selected atoms.

According to these results, the deformation of different parts of the cylinder before the inception of the bands of concerted atomic displacements is predominantly homogeneous character. The small difference to the velocity of the atoms 1 and 2 caused by their proximity to the free surface. Beginning at time $\approx 40\,ps$ a sharp increase of the deformation rate observed in crystallite areas located on the inner surface.
The observed difference in the magnitude of the displacement of various groups of atoms caused by formation of structural defects near the inner free surface of the crystallite. Fig. 4 shows the trajectories of motion of atoms in the central layer of the cylinder at successive times. The time of formation of localized bands displacements of atoms is clearly seen in the time interval from 37 ps to 39 ps (Fig. 4b), despite the fact that at the previous time interval inhomogeneous distribution of the displacement is not observed (Fig. 4a).
A comparison of the localization zones of atomic displacements with the local topology of atomic bonds showed that the atomic displacements are realized in the areas of formed structural defects - stacking faults. This is evident from a comparison of the trajectories of the atoms shown in Figure 4b with Figure 5, which shows the local topology of atomic bonds to atoms of the same dedicated central layer of the crystallite. Figure 5 atoms with an fcc topology atomic bonds (defect-free part of the crystallite) was marked by greem color and red represents the atoms with the local topology of the gpu interatomic bonds.

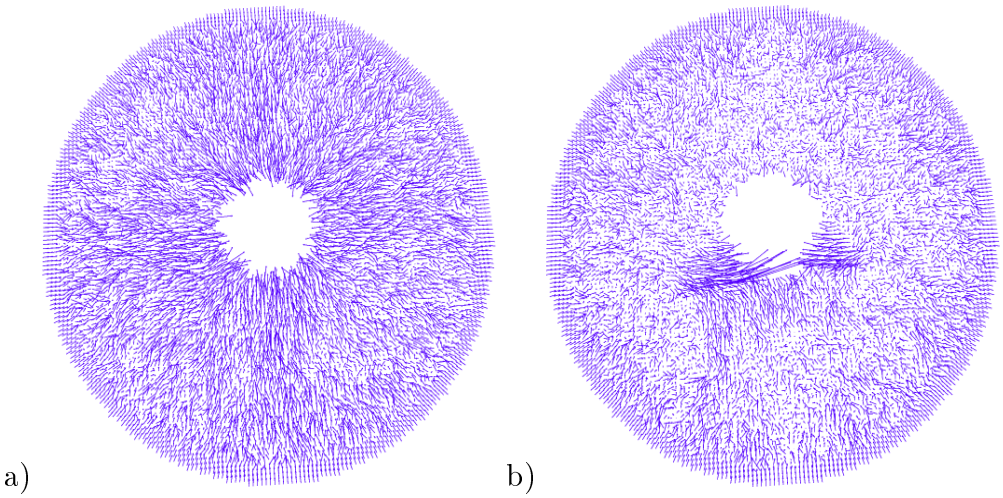

a) b)

Figure 4: Displacements of the atoms of the central layer of the cylinder in the intervals: a) from $t = 34$ ps to $t = 36$ ps and b) from $t = 37$ ps to $t = 39$ ps.

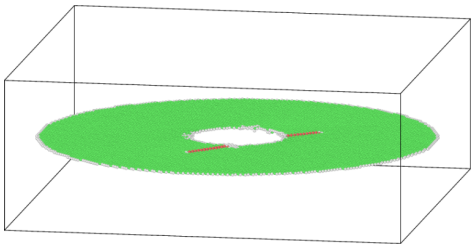

Figure 5: The central layer of the modeled cylinder at time $t = 39$ ps.

According to the results the behavior of the crystallite regions near the inner free surface is largely determined by the peculiarities of the restructuring of the crystal lattice due to the axisymmetric compression. Thus, further reduction of magnitude of the strain rate for the atoms 1 and 2 at time ≈ 80 ps (see. Fig. 3) caused by the collapse of the inner cavity of the cylinder. Character of displacement of atoms 3 and 4 also differs from the other groups of selected atoms. So, areas of cylinder remote from its axis by an amount not less than the half of the wall can be considered for evaluate the deformation properties of the simulated single crystal.

For comparison of deformation properties of cylindrical samples with different crystallographic orientation of their base in the paper average value of strain in 8 atoms in the layer lying remote from the cylinder axis by the same distance as the atoms 5 and 6 in Figure 3 was calculated. The position of the atoms used to estimate the value of the average strain differs by 45° with respect to the axis of the cylinder. The resulting time dependence of the average strain for the three considered crystallites with different crystallographic orientations of base shown in Fig. 6. Schematic representation of the positions of the atoms used for averaging the strain is shown in the upper left corner.

The simulation results showed that the elastic deformation stage for all considered variants identical to the strain 0.03. Further loading causes the deformation rate of the samples that the base (111) and (134) increases as compared with the sample orientation with the base (001) for which this stage of deformation continues until 0.04. At high degrees of loading the rate of deformation of the sample with a base (111) slows down and becomes the minimum of all the considered variants. This dependence, apparently due to the

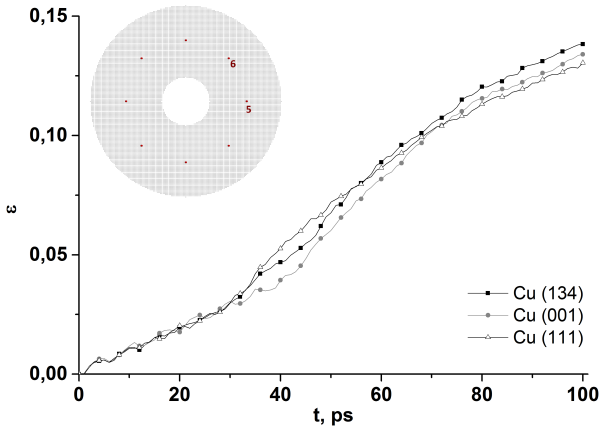

Figure 6: Averaged value of strain for copper samples with different crystallographic orientations their base.

relatively early formation of large number of stacking faults at the simultaneous activation of all possible slip planes. The presence of numerous structural defects leads to a further hardening of the sample. As for the samples with the orientations of a base (001) and (134), then over the entire active phase of loading the calculated average value of deformation for the variant (134) is located above a similar magnitude to case (001).

3 Conclusion

– A computer model of axisymmetric dynamic loading of copper crystallite on the scale of individual atoms showed good agreement between the simulation results and experimental data of explosive loading of copper single crystals. Both in the experiment and in the computer model the order of the activation of slip systems, which is determined by the corresponding value of Schmid factor, was noted. Thus, the proposed numerical model may be used for research of features of origin and development of plastic deformation in crystalline materials.

– It is shown using a computer model the influence of the chosen crystallographic plane of the base of the cylindrical sample on order of connection slip systems and the resulting deformation properties of the simulated object. Thus in a sample with the base parallel to the crystallographic plane (111) slip system activation sequence is not observed, and the generated localized band of atomic displacements formed simultaneously in all possible slip planes. This nature of the response to external loading crystallite leads to the fact that its speed of deformation is maximum of the three modelled variants of sample in the initial stages of the plastic behaviour. During the further loading a relatively early activation of all possible slip planes leads to a slowing of the rate of deformation of the sample and in the final stages of loading, it becomes the minimum of all the considered configurations.

Acknowledgements

Work was performed as part of Fundamental Research Program of SB RAS for 2013-2016.

References

[1] L.B. Zuev, et al., International Journal of Mechanical Sciences 88, 1вЃ“Y7 (2014)

[2] S.C. Yoon, et al., Computational Materials Science. 43(4), 641вЃ“Y645 (2008)

[3] X.D. Wang, et al., Materials Science and Engineering: A. 627, 336вЃ“Y339 (2015)

[4] V.E. Panin Theoretical and Applied Fracture Mechanics. 37, 261вЃ“Y298 (2001)

[5] M.P. Bondar, et al., Combustion, explosion, and shock waves 42, 356-365 (2006)

[6] M.P. Bondar, et al., Phys. Mesomech. 16, 191-199 (2013)

[7] M.P. Bondar, Combustion, explosion, and shock waves 39, 112-114 (2003)

[8] W. Österle, et al., Tribol. Lett. 54, 257-262 (2014)

[9] A. Suzuki, Y. Mishin, Interface Sci. 11, 131вЃ“Y148 (2003)

[10] D.J. Honeycutt, H.C. Andemen, J. Phys. Chem. 91, 4950-4963 (1987)

Nikonov A.Yu., Akademichesky 2/4, 634055, Tomsk, Russia
Dmitriev A.I., Akademichesky 2/4, 634055, Tomsk, Russia

On generalization of the LS-STAG immersed boundary method for Large Eddy Simulation and Detached Eddy Simulation

Valeria V. Puzikova
valeria.puzikova@gmail.com

Abstract

The general approach to the application of the LS-STAG method for the numerical solution of LES and DES equations is suggested. According to the concept of the LS-STAG method normal Reynolds or subgrid stress components are sampled on the base mesh (similar to pressure discretization) and shear ones are sampled in the upper right corners of the base mesh cells. Thus, for the shear Reynolds or subgrid stresses an additional mesh (xy-mesh) is introduced. In case of Reynolds Stress (RSM) LES and DES models, these meshes are used for transport equation solving for Reynolds or subgrid stresses. The result then is taken into account in the Helmholtz equation for the velocity. In case of Eddy Viscosity (EVM) LES or DES models eddy viscosity is sampled on the xy-mesh. In this research it is shown how to obtain the LS-STAG discretization of LES / DES equations and LES / DES turbulence models using the LS-STAG discretization developed for RANS equations and RANS-based turbulence models. To validate this approach the flow past circular airfoil at the Reynolds numbers $\mathrm{Re} = 1000$ and $\mathrm{Re} = 3900$ was simulated.

1 Introduction

The LS-STAG method [1] for viscous incompressible flows simulation combines the advantages of the MAC method, immersed boundary methods and level-set method. This method allows to solve on the Cartesian meshes problems when domain shape is irregular or it changes in the simulation process due to hydroelastic body motion. For these reasons, the LS-STAG method is very useful for solving such complicated problems of computational mechanics as coupled hydroelastic problems, biomechanic problems, problems of solid mechanics with deformable bodies.

However, the LS-STAG method, as all mesh methods, has a significant limitation when simulating flows with high Reynolds number: it requires extremely small space and time steps. It leads to significant increase in computational cost. The traditional method of solving this problem is RANS, LES, DES etc. turbulence models usage. Generalization of the LS-STAG method for LES and DES is presented in this research.

2 Governing equations

The problem is considered for 2D unsteady case when the flow around an airfoil assumed to be viscous and incompressible within the framework of LES and DES approaches. In contrast to direct numerical simulation (DNS) based on solution of Navier—Stokes equations and resolution of all turbulent movement scales, turbulence models usage involves a simulation of a turbulence scales contribution to the averaged motion (in case of RANS approach) or a simulation of scales that do not exceed the filter width Δ (in case of LES approach). In case of RANS approach one speaks of the Reynolds stress simulation and in case of LES approach one speaks of the subgrid stress simulation.
The Reynolds-averaged Navier—Stokes equations are solved in RANS approach, and the filtered Navier—Stokes equations are solved in LES approach instead of the Navier—Stokes equations. Usage of DES approash is means that RANS equations are solved in one part of the computational domain, and LES equations are solved in the other part. It is possible to write down the unified problem statement in dimensionless variables for all approaches, because the form of LES equations is similar to the form of RANS equations. So, the flow is described by the following LES / DES equations:

$$\nabla \cdot \mathbf{v} = 0, \quad \frac{\partial \mathbf{v}}{\partial t} + (\mathbf{v} \cdot \nabla)\mathbf{v} = -\nabla p + \nu \Delta \mathbf{v} + \nabla \cdot \hat{\tau}^t. \tag{1}$$

Here $\mathbf{v}$ is the dimensionless Reynolds averaged of filtrated velocity, p is dimensionless Reynolds averaged of filtrated pressure, t is the dimensionless time, ν is the dimensionless viscosity coefficient, $\hat{\tau}^t$ is the Reynolds or subgrid stresses tensor. The boundary conditions are the following:

$$\mathbf{v}\big|_{\text{inlet}} = \mathbf{v}_\infty, \quad \frac{\partial \mathbf{v}}{\partial \mathbf{n}}\Big|_{\text{outlet}} = 0, \quad \mathbf{v}\big|_{\text{airfoil}} = \mathbf{0}, \quad \frac{\partial p}{\partial \mathbf{n}}\Big|_{\text{inlet \& outlet \& airfoil}} = 0. \tag{2}$$

The relationship between $\hat{\tau}^t$ and Reynolds averaged or filtrated flow variables is given by the turbulence model. In case of Reynolds Stress (RSM) RANS models, for example DRSM, ARSM, EARSM, the Reynolds stress transport equation is solved for simulating of $\hat{\tau}^t$. In case of Eddy Viscosity (EVM) RANS models the eddy viscosity ν^t (and the turbulent kinetic energy k in case of two-equation models) is simulated and Reynolds or subgrid stresses are evaluated using the Boussinesq eddy viscosity assumption [2]:

$$\tau^t_{xx} = 2\nu^t \frac{\partial u}{\partial x} + \frac{2}{3}k, \quad \tau^t_{yy} = 2\nu^t \frac{\partial v}{\partial y} + \frac{2}{3}k, \tag{3}$$

$$\tau^t_{xy} = \nu^t \left(\frac{\partial u}{\partial y} + \frac{\partial v}{\partial x} \right). \tag{4}$$

Here τ^t_{xx} and τ^t_{yy} are the normal Reynolds or subgrid stresses, τ^t_{xy} are the shear Reynolds or subgrid stresses. The equations for ν^t and k, as well as initial and boundary conditions for them are is determined by the turbulence model.

3 Transition from RANS-based turbulence models to subgrid (LES and DES) models

It is possible to distinguish the linear turbulence scale $l_{turb} = l_{turb}(\mathbf{r})$ in all turbulence models. With RANS approach is used this scale l_{turb} is equal to scale $l_{RANS} = l_{RANS}(\mathbf{r})$, which is determined by the turbulence model (table 11).

Table 11: Turbulence scale l_{RANS} for some turbulence models [2]

Turbulence model	l_{RANS}	Comments
SpallartЧAllmaras	d_w	d_w is the distance from the field point to the nearest wall
$k-\varepsilon$	$k^{3/2}\varepsilon^{-1}$	ε is the dissipation rate of the k
$k-\omega$, $k-\omega$ SST	$k^{1/2}(\beta^*\omega)^{-1}$	ω is the specific dissipation rate of the k, $\beta^* = 0.09$

In the case of the turbulence model usage within the LES framework the scale l_{turb} is equal to subgrid scale:

$$l_{LES} = C_{LES}\Delta. \tag{5}$$

Here $\Delta = \Delta(\mathbf{r})$ is the characteristic filter size at the point of computational domain with the radius vector $\mathbf{r}$, and C_{LES} is the empirical constant, which choice depends on the turbulence model and numerical method used to solve the problem (1), (2). Within the DES approach the linear turbulence scale l_{turb} is equal to hybrid linear scale

$$l_{DES} = \min\{l_{RANS}, C_{DES}\Delta\}. \tag{6}$$

Here C_{DES} is the empirical constant similar to C_{LES}, and the maximum of the mesh steps at the point of computational domain with the radius vector $\mathbf{r}$ is used as the characteristic filter size $\Delta = \Delta(\mathbf{r})$. Thus, DES operates as RANS in the domains where the mesh is too coarse and not suitable for resolving turbulent structures, i.e. at $C_{DES}\Delta > l_{RANS}$, and DES operates as subgrid model for LES in the domains where the grid is sufficiently fine [2].

4 Generalization of the LS-STAG method for LES and DES

The Cartesian mesh with cells $\Omega_{i,j} = (x_{i-1}, x_i) \times (y_{j-1}, y_j)$ is introduced in the rectangular computational domain. It is denoted that $\Gamma_{i,j}$ is the face of $\Omega_{i,j}$ and $\mathbf{x}^c_{i,j} = (x^c_i, y^c_j)$ is the center of this cell. Unknown components $u_{i,j}$ and $v_{i,j}$ of velocity vector $\mathbf{v}$ are computed in the middle of fluid parts of the cell faces. These points are the centers of control volumes $\Omega^u_{i,j} = (x^c_i, x^c_{i+1}) \times (y_{j-1}, y_j)$ and $\Omega^v_{i,j} = (x_{i-1}, x_i) \times (y^c_j, y^c_{j+1})$ with faces $\Gamma^u_{i,j}$ and $\Gamma^v_{i,j}$ respectively (fig. 1).
Cells which the immersed boundary intersects are the so-called 'cut-cells' [1]. These cells contain the solid part together with the liquid one. The level-set function φ [3] is used for immersed boundary Γ^{ib} description. The boundary Γ^{ib} is represented by a line segment on the cut-cell $\Omega_{i,j}$. Locations of this segment endpoints are defined by a linear interpolation of the variable $\varphi_{i,j} = \varphi(x_i, y_j)$. The cell-face fraction ratios $\vartheta^u_{i,j}$ and $\vartheta^v_{i,j}$ are introduced. They take values in interval $[0, 1]$ and represent the fluid parts of the east and north faces of $\Gamma_{i,j}$ respectively.
To preserve the five-point structure of the MAC method stencil we need to make distinction between the discretization of the normal and shear stresses (fig. 1). It is proposed to sample

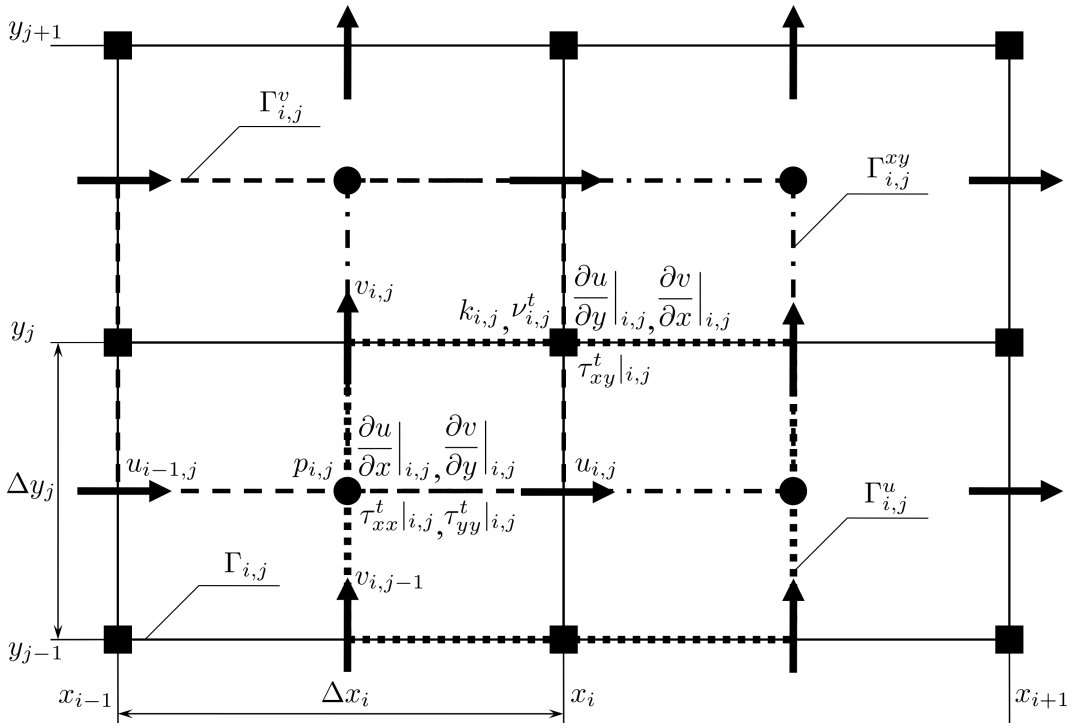

Figure 1: Staggered arrangement of the variables on the LS-STAG mesh

the normal and shear Reynolds or subgrid stresses similarly. It is conveniently to sample the eddy viscosity ν^t and turbulence kinetic energy k at the same points as the shear stresses. Thus, in case of the LS-STAG method usage within LES and DES approaches the fourth mesh with cells $\Omega^{xy}_{i,j} = (x^c_i, x^c_{i+1}) \times (y^c_j, y^c_{j+1})$ is needed. The faces of these cells are $\Gamma^{xy}_{i,j}$ (fig. 1) and their areas are $M^{xy}_{i,j}$. If $i = \overline{1,N}$, $j = \overline{1,M}$, xy-mesh contains $E_{xy} = (N-1)\cdot(M-1)$ cells.
It is posible to assign a weight $\alpha_{i,j}$ to each cell $\Omega_{i,j}$ of the base mesh:

$$\alpha_{i,j} = \begin{cases} 0, & \text{if } \Omega_{i,j} \text{ is the solid cell,} \\ 1/3, & \text{if } \Omega_{i,j} \text{ is the triangular cell,} \\ 1/4, & \text{otherwise.} \end{cases}$$

Then $M^{xy}_{i,j}$ can be expressed through the area of base mesh cells:

$$M^{xy}_{i,j} = \alpha_{i,j-1}V_{i,j-1} + \alpha_{i-1,j}V_{i-1,j} + \alpha_{i,j}V_{i,j} + \alpha_{i,j+1}V_{i,j+1}.$$

Here $V_{i,j}$ is the area of the $\Omega_{i,j}$.
Since ν^t and shear Reynolds or subgrid stresses (4) are sampled at the same points, it follows that

$$\tau^t_{xy}|_{i,j} = \nu^t_{i,j}\Big(\frac{\partial u}{\partial y}\Big|_{i,j} + \frac{\partial v}{\partial x}\Big|_{i,j}\Big),$$

whereas averaged values of turbulent viscosity $\overline{\nu^t}_{i,j}$ and the turbulent kinetic energy $\overline{k}_{i,j}$ should be used for the computation of the normal Reynolds or subgrid stresses (3):

$$\tau^t_{xx}|_{i,j} = 2\overline{\nu^t}_{i,j}\frac{\partial u}{\partial x}\Big|_{i,j} + \frac{2}{3}\overline{k}_{i,j},\ \tau^t_{yy}|_{i,j} = 2\overline{\nu^t}_{i,j}\frac{\partial v}{\partial y}\Big|_{i,j} + \frac{2}{3}\overline{k}_{i,j},$$

$$\overline{\nu^t}_{i,j} = \alpha_{i,j}(\nu^t_{i,j} + \nu^t_{i,j-1} + \nu^t_{i-1,j} + \nu^t_{i-1,j-1}),\ \overline{k}_{i,j} = \alpha_{i,j}(k_{i,j} + k_{i,j-1} + k_{i-1,j} + k_{i-1,j-1}).$$

It is conveniently to sample the linear turbulence scale l_{turb} and the characteristic filter size Δ for LES and DES at the same points as the ν^t and k. We recall that the maximum mesh step at the given point of the computational domain is used as a filter size Δ for DES approach. Since we deal with xy-mesh, the characteristic filter size is defined as a following:

$$\Delta_{i,j} = \Delta_{i,j}^{\max} = \max\{\Delta y_{i-1,j}^{xy}, \Delta y_{i,j}^{xy}, \Delta y_{i+1,j}^{xy}, \Delta x_{i,j-1}^{xy}, \Delta x_{i,j}^{xy}, \Delta x_{i,j+1}^{xy}\},$$

$$\Delta y_{i,j}^{xy} = \frac{1}{2}(\vartheta_{i,j}^{u}\Delta y_j + \vartheta_{i,j+1}^{u}\Delta y_{j+1}),\ \Delta x_{i,j}^{xy} = \frac{1}{2}(\vartheta_{i,j}^{v}\Delta x_i + \vartheta_{i+1,j}^{v}\Delta x_{i+1}).$$

The following filter can also be used on the LS-STAG mesh within LES approach:

$$\Delta_{i,j} = \Delta_{i,j}^{vol} = \sqrt{M_{i,j}^{xy}}.$$

Thus, the LS-STAG discretization of LES / DES equations and turbulence LES / DES models can be easily obtained from the LS-STAG discretization of RANS equations and RANS-based turbulence models developed in [4] by using formulae (5), (6). The development of the LS-STAG discretization for the Spalart—Allmaras (S-A) turbulence model [5] is described in [4] as an example.

5 Numerical experiments

The flow past circular airfoil was simulated using the developed modification of the LS-STAG method at the Reynolds numbers Re = 1000 (on non-uniform meshes 120×148 with $\Delta t = 5 \cdot 10^{-3}$ and 240×296 with $\Delta t = 10^{-3}$) and Re = 3900 (on non-uniform meshes 120×148 with $\Delta t = 10^{-3}$ and 240×296 with $\Delta t = 5 \cdot 10^{-4}$); $C_{LES} = 0.20$, $C_{DES} = 0.65$. The time averaged drag coefficient C_{xa} and the Strouhal number Sh were computed. The coefficient C_{xa} is obtained by averaging over a large period of time the unsteady load $C_{xa}(t) = \dfrac{2F_{xa}(t)}{\rho V_\infty^2}$. Computational results are shown in table 12. These results are in good agreement with experimental data and results of numerical simulations.

6 Conclusion

The key points of the LS-STAG method generalization for LES and DES are described. For the shear Reynolds or subgrid stresses and for the eddy viscosity an additional mesh (xy-mesh) is introduced. It is shown how to obtain the LS-STAG discretization of LES / DES equations and LES / DES turbulence models using the LS-STAG discretization developed for RANS equations and RANS-based turbulence models. To validate this approach the flows past a circular airfoil at the Reynolds numbers Re = 1000 and Re = 3900 were simulated. Computational results are in good agreement with established results from the literature.

Acknowledgements

The work was supported by Russian Federation President's Grant for young scientists [proj. MK-5357.2015.8].

Table 12: Comparison of C_{xa} and Sh with established results from the literature

Turbulence model	Number of cells	Re = 1000		Re = 3900	
		C_{xa}	Sh	C_{xa}	Sh
Experiment [6]		0.98	0.21	0.93	0.22
Experiment [7]		1.12	—	1.01	—
LES [8]	1 103 520	—	—	1.08	—
SV LES [9]	30 720	—	—	1.01	0.22
FV LES [9]	855 040	—	—	1.07	0.24
$k-\varepsilon$ [10]	46 304	0.995	0.15	1.00	0.15
Real $k-\varepsilon$ [10]	46 304	—	0.17	—	0.20
SST $k-\omega$ [10]	46 304	—	0.23	—	0.25
$k-\varepsilon$ [11], ANSYS	388 550	1.17	—	0.74	—
SST $k-\omega$ [11], ANSYS	388 550	0.99	—	0.62	—
LES [11], ANSYS	388 550	1.15	0.21	1.07	—
S-A LES (Δ^{vol}), present study	17 760	1.13	0.26	0.82	0.26
S-A LES (Δ^{vol}), present study	71 040	1.04	0.24	1.09	0.25
S-A LES ($\Delta^{\max}$), present study	17 760	1.13	0.26	0.82	0.17
S-A LES ($\Delta^{\max}$), present study	71 040	1.03	0.24	1.08	0.25
S-A DES, present study	17 760	1.13	0.26	0.81	0.23
S-A DES, present study	71 040	1.00	0.23	1.01	0.23

References

[1] Cheny Y., Botella O. The LS-STAG method: A new immersed boundary/level-set method for the computation of incompressible viscous flows in complex moving geometries with good conservation properties// J. Comput. Phys. 2010. N 229. P. 1043–1076.

[2] Spalart P.R. Strategies for turbulence modelling and simulations// Int. J. Heat and Fluid Flow. 2000. N 21. P. 252–263.

[3] Osher S., Fedkiw R.P. Level set methods and dynamic implicit surfaces. Springer, 2003.

[4] Puzikova V.V., Marchevsky I.K. Extension of the LS-STAG cut-cell immersed boundary method for RANS-based turbulence models // Advanced Problems in Mechanics — 2014 International Summer School-Conference: Book of proceedings. St.-Petersburg, Russia. 2014. P. 411–417.

[5] Spalart P.R., Allmaras S.R. A One-Equation Turbulence Model for Aerodynamic Flows// Recherche Aerospatiale. 1994. N 1. P. 5–21.

[6] Zdravkovich M.M. Flow around circular cylinders. Oxford University Press, 1997.

[7] Zahm A.F. Flow and drag formulas for simple quadrics // NACA Tech. Rept. N 253. 1927. 23 p.

[8] Breuer M. Large Eddy Simulation of the subcritical flow past a circular cylinder: numerical and modelling aspects// Int. J. Numer. Meth. Fluids. 1998. N 28. P. 1281–1302.

[9] Blackburn H.M., Schmidt S. Large Eddy Simulation of flow past a circular cylinder// 14th Australasian Fluid Mechanics Conference, Adelaide University, Adelaide, Australia, 2001.

[10] Rahman M.M., Karim M.M., Alim M.A. Numerical investigation of unsteady flow past a circular cylinder using 2-D finite volume method// J. Naval Arch. and Marine Eng. 2007. N 4. P. 27–42.

[11] Patel Y. Numerical Investigation of flow past a circular cylinder and in a staggered tube bundle using various turbulence models. Master's thesis. Lappeenranta: Lappeenranta University of Technology, 2010.

Valeria V. Puzikova, Russia, 105005 Moscow, 2nd Baumanskaya, 5

Geometrically nonlinear static theory of micropolar elastic thin shallow shells

Armenuhi H. Sargsyan, Samvel H. Sargsyan
armenuhis@mail.ru

Abstract

Micropolar thin shallow shells are considered, the elastic deflections are comparable to their thickness and at the same time are small in relation to the basic size, at the same time as the small angles of relation of the normal to the middle surface before deformation, and their free rotations. Thus, in the deformation tensor and bending-torsion tensor takes into account not only linear but also the nonlinear terms in the gradients of displacements. The hypothesis method is developed and on this base static applied theory of micropolar elastic flexible shallow shells are constructed. Some practical problems are solved.

1 Introduction

In the monographs [1],[2] the geometrically nonlinear static and dynamic general theories of thin plates and shells are constructed on the basis of the classical elasticity theory.
In the works [3],[4] the applied static and dynamic general theories of micropolar thin plates with finite deflections are constructed on the basis of three-dimensional micropolar theory of elasticity.
In the given work as initial, the general variational principle of geometrically nonlinear three-dimensional static theory of micropolar elasticity shallow shells are developed (all basic equations and natural boundary conditions of the specified theory are followed from this principle). The kinematic and static hypotheses of the works [3],[4] are accepted in the basis of construction of the adequate general variational principle of geometrically nonlinear micropolar applied theory of elastic thin shallow shells. By verifying the resulting functional of applied theory of micropolar flexible shallow shells to it's all functional arguments balance equations, physical relations of elasticity, geometrical relations, and also natural boundary conditions are obtained.

2 The geometrically nonlinear model of three-dimensional micropolar elastic shallow shells with independent field of displacements and rotations

The shallow shell with the constant thickness $2h$ is considered as three-dimensional elastic micropolar isotropic body. The shell is attributed to the system of coordinate $x_1,\ x_2,\ z$.

The coordinate surface $x_1,\ x_2$ is combined with the median surface of the shell. The axes Oz is directed along the normal of the median surface.
The variational functional of three-dimensional theory of micropolar elasticity with the finite displacements are resulted and looks like:

$$I = \int_{-h}^{h} \int\int_{S} \Bigg\langle W - \Bigg\{ \sigma_{11} \left[\gamma_{11} - \left(\frac{\partial V_1}{\partial x_1} + \frac{V_3}{R_1} + \frac{1}{2} \left(\frac{\partial V_3}{\partial x_1} \right)^2 \right) \right] +$$

$$+ \sigma_{22} \left[\gamma_{22} - \left(\frac{\partial V_2}{\partial x_2} + \frac{V_3}{R_2} + \frac{1}{2} \left(\frac{\partial V_3}{\partial x_2} \right)^2 \right) \right] + \sigma_{33} \left[\gamma_{33} - \frac{\partial V_3}{\partial z} \right] +$$

$$+ \sigma_{12} \left[\gamma_{12} - \left(\frac{\partial V_2}{\partial x_1} + \frac{1}{2} \frac{\partial V_3}{\partial x_1} \frac{\partial V_3}{\partial x_2} - \omega_3 \right) \right] + \sigma_{21} \left[\gamma_{21} - \left(\frac{\partial V_1}{\partial x_2} + \frac{1}{2} \frac{\partial V_3}{\partial x_1} \frac{\partial V_3}{\partial x_2} + \omega_3 \right) \right] +$$

$$+ \sigma_{13} \left[\gamma_{13} - \left(\frac{\partial V_3}{\partial x_1} + \omega_2 \right) \right] + \sigma_{31} \left[\gamma_{31} - \left(\frac{\partial V_1}{\partial z} - \omega_2 \right) \right] +$$

$$+ \sigma_{23} \left[\gamma_{23} - \left(\frac{\partial V_3}{\partial x_2} - \omega_1 \right) \right] + \sigma_{32} \left[\gamma_{32} - \left(\frac{\partial V_2}{\partial z} + \omega_1 \right) \right] +$$

$$+ \mu_{11} \left[\chi_{11} - \frac{\partial \omega_1}{\partial x_1} \right] + \mu_{22} \left[\chi_{22} - \frac{\partial \omega_2}{\partial x_2} \right] + \mu_{33} \left[\chi_{33} - \frac{\partial \omega_3}{\partial z} \right] +$$

$$+ \mu_{12} \left[\chi_{12} - \frac{\partial \omega_2}{\partial x_1} \right] + \mu_{21} \left[\chi_{21} - \frac{\partial \omega_1}{\partial x_2} \right] + \mu_{13} \left[\chi_{13} - \frac{\partial \omega_3}{\partial x_1} \right] +$$

$$+ \mu_{31} \left[\chi_{31} - \frac{\partial \omega_1}{\partial z} \right] + \mu_{23} \left[\chi_{23} - \frac{\partial \omega_3}{\partial x_2} \right] + \mu_{32} \left[\chi_{32} - \frac{\partial \omega_2}{\partial z} \right] \Bigg\} \Bigg\rangle dx_1 dx_2 dz -$$

$$- \int\int_{S^+} \left[q_1^+ V_1 + q_2^+ V_2 + q_3^+ V_3 + m_1^+ \omega_1 + m_2^+ \omega_2 + m_3^+ \omega_3 \right]_{z=h} dx_1 dx_2 +$$

$$+ \int\int_{S^-} \left[q_1^- V_1 + q_2^- V_2 + q_3^- V_3 + m_1^- \omega_1 + m_2^- \omega_2 + m_3^- \omega_3 \right]_{z=-h} dx_1 dx_2 +$$

$$+ \int_{-h}^{h} dz \int_{l_1'} \left(\sigma_{21}^0 V_1 + \sigma_{22}^0 V_2 + \sigma_{23}^0 V_3 + \mu_{21}^0 \omega_1 + \mu_{22}^0 \omega_2 + \mu_{23}^0 \omega_3 \right) dx_1 +$$

$$+ \int_{-h}^{h} dz \int_{l_1''} \Big[\sigma_{21} \left(V_1 - V_1^0 \right) + \sigma_{22} \left(V_2 - V_2^0 \right) + \sigma_{23} \left(V_3 - V_3^0 \right) +$$

$$+ \mu_{21} \left(\omega_1 - \omega_1^0 \right) + \mu_{22} \left(\omega_2 - \omega_2^0 \right) + \mu_{23} \left(\omega_3 - \omega_3^0 \right) \Big] dx_1 +$$

$$+ \int_{-h}^{h} dz \int_{l_2'} \left(\sigma_{21}^0 V_1 + \sigma_{22}^0 V_2 + \sigma_{23}^0 V_3 + \mu_{21}^0 \omega_1 + \mu_{22}^0 \omega_2 + \mu_{23}^0 \omega_3 \right) dx_2 +$$

$$+ \int_{-h}^{h} dz \int_{l_2''} \Big[\sigma_{21} \left(V_1 - V_1^0 \right) + \sigma_{22} \left(V_2 - V_2^0 \right) + \sigma_{23} \left(V_3 - V_3^0 \right) +$$

$$+ \mu_{21} \left(\omega_1 - \omega_1^0 \right) + \mu_{22} \left(\omega_2 - \omega_2^0 \right) + \mu_{23} \left(\omega_3 - \omega_3^0 \right) \Big] dx_2 \qquad (1)$$

Here surface integrals are extended on the face surfaces $S^+, S^-(z = \pm h)$ and on the lateral surface of the shell, where on one part the external strains and moments are set, and on the other part displacements and rotations are set; quantities with the top indexes zero are the set external force stresses and couple stresses on the certain part l_1 of the contour

of the median surface of the shell and displacements and rotations on the other part l_2 of the same contour, and also $l_1 = l_1' \bigcup l_1'', l_2 = l_2' \bigcup l_2''$. W is the density of potential energy of deformations:

$$W = \frac{1}{2}\Big(\sigma_{11}\gamma_{11} + \sigma_{22}\gamma_{22} + \sigma_{12}\gamma_{12} + \sigma_{21}\gamma_{21} + \sigma_{13}\gamma_{13} + \sigma_{23}\gamma_{23} + \sigma_{32}\gamma_{32} +$$

$$+\mu_{11}\chi_{11} + \mu_{22}\chi_{22} + \mu_{33}\chi_{33} + \mu_{12}\chi_{12} + \mu_{21}\chi_{21} + \mu_{13}\chi_{13} + \mu_{31}\chi_{31} + \mu_{23}\chi_{23} + \mu_{32}\chi_{32}\Big) \quad (2)$$

Here V_i, V_3 are components of the displacement vector; ω_i, ω_3 are components of the independent rotation vector; σ_{ii}, σ_{ij}, σ_{i3}, σ_{3i}, σ_{33} are components of the force stresses tensor; μ_{ii}, μ_{ij}, μ_{i3}, μ_{3i}, μ_{33} are components of the couple stresses tensor; γ_{ii}, γ_{ij}, γ_{i3}, γ_{3i} are components of the deformations tensor; χ_{ii}, χ_{ij}, χ_{i3}, χ_{3i} are components of the bends-torsions tensor.

It is naturally, the functional (1) to call the full functional of three-dimensional micropolar theory of elasticity of shallow shells at finite deflections. On its basis the variational equation ($\delta I = 0$) can be obtained. All general equations and natural boundary conditions of the micropolar elasticity problem at finite displacements are obtained from this equation.

3 The geometrically nonlinear theory of micropolar elastic thin shallow shells with big deflections

Hypothesis of works [3], [4] are accepted in the base of the offered theory of micropolar elastic geometrically nonlinear thin shallow shells for the purpose of reduction the geometrically nonlinear three-dimensional theory of micropolar elasticity to the corresponding tow-dimensional theory. Also, instead of the components of stresses and couple stresses tensors there are entered integrated characteristics, that are statically equivalent to them: strains (T_{ii}, S_{ij}, N_{i3}, N_{3i}), moments (M_{ii}, M_{ij}, L_{ii}, L_{ij}, L_{i3}, L_{33}) and hypermoments (Λ_{i3}):

$$T_{ii} = \int_{-h}^{h} \sigma_{ii} dz,\ S_{ij} = \int_{-h}^{h} \sigma_{ij} dz,\ N_{i3} = \int_{-h}^{h} \sigma_{i3} dz (i \leftrightarrow 3),\ M_{ii} = \int_{-h}^{h} \sigma_{ii} z dz$$

$$M_{ij} = \int_{-h}^{h} \sigma_{ij} z dz,\ L_{mn} = \int_{-h}^{h} \mu_{mn} dz (m,n = 1,2,3),\ \Lambda_{i3} = \int_{-h}^{h} \mu_{i3} z dz \quad (3)$$

The formula of the averaged functional I_0 of micropolar thin shallow shells are obtained from the formula (1) of the three-dimensional theory according to the accepted hypothesis:

$$I_0 = \int\int_S \Bigg\langle W_0 - \Bigg\{ T_{11}\left[\Gamma_{11} - \left(\frac{\partial u_1}{\partial x_1} + \frac{w}{R_1} + \frac{1}{2}\left(\frac{\partial w}{\partial x_1}\right)^2\right)\right] + M_{11}\left[K_{11} - \frac{\partial \psi_1}{\partial x_1}\right] +$$

$$+T_{22}\left[\Gamma_{22} - \left(\frac{\partial u_2}{\partial x_2} + \frac{w}{R_2} + \frac{1}{2}\left(\frac{\partial w}{\partial x_2}\right)^2\right)\right] + M_{22}\left[K_{22} - \frac{\partial \psi_2}{\partial x_2}\right] +$$

$$+S_{12}\left[\Gamma_{12} - \left(\frac{\partial u_2}{\partial x_1} + \frac{1}{2}\frac{\partial w}{\partial x_1}\frac{\partial w}{\partial x_2} - \Omega_3\right)\right] + M_{12}\left[K_{12} - \left(\frac{\partial \psi_2}{\partial x_1} - \iota\right)\right] +$$

$$+S_{21}\left[\Gamma_{21} - \left(\frac{\partial u_1}{\partial x_2} + \frac{1}{2}\frac{\partial w}{\partial x_1}\frac{\partial w}{\partial x_2} + \Omega_3\right)\right] + M_{21}\left[K_{21} - \left(\frac{\partial \psi_1}{\partial x_2} + \iota\right)\right] +$$

$$+N_{13}\left[\Gamma_{13}-\left(\frac{\partial w}{\partial x_1}+\Omega_2\right)\right]+N_{31}\left[\Gamma_{31}-(\psi_1-\Omega_2)\right]+$$
$$+N_{23}\left[\Gamma_{23}-\left(\frac{\partial w}{\partial x_2}-\Omega_1\right)\right]+N_{32}\left[\Gamma_{32}-(\psi_2+\Omega_1)\right]+$$
$$+L_{11}\left[\kappa_{11}-\frac{\partial\Omega_1}{\partial x_1}\right]+L_{22}\left[\kappa_{22}-\frac{\partial\Omega_2}{\partial x_2}\right]+L_{33}\left[\kappa_{33}-\iota\right]+$$
$$+L_{12}\left[\kappa_{12}-\frac{\partial\Omega_2}{\partial x_1}\right]+L_{21}\left[\kappa_{21}-\frac{\partial\Omega_1}{\partial x_2}\right]+L_{13}\left[\kappa_{13}-\frac{\partial\Omega_3}{\partial x_1}\right]+$$
$$+L_{23}\left[\kappa_{23}-\frac{\partial\Omega_3}{\partial x_2}\right]+\Lambda_{13}\left[l_{13}-\frac{\partial\iota}{\partial x_1}\right]+\Lambda_{13}\left[l_{13}-\frac{\partial\iota}{\partial x_1}\right]\Bigg\}\Bigg\rangle dx_1dx_2-$$
$$-\int\int_{S^+}\Big[q_1^+u_1+q_1^+h\psi_1+q_2^+u_2+q_2^+h\psi_2++q_3^+w+$$
$$+m_1^+\Omega_1+m_2^+\Omega_2+m_3^+\Omega_3+m_3^+h\iota\Big]dx_1dx_2+$$
$$+\int\int_{S^-}\Big[q_1^-u_1-q_1^-h\psi_1+q_2^-u_2-q_2^-h\psi_2++q_3^+w+$$
$$+m_1^-\Omega_1+m_2^-\Omega_2+m_3^-\Omega_3-m_3^-h\iota\Big]dx_1dx_2+$$
$$+\int_{l_1'}\left(S_{21}^0u_1+T_{22}^0u_2+M_{21}^0\psi_1+M_{22}^0\psi_2+N_{23}^0w+L_{21}^0\Omega_1+L_{22}^0\Omega_2+L_{23}^0\Omega_3+\Lambda_{23}^0\iota\right)dx_1+$$
$$+\int_{l_1''}\Big[S_{21}\left(u_1-u_1^0\right)+T_{22}\left(u_2-u_2^0\right)+M_{21}\left(\psi_1-\psi_1^0\right)+M_{22}\left(\psi_2-\psi_2^0\right)+N_{23}\left(w-w^0\right)+$$
$$+L_{21}\left(\Omega_1-\omega_1^0\right)+L_{22}\left(\Omega_2-\Omega_2^0\right)+L_{23}\left(\Omega_3-\Omega_3^0\right)+\Lambda_{23}\left(\iota-\iota^0\right)\Big]dx_1+$$
$$+\int_{l_2'}\left(T_{11}^0u_1+S_{12}^0u_2+M_{11}^0\psi_1+M_{12}^0\psi_2+N_{13}^0w+L_{11}^0\Omega_1+L_{12}^0\Omega_2+L_{13}^0\Omega_3+\Lambda_{13}^0\iota\right)dx_2+$$
$$+\int_{l_2''}\Big[T_{11}\left(u_1-u_1^0\right)+S_{12}\left(u_2-u_2^0\right)+M_{11}\left(\psi_1-\psi_1^0\right)+M_{12}\left(\psi_2-\psi_2^0\right)+N_{13}\left(w-w^0\right)+$$
$$+L_{11}\left(\Omega_1-\omega_1^0\right)+L_{12}\left(\Omega_2-\Omega_2^0\right)+L_{13}\left(\Omega_3-\Omega_3^0\right)+\Lambda_{13}\left(\iota-\iota^0\right)\Big]dx_2+ \tag{4}$$

W_0 is the average density of potential energy of deformation of micropolar shallow shell:

$$W_0=\frac{1}{2}\Big(T_{11}\Gamma_{11}+T_{22}\Gamma_{22}+S_{12}\Gamma_{12}+S_{21}\Gamma_{21}+M_{11}K_{11}+M_{22}K_{22}+M_{12}K_{12}+$$
$$M_{21}K_{21}+N_{13}\Gamma_{13}+N_{31}\Gamma_{31}+N_{23}\Gamma_{23}+N_{32}\Gamma_{32}+L_{11}\kappa_{11}+L_{22}\kappa_{22}+$$
$$+L_{33}\kappa_{33}+L_{12}\kappa_{12}+L_{21}\kappa_{21}+L_{13}\kappa_{13}+L_{23}\kappa_{23}+\Lambda_{13}l_{13}+\Lambda_{23}\Big) \tag{5}$$

Let us notice, that in the specified theory the displacements, independent rotations, components of deformation and bend-torsion tensors are expressed by formulas:

$$\gamma_{ii}=\Gamma_{ii}\left(x_1,x_2\right)+zK_{ii}\left(x_1,x_2\right),\ \gamma_{ij}=\Gamma_{ij}\left(x_1,x_2\right)+zK_{ij}$$
$$\gamma_{i3}=\Gamma_{i3}\left(x_1,x_2\right),\ \gamma_{3i}=\Gamma_{3i}\left(x_1,x_2\right)$$
$$\chi_{ii}=\kappa_{ii}\left(x_1,x_2\right),\ \chi_{33}=\iota\left(x_1,x_2\right),\ \chi_{ij}=\kappa_{ij}\left(x_1,x_2\right),\ \chi_{i3}=\kappa_{i3}\left(x_1,x_2\right)+zl_{i3}\left(x_1,x_2\right)$$

$$V_i = u_i(x_1, x_2) + z\psi_i(x_1, x_2),\ V_3 = w(x_1, x_2)$$
$$\omega_i = \Omega_i(x_1, x_2),\ \omega_3 = \Omega_3(x_1, x_2) + z\iota(x_1, x_2) \tag{6}$$

$u_1,\ u_2,\ w$ are displacements of the points of the shallow shell's median surface along the axes $x_1,\ x_2,\ z$; ψ_1, ψ_2 are full angels of the rotation; $\Omega_1,\ \Omega_2,\ \Omega_3$ are free rotations of the initially normal element of the shallow shell's median surface round the lines $x_1,\ x_2,\ z$; ι is intensity of the full rotation along the z; Γ_{ii} are elongation deformations along the $x_1,\ x_2$; $\Gamma_{ij},\ \Gamma_{i3},\ \Gamma_{3i}$ are shears in the corresponding planes; K_{ii} are flexures of the shallow shell's median surface caused by the stresses; K_{ij} are torsions of the shallow shell's median surface caused by the stresses; $\kappa_{ii},\ \kappa_{33}$ are flexures of the shallow shell's median surface caused by the couple stresses; κ_{ij} are torsions of the shallow shell's median surface caused by the couple stresses; l_{i3} are hyper shears of the shallow shell's median surface caused by the couple stresses.

By the verifying I_0 to it's all functional arguments, the general equations and the natural boundary conditions of the micropolar elastic geometrically nonlinear thin shallow shells with the independent fields of displacements and rotations are obtained from the variational equation $\delta I_0 = 0$. These equations and boundary conditions are follows as:

Balance equations

$$\frac{\partial T_{ii}}{\partial x_i} + \frac{\partial S_{ji}}{\partial x_j} = -\left(p_i^+ - p_i^-\right),\ \frac{\partial M_{ii}}{\partial x_i} + \frac{\partial M_{ji}}{\partial x_j} - N_{3i} = -h\left(p_i^+ + p_i^-\right)$$

$$\frac{\partial N_{13}}{\partial x_1} + \frac{\partial N_{23}}{\partial x_2} + \frac{\partial}{\partial x_1}\left[T_{11}\frac{\partial w}{\partial x_1} + \frac{1}{2}(S_{12} + S_{21})\frac{\partial w}{\partial x_2}\right] +$$
$$+\frac{\partial}{\partial x_2}\left[\frac{1}{2}(S_{12} + S_{21})\frac{\partial w}{\partial x_1} + T_{22}\frac{\partial w}{\partial x_2}\right] - \frac{T_{11}}{R_1} - \frac{T_{22}}{R_2} = -\left(p_i^+ - p_i^-\right)$$

$$\frac{\partial L_{ii}}{\partial x_i} + \frac{\partial L_{ji}}{\partial x_j} + (-1)^j(N_{j3} - N_{3j}) = -\left(m_i^+ - m_i^-\right)$$

$$L_{33} - \frac{\partial \Lambda_{13}}{\partial x_1} - \frac{\partial \Lambda_{13}}{\partial x_1} - (M_{12} - M_{21}) = h\left(m_3^+ + m_3^-\right)$$

$$\frac{\partial L_{13}}{\partial x_1} + \frac{\partial L_{23}}{\partial x_2} + (S_{12} - S_{21}) - \frac{L_{11}}{R_1} - \frac{L_{22}}{R_2} = -\left(m_3^+ - m_3^-\right) \tag{7}$$

Elasticity relations

$$T_{ii} = \frac{2Eh}{1-\nu^2}\left[\Gamma_{ii} + \nu\Gamma_{jj}\right],\ M_{ii} = \frac{2Eh^3}{3(1-\nu^2)}\left[K_{ii} + \nu K_{jj}\right]$$

$$S_{ij} = 2h\left[(\mu+\alpha)\Gamma_{ij} + (\mu-\alpha)\Gamma_{ji}\right],\ M_{ij} = \frac{2h^3}{3}\left[(\mu+\alpha)K_{ij} + (\mu-\alpha)K_{ji}\right]$$
$$N_{i3} = 2h\left[(\mu+\alpha)\Gamma_{i3} + (\mu-\alpha)\Gamma_{3i}\right],\ N_{3i} = 2h\left[(\mu+\alpha)\Gamma_{3i} + (\mu-\alpha)\Gamma_{i3}\right]$$
$$L_{ii} = 2h\left[(\beta+2\gamma)\kappa_{ii} + \beta(\kappa_{jj} + \iota)\right],\ L_{33} = 2h\left[(\beta+2\gamma)\iota + \beta(\kappa_{11} + \kappa_{22})\right]$$
$$L_{ij} = 2h\left[(\gamma+\epsilon)\kappa_{ij} + (\gamma-\epsilon)\kappa_{ji}\right],\ L_{i3} = 2h\frac{4\gamma\epsilon}{\gamma+\epsilon}\kappa_{i3},\ \Lambda_{i3} = \frac{2h^3}{3}\frac{4\gamma\epsilon}{\gamma+\epsilon}l_{i3} \tag{8}$$

Geometrically relations

$$\Gamma_{ii} = \frac{\partial u_i}{\partial x_i} + \frac{w}{R_i} + \frac{1}{2}\left(\frac{\partial w}{\partial x_i}\right)^2,\ \Gamma_{ij} = \frac{\partial u_j}{\partial x_i} - (-1)^j\Omega_3 + \frac{1}{2}\left(\frac{\partial w}{\partial x_1}\right)\left(\frac{\partial w}{\partial x_2}\right)$$

$$\Gamma_{i3} = \frac{\partial w}{\partial x_i} + (-1)^j \Omega_j,\ \Gamma_{3i} = \psi_i - (-1)^j \Omega_j,\ K_{ii} = \frac{\partial \psi_i}{\partial x_i} - (-1)^j \iota$$

$$\kappa_{ii} = \frac{\partial \Omega_i}{\partial x_i},\ \kappa 33 = \iota,\ \kappa_{ij} = \frac{\partial \Omega_j}{\partial x_i},\ \kappa_{i3} = \frac{\partial \Omega_3}{\partial x_i},\ l_{i3} = \frac{\partial \iota}{\partial x_i} \tag{9}$$

Boundary conditions (on $x_i = const$)

$$T_{11} = T_{11}^0,\ S_{12} = S_{12}^0,\ M_{11} = M_{11}^0,\ M_{12} = M_{12}^0$$

$$T_{11}\frac{\partial w}{\partial x_1} + \frac{1}{2}\left(S_{12} + S_{21}\right)\frac{\partial w}{\partial x_2} + N_{13} = N_{13}^0,\ L_{11} = L_{11}^0,\ L_{12} = L_{12}^0,\ \Lambda_{13} = \Lambda_{13}^0 \tag{10}$$

The obtained system of the equations (7)-(9) and boundary conditions (10) are the mathematical static model of the geometrically nonlinear micropolar elasticity thin shallow shells with independent fields of displacements and rotations with the full account of shear deformations.

Let us notice, that from constructed model the geometrically linear model of micropolar shallow shells are obtained, if the nonlinear members to ignore, and the geometrically nonlinear Timoshenko type classical model are also obtained, if to put $\alpha = 0$.

It is necessary to have in view, that the mathematical dynamic model of geometrically nonlinear micropolar elastic thin shallow shells with independent fields of displacements and rotations are obtained, if the corresponding inertial members $2\rho h\frac{\partial^2 u_i}{\partial t^2},\ 2\rho h\frac{\partial^2 w}{\partial t^2},\ \frac{2\rho h^3}{3}\frac{\partial^2 \psi_i}{\partial t^2},\ 2Jh\frac{\partial^2 \Omega_i}{\partial t^2},\ 2Jh\frac{\partial^2 \Omega_3}{\partial t^2},\ \frac{2Jh^3}{3}\frac{\partial^2 \iota}{\partial t^2}$ to add.

Let us notice, that the formulated above variational problem corresponds to the most general variational principle of the micropolar elastic thin shallow shells. Therefore, from the last result the Lagrange and Kastiliano type principles of micropolar elastic thin shallow shells will follow as special cases. The direct methods of their approach decision can be made to each of obtained variational equations (in particular Ritz and Galerkin methods). Using these methods, the boundary problem of the theory of flexible micropolar elastic thin shallow shells can be reduce to the decision of the nonlinear algebraic equations system.

As special case, the variational principle of geometrically nonlinear classical theory of elastic thin shallow shells [3],[4] will follow from the variational principle of geometrically nonlinear micropolar theory of elastic thin shallow shells.

Acknowledgements

- This work was supported by State Committee of Science MES RA, in frame of the research project e SCS 13-2C154.

References

[1] *Volmir A. S.* Flexible plates and shells. M.: Gostekhizdat, 1956. 420 p.(in Russian)

[2] *Volmir A. S.* The nonlinear dynamics of plates and shells. M.: "Nauka", 1972. 432 p.(in Russian)

[3] *Sargsyan A. H., Sargsyan S. H.* Variational equation of geometrically nonlinear theory of micropolar elastic thin plates. // The problems of dynamics of interaction of deformable media. Proceedings of VIII international conference, September 22-26. 2014. Goris-Stepanakert. Armenia. "Chartaraget". P. 374-378.(in Russian)

[4] *Sargsyan A. H., Sargsyan S. H.* The mathematical model of geometrically nonlinear theory of micropolar elastic thin plates. // Proceedings of XVII international conference "Modern problems of continuum mechanics". Rostov on Don. South federal university. October 14-17. 2014. P. 180-184.(in Russian)

пњ»

Modelling of Stent Deployment and Deformation in Diseased Arteries by Considering Vessel Anisotropy

A. Schiavone, L.G. Zhao
L.Zhao@lboro.ac.uk

Abstract

In this paper, finite element simulation of stent deployment was carried out using an anisotropic model for the artery, consisting of three individual tissue layers, i.e., intima, media and adventitia. Each layer was modelled as a hyperelastic anisotropic material described by the Holzapfel-Gasser-Ogden (HGO) model. The model parameters were calibrated against the experimental stress-stretch responses in both circumferential and longitudinal directions. The results showed that, at the peak pressure, stent expansion obtained using the anisotropic model was much reduced when compared to that obtained using the isotropic model. However, after deflation, the finally achieved diameter for the anisotropic model is comparable to that for the isotropic model, due to the significant reduction in recoiling for the anisotropic model. Also, the anisotropic model generated slightly higher levels of stress in the artery-plaque system than the isotropic model. For the isotropic model, the high-level stresses were found mainly on the plaque, while, for the anisotropic model, both the intima layer and the plaque experienced high-level stresses. The media and adventitia layers had lower stress levels due to their relatively softer stress-strain response in the circumferential direction as well as limited deformation. Following deployment, deformation of the stent was also modelled by applying relevant biomechanical forces, such as bending and radial compression, to the stent-artery system. The results were utilised to interpret the mechanical performance of stent after deployment.

Key words: Stent deployment; Vessel anisotropy; Finite element; Artery stenosis; Biomechanical forces.

1 Introduction

Coronary stents are essentially scaffolds, made of metallic alloys or biopolymers, used to sustain the blood vessels once expanded inside the obstructed arteries. Stents are generally deployed inside the diseased artery by means of an angioplasty balloon (except for self-expandable stents). The scaffold is placed over the balloon and expands with the balloon

when this is inflated by internal pressure. This surgery procedure has minimal invasive nature and provides fast and effective solutions to patients suffering from coronary stenosis, a major cause of heart attack.

Finite element is an effective tool to simulate the process of stent expansion inside stenotic arteries, which helps to understand the insight of the biomechanical behaviour of the whole stent-artery system during the procedure. The simulations provide essential information regarding stent expansion, recoiling, dogboning and residual stresses, which can be further utilised to guide stent design and surgery procedures [1, 2, 3, 4, 5]. The artery constitutive model is an important factor for simulation of stent deployment. [6] reviewed the state of the art of development of constitutive models in the last ten years to describe the mechanical behaviour of artery tissue. It highlighted the highly nonlinear and anisotropic behaviour of the blood vessel tissue. This work also suggested that in many cases the artery behaves purely elastically and can be characterized by hyperelastic strain energy functions, including the layer specific constitutive models used to describe mechanical behaviour of arteries. However, anisotropic hyperelastic models have seldom been used to simulate expansion and deformation of stent-artery system, and existing studies are dominantly limited to the use of isotropic models.

In this paper, finite element simulation of stent deployment was carried out using an anisotropic model for the artery. In particular, the artery wall was considered to consist of three individual tissue layers, i.e., intima, media and adventitia, which are all described by the Holzapfel-Gasser-Ogden (HGO) hyperelastic anisotropic model [7, 8]. To understand the mechanical performance of stent after deployment, deformation of the stent-artery system was also modelled under relevant biomechanical forces, such as bending and radial compression, focusing on the re-distribution of local stresses and strains in the stent.

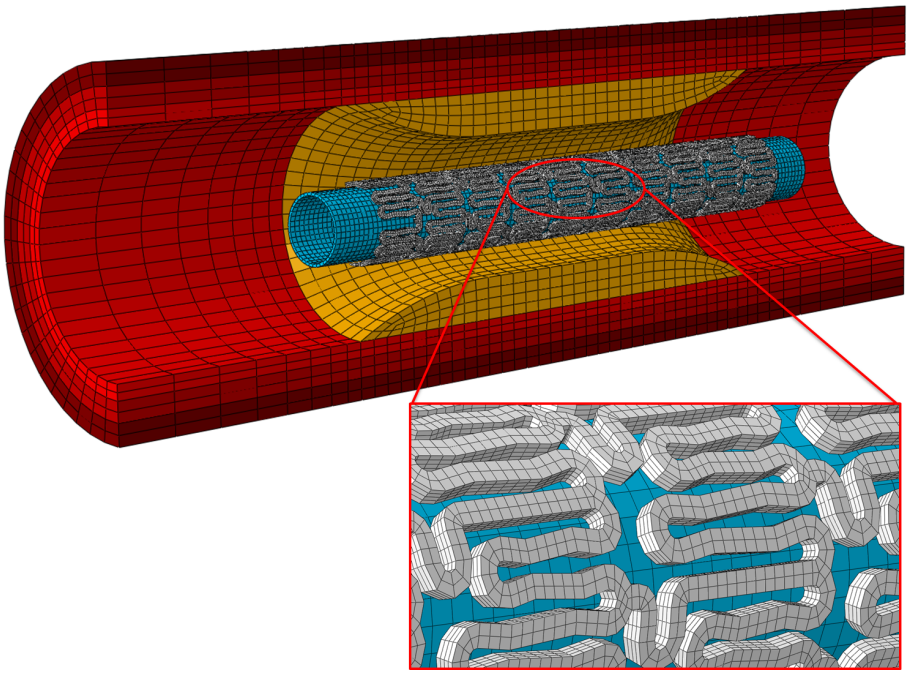

Figure 1: Finite element mesh for the Xience stent, the balloon and the stenotic artery.

2 Finite Element Model

The finite element model for the balloon-stent-artery system is shown in Figure 1. The stent used for this analysis resembles the geometry of Xience stent, one of the latest commercial stents. The stent has a crimped diameter of $1.5mm$, a length of $10mm$ and a strut thickness of $80\mu m$. The artery has a total length of $20mm$, an inner diameter of $4mm$ (healthy region) and a wall thickness of $1mm$. The artery wall is considered to have three layers, namely intima ($0.27mm$), media ($0.35mm$) and adventitia ($0.38mm$). The plaque has a length of $10mm$ and a stenosis of 40%. The balloon has a folded geometry, with a length of $12mm$. The artery and plaque were meshed into hexahedral elements with reduced integration, which are mostly used to increase the computing efficiency and numerical convergence associated with large deformation, especially for soft tissues [9, 10]. The stent was meshed into incompatible hexahedral elements (with full integration) in order to accommodate large bending deformation of the stent strut during expansion [11]. The folded balloon was meshed using 4-node shell elements with reduced integration based on the consideration of computational efficiency.
Contacts between the stent, the artery and the balloon were defined as hard contact with a friction coefficient of 0.25 [12]. The ends of the artery and the balloon were fully constrained to remove rigid body motion. All analyses were carried out using Abaqus explicit solver [11]. The deployment simulations consisted of two steps: the inflation step ($0.1s$) in which the applied pressure increased linearly to the peak value and the deflation step ($0.1s$) in which the pressure dropped linearly to zero to allow the recoil of the artery and the stent. The pressure was applied on the inner surface of the balloon, with a peak pressure of $1.4MPa$. Following the deflation step, a third step was introduced to continue the simulations by applying bending and radial compression to the system. For bending, a displacement of $5mm$ was applied to all the nodes on the cross section at the middle of the artery, while for compression, a pressure of $0.2MPa$ was applied to the outer surface of the artery over the section where the stent was implanted.

3 Material Constitutive Behaviour

3.1. Models for stent, balloon and plaque
The Xience stent is made of Co-Cr L605 which is modelled as an elastic-plastic material with multilinear hardening segments based on the tensile stress-strain curve of the alloy given in [13]. The folded balloon was modelled as a linear elastic material with YoungвЃ™s modulus of $900MPa$ and Poisson ratio of 0.3 [14]. The hypocellular plaque is described by the Ogden hyperelastic model with model parameters given in [15].

3.2. The Holzapfel-Gasser-Ogden model for artery
Experimental tests on human arteries highlighted the anisotropic behaviour of such biological tissues [7, 16]. The Holzapfel-Gasser-Ogden (HGO) anisotropic hyperelastic model [7, 8] was used, with a strain energy potential given as [11]:

$$U = C_{10}\left(\bar{I}_1 - 3\right) + \frac{k_1}{2k_2}\sum_{\alpha=1}^{N}\left\{exp\left[k_2\left\langle\bar{E}_\alpha\right\rangle^2\right] - 1\right\} + \frac{1}{D}\left(\frac{(J^{el})^2 - 1}{2} - lnJ^{el}\right) \tag{1}$$

with

$$\bar{E}_\alpha = \kappa\left(\bar{I}_1 - 3\right) + (1 - 3\kappa)\left(\bar{I}_{4(\alpha\alpha)} - 1\right) \tag{2}$$

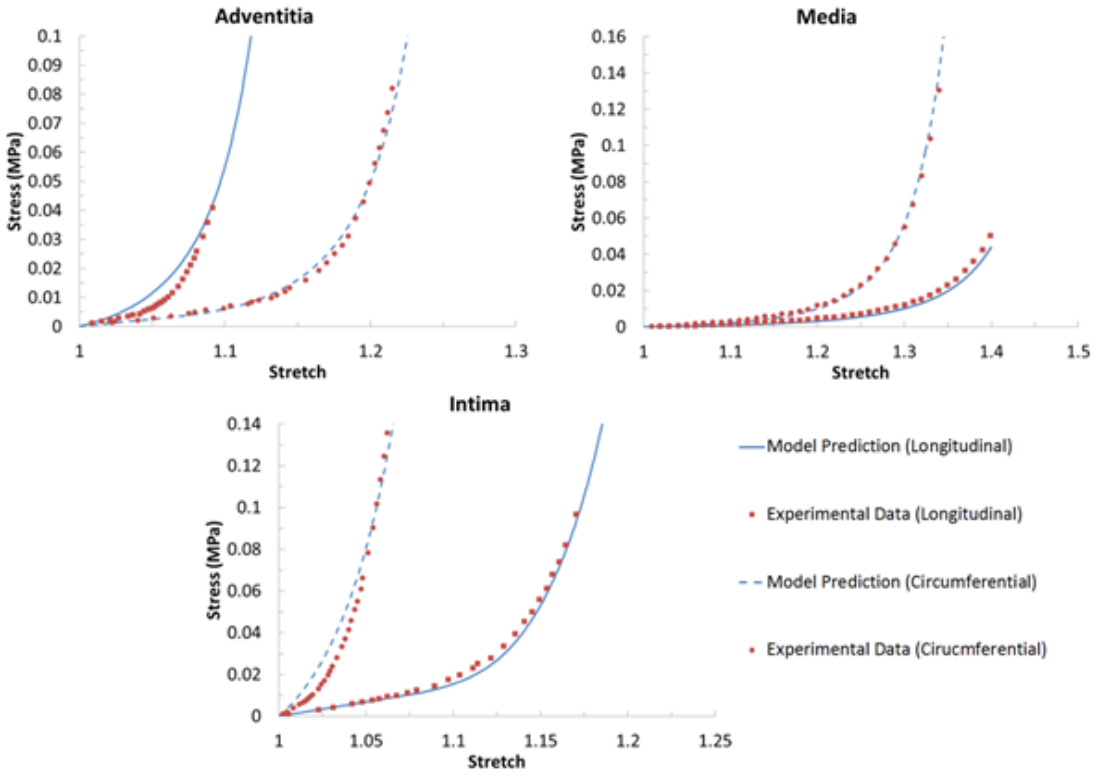

Figure 2: Anisotropic stress-stretch response of the three arterial layers, experimental results [16] versus simulations.

where $\bar{I}_1$ and $\bar{I}_2$ are the first and second stretch invariants, J is the volumetric stretch (or third stretch invariant), C_{10}, D, k_1, k_2 and κ are material parameters, and $\bar{I}_4$ is the invariant of Cauchy-Green deformation tensor. The strain-like quantity $\bar{E}$ characterizes the deformation of the fibre family and the operator $\langle\ \rangle$ stands for the Macauley bracket. The parameters of the model were calibrated to fit the experimental data given in [16]. Fitted model parameters are given in Table 1 for all three vessel layers, which give the stress-stretch responses that are in good agreement with the experimental data in both circumferential and longitudinal directions (Figure 2).

Table 1. Values of the Holzapfel-Gasser-Ogden model parameters for the three vessel layers.

Material	ρ(kg/mm^3)	C_{10}	k_1	k_2	κ	D
Intima	1.07E-6	2.3E-2	25	1200	0.308	8.95E-7
Media	1.07E-6	1.4E-3	0.18	100	0.314	5.31E-6
Adventitia	1.07E-6	8.32E-3	4	1000	0.312	4.67E-6

4 Results and Discussion

4.1. Stent expansion

The result of stent expansion is shown in Figure 3, in a comparison with those obtained from isotropic arterial model. Expansion was shown to have three stages. At the initial

stage, stent deforms elastically and has a lower rate of expansion. At the second stage, plastic deformation occurs and stent seems to expand steadily, together with the artery, at a fairly constant rate. At the final stage, the rate of stent expansion starts to decrease drastically, indicating that the deformation of the stent/artery system seems to reach a saturation stage, i.e., further increase of pressure only results in very limited expansion. This is mainly due to the intrinsic deformation behaviour of the artery which reached a saturation stage of stretch, especially the intima layer (see Fig.2). Consequently, the system becomes considerably resistant to further expansion, resulting in a drastic decrease of expansion rate.

For isotropic model, stent expanded from 1.5mm to 4.8mm at the maximum pressure ($1.4MPa$), with an increase in diameter by more than three folds. At the peak pressure ($1.4MPa$), the maximum diameter achieved using the anisotropic model was only $4.1mm$, which is much reduced when compared to that, i.e. $4.7mm$, achieved using the isotropic model for the layers.

During deflation, recovered elastic deformation and radial pressure from the viscoelastic artery system lead to the recoil of the stent. After recoiling, the diameter was settled at $3.8mm$ for the anisotropic model, which is larger than that ($3.7mm$) computed from the isotropic model. This is due to the significant reduction in recoiling, only 8% for the anisotropic model compared to 22% for isotropic model. The achieved expansion is close to the diameter of a healthy artery.

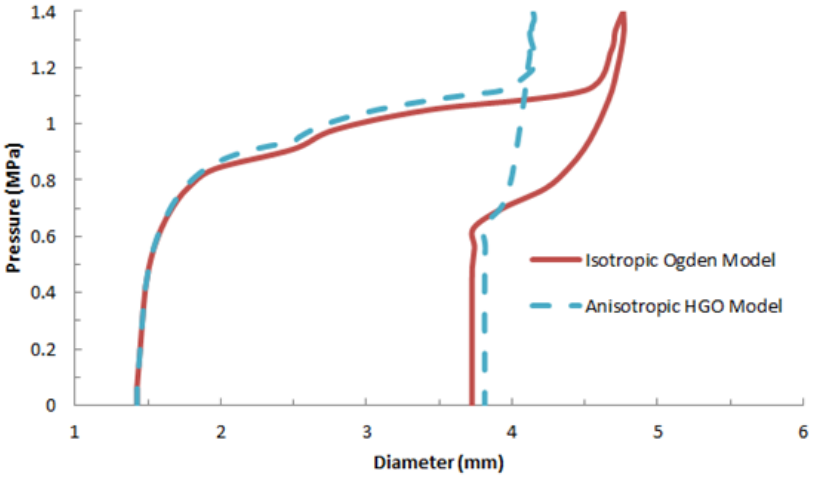

Figure 3: Comparison of diameter change against pressure for stent expansion simulated using isotropic Ogden and anisotropic HGO constitutive models for the artery.

4.2. Stress on the stent

Figure 4 compares the von Mises stress distribution on the stent for the two models following stent deployment. The stent has severe stress concentrations at the U-bends of the cell struts due to highly localised stretch. These are residual stresses which were developed due to the sustained plastic deformation. From the computed results, it appears that the anisotropic artery model increased the magnitude of the von Mises stress on the stent. For isotropic model, the magnitude of residual stress was shown to be around $778MPa$, as opposed to $1384MPa$ for anisotropic model (Figure 4). The stress level is very significant

and implies the potential risk of failure during stent employment. Consequently, optimal design of cell strut U-bends appears to be important for modern stents, which can lead to stress reduction and failure resistance. However, it should be noted that in reality, the stresses on the stents might not reach such high magnitude if the residual stresses developed during stent crimping [17, 18] are considered which shall mitigate the stresses developed during stent expansion.

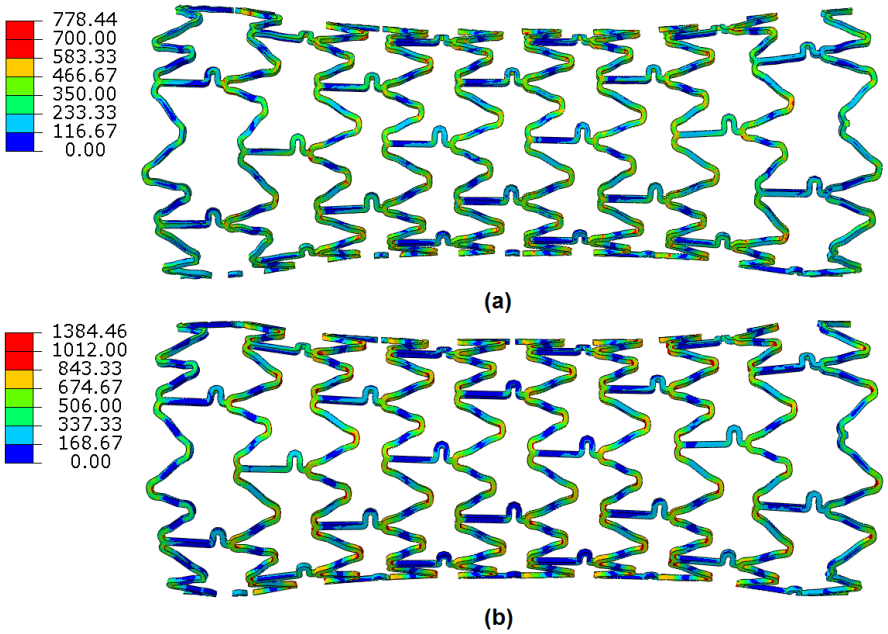

Figure 4: Stress distribution on the stent after deployment simulated using (a) isotropic Ogden and (b) anisotropic HGO constitutive models for the artery.

4.3. Stress on the artery-plaque system

The stress distribution on the artery-plaque system, after stent deployment, is compared in Figure 5, and the anisotropic model generated slightly higher levels of stress than the isotropic model, with a maximum value of $0.70MPa$ ($0.65MPa$ for isotropic model). High stress levels were mainly obtained in the intima layer as well as on the stenotic plaque surface. The media has the lowest stress level due to its soft stress-strain response in the circumferential direction. It was also noticed from our simulation, at the peak inflation pressure, the maximum von Mises stresses on the plaque-artery system were located in the intima layer of the artery with a magnitude of $7.30MPa$, due to the relatively high stiffness of the intima layer as well as the severe constraint on the intima layer imposed by surrounding tissues. After deflation, the maximum stress shifted to the plaque, especially at locations where the stent and the plaque are in full contact.

4.4. Stent deformation under biomechanical forces

For the applied bending, there is hardly any change of stresses on the stent compared to the stress state after deployment. This might be because the metallic material reached a steady-state of stress-strain response in the plastic region and the stress becomes insensitive

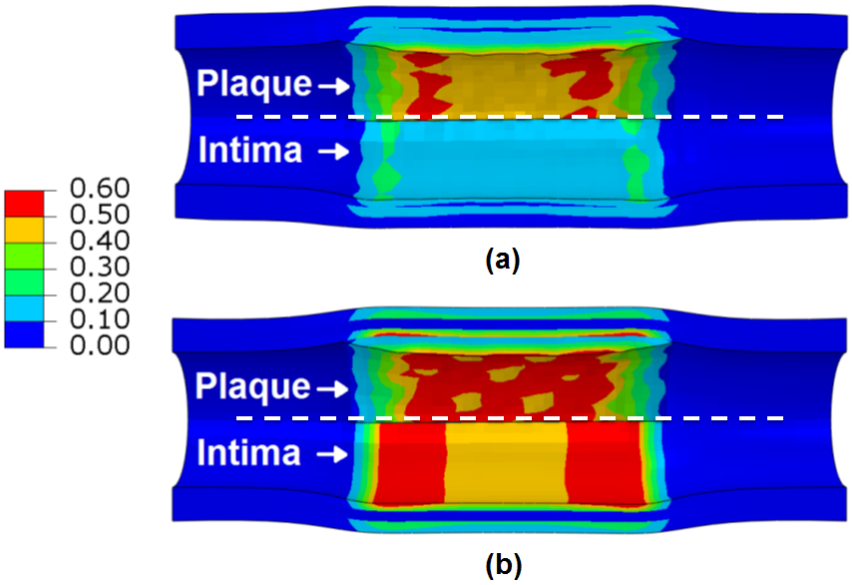

Figure 5: Stress distribution on the artery-plaque system after stent deployment simulated using (a) isotropic Ogden and (b) anisotropic HGOmodels for the artery.

to further deformation. For radial compression, stent collapse started to occur at a pressure of about $0.1MPa$, and also the right end of stent collapsed earlier than the left end due to asymmetry of the stent structure (Figure 6).
We also carried out simulations by excluding the residual stresses generated out of stent deployment. For bending, the maximum stress on the stent was found on one of the bottom longitudinal connective struts in the middle region where the system has the most severe bending deformation. The maximum stress has a value of $651MPa$ which is significantly less than that obtained from simulations by considering the residual stresses. Also stent collapse under compression tended to be delayed when the residual stresses are excluded.

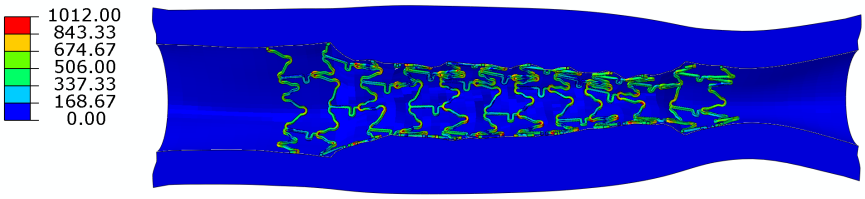

Figure 6: Stress distribution on the deformed stent-artery system at a compressive pressure of 0.2MPa.

5 Conclusions

The anisotropy of blood vessels needs to be considered in order to produce reliable and conclusive results in stent deployment simulations. It is also strongly recommended to take into account the residual stress state, generated out of stent deployment, for further mechanical performance analyses.

Acknowledgements

The research leading to these results received funding from the European Union Seventh Framework Programme (FP7/2007-2013) under grant agreement No. PIRSES-GA-2013-610547 TAMER.

References

[1] Chua SND, McDonald BJ, Hashimi MSJ (2003) Finite element simulation of stent and balloon interaction. J Mater Process Tech 143-144:591-597

[2] Pericevic I, Lally C, Toner D, Kelly DJ (2009) The influence of plaque composition on underlying arterial wall stress during stent expansion: The case for lesion-specific stents. Med Eng Phys 31:428-433

[3] Zhao S, Gu L, Froemming SR (2012) On the importance of modeling stent procedure for predicting arterial mechanics. ASME J Biomech Eng 134:121005-1

[4] Morlacchi L, Colleoni SG, CΓrdenes R, Chiastra C, Diez JL, Larrabide I, Migliavacca F (2013) Patient-specific simulations of stenting procedures in coronary bifurcations: Two clinical cases. Med Eng Phys 35:1272-1281

[5] Schiavone, A., Zhao, L.G., Abdel-Wahab, A.A., 2014. Effects of material, coating, design and plaque composition on stent deployment inside a stenotic arteryвΓΥFinite element simulation. Mater Sci Eng C 42, 479-488

[6] Holzapfel GA, Ogden RW (2010) Constitutive modeling of arteries. Proc R Soc Ser A 466:1551-1597

[7] Holzapfel GA, Gasser TC, Ogden RW (2000) A new constitutive framework for arterial wall mechanics and a comparative study of material models. J Elasticity Phys Sci Solids 61:1-48.

[8] Gasser TC, Ogden RW, Holzapfel GA (2006) Hyperelastic modelling of arterial layers with distributed collagen fibre orientations. J R Soc Interface 6:15-35

[9] Mortier P, De Beule M, Van Loo D, Verhegghe B, Verdonck P (2009) Finite element analysis of side branch access during bifurcation stenting. Med Eng Phys 31:434вΓΥ440

[10] Zahedmanesh H, Kelly DJ, Lally C (2010) Simulation of a balloon expandable stent in a realistic coronary artery - Determination of the optimum modelling strategy. J Biomech 43:2126-2132

[11] ABAQUS (2014) Version 6.13, Dassault SystΓïmes, VΓκlizy-Villacoublay, France.

[12] Ju F, Xia Z, Sasaki K (2008) On the finite element modelling of balloon-expandable stents. J Mech Behav Biomed Mater 1:86-95

[13] Medtronic Technical Bulletin (2003) Advantages of cobalt alloy for coronary stents.

[14] Gervaso F, Capelli C, Petrini L, Lattanzio S, Di Virgilio L, Migliavacca F (2008) On the effects of different strategies in modelling balloon-expandable stenting by means of πæΓnite element method. J Biomech 41:1206-1212

[15] Zahedmanesh H, Lally C (2009) Determination of the influence of stent strut thickness using the finite element method: implications for vascular injury and in-stent restenosis. Med Biol Eng Comput 47:385-393

[16] Holzapfel GA, Sommer G, Gasser CT, Regitnig P (2005) Determination of layer-specific mechanical properties of human coronary arteries with nonatherosclerotic intimal thickening and related constitutive modelling. Am J Phisiol - Heart C, 289:H2048-H2058

[17] Mäller D, Reimers W, Pyzalla A, Fischer A (2001) Residual stresses in coronary artery stents. J J Biomed Mater Res 58:69вЃ“74.

[18] Kleinstreuer C, Li Z, Basciano CA, Seelecke S, Farber MA (2008) Computational mechanics of Nitinol stent grafts. J Biomech 41:2370вЃ“2378.

A. Schiavone & L.G. Zhao, Wolfson School of Mechanical and Manufacturing Engineering, Loughborough University, UK

Mechanical properties of filled elastomers subjected to alternate loading along two orthogonal axes

Vladimir V. Shadrin, Kseniya A. Mokhireva, Anton Yu. Beljaev, Lyudmila A. Komar
shadrin@icmm.ru

Abstract

We present the results of an experimental study of the behavior of carbon black filled rubber and rubber with carbon nanofibers. Tests were carried out using a 4-vector test stand Zwick (biaxial testing machine), a uniaxial testing machine Testometric FS100kN CT and a dynamic mechanical analyzer DMA/SDTA861^e. Our investigations revealed the induced anisotropy of mechanical properties in the material with grain filler — stretching along one axis does not, in any way, affect mechanical properties along the other axis. It is shown that uniaxial stretching of an elastomer with nanofibers changes the structure and mechanical properties of the material in all directions.

Cyclic tests where tensile forces acted in two mutually perpendicular directions were performed to determine the influence of the type of filler on the mechanical properties of filled vulcanizates subjected to external forces. One vulcanizate was prepared by mixing methylstyrene and divinyl rubbers (85 parts by weight of rubber SKMS-30 ARK + 15 parts by weight of rubber SKD), and the other using butadiene-styrene rubber SBR1502. Elastomers were reinforced with different fillers. Carbon black was added to rubber mixture SKMS+SKD: 60 parts by weight of carbon black П514 and 5 parts by weight of carbon black П234 per 100 parts by weight of rubber. Rubber SBR1502 was reinforced by 30 parts by weight of carbon black N220 and 5 parts by weight of carbon nanofibers (CNFs).

The behavior of vulcanizates subjected to complex biaxial loading was investigated using a 4-vector test stand Zwick (biaxial testing machine), a uniaxial testing machine Testometric FS100kN CT and a dynamic mechanical analyzer DMA/SDTA861^e. Preliminary tests on rubbers stretched in two mutually perpendicular directions showed only slight difference in their properties.

Cross-shaped samples were manufactured for tests with a biaxial testing machine (Fig. 1). The working zone of the sample showed in Fig. 1 is a square with a side of 3 cm. The applied load is transferred through a loading tube of length 4.5 cm. To achieve loading uniformity in the central part and, as a consequence, heterogeneity of stress and strain fields, loading tubes are cut into stripes — strands. Hence, the area of uniform stress-strain state distribution covers 73% of the working zone [1].

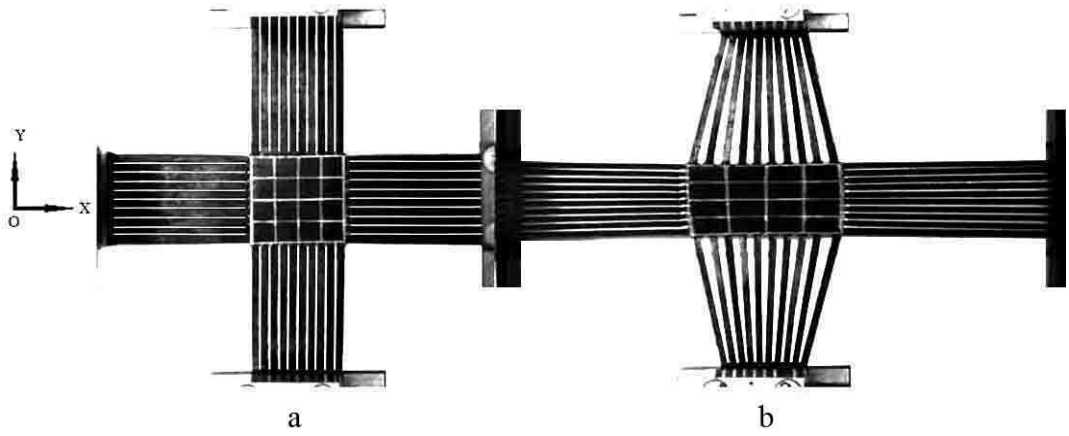

Figure 1: Shape of the cross-shaped sample subjected to cyclic loading along each axis using the biaxial test stand Zwick. The initial state of the sample (a); the sample extended along the 0X-axis (b)

It is known that in cyclic tests on filled elastomers the pronounced Mullins softening effect is observed immediately after the first loading cycle. In addition, elastomers exhibit a viscoelastic behavior that depends on the molecular and structural interfacial layers formed at the filler-matrix boundary [2]. Such a feature can be attributed, in our opinion, to the formation of strands in the case when long molecules are drawn from the polymer surface [3]. Experimental observations support this hypothesis. For example, it was shown that the softening of rubbers is mainly attributable to viscoelastic processes [4, 4]. At a 50% deformation of the sample no internal damages are accumulated in the material, and on unloading the inverse process (polymer molecules return back to their original state) takes place. At temperature of 60°C and over a 24-hour thermostatting period the sample recovers its original structure and properties completely. This process develops much more slowly than the slippage of these molecules off the surface of inclusions under stretching and is temperature dependent. At large deformations, simultaneously with the viscoelastic process, the damage accumulation process begins in rubber, and the stress-strain curve lies below the curve of the undamaged material [4].

Our tests on carbon black filled vulcanizate were performed according to the following scheme. Cross-shaped samples were stretched alternately along the two mutually perpendicular directions 0X and 0Y to elongate by a factor of two. The value of sample elongation was determined utilizing the grid lines given in white color (Fig. 1). Initially, the samples were stretched along the 0Y-axis, and the 0X-axis remained loading-free. To do this, we have developed a special program, where the load is applied along one of the axes, and the grips move along the other axis so that the load remains zero. Then the samples are aged for 7 minutes to achieve complete relaxation, unloaded to the primary position, and aged again for 7 minutes to complete the fast recovery of the material structure. Note that the structure recovery rate is temperature dependent, and therefore at room temperature the structure may not recover its original structure even in a year [4]. Such a sequence of loading-unloading along the 0Y-axis is repeated twice until the softening of the material was stabilized and the repeatability of its cyclic loading curves is achieved.

The same program has been realized along the 0X-axis. In this case, the 0Y-axis remains free of loading. Figure 2 presents the biaxial loading curves: the solid lines denote the behavior of the material in the 0Y-direction, and the dashed lines in the orthogonal 0X-direction.

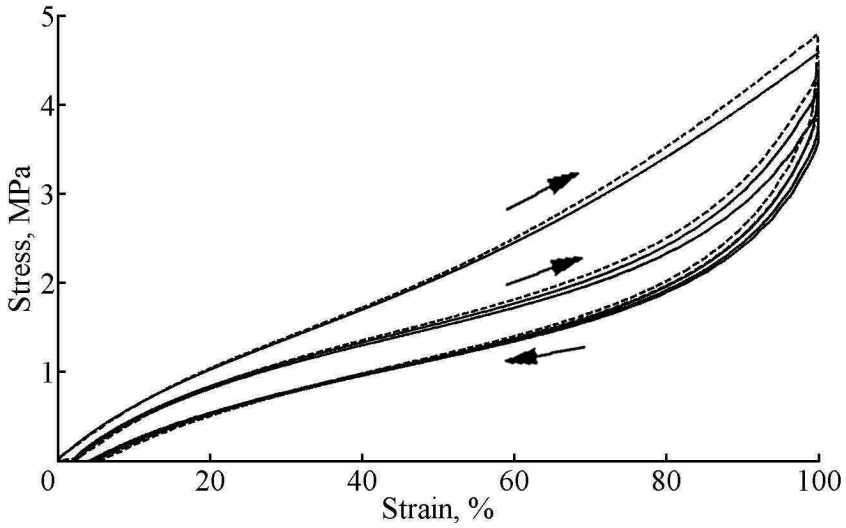

Figure 2: Loading curves for cross-shaped carbon black-filled vulcanizate samples obtained using the biaxial testing machine. Solid line — loading along the 0Y-axis, dashed line — loading along the orthogonal 0X-axis. The arrows show the direction of loading

Typically, during cyclic stretching of rubbers (beginning with the second cycle, the curves for loading along the 0Y-axis are, in fact, repeated), the sample becomes softer, and the hysteresis loss reduces. So, after the second cycle the properties of the sample in this direction are practically stabilized. The analysis of the curves for loading in the orthogonal 0X-direction indicates that the material behaves like it has never been loaded at all — no softening and changes associated with loading along the 0Y axis have been observed. A slight discrepancy between the curves for loading along the 0X- and 0Y-axes can be related to some initial anisotropy of the material caused by the production technique.

We performed analogous tests with the rest of cross-shaped carbon black-filled vulcanizate samples and obtained qualitatively similar results. This evidence led to the conclusion that the loading of the sample in one direction causes the orientation rearrangement of its structure in this direction only. In the orthogonal direction the sample continues to retain its original properties until it is subjected to loading in this direction. That is, being loaded along one direction, the material is solely softened along this direction. In the case of induced anisotropy, the material is softened because of its loading in one direction, which is referred to as the Mullins effect, but its mechanical properties do not change in any way in the perpendicular direction.

A number of experiments have been carried out to study the behavior of the polymer reinforced by 30 parts by weight of carbon black and 5 parts by weight of carbon nanofibers. Firstly, a cyclic load was applied to a sample having the form of a rectangular plate of length 50.6 mm, thickness 2.18 mm and width 28 mm using the uniaxial Testometric FS100kN CT machine. After every loading cycle the sample was returned to its initial position and then aged for 10 minutes to complete rapid recovery of the structure (Fig. 4). As one can see, softening takes place along the loading axis. The material under study possesses some initial anisotropy of mechanical properties that is associated with the production technique (Fig. 3). This circumstance should be taken into account when analyzing the data obtained during the testing along two orthogonal axes. Secondly, samples in the form of rectangular strips of thickness 4 mm and length 28 mm were cut from the plate in two mutually perpendicular directions. The samples cut in the direction of initial stretching of the plate and after its ageing were called "longitudinal", and those cut in the orthogonal direction — "transverse". Tests on these samples were performed 24 hours after they were

stretched in the longitudinal direction.
Some samples were subjected to cyclic loading using the uniaxial machine (Fig. 5), and the remaining ones were tested with the dynamic mechanical analyzer DMA/SDTA861^e (Fig. 6).

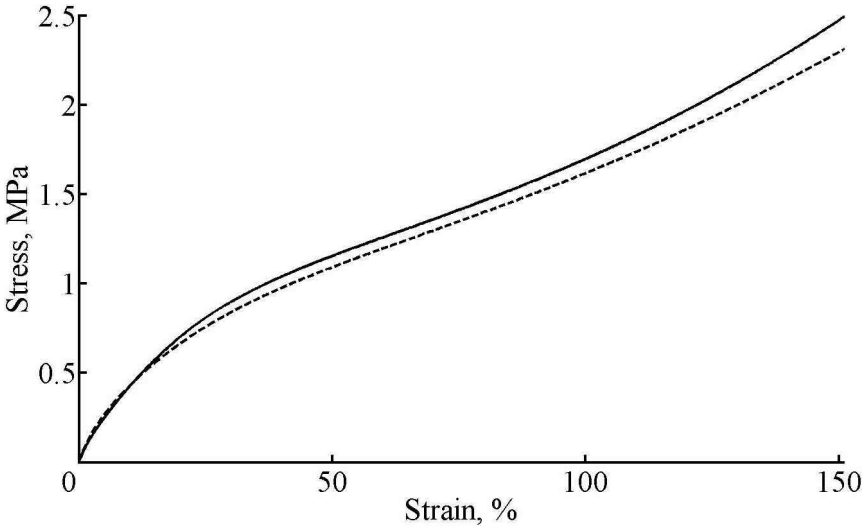

Figure 3: Initial anisotropy of the mechanical properties of the filled elastomeric material. The solid and dashed lines show stretching along two orthogonal directions

The experiments performed with the uniaxial machine indicate that the behavior of the fiber-filled rubber is different from that of the rubber with grain filler. Figure 5 shows that the preliminary ageing in the longitudinal direction causes the material to soften in all directions — longitudinal and transverse. When the initial anisotropy of the material is considered (Fig. 3), softening in the transverse direction corresponds to the same softening in the longitudinal, preliminary aged direction.

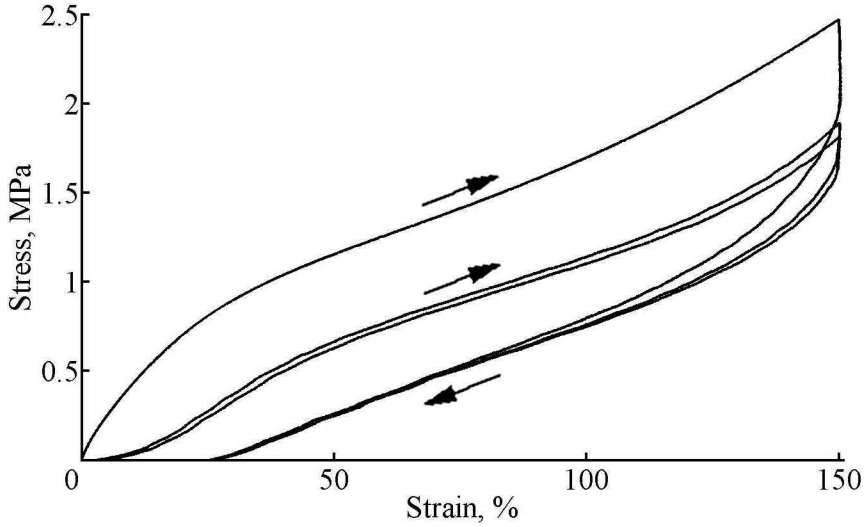

Figure 4: Curves for three cycles of loading of the rectangular plate tested on the uniaxial Testometric FS100kN CT machine. The arrows show the direction of loading

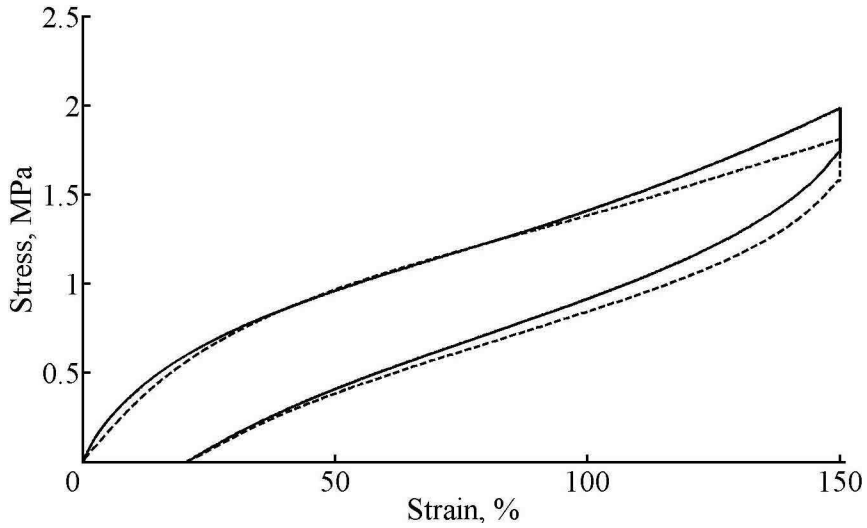

Figure 5: Cyclic testing of longitudinal and transverse samples using the uniaxial Testometric FS100kN CT testing machine. The solid lines show the behavior of longitudinal samples, and the dashed lines the behavior of transverse samples

A comparison of the curves of loading of the longitudinal and transverse samples (solid and dashed lines in Fig. 5) gives evidence that structural changes in the nanofiber filled elastomer under uniaxial deformation take place in all directions. Hence, the suggestion can be made that filler fibers subjected to stretching take a turn, and the long elastomeric molecules slide not only along the axis of elongation, but in the orthogonal direction as well.

Tests with the dynamic mechanical analyzer DMA/SDTA861^e were performed at oscillation frequency of 5, 10, 15, 20 and 30 Hz. This can be seen graphically in Fig. 6, where solid lines indicate the behavior of longitudinal samples, and dashed lines the behavior of transverse samples.

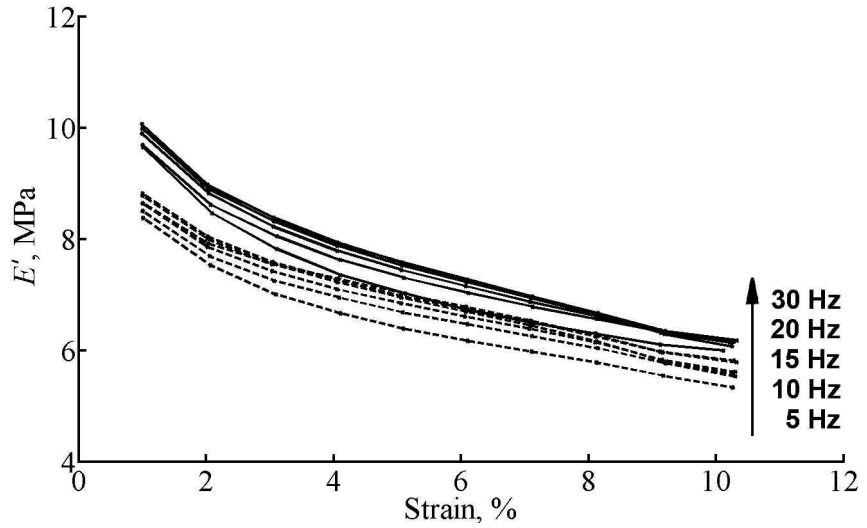

a

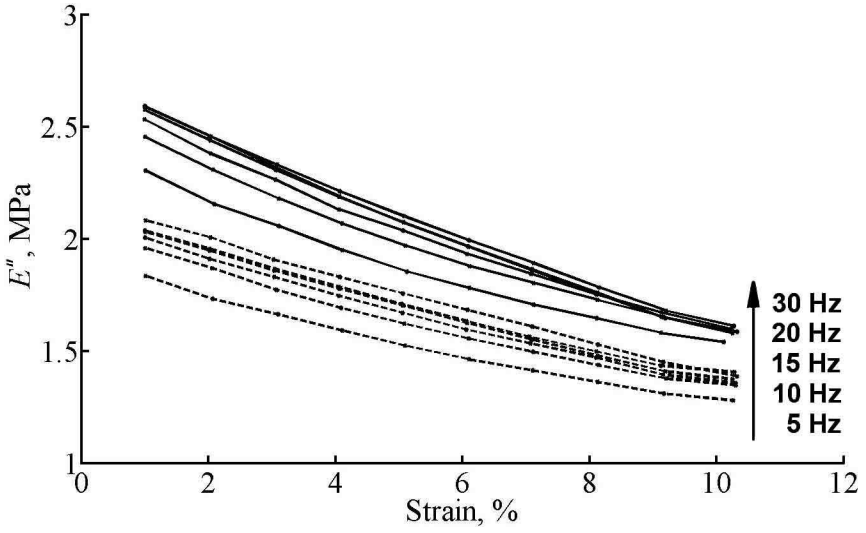

b

Figure 6: Dynamic characteristics of longitudinal and transverse samples obtained in tests with the dynamic mechanical analyzer DMA/SDTA861^e at oscillation frequencies of 5, 10, 15, 20 and 30 Hz; storage modulus E' (a), loss modulus E'' (b). The solid lines show the behavior of longitudinal samples, and the dashed lines — the behavior of transverse samples

During the uniaxial stretching tests it has been found that under small deformations (deformations measured by the DMA/SDTA861^e did not exceed 10%) the fiber filled elastomer exhibits strong softening. The storage modulus E' in the transverse direction turns out to be lower than that in the longitudinal direction (Fig. 6a). The softening of the material in the transverse direction appears to be stronger than in the longitudinal direction, and therefore the loss modulus E'' of the transverse sample is less than that of the longitudinal sample (Fig. 6b). Such a strong softening in the transverse direction can be attributed to the initial orientation of carbon fibers in the elastomeric material, i.e. to the initial anisotropy of the material observed at the stage of its production (Fig. 3). Examination of the properties of elastomers filled with carbon fibers should be extended to elucidate the physical mechanisms underlying structural rearrangements driven by stretching.

Conclusions

We have found that stretching of the elastomer with grain filler in one direction causes the induced anisotropy to appear in the material. The material softens along the extension axis, yet this softening does not, in any way, influence the structural rearrangement along the orthogonal elongation axis and change the mechanical properties of the material along the transverse axis.

When the elastomer with carbon nanofibers is loaded along one of its axis, the structural rearrangement and changes in mechanical properties occur in all directions. Additional studies need to be performed in order to investigate further the behavior of such materials.

Acknowledgements

The study was supported by RFBR and Perm Ministry of Industry of Innovations and

Science (grant 13-01-96016 r_urals_a and grant 14-08-96013 r_urals_a), and the Ministry of Education of Perm Region under agreement C-26/627.

References

[1] Mokhireva K.A., Svistkov A.L., Shadrin V.V. Opredelenie optimal'noi formy obraztsov dlia eksperimentov na dvukhosnoe rastiazhenie // Vychisl. Mekh. Splosh. Cred, 2014. V. 7, No. 4. P. 353–362.

[2] Mullins L., Tobin N.R. Stress softening in rubber vulcanizates. Part I. Use of a strain amplification factor to prescribe the elastic behavior of filler reinforced vulcanized rubber // J. Appl. Polym. Sci., 1965. V. 9. P. 2993–3005.

[3] Zgaevskii V.E., Ianovskii Iu.G. Zavisimost' viazkouprugikh svoistv kompozitov s vysokoelasticheskoi matritsei i zhestkimi chastitsami napolnitelia ot molekuliarnykh i strukturnykh parametrov mezhfaznogo sloia // Mekhanika kompozitsionnykh materialov i konstruktsii, 1998. V. 4, No. 3. P. 106–117.

[4] Machado G., Chagnon G., Favier D. Induced anisotropy by the Mullins effect in filled silicone rubber // Mechanics of Materials, 2012. V. 50. P. 70–80.

[5] Shadrin V.V. Recovery of the mechanical properties of rubber under thermal treatment // Polymer Science. Ser. B, 2005. V. 47, No. 7–8. P. 220–222.

[6] Shadrin V.V., Kornev Iu.V., Gamlitskii Iu.A. Izmenenie svoistv reziny v rezul'tate modifikatsii poverkhnosti chastits uglerodnogo napolnitelia // Mekhanika kompozitsionnykh materialov i konstruktsii, 2009, V. 15, No. 3. P. 401–410.

Vladimir V. Shadrin, Institute of Continuous Media Mechanics UB RAS, Perm, Russia, Perm State National Research University, Perm, Russia
Kseniya A. Mokhireva, Institute of Continuous Media Mechanics UB RAS, Perm, Russia
Anton Yu. Beljaev, Institute of Continuous Media Mechanics UB RAS, Perm, Russia, Perm State National Research University, Perm, Russia
Lyudmila A. Komar, Institute of Continuous Media Mechanics UB RAS, Perm, Russia

Multidimensional pendulum in a nonconservative force field

Maxim V. Shamolin
shamolin@rambler.ru, shamolin@imec.msu.ru

Abstract

In this activity, we systematize the results on the study of the equations of motion of dynamically symmetric multidimensional rigid bodies in nonconservative force fields. The form of these equations is taken from the dynamics of real lower-dimensional rigid bodies interacting with resisting medium by laws of jet flows where a body is influenced by a nonconservative tracing force; under action of this force, the velocity of some characteristic point of the body remains constant, which means that the system possesses a nonintegrable servo constraint.

1 Introduction

In the earlier activities, the author has already proved the complete integrability of the equations of a plane-parallel motion of a body in a resisting medium under the jet flow conditions when the system of dynamical equations possesses a first integral, which is a transcendental (in the sense of the theory of functions of a complex variable) function of quasi-velocities having essential singularities. It was assumed that the interaction of the medium with the body is concentrated on a part of the surface of the body that has the form of a (one-dimensional) plate. In the sequel, the planar problem was generalized to the spatial (three-dimensional) case, where the system of dynamical equations possesses a complete set of transcendental first integrals. In this case, it was assumed that the interaction of the medium with the body is concentrated on the part of the surface of the body that has the form of a planar (two-dimensional) disk.

Moreover, we study the dynamic part of equations of motion of a different four-dimensional dynamically symmetric rigid body where a nonconservative force field is concentrated on a part of the surface of the body, which has the form of a two-dimensional (three-dimensional) disk, and the action of the force is concentrated in the two-dimensional plane (one-dimensional line) perpendicular to this disk.

In this work, we discuss results, both new and obtained earlier, concerning the case where the interaction of the medium with the body is concentrated on the part of the surface of the body that has the form of a $(n-1)$-dimensional disk and the force acts in the direction perpendicular to the disk. We systematize these results and formulate them in the invariant form.

2 Certain General Discourse

First of all for n-dimensional rigid body, we will be interested the case $(1—(n-1))$, i. e., when in some coordinate system $Dx_1 \dots x_n$ attached to the body, the operator of inertia has the form

$$\operatorname{diag}\{I_1, I_2, \dots, I_2\}, \tag{1}$$

i. e., the body is dynamically symmetric in the hyperplane $Dx_2 \dots x_n$ (Dx_1 is the axe of dynamical symmetry).
The configuration space of a free, n-dimensional rigid body is the direct product

$$\mathbf{R}^n \times \mathrm{SO}(n) \tag{2}$$

of the space $\mathbf{R}^n$, which defines the coordinates of the center of mass of the body, and the rotation group $\mathrm{SO}(n)$, which defined rotations of the body about its center of mass and has dimension $n(n+1)/2$.
Therefore, the dynamical part of equations of motion has the same dimension, whereas the dimension of the phase space is equal to $n(n+1)$.
In particular, if Ω is the tensor of angular velocity of a n-dimensional rigid body (it is a second-rank tensor, see [1, 2, 3]), $\Omega \in \mathrm{so}(n)$, then the part of dynamical equations of motion corresponding to the Lie algebra $\mathrm{so}(n)$ has the following form (see [2, 3, 4]):

$$\dot{\Omega}\Lambda + \Lambda\dot{\Omega} + [\Omega,\ \Omega\Lambda + \Lambda\Omega] = M, \tag{3}$$

$$\Lambda = \operatorname{diag}\{\lambda_1, \dots, \lambda_n\}, \tag{4}$$

$$\lambda_1 = \frac{-I_1 + I_2 + \ldots + I_n}{2},\ \lambda_2 = \frac{I_1 - I_2 + I_3 + \ldots + I_n}{2}, \dots,$$

$$\lambda_{n-1} = \frac{I_1 + \ldots + I_{n-2} - I_{n-1} + I_n}{2},\ \lambda_n = \frac{I_1 + \ldots + I_{n-1} - I_n}{2},$$

$M = M_F$ is the natural projection of the moment of external forces $\mathbf{F}$ acting to the body in $\mathbf{R}^n$ on the natural coordinates of the Lie algebra $\mathrm{so}(n)$ and $[.,.]$ is the commutator in $\mathrm{so}(n)$.
Obviously, the following relations hold: $\lambda_i - \lambda_j = I_j - I_i$ for any $i, j = 1, \dots, n$.
For the calculation of the moment of an external force acting to the body, we need to construct the mapping $\mathbf{R}^n \times \mathbf{R}^n \longrightarrow \mathrm{so}(n)$, that maps a pair of vectors $(\mathbf{DN}, \mathbf{F}) \in \mathbf{R}^n \times \mathbf{R}^n$ from $\mathbf{R}^n \times \mathbf{R}^n$ to an element of the Lie algebra $\mathrm{so}(n)$, where $\mathbf{DN} = \{\delta_1, \delta_2, \dots, \delta_n\}$, $\mathbf{F} = \{F_1, F_2, \dots, F_n\}$, and $\mathbf{F}$ is an external force acting to the body. Here $\mathbf{DN}$ is the vector directing from the point D of the coordinate system $Dx_1 \dots x_n$ to the point N of force acting). For this end, we construct the following auxiliary matrix

$$\begin{pmatrix} \delta_1 & \delta_2 & \dots & \delta_n \\ F_1 & F_2 & \dots & F_n \end{pmatrix}. \tag{5}$$

Dynamical systems studied in this activity, are dynamical systems with variable dissipation with zero mean (see [4, 5]). We need to examine by direct methods a part of the main system of dynamical equations, namely, the Newton equation, which plays the role of the equation of motion of the center of mass, i.e., the part of the dynamical equations corresponding to the space $\mathbf{R}^n$:

$$m\mathbf{w}_C = \mathbf{F}, \tag{6}$$

where $\mathbf{w}_C$ is the acceleration of the center of mass C of the body and m is its mass. Moreover, due to the higher-dimensional Rivals formula (it can be obtained by the operator method) we have the following relations:

$$\mathbf{w}_C = \mathbf{w}_D + \Omega^2\mathbf{DC} + E\mathbf{DC},\ \mathbf{w}_D = \dot{\mathbf{v}}_D + \Omega\mathbf{v}_D,\ E = \dot{\Omega}, \tag{7}$$

where $\mathbf{w}_D$ is the acceleration of the point D, $\mathbf{F}$ is the external force acting on the body (in our case, $\mathbf{F} = \mathbf{S}$), and E is the tensor of angular acceleration (second-rank tensor).
Let the position of the body Θ in Euclidean space $\mathbf{E}^n$ is defined by the functions which are the cyclic in the following sense: the generalized force $\mathbf{F}$ and its moment $(\mathbf{DN}, \mathbf{F})$ depend on generalized velocities only (quasi-velocities), and do not depend on the position of the body in the space. Then, the system of equations (3) and (6) on the manifold $\mathbf{R}^n \times \mathrm{so}(n)$ is a *closed* system of dynamical equations of the motion of a free n-dimensional rigid body under the action of an external force $\mathbf{F}$. This system have been separated from the kinematic part of the equations of motion on the manifold (2) and can be examined independently.

3 General Problem on the Motion Under a Tracing Force

Consider a motion of a homogeneous, dynamically symmetric (case (1)), rigid body with Yfront end faceY (a $(n-1)$-dimensional disk interacting with a medium that fills the n-dimensional space) in the field of a resistance force $\mathbf{S}$ under the quasi-stationarity conditions (see [6, 7]).
Let $(v, \alpha, \beta_1, \ldots, \beta_{n-2})$ be the (generalized) spherical coordinates of the velocity vector of the center of the $(n-1)$-dimensional disk lying on the axis of symmetry of the body, Ω be the tensor of angular velocity of the body, $Dx_1 \ldots x_n$ be the coordinate system attached to the body such that the axis of symmetry CD coincides with the axis Dx_1 (recall that C is the center of mass), and the axes $Dx_2, Dx_3, \ldots, Dx_n$ lie in the hyperplane of the disk, and $I_1,\ I_2,\ I_3 = I_2,\ \ldots,\ I_n = I_2,\ m$ are characteristics of inertia and mass.
We adopt the following expansions in the projections to the axes of the coordinate system $Dx_1 \ldots x_n$: $\mathbf{DC} = \{-\sigma, 0, \ldots, 0\}$, $\mathbf{v}_D = v\mathbf{i}_v\,(\alpha, \beta_1, \ldots, \beta_{n-2})$, where

$$\mathbf{i}_v\,(\alpha, \beta_1, \ldots, \beta_{n-2}) = \begin{pmatrix} \cos\alpha \\ \sin\alpha\cos\beta_1 \\ \sin\alpha\sin\beta_1\cos\beta_2 \\ \ldots \\ \sin\alpha\sin\beta_1\ldots\sin\beta_{n-3}\cos\beta_{n-2} \\ \sin\alpha\sin\beta_1\ldots\sin\beta_{n-2} \end{pmatrix} \tag{8}$$

is the single vector on the axe of vector $\mathbf{v}$.
In the case (1) we additionally have the expansion for the function of the influence of the medium on the n-dimensional body: $\mathbf{S} = \{-S, 0, \ldots, 0\}$, i.e., in this case $\mathbf{F} = \mathbf{S}$. Further, the auxiliary matrix (5) for the calculation of the moment of the resistance force has the form

$$\begin{pmatrix} 0 & x_{2N} & \ldots & x_{nN} \\ -S & 0 & \ldots & 0 \end{pmatrix}, \tag{9}$$

then the part of the dynamical equations of motion that describes the motion of the body about the center of mass and corresponds to the Lie algebra $\mathrm{so}(n)$, can be obtained. We

note that system (3), due to the existing dynamical symmetry

$$I_2 = \ldots = I_n, \tag{10}$$

possesses cyclic first integrals

$$\omega_{k_1} \equiv \omega_{k_1}^0 = \text{const}, \ \ldots, \ \omega_{k_s} \equiv \omega_{k_s}^0 = \text{const}, \ s = \frac{(n-1)(n-2)}{2}. \tag{11}$$

Here $k_1 = 1, \ldots, k_s$ are the certain s nonrecurrent numbers from the set $W_1 = \{1, 2, \ldots, n(n-1)/2\}$.
In the sequel, we consider the first integrals (11) of the system on its zero levels:

$$\omega_{k_1}^0 = \ldots = \omega_{k_s}^0 = 0. \tag{12}$$

The choice of nonzero components $\omega_{r_1}, \ldots, \omega_{r_p}$ of tensor Ω consists of $p = n(n-1)/2 - (n-1)(n-2)/2 = n-1$ ones (here $r_1, \ldots, r_p$ are the rest p of numbers from the set W_1, not equal to $k_1, \ldots, k_s$).
If one considers *a more general problem* on the motion of a body under a tracing force $\mathbf{T}$ that lies on the straight line $CD = Dx_1$ and provides the fulfillment of the relation

$$v \equiv \text{const}, \tag{13}$$

throughout the motion, then instead of F_1 system (3), (6) contains $T - s(\alpha)v^2, \ \sigma = DC$. Choosing the value T of the tracing force appropriately, one can achieve the equality (13) throughout the motion. Indeed, expressing T due to system (3), (6), we obtain for $\cos\alpha \neq 0, \ n > 2$ the relation

$$T = T_v(\alpha, \beta_1, \ldots, \beta_{n-2}, \Omega) = m\sigma(\omega_{r_1}^2 + \ldots + \omega_{r_p}^2) +$$

$$+ s(\alpha)v^2 \left[1 - \frac{m\sigma}{(n-2)I_2} \frac{\sin\alpha}{\cos\alpha} \Gamma_v\left(\alpha, \beta_1, \ldots, \beta_{n-2}, \frac{\Omega}{v}\right)\right], \tag{14}$$

$$\Gamma_v\left(\alpha, \beta_1, \ldots, \beta_{n-2}, \frac{\Omega}{v}\right) = |\mathbf{r}_N| = (\mathbf{r}_N, \mathbf{i}_N(\beta_1, \ldots, \beta_{n-2})) =$$

$$= 0 \cdot \cos\frac{\pi}{2} + \sum_{s=2}^{n} x_{sN}\left(\alpha, \beta_1, \ldots, \beta_{n-2}, \frac{\Omega}{v}\right) i_{sN}(\beta_1, \ldots, \beta_{n-2}). \tag{15}$$

Here $i_{sN}(\beta_1, \ldots, \beta_{n-2}), \ s = 1, \ldots, n, \ (i_{1N}(\beta_1, \ldots, \beta_{n-2}) \equiv 0)$ are the components of single vector on the axe of vector $\mathbf{r}_N = \{0, x_{2N}, \ldots, x_{nN}\}$ on $(n-2)$-dimensional sphere $\mathbf{S}^{n-2}\{\beta_1, \ldots, \beta_{n-2}\}$, definied by the equality $\alpha = \pi/2$ as equatorial section of corresponding $(n-1)$-dimensional sphere $\mathbf{S}^{n-1}\{\alpha, \beta_1, \ldots, \beta_{n-2}\}$ (defined by the equality (13)), i. e.,

$$\mathbf{i}_N(\beta_1, \ldots, \beta_{n-2}) =$$

$$= \begin{pmatrix} 0 \\ \cos\beta_1 \\ \sin\beta_1 \cos\beta_2 \\ \ldots \\ \sin\beta_1 \ldots \sin\beta_{n-3} \cos\beta_{n-2} \\ \sin\beta_1 \ldots \sin\beta_{n-2} \end{pmatrix} = \mathbf{i}_v\left(\frac{\pi}{2}, \beta_1, \ldots, \beta_{n-2}\right) \tag{16}$$

(see Eq. (8)). This procedure can be interpreted in two ways. First, we have transformed the system using the tracing force (control) that provides the consideration of the class (13)

of motions interesting for us. Second, we can treat this as an order-reduction procedure. Indeed, system (3), (6) generates the following independent system of following order (due to Eqs. (13), (11), (12)): $n(n+1)/2-(n-1)(n-2)/2-1=2(n-1)$.
Let introduce the new quasi-velocities in system (3), (6). For this, we transform the values $\omega_{r_1},\ldots,\omega_{r_{n-1}}$ by the composition of following $(n-2)$ rotations:

$$\begin{pmatrix} z_1 \\ z_2 \\ \cdots \\ z_{n-1} \end{pmatrix} = T_{n-2,n-1}(-\beta_1)\circ T_{n-3,n-2}(-\beta_2)\circ\ldots\circ T_{1,2}(-\beta_{n-2}) \begin{pmatrix} \omega_{r_1} \\ \omega_{r_2} \\ \cdots \\ \omega_{r_{n-1}} \end{pmatrix}, \quad (17)$$

where the matrix $T_{k,k+1}(\beta),\ k=1,\ldots,n-2$, is obtained from the unit one by the presence of second order minor $M_{k,k+1}$:

$$T_{k,k+1}=\begin{pmatrix} 1 & 0 & 0 & 0 & 0 \\ 0 & \ddots & 0 & 0 & 0 \\ 0 & 0 & M_{k,k+1} & 0 & 0 \\ 0 & 0 & 0 & \ddots & 0 \\ 0 & 0 & 0 & 0 & 1 \end{pmatrix},\ M_{k,k+1}=\begin{pmatrix} m_{k,k} & m_{k,k+1} \\ m_{k+1,k} & m_{k+1,k+1} \end{pmatrix}, \quad (18)$$

$$m_{k,k}=m_{k+1,k+1}=\cos\beta,\ m_{k+1,k}=-m_{k,k+1}=\sin\beta.$$

As we see, we cannot solve the system with respect to $\dot\alpha,\ \dot\beta_1,\ \ldots,\ \dot\beta_{n-2}$ on the manifold

$$O_1'=\{(\alpha,\beta_1,\ldots,\beta_{n-2},\omega_{r_1},\ldots,\omega_{r_{n-1}})\in\mathbf{R}^{2(n-1)}:$$

$$\alpha=\frac{\pi}{2}k,\ \beta_1=\pi l_1,\ldots,\beta_{n-3}=\pi l_{n-3},\ k,l_1,\ldots,l_{n-3}\in\mathbf{Z}\}. \quad (19)$$

Therefore, on the manifold (19) the uniqueness theorem formally is violated. Moreover, for even k and any $l_1,\ldots,l_{n-3}$, an indeterminate form appears due to the degeneration of the spherical coordinates $(v,\alpha,\beta_1,\ldots,\beta_{n-2})$. For odd k, the uniqueness theorem is obviously violated since one of the equation degenerates.
This implies that system (3), (6) outside (and only outside) the manifold (19) can be reduced to the following form $(n>2)$:

$$\dot\alpha=-z_{n-1}+\frac{\sigma v}{(n-2)I_2}\frac{s(\alpha)}{\cos\alpha}\Gamma_v\left(\alpha,\beta_1,\ldots,\beta_{n-2},\frac{\Omega}{v}\right), \quad (20)$$

$$\dot z_{n-1}=\frac{v^2}{(n-2)I_2}s(\alpha)\Gamma_v\left(\alpha,\beta_1,\ldots,\beta_{n-2},\frac{\Omega}{v}\right)-(z_1^2+\ldots+z_{n-2}^2)\frac{\cos\alpha}{\sin\alpha}+$$
$$+\frac{\sigma v}{(n-2)I_2}\frac{s(\alpha)}{\sin\alpha}\left\{\sum_{s=1}^{n-2}(-1)^s z_{n-1-s}\Delta_{v,s}\left(\alpha,\beta_1,\ldots,\beta_{n-2},\frac{\Omega}{v}\right)\right\}, \quad (21)$$

$$\dot z_{n-2}=z_{n-2}z_{n-1}\frac{\cos\alpha}{\sin\alpha}+(z_1^2+\ldots+z_{n-3}^2)\frac{\cos\alpha}{\sin\alpha}\frac{\cos\beta_1}{\sin\beta_1}+$$
$$+\frac{\sigma v}{(n-2)I_2}\frac{s(\alpha)}{\sin\alpha}\{z_{n-1}\Delta_{v,1}\left(\alpha,\beta_1,\ldots,\beta_{n-2},\frac{\Omega}{v}\right)+$$
$$+\sum_{s=2}^{n-2}(-1)^{s+1}z_{n-1-s}\Delta_{v,s}\left(\alpha,\beta_1,\ldots,\beta_{n-2},\frac{\Omega}{v}\right)\frac{\cos\beta_1}{\sin\beta_1}\}-$$

$$-\frac{v^2}{(n-2)I_2}s(\alpha)\Delta_{v,1}\left(\alpha,\beta_1,\ldots,\beta_{n-2},\frac{\Omega}{v}\right), \tag{22}$$

$$\dot{z}_{n-3}=z_{n-3}z_{n-1}\frac{\cos\alpha}{\sin\alpha}-z_{n-3}z_{n-2}\frac{\cos\alpha}{\sin\alpha}\frac{\cos\beta_1}{\sin\beta_1}-$$

$$-(z_1^2+\ldots+z_{n-4}^2)\frac{\cos\alpha}{\sin\alpha}\frac{1}{\sin\beta_1}\frac{\cos\beta_2}{\sin\beta_2}+$$

$$+\frac{\sigma v}{(n-2)I_2}\frac{s(\alpha)}{\sin\alpha}\{\Delta_{v,2}\left(\alpha,\beta_1,\ldots,\beta_{n-2},\frac{\Omega}{v}\right)\left[-z_{n-1}+z_{n-2}\frac{\cos\beta_1}{\sin\beta_1}\right]+$$

$$+\sum_{s=3}^{n-2}(-1)^s z_{n-1-s}\Delta_{v,s}\left(\alpha,\beta_1,\ldots,\beta_{n-2},\frac{\Omega}{v}\right)\frac{1}{\sin\beta_1}\frac{\cos\beta_2}{\sin\beta_2}\}+$$

$$+\frac{v^2}{(n-2)I_2}s(\alpha)\Delta_{v,2}\left(\alpha,\beta_1,\ldots,\beta_{n-2},\frac{\Omega}{v}\right), \tag{23}$$

$$\ldots\ldots\ldots\ldots\ldots\ldots\ldots\ldots\ldots\ldots\ldots\ldots$$

$$\dot{z}_1=\dot{\beta}_{n-2}(-\omega_{r_1}\sin\beta_{n-2}+\omega_{r_2}\cos\beta_{n-2})+$$

$$+(-1)^n\frac{v^2}{(n-2)I_2}s(\alpha)\Delta_{v,n-2}\left(\alpha,\beta_1,\ldots,\beta_{n-2},\frac{\Omega}{v}\right)=$$

$$=z_1\frac{\cos\alpha}{\sin\alpha}\left\{\sum_{s=1}^{n-2}(-1)^{s+1}z_{n-s}\frac{\cos\beta_{s-1}}{\sin\beta_1\ldots\sin\beta_{s-1}}\right\}+$$

$$+\frac{\sigma v}{(n-2)I_2}\frac{s(\alpha)}{\sin\alpha}(-1)^{n+1}\Delta_{v,n-2}\left(\alpha,\beta_1,\ldots,\beta_{n-2},\frac{\Omega}{v}\right)\times$$

$$\times\left\{\sum_{s=2}^{n-1}(-1)^s z_{n+1-s}\frac{\cos\beta_{s-1}}{\sin\beta_1\ldots\sin\beta_{s-1}}\right\}+$$

$$+(-1)^n\frac{v^2}{(n-2)I_2}s(\alpha)\Delta_{v,n-2}\left(\alpha,\beta_1,\ldots,\beta_{n-2},\frac{\Omega}{v}\right), \tag{24}$$

$$\dot{\beta}_1=z_{n-2}\frac{\cos\alpha}{\sin\alpha}+\frac{\sigma v}{(n-2)I_2}\frac{s(\alpha)}{\sin\alpha}\Delta_{v,1}\left(\alpha,\beta_1,\ldots,\beta_{n-2},\frac{\Omega}{v}\right), \tag{25}$$

$$\dot{\beta}_2=-z_{n-3}\frac{\cos\alpha}{\sin\alpha\sin\beta_1}+\frac{\sigma v}{(n-2)I_2}\frac{s(\alpha)}{\sin\alpha\sin\beta_1}\Delta_{v,2}\left(\alpha,\beta_1,\beta_2,\beta_3,\frac{\Omega}{v}\right), \tag{26}$$

$$\ldots\ldots\ldots\ldots\ldots\ldots\ldots\ldots\ldots\ldots\ldots\ldots$$

$$\dot{\beta}_{n-2}=(-1)^{n+1}z_1\frac{\cos\alpha}{\sin\alpha\sin\beta_1\ldots\sin\beta_{n-3}}+$$

$$+\frac{\sigma v}{(n-2)I_2}\frac{s(\alpha)}{\sin\alpha\sin\beta_1\ldots\sin\beta_{n-2}}\Delta_{v,n-2}\left(\alpha,\beta_1,\ldots,\beta_{n-2},\frac{\Omega}{v}\right), \tag{27}$$

$$\Delta_{v,1}\left(\alpha,\beta_1,\ldots,\beta_{n-2},\frac{\Omega}{v}\right)=(\mathbf{r}_N,\mathbf{i}_N\left(\beta_1+\frac{\pi}{2},\beta_2,\ldots,\beta_{n-2}\right)),$$

$$\Delta_{v,2}\left(\alpha,\beta_1,\ldots,\beta_{n-2},\frac{\Omega}{v}\right)=(\mathbf{r}_N,\mathbf{i}_N\left(\frac{\pi}{2},\beta_2+\frac{\pi}{2},\beta_3,\ldots,\beta_{n-2}\right)),$$

$$\ldots\ldots\ldots\ldots\ldots\ldots\ldots\ldots\ldots\ldots\ldots\ldots \tag{28}$$

$$\Delta_{v,n-3}\left(\alpha,\beta_1,\ldots,\beta_{n-2},\frac{\Omega}{v}\right)=(\mathbf{r}_N,\mathbf{i}_N\left(\frac{\pi}{2},\ldots,\frac{\pi}{2},\beta_{n-3}+\frac{\pi}{2},\beta_{n-2}\right)),$$

$$\Delta_{v,n-2}\left(\alpha,\beta_1,\ldots,\beta_{n-2},\frac{\Omega}{v}\right)=(\mathbf{r}_N,\mathbf{i}_N\left(\frac{\pi}{2},\ldots,\frac{\pi}{2},\beta_{n-2}+\frac{\pi}{2}\right)),$$

and function $\Gamma_v\left(\alpha,\beta_1,\ldots,\beta_{n-2},\Omega/v\right)$ can be represented in the form (15).
In right-hand side of the system (20)–(27) after common multiplier

$$\frac{\sigma v}{(n-2)I_2}\frac{s(\alpha)}{\cos\alpha},$$

the values $\Delta_{v,s}\left(\alpha,\beta_1,\ldots,\beta_{n-2},\Omega/v\right),\ s=1,\ldots,n-2$, are represented in linear form (and always $(n-2)$ coefficients precisely). For instance, in Eq. (21) (with left-hand side $\dot{z}_{n-1}$), the functions (28) are represented with all indices s from 1 to $n-2$ (every index per one time), i. e.,

$$1\ 2\ 3\ 4\ \ldots\ n-2. \tag{29}$$

But furthermore, in Eqs. (22)–(24), the set of functions (28) is formed in another way. For instance, in equation with left-hand side $\dot{z}_{n-2}$, the set of functions (28) is formed with corresponding indices (29). But in equation with left-hand side $\dot{z}_{n-3}$, it is already formed with the following indices:

$$2\ 2\ 3\ 4\ \ldots\ n-2 \tag{30}$$

i. e., the function $\Delta_{v,2}\left(\alpha,\beta_1,\ldots,\beta_{n-2},\Omega/v\right)$ is already repeated twice.
What is the general distribution of indices? It can be represented by table 13.

Table 13: General Distribution of Indices in Set of Functions (28)

Left-hand Side of (20)–(27)	Distribution of Indices s in Set of Functions (28)					
$\dot{z}_{n-2}$	1	2	3	4	...	$n-2$
$\dot{z}_{n-3}$	2	2	3	4	...	$n-2$
$\dot{z}_{n-4}$	3	3	3	4	...	$n-2$
$\dot{z}_{n-5}$	4	4	4	4	...	$n-2$
...	...	...	...	...	...	...
$\dot{z}_1$	$n-2$	$n-2$	$n-2$	$n-2$	...	$n-2$

4 Case Where the Moment of a Nonconservative Force Is Independent of the Angular Velocity

Similarly to the choice of Chaplygin analytic functions, we take the dynamical functions $s, x_{2N},\ldots,x_{nN}$ in the following form (using (16)):

$$s(\alpha)=B\cos\alpha,\ \mathbf{r}_N=R(\alpha)\mathbf{i}_N,\ R(\alpha)=A\sin\alpha,\ A,B>0. \tag{31}$$

Herewith, the functions $\Gamma_v\left(\alpha,\beta_1,\ldots,\beta_{n-2},\Omega/v\right)$, $\Delta_{v,s}\left(\alpha,\beta_1,\ldots,\beta_{n-2},\Omega/v\right)$, $s=1,\ldots,n-2$, in system (20)–(27), take the following form:

$$\Gamma_v\left(\alpha,\beta_1,\ldots,\beta_{n-2},\frac{\Omega}{v}\right)=R(\alpha)=A\sin\alpha,\ \Delta_{v,s}\left(\alpha,\beta_1,\ldots,\beta_{n-2},\frac{\Omega}{v}\right)\equiv 0. \tag{32}$$

Then, due to the nonintegrable constraint (13), outside and only outside the manifold (19), system (20)–(27)) has the analytic form

$$\alpha'=-z_{n-1}+b\sin\alpha, \tag{33}$$

$$z'_{n-1}=\sin\alpha\cos\alpha-(z_1^2+\ldots+z_{n-2}^2)\frac{\cos\alpha}{\sin\alpha}, \tag{34}$$

$$z'_{n-2}=z_{n-2}z_{n-1}\frac{\cos\alpha}{\sin\alpha}+(z_1^2+\ldots+z_{n-3}^2)\frac{\cos\alpha}{\sin\alpha}\frac{\cos\beta_1}{\sin\beta_1}, \tag{35}$$

$$z'_{n-3}=z_{n-3}z_{n-1}\frac{\cos\alpha}{\sin\alpha}-z_{n-3}z_{n-2}\frac{\cos\alpha}{\sin\alpha}\frac{\cos\beta_1}{\sin\beta_1}-$$

$$-(z_1^2+\ldots+z_{n-4}^2)\frac{\cos\alpha}{\sin\alpha}\frac{1}{\sin\beta_1}\frac{\cos\beta_2}{\sin\beta_2}, \tag{36}$$

$$\ldots\ldots\ldots\ldots\ldots\ldots\ldots\ldots\ldots\ldots$$

$$z'_1=z_1\frac{\cos\alpha}{\sin\alpha}\left\{\sum_{s=1}^{n-2}(-1)^{s+1}z_{n-s}\frac{\cos\beta_{s-1}}{\sin\beta_1\ldots\sin\beta_{s-1}}\right\}, \tag{37}$$

$$\beta'_1=z_{n-2}\frac{\cos\alpha}{\sin\alpha}, \tag{38}$$

$$\beta'_2=-z_{n-3}\frac{\cos\alpha}{\sin\alpha\sin\beta_1}, \tag{39}$$

$$\ldots\ldots\ldots\ldots\ldots\ldots\ldots\ldots\ldots\ldots$$

$$\beta'_{n-3}=(-1)^n z_2\frac{\cos\alpha}{\sin\alpha\sin\beta_1\ldots\sin\beta_{n-4}}, \tag{40}$$

$$\beta'_{n-2}=(-1)^{n+1}z_1\frac{\cos\alpha}{\sin\alpha\sin\beta_1\ldots\sin\beta_{n-3}}, \tag{41}$$

introducing the dimensionless variables, parameters, and the differentiation as follows:

$$\begin{aligned}&z_k\mapsto n_0 v z_k,\ k=1,\ldots,n-1,\ n_0^2=\frac{AB}{(n-2)I_2}(n>2),\\&b=\sigma n_0,\ <\cdot>=n_0 v<'>\,.\end{aligned} \tag{42}$$

We see that the $2(n-1)$th-order system (33)–(41) (which can be considered as a system on the tangent bundle $T_*\mathbf{S}^{n-1}\{z_{n-1},\ldots,z_1;\alpha,\beta_1,\ldots,\beta_{n-2}\}$ of the $(n-1)$-dimensional sphere $\mathbf{S}^{n-1}\{\alpha,\beta_1,\ldots,\beta_{n-2}\}$, see below) contains the independent $(2n-3)$th-order system (33)–(40) on its own $(2n-3)$-dimensional manifold.

Theorem 1. The system (3), (6) under conditions (13), (11), (12), is reduced to dynamic system (20)–(27) on the tangent bundle $T_*\mathbf{S}^{n-1}\{z_{n-1},\ldots,z_1;\alpha,\beta_1,\ldots,\beta_{n-2}\}$ of $(n-1)$-dimensional sphere $\mathbf{S}^{n-1}\{\alpha,\beta_1,\ldots,\beta_{n-2}\}$.

For the complete integration of $2(n-1)$th-order system (33)–(41), in general, we need $2n-3$ independent first integrals. However, after the change of variables

$$\begin{aligned}&w_{n-1}=z_{n-1},\ w_{n-2}=\sqrt{z_1^2+\ldots+z_{n-2}^2},\ w_{n-3}=\frac{z_2}{z_1},\\&w_{n-4}=\frac{z_3}{\sqrt{z_1^2+z_2^2}},\ \ldots,\ w_2=\frac{z_{n-3}}{\sqrt{z_1^2+\ldots+z_{n-4}^2}},\ w_1=\frac{z_{n-2}}{\sqrt{z_1^2+\ldots+z_{n-3}^2}},\end{aligned} \tag{43}$$

system (33)–(41) splits as follows:

$$\alpha' = -w_{n-1} + b\sin\alpha, \tag{44}$$

$$w'_{n-1} = \sin\alpha\cos\alpha - w_{n-2}^2\frac{\cos\alpha}{\sin\alpha}, \tag{45}$$

$$w'_{n-2} = w_{n-2}w_{n-1}\frac{\cos\alpha}{\sin\alpha}, \tag{46}$$

$$\begin{aligned} &w'_s = d_s(w_{n-1},\dots,w_1;\alpha,\beta_1,\dots,\beta_{n-2})\frac{1+w_s^2}{w_s}\frac{\cos\beta_s}{\sin\beta_s},\\ &\beta'_s = d_s(w_{n-1},\dots,w_1;\alpha,\beta_1,\dots,\beta_{n-2}),\ s=1,\dots,n-3, \end{aligned} \tag{47}$$

$$\beta'_{n-2} = d_{n-2}(w_{n-1},\dots,w_1;\alpha,\beta_1,\dots,\beta_{n-2}), \tag{48}$$

$$\begin{aligned} &d_1 = Z_{n-2}(w_{n-1},\dots,w_1)\frac{\cos\alpha}{\sin\alpha},\\ &d_2 = -Z_{n-3}(w_{n-1},\dots,w_1)\frac{\cos\alpha}{\sin\alpha\sin\beta_1},\\ &\dots\dots\dots\dots\dots\dots\dots\dots\dots\dots\dots\dots\dots\dots\dots\dots\dots\dots\dots\dots\dots\dots\dots\dots\\ &d_{n-2} = (-1)^{n+1}Z_1(w_{n-1},\dots,w_1)\frac{\cos\alpha}{\sin\alpha\sin\beta_1\dots\sin\beta_{n-3}}, \end{aligned} \tag{49}$$

herewith, $z_k = Z_k(w_{n-1},\dots,w_1),\ k=1,\dots,n-2$, are the functions due to the change (43).

We see that for the complete integration of system (44)–(48) it suffices to specify two independent first integrals of system (44)–(46), on one first integral of systems (47), and an additional first integral that YattachesЯ Eq. (48) (*i. e., n in all*).

We have the following transcendental first integral:

$$\Theta_1(w_{n-1},w_{n-2};\alpha) = \frac{w_{n-1}^2 + w_{n-2}^2 - bw_{n-1}\sin\alpha + \sin^2\alpha}{w_{n-2}\sin\alpha} = C_1 = \text{const}. \tag{50}$$

Then the additional first integral obtained has the following structural form:

$$\Theta_2(w_{n-1},w_{n-2};\alpha) = G\left(\sin\alpha, \frac{w_{n-1}}{\sin\alpha}, \frac{w_{n-2}}{\sin\alpha}\right) = C_2 = \text{const}. \tag{51}$$

For the complete integration, as was mentioned above, it suffices to find on one first integral for (potentially separated) systems (47), and an additional first integral that YattachesЯ Eq. (48).

Indeed, we have the desired first integrals as follows:

$$\Theta_{s+2}(w_s;\beta_s) = \frac{\sqrt{1+w_s^2}}{\sin\beta_s} = C''_{s+2} = \text{const},\ s=1,\dots,n-3, \tag{52}$$

$$\Theta_n(w_{n-3},\dots,w_1;\alpha,\beta_1,\dots,\beta_{n-2}) = C''_n = \text{const}, \tag{53}$$

herewith, we must substitute the left-hand sides of the first integrals (52) for $s=n-4,n-3$, in the expressions of first integral (53) instead C_{n-2}, C_{n-1}.

Theorem 2. The $2(n-1)$th-order system (44)–(48) possesses the sufficient quantity (n) of independent first integrals (50), (51), (52), and (53).

Thus, in the case considered, the system of dynamical equations (3), (6) under condition (31) has $(n^2-n+4)/2,\ n>2$, invariant relations: the nonintegrable analytic constraint of the form (13), the cyclic first integrals of the form (11), (12), the first integral of the form (50), the first integral (51), which is a transcendental function of the phase variables

(in the sense of complex analysis) expressed through a finite combination of elementary functions, and, finally, the transcendental first integrals of the form (52), (53).

Theorem 3. System (3), (6) under conditions (13), (31), (11), (12) possesses $(n^2 - n + 4)/2$, $n > 2$, invariant relations (complete set), n of which transcendental functions from the point of view of complex analysis. Herewith, all relations are expressed through finite combinations of elementary functions.

Consider the following $(2n-3)$th-order system:

$$
\begin{aligned}
&\ddot{\xi} + b_*\dot{\xi}\cos\xi + \sin\xi\cos\xi - \\
&- \left[\dot{\eta_1}^2 + \dot{\eta_2}^2\sin^2\eta_1 + \dot{\eta_3}^2\sin^2\eta_1\sin^2\eta_2 + \ldots + \dot{\eta}_{n-2}^2\sin^2\eta_1\ldots\sin^2\eta_{n-3}\right]\frac{\sin\xi}{\cos\xi} = 0, \\
&\ddot{\eta_1} + b_*\dot{\eta_1}\cos\xi + \dot{\xi}\dot{\eta_1}\frac{1+\cos^2\xi}{\cos\xi\sin\xi} - \\
&- \left[\dot{\eta_2}^2 + \dot{\eta_3}^2\sin^2\eta_2 + \dot{\eta_4}^2\sin^2\eta_2\sin^2\eta_3 + \ldots + \dot{\eta}_{n-2}^2\sin^2\eta_2\ldots\sin^2\eta_{n-3}\right]\times \\
&\times\sin\eta_1\cos\eta_1 = 0, \\
&\ddot{\eta_2} + b_*\dot{\eta_2}\cos\xi + \dot{\xi}\dot{\eta_2}\frac{1+\cos^2\xi}{\cos\xi\sin\xi} + \\
&+ 2\dot{\eta_1}\dot{\eta_2}\frac{\cos\eta_1}{\sin\eta_1} - \\
&- \left[\dot{\eta_3}^2 + \dot{\eta_4}^2\sin^2\eta_3 + \dot{\eta_5}^2\sin^2\eta_3\sin^2\eta_4 + \ldots + \dot{\eta}_{n-2}^2\sin^2\eta_3\ldots\sin^2\eta_{n-3}\right]\times \\
&\times\sin\eta_2\cos\eta_2 = 0, \\
&\ddot{\eta_3} + b_*\dot{\eta_3}\cos\xi + \dot{\xi}\dot{\eta_3}\frac{1+\cos^2\xi}{\cos\xi\sin\xi} + \\
&+ 2\dot{\eta_1}\dot{\eta_3}\frac{\cos\eta_1}{\sin\eta_1} + 2\dot{\eta_2}\dot{\eta_3}\frac{\cos\eta_2}{\sin\eta_2} - \\
&- \left[\dot{\eta_4}^2 + \dot{\eta_5}^2\sin^2\eta_4 + \dot{\eta_6}^2\sin^2\eta_4\sin^2\eta_5 + \ldots + \dot{\eta}_{n-2}^2\sin^2\eta_4\ldots\sin^2\eta_{n-3}\right]\times \\
&\times\sin\eta_3\cos\eta_3 = 0, \\
&\ldots\ldots\ldots\ldots\ldots\ldots\ldots\ldots\ldots\ldots\ldots\ldots\ldots\ldots\ldots\ldots\ldots\ldots\ldots\ldots\ldots\ldots \\
&\ddot{\eta}_{n-4} + b_*\dot{\eta}_{n-4}\cos\xi + \dot{\xi}\dot{\eta}_{n-4}\frac{1+\cos^2\xi}{\cos\xi\sin\xi} + \\
&+ 2\dot{\eta_1}\dot{\eta}_{n-4}\frac{\cos\eta_1}{\sin\eta_1} + \ldots + 2\dot{\eta}_{n-5}\dot{\eta}_{n-4}\frac{\cos\eta_{n-5}}{\sin\eta_{n-5}} - \\
&- \left[\dot{\eta}_{n-3}^2 + \dot{\eta}_{n-2}^2\sin^2\eta_{n-3}\right]\sin\eta_{n-4}\cos\eta_{n-4} = 0, \\
&\ddot{\eta}_{n-3} + b_*\dot{\eta}_{n-3}\cos\xi + \dot{\xi}\dot{\eta}_{n-3}\frac{1+\cos^2\xi}{\cos\xi\sin\xi} + \\
&+ 2\dot{\eta_1}\dot{\eta}_{n-3}\frac{\cos\eta_1}{\sin\eta_1} + \ldots + 2\dot{\eta}_{n-4}\dot{\eta}_{n-3}\frac{\cos\eta_{n-4}}{\sin\eta_{n-4}} - \\
&- \dot{\eta}_{n-2}^2\sin\eta_{n-3}\cos\eta_{n-3} = 0, \\
&\ddot{\eta}_{n-2} + b_*\dot{\eta}_{n-2}\cos\xi + \dot{\xi}\dot{\eta}_{n-2}\frac{1+\cos^2\xi}{\cos\xi\sin\xi} + \\
&+ 2\dot{\eta_1}\dot{\eta}_{n-2}\frac{\cos\eta_1}{\sin\eta_1} + \ldots + 2\dot{\eta}_{n-3}\dot{\eta}_{n-2}\frac{\cos\eta_{n-3}}{\sin\eta_{n-3}} = 0,\ b_* > 0,
\end{aligned}
\tag{54}
$$

which describes a fixed n-dimensional pendulum in a flow of a running medium for which the moment of forces is independent of the angular velocity, i.e., a mechanical system in a nonconservative field (see [1, 2]). In general, the order of such a system is equal to $2(n-1)$, but the phase variable η_{n-2} is a cyclic variable, which leads to the stratification

of the phase space and reduces the order of the system.
The phase space of this system is the tangent bundle

$$T\mathbf{S}^{n-1}\{\dot{\xi}, \dot{\eta}_1, \ldots, \dot{\eta}_{n-2}, \xi, \eta_1, \ldots, \eta_{n-2}\} \tag{55}$$

of the $(n-1)$-dimensional sphere $\mathbf{S}^{n-1}\{\xi, \eta_1, \ldots, \eta_{n-2}\}$. The equations that transform system (54) into the system on the tangent bundle of the two-dimensional sphere $\dot{\eta}_2 \equiv \dot{\eta}_3 \equiv \ldots \equiv \dot{\eta}_{n-2} \equiv 0$, and the equations of great circles $\dot{\eta}_1 \equiv 0,\ \dot{\eta}_2 \equiv 0,\ \ldots,\ \dot{\eta}_{n-2} \equiv 0$ define families of integral manifolds.
It is easy to verify that system (54) is equivalent to the dynamical system with variable dissipation with zero mean on the tangent bundle (55) of the $(n-1)$-dimensional sphere. Moreover, the following theorem holds.
Theorem 4. System (3), (6) under conditions (13), (31), (11), and (12), is equivalent to the dynamical system (54).
Indeed, it suffices to set $\alpha = \xi,\ \beta_1 = \eta_1,\ \ldots,\ \beta_{n-2} = \eta_{n-2},\ b = -b_*$.

Acknowledgements

This work was supported by the Russian Foundation for Basic Research, project no. 12-01-00020-a.

References

[1] M. V. Shamolin, "New Case of Integrability in the Dynamics of a Multidimensional Solid in a Nonconservative Field", Doklady Physics, 58:11 (2013), 496–499.

[2] M. V. Shamolin, "New case of integrability of dynamic equations on the tangent bundle of a 3-sphere", Russian Math. Surveys, 68:5 (2013), 963–965.

[3] M. V. Shamolin, "Variety of Integrable Cases in Dynamics of Low- and Multi-Dimensional Rigid Bodies in Nonconservative Force Fields", Journal of Mathematical Sciences, 204:4 (2015), 379–530.

[4] M. V. Shamolin, "A New Case of Integrability in the Dynamics of a Multidimensional Solid in a Nonconservative Field under the Assumption of Linear Damping", Doklady Physics, 59:8 (2014), 375–378.

[5] M. V. Shamolin, "Dynamical Pendulum-Like Nonconservative Systems", Applied Non-Linear Dynamical Systems, Springer Proceedings in Mathematics and Statistics, Vol. 93 (2014), 503–525.

[6] M. V. Shamolin, "A Multidimensional Pendulum in a Nonconservative Force Field", Doklady Physics, 60:1 (2015), 34–38.

[7] M. V. Shamolin, "Classification of Integrable Cases in the Dynamics of a Four-Dimensional Rigid Body in a Nonconservative Field in the Presence of a Tracking Force", Journal of Mathematical Sciences, 204:6 (2015), 808–870.

Maxim V. Shamolin, Lomonosov Moscow State University, Russian Federation

Threshold erosion fracture of aero engine blades

I. Smirnov, G. Volkov, Yu. Petrov, L. Witek, A. Bednarz, N. Kazarinov
i.v.smirnov@spbu.ru

Abstract

A model of erosion wear of blades at threshold velocities of incidence of abrasive particles is presented. In the model the Hertzs classical impact theory is used for modeling the contact interaction of a particle with an elastic half-space. The incubation time fracture criterion is applied for predicting surface fracture.

1 Introduction

Foreign object damage (FOD) is a significant threat on aero engine components. Sources of FOD can be sand particles of various size [1]. However, this particles are small and their impacts will not lead to immediate failure, but may reduce the service life of the component.
The impact speed of dust particles to the surface of the blade greatly affects the magnitude of wear. Obviously, the greater speed of the particle and/or the greater particle size lead to greater wear of the blade. However, the theoretical dependences of blade erosion on a velocity of impact and a particle size are undetermined.
In this work we consider erosion damage of blades by combination of the Hertz problem solution and the incubation time criterion [2]. The aim of the work is to construct a model to predict the threshold erosive wear of blades at different speeds and sizes of abrasive particles.

2 Problem Formulation

Assume that the aircraft is on the ground with running engines. Sand and dust particles are sucked into the engine and falling to the turbine blades. Assume that the particles are identical and have a spherical shape and fall perpendicularly to the blade surface.
The interaction of the particle and the blade can be modeled by solving the contact problem of an impact of a spherical particle of radius R and initial velocity V with a half-space (Hertz problem) [2, 3] . According to the second law of Newton, the equation of particle displacement is as follow:

$$m\ddot{x} = F \tag{1}$$

where m is particle mass; F is determined by the elastic response of the blade. Let us use the Hertzian theory to find it:

$$F = -kx^{3/2}, k = \frac{4}{3}\frac{\sqrt{R}E}{(1-\nu^2)} \tag{2}$$

where E and ν are the Young modulus and the Poisson ratio of the blade.
Assume the initial conditions are the following:

$$x(0) = 0; \dot{x}(0) = V. \tag{3}$$

Hertz solution for the contact problem give the following expression for radial stress:

$$\sigma(t, V, R) = \frac{1-2\nu}{2\pi}\frac{k}{R}\sqrt{x_0 \sin\frac{\pi t}{t_0}} \tag{4}$$

where x_0 is the maximum depth and t_0 is impact duration.
To assess the possibility of fracture in conditions of an erosion process we use the incubation time criterion:

$$\max_t \int_{t-\tau}^{t} \sigma(s)ds \leq \sigma_c \tau \tag{5}$$

where $\sigma(t)$ is the current tearing stress; σ_c is the material static strength, and τ is the brittle fracture incubation time. The incubation time is considered as a physical constant of the material describing the duration of preparation of the medium to fracture or a phase transition, which can be determined experimental or theoretically.
The application of the criterion (5) allow to analyze the behavior of threshold (the minimal external effects causing fracture) characteristics of fracture, such as threshold speed V^* of particle impact.
The determining criteria relation has the form of following equality:

$$f(V, R, \tau) = \max_t \int_{t-\tau}^{t} \sigma_r(V, R, s)ds - \sigma_c\tau \tag{6}$$

where σ_r is the maximal (radial) tearing stress at the surface points adjoining the contact area.
After simplification (6) takes the form

$$\frac{1-2\nu}{2\pi}\frac{k}{R}\sqrt{x_0}\int_{\frac{\lambda-1}{2}}^{\frac{\lambda+1}{2}} \sqrt{\sin\frac{\pi}{\lambda}}[H(\tilde{t}) - H(\tilde{t}-\lambda)]d\tilde{t} = \sigma_c \tag{7}$$

where λ is dimensionless parameter, and it can be expressed through V and R:

$$\lambda = \frac{t_0}{\tau} = \left(\frac{5\pi(1-\nu^2)}{4}\right)^{\frac{2}{5}} \frac{\rho^{\frac{2}{5}}R}{\tau E^{\frac{2}{5}}V^{\frac{1}{5}}}$$

and

$$\frac{1-2\nu}{2\pi}\frac{k}{R}\sqrt{x_0} = \frac{1-2\nu}{2\pi}\left(\frac{5}{3}\pi\right)^{\frac{1}{5}}\left(\frac{4}{3(1-\nu^2)}\right)^{\frac{4}{5}} V^{\frac{2}{5}}\rho^{\frac{1}{5}}E^{\frac{4}{5}}$$

The incubation time of fracture for a material can be found by solving (7) for τ if threshold impact speed V^* of the particle with the radius R is known. Thus, having determined τ, we can predict the impact threshold speeds for particles of an arbitrary size.

3 Results

Figure 1 shows the dependence of the threshold speed of erosion fracture for martensitic steel EI736 [4] on the diameter of erodent particles. This dependence has static and dynamic branches. The static (horizontal) branch has a weak dependence of the threshold speed on the particles diameter. The dynamic branch shows a rapid growth of the threshold speed upon a decrease in the particle size.

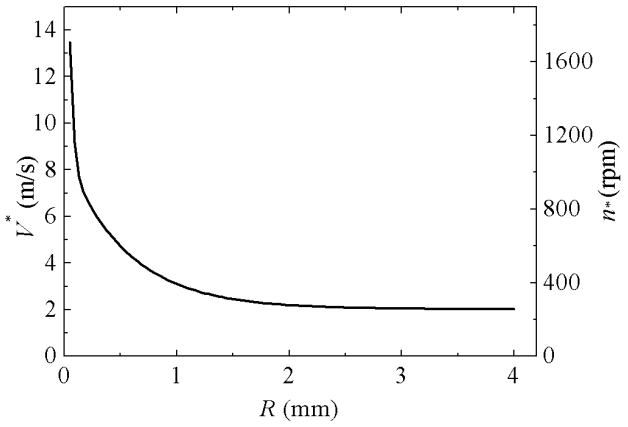

Figure 1: Dependence of the threshold particle (turbine) speed on the particle radius. The speed calculated for points in the centre of the 50 mm blade. The calculated parameters are $\sigma_c = 932$ MPa, $\tau = 10$ μs.

4 Conclusions

This work deals with the problem of erosion damage of engine blades when a blade surface is impacted with abrasive sand particles at the right angle. The Hertzs classical impact theory is used for modeling the contact interaction of a particle with an elastic half-space. To determine the threshold velocity of the particles at which the blade surface does not incur erosive fracture, the incubation time dynamic fracture criterion is applied. The constructed model allows to predict the threshold erosive wear of blades at different speeds and sizes of abrasive particles.

For the development of this work it is expected to consider the influence of different angles of impact and temperature on the threshold velocity of erosion damage of aero engine blades.

Acknowledgements

This work was supported by FP7 EU MARIE CURIE Project TAMER No. 610547

References

[1] E. Silveira, G. Atxaga, A.M. Irisarri. Failure analysis of a set of compressor blades. Engineering Failure Analysis 15 (2008) 666-674.

[2] Yu.V. Petrov and V.I. Smirnov. Interrelation between the threshold characteristics of erosion and spall fracture. Technical Physics 55 (2010) 230-235.

[3] I.I. Argatov, N.N. Dmitriev, Yu.V. Petrov, and V.I. Smirnov. Threshold erosion fracture in the case of oblique incidence. Journal of Friction and Wear 30 (2009) 176-181.

[4] L. Witek, M. Wierzbinska, A. Poznanska. Fracture analysis of compressor blade of a helicopter engine. Engineering Failure Analysis 16 (2009) 1616-1622.

Ivan Smirnov, Saint Petersburg State University, St. Petersburg, Russia
Grigory Volkov, Saint Petersburg State University, St. Petersburg, Russia
Yuri Petrov, Saint Petersburg State University, St. Petersburg, Russia
Lucjan Witek, Rzeszow University of Technology, Rzeszow, Poland
Arkadiusz Bednarz, Rzeszow University of Technology, Rzeszow, Poland
Nikita Kazarinov, Saint Petersburg State University, St. Petersburg, Russia

Numerical simulation of the effect of softening in materials on changes in the stress-strain state of elastomeric articles

Alexander K. Sokolov, Alexander L. Svistkov, Lyudmila A. Komar, Vladimir V. Shadrin, Viktor N. Terpugov
aleksandr_sokol@mail.ru

Abstract

The paper explores the necessity of taking into account the effect of softening encountered in rubbers (Mullins effect) during physical and numerical modeling of industrial rubber articles. For more precise computations, the Ogden-Roxburgh model is modified by changing constants to functions found from the analysis of experimental data. The modified model implemented in commercial package ANSYS allows us to perform a comparative analysis of changes in the stress-strain state of a car tyre with and without taking into account the effect of softening in rubbers.

The effect of softening encountered in rubbers was first observed by Bouasse and Carriere (1903) for unfilled polymers [1]. Despite this fact, the influence of this effect on the stress-strain state of real products is frequently ignored when modeling and designing rubber articles. It is commonly recognized that incorporation of superfine filler particles into rubbers leads to a remarkable improvement in the strength and fatigue properties of the material. However, this also gives rise to an increased softening [2, 3]. In the present paper, we discuss the necessity of taking into account the effect of softening encountered in rubbers during physical and numerical modeling of industrial rubber articles and consider a suitable way to modify the Ogden-Roxburgh model for use in numerical simulations properties.

Experimental data concerning the mechanical properties of filled rubbers were obtained from cyclic tension tests with increasing amplitude. Experiments showed a significant change in the mechanical properties of rubber already in the region of moderate elongations (up to 1.5) (Fig. 1) [4].

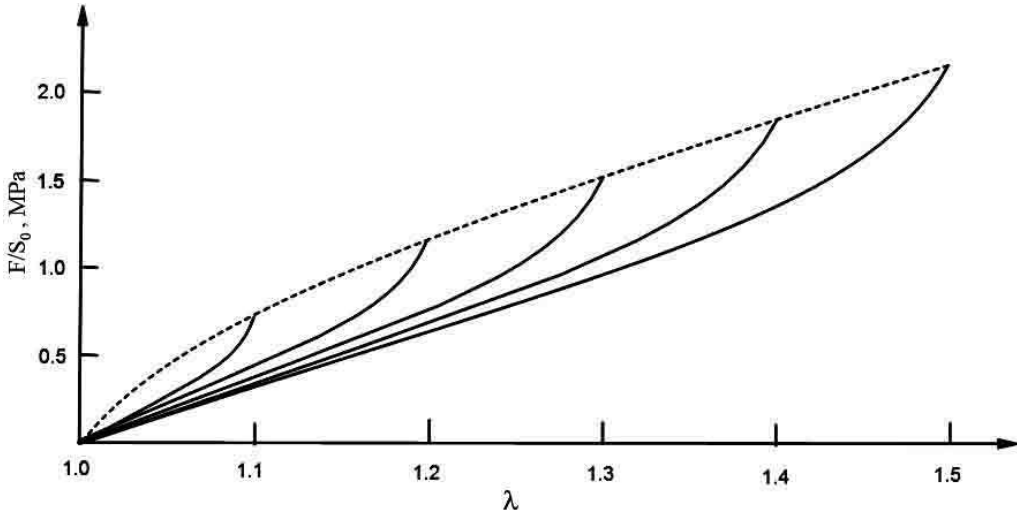

Figure 1: Experimental data obtained for rubber softening under uniaxial loading conditions. The dashed curve indicates the first cycle of loading, and the solid curves show unloading and subsequent loading of the softened material when the value of maximum elongation does not exceed that of elongation achieved during the previous deformation history of the material; F/S_0 — reduced stress; λ — elongation

In our investigation, we have used the Ogden-Roxburgh model describing rubber softening [5]. The strain energy density is split into deviatoric and volumetric parts and can be expressed as

$$U = \eta U_{dev} + U_{vol} + \phi(\eta),$$

where $\phi(\eta)$ is the function used to assess the amount of lost energy; η is the damage parameter. The function $\phi(\eta)$ has the form:

$$\frac{\partial \phi(\eta)}{\partial \eta} = \left(m + \beta U_{dev}^m\right) erf^{-1}\left(r(1-\eta)\right) - U_{dev}^m.$$

The damage of the material $\eta \in (0, 1]$ (at η=1, the material is assumed to be undeformed) is calculated by the formula [3]:

$$\eta = \begin{cases} 1, & \left[U_{dev} > U_{dev}^m\right] \\ 1 - \frac{1}{r} erf\left(\frac{U_{dev}^m - U_{dev}}{m + \beta U_{dev}^m}\right), & \left[U_{dev} < U_{dev}^m\right] \end{cases},$$

where $U_{dev}^m = max(U_{dev})$, $erf(x) = \frac{2}{\sqrt{\pi}} \int\limits_0^x e^{-\omega^2} d\omega$.

The parameters r, m, β can be determined using the experimental recession curves (Fig. 1): r, β are dimensionless; m characterizes the values of strain energy and has the dimensionality of energy; r is related to the degree of softening; β specifies the slope of the softening curve vs. the initial loading curve. When the strain energy reaches the value of the parameter m, the material begins to return to the initial loading curve. The case $m = 0$ is

unrealistic, because complete softening occurs in this case at indefinitely small deformations.

The influence of these parameters on the loading curve obtained for softened material was studied in a series of numerical experiments with MATLAB. The analysis indicates that the Ogden-Roxburgh model used in such commercial packages as ANSYS and ABAQUS is not nearly adequate enough for describing specific features associated with a softening effect encountered in rubbers. In particular, this model cannot be applied to describe the anisotropy of the softening effect. What is more, in the case of high strain data scattering a single set of parameters describes the Mullins effect with significant error. In order to obtain softening curves needed for precise computations, the Ogden-Roxburgh model was modified by changing parameters to special functions fitted to particular loading curves for a wide range of deformations.

The method proposed todescribe the Mullis effect (including changes produced in the Ogden-Roxburgh model) was implemented in the package ANSYS. The developed algorithms made it possible to perform computational experiments devoted to virtual modeling of the motion of a car tyre on a road with and without taking into account rubber softening. The experiments demonstrated that the degree of softening was different in these two cases. Therefore, the stress-strain state of the tyre should be evaluated at each point of its diameter with account for different degree of softening (Fig. 2). The mechanical properties of the tyre were assumed on condition that the car tyre was manufactured from the composite material.

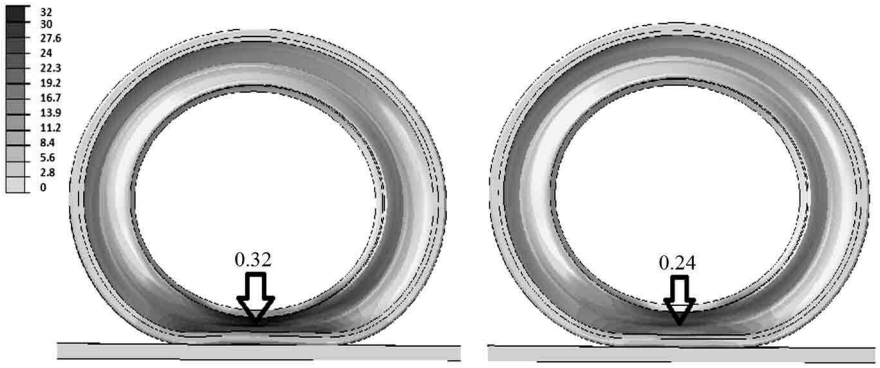

Figure 2: Distribution of the left stretch tensor fields found with (a) and without (b) taking into account the Mullins effect

Conclusions

Computational experiments show that the softening effect in real rubber materials has a profound influence on the stress-strain state of a car tyre and therefore it should be taken into account when developing the design of a car tyre.

Acknowledgements

The study was supported by RFBR and Perm Ministry of Industry of Innovations and Science (grant 13-01-96016 r_urals_a and grant 14-08-96013 r_urals_a), and the Ministry of Education of Perm Region under agreement C-26/627.

References

[1] Bouasse H, Carriere Z. // Ann. Fac. Sci. Toulouse, 1903. V. 5. P. 257–285.

[2] Mullins L., Tobin N.R. Stress softening in rubber vulcanizates. Part I. Use of a strain amplification factor to prescribe the elastic behavior of filler reinforced vulcanized rubber // J. Appl. Polym. Sci., 1965. V. 9. P. 2993–3005.

[3] Patrikeev G.A. Glava XXII. Tekhnologiia kauchuka i reziny. V kn. Obshchaia khimicheskaia tekhnologiia / pod red. S.I. Vol'fkovicha. – M.-ЦIL.: Gosudarstvennoe nauchnoЦItekhnicheskoe izdatel'stvo khimicheskoi literatury, 1946. T. 2. C. 361Ц–427.

[4] Sokolov A.K., Shadrin V.V., Svistkov A.L., Terpugov V.N. Raschet napriazhenno-deformirovannogo sostoianiia avtomobil'noi shiny // Vestnik Permskogo Universiteta. Ser.: Matematika. Mekhanika. Informatika, 2014. T. 2 (25). C. 64–Ц68.

[5] Ogden R.W., Roxburgh D.G. A pseudo-elastic model for the Mullins effect in filled rubber // Proceedings of the Royal Society of London, 1999. V. 455. P. 2861–2877.

Alexander K. Sokolov, Institute of Continuous Media Mechanics UB RAS, Perm, Russia
Alexander L. Svistkov, Institute of Continuous Media Mechanics UB RAS, Perm, Russia, State National Research University, Perm, Russia
Lyudmila A. Komar, Institute of Continuous Media Mechanics UB RAS, Perm, Russia
Vladimir V. Shadrin, Institute of Continuous Media Mechanics UB RAS, Perm, Russia, Perm State National Research University, Perm, Russia
Viktor N. Terpugov, Perm State National Research University, Perm, Russia

Modeling of viscoelastic strain and creep for hardening structures based on cement under temperature gradients

Eleonora P. Solonenko
el-solonenko@yandex.ru

Abstract

During the hardening period, materials based on cement experience deformation due to heat generation and moisture movement or internal consumption of water by cement. All these processes influence the change of material volume. As a result, these factors can lead to water tightness problems, durability problems and damage due to frost, which means that numerical simulation of its properties is important problem. So, in order to predict and prevent these problems, a numerical model should be developed in a proper way. For example, accurate consideration of heat generation and heat loss should be incorporated to calculate the temperature distribution gradients. The first goal of the research is to present numerical model of temperature calculation and then using this data to estimate thermal dilation and autogenous shrinkage during the contraction phase. As is well known, creep also influences on stress state for hardening materials and is a relaxation factor during the cooling period. Finally, the aim is to model a creep effect.

1 Introdiction

As is well known early age concrete behaviour may lead to crack initiation within structures. Scientists have explained it by happening of the high thermal stresses within massive concrete elements. Such measure as using the cooling of the structure has resulted, in some cases, in the surface cracks due to the internal restraints. All these processes happen due to the volumetric deformation within casting concrete structure. and can result in deterioration and damage in structure or degradation of the serviceability. Meanwhile, the presence of cracks and their propagation should be controlled in the details. Generally, to predict and prevent deterioration mechanisms it is significant to model early age deformation in casting concrete and understand the mechanism of deformation occurrence.
The total deformation in young concrete consists of stress-dependent and stress independent deformations. Two driving forces such as thermal dilation and shrinkage are included in the stress-independent deformation and creep effect makes a contribution in stress independent deformation. These deformations depend on the temperature history. There are two methods of determination of the temperature distribution in a structure. One of them is to solve the heat transfer equation, another is applying the heat balance. The describing

of these methods for young concrete could be find in references literature [1] – [3]. In this paper the heat balance is used for finding of the temperature field.
The empirical equations for estimation of the concrete shrinkage have been developed in many theses. E.Holt [4] has described the understanding of the mechanisms due to shrinkage under no moisture movement from or to surroundings (autogenous shrinkage). H.Hedlund [5] has shown the evaluation of shrinkage in three different ways. For example, as a function of relative humidity, based on degree of reaction and combining these methods. In the article, modelling of shrinkage was made by maturity function without moisture transfer through a structure.
The investigation of creep could be carried out by different methods, such as Rate of flow method (RF), Effective modulus method (EM) , Method of superposition, Rate of Creep method (RC), Improved Dischinger method (ID), Trost-Bazant method (TB), Rheological models (RM) and Double power law (DPL) model. In the paper, the calculations of creep effect are made by DPL-model.
The main task here is to develop the model for accurate calculations of stress-dependent and stress-independent deformations.

2 Model for temperature profile

As was mentioned in the introduction the distribution of the temperature is determined by the heat balance between the heat development due to the hydration reactions and heat loss with surroundings.
The factors affect the temperature distribution in the young concrete are:

1. thermal properties (heat of hydration, conductivity and heat capacity);
2. geometry and size of structure;
3. boundary conditions (air temperature, formwork, insulation, and etc);
4. initial conditions (fresh casting temperature).

Hydration process could be presented through the hydration degree which is determined as the ratio of the hydration heat to the ultimate hydration heat.

$$\alpha(t) = \frac{Q(t)}{Q_u(t)}$$

where $\alpha(t)$ is the degree of hydration at time t, Q(t) is the heat of hydration at time t, $Q_u(t)$ is the ultimate heat of hydration.
Heat of hydration is presented as exponential function in the form [6]

$$Q(t) = Q_\infty \cdot e^{\left[-\left(\frac{\tau}{M(t)}\right)^\alpha\right]}$$

where Q_∞ is the total value of the heat generation, τ and α are the model parameters, M(t) is the maturity function describing the effect of the temperature on the rate of the heat reactions.
Maturity function based on Arrhenius equation is written as [7]

$$M(t) = \int_0^t e^{-\frac{E(T)}{R}\cdot\left(\frac{1}{T(\tau)}-\frac{1}{T_{ref}}\right)} \cdot d\tau$$

where E(T) is the activation energy and equal to

$$A + B \cdot (T - 20) \text{ for } T > 20^{\circ}\text{C or } A \text{ for } T < 20^{\circ}\text{C},$$

T_{ref} is the reference temperature, T(τ) is the function of the temperature, R is the universal gas constant.
In this paper, it is proposed that the heat loss from structure to surroundings takes place due to convection. Newton's law defines the heat transmission to surroundings as

$$q = h_c \cdot (T_S - T_A)$$

where q is the convective heat flux per unit area A, h_c is the convective coefficient, T_S and T_A are the surface temperature against environmental temperature. Regarding the different temporary covers the equivalent convective coefficient h'_c is found as [8]

$$h'_c = \frac{1}{h \cdot A} + \sum_{i=1}^{n} \frac{L_i}{k_i \cdot A}$$

where L_i is the thickness of i-curing cover and k_i is the conduction coefficient of i-material. Regarding the initial conditions, next conditions are used

$$T(x, y, t_0) = T_0$$

Finding the temperature profile with regarding the affects described early are made by the next equation

$$T = T_{init} + \int dT_{dev} - \int dT_{loss}$$

where T_{init} is the casting temperature, $\int dT_{dev}$ expresses the increase of the temperature due to the chemical reactions, $\int dT_{loss}$ expresses the decrease of the temperature due to the heat loss.

3 Model for stress-independent deformation

In the hardening concrete, there are two driving forces involves the time-dependent deformation that influence the crack initiation. If we consider isothermal conditions (T=const), autogenous shrinkage effects alone, under normal conditions, where temperature changes occasionally, thermal dilation and autogenous shrinkage operate to produce stresses [3]

$$\varepsilon_{tot} = \varepsilon_T + \varepsilon_{as},$$

where ε_{tot}— total deformation, ε_T — thermal deformation and ε_{as}— autogenous shrinkage. Larson's method can be used to describe the thermal deformation in the details. This method applies only for contraction phase and does not consider the warm period. Tensile stress occurs from Ysecond zero stress time t_2Y and after Ysecond zero stress temperature T_2Y .
Time t_2 is more than time t_1 when structure starts cooling (see Fig. 1) and could be expressed as [9]

$$T_2 - T_s = k_2 \cdot (T_1 - T_s)$$

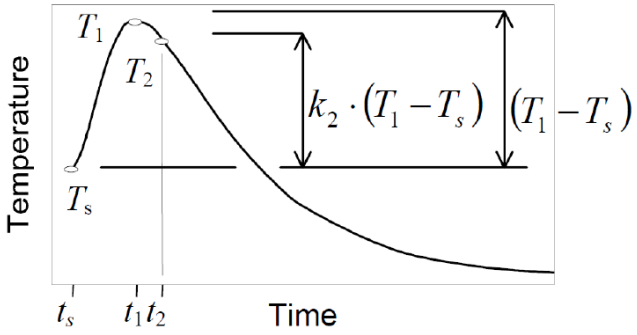

Figure 1: Temperature distribution in hardening period. Tensile stress occurs after time t_2 .

where T_s is the temperature corresponding to time t_s, T_1 is the maximum temperature on the surface of the structure and $k_2 = 1.41 - 1.36 \cdot (w/b)$.
k_2 - factor as we could notice depends on the cement type and has been developed in Sweden. After calculation T_2, at a given point of time t_3 ($t_3 > t_2$), thermal dilation is found as [3]

$$\varepsilon_T = \alpha_T \cdot (T_3 - T_2)$$

where α_T is the thermal expansion coefficient.
The thermal expansion coefficient α_T depends on the type of aggregate and as a literature indicates is in range of $(5.6 - 13) \cdot 10^{-6}$ $1/°C$, but if α_T is unknown, in this case, standard value $10 \cdot 10^{-6}$ 1/°C is used for calculations.
In the hydration process, in spite of the thermal deformation the changes in volume may exist due to shrinkage which occurs because of the moisture transfer through a structure or internal consumption of water by cement. Process of a concrete volume change when moisture flow is negligible is called autogenous shrinkage. It is only a result of internal chemical and structural reaction of the concrete composition.
The evaluation of the autogenous shrinkage is determined, in this paper, as a time function based on the hydration rate. The autogenous shrinkage starts to develop is in the interval from 9 to 24 hours. As a rule, starting time for autogenous shrinkage development is usually chosen to be 24 maturity hours after casting. The autogenous shrinkage $\varepsilon_{sh}(t)$ as a function of time may be written as [5]

$$\varepsilon_{sh}(t) = \varepsilon_{su} \cdot \beta_{s0}(t) \cdot \beta_{ST}(T)$$

where ε_{su} is the final value (ultimate) of autogenous shrinkage,
$\beta_{s0}(t)$ is the relative time of autogenous shrinkage development,
t is the age of concrete.
Distribution of the autogenous shrinkage as a function of time is expressed [5]

$$\beta_{s0}(t) = e^{-\left(\frac{t_{s0}}{t - t_{start}}\right)^{\eta_{sh}}}$$

where t_{start} is the starting time of autogenous shrinkage development (arbitrary time, but not before t_0),
t_{s0}, η_{sh} are the empirical constants. For different concrete composition, these values could be taken from paper [5].
The temperature effects on the autogenous shrinkage may be defined by [5]

$$\beta_{ST}(T) = a_0 + a_1 \cdot (1 - \exp(-(T/T1)^{b1})) + a_2 \cdot (1 - exp(-(T/T2)^{b2}))$$

The total deformation from time t_2 to t_3 is figure out in the next form [3]

$$\varepsilon(t_2, t_3) = \varepsilon_T + \varepsilon(t_2, t_3)$$

4 Model for stress-dependent deformation

When concrete is subjected to constant loads, further deformations will develop after the instantaneous deformation. This phenomenon, of the viscoelastic behaviour, is well known as a creep. Fig.2 shows that the creep is partly reversible deformation. Reversible deformation is relatively small, but it is significant to consider the viscoelastic behaviour of the immature concrete in order for accurate calculations.

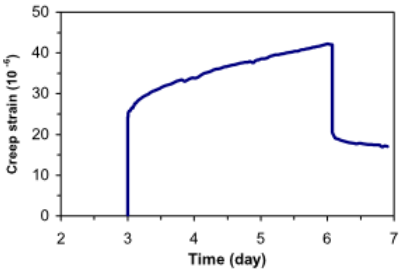

Figure 2: Compressive creep and creep recovery of a HPC specimen.

In this investigation, Double power law (DPL) is used and the basic creep of concrete is determined by the creep function as [3]

$$J(t,t') = \frac{1+\phi(t,t')}{E(t'_e)} \text{ and } \phi(t,t') = \phi_0 \cdot t'^{-d} \cdot (t-t')^p$$

where t_e is the maturity function (or equivalent time), t'_e is the maturity time at loading. t is the actual time, t' is the actual time when the stress increment is applied, and ϕ_0, d and p are the DPL model parameters.
Deformation reflects the creep could be written in the next way

$$\varepsilon = \int_0^t J(t,t') \cdot d\sigma(t')$$

5 Simulation results

In this research the infinite wall is considered. It means that only the wall thickness is considered in calculations. Calculations are made for 28 days. Input data are used for concrete B65. The wall thickness is equal to 4m, the insulation thickness is equal to 0.012m (see fig.3). Thermal conductivity of wood and for hardening concrete are equal to 0.67 kJ/(m·h·°C) against 5.9 kJ/(m·h·°C). The heat capacity is equal to 0.84 kJ/(kg·°C). The analyzed concrete wall consists of cement density - 450 kg/m^3, water density - 160 kg/m^3 and the total density of the concrete mix is equal to 2610 kg/m^3. It is supposed that in 28 days after casting the wooden insulation is removed . In accordance with the hydration model next parameters are used: $\alpha = 2.45, \tau = 10.99$ h and $Q_\infty = 314$ kJ/kg cem. For calculations of the activation energy A=33.5 kJ/mol and B=1.47 kJ/mol·°C.

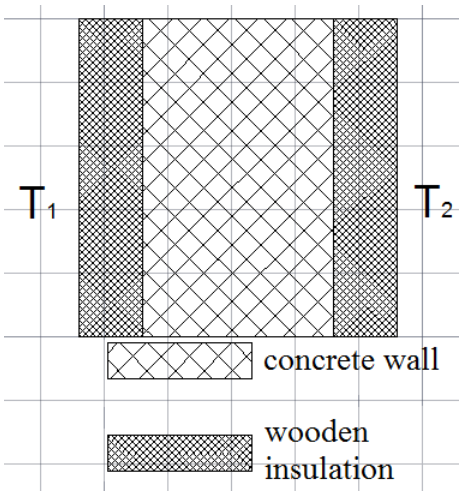

Figure 3: The scheme of the concrete wall.

The total strain involves in the stress independent deformation is calculated by using the next coefficients:t_{s0}=120 h, t_{start}=24h, η_{sh}=0.3, a_0=0.4, a_1=0.6, a_2=0.1, b1=2.9, b2=7, T1=9°C, T2=55°C. Calculations of the creep effect based on the next parameters:ϕ_0=0.33, d=0.27, p=0.56.
The modelling of the temperature and deformations are carried out under different environmental temperatures T_1 and T_2 (see.Fig. 3) where T_1=12°C and T_2=16°C. The initial temperature of the concrete wall is equal to 15°C.

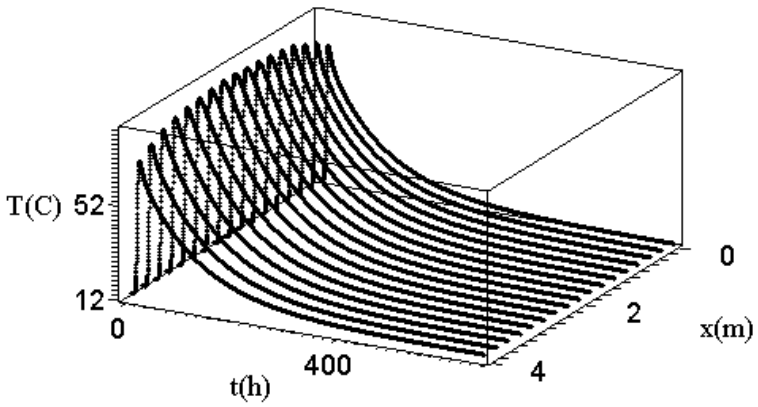

Figure 4: Surface of the temperature distribution through a wall .

Fig. 4 represents the changes in temperature in a wall over the time. Various temperatures in massive concrete occur because hydration, i.e. exotic reactions generated huge amount of heat. The core of the massive concrete elements become hot due to concrete has low thermal conductivity and then it cools down due to dominate of heat loss under heat of hydration. In 28 days the the temperature profile is a linear function.
Graph 5 shows the autogenous shrinkage against thermal deformation. The total strain, in accordance with the equation - $\varepsilon(t_2,t_3) = (T_3 - T_2)\cdot\alpha_T + \varepsilon(t_2,t_3)$ is a little bit more than the thermal strain.
According to DPL-model creep function is calculated and shown on the Fig. 6
Proposed model for the calculations of the thermal strain and viscous deformation as a

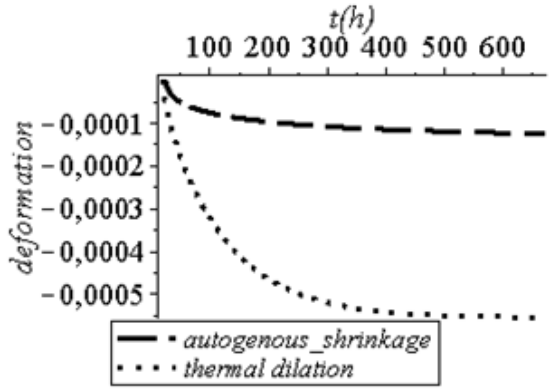

Figure 5: Parts of time-independent deformation.

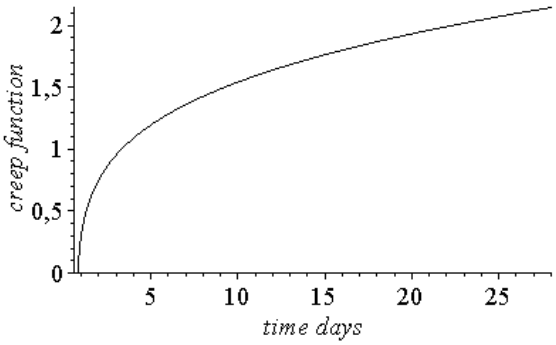

Figure 6: Creep function.

creep in the concrete wall allows to make thermal-stress analysis for concrete wall more accurately.

Acknowledgements

The paper was done as a part of the research project with collaboration of FEFU, NTNU and KVERNER and financed by Norwegian University of Science and Technology and Federal special purpose program event 1.2 Agreement є 14.575.21.0009 ID number RFMEFI57514X0009.

References

[1] Ch.Wang, D.H. Dilger. Prediction of temperature distribution in hardening concrete, in: RILEM Proceedings 25. Spingenschmid(Ed.),Thermal cracking in concrete at early ages, E & FN Spon,London, 1994, pp. 21-28.

[2] J.-E.Jonasson. Modelling of temperature, moisture and stress in young concrete.Ph.D. Thesis, Lulea University of technology, Lulea, 1994.

[3] O. Bjontegaard. Basis for and practical approaches to stress calculations and crack risk estimation in hardening concrete structure. State of the art report. Draft COIN-report, FA 3.1 Crack free structures. 2011-09-21, 96 p.

[4] E. Holt. Early age autogenous shrinkage of concrete. Technical research centre of Finland. Espoo. 2001, 197 p.

[5] H.Hedlund. Hardening concrete: measurements and evaluation of non-elastic deformation and associated restraint stresses. Doctoral Thesis. Division of Structural Engineering, Lulea University of Technology, S-971 87 Lulea, Sweden. December 2000. 414 p.

[6] Smeplass, S. translation by E. Moen, S. Jacobsen. TKT 4215 Con-crete technology 1,Curing technology, Trondheim, Institutt for kon-struksjonsteknikk, NTNU, Chapter 11, pp 1-24.

[7] Azenha, M., Faria, R., Ferreira, D. Identification of early-age con-crete temperature and strains: Monitoring and numerical simulation¥ Cement & Concrete Composites 31 (2009) pp.369-378.

[8] Faria, R., M. Azenha, and J. A. Figueiras. Modelling of concrete at early ages: Application to an externally restrained slab, Cement and Concrete Composites, Vol. 28, pp. 572-585.

[9] M.Larson. Thermal crack estimation in early age concrete. Models and methods for practical application. Doctoral thesis. March 2003.

Eleonora P. Solonenko, Vladivostok, Russia

Hardware-In-the-Loop Modeling system of flight control of the spacecraft "Luna-Glob" at the stage of the automatic landing on the Moon

O. Trifonov, A. Tuchin, D. Tuchin, V. Yaroshevskiy
tob@keldysh.ru

Abstract

The Russian space program lunar exploration involves automatic soft landing on the moon surface of the spacecraft (SC) "Luna-Glob". On-board control system of motion SC is created to implement this task. Integrated on-board computer system is processed measurements of two sets of inertial units, velocity and range Doppler devices. The output parameters of computer system are using for control of SC jet engines: correction and brake, two engines soft landing, four engines correction and stabilization and eight engines stabilization. The HILM system of flight control enabled to begin debug stage of the automatic landing software prior to the creation and assembly of complete sets of equipment SC "Luna-Glob".

Introduction

According to Russian Lunar space program вГЁLuna-GlobвГ№ spacecraft should perform automatic soft landing on Moon surface. Onboard propulsion control software (OMCS) is developed for this purpose. Onboard propulsion control software should function as a part of integrated onboard computer (BIVK) in real-time mode. BIVK performs trajectory measurementsвГЄ processing and then generates commands for engine control system. Development and debugging of complex algorithms for onboard devicesвГЄ control is needed to perform onboard software verification. Usually this problem is handled after spacecraft had been constructed and tested. This research suggests parallel software verification and onboard hardware development.

1 Structure of propulsion control system

Propulsion control system is on of onboard control complexвГЄs (OCC) subsystems. Where:
1 - Electronic unit of drive control,
2 - Pyrotechnics explosion and automatics unit,
3 - Onboard Radio Complex.,
4 - Control Assembly,

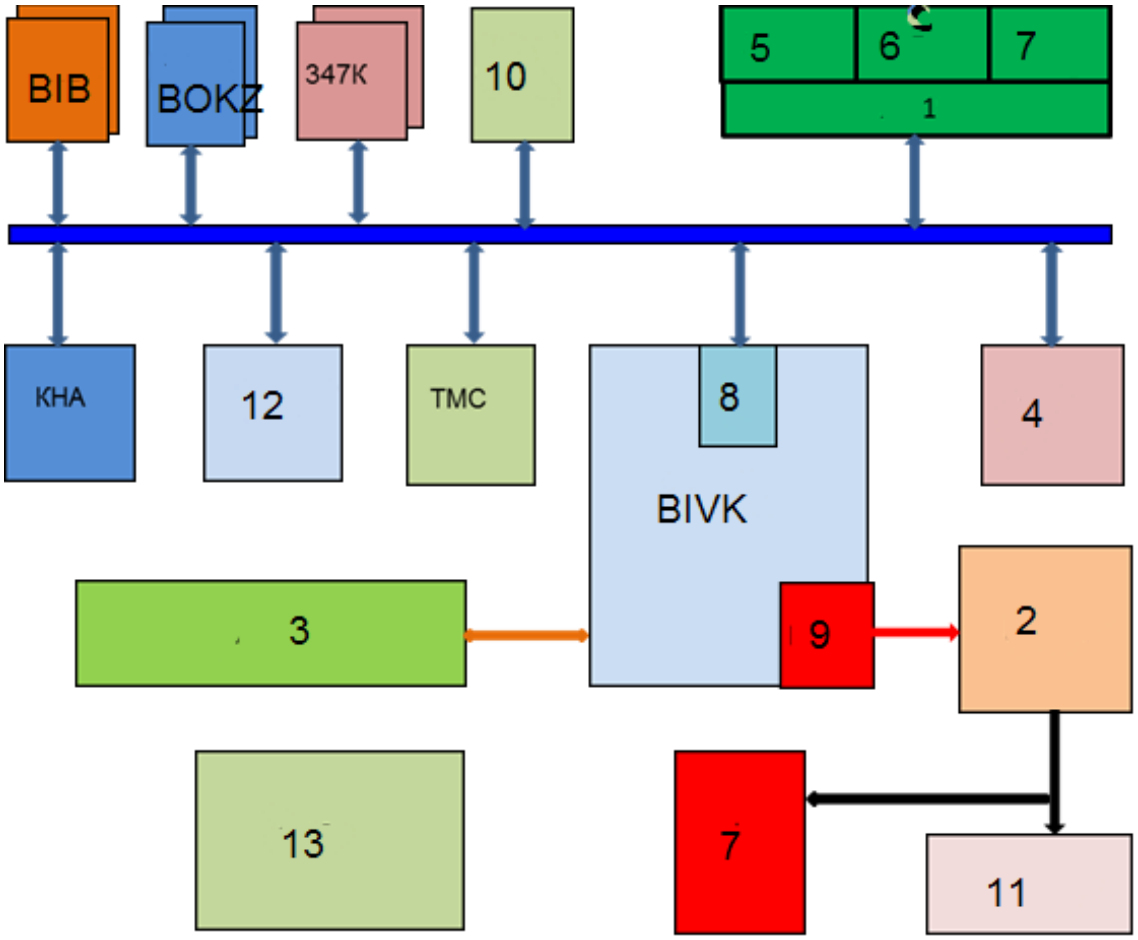

Figure 1: Luna-Glob spacecraft onboard systemsвҐЄ scheme

5 - Antenna attitude control unit (operates after landing),
6 - Correcting and braking engine thrust control unit,
7 - Jet engines,
8 - Controller,
9 - Relay command matrix,
10 - Remote terminal,
11 - Thermal regimes maintenance facilities,
12 - The TV shooting,
13 - Power supply system,

Spacecraft propulsion control system includes:
- Integrated onboard computer (incorporating two subsets) includes,
- Measuring equipment:
+ Two subsets of solar sensors;
+ Two subsets of unit positioning BOKZ stars;
+ Two subsets of strapdown inertial unit BIB;
+ Doppler velocity and distance meter DISD;
- BIVK software performing measuring toolвҐЄs information filtering and processing, calculation of spacecraftвҐЄs orientation in inertial space and various reference frames, cal-

culation of algorithm controlling parameters, elaboration of controlling criterions or commands;
- Executing tools:
+ 1 correction and engine brake (KTD);
+ 8 stabilizing engines;
+ 4 correcting and stabilizing engines ;
+ 2 soft landing engines;
- Surface contact detectors mounted on 4 landing legs.
Information from measuring tools goes to IOC via MIL-STP-1553 multiplex data bus system where IOC is bus controller and all measuring tools are remote terminals. All controlling criterions and commands made in IOC go via MIL-STP to Control Assembly which forms real-time commands for electric automatic units performing direct control of drive and electric pneumatic valves of engine unit. Spacecraft onboard systemsвГЄ block scheme is depicted in Fig 1.

To provide propulsion control systemвГЄs functioning onboard computer has to work within 50 Оёs time cycle. In one cycle onboard computer must receive information from measuring tools, perform its filtering and processing, complete calculations for controlling algorithms, form controlling criterions and commands and send it to Control Assembly [1].

2 вГЁLandingвГ№ propulsion control mode

вГЁLandingвГ№ session moves spacecraft from Lunar orbit to its surface. The session includes preparatory operations and some specific parts of propulsion control. That is why landing session includes three sequential stages: 3-axis stabilization, main braking mode and precise braking mode. Landing scheme is depicted on Fig. 2.
Expected landing sites are located in the Southern lunar hemisphere in BoguslavskyвГЄs crater. Several conditions should be met at the moment when landing legs touch lunar surface:
- Vertical speed must be in the range of 1 ... 3 m/s,
- Horizontal velocity should not exceed 1 m/s,
- Angle between spacecraft OX axis and gravitational normal vector should not overcome 7Bѳ,
- The direction of the spacecraft center to the earth should be located near the plane of the spacecraft XY plane.
Propulsion control in this session is performed with the help of onboard computer BIVK (two subsets), two astronavigation instruments BOKZ (on preparation stage), two subsets of strapdown attitude reference system (BIB) and Doppler velocity and distance meter during the terminal part. Spacecraft orientation at every part of landing session is defined by controlling algorithms with the help of information obtained from measuring tools [2].

3 Experimental testing of software and hardware models

Planning, organization and realization of every test at every stage of spacecraft вГЁLuna-GlobвГ№ unitsвГЄ experimental testing should take in account peculiarity of every single test in order to obtain maximum volume of information to comply with requirements

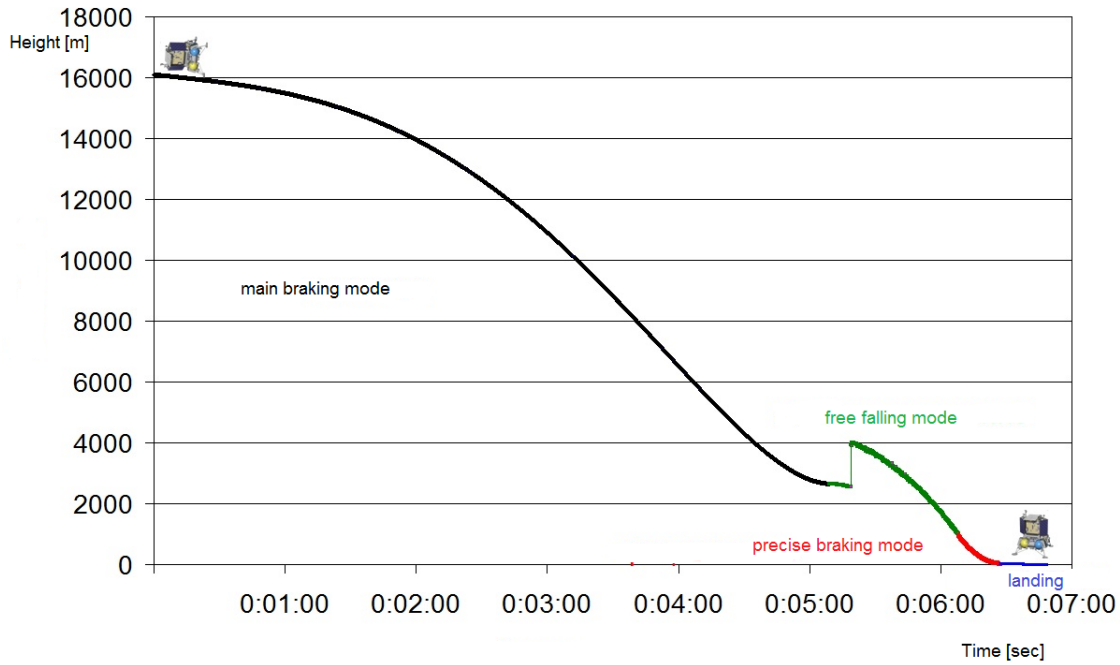

Figure 2: Landiing scheme

specification. A hardware and software modelling stand has been built at Keldysh Institute of Applied Mathematics in order to meet this objective.

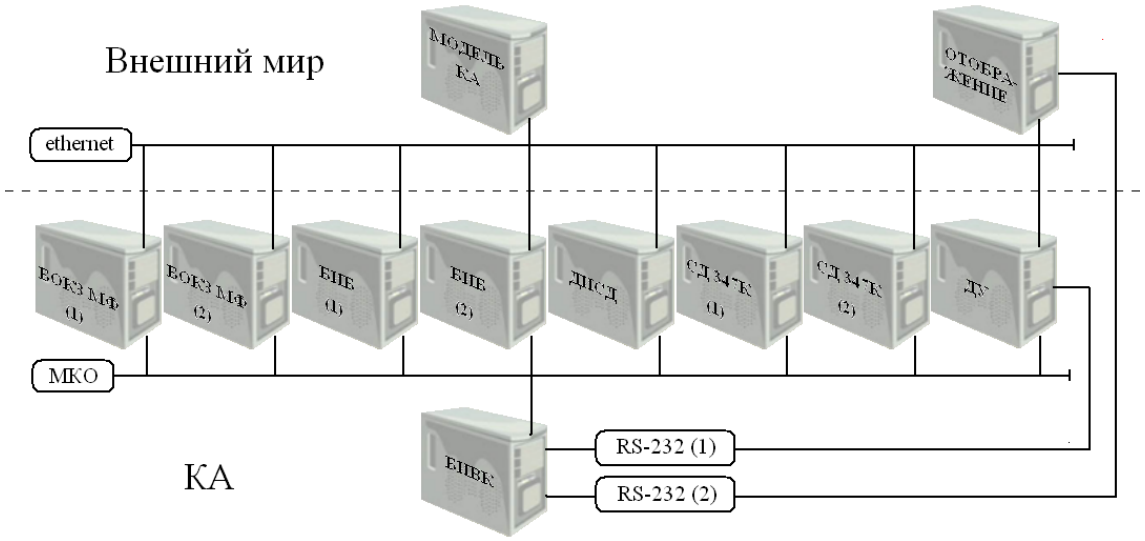

Figure 3: Testing stand structure

Stand structure depicted in fig. 3 includes hardware model of general MIL-STP-1553 data bus, general Ethernet bus and two technological RS232 channels. All engineering and simulation models are plugged to MIL-STP-1553 bus. Usage of spacecraft unitsвГЄ engineering models is limited due to limitations of their usage on Earth surface instead of

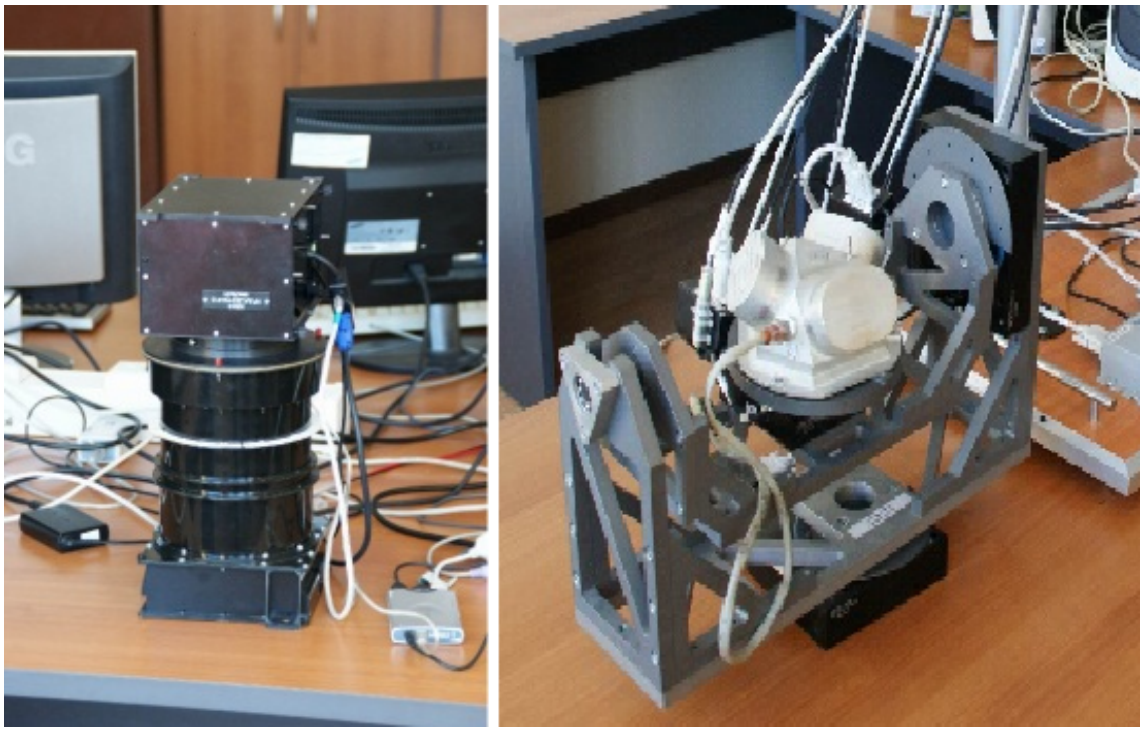

Figure 4: Engineering models of BOKZ astronavigation instrument and strapdown attitude reference system (BIB).

open space. That is why some units в Г Є engineering models are substituted by software simulation models.

Every software simulation model is a single PC with software simulating results that should be produced by unit в Г Є s engineering model. Information traffic between engineering models and software simulation models goes via MIL-STP-1553 data bus in real-time mode. General Ethernet bus and RS232 channels are used to load onboard software and for information transfer in order to synchronize calculation processes.

Stand depicted in fig. 5 is controlled by a separate PC working as a server. Modelling results visualization is performed on the other PC в Г Y it creates 3D graphics depicting landing process in real-time mode (see fig. 6).

Measuring tools mounting and orientation errors as well as functioning errors within requirements specifications for each tool have been variated during modelling process [3].

Conclusion

Hardware and software modelling allowed to perform propulsion control system software debugging before building whole Luna-Glob spacecraft which significantly shortens onboard software testing period. Hardware and software modelling stand developed in Keldysh Institute of Applied Mathematics has been used for assembled onboard software debugging in real-time mode with concurrent usage of spacecraft units в Г Є engineering models and their software simulation models.

Figure 5: General view of the testing stand

References

[1] Tuchin A. Parameter determination of the space craft motion by results of measurements provided a noise is in dynamic system // Preprint KIAM, 2004. Number 2, p 32.

[2] Lavrenov S., Michaylin D., Tuchin A., Tuchin D., Fitenko V.,Yaroshevskiy V. DISD mathematical model for the soft Lunar landing projects // Preprint KIAM, 2013. Number 68, p 15.

[3] Trifonov O., Tuchin A., Tuchin D., Yaroshevsky V. Stand of HIL system control test motion of the SC "Luna-Glob" on stage automatic landing on the moon// Proceed. of conf. "XXXIX Academic Conference on Astronautics", January 30, 2015, Moscow, Russia, pp. 246-247

O. Trifonov, Miusskaya sq.4, Moscow, Russia
A. Tuchin, Miusskaya sq.4, Moscow, Russia
D. Tuchin, Miusskaya sq.4, Moscow, Russia
V. Yaroshevskiy, Miusskaya sq.4, Moscow, Russia

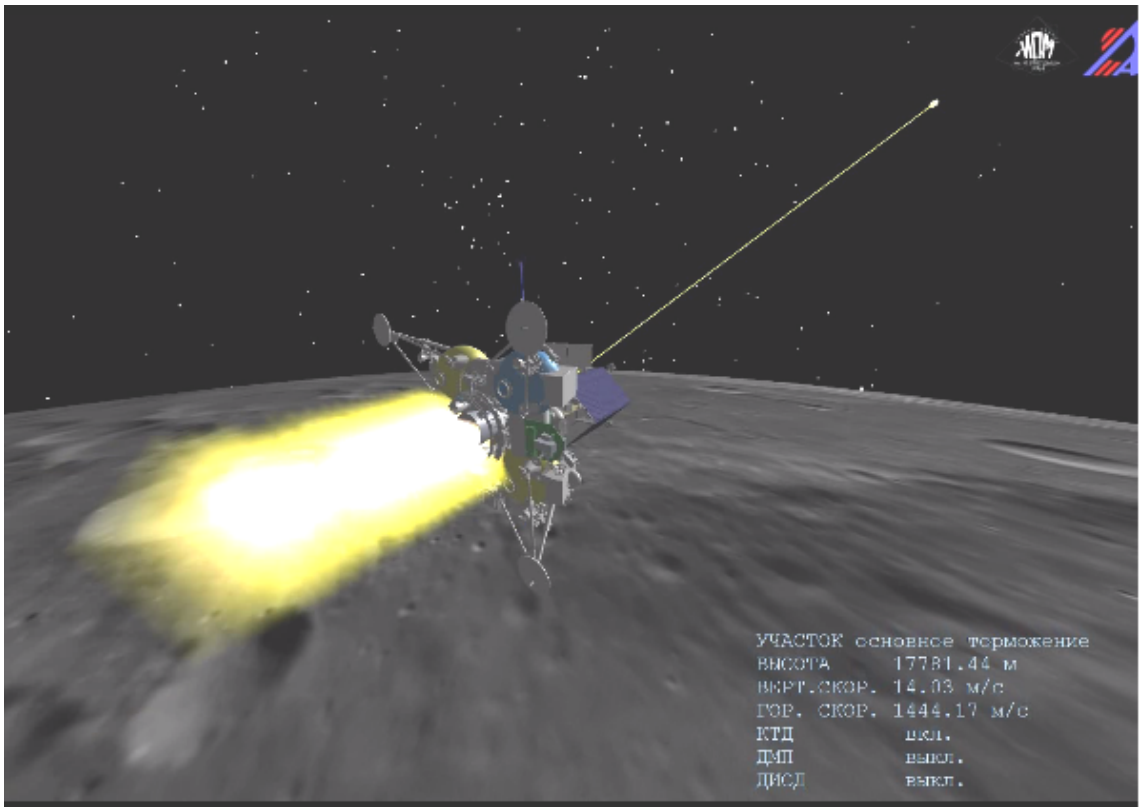

Figure 6: 3D visualization of Lunar landing session modelled by hardware and software modelling stand.

Method for extracting an equivalent Winkler model of the 3D dynamic soil-structure interaction of large-diameter offshore monopile foundations

W.G. Versteijlen, J.M. de Oliveira Barbosa, K.N. van Dalen, A.V. Metrikine
pim.versteijlen@siemens.com

Abstract

The motivation for this work stems from the offshore wind industry, where designers are faced with a discrepancy between the available design methods and the typical dimensions of the offshore wind foundations that call for other design approaches. Throughout the years, much valuable work has been performed in the prediction of long, slender, flexible piles which are most often

applied in the field. For the large-diameter rigidly behaving 'caisson' foundations, less methods are available. These two types of piles (flexible and rigid) interact in a fundamentally different way with the soil. The fact that the observed fundamental frequencies of installed offshore wind structures are higher than designed for, is believed to confirm the underestimation of stiffness associated with the often used 'p-y' design method.

For the damping related part, being it a more complex mechanism, there is even more uncertainty. As a result, conservative low damping ratios are assumed during design. Though it is less straightforward to measure the damping ratios of installed turbines, the published values range from a factor of 1 to 4 with respect to the value used in design. Like for stiffness, empirical relations were derived to estimate damping in the 1970s and 80s based on more advanced 2D and 3D models in combination with field tests and the previously mentioned p-y curves. Again, these relations are restricted to flexible piles, where the pile tip is assumed to be fixed.

To capture the interaction for the currently applied pile dimensions, it is necessary to simulate the 3D interaction between the pile and the soil, and perform full scale tests. The latter are not yet available, but results of a few campaigns are expected in the near future. Advanced 3D numerical models are available, and for the purpose of physical insight and for engineering applications, it is useful to extract a 1D equivalent model that can mimic the 3D simulation.

In this work, a linear elastic dynamic 3D FE model of a pile-soil system is used to extract the static and the frequency dependent displacements. The FE domain is surrounded with perfectly matched layers (PMLs) that absorb the propagating waves at the boundaries for the relevant frequencies of excitation. The soil properties of a design location are used, which have been identified using seismic measurements. A method for the derivation of a 1D equivalent dynamic stiffness (i.e., a Winkler model with distributed springs and dashpots) is derived thereafter. The results obtained with the 1D model for the static response and for a dynamic case are compared to the response of the 3D FE analysis.

1 Introduction

The fundamentally different behaviour between long, slender piles and those with a small ratio of embedded length L over diameter D is widely recognized. Many parametric studies have indicated that this L/D ratio, together with the ratio of the pile stiffness over the soil stiffness is what determines the characteristic response. Pile flexibility factors [1] and characteristic lengths [2] can be calculated to predict the typical response (whether rigid or flexible behaviour is to be expected). In general, piles with a small L/D ratio ($L/D < 7$ for most soil-steel stiffness combinations) bend in a rigid way, interacting on a more global scale with the soil, whereas the displacement and moment distribution of flexible piles can be attributed to local soil reactions. The motivation for the here presented work stems from the offshore wind industry, where rigid behaving foundations (with $4 < L/D < 7$) are designed based on design methods that were developed for flexible long piles with $L/D \approx 30$. In general it holds that many more thoroughly tested methods

have been developed for flexible piles (the most often applied type of pile) than for rigid behaving piles. Not much full-scale testing has so far been performed on rigid behaving piles; however, current numerical (Finite Element Methods (FEM)) competences are more and more capable of capturing the complex 3D nature that characterizes the global soil reaction [8]. This is not only the case for the static reaction; due to successful mitigation of reflections at the boundaries, also dynamic analyses can be performed with higher levels of confidence. Also complicated poro-elastic mechanisms (contributing to both the stiffness and damping characteristics of the soil-structure interaction (SSI)) have been modeled in 3D numerical models [3]. However, as previously mentioned the full-scale testing database needs to become available to fully validate the developed models.

The 3D models are well fit to capture a more realistic response for a certain load case. Nevertheless, their high computational cost makes them incompatible with engineering design. For instance, in the offshore wind industry up to 10.000 simulations of 10min-time responses are run for a single design location and iteration. Despite efficient upcoming numerical substructering techniques [4], it is for many designers not yet feasible to incorporate full 3D numerical models in these kind of design simulations. This is one of the reasons that a more simple and fast equivalent 'engineering' model is desired. The second reason would be the fact that due to the simplification, often more physical insight is gained in capturing the complex 3D nature in a 1D model. In this work, we choose to match the response with a 1D model (and not for instance, a lumped parameter model with discrete springs at the mudline) as this allows to assess the stress distribution in the embedded pile, which is also often assessed in design. Besides these advantages, the coupling terms between the translation and rotation are automatically incorporated.

Before we can build a 3D model, we need to find the continuum (soil) input parameters. This is shortly discussed in Section 2, where we advocate the use of seismic measurements (besides the usual geotechnical in-situ testing) to capture the dynamic properties of the soil. Section 3 gives a brief description of the linear elastic 3D model that incorporates material and radiation damping, and efficiently deals with the reflective boundary problem. Then, being the emphasis of this contribution, the translation method of both the static and the complex (dynamic) 3D modeled response into an equivalent 1D model is given in Section 4. Then, Section 5 closes the paper with a discussion on the presented results.

2 Soil characterization

In this paper we focus on the linear reaction regime of the soil, as it is this regime that defines the modal response of the support structure. To extract the linear elastic properties of a certain site, we suggest to perform in-situ seismic measurements along with the usual geotechnical testing procedures (i.e. Cone Penetration Tests (CPT) and laboratory test on borehole samples). The latter are useful for (local) strength parameters, stratification and density estimation, whereas the seismic measurements capture the true dynamic, small-strain characteristics of the soil.

We emphasize the advantage of *in-situ* seismic measurements because of two reasons: firstly, the in-situ characteristics are always disturbed when retrieving soil samples. Secondly, depending on the frequency of interest, it might be challenging to test soil samples in a laboratory without including sample-boundary effects. It is favorable to be able to capture at least one wave length within a sample, but for the low frequencies (< 1 Hz),

shear-wave lengths are typically in the order of several hundreds of meters ($\lambda = \frac{V_s}{f}$, with λ the shear wave length, V_s the shear wave velocity and f the frequency of interest).

Multiple seismic measurement set-ups exist, among which are Multi-Channel Analyses of Surface Waves (MASW), P&S logging, cross/down/up-hole measurements and the Seismic Cone Penetration Test (SCPT). All these tests have their own inversion techniques. In [5] an inversion method for SCPT data is given.

For this paper, we use a soil profile which was identified using SCPT data (to be published in the near-future). The elastic parameters of this profile are given in Figure 1.

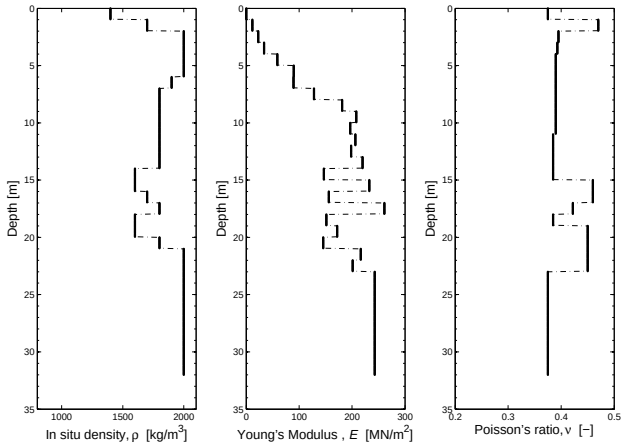

Figure 1: Profiles of the elastic parameters used in the 3D model; density ρ (left panel), Young's modulus E (middle panel) and Poisson's ratio ν (right panel).

With these elastic continuum parameters (Young's modulus E, density ρ and Poisson's ratio ν) at hand, we are ready to construct a 3D elastic model.

3 3D model

For the large diameter rigidly behaving foundations, we need to incorporate 3D effects; the interaction between soil and the large foundation mobilizes more global reactions of the soil instead of local (as is the case for slender piles). This more rigorous model consists of a 2D axisymmetric domain, in which both the soil as the pile are modeled with solid finite elements [6]. To avoid reflections at the edges of the domain, Perfectly Matched Layers (PMLs) (as defined in [7]) are added to the outer boundary of the domain. For very low frequencies, the PMLs are replaced by elastic layers whose dimensions are large enough so that the fictitious boundaries do not influence the results. In order to keep the calculation times small, the size of the elements composing these buffer layers are made successively larger as the distance to the pile increases. The loading scenario of interest is a horizontal load F at the free end of the pile and a bending moment m at the same end. In the more realistic scenario, these loads can be expressed in terms of radial F_R, tangential F_T and vertical F_V forces as

$$F = R \int_0^{2\pi} \left(F_R(\theta) \cos\theta - F_T(\theta) \sin\theta \right) \mathrm{d}\theta, \tag{1}$$

$$m = R^2 \int_0^{2\pi} F_V(\theta) \cos\theta \, \mathrm{d}\theta, \tag{2}$$

where θ is the angle with respect to the horizontal direction of the load F, and R is the radius of the pile. Assuming that the horizontal force F is equally distributed along the perimeter of the pile, then the radial and tangential forces are of the form

$$F_R(\theta) = \frac{F_H}{2\pi R} \cos\theta, \tag{3}$$

$$F_T(\theta) = \frac{F_H}{2\pi R} \sin\theta. \tag{4}$$

Likewise, the force F_V can be described with the cosine of θ as

$$F_V(\theta) = \frac{m}{\pi R^2} \cos\theta. \tag{5}$$

The Fourier expansion of F_R, F_T and F_V leaves us only with terms of first order, and therefore the axisymmetric problem needs to be solved only for the first Fourier term, as explained in reference [6]. Solving this axisymmetric problem is computationally more efficient than solving a complete 3D problem (much smaller linear systems) and produces as accurate results (if not better), provided that the true force distributions along the free end of the pile are as assumed.

For this example, the material damping for both pressure as shear waves was set equal to a ratio of 1%. The soil profile as given in Figure 1 was used. The embedded pile length was set on 32m and its diameter and wall-thickness on 5m and 6cm respectively, giving an L/D ratio of 6.4, which can be considered a rather rigid pile in typical soil conditions. Of course, also typical steel properties were given to the pile; a density of $7850 kg/m^3$, a Young's modulus of $2.1 \times 10^{11} N/m^2$ and a Poisson's ratio of 0.3. The vertical model boundary (horizontal plane) was set at 50m depth. Figures 2 and 3 give a qualitative impression of the 3D pile deflection, and soil-stress response respectively.

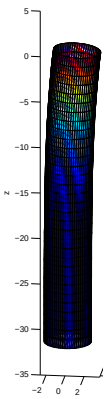

Figure 2: 3D pile deflection due to lateral force

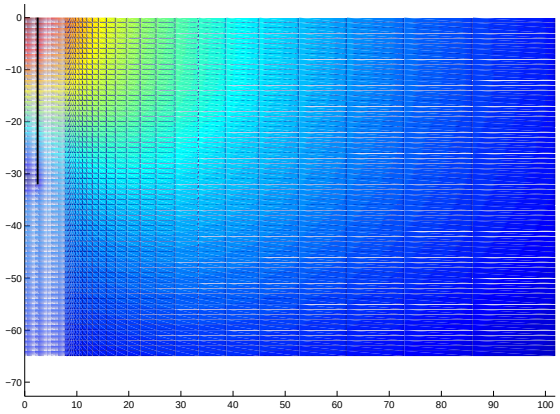

Figure 3: A qualitative impression of soil-stresses in the 3D model

4 An equivalent 1D model

In this paper, the method for finding an equivalent beam on Winkler foundation is demonstrated for the case that only a unit horizontal force of 1N is applied at the top of the pile with a frequency of 0.2 Hz. As the level of the top of the pile in the 3D model is 1cm above mudline, a small bending moment is also applied at mudline. We will only use the averaged 3D horizontal displacement (the centerline of the pile, which is found by averaging the nodes of the cross-sections). This displacement and its derivatives are used within the Euler-Bernoulli formulations for a beam. Though the resistance mechanisms of the soil are quite complex in reality, we will, like often done in engineering models, limit ourselves to only considering distributed lateral springs. To ensure an equilibrium of forces at the boundaries, we do allow discrete lateral and rotational springs at these locations.

First, a static reaction is calculated in the 3D model, in order to find the static soil stiffness $k_s(z)$. Afterwards, a forcing at a frequency of 0.2 Hz is applied. It is then attempted to match both the real as the imaginary part of the resulting 3D deflection in the 1D model by finding an equivalent dashpot distribution $c(z)$, assuming that the stiffness in this case can still be adequately described by the previously found static stiffness $k_s(z)$. Again, we only consider lateral dashpots, including complex discrete lateral and rotational springs at the boundaries. A schematic view of the 1D model is given in figure 4.

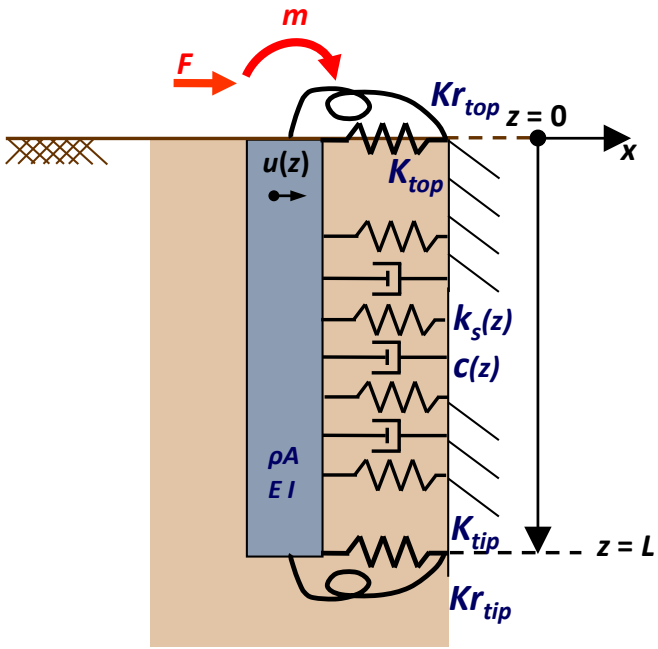

Figure 4: Schematic view of the equivalent 1D model

The material damping in the 3D model was set to a ratio of 1%, by making the Young's modulus of the soil complex. It was implemented as a hysteretic (frequency independent) damping, so also the damping term in the equation of motion (EOM) that will be considered for the beam will be of the hysteretic type. The EOM, considered in the frequency domain, thus reads

$$EI\frac{\partial^4 u(z)}{\partial z^4} + (k_s(z) + \mathrm{i}c(z) - \omega^2\rho A)u(z) = 0, \tag{6}$$

in which $u(z)$ is the complex amplitude of the displacement in the frequency domain, $c(z)$ the depth dependent hysteretic dashpot value, i the imaginary number ($\sqrt{-1}$), ω the angular frequency of the applied load, E the Young's modulus of the steel of the pile, ρ the material density of the steel of the pile and A and I respectively the area and the second moment of area of the cross section of the pile.

The following boundary conditions (BCs) apply:

$$EI\frac{\partial^3 u}{\partial z^3}\bigg|_{z=0} = F - K^*_{top}u(0), \tag{7}$$

$$EI\frac{\partial^2 u}{\partial z^2}\bigg|_{z=0} = m + Kr^*_{top}\frac{\partial u}{\partial z}\bigg|_{z=0}, \tag{8}$$

$$EI\frac{\partial^3 u}{\partial z^3}\bigg|_{z=L} = K^*_{tip}u(L), \tag{9}$$

$$EI\frac{\partial^2 u}{\partial z^2}\bigg|_{z=L} = -Kr^*_{tip}\frac{\partial u}{\partial z}\bigg|_{z=L}, \tag{10}$$

in which the '*' in K^*_{top}, etc. indicates that these discrete lateral and rotational springs are complex-valued dynamic stiffnesses. The magnitude of these springs can be calculated directly using the values of the 3D complex $u(z)$ and its derivatives at these locations. This ensures that the force and moment equilibria at the boundaries are satisfied according to the Euler-Bernoulli beam theory. The magnitude of the distributed springs and dashpots cannot be directly computed due to the fact that $u(z)$ often (for many soil-pile-forcing combinations) has a zero-crossing at a certain depth, which will result in singular values and negative stiffness. We thus try to find an equivalent $k_s(z)$ and $c(z)$ by taking integrals of the EOM over certain parts of the pile. As mentioned previously, first the static distributed stiffness is found by considering the static displacement of the 3D model. Afterwards, it is assumed that this $k_s(z)$ still applies for the dynamic reaction of the soil. Here, we will describe the method for finding $c(z)$, but $k_s(z)$ is found in the same way, (the inertia and damping terms are set equal to zero, and the spring constants of the discrete springs in the BCs are real). Note that for the dynamic case only $k_s(z)$ is used from the static calculation; the discrete springs are recalculated based on the complex deflections (equations 7 to 10). Then, in looking for the magnitude of $c(z)$, we assume a 'free' polynomial form:

$$c(z) = p_0 + p_1 z + p_2 z^2 + p_3 z^3 + p_4 z^4. \tag{11}$$

This expression has 5 unknowns, so we preferably need 5 equations to find these constants. As indicated, we use integrals of the EOM; 2 global integrals (from pile top (z=0) to pile tip ($z = L$)), and 3 local integrals with variable, yet unknown integration bounds. When taking the integral of the EOM (equation 6) over the full length of the pile (from 0 to L) and substituting the BC's where possible, we obtain

$$\begin{aligned}\int_0^L c(z)u(z)dz &= \left\{ -EI\frac{\partial^3 u}{\partial z^3}\bigg|_L + EI\frac{\partial^3 u}{\partial z^3}\bigg|_0 - \int_0^L k_s(z)u(z)dz + \rho A\omega^2\int_0^L u(z)dz \right\}/\mathrm{i} \\ &= \left\{ -K^*_{tip}u(L) + F - K^*_{top}u(0) - \int_0^L k_s(z)u(z)dz + \rho A\omega^2\int_0^L u(z)dz \right\}/\mathrm{i},\end{aligned} \tag{12}$$

However, when computing $c(z)$ in this way, it will become complex due to the fact that $u(z)$ and its derivatives are complex. To avoid this, only the real parts of the left hand

and right hand sides of the above equation are considered;

$$\begin{aligned} &Re(\int_0^L c(z)u(z)dz) = \\ &Re(\Big\{ - K^*_{tip}u(L) + F - K^*_{top}u(0) - \int_0^L k_s(z)u(z)dz + \rho A\omega^2 \int_0^L u(z)dz \Big\}/\mathrm{i}). \end{aligned} \tag{13}$$

This is the case for all the integrals we take, so the '*Re*' indication will be omitted here after. The second integral is equal to the first, but multiplied with z. By doing so, we consider a moment equilibrium instead of a force equilibrium as in equations 6 and 12. Integrating by parts and substituting the BC's where possible, we get

$$\begin{aligned} &\int_0^L zc(z)u(z)dz = \\ &\Big\{ - zEI\frac{\partial^3 u}{\partial z^3}\Big]_L^0 + EI\frac{\partial^2 u}{\partial z^2}\Big]_L^0 - \int_0^L zk_s(z)u(z)dz + \rho A\omega^2 \int_0^L zu(z)dz \Big\}/\mathrm{i} = \\ &\Big\{ - LK^*_{tip}u(L) - Kr^*_{tip}\frac{\partial u}{\partial z}\Big|_L - m - Kr^*_{top}\frac{\partial u}{\partial z}\Big|_0 - \int_0^L zk_s(z)u(z)dz + \rho A\omega^2 \int_0^L zu(z)dz \Big\}/\mathrm{i}, \end{aligned} \tag{14}$$

Now, for the other 3 equations, the same integrals are taken, but with variable integration bounds, focusing on a local part of the pile. The third integral is similar to equation 12 with bounds that are 'swept' with a stepsize ΔL focusing on the top of the pile. Hence, the lower integration bound $z^{(1)}_{f,t}$ ('f' for 'force', 't' for top and '$^{(1)}$' for lower integration bound) will start at the top of the pile ($z = 0$) and the upper will sweep until just above the tip. So,

$$\begin{aligned} z^{(1)}_{f,t} &= 0 \;..\; \Delta L \;..\; (L - 2\Delta L), \\ z^{(2)}_{f,t} &= z^{(1)}_{f,t} + \Delta L \;..\; \Delta L \;..\; L - \Delta L, \end{aligned} \tag{15}$$

Similarly, a local integral of the moment (like equation 14) is computed for the top of the pile, and the 5th integral is also an integral of the moment, but than including the tip of the pile, and not the top. With the 2 global and these 3 local integrals, we have 5 integrals that give a linear set of equations in $p_0..p_4$ (equation 11) and a resulting $c(z)$ for every combination of the integration bounds. All combinations of the 6 integration bounds are evaluated. Every found $c(z)$ is verified to be positive definite, and if so, the corresponding complex deflection and rotation are calculated according to equations 6 to 10, including the previously found complex discrete springs and $k_s(z)$. For the found deflection and rotations of the 1D model, the quality of the fit is assessed by considering the cost of the fit as

$$Cost_{u+u'} = Cost_u + Cost_{u'} = \frac{\sum_{i=0}^{i=L} |u_{3D,i} - u_{1D,i}|}{2\sum_{i=0}^{i=L} |u_{3D,i}|} + \frac{\sum_{i=0}^{i=L} |u'_{3D,i} - u'_{1D,i}|}{2\sum_{i=0}^{i=L} |u'_{3D,i}|}. \tag{16}$$

This cost is calculated for both the imaginary as the real parts of the deflection and rotation separately.

When following this procedure for finding the static stiffness, $k_s(z)$, we get the 'best'

stiffness profile as given by Figure 6. The stiffness profiles given in Figure 6 results in a fit of the displacement u and the rotation (the first derivative of the displacement with respect to z) u' as given in Figure 5. This solution was found by sweeping the integration bounds with a stepsize of $\Delta L = 1.92m$.

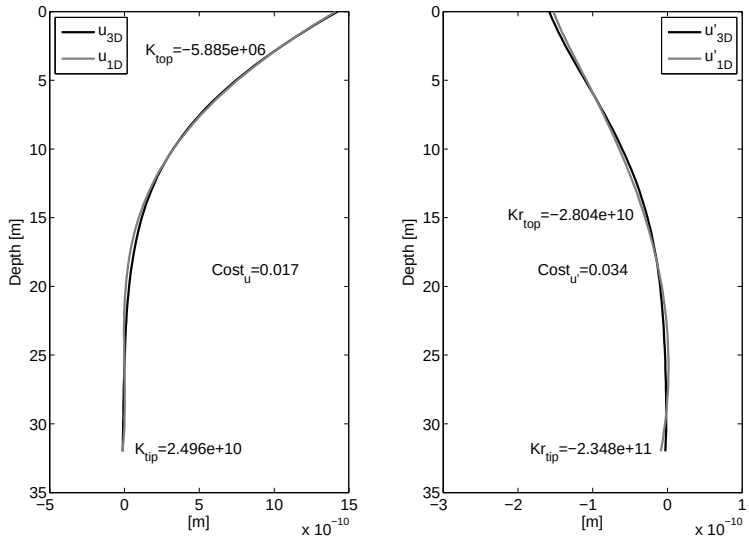

Figure 5: Static deflection u (left panel) and rotation u' (right panel): comparison of the 3D and the equivalent 1D model.

Continuing the above described procedure for the dynamic deflection, resulting from exciting the 3D pile with a unit lateral force (1N, no moment) at a frequency of 0.2 Hz, the $c(z)$ that gives the best solution when sweeping the integral bounds with a stepsize of $\Delta L = 2.13m$, is given in Figure 6. This Figure also includes $k_s(z)$ to be able to compare. Please note that the values of $k_s(z)$ are an order 100 larger than c(z), and that the unit is different.

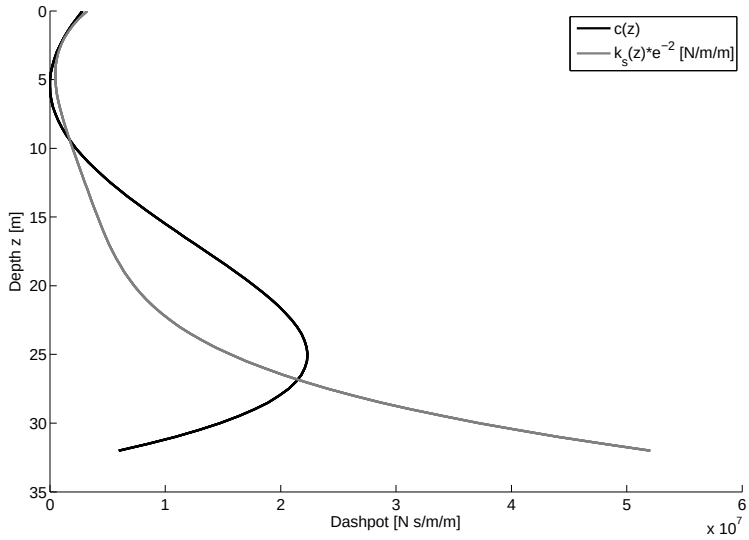

Figure 6: Resulting $k_s(z)$ from the static comparison of the models, and the 'best' c(z) for the case of a dynamic excitation of 0.2 Hz.

The corresponding fit between the imaginary parts of the 3D and 1D complex deflection is given in Figure 7, and the fit of the real parts of the complex rotations are given in Figure 8.

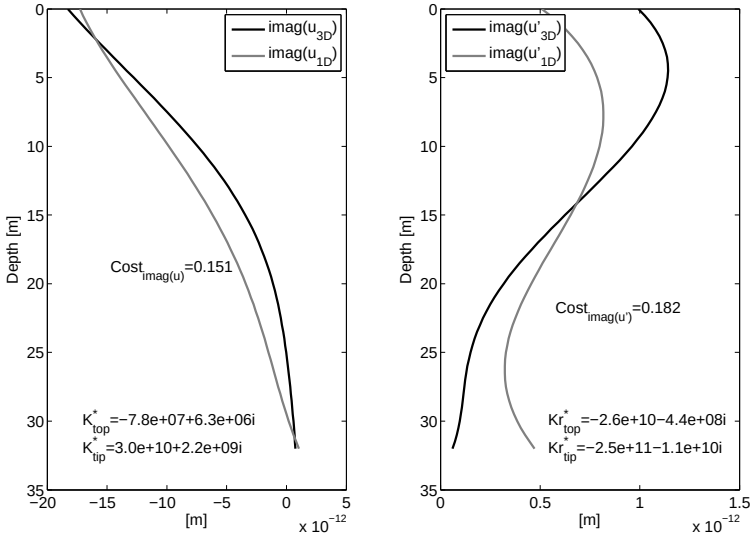

Figure 7: Comparison of the imaginary parts of the deflection (left panel) and rotation (right panel) of the 3D and the equivalent 1D model.

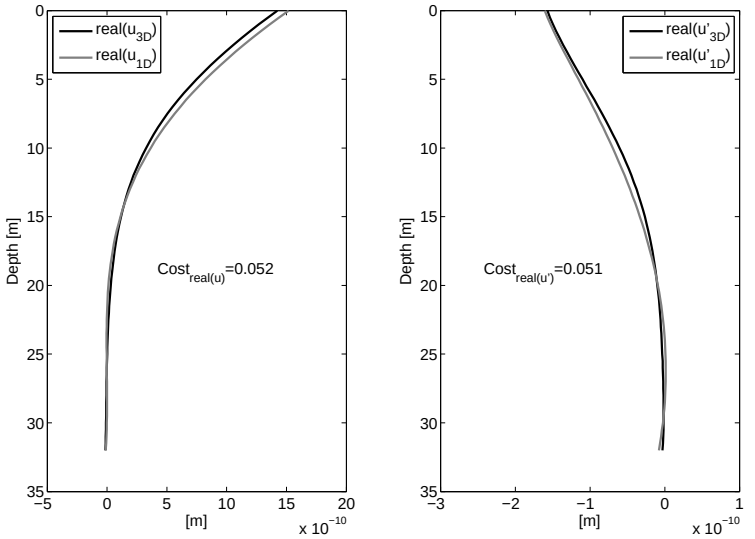

Figure 8: Comparison of the real parts of the deflection (left panel) and rotation (right panel) of the 3D and the equivalent 1D model.

5 Discussion & Conclusions

From the presented Figures (5 to 8) we see that a reasonable correspondence is found between the static deflection and rotation of the 1D and 3D model in case a unit horizontal force is applied at the top of the pile. The cost of the fit of the static displacement over

the full length of the pile is 0.017, which can be multiplied by 2 to yield the percentage difference (see equation 16); 3.4%. The static rotations show a 6.8% difference. Similar matching efforts performed by Varun et al. [8], yielded a difference in static displacement at the top of the pile of 14.0%, and a difference in rotation at the same location of 8.7%. If we also only consider the top of the pile, the match in static deflection at this location is within 1% and the rotation is fitted within 3.4% accuracy.

When the pile is harmonically excited at 0.2 Hz with the same unit horizontal force amplitude, the real part of the complex response matches that of the 3D model with an overall 10.3% difference (10.4% for the displacement and 10.2% for the rotation over the full length of the pile). However, the fit of the imaginary parts of both the deflection and the rotation leave enough room for improvement; 30.2% and 36.4% difference in overall displacement and rotations respectively.

The cause of the discrepancy between the imaginary parts of the complex response will be investigated. One of the reasons could be that we assume that the static soil stiffness $k_s(z)$ (found in the first step where the static models are matched) also applies for the dynamic case. Possibly, this stiffness needs to be updated for the dynamic loading case.

Another aspect of the presented results that raises questions, is the fact that in order for the edges of the 3D pile to match the classic Euler-Bernoulli conditions at the boundaries, negative rotational springs are needed to meet the balance of bending moment (equations 8 and 10). This contradicts our rule of not allowing negative stiffness in the 1D model. The fact that the soil reaction indeed causes a bending moment at the tip of the pile (and also distributed over its length) might not be too surprising. However, the need of the discrete 'balancing' springs at the top of the pile where the load is applied, indicates that discrepancies exist between the 3D pile mechanisms, and the Euler-Bernoulli theory.

References

[1] H.G. Poulos, Behavior of Laterally Loaded Piles I. Single Piles, Journal of Soil Mechanics & Foundations Div, 97.5, Proc paper 8092, 711-731, 1971

[2] B.M. Das, Principles of Foundation Engineering, 5th Edition, 2nd reprint, 2004

[3] P. Cuéllar, et al., A numerical model for the transient analysis of offshore foundations under cyclic loading, Computers and Geotechnics, 59, 75-86, 2014

[4] P.L.C. van der Valk, Coupled Simulations of Wind Turbines and Offshore Support Structures: Strategies based on the Dynamic Substructuring Paradigm, PhD Thesis, Delft University of Technology, 2014

[5] W.G. Versteijlen, et al., Assessing the small-strain soil stiffness for offshore wind turbines based on in situ seismic measurements, Journal of Physics: Conference Series 524.1, p. 012088, IOP Publishing, 2014

[6] O.C. Zienkiewicz and R.L. Taylor, The finite element method for solid and structural mechanics. Elsevier Butterworth-heinemann, 6th edition, 2005.

[7] E. Kausel and J.M. Oliveira Barbosa, PMLs: A direct approach, International Journal for Numerical Methods in Engineering 90.3, 2012, 343-352

[8] Varun, et al., A simplified model for lateral response of large diameter caisson foundations–linear elastic formulation, Soil Dynamics and Earthquake Engineering 29.2, 268-291, 2009

W.G. Versteijlen, Siemens Wind Power, Beatrixlaan 800, 2595 BN Den Haag, The Netherlands
A.V. Metrikine & K.N. van Dalen, Faculty of Civil Engineering and Geosciences, Delft University of Technology, Stevinweg 1, 2628CN Delft, The Netherlands

Buckling and supercritical behavior of axially moving plates

Yury Vetyukov
yury.vetyukov@tuwien.ac.at

Abstract

We consider a flexible plate moving across a domain, bounded by two parallel lines. Velocities of the plate, with which it is entering the domain and leaving it, are kinematically prescribed and may vary in space and time. The deformation of the plate is quasistatically analyzed using the geometrically nonlinear model of a Kirchhoff shell with a mixed Eulerian-Lagrangian kinematic description. In contrast to the formulations, available in the literature, neither the in-plane nor the out-of-plane deformations are unknown a priori and may be arbitrarily large. The particles of the plate travel across a finite element mesh, which remains fixed in the axial direction. The evident advantage of the approach is that the boundary conditions need to be applied at fixed edges of the finite elements. In the paper, we present the mathematical formulation and demonstrate its consistency by comparing the solution of a benchmark problem against results, obtained with conventional Lagrangian finite elements.

1 Introduction

The problem of mathematical modeling of nonlinear deformations of axially moving structures is both challenging and practically important. Numerous papers deal with the transverse vibrations of axially moving beams and strings, see a review paper by Chen, Ref. [1]. While an extension towards nonlinearly coupled in-plane and out-of-plane vibrations of a moving plate is presented in Ref. [5], this model is incapable of representing arbitrarily deformed configurations of the plate. Moreover, the use of Lagrange equations of motion to an open system with influx and outflux of the mass is not justified by the authors of the latter reference.

Large axial deformation and bending of a beam, which can move across a fixed domain, is treated by Humer and Irschik in Ref. [6] using a suitable change of variables. We apply a similar technique for the quasistatic modeling of finite deformations of a plate, which is moving across a given domain in the direction x. The velocities of the plate are prescribed at two boundaries of the domain $x = 0$ and $x = L$, see Fig. 1. Rolling of metal strips, paper production or motion of conveyor belt are a few examples of mechanical engineering problems, which can make use of model at hand. Non-constant profiles of the velocities, with which the particles of the plate are entering the domain $v_{\text{entry}}(y)$ and leaving it $v_{\text{exit}}(y)$, lead to the in-plane deformations. For thin plates this results in various

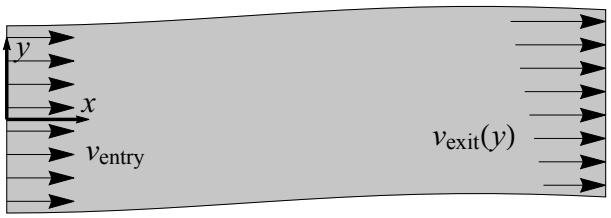

Figure 1: Deformation of a plate with prescribed velocities at the boundaries

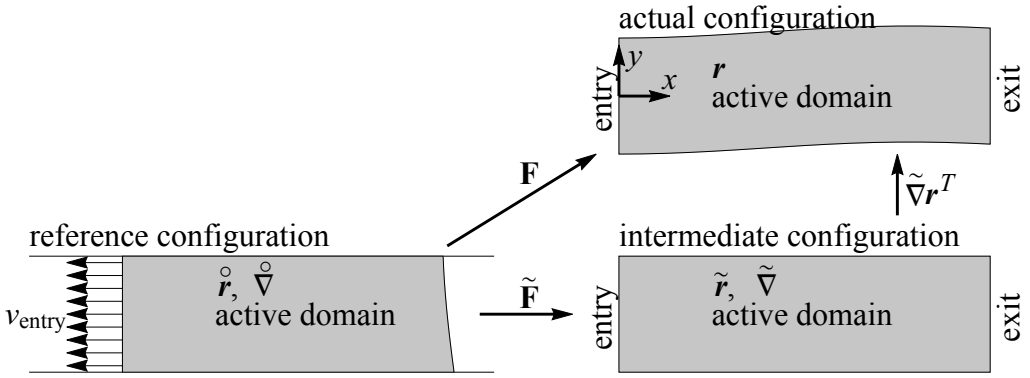

Figure 2: Two-stage mapping from the reference configuration to the actual one: the intermediate configuration is fixed in space

forms of out-of-plane buckling. Accurate simulations using conventional Lagrangian finite element models are difficult because the boundaries of the domain cross the finite element mesh and kinematic boundary conditions need to be imposed inside the elements. The problem is getting even more prominent as the finite element simulations are coupled with a closed-loop control scheme, which is important for practical applications.

2 Mathematical model

In the present study we assume the velocity v_{entry}, with which the plate is entering the domain, to be constant. In the future, arbitrary velocity profiles may be incorporated into the model by using the notion of intrinsic strains and the technique of multiplicative decomposition of the deformation gradient, see Ref. [7]. The varying velocity profile $v_{\text{exit}}(y)$, with which the material particles of the plate are leaving the domain at $x = L$, leads to the time varying deformation. Seeking a sequence of quasistatic equilibrium states of the elastic structure, we need to minimize the total energy of the active region of the plate, which is currently residing in the considered domain. Not going into details concerning the time integration, which is intended to be discussed in future publications, we focus on the kinematic modeling of the deformation of the plate.

The plane reference configuration $0 \leq \mathring{y} \leq w$ is straight (w is the undeformed width and $\mathring{\boldsymbol{r}} = \mathring{x}\boldsymbol{i} + \mathring{y}\boldsymbol{j}$ is the position vector in the reference configuration), see Fig. 2. The present mixed Eulerian-Lagrangian kinematic description makes use of a fixed intermediate configuration with the position vector $\tilde{\boldsymbol{r}}$ such, that the mapping of the positions of particles

from the reference configuration to the actual one $\boldsymbol{r} = \boldsymbol{r}(\overset{\circ}{\boldsymbol{r}})$ comprises two stages:

$$\begin{aligned} \tilde{\boldsymbol{r}} &= \overset{\circ}{\boldsymbol{r}} + u_x(\tilde{\boldsymbol{r}})\boldsymbol{i}, \\ \boldsymbol{r} &= \tilde{\boldsymbol{r}} + u_y(\tilde{\boldsymbol{r}})\boldsymbol{j} + u_z(\tilde{\boldsymbol{r}})\boldsymbol{k}. \end{aligned} \tag{1}$$

Simplicity of this description essentially distinguishes it from the known Arbitrary Lagrangian-Eulerian formulation, Ref. [2]: neither re-meshing nor transport of mechanical fields between the time steps are required. All fields are functions of the place in the fixed intermediate configuration, in which a finite element discretization of the field of displacements $\boldsymbol{u} = u_x\boldsymbol{i} + u_y\boldsymbol{j} + u_z\boldsymbol{k}$ is performed.
We apply the classical Kirchhoff model of a shell with five degrees of freedom of particles, see Refs. [3, 4, 8]. Expressions for the strain measures require the gradient of deformation of the plate from the reference configuration to the actual one

$$\boldsymbol{F} = \overset{\circ}{\nabla}\boldsymbol{r}^T, \tag{2}$$

in which

$$\overset{\circ}{\nabla} = \boldsymbol{i}\frac{\partial}{\partial \overset{\circ}{x}} + \boldsymbol{j}\frac{\partial}{\partial \overset{\circ}{y}} \tag{3}$$

is the differential operator of the reference state. As the finite element discretization is performed in the intermediate configuration, we need to express $\boldsymbol{F}$ using the corresponding differential operator

$$\tilde{\nabla} = \boldsymbol{i}\frac{\partial}{\partial \tilde{x}} + \boldsymbol{j}\frac{\partial}{\partial \tilde{y}} = \boldsymbol{i}\frac{\partial}{\partial x} + \boldsymbol{j}\frac{\partial}{\partial \overset{\circ}{y}}, \tag{4}$$

the axial coordinate in the intermediate configuration $\tilde{x}$ equals the actual one, and the transverse coordinate $\tilde{y}$ equals the reference one according to (1). Now, the two differential operators are related by the gradient of deformation from the reference configuration to the intermediate one $\tilde{\boldsymbol{F}}$:

$$\overset{\circ}{\nabla} = \tilde{\boldsymbol{F}}^T \cdot \tilde{\nabla}, \quad \tilde{\boldsymbol{F}}^T = \overset{\circ}{\nabla}\tilde{\boldsymbol{r}}^T. \tag{5}$$

Finally, total gradient of deformation of the plate with the differential operator of the intermediate configuration $\tilde{\nabla}$ results in the form

$$\begin{aligned} \boldsymbol{F} &= \overset{\circ}{\nabla}\boldsymbol{r}^T = \tilde{\nabla}\boldsymbol{r}^T \cdot \tilde{\boldsymbol{F}}, \\ \tilde{\boldsymbol{F}} &= \left(\boldsymbol{I}_2 - \boldsymbol{i}\tilde{\nabla}u_x\right)^{-1}. \end{aligned} \tag{6}$$

Here $\boldsymbol{I}_2 = \boldsymbol{ii} + \boldsymbol{jj}$ is the in-plane identity tensor, and the expression for the in-plane tensor $\tilde{\boldsymbol{F}}$ follows from

$$\boldsymbol{I}_2 = \overset{\circ}{\nabla}\overset{\circ}{\boldsymbol{r}} = \tilde{\boldsymbol{F}}^T \cdot \tilde{\nabla}(\tilde{\boldsymbol{r}} - u_x\boldsymbol{i}). \tag{7}$$

The strain measures of a classical shell

$$\begin{aligned} \boldsymbol{E} &= \frac{1}{2}\left(\boldsymbol{F}^T \cdot \boldsymbol{F} - \boldsymbol{I}_2\right), \\ \boldsymbol{K} &= \boldsymbol{F}^T \cdot \boldsymbol{b} \cdot \boldsymbol{F} \end{aligned} \tag{8}$$

feature the actual second metric tensor $\boldsymbol{b} = -\nabla\boldsymbol{n}$, in which $\boldsymbol{n}$ is the vector of unit normal and $\nabla = \boldsymbol{F}^T \cdot \overset{\circ}{\nabla}$ is the differential operator on the deformed surface. After mathematical transformations we express the tensor of bending strains with the operator of the intermediate configuration:

$$\boldsymbol{K} = \tilde{\boldsymbol{F}}^T \cdot \tilde{\boldsymbol{K}} \cdot \tilde{\boldsymbol{F}}, \quad \tilde{\boldsymbol{K}} = \tilde{\nabla}\tilde{\nabla}\boldsymbol{r} \cdot \boldsymbol{n}. \tag{9}$$

Here we restrict the analysis to pure elastic material behavior. The strain energy of the plate per unit area in the reference configuration is computed as a quadratic form

$$U = \frac{1}{2}\left(A_1(\operatorname{tr}\boldsymbol{E})^2 + A_2\boldsymbol{E}\cdot\cdot\boldsymbol{E} + D_1(\operatorname{tr}\boldsymbol{K})^2 + D_2\boldsymbol{K}\cdot\cdot\boldsymbol{K}\right) \tag{10}$$

with known coefficients, see Refs. [4, 8]. The total strain energy

$$U^\Sigma = \int_0^L \int_{-w/2}^{w/2} U(\det\tilde{\boldsymbol{F}})^{-1}\mathrm{d}\tilde{y}\,\mathrm{d}x \tag{11}$$

is integrated in the intermediate configuration using the finite element discretization of displacements $\boldsymbol{u}$ and minimized at each time step of the quasistatic simulation. As discussed after (16), known velocities of particles v_{entry} and v_{exit} determine the time variations of the axial displacements u_x at the boundaries $x = 0$ and $x = L$, which means that the material volume of the active domain is prescribed for each time step. This allows seeking static equilibrium configurations by minimizing the total strain energy of this material volume, which is changing during the simulation, but is known for each time step.

3 Time stepping scheme

In a numerical simulation, we discretize the evolution of the system in time and need to formulate an algorithm of transformation of the solution from one time step t^k to the next one $t^{k+1} = t^k + \tau$. In the beginning of a time step, the field of displacements $\boldsymbol{u}^k(\tilde{\boldsymbol{r}})$ is known in the form of a finite element approximation. Now, each particular material point moves with the velocity $\dot{\boldsymbol{u}}$, in which the full time derivative is defined for a fixed material particle as

$$(\ldots)^{\cdot} \equiv \left.\frac{\partial\ldots}{\partial t}\right|_{\overset{\circ}{\boldsymbol{r}}=\text{const}}. \tag{12}$$

The notion of a local time derivative with fixed $\tilde{\boldsymbol{r}}$ is relevant for the description in the intermediate configuration:

$$\partial_t(\ldots) \equiv \left.\frac{\partial\ldots}{\partial t}\right|_{\tilde{\boldsymbol{r}}=\text{const}}. \tag{13}$$

The transformation between the full and the local time derivatives can be easily derived by considering a field $\boldsymbol{u}(\tilde{\boldsymbol{r}}, t)$, which is defined in the intermediate configuration. Computing $\dot{\boldsymbol{u}}$, we take into account that $\tilde{\boldsymbol{r}} = \tilde{\boldsymbol{r}}(\overset{\circ}{\boldsymbol{r}}, t)$ changes in time for $\overset{\circ}{\boldsymbol{r}} = \text{const}$, and arrive at

$$\dot{\boldsymbol{u}} = \partial_t\boldsymbol{u} + \dot{\tilde{\boldsymbol{r}}} \cdot \tilde{\nabla}\boldsymbol{u}. \tag{14}$$

Using the first relation in (1) and taking into account that the full time derivative $\overset{\circ}{\boldsymbol{r}}{}^{\cdot} = 0$, we find

$$\dot{\boldsymbol{u}} = \partial_t\boldsymbol{u} + \dot{u}_x\boldsymbol{i} \cdot \tilde{\nabla}\boldsymbol{u} = \partial_t\boldsymbol{u} + \dot{u}_x\partial_x\boldsymbol{u}. \tag{15}$$

This results in

$$\dot{u}_x = \partial_t u_x \left(1 - \partial_x u_x\right)^{-1}. \tag{16}$$

The definitions of material and local time derivatives are used to formulate a strategy for the time stepping. Neglecting the dynamic effects, we consider the time evolution of the deformation of the plate owing to the prescribed velocities at the boundaries of the domain. Seeking for an equilibrium state at each time step, we minimize the total strain energy of the active domain U^{Σ}. Although the material of the plate is flowing across the intermediate configuration, this approach is justified as the material volume within the active domain is fixed for the end of the time step. Indeed, according to the boundary conditions, discussed below, the displacements at the two boundaries of the domain (19) are known for the end of the time step $t = t^{k+1}$. This means that the boundaries of the active domain in the reference configuration are fixed according to the first relation in (1), and seeking the equilibrium of this material volume is equivalent to minimizing its total energy.

4 Boundary conditions at a time step

In this section, we discuss the time evolution of the displacements of the plate at the boundaries of the domain $x = 0$ and $x = L$. We interpret the velocity at the entry to the active domain v_{entry} as the time rate of material generation. This is relevant e.g. for modeling rolling processes, in which the time rate of the material volume flowing across a roll gap is known. Owing to the deformation, the particles acquire a different material velocity after entering the active domain. In contrast, v_{exit} is the material velocity, with which the particles of the plate leave the domain at the entry to the subsequent roll gap.
The analysis in the present paper is restricted to a particular case of constant entry velocity. The left boundary of the intermediate configuration moves across the reference one to the left with $v_{\text{entry}} = \text{const}$, which means that an infinitesimally thin layer of the plate with the length $v_{\text{entry}}\mathrm{d}t$ enters the active domain during the time $\mathrm{d}t$. The local time derivatives here are known:

$$x = 0: \quad \partial_t \mathring{\boldsymbol{r}} = -v_{\text{entry}}\boldsymbol{i}, \quad \partial_t \tilde{\boldsymbol{r}} = 0; \quad (1) \quad \Rightarrow \quad \partial_t \boldsymbol{u} = v_{\text{entry}}\boldsymbol{i}. \tag{17}$$

We immediately conclude that $u_x = v_{\text{entry}} t$ and $v_y = 0$ at the left boundary.
At the right boundary we know material velocities, and the local time derivatives follow:

$$x = L: \quad \dot{\boldsymbol{u}} = v_{\text{exit}}\boldsymbol{i}; \quad (15) \quad \Rightarrow \quad \partial_t \boldsymbol{u} = v_{\text{exit}}(\boldsymbol{i} - \partial_x \boldsymbol{u}). \tag{18}$$

It is important to notice, that although the material time derivative here is always directed along x, the line of contact would still travel in the transverse direction because $\partial_t \boldsymbol{u} \cdot \boldsymbol{j} \neq 0$ as long as the plate is inclined and $\partial_x u_y \neq 0$.
In the beginning of a time step $t = t^k$, the local time derivatives $\partial_t \boldsymbol{u}$ are available at the boundaries $x = 0$ and $x = L$. Experience shows, that an explicit time integration scheme for the boundary conditions with a moderately small time step size τ leads to accurate simulation results, which rapidly converge as $\tau \to 0$:

$$x = 0, L: \quad \boldsymbol{u}^{k+1} = \boldsymbol{u}^k + \tau\, \partial_t \boldsymbol{u}. \tag{19}$$

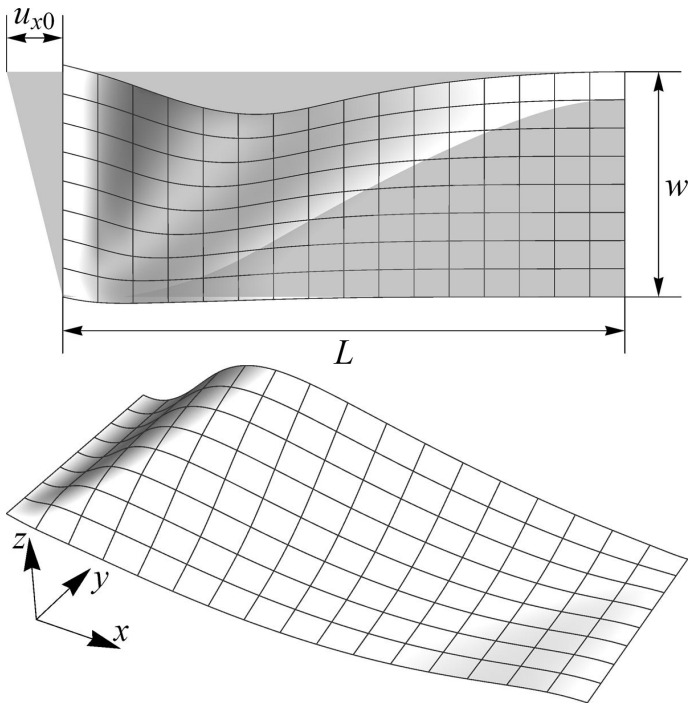

Figure 3: Deformation of a trapezoidal plate, seen from above (together with the undeformed configuration) and from the side

5 Numerical benchmark problem

While the results of numerical modeling of deformation of axially moving plates will be reported in future publications, here we test the formulation by seeking the equilibrium of a trapezoidal plate of the width w and side lengths L and $L + u_{x0}$, see Fig. 3. The inclined edge is rotated parallel to the right one by kinematically prescribed displacements u_x and u_y such, that the actual configuration is bounded by the lines $x = 0$ and $x = L$; the length of the edge is preserved constant to avoid large in-plane strains. The mapping (1) is thus possible with the intermediate configuration $0 \leq x \leq L$, $0 \leq \tilde{y} \leq w$, which is discretized using C^1 continuous finite element approximation of displacements, presented by the author in Refs. [8, 9].

The compressed shell buckles out of plane, and the region with $u_z < 0$ is "shadowed" by the gray initial configuration in Fig. 3. The transverse edges of the finite element mesh remain parallel in the deformed configuration. This corresponds to the second relation in (1), as the mapping $\boldsymbol{r}(\tilde{\boldsymbol{r}})$ features only u_y and u_z.

The considered parameters of the model in SI system are $L = 1$, $w = 0.4$, thickness of the plate $5 \cdot 10^{-3}$, Young modulus $2.1 \cdot 10^{11}$ and Poisson ratio 0.3. In Table 14 we summarized the maximal and minimal values of the out-of-plane displacements, computed for various discretizations using the present method as well as the conventional shell finite elements with Lagrangian description, discussed in the above references. These maximal and minimal displacements take place at the opposite edges of the plate. We initiated out-of-plane displacements by applying and then releasing a transverse distributed load in the positive direction of z axis, which determined the direction of buckling in all simulations. The current implementation of the mixed Eulerian-Lagrangian finite element formulation using *Wolfram Mathematica* is yet restricted concerning the size of the mesh, but one can

Table 14: Mesh convergence and comparison of the mixed Eulerian-Lagrangian and traditional Lagrangian frameworks

Discretization,	Mixed E.-L.		Lagrangian	
$n_x \times n_y$	$\min u_z$	$\max u_z$	$\min u_z$	$\max u_z$
4×2	-0.07270	0.18577	-0.07322	0.18138
8×4	-0.05846	0.18427	-0.05831	0.18256
16×8	-0.05542	0.18319	-0.05527	0.18259
32×16	—	—	-0.05490	0.18262

conclude that the results converge to the same solution.

Acknowledgements

This work has been partially carried out at LCM GmbH as part of a K2 project. K2 projects are financed using funding from the Austrian COMET-K2 programme. The COMET K2 projects at LCM are supported by the Austrian federal government, the federal state of Upper Austria, the Johannes Kepler University and all of the scientific partners which form part of the K2-COMET Consortium.

References

[1] Chen, L.-Q., Analysis and control of transverse vibrations of axially moving strings, *Appl Mech Rev*, 58, pp. 91-116, 2005.

[2] Donea, J., Huerta, A., Ponthot, J.-P. and Rodriguez-Ferran, A., *Arbitrary Lagrangian-Eulerian methods*, in *Encyclopedia of Computational Mechanics*, vol. 1: Fundamentals, Stein, E., de Borst, R. and Hughes, T. (eds.), chap. 14, John Wiley & Sons, Ltd, 2004.

[3] Eliseev, V., *Mechanics of deformable solid bodies* (in Russian). St.Petersburg State Polytechnical University Publishing House, 2006

[4] Eliseev, V. and Vetyukov, Y., Finite deformation of thin shells in the context of analytical mechanics of material surfaces, *Acta Mech*, 209, pp. 43-57, 2010.

[5] Ghayesh, M. H., Amabili, M. and Païdoussis, M. P., Nonlinear dynamics of axially moving plates, *J Sound Vib*, 332, pp. 391-406, 2013.

[6] Humer, A. and Irschik, H., Large deformation and stability of an extensible elastica with an unknown length, *Int J Solids Struct*, 48, pp. 1301-1310, 2011.

[7] Humer, A. and Krommer, M., Modeling of piezoelectric materials by means of a multiplicative decomposition of the deformation gradient, *Mech Adv Mat Struc*, 22, pp. 125-135, 2015.

[8] Vetyukov, Y., *Nonlinear Mechanics of thin-walled structures. Asymptotics, direct approach and numerical analysis*, Springer, Vienna, 2014.

[9] Vetyukov, Y., Finite element modeling of Kirchhoff-Love shells as smooth material surfaces, *ZAMM*, 94, pp. 150-163, 2014.

Yury Vetyukov, Institute of Mechanics and Mechatronics, Vienna University of Technology, Getreidemarkt 9, 1060 Vienna, Austria

Modeling of the flow ignition in a planar vortex chamber

Dmitriy V. Voronin
voron@hydro.nsc.ru

Abstract

The numerical calculations of the flowfield in a planar vortex chamber have been performed. The model is based on conservation laws of mass, momentum and energy for nonsteady two-dimensional compressible gas flow in case of swirl axial symmetry. The processes of viscosity, heat conductivity and turbulence have been taken into account. It was found that transition of kinetic energy of gas into heat due to processes of dissipation generates "hot spots" in boundary layers at the chamber walls. The gas temperature at the spots may exceed the temperature of gas ignition, while the surrounding regions remain still cold. It may be the reason of cold gas self-ignition observed in experiments.

1 Introduction

It is known that mixing of a fuel and oxidizer in a cold chamber leads to self-ignition for some particularly reactive fuel compositions, for example, for fluorine oxidizers [1]. The most frequently used mixtures of hydrocarbon fuels and hydrogen with air and oxygen ignite only as a result of additional external actions, such as rapid compression by a piston, compression by a shock wave, a spark, or a contact with a hot body. Spontaneous ignition of residual hydrocarbon fuels upon their contact with oxygen is known from the experience of exploitation of oxygen and high-pressure air tanks and pipelines [2]. In these cases, the phenomenon usually finds satisfactory explanation in the emergence of sparks due to accidental solid particles rubbing against the wall or by heating of some portions of the mixture upon its compression by a high-speed unsteady gas flow. For the first time spontaneous ignition of widely used fuel mixtures in a nonheated straight-flow chamber of the vortex type was obtained in paper [3]. The phenomenon had been observed accidentally in experiments on continuous detonation combustion of mixtures, where detonation was initiated by an electric discharge or by an explosion of a an electric microdetonator after the mixture fills the chamber. Examining the streak records of the processes it was found [3] that the glow in the chambers sometimes appears earlier than the triggering pulse. In subsequent experiments the regular self-ignition of hydrogen and kerosene was registered upon their mixing with oxygen-enriched air in a straight-flow vortex chamber. The nature of the ignition observed remained unclear. The present paper devoted to numerical calculations of the flowfield in planar vortex chamber. The determination of non-stationary fields of main thermodynamic parameters allows to find possible regions of gas self-ignition. The geometry and main physical characteristics correspond to experimental data [3].

2 Problem Formulation

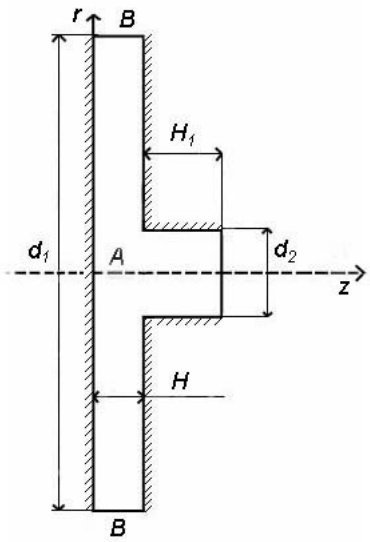

Figure 1: The scheme of the vortex chamber

Let's consider a planar-radial circular chamber (Fig. 1). The chamber has axial symmetry form, where line A is a symmetry axis. The inner volume has the form of a disc of diameter $d_1 = 204$ mm and length H = 15 mm. The central outlet in one radial wall had a length $H_1 = 42$ mm and served to exhaust the products into atmosphere. The outlet diameter d2 was equal to 40 mm. Gas components were fed into the chamber through circular inlet surface B (separating the chamber from the receiver) at an angle of 45 to the surface. The angle ensured rotational motion of the gas mixture in the chamber. The form and parameters of the chamber correspond to the experimental facility [3]. At the instant t = 0, the entire chamber is filled by air of density ρ_0 and pressure p_0. At $t > 0$, the tangential injection of air begins from the cylindrical wall $r = r_1$ (the inlet surface B). It is required to find the values of velocity, pressure, density and temperature of the gas as functions of time. Unsteady motion of viscid compressible turbulent fluid was described by Reynolds equations [4]:

$$\frac{\partial \vec{Q}}{\partial t} + \frac{\partial \vec{U}}{\partial r} + \frac{\partial \vec{F}}{\partial z} = \vec{G} \tag{1}$$

where r, z - radial and axial (along symmetry axis) cylindrical coordinates. The vectors $\vec{Q}, \vec{U}, \vec{F}, \vec{G}$ are defined by the equations

$$\vec{Q} = \begin{pmatrix} r\rho \\ r\rho u_r \\ r\rho u_\theta \\ r\rho u_z \\ rE \end{pmatrix}, \vec{U} = \begin{pmatrix} r\rho u_r \\ r(\rho u_r^2 + p - \tau_{11}) \\ r(\rho u_r u_\theta - \tau_{12}) \\ r(\rho u_r u_z - \tau_{13}) \\ r(E+p)u_r - r(u_r\tau_{11} + \\ u_\theta\tau_{12} + u_z\tau_{13} + q_r) \end{pmatrix}, \vec{F} = \begin{pmatrix} r\rho u_z \\ r(\rho u_r u_z - \tau_{13}) \\ r(\rho u_\theta u_z - \tau_{23}) \\ r(\rho u_z^2 + p - \tau_{33}) \\ r(E+p)u_z - r(u_r\tau_{13} + \\ u_\theta\tau_{23} + u_z\tau_{33} + q_z) \end{pmatrix},$$

$$\vec{G} = (0, \rho u_\theta^2 + p - \tau_{22}, -\rho u_r u_\theta + \tau_{12}, 0, 0)$$

here the components of the shear stress tensor have the form

$$\tau_{11} = (2/3)\mu_e(3e_{11} - div\vec{V}), \tau_{12} = \mu_e e_{12}, \tau_{22} = (2/3)\mu_e(3e_{22} - div\vec{V}), \tau_{13} = \mu_e e_{13},$$

$$\tau_{33} = (2/3)\mu_e(3e_{33} - div\vec{V}), \tau_{23} = \mu_e e_{23}.$$

The components of heat flux vector are

$$q_r = -\lambda_e \frac{\partial T}{\partial r}, q_z = -\lambda_e \frac{\partial T}{\partial z}.$$

Here

$$e_{11} = \partial u_r/\partial r, e_{22} = u_r/r, e_{33} = \partial u_z/\partial z, div\vec{V} = e_{11} + e_{22} + e_{33}, e_{12} = \partial u_\theta/\partial r - u_\theta/r,$$

$$e_{13} = \partial u_r/\partial z + \partial u_z/\partial r, e_{23} = \partial u_\theta/\partial z,$$

$$E = \rho(e + q^2/2), e = p/((\gamma - 1)\rho), q = u_r^2/2 + u_\theta^2/2 + u_z^2/2$$

.

the velocity vector has radial u_r, circumferential u_θ and axial u_z components; p, ρ, T and $\gamma = c_p/c_v$ are the pressure, density, temperature and the ratio of specific heats, respectively; μ_e and λ_e are the effective viscosity and effective thermal conductivity of the gas. μ_e is a sum of molecular μ and turbulent μ_t viscosities, , Pr and Pr_t are molecular and turbulent Prandtl numbers.
The law of Sazerland is used for the values of molecular viscosity

$$\frac{\mu}{\mu_*} = \left(\frac{T}{T_*}\right)^{3/2} \frac{T_* + S_0}{T + S_0} \tag{2}$$

where $\mu_* = 1.68 \cdot 10^{-5} kg/(m \cdot s), T^* = 273, S_0 = 110$ for air. The processes of turbulence were described according to $k - \epsilon$ model:

$$\frac{\partial \rho k}{\partial t} + (\rho\vec{V} \cdot \bigtriangledown)k = \bigtriangledown\left(\left(\mu + \frac{\mu_t}{\sigma_k}\right) \bigtriangledown k\right) + P^* - \rho\epsilon, \tag{3}$$

$$\frac{\partial \rho \epsilon}{\partial t} + (\rho\vec{V} \cdot \bigtriangledown)\epsilon = \bigtriangledown\left(\left(\mu + \frac{\mu_t}{\sigma_\epsilon}\right) \bigtriangledown \epsilon\right) + \frac{\epsilon}{k}\left(C_{\epsilon 1} P^* - C_{\epsilon 2}\rho\epsilon\right). \tag{4}$$

with values $\sigma_k = 1.0, \sigma_\epsilon = 1.3, C_{\epsilon 1} = 1.44, C_{\epsilon 2} = 1.92$. Here k is turbulence kinetic energy, ϵ is its rate of dissipation, term P^* represents the production of turbulence kinetic energy, $P^* = \mu_t S^2, S = \sqrt{e_{ij}e_{ij}}$. Turbulent viscosity was defined according to Kolmogorov-Prandtl formula:

$$\mu_t = \frac{C_\mu \rho k^2}{\epsilon}, C_\mu = 0.09.$$

The following boundary conditions are imposed: on the planar radial walls of the chamber ($z = 0, 0 < r < r_1$, and $z = H, r_2 < r < r_1, r_1 = d_1/2, r_2 = d_2/2$) the condition of gas adhesion $u_r = u_z = u_\theta = 0$ and constant gas temperature on it: $T = T_0$; on the inlet surface B ($r = r_1, 0 < z < H$), $p = p^*(r_1, z, t), \rho = \rho^*(r_1, z, t), u_z = 0, u_\theta = u_\theta^*(r_1, z, t), u_r = u_r^*(r_1, z, t)$. Functions $p^*, \rho^*, u_\theta^*, u_r^*$ depend on the dynamics of air overflow from the collector to the chamber and are defined according to [3]; at the exit ($z = H + H_1, 0 < r < r_2$) the conditions of equality to zero of the first derivatives of the thermodynamic parameters with respect to z, are valid.

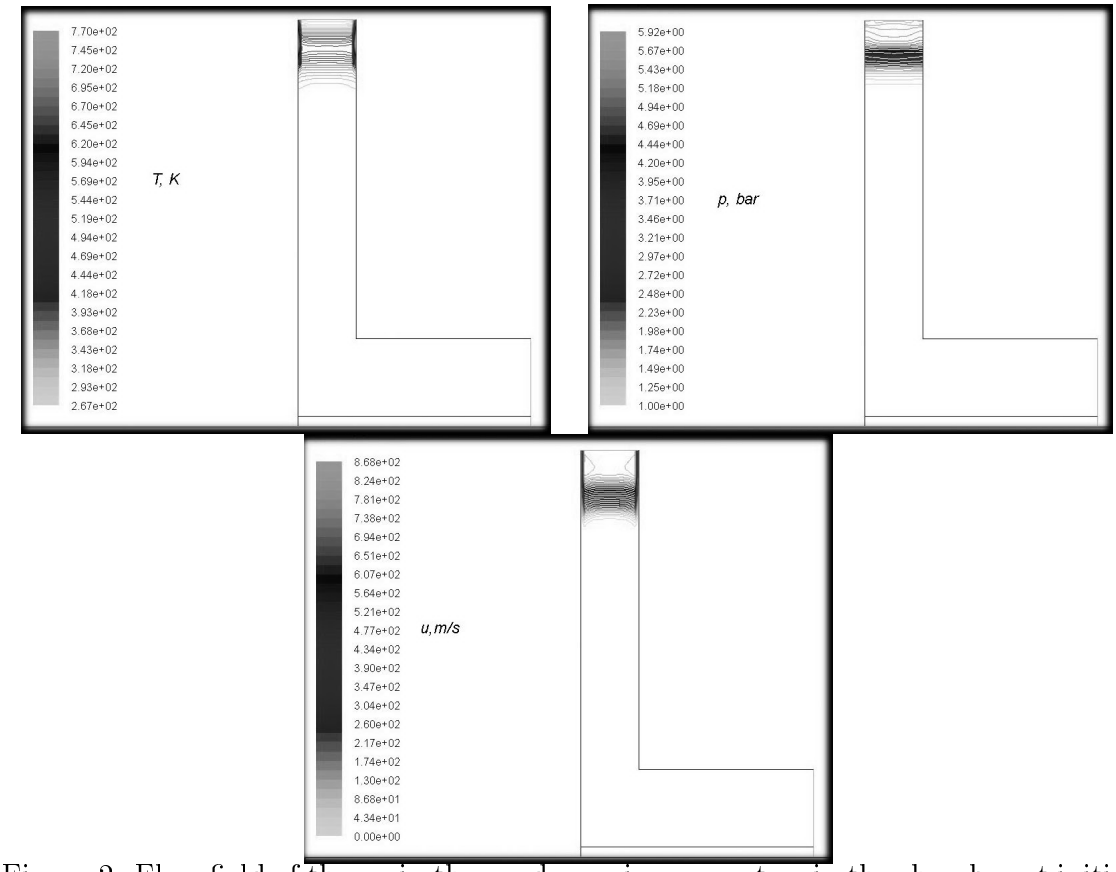

Figure 2: Flow field of the main thermodynamic parameters in the chamber at initial stage of the processes, $t = 1.0 \cdot 10^{-4}$ s.

3 Numerical solution of the problem

The calculations were performed for the following initial values of air: $p_0 = 1bar, \rho_0 = 0.1225kg/m^3, \gamma = 1.4, u_{r0} = u_{z0} = u_{\theta 0} = 0$; initial values of air pressure p_r and density ρ_r in the receiver : $p_r/p_0 = 10, \rho_r/\rho_0 = 10$. The problem stated above, was solved numerically with the help of the method of large particles [5].

The initial stage of numerical simulations is presented in Fig. 2. Here $u = \sqrt{u_r^2 + u_\theta^2 + u_z^2}$. It could be seen that a compression wave starts to propagate from the inlet surface B to the symmetry axis A. The pressure amplitude in the wave is up to 5.92 bar. The flow friction at the chamber walls results in mass growing of gas at the walls due to processes of dissipation, and subsequent transition of gas kinetic energy into heat starts. The values of temperature in generated boundary layers is growing up to 770 K (z = 0), while in the center of the channel it is equal to 520 K (at the same r and z = H/2). The subsequent

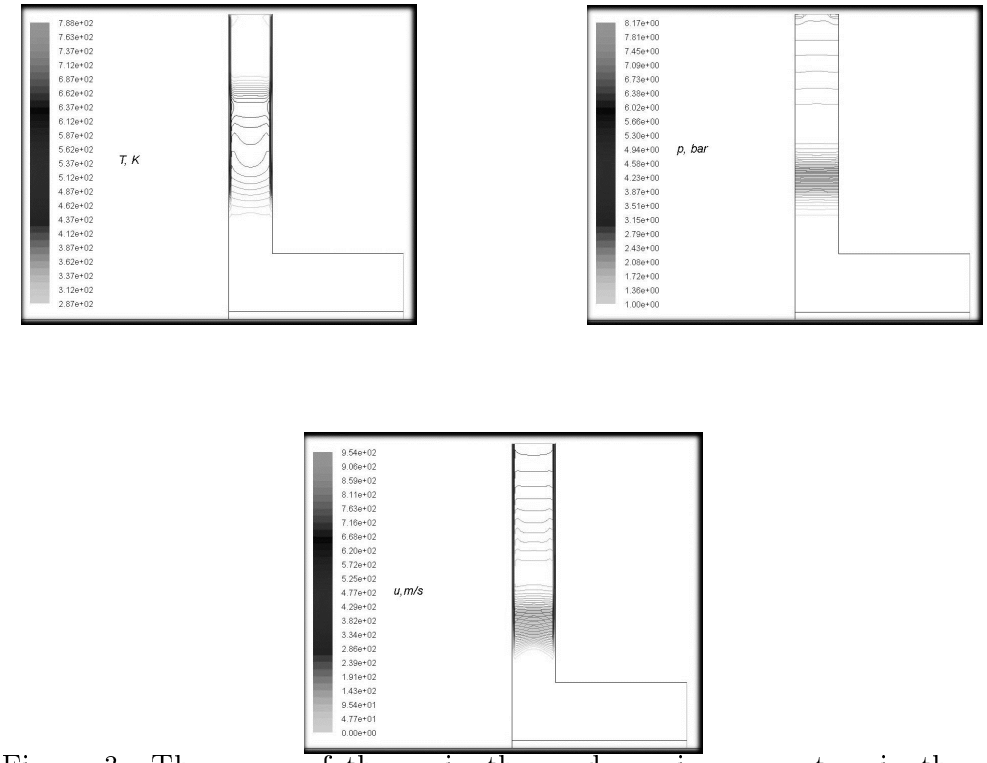

Figure 3: The maps of the main thermodynamic parameters in the chamber at $t = 5.0 \cdot 10^{-4}$ s.

stage of the processes is presented in Fig. 3. The compression wave continues to propagate nearly at the same amplitude. The sizes of hot boundary layers are growing along with temperature values in them. The giant vortex is generated in the chamber at the walls. Its axes is the axes of symmetry A. The vortex is gradually coming down to the axes A. In recent simulations the initial pressure in the receiver pr = 10 bar. In the experiments [3] it may be up to 100 bar. Then the temperature in the boundary layers (in the vortex) exceeds the ignition temperature $T_{ig} = 1200$ K. That results in self-ignition of gas in a whole volume observed in the experiments [3]. When the vortex comes down to the axes A, and gas masses collide (Fig. 4), the temperature amplitude reaches the value of 1480

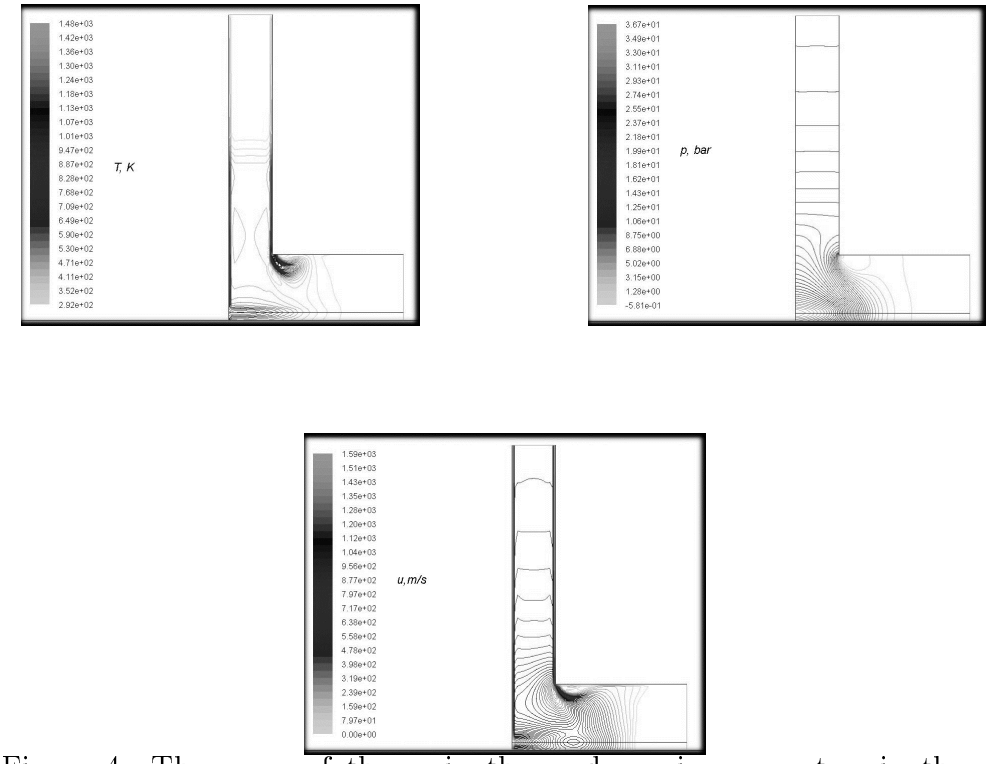

Figure 4: The maps of the main thermodynamic parameters in the chamber at $t = 9.0 \cdot 10^{-4}$ s.

K, that initiates the processes of gas self-ignition even at present $p_r = 10$ bar. But the maximum of temperature takes place not at the axes of symmetry A but in the heated spot at the chamber corner ($r = r_2, z = H$), where the boundary layer tearing off from the chamber walls occurs.

Interaction of the heated spot with reflected shock waves (from the symmetry axes A) and gas acceleration in the spot (due to rarefaction wave) from the outlet surface result in subsequent temperature growth. At the course of time the temperature values in the spot exceed 2000 K (Fig. 5).

Dynamics of the maximum values of gas temperature we can see in Fig. 6. The dotted line in the figure corresponds to the value of ignition temperature T_{ig}. We can determine six stages of the processes. The initial stage 1 is a temperature growth from 300 K to 800 K, when the shock wave starts to propagate from the receiver to the chamber through the inlet surface B. The stagnation period 2 corresponds to the shock wave propagation to the center of the chamber (the symmetry axes A). The temperature growth at the stage 3 is a result of shock waves collision at the symmetry axes A. Here the gas temperature at the axes is increased up to 1500 K and exceeds the value of T_{ig}. That may result in gas self-ignition in the region. The interval 4 is the processes discharge in the direction of the outlet surface. The stage 5 is a temperature growth in the tearing off boundary layer at the chamber corner at its interaction with reflected shock wave. The temperature here exceeds here the value of 2100 K. The stage 6 lasts till rarefaction wave from the outlet surface appearance at the corner. To appreciate the influence of turbulence on the gas self-ignition, the numerical simulations of laminar flow were performed on the base of

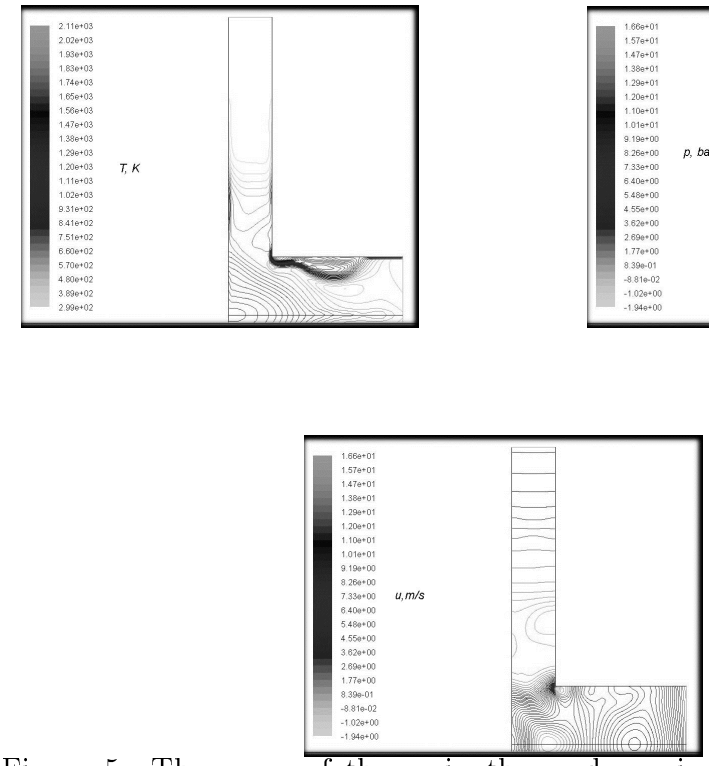

Figure 5: The maps of the main thermodynamic parameters in the chamber at $t = 1.4 \cdot 10^{-3}$ s

Navier-Stokes equations (Fig. 7) at the same initial values of the problem parameters. It could be seen from the figure that for laminar flows the mixture self-ignition may occur as well. Although the maximum value of temperature in laminar hot spot T = 1370 K is significantly less than turbulent T = 2110 K at the same instant.

4 Conclusion

The numerical calculations of the flowfield in a planar vortex chamber on the base of Reynolds equations have been performed. The model is based on conservation laws of mass, momentum and energy for nonsteady two-dimensional compressible gas flow in case of swirl axial symmetry. The processes of viscosity, heat conductivity and turbulence have been taken into account. It was found that transition of kinetic energy of gas into heat due to processes of dissipation generates "hot spots" in boundary layers at the chamber walls. The gas temperature at the spots may exceed the temperature of gas ignition, while the surrounding regions remain still cold. It may be the reason of cold gas self-ignition observed in experiments. The flow turbulence may play decisive role in possibility of gas self-ignition.

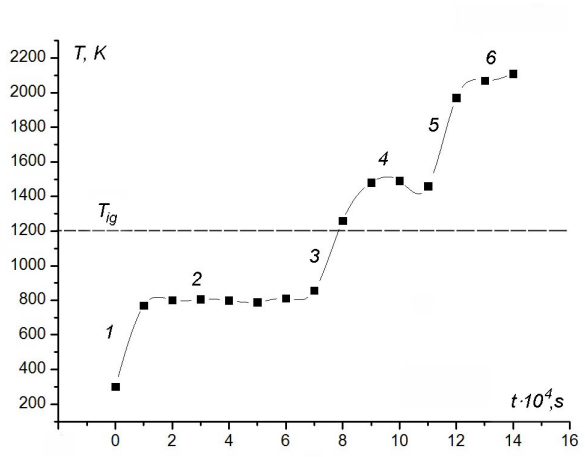

Figure 6: Dynamics of the temperature maximum in the chamber.

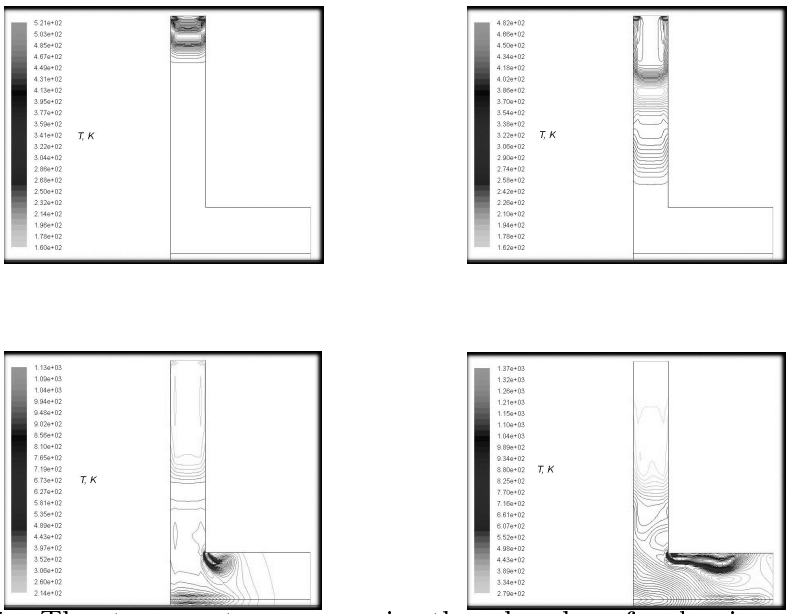

Figure 7: The temperature maps in the chamber for laminar flow at various instants:$t_1 = 1.0 \cdot 10^{-4}$ s, $t_2 = 5.0 \cdot 10^{-4}$ s,$t_3 = 9.0 \cdot 10^{-4}$ s,$t_4 = 1.4 \cdot 10^{-3}$ s.

Acknowledgements

The work was performed with financial support of Russian Foundation of Basic Research (grant N 14-08-0080).

References

[1] Mel'kunmov T.M., Melic-Pashaev N.I., Chistyakov P.G., Shuikov A.G., Rocket engines, Moscow, Mashinosnroenie, 1968.

[2] Protection of labor in research institutions of the USSR Academie of Sciences, Section Two: Safety engineering during exploitation of tanks operating at high pressures, Moscow, Nauka, 1972.

[3] Bykovskii F.A., Zhdan S.A., Mitrofanov V.V., Vedernikov E.F. Self-ignition and special features of flow in a planar vortex chamber, Fizika gorenia i vzryva, 2000, Vol. 35, No 6. pp. 26 - 41.

[4] Anderson D., Tannehill J., Pletcher R. Computational fluid mechanics and heat transfer, New York, Hemisphere, 1984.

[5] Belotsercovskii O.M., Davydov Yu.M. Method of large particles in gas dynamics, Moscow, Nauka, 1984.

Dmitriy V. Voronin, Lavrentyev str. 15, 630090, Novosibirsk, Russia

On the pulse pneumatic transportation of metal radioactive waste materials at atomic electric power stations

Dmitriy V. Voronin, Vyacheslav L. Istomin
voron@hydro.nsc.ru

Abstract

A problem of metal particles movement in a tube under action of a pulse gas flow was numerically and experimentally solved. Comparison of computational and experimental data was carried out. On the basis of researches the optimum characteristics of the work of pulse pneumatic transportation of metal radioactive waste materials are determined. Modeling was performed within the framework of model of non-stationary two-dimensional motion of ideal compressible media on the basis of laws of conservation of mass, pulse and energy in case of axial symmetry. The thermodynamic flow field has been computed both in gas and solid phases. Processes of particles mutual interactions, coalescence, fragmentation, interaction with a tube walls and motion have been investigated in detail. Interface borders have been considered as contact discontinuity surfaces, where a condition of a continuity of normal to the surface component of a flow velocity vector and the continuity of normal component of tension tensor were satisfied. Modeling was performed numerically on the basis of the method of individual particles. The comparison of the computational and experimental data confirms the reliability of numerical algorithm. The optimum pipeline parameters (optimum nozzle diameter is 37 mm, pressure of gas in receiver chamber is about 8 MPa) are determined, at which the effective pulse cleaning of pipelines from metal wastes with the least expenses is possible. It was found that series of pulses is more effective mode of transportation than a single pulse, having similar total power.

1 Introduction

Significant share in high radioactive waste materials, formed in factories on regeneration of worked off nuclear fuels in nuclear electric power stations, make metal wastes as fragments of constructional materials from processing nuclear reactors. One of labor-consuming and dangerous operations in technological process of processing reactors is the operation on transportation of firm wastes, as it is necessary to take into account the danger of materials to an environment and their harmful influence on health of the attendants and population. The various devices for transportation of high radioactive waste materials are known [1, 2, 3]. Now most widespread is their delivery to a burial place in containers by the

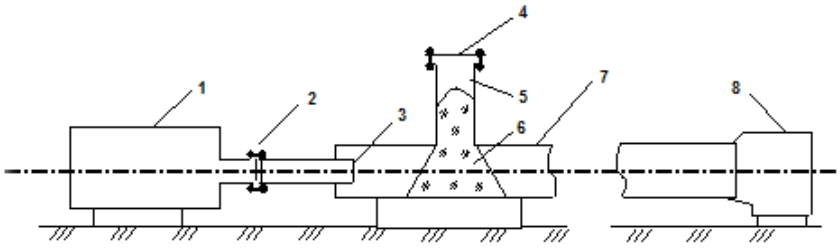

Figure 1: The scheme of experimental installation of pulse pneumatic transportation: 1 - receiver; 2 - valve; 3 - nozzle; 4 - cover; 5 - bunker; 6 - metal pieces; 7 - pipeline; 8 - accumulating chamber.

specially equipped automobiles or railway transportation. Such approach alongside with advantages has essential lacks: in places of loading and the unloadings there are inevitable losses, that can result in jamming the container, and the repair thus is necessary in view of a radioactivity. The best transport of firm radioactive wastes represents pipeline, based on pneumatic transportation and allowing sharply to locate a zone of distribution of radioactive particles, to improve sanitary - hygienic conditions. Such transport has a high degree of automatisation and provides moving a material in a complex line. Here occurrence of emergency conditions is possible as well, in case of a stop of work of the device for pneumatic transportation at blocking, owing to fall of operating pressure values. Especially it is essential for materials with high specific density. However, the latter lack is possible to avoid, using pulsed pneumatic transport [4]. The recent paper is devoted to theoretical and experimental determination of various modes of operations of pulsed pneumatic transport devices, which combines the advantages of usual pneumatic transport and is deprived of the mentioned above lacks. This system is applied now at industrial facilities of "Mayak" groop. The gas was used as an inflator in the pipeline, as the clearing of a liquid is more difficult problem. The scheme of experimental installation for research of parameters of pulse pneumatic transportation is submitted in Fig. 1. A portion of metal pieces was loaded into the bunker and closed by a cover. The gas (air) was pumped into receiver chamber, and after opening of the special valve it penetrates in the pipeline (where the pieces are transported to the accumulating chamber) through a nozzle. In the experiments the simulators of metal pieces of firm wastes with granular structure were used, which were obtained at their mechanical crushing in cutting devices. The size of basic groop of pieces (particles) is about 30-40 mm. A diameter of the pipeline is 250 mm. The purpose of the paper is a calculation of the various characteristics of the process with the subsequent determination of optimum parameters values, ensuring fast and effective clearing off the pipeline: a nozzle diameter, pressure of gas in the receiver chamber and total gas charge.

2 Modeling

Basing on experimental data (obtained with pneumatic transportation device) and knowing its characteristics, we describe the statement of a model problem. The scheme of simulated

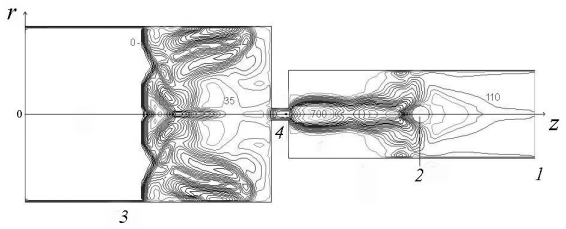

Figure 2: Isolines of gas velocity in the installation.

flow is submitted in Fig. 2. Initially motionless steel particle or conglomerate of particles with diameter d_0 (region 2) is placed within a pipeline having diameter D_0 (region 1). Regions 3 and 4 are the receiver (diameter $2D_0$) and the nozzle correspondingly. The nozzle and the pipeline are initially separated by a diaphragm. All the regions, except for 2, are filled with air. The gas is pumped in regions 3 and 4 for obtaining increased values of initial pressure there. The initial pressure of gas in region 1 is $p_0 = 1$ bar. The whole system is under condition of dynamic balance and has zero value of gas initial velocity in all the regions $u_0 = 0$. At the instant $t = 0$ the diaphragm is removed and propagation of gas pulse from the nozzle within the pipeline starts at constant values of pressure p and gas velocity (equal to sound velocity C_0) at the nozzle. The mathematical model of flow is based on the laws of conservation of mass, pulse and energy for two dimensional non-stationary motion of two-phase compressible medium with obvious allocation of borders between the phases in case of axial symmetry . The basic equations and numerical method are stated in paper [5]. The meanings of characteristic constants correspond to the experimental data described above and are chosen according to [6]. For the firm phase in system of units gram - centimeter-microsecond the following values of characteristic constants have been used: $a_1 = 7,78, a_2 = 31,18, b_0 = 9,591, b_1 = 15,676, b_2 = 4,634, c_0 = 0,3984, c_1 = 0,5306, \phi_0 = 9,0, \rho_0 = 7,86$; for gas $\rho_0 = 0,00122, \gamma = 1,4$. A diameter of the pipeline is $D_0 = 250$ mm, diameter of a particle or their conglomerate is $d_0 = 40$ mm. Let's note, that the problem was solved numerically in dimensionless mode. One of dimensionless combinations of the basic parameters of the problem (determining the flow process) was the ratio $\overline{d} = \frac{D_0}{d_n}$, where d_n is the nozzle diameter. Therefore proportional change of the geometrical characteristics of the problem (at the fixed value of the ratio d_n/d_0) did not change a flowfield of the basic thermodynamic parameters. Due to technological features of pneumatic transportation device [4] the distance l between the particles and the nozzle could not be less than 20 cm. According to computation results, at $l > 20$ cm the main characteristics of the process poorly depend on this parameter, since the losses of a pulse and energy owing to friction of gas at the wall of the pipeline are not taken into account in the model. Therefore the results stated below are obtained at fixed $l = 35$ cm. One of the important technological constants determining characteristic of pipeline transportation, is the velocity of particles starting off U_T. Usually it is considered as lower value of average gas velocity in a cross section of the pipe, at which a particle of definite size is not soared in the flow any more. This hydraulic characteristic of carrying ability of the flow can be considered [3], as the characteristic of some limiting condition, when the frontal influence of a flow on a particle causes its sliding along the wall of the pipe, and the elevating force tries to lift it on some height. According to [3] we have

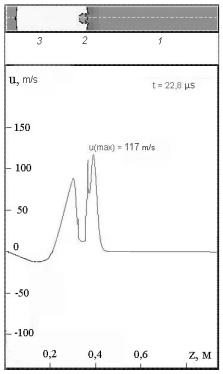

Figure 3: Map of velocity u at the centre of the pipe at $t = 22,8\mu s$.

$$U_T = \sqrt{agd_0/Fr}, \tag{1}$$

$$a = \frac{\rho_2}{\rho} - 1, Fr = \psi_1 + \psi_2\delta^2 \tag{2}$$

Here, ρ, ρ_2 are density of gas and particles accordingly, g is acceleration of force of gravity, d_0 is a diameter of particles, Fr is Froude number , δ is the ratio of the diameter of a particle to the diameter of a pipe; ψ_1, ψ_2 are experimental constants. For the characteristic geometrical sizes of the problem (as the change of the particle form in course of time from just splintered to smoothed ones was taken into account and $\psi_1 = 0,7 \div 1,35$ according to [3]) the value of U_T varies from 14,4 m/s up to 24,8 m/s. The maximal value of the velocity of particles starting off $U_T = 25$ m/s was taken in the numerical calculations stated below. To minimize the time of obtaining U_T, it is necessary to pick up the optimum size of a nozzle. The necessity of such a nozzle for submission of gas into the pipeline is caused by two main reasons. First, the velocity of a gas flow for steady motion of particles in the pipeline should be $2 - 3$ times more than the velocity of particles starting off. Secondly, used in experiments the receiver has limited volume.

The flow-field of gas velocities in the pipeline at instant $t = 2$ ms from a beginning of diaphragm breaking at the initial pressure value in the receiver $\overline{P} = 7$ MPa is submitted in Fig. 2. Twenty ranges of velocities in an interval from 0 up to 750 m/s are represented here. The length of receiver is 70 cm. In experiments the duration of a gas pulse τ, acting from the nozzle into the pipeline, is sometimes adjusted with the help of a latch in the nozzle. The results of such a numerical modeling in the pipeline are submitted in Fig. 3 at $\tau = 0,8$ ms for longitudinal velocity u at the instant 1,1 ms from the moment of diaphragm break ($\overline{P} = 8$ MPa). Here region 1 is gas at initial pressure $p_0 = 1$ bar ($\rho_0 = 0,001225g/cm^3$), region 2 is for particles of steel, 3 is a pulse, moving to the left hand side from the nozzle into the pipeline, with compressed air at $\overline{P} = 8$ MPa ($\rho = 0,098g/cm^3$). We name an interval between the beginning of interaction of a particle with the pulse and moment of reaching the meaning of U_T as the time of obtaining of the velocity of particles starting off. Its meaning was determined from the generated slides with a step of 0,2 ms, showing the further stages of the process. For the recent variant such time is equal to $22,8\mu s$. Here readout of z coordinate is conducted from the nozzle. The required velocity of particles

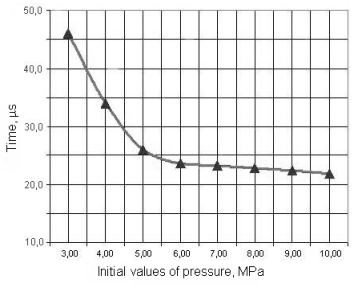

Figure 4: Time dependence of achievement of Ut from initial pressure of gas

starting off was determined from a structure of longitudinal velocity at the centre of the pipe. As it is visible from the figure, by this moment the particle velocity begins to exceed the meaning of the velocity of particles starting off.

Table 1. Time dependence of achievement U_T from pressure of working gas.		
number of calculation	initial pressure of gas, MPa	time for achievement U_T
1	1	-
2	3	46,00
3	4	34,00
4	5	26,00
5	6	23,60
6	7	23,20
7	8	22,80
8	9	22,40
9	10	21,80

Variations of time of reaching U_T meanings are represented in Tab. 1. As it is visible from the table, at the fixed nozzle diameter $d_n \in [10, 200]$ mm and $\overline{P} > 6$ MPa the time of reaching the velocity of particles starting off begins poorly to depend on growth of initial pressure values. As is clear from numerical simulations, at the fixed pressure of gas in the receiver for meanings presented in Tab. 1, the least time of achievement of the velocity of particles starting off corresponds there the meaning $\overline{d} = 6,8$. With the reduction of $\overline{d}$, the gas in the pipeline has the velocity insufficient for steady motion of particles, and at the very large diameter of nozzle, the pulse of gas is short, i.e. the time of its influence on the particles is insignificant. If $d_0 = 40$ mm, then the optimum diameter of nozzle is 37 mm, that is close to experimental data [4], where it is equal to 35 mm. In Fig. 4 we can see the time diagram of reaching the value of the velocity of particles starting off U_T from the initial pressure of gas. It is visible from the diagram,

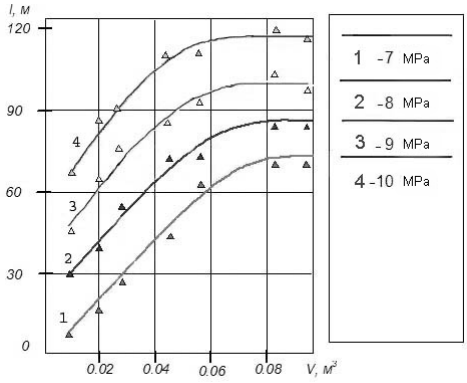

Figure 5: Influence of the receiver volume and initial pressure of gas on the distance of particles motion.

that the time has radical changes at pressure values diapason from 3 MPa up to 6 MPa, but at the further increase of pressure its change are insignificant. Optimum parameter value for the present scheme is pressure $\overline{P} = 8$ MPa, the further increase is inexpedient, since it will result in the over-expenditure of energy. In subsequent simulations we use this meaning of pressure. Now we must determine the optimum charge of gas that is necessary for the pipeline cleaning. The distance of particles motion (at fixed nozzle diameter and variating pressure and the receiver volume) is important factor here. Let's note, that as the distance of transportation we consider one from initial place up to the position of the inertia centre for the conglomerate of particles after their motion under action of the pulse of gas. In technological installations that distance is about tens meters. Such range is achieved, if average gas velocity in cross section is 2-3 times higher than the velocity of particles starting off. For the comparison with experimental data it was assumed in numerical simulations, that the value of gas velocity $u = 2,5U_T$ provides such a distance. The comparison of experimental and numerical (continuous lines) data is presented in Fig. 5. The deviations of numerical curves from experimental data do not exceed 7 percents. It is visible from the figure, that with growth of the receiver volume at fixed initial pressure of gas in it, the distance of particle motion initially grows linearly and at achievement of some critical volume remains practically constant. At the increase of initial pressure of gas in the receiver this curve moves above. Thus, there exists an optimum technological volume of the receiver (about $0,078m^3$), and its further increase becomes inexpedient. In Tab. 2 the computation of the charge of gas is presented at the fixed initial pressure $\overline{P} = 8$ MPa. It is visible from the table, that there is an optimum technological volume here as well, that at its further increase the time of achievement of the velocity of particles starting off varies poorly. As well as in the previous problem we determine the time of achievement of the velocity of particles starting off U_T . In experiments for breadboard models of pulse pneumatic device [4] not a single pulse was used, but alternation of pulses. For the checking of efficiency of such an approach, the simulations with two pulses were performed, when the total duration is equal to one submitted in Fig. 3. All other values of a flow parameters of these problems are similar. As numerical study reveals, the alternation of the phases of compression and rarefaction, that is usual for the complex of two pulses, results in strong distortion of the form of the conglomerate of particles owing to instability

of interface border that promotes the development of the splitting phenomena. Therefore alternation of pulses is more effective means of clearing of the pipeline, than having pulse at fixed velocity and pressure that proves to be true by the experimental data [4]. The numerical simulations confirm that with increase of gas volume its duration of action is increased as well, but the meaning $V_{opt} = 0,095m^3$ is optimal, since at smaller volume the object exposed to influence of a wave of compression, has not necessary velocity for steady motion. The results of modeling on revealing of parameters for the optimum mode of transportation, well coincide with parameters obtained by experimental way.

Table 2. Determination of the optimum charge of gas.

number of calculation	time of achievement $U_T, \mu s$	time of action, μs	volume of gas in a pulse, m^3	the charge of gas, kg
10	-	26,0	0,088	8,624
11	30,0	32,4	0,095	9,31
12	26,4	36,8	0,106	10,388
13	22,8	38,2	0,15	14,7
14	22,4	42,2	0,176	17,248
7	22,0	46,0	0,196	19,208

3 Conclusions

The problem of metal particles motion in a pipe under action of a pulsed gas flow is numerically solved in the paper. The comparison of the numerical data with experimental ones testifies about reliability of the numerical algorithm. The optimum value of device parameters are determined (optimal nozzle diameter is about 37 mm, pressure of gas in the receiver is about 8 MPa and appropriate gas charge corresponds to the values), at which the effective pulse clearing of pipelines from metal wastes with the least expenses is possible.

References

[1] Ginniff M. A burial place of radioactive wastes // Nuclear engineering abroad. - 1984. N 7. - P. 42.

[2] Borisov G.B., Saveliiev V.F. Processing and storage of metal wastes from regeneration of the worked out nuclear fuel // Nuclear engineering abroad. - 1978. N 8. - P. 23.

[3] Smoldyrev A.K. Pipeline transportation. - Moscow: Nedra, 1970, 272 pp.

[4] Istomin V.L. Pulse pneumatic transportation of metal radioactive wastes at nuclear power stations // Atomic Energy. - 1994. - V. 77. - N. 3. - P. 231.

[5] Voronin D.V., Istomin V.L. Modeling of pulse pneumatic transportation of metal radioactive wastes from processing at nuclear power stations // Problems of radioactive safety. - 2011 - є4 - P. 61.

[6] Loytsianskiy L.G. The mechanics of a liquid and gas. - Moscow: Nauka, 1987, 840 pp.

Dmitriy V. Voronin, Lavrentyev Institute of Hydrodynamics of SB RAS, Lavrentyev str. 15, 630090, Novosibirsk, Russia
Vyacheslav L. Istomin, Lavrentyev Institute of Hydrodynamics of SB RAS, Lavrentyev str. 15, 630090, Novosibirsk, Russia

Crack propagation analysis of compressor blade subjected to resonant vibrations

Lucjan Witek, Arkadiusz Bednarz, Feliks Stachowicz, Nikita Kazarinov, Ivan Smirnov
lwitek@prz.edu.pl, i.v.smirnov@spbu.ru

Abstract

In this work the crack propagation analysis of the compressor blade of aero engine was performed. During investigations the blade with mechanical defect (notch) was considered. In experimental analysis the blade was subjected to resonant vibration. During transverse vibrations, a high stress occurs in the blade. Pulsation of stress causes the fatigue of material. In results of proposed investigations both the number of load cycles to initiation and also the crack growth dynamics was obtained for the blade working in resonance condition. In second part of work the maximum principal stress distributions in the vibrated blade were determined using finite element method.

1 Introduction

High-cycle fatigue (HCF) is often concerned with vibration of aero engine components. Compressor blades have a small bending stiffness and are particularly susceptible to HCF. During work of engine, blades are excited by an unbalanced rotor. The worst case is when the frequency of excitation overlaps with the resonant frequency of the blade. During resonance, large amplitude of stress causes that the blade can be damaged in relatively short time. The fatigue process is often accelerated by mechanical defects (notches) created during collision of rotated blade with hard objects suctioned from a ground. If aBrproblem arises in the compressor section it will significantly affect the whole engine function and safety of the aircraft.
The broken blade could cause the puncture of the engine casing. Failures of any high speed rotating components (jet engine rotors, centrifuges, high speed fans, etc.) can be very dangerous to passengers, personnel and surrounding equipment and must always be avoided. The failure analysis of the compressor blade has received the attention of several investigations. The problem of fatigue fracture of the aero engine blades was described in works [1-10].
The objective of presented investigation is to determine both the number of load cycles to crack initiation and also the crack growth dynamic for the compressor blade of aero engine (including artificially created mechanical defects), subjected to resonant vibrations. Created defects (notches) simulate the foreign object damage (FOD) of the blade. An additional aim of work is numerical determination of maximum principal stress values in the blade with the notch subjected to resonant vibration.

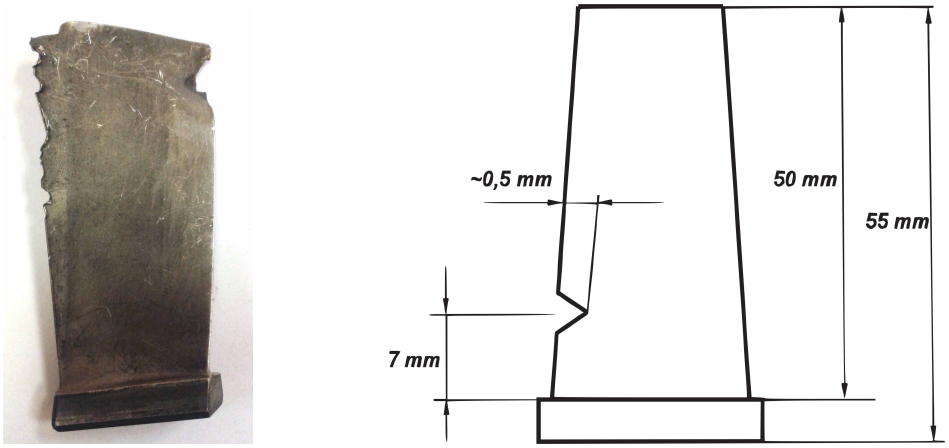

Figure 1: View of blade damaged by foreign object (a), dimension of the investigated blade with v-noth (b).

2 Experimental investigations

In investigated blade a V-notch presented in Fig. 2 was created. The depth of notch was about $0.5mm$ whereas the apex angle 90 degrees. The notch in the blade was created by machining. The compressor blade was made out of $EI-961$ steel ($0.11C$; $11Cr$; $1.5Ni$, $1.6W$; $0.18V$; $0.35Mo$; $0.025S$; $0.03P$) with the following properties (measured in temperature 20^oC): Ultimate tensile strength $900-1000MPa$, Yield stress $800-900MPa$, Young modulus $200GPa$, Poisson ratio 0.3. The high cycle fatigue tests of the blade were made using the Unholtz-Dickie UDCO TA-250 electrodynamic vibration system, presented in Fig. 3 at Laboratory of Turbomachinery of Rzeszow University of Technology. The blade with a notch was horizontally mounted on the movable head of vibrator (Fig. 4). Next the head of shaker was entered into harmonic vibration. In first step of analysis the resonance frequency was determined (for first mode of transverse vibration). The fatigue test was started from frequency close to resonant. During investigations two main parameters were periodically monitored: vibration amplitude of the blade tip and the size (or existence) of the crack. For control of amplitude the laser scanning vibrometer POLYTEC PSV H-400S were used. To measure the length of the crack a nondestructive fluorescent penetrant method was utilized.

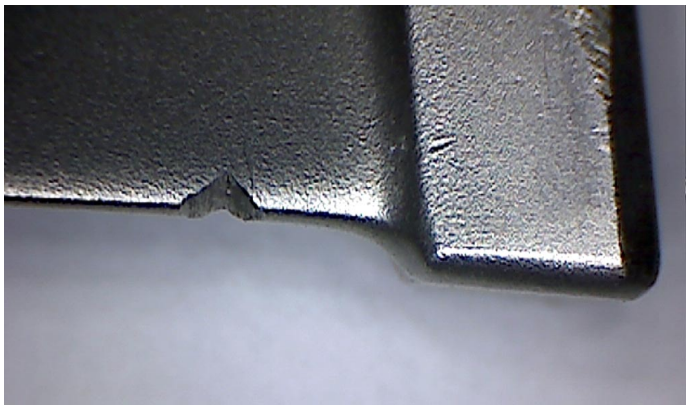

Figure 2: V-noth created on the attack edge of investigated blade.

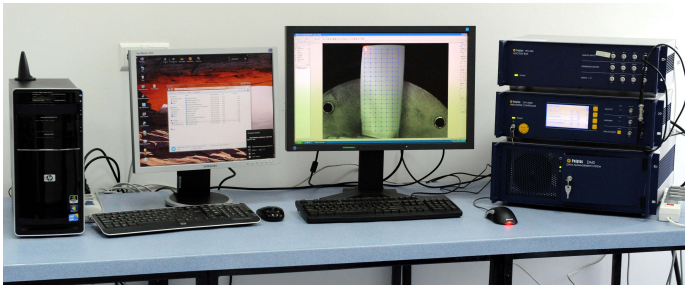

Figure 3: View of control systems of both laser scanning vibrometer and the shaker used in experimental investigations.

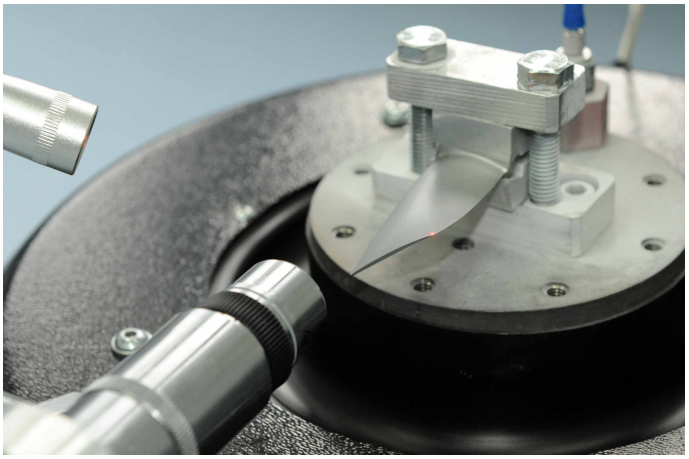

Figure 4: Compressor blade fixed to movable head of vibrator.

The control parameters of vibration system and results obtained for compressor blade are shown in Tab. 1. The resonant frequency (F_{rez}) of blade was $796.6Hz$. As seen from Tab. 1, the fatigue test started from frequency $2.2Hz$ higher than F_{rez} ($798.8Hz$). Just for this frequency, the vibration amplitude $A = 1.2mm$ was achieved. After 12.46×10^6 total number of cycles (N), an amplitude of blade tip decreased from $1.20mm$ to $1.08mm$. During fracture, the bending stiffness of blade is not constant. This information is important from practical point of view, because decrease of amplitude at constant intensity of excitation is always related to start of crack initiation process. In present case $2.5mm$ long crack (a dimension in Fig. 8) was detected. From $N = 12.82 \times 10^6$ number of load cycles, the excitation frequency decreased with different rate. Preliminary, the rate of change of frequency was $0.025Hz/s$. It allowed to maintain the vibration amplitude on constant level (about $1.2mm$). In first stage of blade fracture the intensity of acceleration of vibrator head was constant to crack length $a = 6.5mm$. After that the intensity of head acceleration was increased to $12g$ and $14g$ adequately. In spite of increase of acceleration, the blade amplitude was not constant in the final stage of fracture (for crack length $a = 6.5 - 19mm$).

Obtained results (Tab. 1) showed that the blade with v-notch created by machining, needs $N = 12 \times 10^6$ total number of load cycles to crack initiation. The crack propagation process was much shorter. The crack needs $N = 1.87 \times 10^6$ number of load cycles for propagation from length $a = 0$ to final crack size a = 19 mm (at which the blade was broken). Thus, in presented case the crack initiation process ($N = 12 \times 10^6$) is a main part of fatigue life of the blade ($N = 13.87 \times 10^6$).

Table 15: Control parameters of vibration system and results of fatigue test of the blade.

Initial freq.	Final freq.	Rate of change of freq.	Intensity of excitation	Partial no. of cycles	Total no. of cycles	Total no. of cycles (crack prop.)	Crack length	Amplitude of crack tip
F_{init} $[Hz]$	F_{fin} $[Hz]$	dF/dt $[Hz/s]$	$[g]$	N_{part} $\times 10^6$	N $\times 10^6$	N_{cp} $\times 10^6$	a $[mm]$	A $[mm]$
798.8	798.8	0	10	0	0	-	0	1.20
798.8	798.8	0	10	3	3	-	0	1.20
798.8	798.8	0	10	3	6	-	0	1.20
798.8	798.8	0	10	3	9	-	0	1.20
798.8	798.8	0	10	3	12	0	0	1.19
798.8	798.8	0	10	0.46	12.46	0.46	2.5	1.08
798.8	789.3	0.025	10	0.36	12.82	0.82	4.0	1.21
789.3	770.0	0.036	10	0.40	13.22	1.22	6.5	1.14
770.0	699.0	0.260	12	0.20	13.42	1.42	9.0	1.03
699.0	500.0	0.370	14	0.32	13.74	1.74	15.0	0.95
500.0	100.0	0.130	14	0.13	13.87	1.87	19.0	0.91

The assumption of work was to maintain the blade tip displacement amplitude (vibration amplitude) on constant level. However this condition is difficult for satisfy during all fatigue test. The vibration amplitude in the blade was constant until about $N = 12 \times 10^6$ number of cycles (Fig. 6). Just after crack initiation, the blade stiffness decreases and in consequence of them the lower value of blade amplitude ($A = 1.08mm$) was observed (at $N = 12.46 \times 10^6$). To maintain the blade amplitude on level $A = 1.2mm$ the frequency of excitation was next decreased. In the range of $N = 12.82 - 13.10 \times 10^6$ number of load cycles, the blade amplitude was close to initial value, but after $N = 13.42 \times 10^6$ the vibration amplitude decreased more quickly. The last part of fracture is highly unstable process. The increase of intensity of vibration (to value of $12g$ and $14g$) in finish part of fatigue (Fig. 7) caused that the vibration amplitude was still not constant (Fig. 6).
Shape of crack in preliminary phase of growth is presented in Fig. 8a. As seen from this figure, the crack in first phase of growth propagates more quickly along the concave surface of the blade profile. In Fig. 8a is also distinguished the crack length (a dimension) used to description of vertical axis of plot presented in Fig. 5. The blade after finish of the fatigue test is visible in Fig. 8b. The crack direction is not parallel to blade lock. The crack starts from the notch located $7mm$ above the lock. The crack in finish part of fracture achieved the trailing edge of the blade, about $5mm$ above the lock.

3 Numerical stress analysis of the compressor blade subjected to vibration

For definition of stress state in the blade subjected to HCF, the finite element analysis (FEA) was performed. In this analysis the first mode of transverse vibration was considered. To solve this problem, the Patran program was used to both geometrical and the finite element model preparation. In Fig. 9a the discrete model of blade with the notch located $7mm$ above the lock was shown. In the notch vicinity the finite element mesh was concentrated (Fig. 9b). In the next part of work Abaqus software were used for stress and modal analysis of the compressor blade. Results of FEM analysis (Fig. 9c) showed that

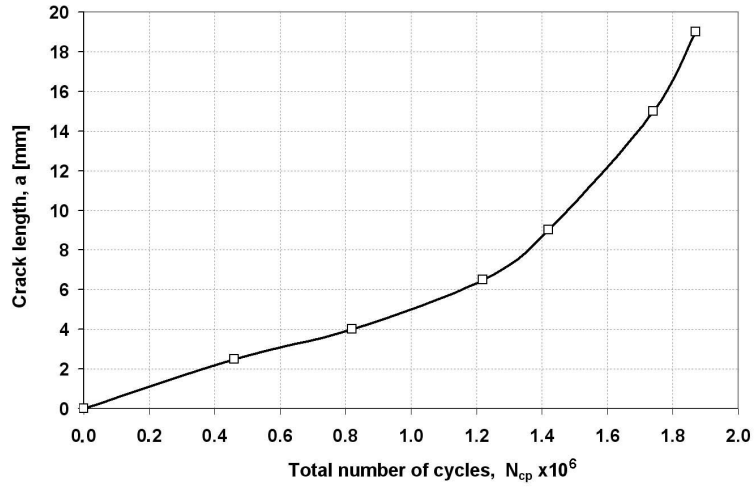

Figure 5: The crack length in function of number of load cycles N_{cp} (counted from crack initiation) for blade subjected to resonant vibration (first mode, $A = 1.2mm$).

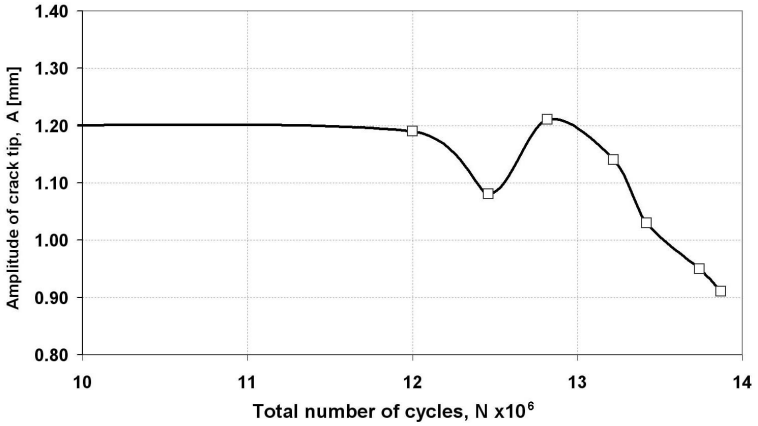

Figure 6: Amplitude of crack tip displacement (vibration amplitude) as a function of number of load cycles N.

during first mode of resonant vibration the blade are subjected to cyclic bending. During transverse vibration the maximum value of amplitude of displacement (on blade tip) is equal to $1.2mm$. All numerical results are obtained for the same vibration amplitude ($A = 1.2mm$) and for left blade deflection at which the maximum principal stress in the blade was observed. Figure 10a showed that value of maximum principal stress value in the zone located near the attack edge of blade is about $225 - 280MPa$. The area of maximum stress ($771MPa$) is located in the notch vicinity (Fig. 10b). Maximum principal stress values in cross-section of blade (in fracture plane) showed that during left blade deflection the tension stress occurred in the zone near concave surface of blade (Fig. 11). Just in this region the crack propagate more quickly than in convex profile area. Obtained results showed that cyclic tension stress in blade cross section is a main reason for crack initiation and crack propagation of the blade subjected to resonant vibration.

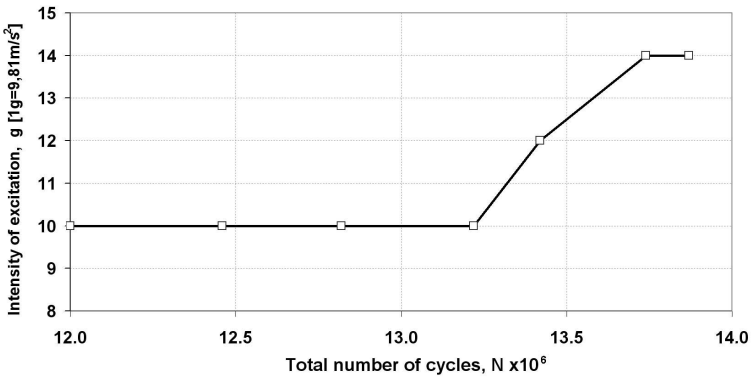

Figure 7: Intensity of excitation (vibration) in function of number of load cycles N.

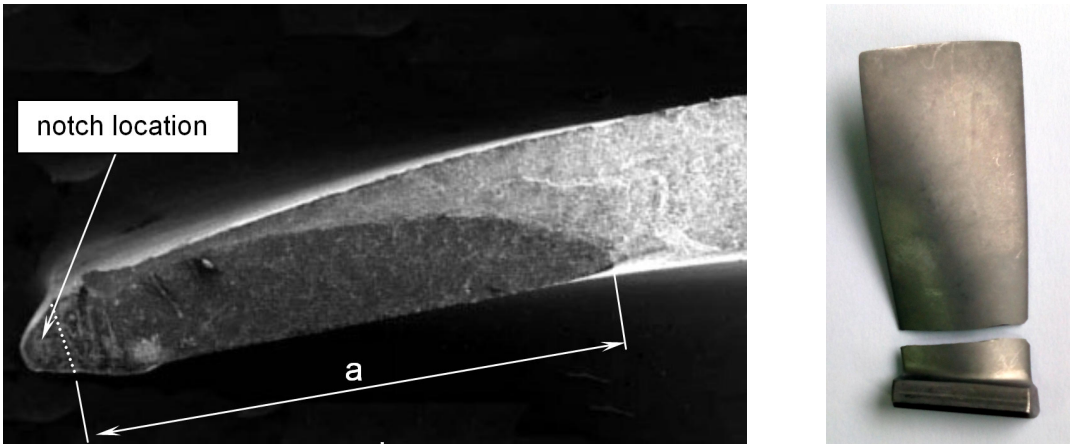

Figure 8: Fracture of blade with $6.5mm$ long crack ($a = 6.5mm$) (a) and the blade after finish of fatigue test (b).

4 Conclusions

In this study the experimental analysis were performed to investigate both the crack initiation and the crack propagation process of compressor blade with preliminary defect. This mechanical defect simulates the foreign object damage. The complex experiment was performed in resonance condition. In experimental investigation a modern vibration system and the laser scanning vibrometer were used. In results of performed work, the following conclusions were formulated:

1. Foreign object damage is very dangerous for the compressor blades. In most cases defects obtained in results of FOD (as V-notches) is potential crack origin. After phase of initiation, the crack propagates from notch inside the structure in relatively short time.

2. The crack in the blade working in resonance conditions (first mode of vibrations, $A = 1.2mm$) initiates after about $N = 12 \times 10^6$ total number of load cycles.

3. The crack needs $N = 1.87 \times 10^6$ number of load cycles for propagation from length $a = 0$ to final crack size $a = 19mm$ (at which the blade was broken).

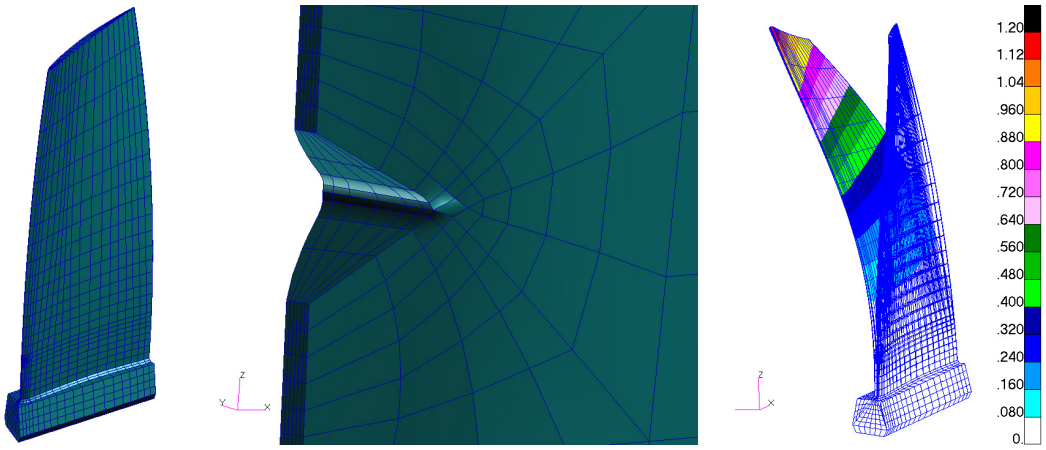

Figure 9: View of numerical model of compressor blade (a), magnified notch area (b) and values of displacement of blade during first mode of free vibrations, $[mm]$ (c).

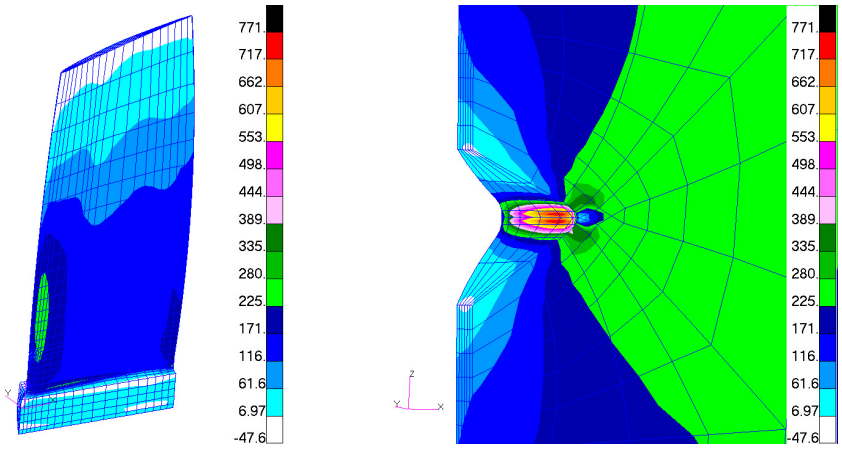

Figure 10: Values of maximum principal stress for the blade (a) and in the vicinity of notch (b), $[MPa]$.

4. The crack initiation process (number of cycles for initiate of crack from $a = 0$ to blade damage) is a small part (about 13.5%) of total fatigue life of blade ($N = 13.87 \times 10^6$).

5. Maximum principal stress area in the blade is located on tip of notch. In the blade vibrated with amplitude $1.2mm$ a maximum stress on the notch has a value of $771MPa$. This value is close to yield stress of blade material.

6. Maximum principal stress value (for left deflection) in the blade without defects is about 3 times lower then the local stress in the notch.

In the case of old aircraft structures, which are operated according to the damage tolerance method, the information about crack dynamics is very important from practical point of view. In aerospace engineering, structure is considered to be damage tolerant if implemented maintenance program can stop operation of structure with a small (safe) fatigue crack. The operation of structures according to damage tolerance methodology can cause a significant reduction of costs because the aircraft or aero-engine can be safety operated to the real fatigue limit.

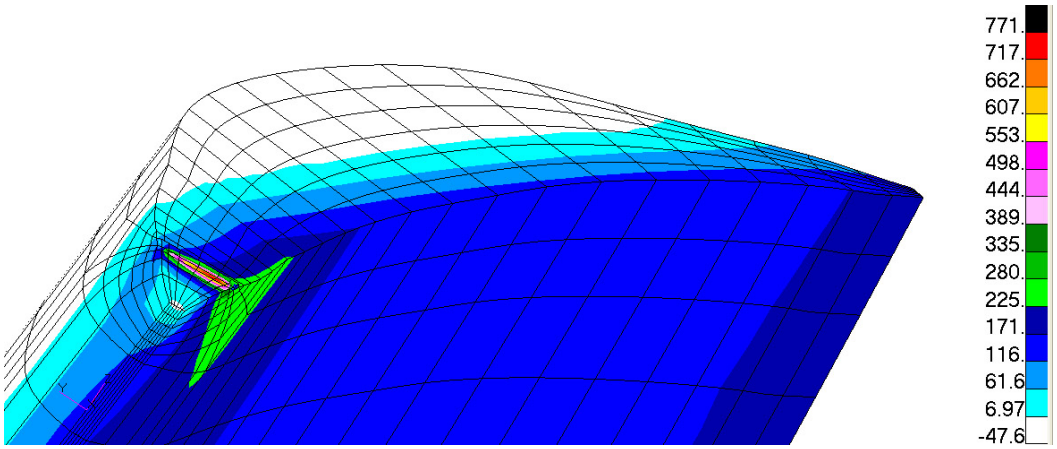

Figure 11: Values of maximum principal stress in cross-section of blade (at level of notch), $[MPa]$.

Acknowledgements

The research leading to these results has received funding from the People Programme (Marie Curie International Research Staff Exchange) of the European Union's Seventh Framework Programme FP7/2007-2013/ under REA grant agreement nBo PIRSES-GA-2013-610547.

References

[1] Kermanpur A., Sepehri A.H., Ziaei-Rad S., Nourbakhshnia N., Mosaddeghfar M., Failure analysis of Ti6Al4V gas turbine compressor blades, Engineering Failure Analysis, Vol. 15, pp: 1052-1064; 2008.

[2] Lourenco N.J., Graca M.L.A., Franco L.A.L., Silva O.M.M., Fatigue failure of a compressor blade, Engineering Failure Analysis, Vol. 15, pp: 1150-1154, 2008.

[3] Park M., Hwang Young H., Choi Y.S, Kim T.G., Analysis of a J69-T-25 engine turbine blade fracture. Engineering Failure Analysis, Vol. 9, pp: 593-601, 2002.

[4] Song K.S., Kim S.G., Jung D., Hwang Y.H. Analysis of the fracture of a turbine blade on a turbojet engine, Engineering Failure Analysis, Vol. 14, pp: 877-83, 2007.

[5] Troshchenko V.T., Prokopenko A.V., Fatigue strength of gas turbine compressor blades. Engineering Failure Analysis, Vol. 7, pp: 209-220, 2000.

[6] Witek L., Simulation of crack growth in the compressor blade subjected to resonant vibration using hybrid method, Engineering Failure Analysis, Vol. 49, pp: 57-66, 2015.

[7] Witek L., Crack propagation analysis of mechanically damaged compressor blades subjected to high cycle fatigue, Engineering Failure Analysis, Vol. 18, pp. 1223-1232, 2011.

[8] Witek L., Fatigue Investigations of the Compressor Blades with Mechanical Defects, Key Engineering Materials, Vol. 598, pp. 269-274, 2014.

[9] Vardar N, Ekerim A. Failure analysis of gas turbine blades in a thermal power plant, Engineering Failure Analysis, Vol. 14, pp: 743-749, 2007.

[10] Xu X., Yu Z., An investigation on the failed blades in a locomotive turbine, Engineering Failure Analysis, Vol. 14, pp: 1322-1328, 2007.

Lucjan Witek, Arkadiusz Bednarz, Feliks Stachowicz,
Faculty of Mechanical Engineering and Aeronautics, Rzeszow University of Technology Al. Powstancow Warszawy 8, 35-959 Rzeszow, Poland
Nikita Kazarinov, Ivan Smirnov,
Department of Elasticity Theory, Saint Petersburg State University, Universitetskiy prospekt 28, Peterhof, St. Petersburg, 198504, Russia

Starting inertially excited trans-resonant vibration machines with several degrees of freedom of the carrier system

N.P. Yaroshevich, A.V. Sylyvonyuk, I.P. Zabrodets
Andriy.Sylyvonyuk@gmail.com, m_yaroshevich@mail.ru

Abstract

Expressions for vibration moments (additional dynamic loading caused by the vibrations of bearing body) during the passage of resonant zone by vibration machines with the flat vibrations of bearing body both with one arbitrarily located vibration exciter and with two self-synchronization vibration exciters for the different modes of starting are got in an analytical form by method of direct division of motions. Using approaches of vibration mechanics of I.I. Blekhman possibilities of improvement of process of running approach of vibration machines with unbalanced vibration exciters are demonstrated by using of methods the "double" (in case of one vibration exciter) and "separate" starting of electric motors (in case of two vibration exciters). It is shown that the first method is based on using semislow vibrations arising in the resonant zone. The necessary condition of the successful using of this method is motion on the rotor of exciter in the moment of the repeated including of engine of rotary-type vibration moment. The conditions when the separate starting is effective are shown. Conclusions and practical recommendations that allow to facilitate starting of vibration machines with an unbalanced drive are pointed.

1 Posing the problem and its connection with the main scientific tasks

Solutions of problems of run-up and run-down of vibrational systems with inertial drive is of considerable interest for vibrational technical devices. When inertial vibroexciter passes the zone of natural frequencies an unset of resonance vibrations is possible which cause both a sufficient rise of dynamic loads on the rotor of electric motor, on elements of machine bearing construction and additional losses of power in the system. So, the start of vibration machine with unbalanced drive needs the power of the drive with sufficiently exceed the power needed for operating in stationary mode (2-5 times as large by some data). In addition to that, in case of large machines with the drive from electric motors of asynchronous type the striking starting current exerts negatively upon the feeding electrical network.

In order to lower the level of vibrations when passing the resonance zone various means are used – from vibroexciters with automatically regulated static moment of unbalance mass

to algorithms with feedback. No doubt, to successful realization of the lasts it is important to have more thorough conception of dynamics of the occurring processes.

2 Analysis of the latest investigations

The survey of investigations, concerning the passing of the resonance zone by inertial vibroexciter one may find in [1-3]. In the last years a number of tasks are solved on the basis of vibrational mechanics approaches, in particular, by using the method of direct separation of motions. In [3] it is shown by the example of the simplest system with linear vibrations of the bearing body and one unbalanced exciter that the important merit of such approach is its comperative simplicity and physical integration of the results.
In work [2] attention is paid to the peculiarity of the motion of the system nearby the resonance – the availability of the so called inner pendulum and its YsemislowY motions, which are physical base of the efficiency of some methods of controlling the starting of vibration machines with inertial exciting of vibration.
A great number of works are dedicated to the use of the phenomenon of selfsynchronization in vibration machines and devices, they are shown in [1, 3], and the latest ones in [4-6]. However, no attention was paid to the dynamics of starting of such vibrations machines. The presented paper is dedicated to generalization and development of the results of works [2, 7-9].

3 Statement of the task

The majority of vibration machines with unbalanced drive may be idealized in the form of a system, consisting with a single lifting rigid body, which may execute plane-parallel motion and is connected with stationary base with elastic and damping elements (Fig. 1). As exciters of vibrations of lifting body mostly unbalanced vibroexciters (disbalanced rotors) drived by the electric motors of asynchronous type are used. Motion equations of such system may be written down in the following form (see, for instance, [1-3]):

$$M\ddot{x} + \beta_x\dot{x} + c_x x = \sum_{i=1}^{s} m_i\varepsilon_i(\ddot{\varphi}_i \sin\varphi_i + \dot{\varphi}_i^2 \cos\varphi_i),$$

$$M\ddot{y} + \beta_y\dot{y} + c_y y = \sum_{i=1}^{s} m_i\varepsilon_i(\ddot{\varphi}_i \cos\varphi_i - \dot{\varphi}_i^2 \sin\varphi_i), \quad (1)$$

$$J\ddot{\varphi} + \beta_\varphi\dot{\varphi} + c_\varphi\varphi = \sum_{i=1}^{s} m_i\varepsilon_i r_i(\ddot{\varphi}_i \cos(\varphi_i + \delta_i) - \dot{\varphi}_i^2 \sin(\varphi_i + \delta_i)), (s = 1...n)$$

$$I_i\ddot{\varphi}_i = L_i(\dot{\varphi}_i) - R_i(\dot{\varphi}_i) + m_i\varepsilon_i(\ddot{x}\sin\varphi_i + \ddot{y}\cos\varphi_i + r_i\ddot{\varphi}_i\cos(\varphi_i + \delta_i) + g\cos\varphi_i), \quad (2)$$

where M, J – are correspondingly, mass and moment of inertia of the lifting body as to the axis which passes through its center of gravity; x, y, φ – are coordinates, determining the position of the lifting body; φ_i – are the angles of rotation of vibroexciter; r_i and δ_i – are polar coordinates of axes of vibroexciters; m_i, ε_i – are, correspondingly, mass and accentricity of the exciter; I_i – is applied to the shaft of the vibroexciter moment of inertia of the rotating parts of the drive; c_x, c_y, c_φ – are horizontal, vertical and rotational rigidity of the elastic elements; β_x, β_y, β_φ – are coefficients of viscous resistance; $L_i(\dot{\varphi}_i)$, $R_i(\dot{\varphi}_i)$ – is the torque of the electric motor and moment of forces of resistance to rotation; g – is a free-fall accekeration.

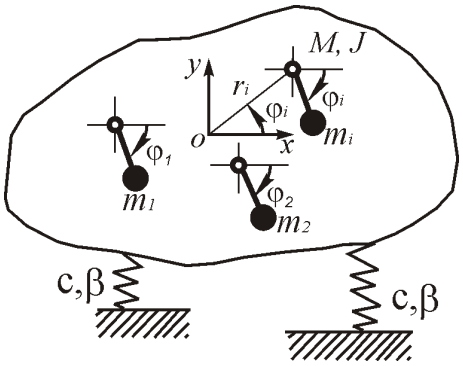

Figure 1: General diagram of vibrational system with unbalanced vibroexciters.

4 Exposition of the basic material

To solve the set of equate ions (1), (2) we use the method of direct separation of motions [1, 3]. Set us accept as a zero-order approximation $\varphi_i = \omega t$, $q_i = P_i \sin\omega t + Q_i \cos\omega t$ where $\omega = \omega(t)$ -Ц are slowly and $q_i = x,y,\varphi$ – fast changing time functions. Then it is not complicated to come from the original system of equations of vibroexciters rotors motion (2) to the equations of their rotation in the resonance zone in the form, obtained in [3]:

$$I_i\dot{\omega} = L_i(\omega) - R_i(\omega) + V_i(\omega), \tag{3}$$

where $V_i(\omega) = m_i\varepsilon_i\langle\ddot{x}\sin\varphi_i + \ddot{y}\cos\varphi_i + r_i\ddot{\varphi}_i\cos(\varphi_i + \delta_i)\rangle$.
French quotes in (3) point out at averaging for the $T = 2\pi$ by fast time $\tau = \omega t$.
It should be noted that equation (3) differs from classic equation of machine assembly by presence of item $V_i(\omega)$ – vibrational moment which defines the peculiarity of vibrational system conduct. Presence of vibrational moment explains both ZommerfieldЎs effect and selfsynchronization of vibroexciters. Determination of the vibrational moment is of main interest.
It should be noted that equation (3) keeps its form, obtained for the system with linear vibrations of the lifting body [3] for the examined more general case as well. Only expression for vibrational moment has more complicated structure, algorithm of its obtaining remains previous, only computing difficulties grow up.

4.1 Vibrational systems with one vibroexciter ZommerfieldЎs effect

Certain part of operating at present machines has one unbalanced vibroexciter. It is not complicated to obtain expressions of vibrational moment in the resonance zone for the case of vibroexciter, placed arbitrarily as to centre of masses of the lifting body in plane vibration in the form:

$$V(\omega) = -\frac{(m\varepsilon\omega)^2}{M}\left[\frac{n_x}{B_x^2} + \frac{n_y}{B_y^2} + \frac{Mr^2}{J}\frac{n_\varphi}{B_\varphi^2}\right], \tag{4}$$

$$B_q = \sqrt{(1-\lambda_q^2)^2 + 4n_q^2};\ \lambda_q = \frac{p_q}{\omega};\ n_q = \frac{\beta_q}{2M_q\omega},$$

where p_q – are the frequencies of the natural vibration of the system.
Here, if $q = x$, y, then $M_q = M$, if $q = \varphi$, then $M_q = M\frac{\rho^2}{h^2}$; in addition to that, $n_\varphi = \frac{\beta_\varphi}{2J\omega}$.

One can see that all items in formula (4) are negative. Hence, vibrational moment is always braking one, that is, it is an additional dynamic load upon the rotor of the engine, its dependence from frequency is of resonance character and, therefore, an essential braking exercion is manifested in comparatively narrow range of natural frequencies. In addition to that, rapid growth of value $V(\omega)$ at approaching to resonance just explains the possible Ysticking¥ of frequency in the process of starting (Zommerfield¥s effect) and, as consequence, the necessity of overrated (from starting conditions) power of the drive of postresonance vibromachines. Such conclusion follows from diagramic presentation of dependences $L(\omega)$ and $M_{sum} = R(\omega) + V(\omega)$ (fig. 2), abscissas of intersection points correspond to possible stationary modes (curves L describe statical characteristics of electric engines. Stability of motions is easily determined geometrically by the sign and values of slope angles tangent to curves $L(\omega)$ and M_{sum}. It is evident that right slopes of resonance curve cannot be realized. According to the figure, the presence of several resonance peaks of the curve of vibrational moment may lead to the emergence (as compared with the system of linear vibration of the lifting body) points of curves intersection. So, there exists a possibility of several stationary modes of motions, having different angular velocities (up to seven, four of them may be stable). However, there are only two, different in lessence modes of motion: Ysticking¥ (curves 1) of the system with engine of deficient power in the resonance zone (motor) on having come in the process of running to this mode, would not be able to overcome the resonance peak and far postresonance mode with frequency of electric motor. If the motor power is sufficient, then, as a rule, after some breaking in the resonance zone, the system rapidly (upsetting) passes to far postresonance modes of motion (curves 2).

So, to reach by the exciter the working frequency, the moment of the motor should overcome vibrational moment $V(\omega)$ during its running. According to (4), maximal (peak) value of moment $V(\omega)$ is as much large as a damping of n_q becomes less and higher of the own vibrations of system p_q. Hence, it is important not to overrate the value of rigidity of elastic elements; the use of elastic suspension may be effective; it is possible to lower resonance peak values of vibrations as well as the power of the drive by installation of dampers of maximal vibrations. Expression (3) may be presented in the form of the sum of Ypartial¥ vibration movements ν_q, which characterize the impact of vibrations, corresponding to each of the generalized coordinates: $V(\omega) = \sum_{q=x,y,\varphi} \nu_q$ where $\nu_q = \frac{1}{2} F a_q \sin\gamma_q$; $\sin\gamma_q = -\frac{2n_q}{B_q}$; $a_q = \frac{m\varepsilon}{M_q B_q}$; $F = m\varepsilon\omega^2$. It is natural that maximal breaking exertion is effected by Ypartial¥ vibrational moment which corresponds to the highest natural frequency of vibrations p_q, so it is often enough to use damper of only suck vibrations.

It is clear from formula (4) that start of vibromachine at the absence of working load is more complicated than at its presence; that to make the start easier it is advisable to install vibroexciter in the centre of masses of the system or as close to it, as possible. So, the breaking vibrational moment, resonance vibrations and, correspondingly, the necessary power of the motor are sufficiently less for centre-drilled system (fig. 3, a) than, for instance, for the diagram shown in fig. 3, b (in the first case the last component in formula of vibrational moment (4) disappears). It should also be noted that Yrapid¥ (with frequency 2ω) vibrations of vibrational moment do not take place in such system in the steady mode, which is favorable for the durability of the system.

On the other hand, taking into account the fact that the value of the vibrational moment depends, first of all, on the velocity of running of the rotor of vibroexciter, to make easier the start, engines with higher starting moment are recommended (it facilitates, also, the solution of the problem of lifting the unbalanced mass at first half-turn). At prescribed static moment unbalance mass should be designed with minimal moment of inertia. So,

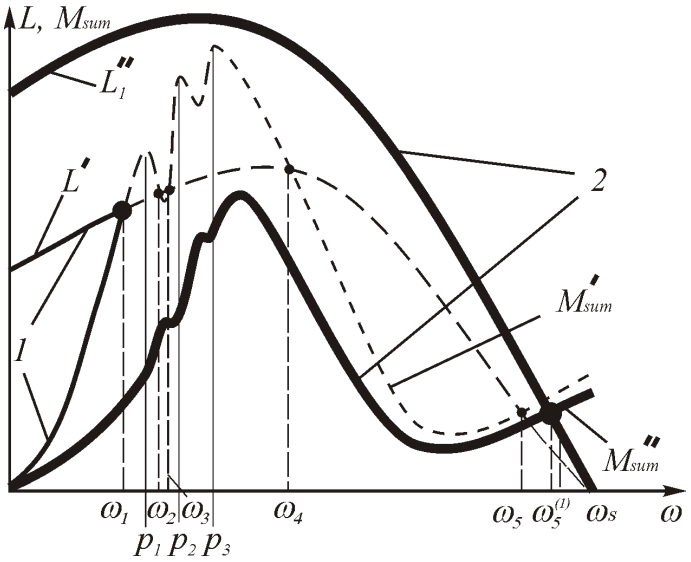

Figure 2: Stationary modes of rotation of vibroexciter: 1 – YstickingY in resonance zone; 2 – far postresonance mode

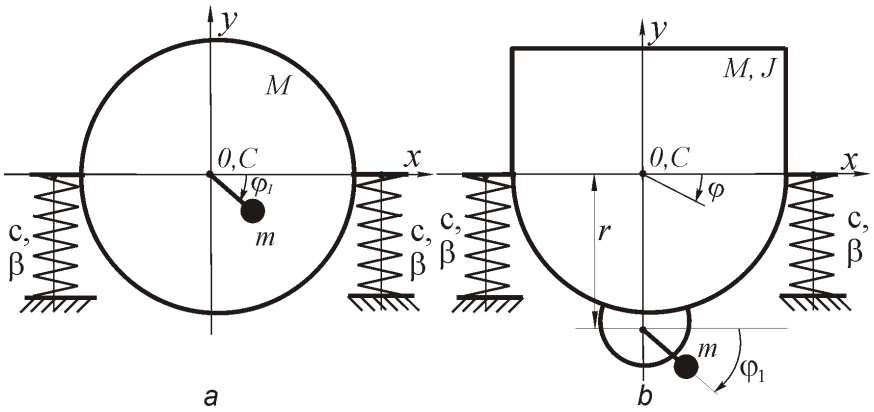

Figure 3: Diagrams of vibromachines: a) with centrally installed vibroexciter; b) with shifted vibroexciter

constructions of vibroexciters with laid on unbalanced mass are more preferable for changing the amplitude of vibrations, then those, having regulated static moment. In addition to this, it is recommended to exclude from the construction (if they are available) synchronizers, mechanical transmissions and so on, using the phenomena of selfsynchronization, employing controlled electric drive.

Manifestation of ZommerfieldŸs effect during the run-up of vibromachine is visually demonstrated by the results of numerical modelling, obtained for vibrational system (fig. 3, a) with parameter $M = 330\ kg$; $J = 8.02\ kg \cdot m^2$; $c_y = c_x = 4.5 \cdot 10^5\ N/m$; $c_\varphi = 2.8 \cdot 10^4\ N{\cdot}m$; $m = 10\ kg$; $\varepsilon = 0.036\ m$, electric engine – asynchronous, with frequency of rotation $n_c = 1500\ rpm$, of power $P = 1.5\ kW$. According to fig. 4, at passing the natural frequencies zone ($t = 0.15 - 0.4\ s$) dynamic load upon the rotor of electric engine grows sufficiently (curve 1); one can see that the value of vibrational moment is larger, than in stationary mode several times as much and its maximal vibrations are compatible with starting moment of the engine.

Correspondingly, the velocity of running of the rotor of exciter shows down intensively up to

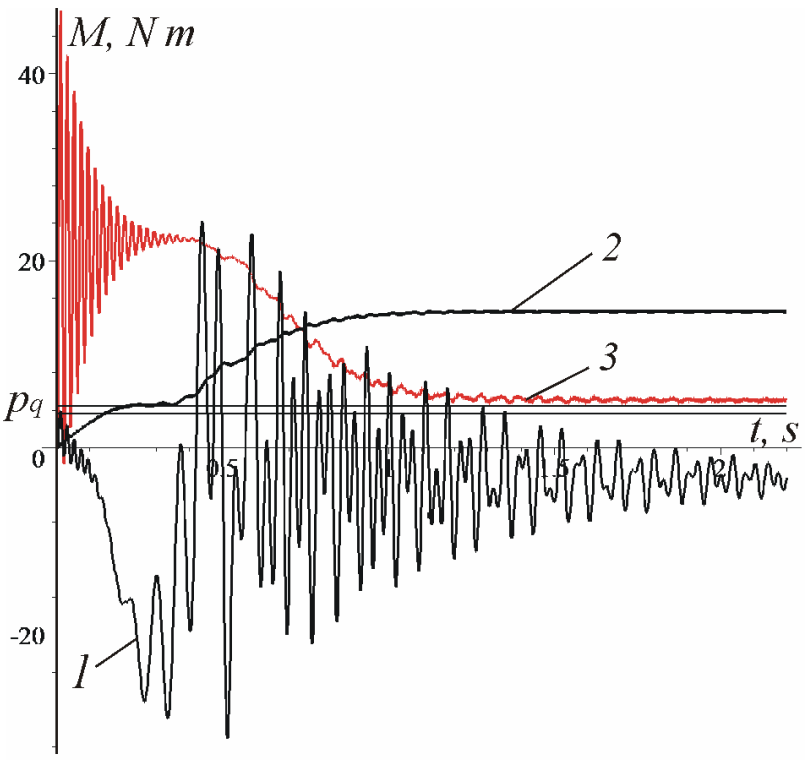

Figure 4: Changing in time: 1 – of engine moment; 2 – of vibrational moment; 3 – of vibroexciter velocity

short-term stabilization of the frequency of rotation (curve 2), in addition to that, maximal resonance vibration of the lifting body are excited. Just after passing the resonance the value of vibrational moment decreases sufficiently fast and its vibrations cover positive zone, that is it becomes rotating in some moments of time. Then their damping takes place as to small negative level (determined by resistance to the vibrations of the lifting body); the amplitude of vibrations of lifting body decreases as fast and the value of rotating moment of the engine changes from starting to nominal value (curve 3).
As it follows from the diagrams of velocity of rotation of vibroexciter for cases of different powers of driving electric motor (fig. 5) at replacing motor of power $P = 1.5\ kW$ with motor of power $P = 2.2\ kW$, slowing down of velocity of exciter in resonance zone is practically absent (curve 3) while its steady postresonance mode of operating becomes impossible (curve 2 – YstickingY of angular velocity in postresonance zone).

4.2 Double start of vibrational machines with unbalanced drive

In practical use of such machines the so called method of Ydouble startingY is applied for lowering the level of vibrations during passing the resonance frequencies. Its technical realization is rather simple. Method consists in switching-off and next switching-on the electric motor in the resonance zone in predetermined moment of time. Theoretical grounding of the method with account of standpoints of vibrational mechanics facilitates its wider use. The basis of the method lies in two existing appropriatenesses of motion of the system close to the region of manifestation of ZommerfieldŸs effect: the first one – at switching-off the motor in the resonance zone vibrational moment effecting the rotor of vibroexciter becomes

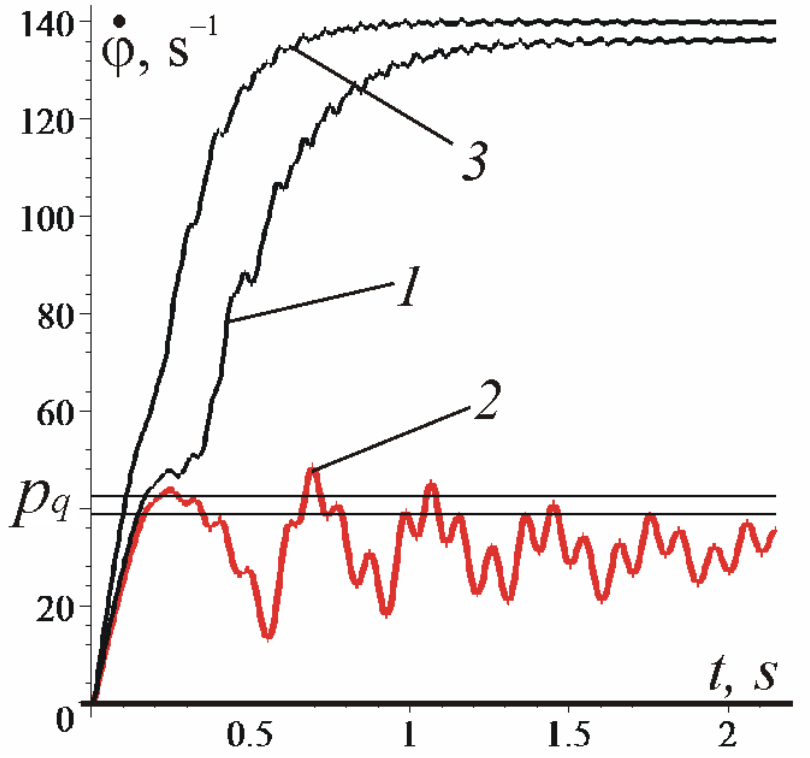

Figure 5: Changing in time the vibroexciter velocity: 1 – $P = 1.5\ kW$; 2 – $P = 1.1\ kW$ (YstickingY of velocity); 3 – $P = 2.2\ kW$

positive, that is, rotating (it follows from the basic equation of vibrational mechanics (3), written down for the case of stationary mode); the second one – availability of so called inner pendulum and its YsemislowY motions. So, using the method of direct separation of motions and accepting as the first approximation $\varphi_1 = \varphi_1^{(1)} = \omega t + \psi$, $q = q^{(0} + q^{(1}$, for general system (fig. 1) in case of one vibroexciter it is not complicated to obtain equation of YsemislowY vibrations of velocity of rotor in the form [2]:

$$\ddot{\Psi} + 2n_1\dot{\Psi} + B\sin\Psi - P\sin^2\frac{\Psi}{2} = 0, \tag{5}$$

for the system under consideration $B = \sum_{q=x,y,\varphi} b_q$; $b_q = \frac{(m\varepsilon\omega^2)^2}{2MI}\frac{p_q^2-\omega^2}{(p_q^2-\omega^2)^2+4n_q^2\omega^4}$; $P = \sum_{q=x,y,\varphi}\rho_q^2$; $\rho_q = \frac{(m\varepsilon\omega^2)^2}{MI}\frac{p_q^2-\omega^2}{(p_q^2-\omega^2)^2+4n_q^2\omega^4}$; $2n_1 = k/I$; k – is a coefficient of damping.
The value $q = \sqrt{|B|}$ is frequency of small free vibrations of the inner pendulum on condition of slow changing of the frequency of rotation of rotor ω. It should be noted that at $B < 0$, the stable position of the inner pendulum simply changes; it is look like it turns [2]. The effect of appearance of semislow vibrations in the resonance zone may be observed in the fig. 5-7. In addition to that, according to fig. 6, a (curve 1) semislow (with frequency $2q$) vibrations of vibrational moment take place after switching-off of the motor with regard to the shifted to the positive side level.
Fig. 6, b and fig.7 demonstrate the possibility of realization of running ang coming to the mode of rotation with frequency, close to nominal of the motor of YunsufficientY power ($P = 1.1\ kW$) with the help of method of double starting as one can see, the necessary condition of successful use of the method is, first of all, effect upon the rotor of

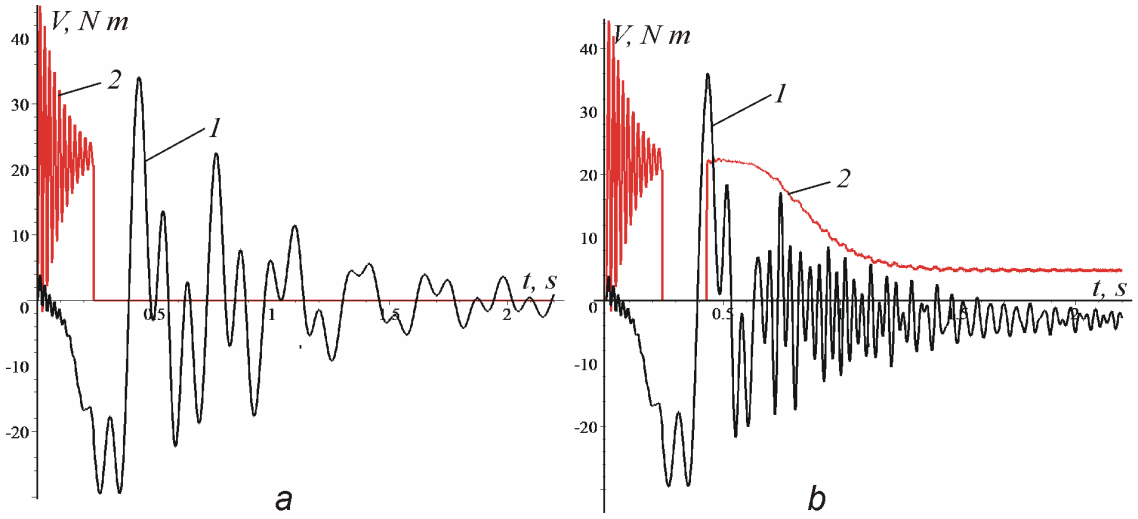

Figure 6: Changing in time: 1 – of vibrational moment; 2 – of motor moment ($P = 1.1\ kW$): a) switching-off of the motor in the resonance zone, $t_{sw.-off} = 0.3\ s$; b) double starting of the engine, $t_{sw.-off} = 0.3\ s$, $t_{rep.sw.-on} = 0.48\ s$

vibroexciter in the moment of repeated switching-on of the motor (in figures $t_{rep.sw.-on} = 0.48\ s$) of rotating vibrational moment commensurable with its starting moment. The abovementioned condition is not complicated to realize with the help of modern means of controlling the electric motors. Applied recommendations to switch off the motor in the moment of growing of intensive resonance vibrations of the lifting body and at once (in a period of time of semiperiod of semislow vibrations $t = 2/q$) switch it on again.

4.3 Vibrational systems with two selfsynchronizing exciters. Separate starting

Many modern vibrational machines, in particular, screens and platforms with directed vertical (horizontal) vibrations are realized by the diagram, shown in fig. 8. Expressions for vibrational moments influencing in resonance zone upon the rotors of exciters rotating in opposite directions are presented in the form:

$$V_i(\omega) = -\frac{1}{2}\frac{(m\varepsilon\omega)^2}{M}\frac{n_y}{B_y^2}, \tag{6}$$

Vibrational machines with selfsynchronizing exciters permit the possibility of separate (in turns) start of electric motors, however, it is not applied in practice. Using the approach under consideration, it is possible to demonstrate possibility advantages of such start.
It is not complicated to establish that vibrational moment in case of running only one of vibroexciters will equal $V_{separ}(\omega) = \frac{1}{2}V(\omega)$, where $V(\omega)$ is determined by formula (4). It follows from analysis (4) that if natural frequencies of vibrational system p_q differ sufficiently enough (it may always be reached by the choice of elastic elements), then with the grows of frequency ω in the process of running each item (except the one corresponding to $\omega \approx p_q$) will be disregardly small. Taking into account the fact that ratio $Mr^2/2$ is for the dynamic system in consideration, sufficiently less than unity it is possible to come to the following estimation of the value of vibrational moment, functioning in the resonance zone

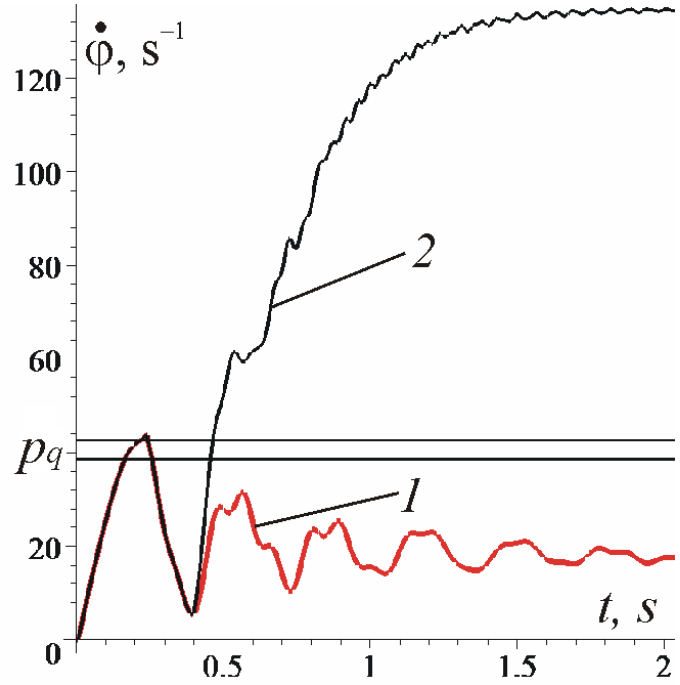

Figure 7: Changing in time of the velocity of vibroexciter ($P = 1.1\ kW$):
1– switching-on the motor in the resonance zone, $t_{sw.-off} = 0.3\ s$; 2 – double start of the motor, $t_{sw.-off} = 0.3\ s$, $t_{rep.sw.-on} = 0.48\ s$

in case of separate start of its electric motors: $V_{separ}(\omega) \approx \frac{1}{2}V_i(\omega)$. So, by corresponding choice of the parameters of the system at separate start of motors it is possible to attain the decrease of resonance vibrational moments and, as a result, to attain all connected with this possible of improvement of dynamic and power characteristics of vibromachines. In favor of decrease of vibrational moments at separate start of selfsynchronizing vibroexciters are the facts that, owing to the differences between their phases, some Ycollateral¥ vibrations of the lifting body occur and that it is necessary at more precise determination of vibrational moment of the exciter under consideration, to take account of the effect of other exciters. That is, at calculation of vibrational moment it should be presented in the form of the sum of two items, one of which (being determined above) represents additional load , caused by losses of power at vibrations, and the second (noticeably less in the resonance

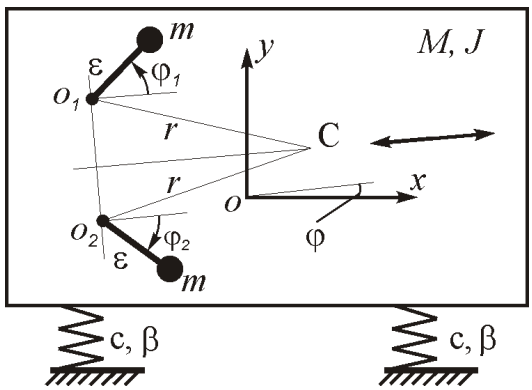

Figure 8: Diagram of vibrational machine with selfsynchronizing exciters

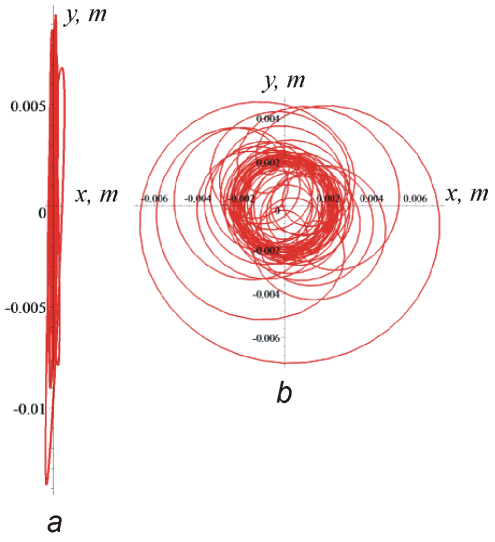

Figure 9: Trajectories of the centre of masses of lifting body: a – synchronous (ordinary) start of motors; b – start of one motor (separate start)

zone, as a rull) is caused by the influence of other vibroexciters. It should be noted, that the second item represents redistribution of power between the vibroexciters. Formulas for determination of its value for many of vibrational systems may be found in specialize literature [1, 3]. The positive effect may be magnified by installation of damper of vertical vibrations. Besides, in case of using separate start of motoes, the decrease (almost twice as much) of starting currents is rather important.

It should be noted that somewhat excessive power of electric drive is recommended for easing the start in case of vibromachines with two selfsynchronizing exciters. In addition to that, effect of vibrational support of rotation of unbalanced exciter in steady state should be used, working with one switched off motor. Especially as mode of vibrational support of rotation is the most stable for the dynamic system under consideration. It follows from comparison (4) and (6) that dynamic load upon the rotors of electric motors and, correspondingly, the necessary total power of electric drive in case of vertical vibrations of the working part of vibromachine will be sufficiently less than at elliptic trajectory.

Results of simulation confirm the advantages of separate start. Thus, for instance, according to fig. 9 ($Mr^2/J = 0.52$), in case of such start resonance amplitudes of vibration of masses centre of the lifting body are sufficiently less than those at synchronous start of the motors. In addition to that amplitudes of horizontal and turning resonance vibrations grow. However, their amplitudes are far from maximal values of amplitudes of vertical vibrations.

5 Findings

Thus, the majority of mechanisms of behavior of inertial vibroexciters and vibrational system in general at passing the resonance zone may be explained on the basis of approaches of vibrational mechanics. On this ground practical conclusions and recommendations improving dynamic and power characteristics of vibromachines with unbalanced drive may be obtained. Methods of double and separated start are effective for easing the start of postresonance vibromachines with unbalanced drive.

References

[1] Blekhman I.I. Theory of vibration processes and devices. Vibration mechanics and vibration technology. The Publishing House "Ore and Metals", 2013. – 640p.

[2] Blekhman I.I., Indieytshev D.A., Fradkov A.I. Slow motions in systems with inertial excitation of oscillations // Problems of machine building and reliability of machines. – Vol. 1, 2008. pp. 25-31. (in Russian).

[3] Blekhman I.I. Vibrational Mechanics, World Scientific, Singapore, 2000.

[4] Li Y., Li H., Wei X., Wen B. Self-synchronization theory of a vibrating system with a two-stage vibration isolation frame driven by two motors Zhendong yu Chongji, Dongbei Daxue Xuebao, Journal of Northeastern University. – Vol. 35, 2014. – pp. 836-840.

[5] Zhang X., Wen B., Zhao C. Vibratory synchronization and coupling dynamic characteristics of multiple unbalanced rotors on a mass-spring rigid base, Journal of Mechanical Science and Technology. – Vol. 28, 2014. – pp. 249-258.

[6] Franchuk V.P., Savluk N.V. Applying of self-synchronisation in mountain vibration machines, Vibrations in technics and technology. – Vol. 1(33), 2004. – pp. 12-14.

[7] Blekhman I.I., Yaroshevich N.P. Transition regimes in inertially excited trans-resonant vibration devices with several degrees of freedom of the carrier system / Nonlinear problems of theory of oscillation and theory of control Vibrational Mechanics. – SPb.: Nauka, 2009. –pp. 215-238.

[8] Blekhman I.I., VasilЎkov V.B., Yaroshevich N.P. On Some Opportunities for Improving Vibration Machines with Self-Synchronization Inert Vibration Exciters. Journal of Machinery manufacture and reliability, Vol. 42 (3), 2013.– pp. 192-195

[9] Yaroshevich N.P., Sylyvonuk A.V. About some features of dynamic acceleration of vibration mashines with self-synchronisation inertion vibroexciters, Scientific Bullietin of National Mining University, Vol. 4 (136), 2013. – pp. 70-75.

N.P. Yaroshevich, 75 Lvivska Str., Lutsk, 43018, Ukraine
A.V. Sylyvonyuk, 75 Lvivska Str., Lutsk, 43018, Ukraine
I.P. Zabrodets, 75 Lvivska Str., Lutsk, 43018, Ukraine